Tungsten and rare-metal (Nb, Ta, Sn) hydrothermal metallogenic systems in the late-variscan orogenic context : example of the French Massif Central

Matthieu Harlaux

Ecole Doctorale RP2E « Ressources, Procédés, Produits, Environnement »
Collegium Sciences et Technologies
Université de Lorraine – LabEx Ressources 21
UMR 7359 GeoRessources

THÈSE

Présentée pour l'obtention du titre de

Docteur de l'Université de Lorraine
Spécialité Géosciences

Par

Matthieu Harlaux

Les systèmes métallogéniques hydrothermaux à tungstène et métaux rares (Nb, Ta, Sn) dans le contexte orogénique fini-varisque : exemple du Massif Central Français

Tungsten and rare-metal (Nb, Ta, Sn) hydrothermal metallogenic systems in the late-Variscan orogenic context: example of the French Massif Central

---

Soutenance publique le 1er Décembre 2016

Membres du jury :

Rapporteurs :	Robert L. Linnen	Professeur, Université de Western Ontario, Canada
	Johann G. Raith	Professeur, Université de Leoben, Autriche
Examinateurs :	Ru Cheng Wang	Professeur, Université de Nanjing, Chine
	Rolf L. Romer	Professeur, GFZ Potsdam, Allemagne
	Philippe Muchez	Professeur, Université de Louvain, Belgique
	Michel Cathelineau	Directeur de Recherche CNRS, GeoRessources, France
Directeur de thèse :	Michel Cuney	Directeur de Recherche CNRS Emérite, GeoRessources, France
Invités :	Christian Marignac	Professeur Emérite, Ecole des Mines de Nancy, France
	Julien Mercadier	Chargé de Recherche CNRS, GeoRessources, France

Faculté des Sciences et Technologies – Campus des Aiguillettes – 54506 Vandœuvre-lès-Nancy Cedex

« On fait la science avec des faits comme une maison avec des pierres ; mais une accumulation de faits n'est pas plus une science qu'un tas de pierres n'est une maison. »

Henri Poincaré
La Science et l'hypothèse (1908)

Résumé :

Le tungstène (W) fait partie des « ressources minérales critiques » définies par la Commission Européenne en terme d'approvisionnement pour de nombreuses applications technologiques. Le Massif Central Français (MCF), localisé dans la partie interne de la Chaîne Varisque Européenne, possède un potentiel économique significatif en W (>45 kt WO_3) essentiellement sous forme de minéralisations disséminées dans des granites spécialisés ou associées à des systèmes filoniens hydrothermaux péri-granitiques à quartz-wolframite±cassiterite. Le but de cette thèse est (i) de caractériser les sources des fluides et des métaux impliquées dans la formation des minéralisations à W et (ii) de dater ces événements métallogéniques afin de les relier avec l'évolution orogénique de la Chaîne Varisque et notamment avec les événements métamorphiques et magmatiques fini-carbonifères. Ce travail est basé sur l'étude de plusieurs gisements hydrothermaux à W±Sn dans le MCF dans une approche multidisciplinaire combinant pétrographie et minéralogie détaillée, géochimie minérale et isotopique, géochimie en roche totale des granites et roches métamorphiques, géochronologie et étude des inclusions fluides. Les datations U-Pb des wolframites montrent que les minéralisations à W résultent d'événements hydrothermaux distincts sur une période d'au moins 40 Ma, correspondant à trois épisodes géodynamiques majeurs affectant la Chaine Varisque : (i) des minéralisations viséo-namuriennes (333-327 Ma) contemporaines de la compression syn-orogénique et de la mise en place des complexes leucogranitiques peralumineux à 335-325 Ma; (ii) des minéralisations namuro-westphaliennes (315-310 Ma) associées au jeu complexe de conditions compressives et extensives dans les zones internes de la Chaîne Varisque qui caractérise la fin du Carbonifère; (iii) des minéralisations stéphano-permiennes (298-274 Ma) mises en place en contexte post-collisionnel. L'analyse *in situ* des éléments mineurs et traces dans la wolframite a révélé l'existence de différents types de signatures géochimiques régionales, qui montrent de nombreuses similarités avec celles de granites évolués riches en métaux rares. L'étude détaillée du gisement de Puy-les-Vignes, exemple exceptionnel de minéralisation hydrothermale à W associée à un pipe bréchique, a permis de démontrer la superposition d'un stade à Nb-Ta sur la paragenèse primaire à W, interprété comme la contribution d'un fluide magmatique issu d'une coupole granitique à métaux rares. Ce résultat apparait similaire avec ceux déjà obtenus dans le cas du gisement de W d'Echassières, où le stockwerk à quartz-wolframite de La Bosse est recoupé par le granite à métaux rares de Beauvoir. De même, des aplites et pegmatites à métaux rares impactant les minéralisations à W±Sn ont été mises en évidence à Puy-les-Vignes et à St-Mélany. L'analyse par LA-ICPMS des inclusions fluides du granite de Beauvoir et du stockwerk de la Bosse a permis de caractériser la composition chimique des fluides primaires exsolvés lors de la transition magmatique-hydrothermale et de montrer leurs concentrations très élevées (10^2-10^3 ppm) en métaux rares (Sn, W, Nb) et la plus grande mobilité hydrothermale du Nb par rapport à celle du Ta. L'analyse minéralogique et géochimique de minéraux marqueurs des circulations fluides, tels que la tourmaline et les oxydes de titane, apporte de nouvelles évidences sur l'importance du rôle joué par les fluides métamorphiques régionaux précoces pour la mise en place des minéralisations à W-Sn. Enfin, cette thèse apporte des mises au point de développement méthodologique pour l'analyse multi-élémentaire des inclusions fluides et de la wolframite par LA-ICPMS.

Mots-clés : minéralisation à tungstène ; métaux rares ; fluides hydrothermaux ; Chaîne Varisque ; Massif Central Français.

Abstract:

Tungsten (W) is part of the “critical mineral resources” as defined by the European Commission in terms of supply for several technological applications. The French Massif Central (FMC), located in the internal part of the European Variscan belt, is the host for a significant economic potential in W (>45 kt WO_3), mainly as disseminated mineralization in specialized granites or associated with peri-granitic quartz-wolframite±cassiterite hydrothermal vein systems. The aim of this thesis is (i) to characterize the fluids and metals sources involved in the genesis of W mineralization and (ii) to date these metallogenic events in the framework of the orogenic evolution of the Variscan belt, especially in link with the late-Carboniferous metamorphic and magmatic events. This work is based on the study of several W±Sn hydrothermal deposits in the FMC using a multidisciplinary approach combining petrography and detailed mineralogy, mineral and isotope geochemistry, whole-rock geochemistry of granites and metamorphic rocks, geochronology and fluid inclusions study. U-Pb dating of wolframite show that the W mineralization formed during several distinct hydrothermal events in a period of at least 40 Ma, corresponding to three major geodynamic episodes affecting the Variscan belt: (i) Visean-Namurian (333-327 Ma) mineralization coeval with the syn-orogenic compression and the emplacement of peraluminous leucogranitic complexes at 335-325 Ma; (ii) Namurian-Westphalian (315-310 Ma) mineralization associated with a complicated setting characterized by coeval compressive and extensive conditions in the internal zones of the Variscan belt, typical of the late-Carboniferous; (iii) Stephanian-Permian (298-274 Ma) mineralization emplaced in post-collisional context. *In situ* analysis of minor and trace elements in wolframite showed the existence of different types of regional geochemical signatures, which share several similarities with those from rare-metal-rich evolved granites. The detailed study of the Puy-les-Vignes deposit, an exceptional case of hydrothermal W mineralization associated with a breccia pipe, allowed to demonstrate the superposition of a Nb-Ta stage on the primary W paragenesis, which is interpreted as the contribution of a magmatic fluid derived from a rare-metal granitic cupola. This result appears similar with those already obtained in the Echassières W deposit, where the La Bosse quartz-wolframite stockwork is cut by the Beauvoir rare-metal granite. Similarly, rare-metal aplites and pegmatites overprinting W±Sn mineralization have been shown in the Puy-les-Vignes and St-Mélany deposit. LA-ICPMS analysis of fluid inclusions from the Beauvoir granite and the La Bosse stockwork allowed to characterize the chemical composition of the primary fluids exsolved during the magmatic-hydrothermal transition and to show their very high concentrations (10^2-10^3 ppm) in rare-metals (Sn, W, Nb), and the higher hydrothermal mobility of Nb compared to Ta. Mineralogical and geochemical analyses of minerals markers of fluid circulations, such as tourmaline and titanium oxides, bring new evidences of the important role played by the early regional metamorphic fluids in the emplacement of W-Sn mineralization. Finally, this thesis gives new methodological developments for the multi-element analysis of fluid inclusions and wolframite by LA-ICPMS.

Keywords: tungsten mineralization; rare metals; hydrothermal fluids; Variscan belt; French Massif Central.

TABLE OF CONTENTS

Remerciements

Ce travail de doctorat a été financé par le Laboratoire d'Excellence Ressources 21 à travers le programme national des « Investissements d'avenir » avec le soutien de l'Institut Carnot ICÉEL et a également bénéficié du support financier du réseau EraMin et du CNRS. Je remercie donc dès à présent l'ensemble des personnes qui ont contribué à la naissance de ce projet et son avancement. Je tiens à remercier en particulier Michel Cathelineau, Directeur Scientifique du Labex Ressources 21 et Responsable de l'équipe Ressources Minérales au sein du laboratoire GeoRessources, qui m'a accompagné lors de mon arrivée au G2R en 2011 en Master Recherche, me donnant ainsi le goût et l'envie de poursuivre en doctorat. Je le remercie notamment pour la confiance et la liberté de travail qu'il m'a accordées.

Je tiens ensuite à remercier mes encadrants de thèse qui m'ont accompagné et soutenu tout au long de ces trois années de doctorat :

- Michel Cuney, mon directeur de thèse, qui m'a fait confiance dès le début en me proposant ce sujet et qui m'a fait partager en permanence son enthousiasme pour ce travail, ainsi que sa connaissance sur les granites à métaux rares, en répondant toujours à mes questions, et ce depuis les quatre coins du globe. Je suis fier d'avoir été ton dernier thésard, qui plus est sur un sujet ayant trait au tungstène et non à la métallogénie de l'uranium !

- Christian Marignac, mon co-directeur de thèse, qui s'est énormément investi dans ce projet en étant toujours à l'écoute et en m'accordant une très grande disponibilité. Merci d'abord pour m'avoir fait découvrir la beauté de la science métallogénie lorsque j'étais encore élève à l'ENSG et dont j'ai eu la chance d'être parmi tes derniers étudiants. Merci également pour ta gentillesse, ta pédagogie et pour m'avoir fait partager ta connaissance encyclopédique sur la métallogénie du tungstène et la géologie du Massif Central et m'avoir appris que l'essentiel se cache dans les détails !

- Julien Mercadier, mon troisième encadrant, sans qui cette thèse n'aurait sans nul doute pas pris la même tournure. Bien qu'encadrant non-officiel de ce travail, tu t'es investi dès le début de ce projet avec une vision neuve du sujet et débordant d'idées fraîches, tout en voulant apporter tes compétences analytiques à ce projet. Merci pour ton dynamisme et ton énergie sans faille, pour m'avoir transmis ton expérience en spectrométrie de masse et pour ton soutien et ta confiance pour les nombreux projets en collaborations.

Je tiens désormais à exprimer mes sincères remerciements aux membres du jury qui m'ont fait l'honneur d'évaluer ce travail :

- Messieurs Robert Linnen et Johann Raith, qui ont accepté de juger ce manuscrit de thèse en tant que rapporteurs. Merci pour les discussions très intéressantes et votre grand intérêt pour ce sujet.

- Monsieur Michel Cathelineau, qui a accepté d'être Président du jury et examinateur interne de ce travail. Merci pour avoir apporté tes connaissances sur les gisements de tungstène varisques et pour l'intérêt porté tout du long à mon travail.

- Monsieur Rolf Romer, avec qui nous avons eu une excellente collaboration sur la datation de la wolframite et qui a contribué de manière importante à ce travail. Merci pour ta grande disponibilité, ta confiance et m'avoir fait bénéficié de ton expertise et de l'accès à ton laboratoire au sein du GFZ à Potsdam.

- Monsieur Philippe Muchez, qui a accepté d'examiner ce travail et m'a fait partager ses connaissances et son enthousiasme sur les gisements de tungstène africains.

- Monsieur Ru Cheng Wang, qui n'a pas pu faire le déplacement dû à un emploi du temps très chargé, mais que je remercie grandement pour avoir examiné ce travail ainsi que pour son support à l'organisation de la mission de terrain en Chine.

Comme tout projet scientifique, celui-ci a été le fruit de nombreuses collaborations, nationales et internationales, et je tiens ici à exprimer mes chaleureux remerciements à toutes les personnes qui ont pris part, de près ou de loin, à ce travail :

- ETH Zürich : Detlef Günther pour avoir accepté de m'accueillir au sein de son laboratoire. Merci pour votre confiance, votre enthousiasme en ce projet, ainsi que pour m'avoir initié à « l'art » de l'ablation laser des inclusions fluides et devenir ainsi un « fluid inclusion exclusionist ». Un grand Merci également à Olga Borovinskaya, Daniel Frick, Daniel Tabersky, Sabrina Gschwind, Bodo Hattendorf et Marcel Burger pour votre aide aux analyses spectrométriques et le traitement des données. Avec une mention spéciale à Olga, l'experte en TOFMS, qui m'a aidé jusqu'au bout de ce projet et même après.

- CRPG Nancy : Merci à Christophe Cloquet et au SARM pour les analyses de dissolution des wolframites, malgré un matériel particulièrement coriace ! Je remercie également Johan Villeneuve, Andrey Gurenko, Nordine Bouden, Michel Champenois et Etienne Deloule pour les nombreuses heures d'analyses à la sonde ionique.

- Université de Genève : Kalin Kouzmanov pour nous avoir accueilli au sein de son laboratoire et nous avoir permis de se familiariser à l'analyse des inclusions fluides dans la

wolframite par microscopie infra-rouge. Merci à Vincent Casanova et Bertrand Rottier pour leur aide durant les analyses microscopiques et microthermométriques.

- Université de Rennes : Marc Poujol, Christophe Ballouard et Philippe Boulvais pour les analyses de datations des rutiles, les nombreuses discussions et conseils avisés, ainsi que pour leur aide à l'organisation de l'excursion de terrain en Bretagne.

- GeoRessources : Un grand Merci à tout le personnel technique et administratif du labo pour leur gentillesse et leur professionnalisme, en particulier : Alexandre Flammang, John Moine et Cédric Demeurie pour la réalisation des lames et les nombreuses discussions autour d'un café ; Patrick Lagrange pour son aide logistique et sa bonne humeur permanente, malgré mes demandes souvent de dernière minute ; Sandrine Mathieu, Andreï Lecomte, Olivier Rouer, Christophe Morlot et Lise Salsi pour les très nombreuses séances de microscopie, sonde électronique et tomographie ; Marie-Camille Caumon et Odile Barrès pour les analyses de spectrométrie Raman et FTIR ; Marie-Christine Boiron et Chantal Peiffert pour les séances de LA-ICPMS ; Marie-Odile Campadieu pour sa grande gentillesse et son aide à la gestion financière des missions ; Merci également à Isabelle Abildtrup et Elisabeth Meyer du Labex Ressources 21.

- Imerys : Hubert Sauvage et Dominique Duhamet pour nous avoir permis d'accéder au site de Beauvoir, ainsi que pour leur intérêt dans nos travaux de recherche.

- Merci à Bernard Mouthier pour l'accès au site et aux échantillons de Puy-les-Vignes, sa gentillesse et son intérêt passionné dans l'étude de cette ancienne mine. Merci également à Hossein Ahmadzadeh et au Musée Minéralogique de l'Ecole des Mines d'Alès pour le prêt des échantillons de collection.

- Merci enfin aux étudiants de l'ENSG : Yann Foucaud, Wilédio Bonzi, Clotilde Schnell et Valentin Kremer, qui ont participé à l'avancement de ce travail.

Enfin, j'adresse ici mes remerciements à tous mes collègues chercheurs, enseignants-chercheurs, techniciens, administratifs et étudiants du laboratoire pour leur convivialité et leurs encouragements. Un grand Merci en particulier à toute la fine équipe de thésards et postdocs (anciens et nouveaux) de GeoRessources, avec qui ces trois années de thèse se sont déroulées tout du long dans la bonne humeur et la bonne ambiance. Cela fait beaucoup de monde à remercier ! Je remercie en particulier, dans l'ordre d'arrivée/départ : Aurélien Eglinger, Christophe Bonnetti, Julien Bonnet, Maxime Dargent, Adeline Delonca, Justine Jaguin, Thomas Hauquin, Christophe Scheffer, Jérémy Lerat, Guillaume Barré, François Turlin, Hélène Legros, Pierre Martz, Valérie Payré, Maïa Riehl, Yoram Teitler, Benoit

Quesnel, Raphaël Vasseur, Zeying Zhu, Eleonora Carocci, Héloïse Verron et Joséphine Gigon. Enfin, un remerciement tout particulier à Roland Salardon, mon collègue de bureau, compagnon de thèse et ami sincère, grâce à qui la thèse a été une véritable aventure humaine. Quelle idée d'avoir placer un Ch'ti et un Marseillais dans le même bureau ! Merci à vous tous pour les nombreux délires aux pauses cafés, les soirées vins et fromages du vendredi soir, les franches rigolades, les moments de craquages et de décompressions véhéments (Nerf), ainsi que pour vos encouragements et votre soutien en fin de thèse.

Je remercie également mes colocs du 126, qui m'ont accueilli chaleureusement à mon début de thèse et m'ont permis de passer trois superbes années à leurs côtés dans les meilleures conditions possibles. Et pour terminer, je remercie mes amis proches et ma famille, en particulier mes parents, qui m'ont toujours soutenu depuis toutes ces années et ont toujours cru en moi, en me permettant de réaliser mes projets. Merci à vous ! Et enfin, « the last but not the least », merci à toi pour m'avoir accompagné et soutenu durant ces derniers mois.

Résumé étendu

Le sujet de cette thèse concerne l'étude des minéralisations hydrothermales à tungstène (W) et métaux rares associés, incluant l'étain (Sn), le niobium (Nb) et le tantale (Ta), dans la Chaîne Varisque Européenne sur l'exemple du Massif Central Français (MCF). Le tungstène fait partie des « ressources minérales critiques » définies par la Commission Européenne (2014) en termes d'importance économique et de risque d'approvisionnement pour de nombreuses applications technologiques. En Europe, la Chaîne Varisque formée au cours du Paléozoïque Supérieur durant la collision continentale entre les continents Gondwana et Laurussia, est relativement riche en minéralisations à W-Sn et métaux rares, localisées principalement en Cornouailles, le Massif Ibérique, le Massif de Bohême, le Massif Armoricain et le MCF. En France, ce dernier représente la plus large zone de terrains varisques et possède un potentiel économique significatif en W (>45 kt WO_3), essentiellement sous forme de minéralisations disséminées dans des granites spécialisés ou associées à des systèmes filoniens hydrothermaux péri-granitiques à quartz-wolframite±cassitérite.

Le but de cette thèse est de mieux comprendre la métallogenèse des systèmes hydrothermaux à W-Sn et métaux rares en lien avec l'évolution orogénique de la Chaîne Varisque Européenne à la fin du Carbonifère. Dans le cadre de cette problématique, ce travail de thèse vise trois principaux objectifs scientifiques : (i) dater les événements métallogéniques à W dans le MCF afin de les relier avec l'évolution orogénique de la Chaîne Varisque et notamment avec les événements métamorphiques et magmatiques fini-carbonifères ; (ii) déterminer la source et le comportement des métaux rares dans les fluides minéralisateurs ; (iii) caractériser les sources des fluides impliqués dans la formations des systèmes hydrothermaux à W.

Afin d'atteindre ces objectifs, ce travail intégré est basé sur l'étude de plusieurs gisements hydrothermaux à W-Sn dans le MCF dans une approche multidisciplinaire combinant pétrographie et minéralogie détaillée, géochimie des roches et des minéraux, géochimie isotopique et géochronologie et étude des inclusions fluides. Ce manuscrit de thèse est organisé en trois parties, subdivisées en 8 chapitres indépendants, rédigés sous la forme d'articles scientifiques. Une discussion générale et une conclusion intègrent l'ensemble des résultats obtenus et proposent un modèle métallogénique conceptuel pour la formation des systèmes hydrothermaux à W dans le MCF, ainsi que de nouvelles perspectives scientifiques.

PARTIE I : Datation isotopique et traçage géochimique de la wolframite et avancées méthodologiques

Chapitre 1 : 40 Ma de minéralisations hydrothermales à W au cours de l'évolution orogénique du Massif Central Français révélés par la datation U-Pb de la wolframite

La Chaîne Varisque Ouest Européenne possède de nombreuses minéralisations hydrothermales à W-Sn en association spatiale avec des granites carbonifères syn- à tardi-orogénique. La formation de ces minéralisations au cours de l'évolution orogénique de la Chaîne Varisque Européenne est toujours débattue, en particulier les liens temporels et génétiques entre les différents épisodes de magmatisme et d'hydrothermalisme, qui restent peu contraints du fait de l'absence de datation directe des gisements. Cette étude présente des âges U-Pb obtenus par TIMS de wolframites provenant de plusieurs gisements hydrothermaux à W±Sn dans le MCF, localisé dans la zone interne de la Chaîne Varisque Ouest Européenne. Les échantillons de wolframite étudiés sont caractérisés par des concentrations variables en U et Pb et montrent des variations significatives dans leurs compositions isotopiques en Pb radiogénique. Les faibles teneurs en U (< 10 ppm en moyenne) reflètent probablement la disponibilité limitée de l'U dans les fluides réducteurs du système hydrothermal précipitant la wolframite et indique possiblement que seule la wolframite issue de systèmes relativement oxydés est appropriée pour la datation isotopique. Bien que la plupart des wolframites donnent des âges concordants, certains échantillons possèdent des compositions isotopiques variables donnant des âges discordants dû à la réouverture du système U-Pb pendant l'altération hydrothermale (e.g., ferbéritisation) ou à la présence de micro-inclusions (e.g., scheelite, sulfures). En considérant ces processus perturbants potentiels, ainsi que leurs effets sur les âges isotopiques U-Pb calculés, il apparaît que les âges U-Pb obtenus pour les wolframites du MCF forment trois groupes géochronologiques distincts liés à des contextes géodynamiques différents : (i) des minéralisations d'âge Viséen-Namurien (333-327 Ma) mises en place en contexte de compression syn-orogénique et contemporaines de l'emplacement de leucogranites peralumineux (ca. 335-325 Ma) ; (ii) des minéralisations d'âge Namurien-Westphalien (317-315 Ma) synchrones de l'extension tardi-orogénique dans les zones internes de la Chaîne Varisque et de la mise en place de granites syn-tectoniques (ca. 315-310 Ma) ; (iii) des minéralisations d'âge Stéphanien-Permien (298-274 Ma) formées durant l'extension généralisée post-orogénique du MCF, qui est contemporaine du volcanisme Permien et de la

mise en place de dykes de lamprophyres et de vaugnérites dans l'ensemble de la Chaîne Varisque. Les plus jeunes âges obtenus (276-274 Ma) reflètent probablement la réouverture du système isotopique U-Pb après la cristallisation de la wolframite et qui pourrait résulter d'une altération hydrothermale tardive (e.g., ferbéritisation). Les données isotopiques du Pb dans des minéraux de veines associés aux différentes générations de wolframites indiquent que le W provient des roches dérivées du Gondwana. Ces résultats démontrent par conséquent pour la première fois que les minéralisations à W(±Sn) dans le MCF se sont formées au cours d'au moins trois événements hydrothermaux distincts dans des contextes tectono-métamorphiques différents et pendant un intervalle temporel d'au moins 40 Ma.

Chapitre 2 : Analyse des éléments mineurs et traces dans la wolframite par LA-ICPMS : traçage géochimique des gisements de tungstène varisque du Massif Central Français

La wolframite représente le principal minerai dans les gisements hydrothermaux de tungstène et peut être une phase porteuse de métaux critiques de haute technologie, tels que Nb, Ta, Sc et REE. Analyser la composition en éléments traces de la wolframite permet d'établir une signature géochimique des gisements de tungstène pour l'exploration minérale, ainsi que de caractériser la composition des fluides minéralisateurs afin de déterminer la source des fluides. Ce travail concerne l'analyse par LA-ICPMS des éléments mineurs et traces dans des wolframites provenant de plusieurs gisements hydrothermaux à W±Sn dans le MCF. Une étude préliminaire réalisée sur des cristaux de wolframite homogènes provenant du gisement de Maoping (Chine) a permis de démontrer l'absence d'effets de matrice significatifs durant l'analyse par LA-ICPMS de la wolframite. Les wolframites des échantillons sélectionnés ont révélé des variations intra-cristallines dans les concentrations en éléments traces, principalement en Nb, Ta et Sn, ce qui reflète une zonation de croissance au cours de la cristallisation de la wolframite. L'analyse des éléments traces des wolframites provenant des gisements à W dans le MCF montre des variations régionales de compositions, caractérisées par des enrichissements et des appauvrissements variables en plusieurs éléments par rapport à la croûte continentale supérieure. Quatre principaux groupes régionaux de wolframite peuvent être ainsi distingués : (i) Vaulry, St-Goussaud et St-Mélany ; (ii) Enguialès, Leucamp et Puy-les-Vignes ; (iii) Echassières (La Bosse et Les Montmins) ; et (iv) Montredon-Labessonnié. Ces signatures géochimiques régionales reflètent des variations de la composition chimique des fluides hydrothermaux, ce qui suggère que les concentrations en

éléments traces dans la wolframite représentent des marqueurs directs de la source des fluides. L'incorporation des éléments traces, tels que les REE, apparaît fortement contrôlée au premier ordre par la cristallochimie de la wolframite. La comparaison des signatures en éléments traces des wolframites du MCF montre de nombreuses similitudes avec la composition de granites évolués, suggérant que les wolframites ont cristallisé à partir de fluides hydrothermaux équilibrés avec des granites évolués. Cependant, l'incorporation de certains éléments (e.g., Zn, U, Mo) semble plutôt expliquée par une contribution de métapélites. En conclusion, ces résultats suggèrent que la composition géochimique des wolframites résulte du mélange de différentes sources de fluides.

Chapitre 3 : Capacités des systèmes LA-ICPMS séquentiels et quasi-simultanés pour l'analyse multi-élémentaire de petites quantités de liquides (pl à nl) : apport de l'analyse des inclusions fluides

Trois configurations de spectromètres de masse couplé à un plasma induit (ICPMS), à savoir un quadrupole (QMS) et un champ magnétique (SFMS), tous deux équipés avec une cellule d'ablation cylindrique standard, et un temps de vol orthogonal (TOFMS) équipé avec une cellule d'ablation à vidange rapide, ont été couplés avec le même système d'ablation laser Excimer 193 nm afin d'évaluer leurs capacités pour l'analyse multi-élémentaire mineurs et traces dans de petites quantités de fluides (pl à nl), tels que les inclusions fluides. Les analyses ont été réalisées sur différents objets : (i) des solutions multi-élémentaires scellées dans des capillaires de silice d'un diamètre interne de 20 µm servant d'analogues synthétiques à des inclusions fluides naturelles ; (ii) des inclusions fluides naturelles biphasées (liquide + vapeur) de faible salinité (ca. 4.8 wt.% éq NaCl) et de compositions homogènes, piégées dans des cristaux de quartz des Alpes ; (iii) des inclusions fluides naturelles multi-phasées (liquide + vapeur + solides multiples) de salinité élevée (ca. 13-15 wt.% éq NaCl) et de compositions homogènes, piégées dans des cristaux de quartz de la Copperbelt de Zambie. Cette étude démontre que le SFMS et le TOFMS apportent des améliorations, notamment en termes de limites de détections (LOD) et de précision, en comparaison avec le QMS traditionnellement utilisé pour l'analyse des inclusions fluides. Le SFMS montre en moyenne des LOD inférieures d'un ordre de grandeur comparé au QMS et TOFMS, mais la précision et la justesse sont inférieures du fait de temps de cycles d'acquisition plus longs. Le TOFMS présente à la fois l'avantage d'avoir une acquisition rapide et quasi-simultanée des isotopes

depuis le ^{6}Li jusqu'à l'^{238}U dans un temps de cycle très court de 30 µs avec des précisions plus élevées et des LOD plus faibles que le QMS pour les isotopes avec un m/Q > 11. Son utilisation couplée avec une cellule d'ablation à vidange rapide conduit à (i) une amélioration pour l'analyse d'inclusions fluides de petites tailles (< 10 µm) et multi-phasées et (ii) la détection d'un plus grand nombre d'isotopes comparé au QMS et SFMS, qui sont tous les deux limités par le nombre d'isotopes mesurés à partir des signaux transitoires des inclusions fluides. Par conséquent, le TOFMS testé couplé avec une cellule d'ablation à vidange rapide apparaît comme un instrument prometteur pour l'analyse des inclusions fluides naturelles par LA-ICPMS, et en particulier pour l'analyse d'inclusions de petites tailles, multi-phasées et/ou de faibles salinités.

PARTIE II : Etudes de cas de gisements hydrothermaux à W : analyse détaillée des processus de minéralisation

Chapitre 4 : Le gisement à W±Nb-Ta de Puy-les-Vignes (Massif Central, France) : contraintes pétrologiques, géochimiques et géochronologiques sur la mise en place d'un cas atypique de pipe bréchique minéralisée à W dans la Chaîne Varisque

Le gisement de Puy-les-Vignes, localisé dans la région Limousin (NO MCF) représente une occurrence rare de pipe bréchique à quartz-wolframite-tourmaline dans la Chaîne Varisque Ouest Européenne. La formation de la minéralisation résulte de plusieurs épisodes de circulations fluides, qui ont conduit à la structuration finale du gisement. Une étude intégrée pétrographique, géochimique et géochronologique de ce gisement atypique a permis de proposer une chronologie détaillée en cinq stades :

(i) Une altération hydrothermale précoce (greisenisation et tourmalinisation) des roches encaissantes, datée à ca. 327-325 Ma, précède l'épisode de bréchification majeure daté à ca. 323-321 Ma, conduisant à la structure de pipe bréchique composée par des fragments hétérométriques des roches encaissantes altérées (principalement gneiss et granites). L'épisode de greisenisation est contemporain de la mise en place d'un dyke de leucogranite daté à 324.7 ± 4.2 Ma, dont la géochimie roche totale est caractéristique d'un granite évolué de type Limousin, ce qui indiquerait la présence d'une coupole leucogranitique cachée sous le gisement de Puy-les-Vignes.

(ii) Une minéralisation à W-As-Nb-Ta est associée à la mise en place de veines

hydrothermales à quartz-wolframite-arsénopyrite au cours d'un second épisode de bréchification affectant le pipe bréchique. L'épisode à W est daté indépendamment par un âge U-Pb sur wolframite à ca. 317 Ma (voir Chapitre 1), ce qui indique que la minéralisation principale est déconnectée temporellement des stades précoces d'altération hydrothermales et de bréchification. Une minéralisation à Nb-Ta, associée à la formation d'oxydes de métaux rares, se met en place après le dépôt de la wolframite et pourrait résulter d'un fluide magmatique-hydrothermale issu d'un granite à métaux rares en profondeur. La présence d'une coupole granitique à métaux rares est mise en évidence indirectement par un échantillon d'aplo-pegmatite à métaux rares, qui présente l'ensemble des caractéristiques minéralogiques, texturaux et géochimiques d'un dyke granitique à métaux rares issu d'une coupole de granite très évolué en profondeur. Cet échantillon a été daté à 314 ± 5.2 Ma par un âge Ar-Ar sur muscovite magmatique, ce qui est cohérent avec l'intervalle temporel des autres granites et pegmatites à métaux rares mis en place dans le Limousin à ca. 315-310 Ma.

(iii) Une minéralisation mineure à Fe-Cu-Zn composée par une association à pyrite, chalcopyrite et sphalérite, recoupant les paragenèses minérales des stades précédents.

(iv) Une minéralisation hydrothermale tardive à Nb-Ti-Y-HREE correspond à la formation d'une crackle-breccia avec une matrice d'adulaire, tourmaline et de chlorite vermiculaire, qui recoupe les veines de quartz minéralisées après l'épisode de déformation ductile majeure La brèche contient de nombreux minéraux accessoires disséminés au sein de la matrice d'adulaire composés de cristaux de monazite, xénotime, zircon, rutile-Nb-Fe-W et d'oxydes de Nb-Ti-Y-HREE-W-U. Ce stade est caractérisé par une signature géochimique à P, Y, HREE, Nb, Ti, Zr, U et est interprété comme la contribution d'une source magmatique peralcaline en profondeur (voir Chapitre 5).

(v) Une minéralisation discrète à Bi±Au-Ag remplie les microcavités et microfractures dans les minéraux des stades précédents avec une paragenèse similaire à celle des gisements mésothermaux d'or du MCF et en particulier de la région Limousin. Un âge Ar-Ar à 301.3 ± 3 Ma a été obtenu sur adulaire du stade de crackle-breccia hydrothermale tardive (stade iv), ce qui représente le plus jeune âge obtenu dans cette étude et pourrait enregistrer le dernier épisode hydrothermal connu régionalement dans la région Limousin.

Chapitre 5 : Oxydes de Nb-Ti-Y-HREE-W-U de composition singulière associés à la minéralisation à tungstène du gisement de Puy-les-Vignes (Massif Central, France) : évidence de mobilisation des métaux rares par des fluides hydrothermaux de signature peralcaline

Le gisement de Puy-les-Vignes, localisé dans la partie nord-ouest du MCF, est une occurrence originale dans la Chaîne Varisque Ouest Européenne d'une minéralisation hydrothermale à tungstène associée à une structure de pipe bréchique. L'un des derniers stades de minéralisation consiste en une paragenèse minérale composée de zircon, xénotime, monazite, rutile-Nb-Fe-W et d'oxydes de Nb-Ti-Y-HREE-W-U (ci-après nommés NTox) disséminés au sein d'une matrice d'adulaire-tourmaline-chlorite. Cette étude est focalisée sur ces oxydes de métaux rares qui possèdent des textures internes complexes ainsi que des compositions chimiques originales avec des concentrations variables en Nb, Ti, Y, HREE et W, non décrits jusqu'à présent. Ils sont également caractérisés par des totaux analytiques faibles en microsonde (76 à 95%) et par la présence de groupements OH^- dans la structure cristallographique détectés par spectroscopie FTIR, qui sont interprétés comme le résultat d'altération, telle que l'hydratation et/ou la métamictisation. L'étude cristallochimique montre que ces cristaux apparaissent comme des solutions solides multi-polaires complexes, impliquant un mélange chimique entre deux groupes de solutions solides binaires : un premier groupe de solution solide anatase – columbite et un second groupe de solution solide euxénite-(Y) – columbite. L'interprétation de leurs textures internes et de leurs chimies suggèrent que les NTox se sont formés au cours d'une cristallisation multi-phasée dans un système ouvert par le mélange de deux fluides hydrothermaux différents : un premier fluide L_1 enrichi en Ti>Nb, Fe, W, avec la même signature géochimique que la minéralisation principale, et un second fluide L_2 enrichi en Nb>Ti, Fe, Y, REE, W, avec une signature géochimique contrastant nettement avec la première et contemporaine de la cristallisation d'adulaire, xénotime, monazite, zircon et rutile. Cette paragenèse minérale est caractérisée par une signature géochimique à P, Y, HREE, Nb>Ta, Ti, Zr, U, typique du magmatisme peralcalin à métaux rares, ce qui suggère la mobilisation de métaux rares par des fluides hydrothermaux tardifs avec une signature peralcaline, possiblement issus d'une source inconnue en profondeur (e.g., pegmatites de type NYF ou granite associé) au cours des derniers stades métallogéniques à Puy-les-Vignes.

Chapitre 6 : Mobilisation du W durant le métamorphisme tardi-varisque : exemple du gîte à Sn-W de St-Mélany (Cévénnes, Massif Central Français)

Le gîte à Sn-W de St-Mélany, localisé dans la région des Cévennes (SE MCF) représente un cas intéressant de système de veines hydrothermales à quartz-cassitérite-wolframite encaissé dans des micaschistes mésozonaux à proximité de deux granites hétérochrones mis en place dans un contexte régional tectono-métamorphique polyphasé. L'étude structurale et pétrographique des veines minéralisées a montré que le système hydrothermal s'est formé durant une ouverture de veines polyphasée suivant un mécanisme de fracturation hydraulique et fut par la suite affecté par une déformation plastique en conditions compressives pendant le métamorphisme BP-HT (M3) à ca. 315 Ma, synchrone de l'emplacement du granite de Rocles au nord. Les analyses géochimiques des principales roches magmatiques ont révélé l'existence de deux sources potentielles en métaux rares dans la région de St-Mélany : (i) le faciès à muscovite du granite de Rocles, correspondant à un granite évolué mis en place à ca. 315 Ma ; (ii) des aplites et pegmatites à métaux rares recoupant l'indice de St-Mélany et mises en places à ca. 305 Ma. Tandis que ces dernières sont clairement déconnectées temporellement de la minéralisation à Sn-W, le premier s'est mis en place au cours du métamorphisme prograde M3 et pourrait représenter une source potentielle de Sn-W pour le gîte de St-Mélany. La géochimie en roche totale des micaschistes cévenols a révélé une anomalie en W dans les environs de St-Mélany. Un profil géochimique réalisé le long de la vallée de la Beaume dans les micaschistes progrades en direction du contact avec le granite de Rocles a révélé une diminution progressive en W et Sn depuis l'épizone jusqu'à la transition mésozone-catazone, suggérant ainsi un appauvrissement progressif au cours du métamorphisme prograde. L'étude minéralogique et géochimique détaillée des oxydes de Ti contenus dans les micaschistes de la vallée de la Beaume a montré une dissolution progressive de l'ilménite initiale et la cristallisation d'anatase et de rutile au cours du métamorphisme prograde M3, ce qui libère des quantités significatives de W. Des enrichissements locaux en métaux rares (W, Nb, Sn, Ta) ont été observé dans des cristaux d'anatase présents dans les micaschistes encaissants la minéralisation de St-Mélany, ce qui suggère l'interaction locale avec un fluide hydrothermal enrichi en métaux rares au cours du métamorphisme M3. En intégrant ces résultats, un modèle en deux stades peut être proposé pour expliquer la formation du gîte de St-Mélany pendant le métamorphisme régional BP-HT : (i) un stade de préconcentration par des fluides magmatiques-hydrothermaux issus du granite à muscovite de Rocles et résultant en une anomalie régionale à W stockée dans les oxydes de

Ti ; (ii) un stade de remobilisation correspondant à un lessivage partiel du stock de W par des fluides métamorphiques régionaux pendant le métamorphisme prograde M3 conduisant à leur concentration progressive à St-Mélany formant le système de veines minéralisées. Ce travail souligne l'importance du rôle joué par les fluides métamorphiques dans un contexte tectono-métamorphique polyphasé pour la formation de minéralisations à Sn-W péri-batholitihiques et ouvre de nouvelles perspectives pour la compréhension de ces systèmes hydrothermaux complexes à l'échelle crustale.

PARTIE III : Caractérisation des sources des fluides et des métaux : comparaison de gisements hydrothermaux et magmatiques

Chapitre 7 : Les sources fluides associées aux minéralisations à W-Sn dans le Massif Central Français varisque : analyse détaillée de la composition chimique et isotopique du bore de la tourmaline

La tourmaline est communément associée avec les minéralisations à Sn-W dans la Chaîne Varisque Européenne, où elle représente une phase minérale accessoire, localement abondante, dans les granites et pegmatites associées, les greisens, les veines de quartz hydrothermales et les systèmes de pipes bréchiques. Ce travail s'intéresse à l'étude de la tourmalinisation associée à trois gîtes hydrothermaux à W±Sn (Puy-les-Vignes, Enguialès, St-Mélany) localisés dans le MCF via une approche intégrée combinant observations minéralogiques et texturales, analyses des compositions chimiques des éléments majeurs, mineurs et traces et analyse isotopique du bore dans la tourmaline. Dans les trois gîtes étudiés, la tourmalinisation représente la principale altération hydrothermale et apparaît systématiquement au cours d'un processus multi-phasé, soit durant l'altération hydrothermale précoce, pendant la formation des veines minéralisées ou au cours d'épisodes de fracturation tardifs. Les générations successives de tourmalines identifiées montrent de nombreuses similitudes entre les trois gîtes, ce qui indique que la tourmalinisation se produit via un mécanisme de métasomatisme boré commun à l'échelle régionale, impliquant différentes circulations de fluides hydrothermaux au cours du temps. L'analyse détaillée de cristaux de tourmaline représentatifs indique que la tourmalinisation résulte d'un processus discontinu de mélange de fluides en système ouvert, impliquant des apports périodiques de fluides hydrothermaux avec des compositions différentes au cours du temps. En représentant la

composition chimique des tourmalines dans le diagramme classique Al-Fe-Mg de Henry et Guidotti (1985), il apparaît que quatre principaux pôles fluides sont suffisants pour décrire la zonation chimique des tourmalines en impliquant des vecteurs de mélange entre ces différents pôles purs. L'interprétation de ces pôles fluides en termes de réservoirs crustaux a été réalisé à partir de l'analyse des éléments traces des tourmalines et a révélé la contribution de fluides équilibrés avec des granites, des orthogneiss et des roches métasédimentaires. En combinant les compositions en éléments traces et les signatures isotopiques du bore des tourmalines, il est proposé que la source du bore provient en majorité des roches métasédimentaires dans les trois gîtes étudiés. A cet égard, l'Unité Para-Autochtone, localisée à la base du système de pile de nappes du MCF, représente un important réservoir métamorphique de bore à l'échelle régionale. Enfin, les tourmalines des gîtes de Puy-les-Vignes, Enguialès et St-Mélany montrent communément des enrichissements en Sn (36 ppm en moyenne) et W (2.5 ppm en moyenne) avec des teneurs Sn>W. En comparaison, les tourmalines provenant de veines de quartz stériles situées à proximité de St-Mélany ne montrent aucun enrichissement en Sn et W et possèdent une signature isotopique en B distincte. Par conséquent, il peut être proposé que la composition en éléments traces ainsi que la composition isotopique du B dans la tourmaline pourrait servir comme indicateur proximal de minéralisation à Sn-W, pouvant ainsi permettre de faire la distinction entre des zones minéralisées et stériles.

Chapitre 8 : Signature géochimique des fluides magmatiques à métaux rares exsolvés du granite de Beauvoir (Massif Central, France) à partir de l'analyse par LA-ICPMS des inclusions fluides primaires

Le granite de Beauvoir, localisé dans le complexe granitique d'Echassières dans la partie nord-est du MCF, représente un cas exceptionnel dans la Chaîne Varisque Européenne d'un granite à métaux rares recoupant un stockwork à quartz-ferbérite (La Bosse) avec un développement vertical de plus de 100 m. Ce dernier a été fortement remanié par les fluides magmatiques-hydrothermaux issus du granite de Beauvoir résultant en une intense topazification. Cette étude focalise sur l'analyse par LA-ICPMS des inclusions fluides primaires contenues dans le quartz et la topaze du granite de Beauvoir et dans le stockwork de La Bosse afin de caractériser la composition géochimique des fluides magmatiques exsolvés du granite à métaux rares de Beauvoir. Les inclusions de type L1 représentent les enregistrements les plus précoces des fluides primaires dans le granite de Beauvoir. Les

données microthermométriques ont montré que ces fluides sont de haute température (500 à >600°C), salés (17-28 wt.% éq NaCl) et riches en Li (T_e < -70°C) avec des ratios Na/Li < 0.5. Les analyses LA-ICPMS montrent que la composition chimique du fluide est dominée principalement par Li, Na, K, Cs, Sn, Rb comme cations majeurs avec des concentrations significatives (10^2-10^3 ppm) en Nb, Ta et W comme éléments mineurs. L'ébullition du fluide L1 conduit à la séparation de phase d'une vapeur de salinité faible à modérée (V2 ; 4.7-22 wt.% éq NaCl) et d'une saumure de salinité élevée (L2 ; 32-48 wt.% éq NaCl) à ca. 450°C. Les analyses LA-ICPMS de ces deux types d'inclusions fluides ont révélé que les inclusions fluides de type L2 possèdent les concentrations les plus élevées en métaux et montrent un enrichissement préférentiel dans la plupart des éléments par comparaison aux inclusions fluides de type V2. L'évolution des fluides exsolvés à distance du granite de Beauvoir est caractérisée par une diminution en température et en salinité, ce qui peut s'interpréter en terme de refroidissement et d'équilibrage thermique autour de l'intrusion. En outre, la diminution de salinité indique que les fluides magmatiques-hydrothermaux issus du granite de Beauvoir ont été plus ou moins dilués par un fluide de très faible salinité, qui pourrait être possiblement de l'eau météorique, considérant la mise en place relativement peu profonde (ca. 3 km) du granite de Beauvoir. Ces résultats démontrent que les inclusions fluides de type L1 ont conservé la signature géochimique magmatique originelle du granite de Beauvoir et que cette signature a été préservé au sein des inclusions fluides du stockwork de La Bosse métasomatisé et ce malgré la distance à la coupole granitique (> 100 m) et l'interaction avec des fluides externes. Par conséquent, la signature géochimique des inclusions fluides pourrait servir de marqueur robuste pour la découverte de coupoles cachées de granites à métaux rares à Echassières et plus largement dans la région Limousin.

CONCLUSIONS GÉNÉRALES

Ce travail a permis de proposer un nouveau modèle métallogénique pour les systèmes hydrothermaux péri-batholithiques à W-Sn dans le MCF. Ce modèle de type magmatique-hydrothermal inclus : (i) un rôle fondamental joué par un granite évolué en profondeur comme source du W et/ou Sn, qui peuvent être mobilisés depuis le magma et transférés dans les roches encaissantes par les fluides magmatiques ; (ii) l'importance du métamorphisme régional prograde BP-HT pour la remobilisation de ce stock métal péri-granitique par les fluides métamorphiques ; (iii) un rôle déterminant de la focalisation progressive de ces fluides

vers une structure tectonique drainante permettant le mélange de fluides avec des fluides externes et la précipitation des métaux. Ce modèle présente l'avantage d'expliquer l'absence apparente de la trace des fluides magmatiques dans le système hydrothermal et ne requiert pas la présence d'un granite évolué contenant des concentrations élevées en W et/ou Sn. Cette juxtaposition de plusieurs processus géologiques indépendants aide ainsi à comprendre le paradoxe entre la faible proportion de gisements de W et le grand nombre de granites dans le MCF, alors qu'il est connu expérimentalement que le W est facilement extrait des magmas granitiques par les fluides magmatiques exsolvés et mobilisé comme espèces tungstates. Néanmoins, il demeure que le modèle proposé s'applique aux minéralisations hydrothermales à W-Sn associées à des granites mis en place en conditions de moyenne profondeur (i.e., 1-2 kbar), étant admis que les intrusions plus superficielles pourraient amener à la formation directe de minéralisations magmatiques-hydrothermales.

A une échelle régionale, il apparaît suite à ce travail de thèse que les systèmes hydrothermaux à W dans le MCF sont caractérisés par une extension verticale plutôt que latérale, qui peut connecter plusieurs réservoirs géologiques à l'échelle crustale, tel que proposé dans le cas du gisement de Puy-les-Vignes où plusieurs événements magmatiques et hydrothermaux se superposent dans le temps. De plus, il semble fort probable que plus le système initial sera riche en métaux, plus sa taille sera importante, pouvant amener à la formation d'un système de dimension crustale. Enfin, il apparaît de manière remarquable que des granites à métaux rares succèdent temporellement et parfois se superposent spatialement à des systèmes minéralisés à W-Sn, tels que observés à Puy-les-Vignes, Echassières et St-Mélany. Le modèle métallogénique proposé dans cette thèse peut potentiellement être étendu à d'autres systèmes minéralisés péri-batholithiques à W-Sn connus ailleurs, et en particulier dans la Chaîne Varisque Européenne, dans lesquels les fluides identifiés correspondent à des fluides aquo-carbono-azotés de haute température et peu salés, sans indication claire de l'implication de fluides magmatiques. Ces résultats ouvrent de nouvelles perspectives scientifiques pour la reconsidération de la métallogénie des minéralisations à W-Sn péri-granitiques dans la Chaîne Varisque Européenne, ainsi que de nouvelles perspectives en terme d'exploration minérale pour la découverte de gisements à W cachés dans des régions, où des systèmes magmatiques-hydrothermaux sont déjà connus.

INTRODUCTION

1. General context of the thesis and problematic

This thesis is part of the scientific project from the Laboratory of Excellence Resources 21 so-called "Strategic metals in the 21th century", which aims to better understand and to manage the strategic metal resources with a specific emphasis on the processes leading to the formation of ore deposits. The subject of this PhD thesis concerns the study of hydrothermal tungsten (W) mineralization and associated rare-metals, including tin (Sn), niobium (Nb) and tantalum (Ta), in the European Variscan belt on the example of the French Massif Central deposits.

1.1. Economic importance of tungsten for the European Union

Tungsten is part of the "critical mineral resources" as defined by the European Commission (2014) in terms of both economic importance for Europe and supply risk for several high technology applications (Fig. 1). In reason of its exceptional physical properties (high density, corrosion-resistance and highest melting temperature), W is used in a wide range of industrial applications, especially for the manufacturing of cemented carbides for metal-cutting and drilling-tools (ca. 60%) and for the production of special high-temperature alloys for the aero-spatial industry (ca. 23%). In 2014, the world annual W production was estimated at ~83 kt, for which the European consumption represented around 10% of the world total, i.e. ~15 kt (European Commission, 2014). China represents the world's largest W consumer with approximately half of the total world consumption, followed by the USA (14%) and Japan (11%). In 2014, about 82% of the world's W production came from China (~68 kt W), which hosts the largest resources in the world estimated at 6.4 Mt W. The W production in Europe remains minor (~2 kt W, 2.5% world production) and is not sufficient to supply the European economy, whose the annual W importation increases every year since 2010. In this global context, the European Union is consequently highly dependent on its W imports and need to secure its supply regarding an increasing worldwide demand. Recycling, although desirable, is far to be able to sustain the European demand. To answer this challenge, it appears necessary for Europe to discover new resources on the one hand and to mine new ore deposits on the other hand. Except at Mittersill (Austria) and Panasqueira (Portugal), tungsten production was practically stopped in Europe for more than 25 years and it is only until recently that new exploration projects were started and that new mines were opened or reopened, notably in Spain (Los Santos, Barruecopardo) and in England (Hemerdon). In

France, W mining production was about 25 kt WO_3 during the 20th century and stopped in 1986 with the closure of the Salau mine (Ariège, Pyrenees). Numerous W deposits are known in France with potential resources estimated >80 kt WO_3 (Audion and Labbé, 2012).

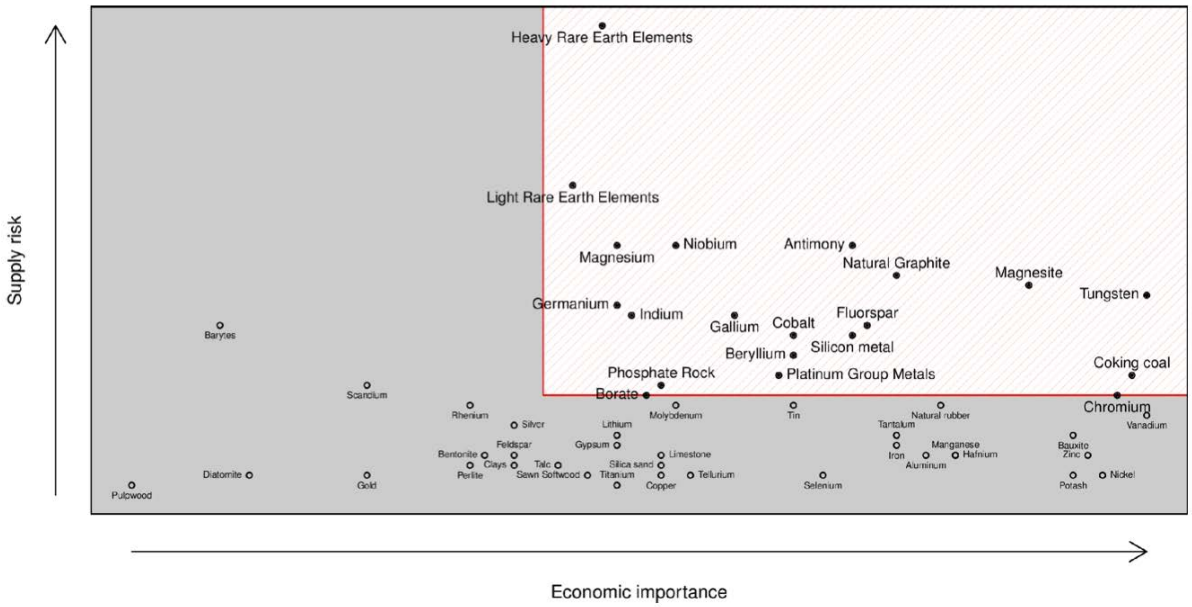

Fig. 1: Criticality matrix published by the European Commission (2014) defining 20 critical raw materials (red zone).

1.2. General problematic of the thesis

Tungsten deposits associated with quartz-wolframite±cassiterite vein systems have been known for long in the European Variscan belt (Fig. 2), which is by far the best endowed in ra-rare-metal terranes in Europe with world-class districts for W-Sn and rare-metals (Nb, Ta, Li, Be) deposits in Cornwall, the Iberian Massif, the Bohemian Massif, the Armorican Massif and the French Massif Central (FMC). In France, the latter represents the largest area where Variscan terranes are exposed and hosts several W deposits with a significant economic potential (> 45 kt WO_3), mainly as disseminated mineralization in specialized granites or associated with peri-batholitic quartz-wolframite±cassiterite hydrothermal vein systems (Marignac and Cuney, 1999). The W mineralizing event(s) occurred at the end of the continental collision between Gondwana and Laurussia through the Upper Paleozoic, in a complicated geodynamic setting characterized by coeval compressive and extensive conditions, typical of lithospheric delamination processes. At the end of the Carboniferous, while the lower crust suffered granulitization, several batches of granitic magmas were

emplaced at variable depths in various local tectonic regimes from extensional to compressional. Granite magmas of both deep and middle crustal origin were produced. The former are characterized by strong interaction (mingling/mixing) with mafic melts issued from the partial melting of a metasomatized SCLM (sub-continental lithospheric mantle), whereas the latter are typically peraluminous (from cordierite-bearing to two mica leucogranites and evolved rare metal granites), to which are spatially associated the W-Sn-Ta-Nb mineralization. However, the timing of the W-Sn mineralization and the temporal links with specific magmatic and metamorphic events remains poorly constrained due to the lack of direct dating of the deposits. Earlier works in the FMC or Iberia (e.g., Noronha et al., 1999; Vallance et al., 2001) have shown that the dominant fluids associated to the quartz-wolframite hydrothermal systems are part of the C-O-H-N system, with a clear "metamorphic" signature, whereas characteristic magmatic fluids are typically lacking. The question of the role of such fluids in the mineralizing process, as well as symmetrically the role possibly taken by the granite magmas, remains therefore open. In the same way, the sources of the metals and the exact role played by granites remain currently poorly understood for this type of granite-related mineralization.

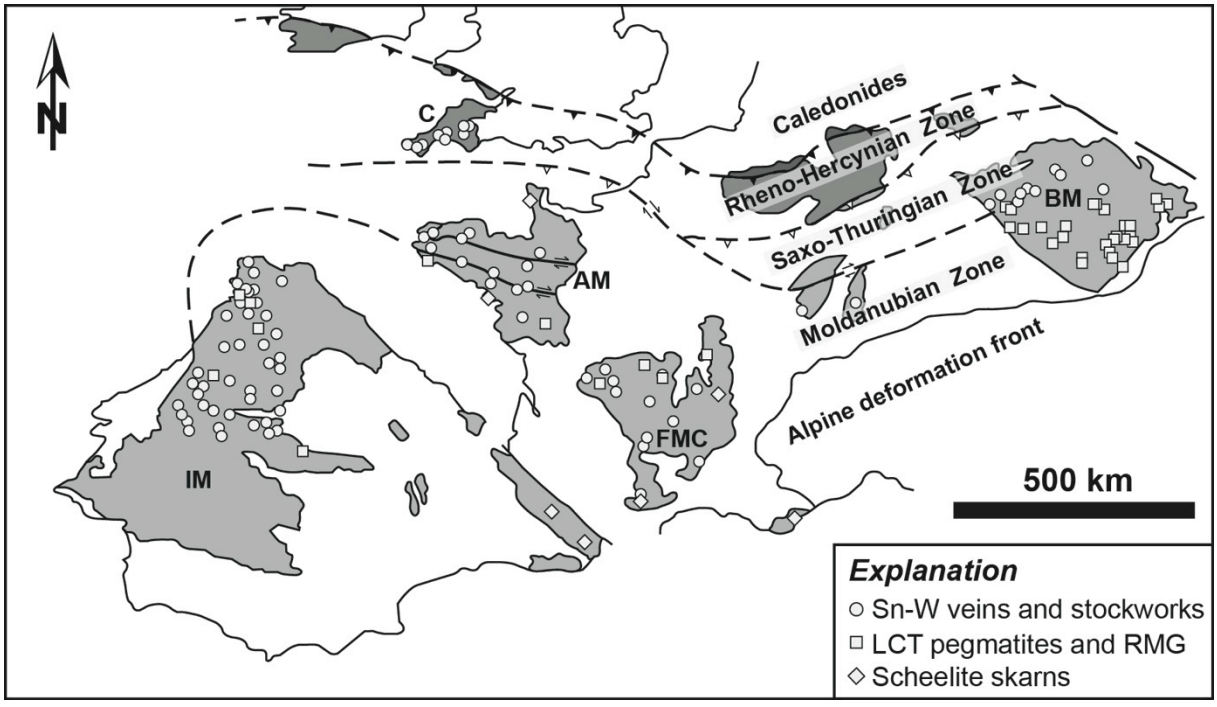

Fig. 2: General framework of the European Variscan belt (modified from von Raumer et al., 2003) showing the main Variscan domains and the distribution of W-Sn and rare-metal deposits: Iberian Massif (IM), French Massif Central (FMC), Armorican Massif (AM), Cornwall (C) and Bohemian Massif (BM).

2. Scientific objectives

The main aim of this thesis is to better understand the metallogenesis of hydrothermal W and rare-metals mineralization in link with the late-Carboniferous evolution of the European Variscan belt. To address this problematic, this PhD thesis aims three main scientific objectives:

(i) The first objective is to address the timing of the hydrothermal W mineralization in the FMC in order to better understand the temporal relationships with the late-Carboniferous tectono-metamorphic evolution of the Variscan belt. Indeed, available geochronological data seem to indicate that there are at least two W-mineralizing episodes in the FMC during the Upper Carboniferous (Marignac and Cuney, 1999; Cuney et al., 2002): a first episode during the Namurian at ca. 325 Ma coeval with the syncollisional extension of the Variscan belt, and a second episode during the Westphalian at ca. 310 Ma, linked with the development of the Central European Extensional Province. Nevertheless, the data remain limited and do not date directly the mineralization, and it remains possible to sustain the idea of only one W event correlated with gold deposition at the very end of the Carboniferous ("ca. 300 Ma W-Au event" of Bouchot et al., 2005). Thus, direct dating of the wolframite and associated minerals appears necessary to better constrain the timing of the W-events in the FMC.

(ii) The second objective concerns the behaviour and the source of rare-metals (Nb, Ta) in the hydrothermal fluids precipitating the mineralization. Few data exist in the literature on the trace element geochemistry of wolframite and associated minerals (Ti-oxide, columbo-tantalite, wolframoixiolite), which are known to be potential carriers of critical high-technology metals, such as Nb, Ta, Sc and REE. These minerals also represent mineralogical markers of magmatic-hydrothermal processes and give information about the mobility of rare-metals in hydrothermal conditions, as well as the possible sources of metals through the definition of geochemical signatures ("fingerprints") with eventual economic implications at the deposit scale.

(iii) The third objective concerns the characterization of fluid reservoirs involved in the formation of the hydrothermal W mineralization in order to assess the importance of magmatic, metamorphic and meteoric fluids. Indeed, the nature of the mineralizing fluids is not clear. In many quartz-wolframite vein-type deposits, the deposition of the mineralization

result from the mixing between early high-temperature (350-500°C) and moderately saline (< 15 wt.% eq. NaCl) with late low-temperature and low-salinity fluids. Whereas the latter are likely derived from meteoric water, the origin of the former remains controversial. The dominant fluids appear to be of "metamorphic" origin, i.e., equilibrated with graphite-bearing metamorphic enclosing rocks, whereas the presence of magmatic fluids is at present poorly or not documented. Yet, this question is of paramount importance for the identification of the granite-ore deposits relationships, given the multiplicity of granite occurrences in the mineralized areas.

In order to reach these objectives, this work is based on the study of several W±Sn hydrothermal deposits located in different areas from the FMC using a multidisciplinary approach, now classically used in economic geology, combining petrography and detailed mineralogy, mineral and isotope geochemistry, whole-rock geochemistry of granites and metamorphic rocks, geochronology and fluid inclusions study. By the way, it was necessary to improve some geochemical approaches, in cooperation with the German Research Centre for Geosciences (GFZ Potsdam, Germany) and with the Laboratory of Inorganic Chemistry from ETH Zurich (Switzerland). The final goal of this work is to propose an integrative model for the W-Sn and rare-metals hydrothermal metallogenic systems in the late-Variscan orogenic context.

3. Organization of the manuscript

This PhD manuscript is organized in three main parts, sub-divided in 8 chapters written as independent articles.

The first part is devoted to methodological developments and/or their application. It concerns the isotopic dating and the geochemical tracing of wolframite and methodological advances. It is composed by three chapters. ***Chapter 1*** focuses on the U-Pb dating of wolframite and the relationships with the late-Variscan evolution of the FMC. Here, the methodology was already developed (Romer et al., 2006), and the aim was to test the feasibility of dating Variscan wolframites in collaboration with the GFZ (Potsdam, Germany). ***Chapter 2*** concerns the geochemical tracing of wolframite through LA-ICPMS analysis of minor and trace elements in order to characterize the fingerprints of W deposits in the FMC. Here, the potential matrix effects during LA-ICPMS analysis of wolframite were firstly

investigated in order to avoid any analytical bias. ***Chapter 3*** presents analytical developments on quasi-simultaneous LA-ICPMS applied to fluid inclusions analysis. This work was done in collaboration with the ETH (Zürich, Switzerland) and allowed to compare the capabilities of sequential and quasi-simultaneous LA-ICPMS for the multi-element analysis of fluid inclusions.

The second part focuses on case studies of hydrothermal W deposits in the FMC with an emphasis on the mineralization processes. It includes thee successive chapters. ***Chapter 4*** is devoted to the detailed study of the Puy-les-Vignes deposit, located in the Limousin area (NW FMC), which represents an atypical case of hydrothermal W mineralization associated with a breccia pipe structure. Here, an integrative petrological, geochemical and geochronological study allowed to understand the emplacement of the W mineralization during a multiphase history. ***Chapter 5*** is in continuity of the preceding chapter and provides a detailed description of uncommon Nb-Ti-Y-HREE-W-U oxides associated with the W mineralization in the Puy-les-Vignes deposit. ***Chapter 6*** concerns the study of the St-Mélany deposit, located in the Cévennes area (SE FMC), which representing a possible case of syn-metamorphic W-Sn hydrothermal mineralization.

The third part is about the characterization of fluids and metals sources through a comparison between hydrothermal and magmatic deposits. ***Chapter 7*** presents a comparative study of the tourmalinization process from three hydrothermal W-Sn deposits in the FMC (Puy-les-Vignes, St-Mélany, Enguialès) through the chemical and isotopic analysis of tourmaline. Here, the objective was to use tourmaline as a marker of hydrothermal fluid circulations, temporally and spatially associated with the W-Sn mineralization, in order to determine the different fluid reservoirs involved. ***Chapter 8*** gives a focus on the characterization of the rare-metal magmatic fluids exsolved from the Beauvoir granite, intrusive in the Echassières granitic complex, in the Limousin area. This last chapter aims to establish a typical geochemical signature of rare-metal magmatic fluids in order to compare with the signature of hydrothermal W deposits.

This manuscript ends with a **general discussion and conclusions**, which integrates the obtained results and proposes a conceptual model for the genesis of the hydrothermal W mineralization in the FMC and gives further perspectives for the understanding of these complex metallogenic systems.

PART I: Isotopic dating and geochemical tracing of wolframite and methodological advances

Chapter 1: 40 Ma of hydrothermal W mineralization during the Variscan orogenic evolution of the French Massif Central revealed by U-Pb dating of wolframite

Matthieu Harlaux[1], Rolf L. Romer[2], Julien Mercadier[1], Christophe Morlot[1], Christian Marignac[1] and Michel Cuney[1]

Article submitted to *Mineralium Deposita*

1: Université de Lorraine, CNRS, CREGU, GeoRessources, F-54506 Vandœuvre-lès-Nancy, France.
2: GFZ German Research Centre for Geosciences, Telegrafenberg, D-14473 Potsdam, Germany.

Abstract

The West European Variscan belt is the host of regionally important hydrothermal W-Sn mineralization in spatial association with syn- to late-orogenic Carboniferous granites. The formation of these mineralization during the orogenic evolution of the European Variscan belt is still debated, and particularly the temporal and genetic links between the various episodes of magmatism and hydrothermalism, which remain poorly constrained due to the lack of direct dating of the ore deposits. This study presents U-Pb TIMS ages of wolframites from several granite-related hydrothermal W±Sn deposits in the French Massif Central (FMC), located in the internal zone of the West European Variscan belt. The studied wolframite samples are characterized by variable U and Pb contents and show significant variations in their radiogenic Pb isotopic compositions. The low U contents (<10 ppm in average) probably reflect the restricted availability of U in the reduced fluids of the hydrothermal system precipitating wolframite and possibly indicate that only wolframite from relatively oxidized systems is suitable for isotopic dating. Although most wolframite ages are obtained from concordant samples that cluster in a single group, there are also samples that are variably normally and reversely discordant or show excess scatter due to reopening of the U-Pb system

during hydrothermal alteration (e.g., ferberitization) or the presence of micro-inclusions (e.g., scheelite, sulphides). Considering these potential disturbing processes and their effect on the calculated U-Pb isotopic ages, the obtained U-Pb ages for the wolframites from the FMC define three distinct geochronological groups related to three contrasting geodynamic settings: (i) Visean to Namurian mineralization (333-327 Ma) coeval with the syn-orogenic compression and the emplacement of large peraluminous leucogranites (ca. 335-325 Ma); (ii) Namurian to Westphalian mineralization (317-315 Ma) synchronous with the onset of the late-orogenic extension in the internal zones of the Variscan belt and the emplacement of syn-tectonic granites (ca. 315-310 Ma); and (iii) Stephanian to Permian mineralization (298-274 Ma) formed during the global post-orogenic extension of the FMC, which is contemporaneous with the Permian volcanism and the emplacement of lamprophyres and vaugnerites dykes throughout the entire Variscan belt. The youngest ages (276-274 Ma) obtained likely reflect reopening of the U-Pb isotopic system after wolframite crystallization and may correspond to late hydrothermal alteration (e.g., ferberitization). Pb isotopes data of vein minerals associated with the different generations of wolframites indicate that most of the W was derived from the Gondwana-derived rocks. These results consequently demonstrate for the first time that W(±Sn) mineralization in the FMC formed during at least three distinct hydrothermal events in different tectono-metamorphic settings, and over a time range of at least 40 Ma, which temporally overlaps a significant part of the global geodynamic evolution of the West European Variscan belt.

Keywords:
U-Pb dating; wolframite; tungsten deposits; French Massif Central; Variscan belt.

1. Introduction

Dating of ore deposits represents a major challenge in economic geology as age data provide key information to better understand the relation between the source rocks, the local geological and tectonic development, and the deposition of metals, and consequently allow to assess the relevance of different metallogenic models for a particular deposit or deposit-type. There are two approaches to date mineralization: (i) direct dating of the ore minerals; and (ii) indirect dating of the ore.

Direct dating of ore minerals represents the ideal situation to determine the age of mineralization as well as the age of possible later metal redistribution. A wide range of ore minerals and geochronometers have been successfully used for direct dating of deposits, such as: U-Pb for dating of uraninite (e.g., Ludwig et al., 1987; Bowles, 1990; Fayek et al., 2002), heterogenite (e.g., Decrée et al., 2010, 2014), columbite-tantalite (e.g., Romer and Wright, 1992; Romer and Lehmann, 1995; Smith et al., 2004), wolframite (e.g., Frei et al., 1998; Romer and Lüders, 2006) and cassiterite (e.g., Gulson and Jones, 1992; Yuan et al., 2008); Rb-Sr for sphalerite (e.g., Nakai et al., 1993; Christensen et al., 1995); Re-Os for sulphide minerals (e.g., Stein et al., 1998, 2000; Morelli et al., 2005); K-Ar and Ar-Ar for Mn-oxides (e.g., Vasconcelos et al., 1992; Ruffet et al., 1996; Spier et al., 2006); or Sm-Nd for fluorite (e.g., Chesley et al., 1991, 1994) and scheelite (e.g., Bell et al., 1989; Anglin et al., 1996).

Indirect dating represents an alternative approach to date an ore deposit when direct dating is not possible. Indirect approaches include dating of gangue minerals that are presumed to be cogenetic with the ore minerals and dating of alteration, magmatic or metamorphic minerals that are more or less coeval with the emplacement of the mineralization. Nevertheless, a major issue remains that the cogenetic relation between the dated minerals and the ore minerals cannot always be established by textural observations. Moreover, the age of the dated gangue mineral may be disturbed by recrystallization during late hydrothermal fluid circulations (e.g., Tartèse et al., 2011).

The French Massif Central (FMC) hosts several hydrothermal W±Sn deposits that are spatially associated to Carboniferous granites emplaced from the syn-orogenic compression to the post-orogenic extension of the West European Variscan belt. However, the timing of the mineralizing event(s) remains poorly constrained for several reasons: (i) only K-Ar and Ar-Ar mica ages associated with tungsten mineralization exist for some deposits (Merceron et al., 1987; Bril et al., 1991; Monié et al., 2000; Alexandre et al., 2002; Cuney et al., 2002); (ii) The dated micas have not been systematically checked for internal zoning or recrystallized

selvages; (iii) Some micas may not be cogenetic with wolframite deposition within the same vein. Therefore, available age data do not necessary reflect the age of tungsten deposition in the various veins, but may date late fluid episodes (alteration, recrystallization). Wolframite ([Fe,Mn]WO_4) represents the most suitable tungsten ore mineral for direct dating of these deposits. Indeed, scheelite ($CaWO_4$), the second important tungsten ore mineral, is not ubiquitous in the mineralized veins and generally forms after wolframite (Wood and Samson, 2000). Moreover, scheelite is likely to contain high contents of common Pb in its crystal lattice due to the substitution of Pb^{2+} for Ca^{2+}.

Only few attempts of U-Pb dating of wolframite have been published (Frei et al., 1998; Romer and Lüders, 2006; Pfaff et al., 2009; Lecumberri-Sanchez et al., 2014). Common to these studies is the relatively high content of U in wolframite (tens to hundreds ppm) and low common Pb content (few ppm), which yields radiogenic Pb isotopic compositions, allowing to determine precise ages. It is, however, not clear whether wolframite generally has high U contents, which would make this mineral attractive for U-Pb dating, or if U is integrated in mineral inclusions or in alteration phases, both of them potentially being formed significantly after wolframite crystallization. Low U content in wolframite (few ppm), however, would strongly reduce the potential of wolframite for U-Pb dating, in particular if U- and/or Pb-rich micro-inclusions or alteration phases are present, which may disturb the U-Pb system.

In order to better understand the U-Pb isotope systematics of wolframite and to provide new geochronological constraints on the timing of W mineralization in the FMC, this study provides U-Pb ages on wolframite from several tungsten deposits in the FMC, whose ages are currently constrained by dated regional structures and granites. The objectives of this paper are: (i) to determine the timing of tungsten mineralization and its relation with the late-Carboniferous geodynamic, metamorphic and magmatic evolutions of the Variscan belt; (ii) to investigate the U distribution in wolframite and the role of micro-inclusions and late alteration phases for U-Pb dating; and (iii) to use the initial Pb isotopic composition of gangue minerals associated with wolframite as fingerprint for the metal source(s) on a regional scale.

2. Geological setting

2.1. The French Massif Central as part of the Variscan orogen

The late Paleozoic collision of Laurussia with Gondwana was diachronous along the Rheic suture and resulted in the formation of the Acadian, Variscan, Alleghenian, and

Ouachita orogenic belts that range in age from 400 Ma to 250 Ma (e.g., Matte, 2001; Kroner and Romer, 2013). The Variscan belt extends from the Bohemian Massif in the east to Iberia and Morocco in the west. The irregular shape of the Variscan belt (Fig. 3a) is the result of the complex interaction of low-strain and high-strain domains of continental crust between the two colliding continents Laurussia and Gondwana. The low-strain domains are blocks of thick continental crust that were only little deformed during the Variscan orogeny (e.g., Armorica, the Teplá-Barrandian Unit, Lusatia, Iberia). Typically, they consist of a Cadomian basement and a relatively thin cover of Cambrian to Carboniferous siliciclastic sedimentary rocks (Linnemann et al., 2010). The high-strain domains have experienced extensive Variscan deformation. They represent domains of former relatively thin continental crust, which formed during the late Cambrian to early Ordovician extension of northern Gondwana. They are characterized by large volumes of continent-derived sediments, which have been deposited into the evolving basins. These domains of thick and thin continental crust together constitute the leading part of Gondwana during the Variscan orogeny, i.e., the Armorican Spur, and were integral parts of the Gondwana plate that behaved differently during the Variscan orogeny (Kroner and Romer, 2013): blocks of thick continental crust were not subductable, whereas areas of thin continental crust were subductable (e.g., Cloos, 1993; Kroner and Romer, 2010).

The collision of blocks of thick continental crust resulted in the formation of a new subduction zone behind the colliding block. In these intra-continental subduction zones, thinned continental crust with its sedimentary cover was subducted. These rocks were in part exhumed and are preserved in the high-strain domains of the Variscan belt, as for instance in the Moldanubian Zone, the Saxo-Thuringian Zone, and the FMC (Kroner and Romer, 2010, 2013). After the consumption of the various domains of thin continental crust during the Variscan orogeny, the final closure of the Rheic Ocean was accomplished by westward displacement of Gondwana leading to the Alleghenian-Mauritanide orogeny synchronous with crustal extension in Central Europe. The transition from compressional tectonics to extensional tectonics in Central Europe possibly started around 310-300 Ma (e.g., Wilson et al., 2004; Kroner and Romer, 2013). Magmatism within the Variscan belt falls in three groups that on a regional scale are not strictly coeval: (i) magmatism synchronous with the emplacement of the high-strain domains as piles of nappes onto the low-strain domain; (ii) late-Variscan crustal melts post-dating the emplacement of the metamorphic units; and (iii) post-Variscan granitic rocks that were emplaced during crustal extension (Kroner and Romer, 2013).

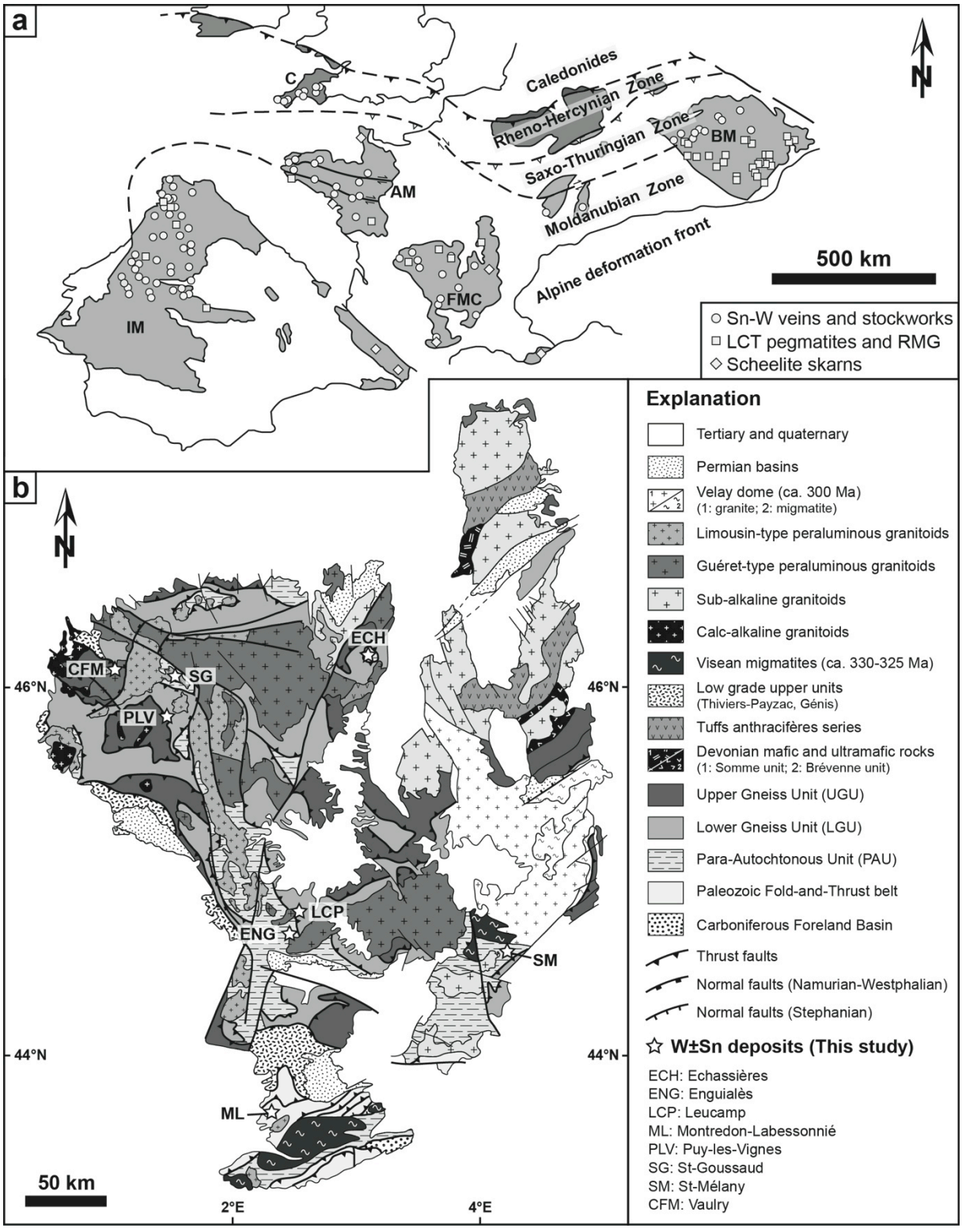

Fig. 3: (a) General framework of the European Variscan belt (modified from von Raumer et al., 2003), showing the main Variscan provinces and the distribution of W-Sn and rare-metal deposits: Iberian Massif (IM), French Massif Central (FMC), Armorican Massif (AM), Cornwall (C) and Bohemian Massif (BM); (b) Geological map of the French Massif Central (modified from Faure et al., 2009), with the location of W±Sn deposits selected for this study.

The geological structure of the FMC (Fig. 3b) has been classically described as a stack of metamorphic nappes that from the north to the south define three major units (Ledru et al., 1989; Faure et al., 2009): (i) the Upper Gneiss Unit (UGU), which is composed of migmatitic ortho- and paragneisses and contains the so-called "leptynite – amphibolite complex", formed by the bimodal association of mafic/ultramafic rocks with acidic rocks; (ii) the Lower Gneiss Unit (LGU) which consists of ortho- and paragneisses similar to those of the UGU; and (iii) the Para-Autochtonous Unit (PAU), dominated by metasedimentary units (micaschists, meta-greywackes and quartzites) that generally experienced Variscan low-grade metamorphism. To the south, these metamorphic units are overthrusted onto the non-metamorphic rocks of the external zone with its fold-and-thrust belt and its foreland basin. The three main tectonic units of the FMC, i.e. the UGU, the LGU and the PAU, are overthrusted by allochtonous low-grade units, corresponding to the Brévenne and Somme units and the "Tuffs anthracifères" series to the ENE and the Thiviers-Payzac and Génis units in the WSW (Faure et al., 2009).

There are three groups of syn- to late-orogenic granitoids that intrude the rocks of the metamorphic nappes of the FMC: (i) Late Devonian to early Carboniferous intrusions (ca. 360-350 Ma) forming large bodies of peraluminous cordierite-biotite granites (e.g., Duthou, 1978; Duthou et al., 1984; Bertrand et al., 2001; Cuney et al., 2001) similar to the Guéret batholith in the northern part of the FMC (Guéret-type of Stussi, 1989) and synchronous with the emplacement of low to highly potassic calc-alkaline gabbro-dioritic to granitic rocks along the so-called "Limousin tonalitic line" (Shaw et al., 1993; Bertrand et al., 2001; Cuney et al., 2001); (ii) Visean to Namurian intrusions (ca. 335-325 Ma) are dominated by two–mica peraluminous leucogranites (Limousin-type of Stussi, 1989) and occur mainly in the northwestern part of the FMC, i.e., in the Limousin area. The most prominent intrusions of this type are those of St-Sylvestre, Millevaches, and St-Mathieu (e.g., Holliger et al., 1986; Scaillet et al., 1996); (iii) Late Namurian to Westphalian intrusions (ca. 310 Ma) are generally peraluminous and were emplaced in a late-orogenic extensional setting (e.g., Cheilletz et al., 1992; Alexandrov et al., 2002; Cuney et al., 2002; Le Carlier de Veslud et al., 2013; Melleton et al., 2015), linked with the development of granulite-facies metamorphism in the lower crust (Cuney and Barbey, 2014). They occur mainly in the Limousin area and typically form small, highly fractionated rare-metal granites (RMG) such as Beauvoir, Blond, Montebras and Chavence (Aubert, 1969; Mourey, 1985; Soufi, 1988; Cuney et al., 1992; Raimbault et al., 1995; Belkasmi and Cuney, 1998), LCT-type pegmatites such as Chèdeville (Raimbault, 1998; Deveaud et al., 2013, 2015) and even rhyolites such as Richemont (Ebougué, 1995; Raimbault and Burnol, 1998).

The European Variscan belt represents an important metallogenic province with world-class districts for W-Sn and rare-metals (Nb, Ta, Li, Be) deposits in Cornwall, the Iberian Massif, the Bohemian Massif, the Armorican Massif and the FMC (Fig. 3a), U in the Bohemian Massif and the FMC, as well as numerous Au-Ag±Sb, Pb-Zn±Cu, and F±Ba deposits (e.g., Jackson et al., 1989; Bril et al., 1994; Chauris and Marcoux, 1994; Breiter et al., 1999; Marignac and Cuney, 1999; Tornos et al., 2002; Cuney and Kyser, 2008). Despite of its old mining history and the large number of workings, the FMC appears as a region relatively poor in tungsten deposits in comparison with other Variscan provinces (Fig. 3a). According to Audion and Labbé (2012) such a low endowment may be due to under-exploration of the FMC with respect to tungsten, although resources of at least 45,000 t WO_3 are estimated. The tungsten occurrences in the FMC are granite-related deposits forming either peribatholitic or intragranitic stockworks, greisen, scheelite skarns or rarely breccia pipes. Most of these occurrences are hydrothermal vein-type deposits that are spatially associated with large Guéret-type batholiths or two-mica leucogranites (Stussi, 1989; Marignac and Cuney, 1999; Bouchot et al., 2005). Available ^{40}Ar-^{39}Ar ages seem to indicate that there are at least two W-mineralizing episodes in the FMC (Cuney et al., 2002): a first episode during the Namurian at ca. 325 Ma, i.e., coeval with the syncollisional extension of the Variscan belt, and a second episode during the Westphalian at ca. 310 Ma, linked with the development of the Central European Extensional Province and associated with granulite-facies metamorphism in the lower crust (Cuney and Barbey, 2014). Nevertheless, it has also been proposed that the W deposits may be linked with a single late-Variscan Au episode at ca. 305-300 Ma (Bouchot et al., 2005 and references therein).

2.2. Geology of the tungsten deposits

The samples used for U-Pb dating of wolframite were taken from eight tungsten deposits in the FMC. These hydrothermal quartz-wolframite±cassiterite deposits are located in four districts (Fig. 3b): Limousin (Vaulry, St-Goussaud, Echassières, Puy-les-Vignes), La Châtaigneraie (Leucamp, Enguialès), Cévennes (St-Mélany) and Tarn (Montredon-Labessonnié).

2.2.1. Vaulry deposit (sample CFM-16)

The Vaulry deposit (Limousin area) is located in the northwestern part of the FMC at

the eastern margin of the peraluminous Blond granite that intruded at the contact between the UGU and the LGU (Soufi, 1988). The deposit consists of a network of NNE-trending quartz-wolframite±cassiterite veins that crosscut the Blond massif and metamorphic rocks (Vallance et al., 2001). The veins are a few centimetres wide and are surrounded by a greisenized envelope that is older than the tungsten mineralization, similar to other intragranitic Sn-W deposits as for instance Cligga-Head in Cornwall (Charoy, 1979; Jackson et al., 1989). The emplacement of the Blond granite is dated at ca. 313 Ma (^{40}Ar-^{39}Ar on muscovite; Alexandrov et al., 2002) and was followed by late hydrothermal fluid circulations at ca. 305 Ma, likely responsible for the formation of the quartz veins (Vallance et al., 2001; Alexandrov et al., 2002). ^{40}Ar-^{39}Ar dating of muscovite from the greisen and biotite from the wall of the veins gave ages of 309 ± 1.4 Ma and 311.1 ± 0.7 Ma, respectively (Cuney et al., 2002). These ages are likely to refer to an early episode of hydrothermal alteration of the granite rather than to the emplacement of the mineralization itself. Tungsten mineralization postdates the early hydrothermal alteration and should yield a Westphalian to Stephanian age, i.e., less than ca. 310 Ma. The dated sample CFM-16 was collected from mineralized blocks of the old, now inaccessible, mine workings, and consists in W-bearing intragranitic quartz veins.

2.2.2. St-Goussaud deposit (sample BOS3c)

The St-Goussaud leucogranite (Limousin area) is intrusive in the LGU and belongs to the most differentiated unit of the eastern part of the Brâme-St-Sylvestre leucogranitic complex (Cuney and Friedrich, 1987; Cuney et al., 1990). The emplacement of the Brâme-St Sylvestre complex has been dated at 324 ± 4 Ma (U-Pb on zircon and monazite; Holliger et al., 1986). The younger ^{40}Ar-^{39}Ar age of ca. 305 Ma obtained on muscovite from the granite, close to the W mineralization, is thought to reflect closure of the Ar-Ar system during the exhumation of the Brâme-St Sylvestre complex (Scaillet et al., 1996). Several W±Sn vein systems crosscut both the St-Goussaud granite, at its northern and southern contacts, and the enclosing metamorphic rocks of the LGU. These peribatholitic and endogranitic deposits form a network of N20°E and N170°E striking cm-thick quartz-wolframite±cassiterite veins that are interpreted to reflect conjugate fractures that opened in a NNW-SSE compressional regime (Alikouss, 1993). As the direction of shortening closely corresponds to the direction of magmatic foliation in the granite and the quartz-wolframite veins are affected by ductile shearing, it has been proposed that tungsten mineralization is syn-tectonic and formed during the late stages of the emplacement of the St-Goussaud granite in the Namurian to Westphalian

(Alikouss, 1993). Sample BOS3c comes from the Bossabut W±Sn showing located at the margin but within the St-Goussaud granite.

2.2.3. Echassières deposit (samples ECH-X1 and MTM-1)

The Echassières complex in the northeastern part of the FMC includes at least three successive granitic units that intruded into the micaschists of the PAU (Cuney et al., 1992; Raimbault et al., 1995). From the older to the younger, these granitic units are: (i) the La Bosse granite, concealed at depth, is presumed to be related to the genesis of the tungsten deposit; (ii) the Colettes granite, which is a porphyritic biotite-muscovite-cordierite granite; and (iii) the Beauvoir topaz-lepidolite-albite granite, consisting of a peraluminous high phosphorus RMG with disseminated Sn-Li-Ta-Nb-Be mineralization. The Beauvoir granite constitutes the latest of these intrusions, crosscutting the Colettes granite, and was emplaced at ca. 308 ± 2 Ma (^{40}Ar-^{39}Ar on lepidolite; Cheilletz et al., 1992). A recent U-Pb age on columbite-tantalite yields an age of 317 ± 6 Ma (Melleton et al., 2015), which is significantly older than the previous ^{40}Ar-^{39}Ar age. Several mostly N10-N40°E striking W±Sn vein deposits are located both to the north (Le Mazet, Les Montmins) and to the south (La Bosse) of the Echassières complex (Aubert, 1969). The La Bosse stockwork represents the most significant among these tungsten deposits in the area and was mined until 1962 producing ca. 3,900 t WO_3 at an average grade of 0.25% WO_3 and contains additional inferred resources estimated to ca. 5,000 t WO_3 (Audion and Labbé, 2012). The stockwork is formed by up to 0.6 m thick quartz-ferberite veins that crosscut the micaschists. There are two sets of veins, one parallel and one oblique to the regional foliation. Tungsten mineralization is polyphased at the vein scale, since three generations of quartz-ferberite veins have been recognized, emplaced by a crack-and-seal mechanism (Aubert, 1969; Aïssa et al., 1987a). The quartz-ferberite stockwork is cut by the Beauvoir and Colettes granites, which provide a minimum age for the emplacement of the tungsten mineralization (Aubert, 1969). K-Ar dating of phengites from selvages of the quartz-ferberite veins gave an age of ca. 325-320 Ma (Merceron et al., 1987). The dated veins are considered to represent the earliest episode of hydrothermal alteration at Echassières (Merceron et al., 1992). Consequently, the tungsten mineralization is likely to have formed during the late Visean to early Namurian. The dated samples ECH-X1 and MTM-1 come from the La Bosse and the Les Montmins localities, respectively.

2.2.4. Puy-les-Vignes deposit (sample PLV-7594)

The Puy-les-Vignes deposit (Limousin area) represents the only known W-bearing breccia pipe and associated vein system occurrence in the FMC. The deposit is hosted in biotite-sillimanite migmatitic gneisses of the LGU in close vicinity of the Auriat granite dated at 324 ± 1 Ma (U-Pb on zircon; Gebauer et al., 1981) and the Aureil granite dated at 346 ± 14 Ma (Rb-Sr on whole rock; Duthou, 1978), which are peraluminous granites of Limousin-type and Guéret-type, respectively (Stussi, 1989). The W-mineralized veins were mined underground until 1957 and have produced ca. 4,000 t WO_3 at an average grade of 0.5% WO_3 (Weppe, 1958). Tungsten resources may be significant as only half of the pipe was explored and the breccia itself represents a potential low-grade tungsten resource (Mouthier, 2005). Several mineralized showings are known in the surroundings of Puy-les-Vignes, such as quartz-wolframite vein deposits (Lifarnet, Moulards, Clauds, Etivaud) (Weppe, 1958). The Puy-les-Vignes breccia pipe has an 80 x 340 m oval surface outcrop and is cut in two parts by a N30°E sinistral strike-slip fault with a 120 m horizontal displacement (Weppe, 1951, 1958). The breccia body is composed of centimetre to meter large clasts of the enclosing gneisses and granites, cemented by a quartz matrix and altered by successive greisenization and tourmalinization during an early hydrothermal episode (Alikouss, 1993; Harlaux et al., 2015a). The mineralization is hosted in 0.5 to 1 m wide quartz-wolframite-sulphides veins that either crosscut the breccia pipe ("plateures" and "filons") or delineate the contacts between breccia and country rocks ("gaine"). A late hydrothermal stage with a peralkaline signature remobilizes rare-metals from the early stages and is associated with the deposition of Nb-Ti-Y-HREE-W-U oxide minerals with uncommon compositions (Harlaux et al., 2015b). ^{40}Ar-^{39}Ar dating on muscovite closely associated with wolframite yielded to a plateau age of 323 ± 0.9 Ma (Cuney et al., 2002), suggesting a Namurian emplacement age of the tungsten mineralization. The dated sample PLV-7594 was taken from a quartz-wolframite-sulphides vein ("filon A", 15th level) in the old underground workings, non-accessible today.

2.2.5. Leucamp and Enguialès deposits (samples LCP-35a and ENG-21b)

The Leucamp and Enguialès deposits are located in the La Châtaigneraie district in the southwestern part of the FMC. This district hosts several tungsten occurrences, including quartz-wolframite vein deposits (Leucamp, Enguialès, Le Viala, Murols, Teissières-les-Bouliès, La Granière), intragranitic scheelite-bearing episyenite veins (La Feuillade-en-Vézie)

and disseminated scheelite deposits in calc-silicate rocks (Cazottes, Manhaval, Picatière) (Bogdanoff et al., 1987). Leucamp and Enguialès represent the two most important deposits in the district, with potential resources of at least 12,000 t WO_3 (Audion and Labbé, 2012). They consist of dense networks of quartz-ferberite veins, typically 10 to 50 cm thick, hosted in the micaschists of the LGU and cutting the regional schistosity in the contact metamorphic aureoles of two large Namurian biotite-cordierite porphyroid granites (Bogdanoff et al., 1989): (i) the Entraygues granite to the south corresponds to the western part of the Margeride batholith and has been dated at ca. 315-310 Ma (^{40}Ar-^{39}Ar on biotite; Monié et al., 2000). Geochronological data on the Margeride complex yielded ages of 334 ± 7 Ma (U-Pb on zircon; Respaut, 1984), 323 ± 12 Ma (Rb-Sr on whole rock; Couturié et al., 1979), 314 ± 3 Ma (U-Pb on monazite; Pin, 1979), 310 ± 3 and 306 ± 3 Ma (^{40}Ar-^{39}Ar on biotite; Monié et al., 2000); (ii) the Veinazès granite to the north which yields ages of 323 ± 15 Ma (U-Pb on zircon; Monié et al., 2000), 314 ± 3 Ma and 313 ± 3 Ma (^{40}Ar-^{39}Ar on biotite; Monié et al., 2000). These contrasting ages suggest that the Margeride granite may have suffered several stages of sub-solidus high-temperature alterations during late fluid-rock interactions, as exemplified in the Armorian Massif (Tartèse et al., 2011). Although the Enguialès and Leucamp deposits are spatially close and present similarities in term of vein filling, structural studies suggest that they formed during different periods. At Enguialès, veins formed during a NNE-SSW compression prior to kink-bands folding and brittle deformation (Bonne and Moreau, 1973; Derré, 1983; Caia, 1989). At Leucamp, the structural relations appear more complex than at Enguialès, possibly indicating two successive stages of tungsten mineralization during the Namurian to Westphalian (Demange et al., 1988a; Gama, 2000). The formation of the quartz-wolframite veins at Leucamp appears to be controlled by structures related to the NNE-SSW compression and by structures related to late-kinematic WNW-ESE compression (Nicolas, 1985; Demange et al., 1988a). Muscovite from the selvage of a quartz-wolframite vein at Enguialès yielded ^{40}Ar-^{39}Ar ages of 305 ± 3 Ma and 306 ± 3 Ma, whereas a plateau age of 312 ± 3 Ma was obtained for a muscovite within the vein (Monié et al., 2000). The earlier ages, in combination with O-D isotope data, have been interpreted as the age of tungsten mineralization at Enguialès (Lerouge et al., 2000; Lerouge and Bouchot, 2009). Nonetheless, they could also represent younger ages since they are contemporaneous with the emplacement of small fine-grained leucogranite dykes at 306 ± 3 Ma and 307 ± 3 Ma (^{40}Ar-^{39}Ar on muscovite; Monié et al., 2000), which intruded into the Entraygues granite. At Leucamp, the quartz-wolframite veins are cut by late microgranitoid and microdiorite dykes (Nicolas, 1985; Demange et al., 1988a,b). A whole rock K-Ar age of

274 ± 8 Ma has been obtained for a similar microdiorite dyke in the north of the Entraygues granite (Bellon and Gibert, 1981). This age could represent therefore an upper limit for the age of the W mineralization. Samples LCP-35a and ENG-21b have been collected from the mining dumps from Leucamp and Enguialès, respectively.

2.2.6. St-Mélany deposit (sample SM-1)

The St-Mélany Sn±W showing (Cévennes area) is located in the southeastern part of the FMC, around 10 km to the south of the southern boundary of the Velay migmatitic dome. The deposit is close to two granites: (i) the Rocles granite in the northeast was emplaced during the regional LP-MT compressive event dated at ca. 315 Ma during the Namurian (Barbey et al., 2015 and references therein). Chemical U-Th-Pb ages on monazite from the Rocles granite yield ages between 325 ± 4 Ma, 324 ± 4 Ma and 318 ± 3 Ma (Be Mezeme et al., 2006, 2007); (ii) the Borne granite in the southwest represents the eastern part of the Mont Lozère massif and yields ages between 315 ± 5 Ma (Rb-Sr on whole rock; Mialhe, 1980), 307 ± 11 Ma (U-Pb on zircon; François, 2009) and 303 ± 3 Ma (U-Pb on monazite; Brichau et al., 2008). Recent dating of the Largentière granite, an eastern equivalent of the Borne granite in the same area, yields a Westphalian age of 304 ± 6 Ma (U-Pb on zircon; Couzinié et al., 2014), interpreted as the emplacement age of the Borne granite. Although other tungsten showings are known in the surroundings of St-Mélany, such as quartz-wolframite veins (Serrecourte), wolframite-scheelite-bearing muscovite episyenite (St-Cierge-la-Serre) and disseminated scheelite in calc-silicate rocks, the metallogenic potential of the Cévennes remains largely unexplored (Ramboz, 1980; Ramboz et al., 1985; Noyé, 1985). The St-Mélany deposit is formed by a network of up to 40 cm wide N110-140°E striking quartz-cassiterite±wolframite veins hosted in the micaschists of the PAU (Noyé, 1985). The quartz veins cut the regional schistosity and are deformed during regional LP-MT compression that is coeval with the emplacement of the ca. 315 Ma old syn-tectonic Rocles granite (Barbey et al., 2015). The Sn±W veins are cut by younger N20-N60°E striking dykes of aplo-pegmatites that yield a ^{40}Ar-^{39}Ar muscovite age of 306.5 ± 3.1 Ma (Chauvet et al., 2012). Several intrusions of lamprophyres crosscut also the St-Mélany vein system and are likely related to the mafic magmatism episode during the melting of the lower Variscan crust at ca. 305 Ma (Couzinié et al., 2014; Barbey et al., 2015). Consequently, considering these structural relationships, an early Namurian age can be proposed for the emplacement of the Sn±W mineralization at St-Mélany. Sample SM-1 comes from a surface sampling of the quartz-

cassiterite-wolframite veins.

2.2.7. Montredon-Labessonnié deposit (sample ML-1)

The Montredon-Labessonnié tungsten district (Tarn area) is located in the southwestern part of the FMC in the north of the Montagne Noire. Several tungsten occurrences are known in the district such as quartz-wolframite±scheelite vein deposits (Lacoste-La Frégère, Budel, Auriole, l'Hom-Haut), scheelite strata-bound deposits (l'Hom-Haut, Auriole, Cavaillé) and scheelite skarns (Fumade) (Béziat et al., 1980; Ramboz, 1980; Severac, 1982; Guion, 1984; Tessier, 1989; Gibert et al., 1992). The Lacoste-La Frégère vein system represents one of the most important tungsten deposits of the Montredon-Labessonnié district. It was mined from 1958 to 1962 producing about 864 t WO_3 at 1.08%, but the ore body has been evaluated to contain about 10,500 t WO_3 with an average grade of 0.7% WO_3 (Béziat et al., 1980). The deposit consists of a network of quartz-wolframite±cassiterite veins that are 0.3 to 2 m thick. The deposit is hosted in the Montredon orthogneiss and the overlying micaschists (Béziat et al., 1980; Guion, 1984). The N110-160°E striking vein system, which cuts the regional schistosity, is interpreted as tension joints that opened during the late Variscan NW-SE compression (Béziat et al., 1980). Although the mineralization is rooted in the Montredon orthogneiss, there is no clear evidence for a genetic link between the orthogneiss and the tungsten mineralization (Guion, 1984). Gravimetric data and local contact metamorphism evidence indicate that there is a hidden granite at depth (Guérangé-Lozes and Burg, 1990) that may be related to the quartz-wolframite vein system. Muscovite and biotite related to this thermal metamorphism yielded ^{40}Ar-^{39}Ar ages of 300.3 ± 3.1 Ma and 302.5 ± 3.2 Ma, respectively (Costa, 1990). These Stephanian ages represent the maximum age for the emplacement of the tungsten mineralization at Montredon-Labessonnié. Sample ML-1 was collected from the old mining dumps.

3. Materials and analytical methods

Mineralogical characterization and chemical analyses of wolframite were performed at GeoRessources Laboratory (Université de Lorraine, Vandœuvre-lès-Nancy, France). Polished thick sections were prepared for subeuhedral, up to several centimetre large wolframite crystals to determine the internal texture and the major element composition and to identify crystals that do not have micro-inclusions such as sulfides, quartz, scheelite, or cassiterite and

that do not show evidence for secondary processes, such as phase exsolution, replacement, and recrystallization. Indeed, inclusions of Pb-rich and/or U-rich phases would strongly reduce the potential of wolframite for U-Pb dating and secondary phases may disturb the U-Pb system. Textural characterization and major element composition (W, Fe, Mn, Mg) of wolframite samples were determined using a Jeol J7600F scanning electron microscope (SEM) equipped with a SDD-type EDS spectrometer coupled to an Oxford Wave WDS spectrometer. Backscattered electron (BSE) images were obtained on polished thick sections with an acceleration voltage of 15 kV, adjusting the electronic contrast to reveal internal zoning within wolframite crystals. Homogeneity for major elements in wolframite samples was systematically checked at several scales up to the micrometre scale, to determine the presence of micro-inclusions (e.g., sulphides, scheelite) or alteration phases (e.g., ferberite). The measured elements (W, Fe, Mn, Mg) were calibrated using the following standards: $CaWO_4$ for W, Fe_2O_3 for Fe, $MnTiO_3$ for Mn and $(Mg,Fe)_2SiO_4$ for Mg. Major element compositions are expressed in weight per cent oxides (wt.%). The analytical errors are 0.7 wt.% for WO_3, 0.4 wt.% for FeO, 0.3 wt.% for MnO and 0.1 wt.% for MgO. In the following, we refer to wolframite series samples with $Fe/(Fe+Mn) > 0.8$ as ferberite and those with $0.2 < Fe/(Fe+Mn) < 0.8$ as wolframite.

Relative concentrations of U and Pb isotopes in wolframite samples were measured by laser ablation - inductively coupled plasma mass spectrometry (LA-ICPMS) using a Agilent 7500c quadrupole ICPMS coupled with a 193 nm GeoLas ArF Excimer laser (MicroLas, Göttingen, Germany). LA-ICPMS was used for a first screening of samples with a two-fold purpose: (i) select samples that may be suitable for U-Pb dating by isotope dilution, i.e., samples with radiogenic Pb isotopic compositions; (ii) investigate the spatial distribution of U and Pb within wolframite and the isotopic compositions of micro-inclusions. For these reasons and due to the absence of reference material currently available for wolframite, the intensities of U and Pb isotopes measured via the ICPMS were used only qualitatively. Laser ablation was performed on the same thick sections previously studied by SEM by focussing the beam at the sample surface with a constant 10 Hz pulse frequency and a constant fluence of 7 J/cm^2. Helium was used as carrier gas to transport the laser-generated particles from the ablation cell to the ICPMS and argon was added as an auxiliary gas via a flow adapter before the ICP torch. Typical flow rates of 0.5 L/min for He and 1 L/min for Ar were used. LA-ICPMS calibration was optimized on the NIST SRM 610 reference material for highest sensitivity on U and Pb isotopes, while maintaining $U/Th \sim 1$ and $ThO/Th < 0.5\%$. Ablation lines of 500 µm in length were analysed with a constant laser spot diameter of 120 µm and a

speed of 2 µm/s. Single-spot analysis were done with a laser spot diameter of 60 µm. The following isotopes were measured: ^{180}W, ^{55}Mn and ^{57}Fe with a dwell time of 10 ms, and ^{204}Pb, ^{206}Pb, ^{207}Pb, ^{208}Pb, ^{235}U and ^{238}U with a dwell time of 60 ms for each.

Following the *in situ* analyses, the wolframite samples selected for dating were crushed in an agate mortar and fragments free of surface alteration, fractures and visible overgrowths were picked under the binocular microscope. To constrain the initial Pb isotopic composition of wolframite, gangue minerals (quartz, pyrite, and/or scheelite) closely associated with wolframite were also separated. Pyrite and scheelite, which commonly have high Pb content and low $^{238}U/^{204}Pb$ values, did not occur in all samples. Therefore, the quartz forming the main gangue in all samples was also separated, using Pb from fluid inclusions as best estimate to the initial Pb isotopic composition of wolframite.

U-Pb isotopic analyses of wolframite and related gangue minerals were done at GFZ German Research Centre for Geosciences (Potsdam), following the analytical procedure described in detail in Romer and Lüders (2006). After removing surface contamination by washing the samples in warm 7N HNO_3, H_2O and acetone, and addition of a mixed ^{205}Pb-^{235}U tracer, the samples were dissolved in 40% HF on a hot plate for one day. While precipitation of wolframate reduced the ion-load on the column, precipitation before complete dissolution of wolframite represents a problem as it is likely to prevent complete homogenization of U and Pb from sample and tracer. Therefore, an excess of HF was used and all samples were inspected visually for absence of precipitates before HF was evaporated. Pb and U were separated using ion-exchange chemistry (Romer et al., 2005). Pb and U were loaded with H_3PO_4 and silica gel on separate Re single-filaments. The isotopic ratios of U and Pb were measured using a Triton thermal ionization mass-spectrometer (TIMS) operated in static or dynamic multi-collection using Faraday collectors and an ion counter, depending of the signal intensity. The common Pb isotopic composition of quartz, sulphides, and scheelite was measured on Faraday collectors using static multi-collection. Pb was analysed at 1200-1260°C and U at 1300-1360°C. All isotopic ratios were corrected for mass fractionation (1‰/A.M.U.), U and Pb blank, and tracer and common Pb composition of quartz, pyrite and/or scheelite (Table 2). Data reduction followed the procedures described in Schmid et al. (2003). Uncertainties in tables and text are given at the 2σ level. The data were plotted using ISOPLOT v.3.75 (Ludwig, 1993).

X-ray computed tomography (CT) is used to investigate the internal structure of wolframite and to provide three-dimensional information about the relative proportions and the spatial distribution of micro-inclusions. CT is a non-destructive 3D imaging technique that

has been applied since many years for a large variety of materials and research fields, and in particular in geosciences for morphological and textural analysis, spatial distribution of defects (inclusions, pores) and structural analysis of micro-fractures for instance (e.g., Cnudde and Boone, 2013; Kyle and Ketcham, 2015). X-ray images were acquired with a Phoenix Nanotom S scanner at GeoRessources Laboratory (Université de Lorraine, Vandœuvre-lès-Nancy, France), using a nanofocus X-ray tube tension of 105 kV and a beam current of 120 µA. The obtained images are an average of four images with an exposure time of 1 s. Virtual cross-sections from all axes were extracted from the 3D volume to observe the physical structure (e.g., inclusions and porosity) and to detect the presence of phases with different densities. The Nanotom scanner produces files with voxel (3D pixel) resolutions between 30 and 0.6 µm as a function of sample size and density. The high density of wolframite and the X-ray absorption properties of tungsten impair the acquisition of CT images. Therefore the analysed wolframite crystal from the St-Mélany deposit (SM-1 sample) was small (2 x 2 x 1.25 mm) and CT analysis was done at a resolution of 1.5 µm/pixel, i.e., 3.4 μm^3/voxel.

4. Results

4.1. SEM and LA-ICPMS data of wolframite

Selected crystals of wolframite are mostly characterized by homogeneous internal texture in BSE images (Fig. 4a). They rarely display internal zoning, except for three samples (SM-1, ECH-X1 and MTM-1), which present a growth zoning marked by successive micrometer-scale bands, reflecting intra-crystalline variations of the W content and minor variations in the Fe/Mn ratio along the crystallographic axis (Fig. 4b). Most of the crystals are characterized by a strongly developed internal porosity, corresponding either to (i) sets of micro-cracks cross-cutting the crystals, or to (ii) disseminated ovoid pores of around 10 µm in diameter, which are sometimes organized along regular trails (Fig. 4a). Such features could correspond to fluid inclusions planes within wolframite. Samples ECH-X1 and MTM-1 are characterized by Nb-rich bands (Fig. 4c), which correspond to growth zoning (Aïssa et al., 1987a). Minor surface alteration has been occasionally observed for some samples (BOS3c, LCP-35a, ML-1), related to the formation of ferberite ($FeWO_4$) in replacement to wolframite along crystalline borders or micro-cracks (Fig. 4d). Micro-inclusions are rare and include isolated crystals of scheelite, pyrite, bismuthinite or native Bi, of 10 to 100 µm in size (Fig. 4e,f). Major element compositions determined for wolframite are given in Table 1.

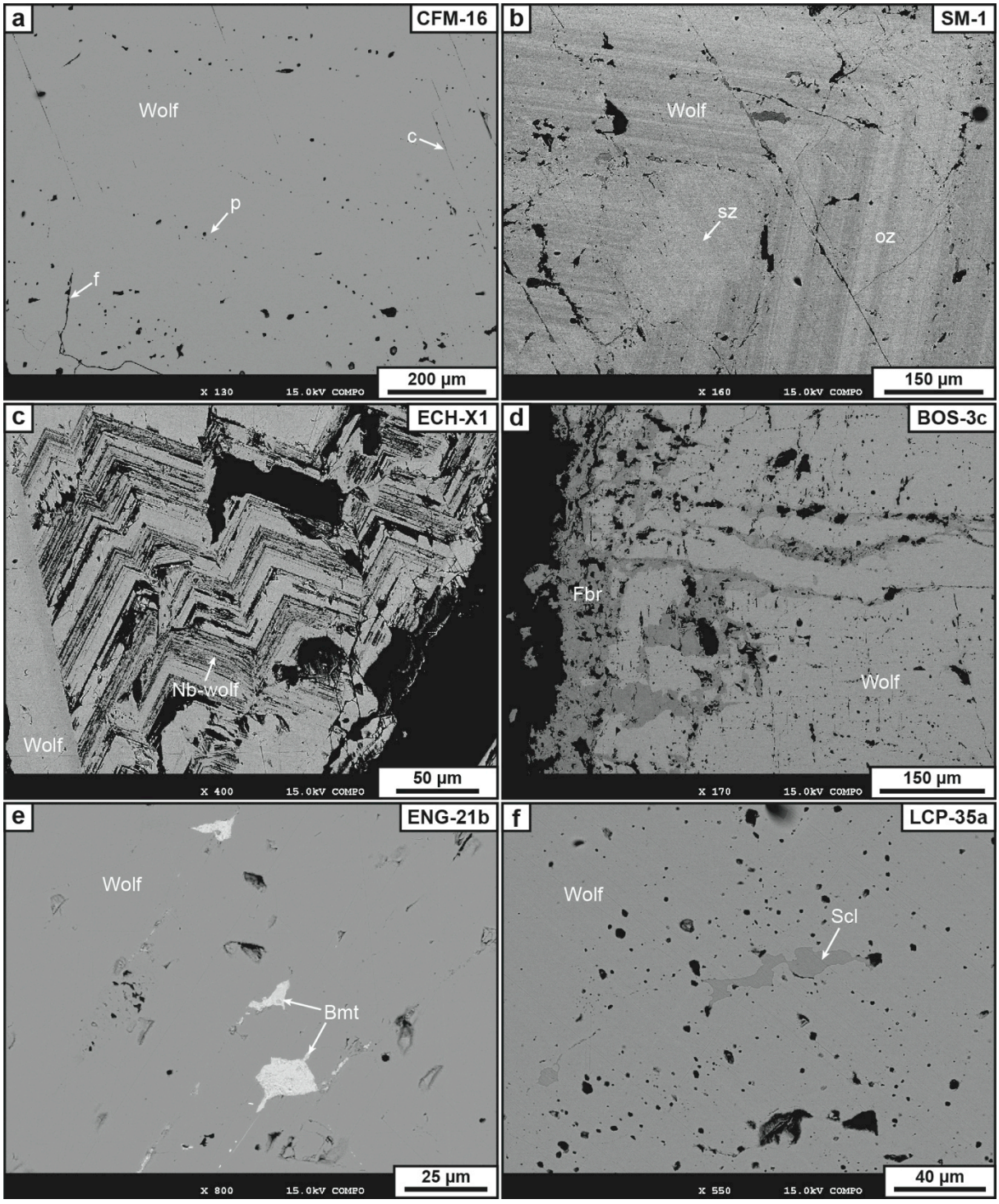

Fig. 4: Selected BSE images of wolframites (Wolf). (a) Typical homogeneous wolframite, showing cleavage planes (c), fluid inclusions planes (p) and micro-fractures (f) (sample CFM-16); (b) Growth zoning in a wolframite crystal, showing both oscillatory (oz) and sector zoning (sz) (sample SM-1); (c) Wolframite with Nb-rich growth bands (Nb-wolf) (sample ECH-X1); (d) Ferberite (Fbr) alteration along crystal border of a wolframite crystal (sample BOS3c); (e) Micro-inclusions of bismuthinite (Bmt) in wolframite (sample ENG-21b); (f) Micro-inclusion of scheelite (Scl) in wolframite (sample LCP-35a).

The wolframite samples show variable compositions, marked by FeO and MnO contents ranging from 12.8 – 19.5 and 2.61 – 9.71 wt.%, respectively (Table 1). Mg contents are above detection limit only for two samples (PLV-7594 and LCP-35a; Table 1), but remain always <1 wt.%.

LA-ICPMS analyses of wolframite show small-scale variations in U and Pb contents, without correlations with major elements, both between different samples and within individual samples. The anomalous high U and Pb counts systematically observed during the first ca. 10 seconds of the LA-ICPMS spectra (Fig. 5) are likely due to the laser ablation process itself and not to sample heterogeneity or surface contamination.

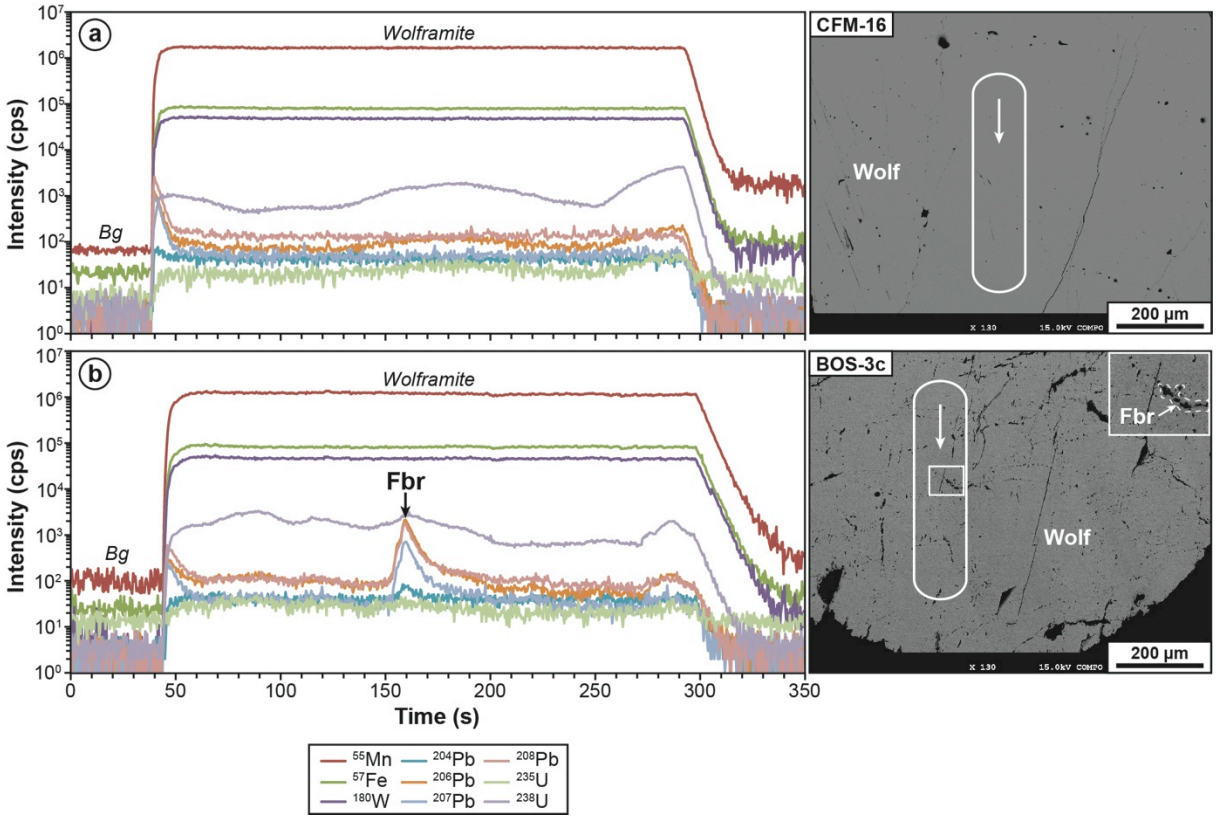

Fig. 5: Typical LA-ICPMS spectra of wolframite (Wolf). (a) Homogeneous wolframite in BSE imagery showing intra-crystalline variations of U content (sample CFM-16); (b) Wolframite containing a micro-inclusion of ferberite (Fbr), hardly visible on SEM image (see zoomed image in inset in the right corner) (sample BOS3c). Ablation lines are 500 µm long and were realised with a constant laser spot diameter of 120 µm, a speed of 2 µm/s and a repetition rate of 10 Hz (see text for details). Bg: background.

LA-ICPMS spectra of wolframite (Fig. 5a) show a positive correlation between ^{238}U and ^{206}Pb signals without correlation with ^{204}Pb. The latter was detected in wolframite with low intensity and shows no visible signal variations, thus indicating that some common Pb

(represented by ^{204}Pb) is incorporated in the crystal lattice of wolframite. Whereas the variations of the ^{206}Pb largely reflect post-crystallization radiogenic Pb growth, the observed variations in the signal intensity of U imply that U is present in the crystal lattice of wolframite and the variations in U content do not reflect crystallographic controls, but are related to variations in fluid compositions at the fluid-crystal interface.

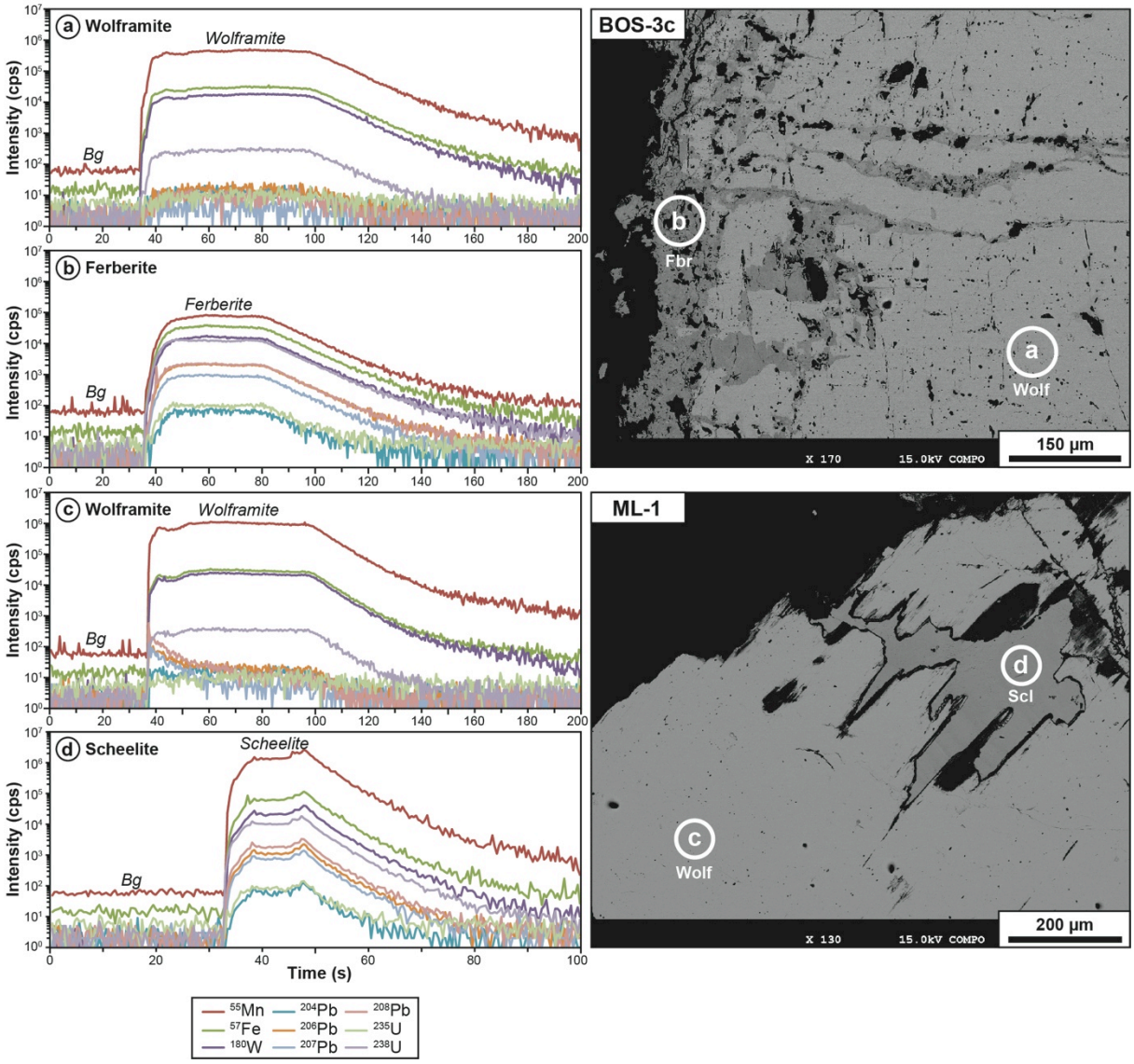

Fig. 6: Typical LA-ICPMS spectra of ferberite (Fbr) and scheelite (Scl) associated with wolframite (Wolf). (a) Homogeneous wolframite in BSE imagery, partially replaced by ferberite (b) along crystalline borders (sample BOS3c). (c) Homogeneous wolframite hosting inclusions of scheelite (d) in replacement (sample ML-1). Single-spot laser analysis using 60 µm spot diameter and 10 Hz repetition rate (see text for details). Bg: background.

Locally, there are Pb-rich micro-inclusions within wolframite (Fig. 5b), such as inclusions of ferberite and/or scheelite (Fig. 6). Isolated micro-inclusions of ferberite are

generally not easily visible on SEM image because of their dimension (generally tens of μm), but can be detected by LA-ICPMS (Fig. 5b). The constant Fe/Mn ratio in the LA-ICPMS spectrum is related to the relatively small volume of ferberite compared to the large volume of wolframite ablated. Ferberite also occurs as alterations along crystal boundaries. This ferberite displays U contents that are one to two orders of magnitude higher than those of wolframite and typically has higher $^{206}Pb/^{204}Pb$ values than wolframite (Fig. 6a,b). Scheelite micro-inclusions have U and Pb contents that are also one to two orders of magnitude higher than those of wolframite (Fig. 6c,d), but does not show high $^{206}Pb/^{204}Pb$ values as in situ ^{206}Pb growth is overwhelmed by high common Pb contents. Because of their higher U and Pb contents, micro-inclusions may significantly influence the U-Pb system of bulk wolframite samples. Scheelite and sulphides may shift the Pb isotopic composition to unradiogenic compositions, whereas ferberite may shift the Pb isotopic composition of the bulk sample to more radiogenic compositions. Significant contributions of ferberite, therefore, may yield anomalously young ages, i.e., the age of ferberite alteration (ferberitization), which may be a problem if wolframite formation and ferberite alteration do not represent early and late stages of a single short-lived process, but are related to two different processes widely separated in time.

4.2. Pb isotopic composition of scheelite, pyrite and quartz

The Pb isotopic composition and the U and Pb contents of scheelite, pyrite, and quartz associated with wolframite samples are shown in Table 2. Initial $^{206}Pb/^{204}Pb$ and $^{207}Pb/^{204}Pb$ values as used for the calculation of the $^{206}Pb/^{238}U$ and $^{207}Pb/^{235}U$ values of wolframite (Table 3) were estimated using these data for an age of 300 Ma. Initial $^{208}Pb/^{204}Pb$ values were not calculated, as Th contents have not been determined. Because of the lower solubility of Th in comparison to U, it is likely that the correction of *in situ* ^{208}Pb growth is even less significant that the one for *in situ* growth of ^{206}Pb and ^{207}Pb. Scheelite and pyrite have relatively high Pb contents (Table 2) and *in situ* Pb growth was relatively insignificant, despite U contents of 210 to 300 ppm in scheelite and 2 to 78 ppm in pyrite (Table 2). Several samples do not contain scheelite or pyrite and, therefore, the initial Pb isotopic composition of wolframite was estimated using quartz. Quartz has very low Pb and U contents (Table 2), which are likely to be hosted in fluid inclusions rather than in the crystal lattice. For some samples the initial Pb isotopic composition of quartz and the one of scheelite and pyrite closely correspond to each other, whereas for other samples there are distinct differences. Actually, there are also

differences between quartz samples from the same vein. There are two reasons for this heterogeneity: (i) Pb is leached from source and local wall rocks and, therefore, may have different isotopic compositions during different stages of vein formation; (ii) Quartz and wolframite are not necessarily strictly coeval and record several generations of fluid circulations, as commonly observed in quartz crystals associated with wolframite (e.g., Vallance et al., 2001). Especially if there are several generations of fluid inclusions, the initial Pb isotopic composition of quartz may not be identical with the one of pyrite, scheelite, and wolframite.

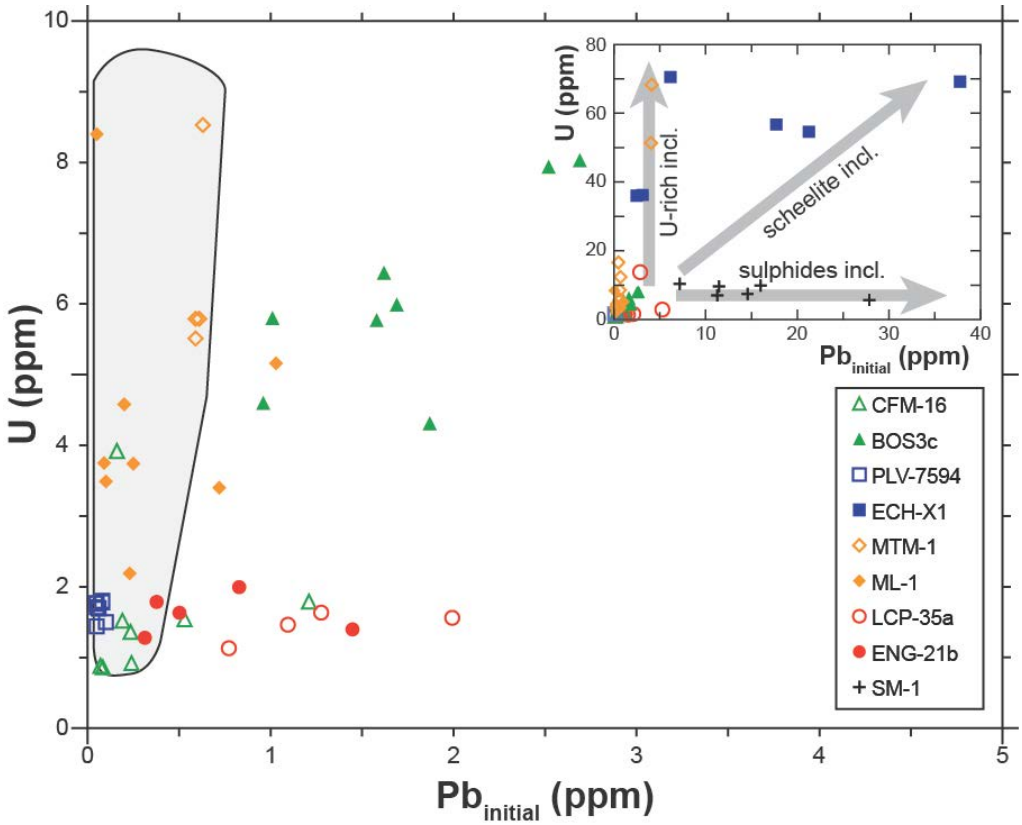

Fig. 7: U vs. $Pb_{initial}$ contents in wolframite samples from the FMC. Data for wolframite samples are given in Table 3 and Table 4. Arrow in the inset shows the mixing trends between typical wolframite and U-rich inclusions (high U and low Pb), scheelite (high Pb and high U) and sulphides (high Pb and low U) inclusions. The grey field correspond to the samples with high μ values, which developed high Pb radiogenic composition and are the most suitable for U-Pb dating.

4.3. U-Pb age data of wolframite

The wolframite samples are characterized by variable contents of U and Pb ranging from 0.86 to 70.55 ppm (typically <10 ppm) and from 0.11 to 41.1 ppm (typically <3 ppm),

respectively, and show variably radiogenic Pb isotopic compositions with $^{206}Pb/^{204}Pb$ values between 19.3 and 154.2 (Table 3,Table 4). The low $^{206}Pb/^{204}Pb$ values of some samples are due to variable contents of Pb_{inital} in some wolframite samples (0.04 to 37.8 ppm). Although most of the wolframite samples fall in a cluster characterized by low U and low Pb_{inital} contents, a few samples have higher U and/or Pb_{inital} contents (Fig. 7). The remaining samples define three different trends that reflect inclusions of sulphides (high Pb and low U) or scheelite (high Pb and high U). The third trend, characterized by variable U contents and low Pb_{inital}, includes samples that develop radiogenic Pb isotopic compositions (Fig. 7), which makes them suitable for isotopic dating. U in these samples may be hosted in the wolframite lattice or in micro-inclusions of U-rich minerals such as columbite. U-Pb data for wolframite are given in Table 3 and Table 4.

4.3.1. Vaulry deposit (sample CFM-16)

Wolframite from Vaulry has very low U contents (0.86 to 3.92 ppm) and low Pb contents (0.11 to 0.34 ppm), whereby most of the Pb is unradiogenic (Pb_{inital}: 0.07 to 0.24 ppm) (Table 3). Five samples are concordant and coincide within error (Fig. 8a). Two samples are strongly discordant (Table 3). The discordant samples, one of which has a distinctly higher Pb_{inital} content (1.2 ppm), have not been included in the age calculation. The five concordant samples define a concordia age of 298 ± 1.2 Ma (2σ, MSWD = 0.42; Fig. 8a), interpreted as the age of the wolframite crystallization. This age is significantly younger than the previous $^{40}Ar/^{39}Ar$ ages of 311-309 Ma obtained on micas from the selvages of the quartz-wolframite veins (Cuney et al., 2002).

4.3.2. St-Goussaud deposit (sample BOS3c)

Wolframite from St-Goussaud has U contents between 4.3 and 8.0 ppm and Pb contents between 1.2 and 3.1 ppm (Table 3). Despite the relatively high U content, the Pb isotopic composition is not very radiogenic, with $^{206}Pb/^{204}Pb$ ratios ranging from 37.2 to 47.5. *In situ* Pb growth, which contributes 0.25 to 0.39 ppm to the Pb content, is compensated by high contents of Pb_{inital} of 1.01 to 2.69 ppm (Table 3). There is a scattered correlation between U and Pb_{inital} contents (Fig. 7) that may indicate that (i) U and Pb in wolframite are coupled to some extent or (ii) the analysed sample corresponds to a two-component mixture consisting of a mineral phase having low contents of U and Pb and another mineral phase having high

contents of U and Pb. It should be noted in case (ii) that the low-Pb phase has a higher $^{238}U/^{204}Pb$ ratio than the high-Pb phase. The first explanation is unlikely, as wolframite samples from the Grube Clara, Sweet Home Mine or Wutong deposits, which have similar or higher U contents, all have very low contents of Pb_{inital} (Romer and Lüders, 2006; Pfaff et al., 2009; Lecumberri-Sanchez et al., 2014). Moreover, Pb does not fit well into the crystal lattice of wolframite, due to the larger ionic radii of Pb^{2+} compared to W^{6+}, Fe^{2+} and Mn^{2+} (Shannon, 1976). The second possibility actually explains several features observed for BOS3c data: (i) if the high-Pb and the low-Pb minerals do not have the same age, the data will scatter along the discordia between the ages of the two minerals; (ii) if the high-Pb phase is a secondary phase and incorporates Pb much more readily than U, it is likely that it incorporates Pb released from precursor wolframite to a much higher extent than U released from precursor wolframite. As the Pb from precursor wolframite also contains contributions of *in situ* grown radiogenic Pb, such a fractionation between U and Pb during growth of the high-Pb phase would generate reversely discordant U-Pb systems for the mixture (Table 3). Such a reverse discordance by inheritance of radiogenic lead has been shown for titanite grown at the expense of older rutile (e.g., Romer and Rötzler, 2003, 2011). In this sample (and others with similar disturbances), secondary scheelite may account for the anomalous data pattern. In the $^{206}Pb/^{204}Pb$ vs. $^{238}U/^{204}Pb$ diagram, four wolframite samples together with the quartz sample define an isochron that corresponds to an age of 327.6 ± 5.7 Ma (2σ, MSWD = 0.39; Fig. 9d) and a very high initial $^{206}Pb/^{204}Pb$. This radiogenic initial Pb isotopic composition yields concordant wolframite data in the $^{206}Pb/^{238}U$ vs. $^{207}Pb/^{235}U$ diagram for samples used to define the isochron and reduces the reverse discordance of the other samples. Thus, wolframite from St-Goussaud is anomalous in two respects, i.e., (i) it has an anomalous initial Pb isotopic composition and (ii) the U-Pb system is likely to be bound to two different mineral phases.

4.3.3. Echassières deposit, La Bosse (sample ECH-X1)

Wolframite from La Bosse (Echassières deposit) has high U (36 to 70 ppm) and Pb_{inital} (2.47 to 37.8 ppm) contents (Table 3), which indicates that the analysed samples have a two-component U-Pb system similar to the one of specimen BOS3c from St-Goussaud, possibly related to U-rich inclusions and to scheelite inclusions (Fig. 7). Wolframite from La Bosse, however, shows no sign of reverse discordance, indicating that the two-component system is a primary feature or the formation of the secondary mineral phases occurred at a late stage of

mineralization, i.e., before sufficient time had elapsed to grow significant amounts of radiogenic Pb. The Nb-rich growth bands observed within wolframite correspond likely to U-rich nano-inclusions of columbite-tantalite minerals, which would therefore be coeval with the crystallization of wolframite (Aïssa et al., 1987a). The three concordant samples define a concordia age of 333.4 ± 2.4 Ma (2σ, MSWD = 7.0; Fig. 8c). This age is interpreted as the age of crystallization of this wolframite sample. It is significantly older than the K-Ar ages of 325-320 Ma obtained on phengites from selvages of the quartz-ferberite veins (Merceron et al., 1987).

4.3.4. Echassières deposit, Les Montmins (sample MTM-1)

Wolframite from Les Montmins (Echassières deposit) shows a very large range of U and Pb content, ranging from 5.8 to 68.3 ppm and from 0.87 to 7.4 ppm, respectively (Table 3). The contents of U and Pb_{inital} (0.47 to 4.1 ppm) correlate (Fig. 7), indicating that the U-Pb system of sample MTM-1 consists of a two-component system similar to the one of samples BOS3c and ECH-X1. Sulfides or scheelite inclusions, however, do not play a role. Instead, the range in U content just may reflect contrasting U availability during wolframite growth, yielding both low-U wolframite and high-U wolframite (Fig. 7). Five concordant samples define a concordia age of 334.4 ± 1.7 Ma (2σ, MSWD = 3.6; Fig. 8d). The coincidence of these five samples implies – as for sample ECH-X1 – that the development of a two-component system is a primary or late-stage feature, rather than a much younger secondary event. In this respect, this age is considered to date the crystallization of the wolframite.

4.3.5. Puy-les-Vignes deposit (sample PLV-7594)

Wolframite from Puy-les-Vignes has low U content of 1.44 to 1.80 ppm and low Pb_{inital} contents of 0.04 to 0.10 ppm (Table 3). The analysed samples do not contain mineral inclusions. Six concordant samples define a concordia age of 317.7 ± 0.7 Ma (2σ, MSWD = 5.7; Fig. 8b). This age is interpreted to date the crystallization of the wolframite. It is slightly younger than the $^{40}Ar/^{39}Ar$ age obtained on the muscovite associated with the quartz-wolframite veins (323 ± 0.9 Ma; Cuney et al., 2002) and younger than the ages of the spatially associated granites in the region (324 ± 1 Ma to 346 ± 14 Ma; Duthou, 1978; Gebauer et al., 1981).

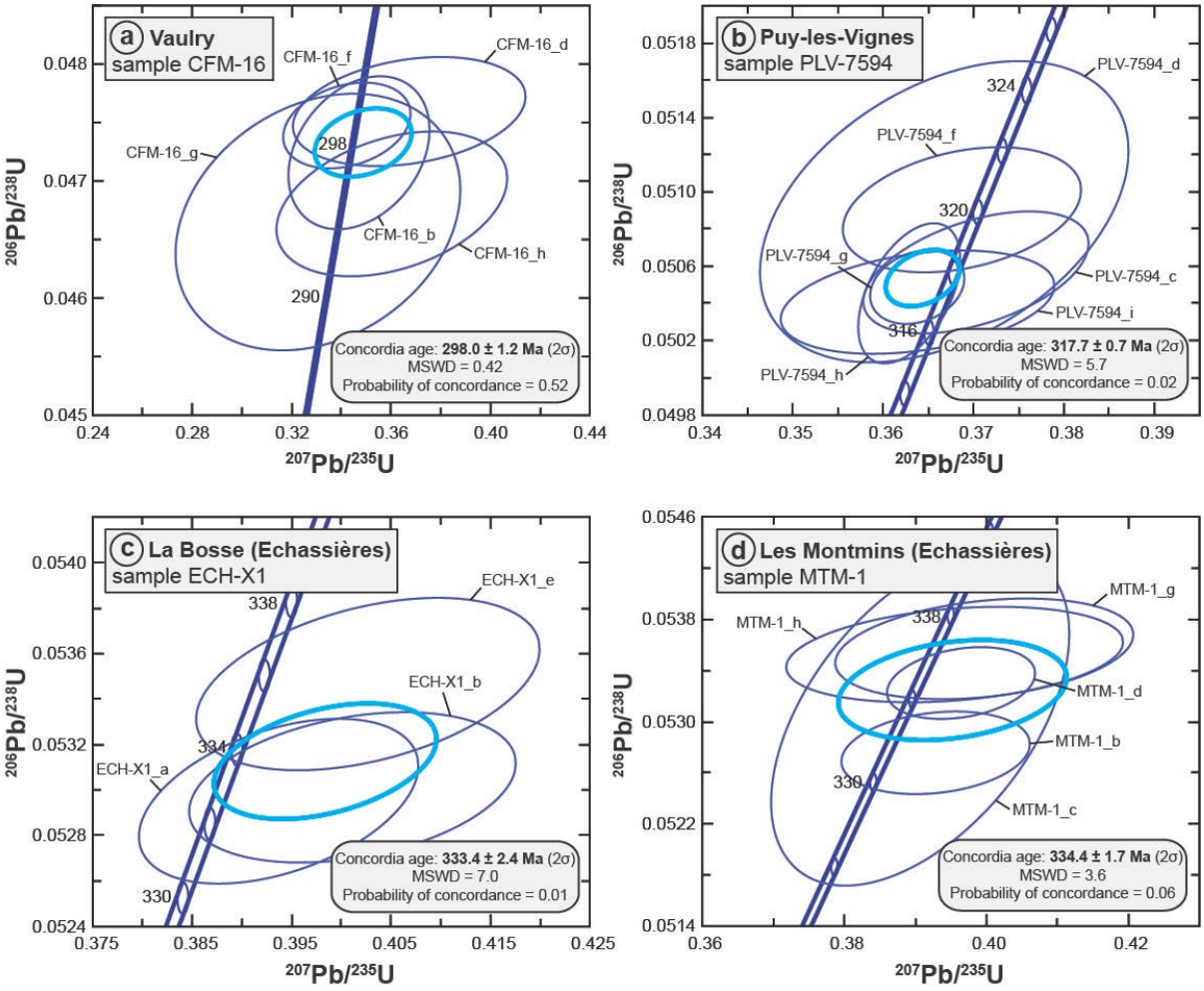

Fig. 8: Concordia diagrams for wolframite from the Vaulry (a), Puy-les-Vignes (b), La Bosse (c) and Les Montmins (d) W deposits, French Massif Central. The concordia age is calculated using concordant data of wolframite. Error ellipses show data (thin lines) and calculated concordia age (thick line) at 2σ level. All data for wolframite are given in Table 3.

4.3.6. Enguialès deposit (sample ENG-21b)

Wolframite from Enguialès shows a broad range of U contents (1.13 to 13.7 ppm) that broadly correlate with the Pb_{inital} contents (0.77 to 5.37 ppm) (Table 4). Such a correlation may be indicative for a two-component mixture similar to the one discussed for the St-Goussaud samples. Four samples together with quartz from the same specimen constrain a $^{206}Pb/^{204}Pb$ vs. $^{238}U/^{204}Pb$ isochon that corresponds to an age of 273.7 ± 6.5 Ma (2σ, MSWD = 2.1; Fig. 9a). The sample with the highest measured $^{206}Pb/^{204}Pb$ value (Table 4) falls far below that isochron, indicating later disturbance. The U-Pb age of 273.7 ± 6.5 Ma is markedly younger than the ages determined for muscovite associated with the quartz-wolframite veins

(312 ± 3 to 305 ± 3 Ma; Monié et al., 2000) and the ages of the spatially associated granites in the region (323 to 310 Ma; Monié et al., 2000). Therefore, it seems clear that this age dates a later episode after the crystallization of wolframite, which could correspond for instance to the ferberitization event.

4.3.7. Leucamp deposit (sample LCP-35a)

Wolframite from Leucamp has low U contents (1.28 to 1.99 ppm) and variable Pb contents (0.35 to 1.50 ppm) (Table 4). The measured $^{206}Pb/^{204}Pb$ values are low (21.06 to 31.52), but allow the definition of a discordia that corresponds to an age of 276.5 ± 2.9 Ma (2σ, MSWD = 1.7; Fig. 9b). As for the Enguialès deposit, this age reflect likely the isotopic disturbance of wolframite and could be related to a late hydrothermal alteration episode, such as ferberitization.

4.3.8. St-Mélany deposit (sample SM-1)

Wolframite from St-Mélany has relatively high U contents (5.68 to 10.37 ppm) in comparison with most other dated wolframite samples from the FMC (Table 3 and Table 4) and variable, but high Pb_{inital} contents (7.16 to 27.9 ppm). In the U vs. Pb_{inital} diagram (Fig. 7), these samples define a horizontal trend, indicating that Pb_{inital} is bound to sulphide inclusions. Because of the high Pb_{inital} contents, the measured Pb isotopic composition is not very radiogenic, with $^{206}Pb/^{204}Pb$ values ranging from 19.93 to 22.75 (Table 4). The wolframite samples define together with pyrite and quartz an isochron in the $^{206}Pb/^{204}Pb$ vs. $^{238}U/^{204}Pb$ diagram (Fig. 9c) that corresponds to an age of 315 ± 15 Ma (2σ, MSWD = 25; Fig. 9c). The large MSWD is mainly due to the slight difference in the Pb isotopic composition between the pyrite and quartz samples, whereas the relatively large uncertainty is mainly due to the MSWD and the small spread of the data (Fig. 9c). The age of 315 ± 15 Ma is interpreted to date the crystallization of wolframite.

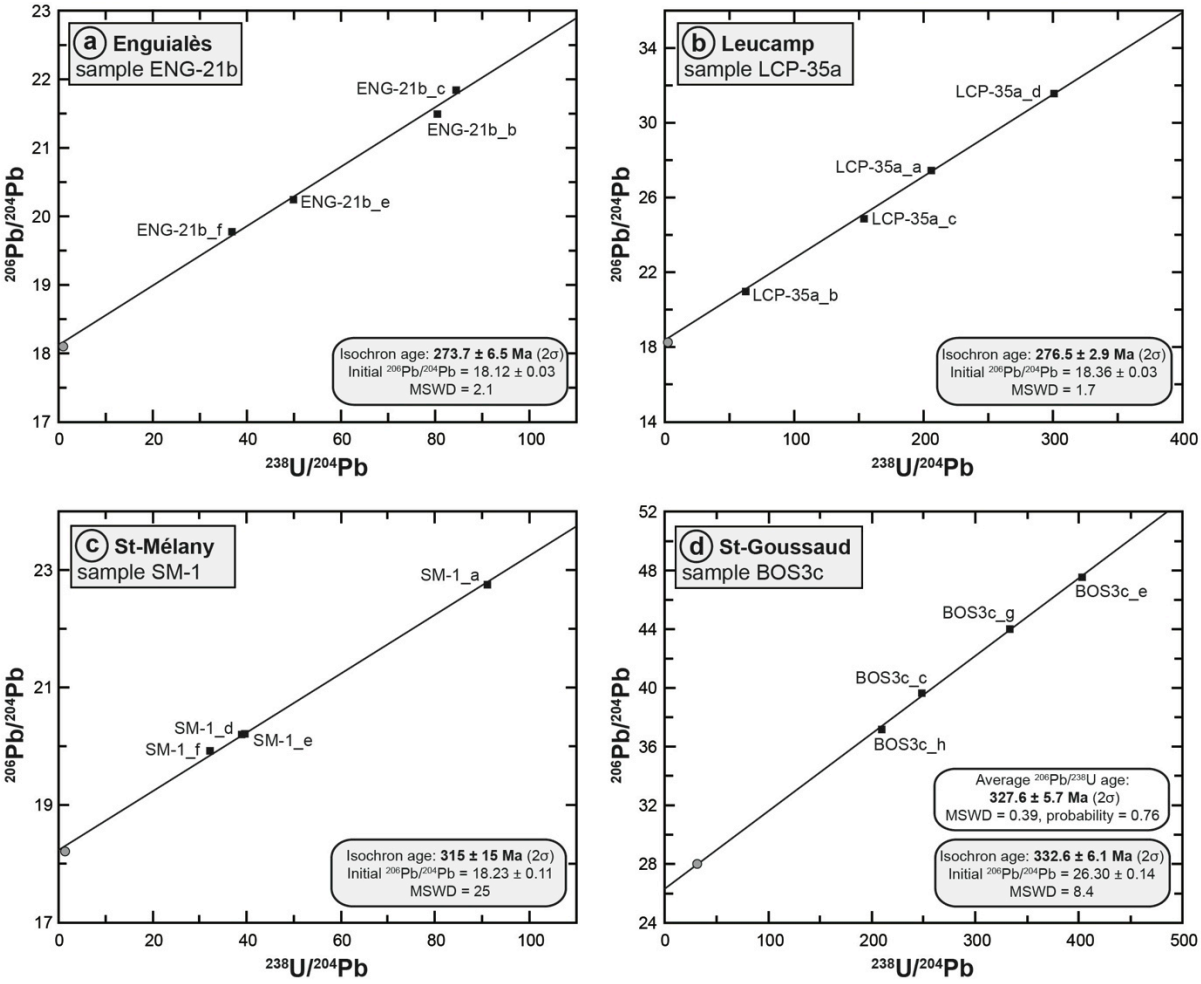

Fig. 9: $^{206}Pb/^{204}Pb$ vs. $^{238}U/^{204}Pb$ isochron diagrams for wolframite from the Enguialès (a), Leucamp (b), St-Mélany (c) and St-Goussaud (d) W deposits, French Massif Central. Wolframite samples are shown as squares, associated low $^{238}U/^{204}Pb$ minerals (quartz, pyrite or scheelite) are shown as circles. Note, most of the isochrons show excess scatter, most significantly for St-Mélany wolframite (c). For this sample, excess scatter is largely due to quartz and pyrite that do not fall on the isochron defined by the wolframite samples alone (for discussion see text). The initial Pb isotopic composition of the St-Goussaud samples is unusually radiogenic. All data for wolframite are given in Table 3 and Table 4. Data for vein minerals (quartz, pyrite or scheelite) are given in Table 2.

4.3.9. Montredon-Labessonnié deposit (sample ML-1)

Six wolframite samples from Montredon-Labessonnié have low contents of U (2.19 to 4.58 ppm) and Pb_{inital} (0.09 to 0.72 ppm) and relatively high radiogenic Pb isotopic compositions with $^{206}Pb/^{204}Pb$ values ranging from 31.32 to 151.3 (Table 3). The six samples show a wide range of apparent $^{206}Pb/^{238}U$ ages and define a discordia with an upper intercept of 315.9 ± 2.3 Ma (2σ, MSWD = 1.8; Fig. 10) and an anomalous negative lower intercept (see

discussion below). Most of the excess scatter is due to one sample (Fig. 10). We interpret the upper intercept as the age of wolframite crystallization.

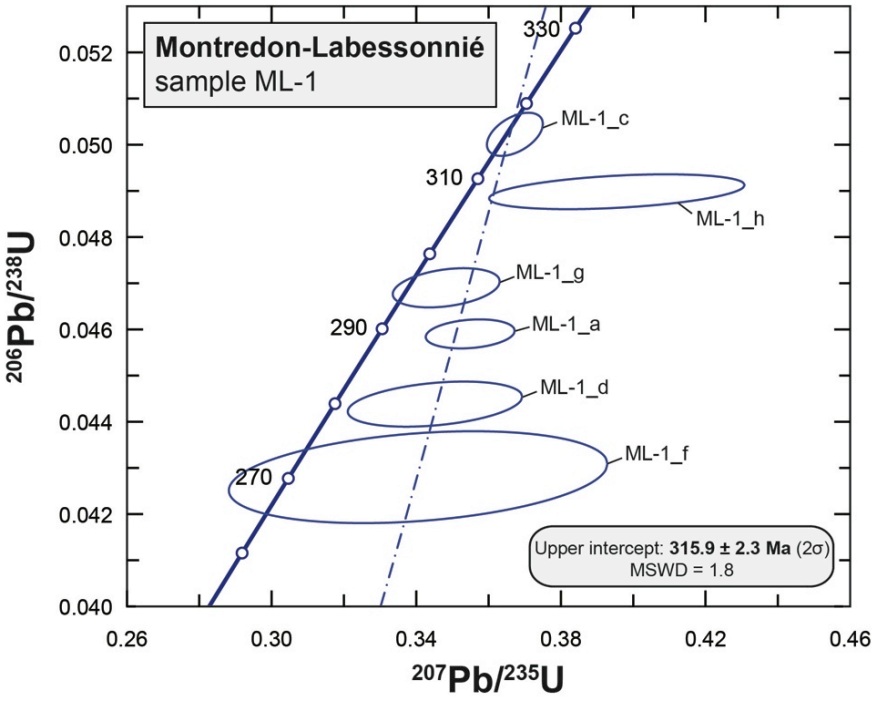

Fig. 10: Concordia diagram for wolframite from the Montredon-Labessonnié W deposit, French Massif Central. Error ellipses show data (thin lines) at 2σ level. The discordia has an anomalous lower intercept that implies multi-stage development of the U-Pb system (for discussion see text). Data for wolframite are given in Table 3.

4.4. X-ray computed tomography of wolframite

CT images of the wolframite crystal from the St-Mélany deposit (SM-1 sample) are shown in Fig. 11. The 3D volume reconstructed from CT images show that defects, i.e., micro-fractures or mineral phases, are minor on the mineral surface (Fig. 11a), as observed in BSE imagery. However, virtual cross-sections through the 3D volume reveal that the number of defects within wolframite is significant and is under-estimated from a single 2D view (Fig. 11b,c). The defects may correspond either to regular cleavage planes, fractures planes or to irregularly shaped micro-inclusions. Due to the high density and X-ray absorption of tungsten, CT do not allow distinguishing porosity from mineral phases, which have the same absorption contrast on the images. Most of the defects in wolframite form a highly irregular and complex three-dimensional network (Fig. 11c,d). The largest defects are generally connected with each other, whereas the smallest ones are isolated or form disseminated

clusters. The frequency histogram of the individual defect volumes, estimated from the 3D reconstruction, show a skewed distribution with a median value of 500 μm^3 (Fig. 11e). The shape of the defects is also highly variable and is best estimated by the sphericity index, which shows a skewed distribution with a median value of 0.55 (Fig. 11f). These results indicate that the majority of the defects within the sample SM-1 are small and have an irregular shape. Integration of the 3D models allows to estimate a total volume of the defects correspond to ca. 3.5% of the crystal volume. CT images of wolframite, thus, confirm that sample SM-1 contains micro-inclusions, as inferred from the SEM data (Fig. 4) and U-Pb concentration data (Fig. 7). The analysed SM-1 sample is approximately twice the size of the crushed crystals of wolframite (ca. 1 mm^3) selected for U-Pb dating. Therefore, the relatively small contribution of defects and/or inclusions may represent actually a severe issue for U-Pb dating if the micro-inclusions are not cogenetic with wolframite or contain high contents of common Pb, as detected in scheelite and ferberite by LA-ICPMS (Fig. 6). Consequently, CT appears to be a powerful method to investigate both the relative proportions and the spatial distribution of micro-inclusions within wolframite and, thus, may represent an efficient and timesaving technique to select samples suitable for U-Pb TIMS dating, i.e. samples that are free of micro-inclusions.

5. Discussion

5.1. Disturbance of the U-Pb isotope system of wolframite

Wolframite is generally stable over a large range of temperature and pressure (300-900°C, 0.5-2 kbar) and under hydrothermal conditions over a large range of fO_2 values (Hsu, 1976; Wood and Samson, 2000; Linnen and Cuney, 2005; Che et al., 2013). Nevertheless, little information is available about the stability of the U-Pb isotope system in wolframite. Although most of the samples from the same specimen cluster and overlap in a single isotopic group, there are also samples that are variably normally and reversely discordant in the $^{206}Pb/^{238}U$ – $^{207}Pb/^{235}U$ diagram, show excess scatter in the $^{206}Pb/^{204}Pb$ – $^{238}U/^{204}Pb$ diagram, or define a discordia with a negative lower intercept. All these features indicate that the U-Pb system of wolframite may be disturbed by a wide range of processes, including laboratory treatment and geological processes.

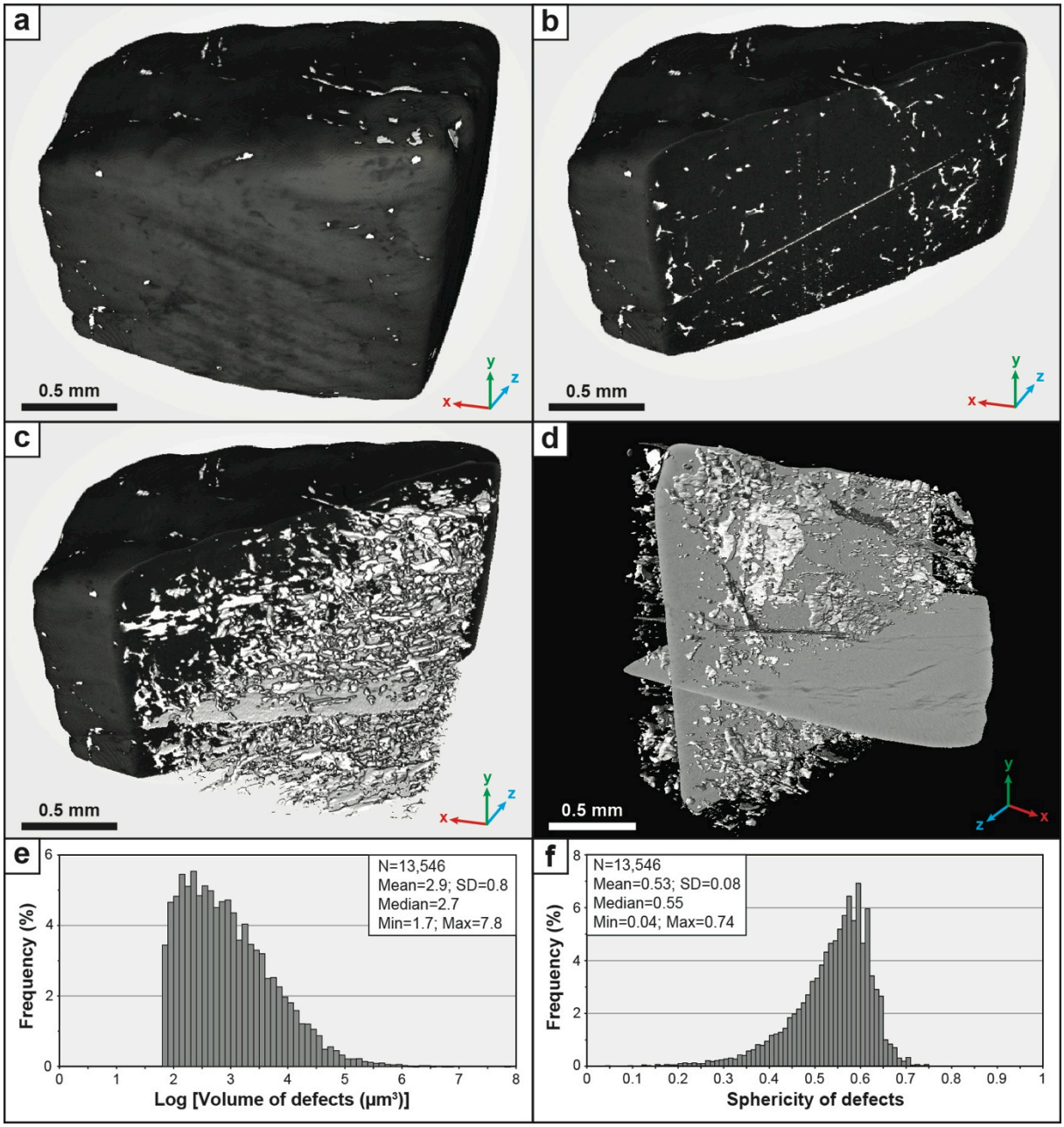

Fig. 11: 3D volumes of a wolframite crystal from the St-Mélany deposit (SM-1 sample) reconstructed from X-ray computed tomography (CT) images. (a) Global view of the wolframite crystal showing minor defects on surface (in white). (b) Virtual cross-section through the 3D volume showing cleavage planes and internal defects. (c) Reconstructed 3D volumes of the defects (white colour) within wolframite showing a complex internal network. (d) Reconstructed 3D volumes of the defects superposed on CT cross-section images showing the internal distribution of the defects. (e) Distribution histogram of volume of the defects within wolframite. (f) Distribution histogram of sphericity of the defects within wolframite.

5.1.1. Disturbance due to laboratory treatment

Wolframite readily dissolves in concentrated HF on the hot plate. Tungsten may precipitate as tungstates, which may scavenge U and Pb. If precipitation starts after complete dissolution of wolframite and complete homogenization of sample and tracer U and Pb, scavenging of some Pb and U by the precipitates has no effect on the dating. In contrast, if precipitation of tungsten starts before complete dissolution of wolframite, the isotopic composition of U and Pb scavenged by the precipitate may differ from the isotopic composition of U and Pb in the final solution, resulting in incorrect concentration determinations for U and/or Pb and in a shift of the data along a discordia through the origin of the concordia diagram toward discordant and reverse discordant values. All HF solutions were systematically checked visually for precipitates after the dissolution of wolframite and a small amount of H_2SO_4 was added to stabilize the samples. Although only samples without visible precipitates were used for dating, the possibility of U-Pb scavenging before homogenization of the solution cannot be ruled out completely. As it is unlikely that several samples are disturbed in the same way, the coincidence within error of several samples in the concordia diagram, however, provides strong argument against incomplete homogenization of tracer and sample.

5.1.2. Disturbance due to geological processes

Post-crystallization fluid-mineral interaction may form a second generation of wolframite or result in the replacement of the original wolframite by secondary minerals (Fig. 4; e.g., ferberite and/or scheelite) and thereby redistribute U and Pb. Only in the ideal case of complete loss of Pb, such a later redistribution of U and Pb would completely reset the dating system and and the obtained age would date the younger event, i.e. the age of the alteration episode. But generally, resetting is not complete, which results in mixed ages.

The formation of secondary minerals may disturb the U-Pb system of wolframite in a very complex way. Mineral exsolution within wolframite may result in secondary minerals that strongly fractionate U and Pb, essentially yielding a sample with two different chronological systems, i.e., one bound to the host wolframite and one bound to the exsolution. In this case, the bulk system will appear undisturbed, as long as the separation in two U-Pb systems occurs on a much smaller scale than the size of the individual sample used for dating. The bulk system only will appear disturbed if one of the sub-systems behaves open and if (i)

there had been exchange between the two systems (for a systematic discussion see Romer et al., 2007). Replacement of wolframite by scheelite (e.g., Ferenc and Uher, 2007; Goldmann et al., 2013) similarly may yield a disturbed U-Pb system. Scheelite may take up considerable amounts of Pb that substitutes for Ca. Unradiogenic lead only would reduce the $^{206}Pb/^{204}Pb$ that develops with time (and thus would reduce the precision of the age), but radiogenic Pb released from other minerals and incorporated into scheelite would result in reversely discordant data with too old apparent ages.

Recurrent fluid-flow in hydrothermal systems is particularly prone to result in the formation of secondary minerals at grain boundaries and along crystal fractures and therefore, sample selection is critical for isotopic dating. In this respect, CT may be a very efficient tool to select samples without micro-inclusions for the U-Pb dating. The U-Pb system of sample ML-1 provides an example for the highly anomalous data pattern of samples with micro-inclusions and a two-component U-Pb system. Data of this sample yield a discordia with a negative lower intercept (Fig. 10). Whereas the variable discordance of the data reflects Pb loss, the negative lower intercept cannot be explained by Pb loss alone. Instead, such lower intercepts are observed for systems that have experienced intermediate daughter loss in the ^{238}U decay series (e.g., Ludwig and Simmons, 1991; Romer, 2003) and are primarily related to micro-crystalline material or to material with closely spaced crystal defects that allow loss of the short-lived intermediate daughter isotopes of the ^{238}U decay series. It is important to note that the intermediate daughters have to be lost continuously to result in the observed effect.

5.2. Contrasting uranium content of wolframite

Wolframite samples from the FMC show variable U concentrations, ranging from 0.8 to 70 ppm and <10 ppm in average (Table 3 and Table 4), both on the scale of individual samples as well as on the regional scale. Most low-U wolframite samples show a relatively small range of U content (generally 1-10 ppm), whereas high-U wolframite samples have a larger range up to one order of magnitude (5.5-68 ppm; sample MTM-1). Especially if the high U contents correlate with high contents of initial Pb, it is likely that they reflect contributions of scheelite or sulphides inclusions, which may have both high contents of U and Pb (Fig. 7, Table 2). High U contents at low Pb_{inital} contents, however, are likely to reflect higher availability of U in the fluid from which wolframite crystallized. The majority of the wolframite samples from the investigated tungsten deposits in the FMC have low U contents.

Limited minor and trace element data of wolframites from other worldwide areas also showed that U concentrations in wolframite generally are very low and typically fall in the low ppm (< 5 ppm) range (e.g., Swart and Moore, 1982; Tindle and Webb, 1989; Ferenc and Uher, 2007; Goldmann et al., 2013). In contrast, wolframite samples for which U-Pb ages have been published commonly have higher U contents, ranging from 4.8 ppm up to 419 ppm, and generally >100 ppm (Frei et al., 1998; Romer and Lüders, 2006; Pfaff et al., 2009; Lecumberri-Sanchez et al., 2014). Similar broad ranges of U concentrations from sub-ppm to several hundred ppm also have been found in other studies on wolframite composition (n>100 samples; pers. comm. F. Melcher, Leoben).

The large variation of U content raises questions about both the distribution and localization of U in wolframite and the role of the availability of U in the fluid. There are three possible mechanisms for U incorporation in wolframite: (i) U may substitute by coupled substitution for Fe^{2+} and Mn^{2+} in the crystal lattice with creation of a vacancy, since octahedrally coordinated U^{4+} has a ionic radius of 0.89 Å, close to the ones of octahedrally coordinated Fe^{2+} (0.78 Å) and Mn^{2+} (0.83 Å), respectively (Shannon, 1976). Substitution may be homogeneous and random or it may result in concentration along regular crystal growth surfaces as described by Swart and Moore (1982). Highly heterogeneous distribution may reflect availability control on U concentration in wolframite rather than crystallographic control; (ii) U may be hosted by U-rich micro-inclusions such as pyrochlore or columbo-tantalite group minerals. Micro-inclusions may be either “trapped” during crystallization of wolframite such as columbite nano-crystals in Nb-rich growth zones (e.g., Aïssa et al., 1987a; Tindle and Webb, 1989) or may result from exsolution (for an analogue in cassiterite, see Neiva, 1996, 2008). Moreover, they would result in two independent U-Pb systems within wolframite that may behave contrastingly during later processes (e.g., Romer, 2003; Romer et al., 2007); (iii) U may be present in the aqueous phase of fluid inclusions within wolframite. Although U may be incorporated too in the wolframite lattice, preferential residence of the chronologically exploitable element-pair in fluid inclusions rather than in the host mineral is possible and has been demonstrated for Rb-Sr in sphalerite (e.g., Nakai et al., 1993; Christensen et al., 1995), Rb-Sr in quartz (e.g., Shepherd and Darbyshire, 1981; Pettke and Diamond, 1995) and U-Pb in hematite (e.g., Lüders et al., 2005).

Low U contents in wolframite may firstly reflect low concentrations of U in the hydrothermal fluid crystallizing the wolframite. The mobility of U in aqueous solutions is mainly controlled by its redox state and the availability of complexing ligands (Langmuir, 1976). Indeed, U is known to be highly mobile as hexavalent uranyle ion (UO_2^{2+}) under

oxidizing conditions, whereas the solubility of U^{4+} is extremely low in reduced conditions. Thus, U content in wolframite may be controlled by the redox conditions both of the metal source and of the transporting fluid(s). In hydrothermal systems, Sn and W behave differently than U, due to their contrasting redox behaviour (Dubessy et al., 1987; Heinrich, 1990; Wood and Samson, 2000). Sn-W mineralizations are generally spatially associated with reduced granites (Fig. 12), which may have played a genetic role either as direct metal source or as thermal source driving hydrothermal fluid circulations. U-rich granites are also generally reduced (Fig. 12) and contain dominantly uraninite, which crystallizes directly in the magma, as well exemplified by the peraluminous leucogranites of the Limousin-type, the St Sylvestre granite representing one of the best example (Cuney and Kyser, 2008 and references therein). Melt-fluid fractionation at the magmatic-hydrothermal transition results thus in very low U concentrations in the exsolved fluid. Consequently, reduced U-rich granites do not generate U-rich magmatic fluids and wolframite crystallizing from such fluids may have low U content.

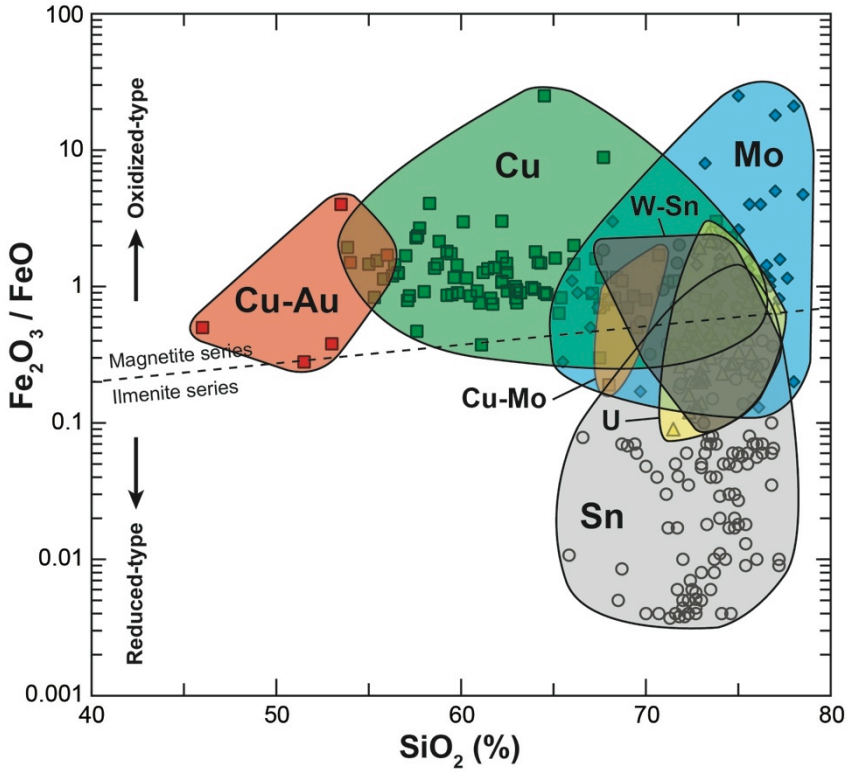

Fig. 12: Fe_2O_3/FeO - SiO_2 diagram for granitoid rocks associated with mineral deposits of Cu-Au, Cu, Mo, W-Sn, Sn and U. The different fields are represented with data compiled from Cuney et al. (1984), Kontak (1990), Lehmann (1990), Breiter et al. (1991), Blevin and Chappell (1995), Breiter et al. (1997), Gomes and Neiva (2002), Štemprok et al. (2005), Linnen and Cuney (2005), Sinclair (2007) and Breiter and Škoda (2012). The dividing line between the magnetite (oxidized-type) and ilmenite (reduced-type) series is from Ishihara (1981).

There are two exceptions where wolframite crystallizing from hydrothermal fluid may have high U contents: (i) Fluid derived from an oxidized granite may mobilize U in solution, i.e., U does not precipitate as uraninite in the magma but is fractionated preferentially in the aqueous fluid phase. For instance, wolframite from the Sweet Home Mine deposit (Romer and Lüders, 2006) contains relatively high U content (6.3 – 30 ppm) and is associated with hübnerite-rhodochrosite veins, related to an oxidized Mo porphyry granitic system, similar to those of other hübnerite-rhodochrosite mineralization in the external zones of porphyry molybdenite granites of the Colorado Mineral Belt (e.g., Seedorff and Einaudi, 2004); (ii) Fluid-rock interactions between U-bearing reduced granite or U-rich metamorphic shales with external oxidized fluids may result in U leaching and mobilization. For instance, wolframite from the Clara deposit (U content: 4.8 – 419 ppm) occurs on fractures that are more than 100 Ma younger than the last magmatic event in the region (Pfaff et al., 2009), whereas wolframite from the Wutong deposit (U content: 72 – 155 ppm) formed from crust-derived oxidized fluids (Lecumberri-Sanchez et al., 2014). The wolframite from these two deposits likely derived its high U content from the leaching of U-rich granitic or metamorphic local host-rocks by oxidizing fluids. The U content in wolframite, thus, seems to reflect the availability of U in the hydrothermal system during the crystallization of wolframite and the evolution of the redox properties of the fluids during fluid-rock interactions. The low U content in wolframite represents a major limitation for U-Pb dating as wolframite may have variable Pb contents due to Pb-rich micro-inclusions (e.g., sulphides, scheelite). Fluid-rock interactions with country rocks not only may leach U, but may also mobilize Pb with locally highly variable Pb isotopic compositions (e.g., the highly radiogenic initial Pb of quartz and wolframite from the St-Goussaud deposit; Table 2 and Table 3), which may account in a heterogeneous Pb isotopic composition during wolframite crystallization from the fluid. The variable U contents observed in some samples in this study (e.g., sample MTM-1; Table 3) likely represent variable U concentrations in the hydrothermal fluid during the crystallization of wolframite.

5.3. Lead isotope composition of vein minerals as marker of fluid sources

The initial Pb isotopic composition of rocks and minerals varies regionally depending on the geological history of their precursors in terms of time and variations in $^{238}U/^{204}Pb$ (= μ), $^{232}Th/^{204}Pb$ (= ω), and $^{232}Th/^{238}U$ (= κ). Although the isotope ratios $^{206}Pb/^{204}Pb$, $^{207}Pb/^{204}Pb$, and $^{208}Pb/^{204}Pb$ increase monotonously with time, the rate of change depends on

their initial μ and ω ratios, and for $^{207}Pb/^{204}Pb$ also on the early history of the protoliths as most ^{235}U decayed before the beginning of the Proterozoic. This also means that most ^{207}Pb formed before the Proterozoic and, therefore, only rocks and minerals that are derived from a source that had a high μ-value already in the Archean may acquire high $^{207}Pb/^{204}Pb$ values, whereas Archean rocks with a low μ-value develop significantly lower $^{207}Pb/^{204}Pb$ values. The elements Th and U may separate from each other during high-grade metamorphism and during fluid mediated processes, especially depending on the redox conditions. Loss of U and to some extent of Pb during high-grade metamorphism results in low μ-values and high ω-values, i.e., in retarded and enhanced increase of $^{206}Pb/^{204}Pb$ and $^{208}Pb/^{204}Pb$, respectively, with time. In contrast, the low solubility of Th in most aqueous fluids results in low ω-values and variable μ-values, i.e., with time in enhanced and retarded increase of $^{206}Pb/^{204}Pb$ and $^{208}Pb/^{204}Pb$, respectively. Zartman and Doe (1981) take these observations into account in their "plumbotectonic model", which presents average Pb-growth curves for different geological reservoirs, i.e., "upper crust", "lower crust", and "mantle" (Fig. 13). The upper crust reservoir is best represented by low-deformed Archean cratons, recycled ancient crust, and erosional debris derived from them. In contrast, the lower crust reservoir represents rocks that have experienced ancient (e.g., Archean or early Proterozoic) high-grade (granulite-facies) metamorphism. An additional reservoir defined by Zartman and Doe (1981), i.e., the "orogene" reservoir (Fig. 13), reflects the mixing and recycling of Pb from the others three reservoirs in a continental magmatic arc. As younger rocks inherit the Pb isotopic composition of their precursor rocks, Pb isotopes represent fingerprints of the protoliths that allow distinguishing rocks derived from protoliths of contrasting geological history.

The initial Pb isotopes compositions of the vein minerals (quartz, pyrite, scheelite; Table 2) associated with wolframite are shown in the $^{208}Pb/^{204}Pb$ - $^{206}Pb/^{204}Pb$ and $^{207}Pb/^{204}Pb$ - $^{206}Pb/^{204}Pb$ diagrams (Fig. 13). Most samples have initial $^{206}Pb/^{204}Pb$, $^{207}Pb/^{204}Pb$ and $^{208}Pb/^{204}Pb$ values falling in the range of 17.8 – 18.6, 15.5 – 15.7 and 37.8 – 38.9, respectively. Only two samples have markedly higher $^{206}Pb/^{204}Pb$ values, i.e., those from the Vaulry (CFM-16; $^{206}Pb/^{204}Pb$ = 19.6) and the St-Goussaud (BOS3c; $^{206}Pb/^{204}Pb$ = 26.5, not shown in Fig. 13) deposits.

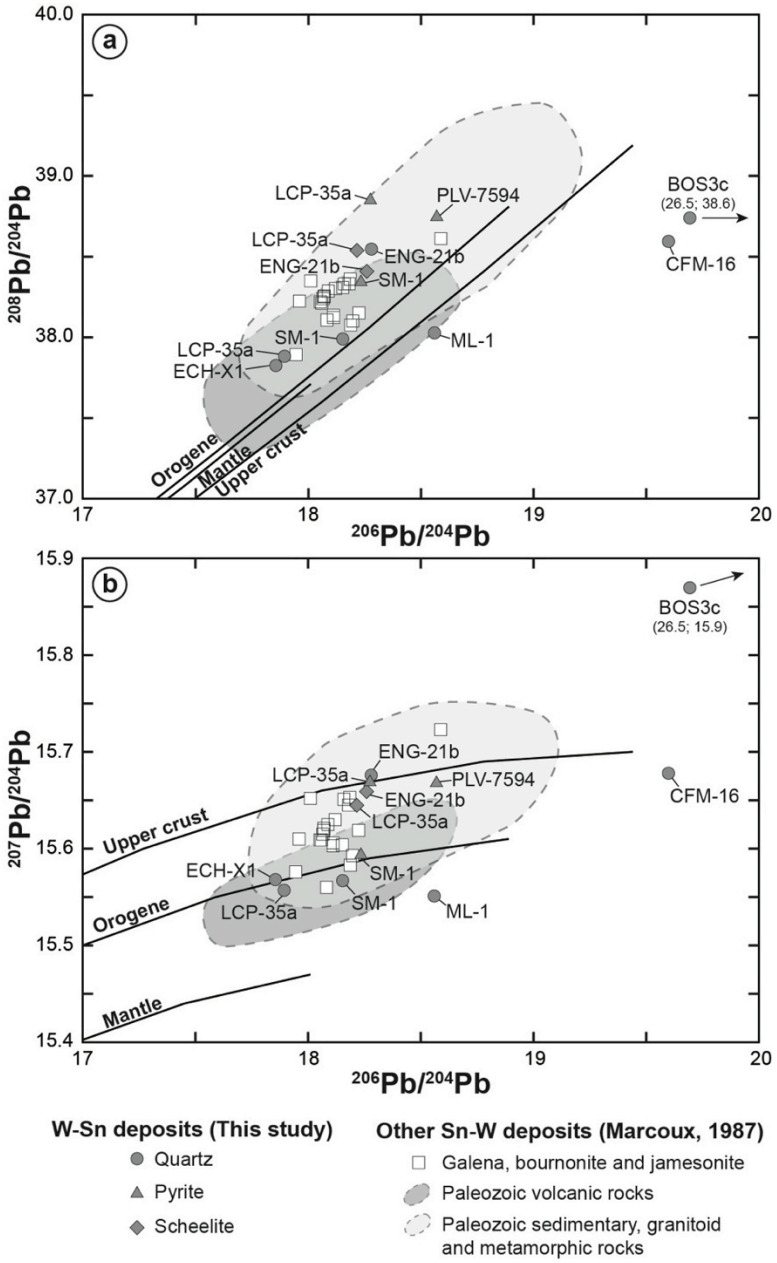

Fig. 13: Lead isotope composition of the W-Sn deposits from the French Massif Central. The Pb isotope data for vein minerals (scheelite, pyrite, quartz; see Table 2), associated with the wolframite, are compared with data available for sulphides from other Sn-W deposits in the French Massif Central and Armorican Massif (Marcoux, 1987). The data point for the St-Goussaud deposit (sample BOS3c, quartz) is not shown, because it is out of scale. The two fields represent a compilation of all available Pb isotope data for sulphides associated with mineral deposits from the different Variscan domains in France (Armorican Massif, French Massif Central, Vosges, Pyrenees, Alps and Maures), by distinguishing the deposits hosted in volcanic rocks (dark grey field) and in the sedimentary, granitoid and metamorphic rocks (light grey field). Data sources: Lancelot et al. (1971, 1984), Brevart et al. (1982), Marcoux and Bril (1986), Marcoux (1987), Marcoux et al. (1988, 1990, 1991, 1993), Marcoux and Moelo (1991), Oh et al. (1989), Cathelineau et al. (1990), Le Guen et al. (1991, 1992), Respaut et al. (1991), Cardellach et al. (1996), Velasco et al. (1996), Gloaguen et al. (2007), García-Sansegundo et al. (2014), Munoz et al. (2015). The model Pb growth curves ("mantle", "upper crust" and "orogen") are from Zartman and Doe (1981).

Two groups of data points can be distinguished with respect to their $^{207}Pb/^{204}Pb$ and $^{206}Pb/^{204}Pb$ values (Fig. 13b), i.e.: (i) a group with $^{207}Pb/^{204}Pb$ values (15.64 – 15.68) close to the "upper crust" curve of Zartman and Doe (1981), including the deposits of Enguialès, Leucamp and Puy-les-Vignes; and (ii) a group with $^{207}Pb/^{204}Pb$ values (15.55 – 15.60) close to the "orogene" curve, including the deposits of Echassières, St-Mélany and Montredon-Labessonnié. There is no correlation between the Pb isotope composition of the vein minerals, the locality of the deposits (i.e. the local geology) and the age of wolframites. Although the analysed vein minerals are not necessarly coeval with the wolframite deposition, their Pb isotopic composition may be tentatively used as fingerprint to trace the source of W on the regional scale. In this regard, the contrasting Pb isotope signatures of the different W deposits may be interpreted as reflecting different source materials on the regional scale. Wolframite mineralization of group (i) fall in the field defined by mineral deposits hosted in Paleozoic sedimentary, granitoid, and metamorphic rocks, all of which are dominated by materials derived from the old cratonic areas of Gondwana (e.g., Linnemann and Romer, 2002), whereas wolframite mineralization of group (ii) fall in the field defined by mineralization hosted in Devonian volcanic rocks, such as VMS deposits (Fig. 13b). Whereas the first group represents Pb derived from recycled crust from Gondwana, the second group may correspond to Pb derived from more juvenile materials incorporated during the Variscan orogeny. The broad overlap of the compositional fields of the protoliths and the contrasting Pb isotopic composition just reflect more or less dilution of the protoliths with young materials. The Pb isotopic composition of samples from the Enguialès, Leucamp, Puy-les-Vignes and St-Mélany deposits, fall into the field of the FMC granites, which are characterized by $^{206}Pb/^{204}Pb$, $^{207}Pb/^{204}Pb$ and $^{208}Pb/^{204}Pb$ values, ranging in 18.0 – 18.9, 15.6 – 15.7 and 38.1 – 38.8, respectively (Michard-Vitrac et al., 1981; Brevart et al., 1982; Le Guen et al., 1991; Sinclair et al., 1993; Downes et al., 1997).

Samples with higher $^{206}Pb/^{204}Pb$ values (BOS3c and CFM-16; Fig. 13) fall on the same evolution trend, but may have acquired their more radiogenic composition in the time gap between granite emplacement and wolframite mineralization. The anomalously high initial $^{206}Pb/^{204}Pb$ value of quartz from the St-Goussaud deposit (sample BOS3c; Table 2) indicates that the fluid, which precipitated the wolframite, was derived from a source that had a high μ-value. As the initial $^{208}Pb/^{204}Pb$ value of quartz falls in the same range as all other samples, the source of this Pb must have had a very low ω-value. Possible sources for such Pb could be U-rich organic-rich shales or granitic rocks that have assimilated important proportions of such organic-rich sediments or that contain U-rich minerals (e.g., uraninite). The second hypothesis

is highly likely since the St-Goussaud deposit is hosted in the eastern part of the Brâme-St-Sylvestre peraluminous leucogranitic complex, which is composed of multiple U-rich granitic intrusions with 10 - 30 ppm U in average and up to 60 ppm U in the most differentiated facies (Cuney et al., 1990). Leaching of such rocks would mobilize not only Pb with similar fingerprints as found in the quartz-vein from St-Goussaud, but would also mobilize U. Late remobilization of magmatic U pre-concentrations at the Stephanian to Permian transition (290-270 Ma), eventually forming important vein-type U districts, have been documented for the FMC (Cathelineau et al., 1990), the Armorican Massif (Ballouard et al., 2017), the Erzgebirge (Förster et al., 2008) and the Fichtelgebirge (Förster, 2010). The Pb isotopic composition of quartz from the Vaulry deposit (sample CFM-16; Table 2), which is hosted in the Blond peraluminous leucogranite, may be explained in a similar way by involving the leaching from U-rich country rocks (gneiss or granite). Furthermore, it should be noted that the Pb isotopic composition of quartz itself may represent a mixture of highly radiogenic Pb from the U-rich organic sediments or U-rich minerals in the granite (Pb isotopes do not allow to distinguish between these two possibilities) and non-radiogenic Pb released from sulphides and feldspars that decomposed during metal mobilization. In conclusion, the contrasting $^{206}Pb/^{204}Pb$ values of quartz from St-Goussaud and Vaulry reflect different contributions of radiogenic and non-radiogenic Pb rather than different source rocks.

5.4. Metallogenic implications for the timing of Variscan W mineralization

Tin, tungsten, and tantalum mineralization are genetically closely related to similar source rocks and are commonly related to highly evolved peraluminous granitoids (e.g., Černý et al., 2005; Linnen and Cuney, 2005; Cuney and Barbey, 2014). However, these metals generally occur separated in time and space as they are mobilized in their source at different melting temperatures and transported by different complexes during hydrothermal processes, possibly under contrasting redox conditions (e.g., Heinrich, 1990; Wood and Samson, 2000; Linnen and Cuney, 2005). Lead isotope data (Fig. 13) show that Gondwana-derived sedimentary rocks represent an important source of W in the FMC. Chemically intensely weathered Cambrian sediments occurred throughout entire northern Gondwana (e.g., Noblet and Lefort, 1990) and were redeposited during Gondwana breakup to form voluminous early Ordovician sedimentary packages at the margin of major crustal blocks (Noblet and Lefort, 1990; Romer and Kroner, 2015, 2016). Partial melting and metal mobilization from these anomalously W-Sn-enriched sedimentary rocks is related to heat input from the mantle during

continental collision, nappe stacking, or post-orogenic crustal extension (Romer and Kroner, 2015, 2016). The complex structure of the Variscan orogen and the distribution of geochemically diverse granitoids and associated Sn-W deposits (Fig. 3a) are the result of the distribution of crustal domains of contrasting rheological properties during the Variscan geodynamic evolution (Kroner and Romer, 2013). The obtained U-Pb wolframite ages from the FMC define three distinct geochronological groups in contrasting geodynamic settings during the orogenic evolution of the FMC (Fig. 14):

(i) The first group of wolframite, i.e. 334-327 Ma, obtained for the Echassières and St-Goussaud deposits falls in the same age as the widespread development of peraluminous Visean to Namurian granites (ca. 335-325 Ma) that are mainly emplaced in the northwestern part of the FMC (Limousin area) and are coeval with the syn-orogenic compression in the FMC (Faure et al., 2009 and references therein). This first episode of W mineralization is also coeval with the emplacement of the rare-element pegmatites in the Bohemian Massif (Fig. 3a) dated at ca. 333 ± 3 Ma and 325 ± 4 Ma (U-Pb on columbite-tantalite; Melleton et al., 2012), as well as the emplacement of the Argemela rare-metal granite in the Iberian Massif at ca. 326 ± 3 Ma (U-Pb on columbite-tantalite; Melleton et al., 2015).

(ii) The second group of wolframite ages, i.e. 317-315 Ma, including the Puy-les-Vignes, Montredon-Labessonnié and St-Mélany deposits, correspond to the onset of the late-orogenic extension of the internal zones of the Variscan belt (e.g., Faure et al., 2009; Le Carlier de Veslud et al., 2013). This second episode of W mineralization is contemporaneous with or followed by the emplacement of late Namurian to Westphalian (ca. 315-310 Ma) peraluminous leucogranite intrusions, such as the Blond granite, and the peraluminous high-phosphorous rare-metal granites and pegmatites in the FMC (Cuney et al., 2002; Melleton et al., 2015). This time interval corresponds to a late-orogenic extensional setting, potentially associated with the development of the granulite-facies metamorphism in the lower crust (Cuney and Barbey, 2014). It is also contemporaneous with the first intrusions of rare-metals pegmatites in the Iberian Massif at ca. 310 ± 5 Ma (U-Pb on columbite-tantalite; Melleton et al., 2015).

(iii) The third group of wolframite, i.e. 298-274 Ma, including the Vaulry, Leucamp and Enguialès deposits, falls into a period of post-orogenic extension, which is related to the reorganization of the plate movement between Gondwana and Laurussia and resulted in important heat input from the mantle (Kroner and Romer, 2013), as attested by widespread Permian volcanism and the emplacement of lamprophyres and vaugnerites dykes throughout the entire Variscan belt (e.g., Perini et al., 2004; von Seckendorff et al., 2004). This third

episode of W mineralization is synchronous with the emplacement of the last generation of rare-metal pegmatites in the Iberian Massif at ca. 301 ± 3 Ma (U-Pb on columbite-tantalite; Melleton et al, 2015) and occurs during the end of the formation of the Au±Sb deposits in the FMC (Bouchot et al., 2005). However, the youngest ages, falling in the range of 280-267 Ma within age uncertainty, obtained for the Enguialès and Leucamp deposits reflect likely the reopening of the U-Pb isotopic system after the wolframite crystallization and could be related to ferberitization episode(s) during late hydrothermal alteration. This time interval (290-270 Ma) corresponds also to the formation of major hydrothermal U vein-type deposits during the Permian (Cathelineau et al., 1990; Förster et al., 2008; Förster, 2010; Ballouard et al., 2017), related to the post-orogenic extension in the Variscan belt with the development of extensive rifting and volcanism (e.g., Praeg, 2004; McCann et al., 2006; McCann, 2008). The most important tin and tungsten mineralization of the Variscan belt, i.e., those of Cornwall, fall into this period (Chen et al. 1993; Romer and Kroner, 2015).

The U-Pb ages of wolframite crystallization obtained in this study (Fig. 14) range from 336 to 296 Ma within age uncertainty. They indicate that W mineralization in the FMC formed during several distinct hydrothermal episodes over a time range of at least 40 Ma and in contrasting geodynamic settings from remobilized Gondwana-derived rocks. Therefore, these results do not support models of a single late-Variscan tungsten metalliferous peak at ca. 300 Ma as previously proposed (e.g., Bouchot et al., 2005). This timing is similar to the one in other parts of the Variscan belt (Fig. 3a), such as the Erzgebirge in the Bohemian Massif, where tin mineralization fall in two age groups at 327-318 Ma and 305-290 Ma (e.g., Förster and Romer, 2010; Romer and Kroner, 2015) and the Iberian Massif, where granitic magmatism with mineralization fall in the ranges 320-310 Ma and 305-290 Ma (e.g., Neiva et al., 2012; Costa et al., 2014). Our data show a clear temporal relation between the formation of W mineralization and the emplacement of large peraluminous granites in different geodynamic settings ranging from syn-collisional compression to post-orogenic extension. Our results demonstrate that wolframite mineralization in the FMC was polyphase, (i) supporting the claim of Marignac and Cuney (1999) that W mineralization was distinctly non-contemporaneous eventhough it formed under similar conditions, and (ii) closely corresponding to the suggestion of Romer and Kroner (2015, 2016) that distinct phases and styles of tin, tungsten, and tantalum mineralization reflect changes in the tectono-metamorphic evolution of the Variscan belt with time.

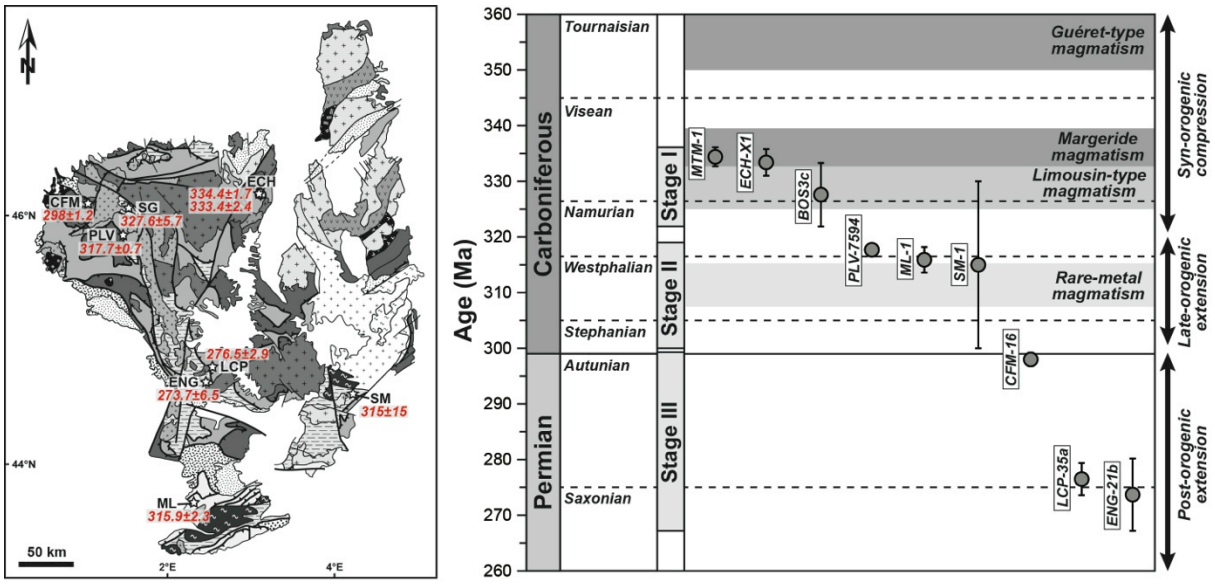

Fig. 14: Synthesis of the U-Pb ages of wolframite obtained in this study and comparison with the ages of the main tectono-metamorphic and magmatic episodes in the French Massif Central (Faure et al., 2009 and references therein). Subdivisions for the Carboniferous and Permian timescales are from McCann (2008).

6. Conclusions

This integrated study of wolframite combining mineralogical observations, chemical composition analyses of major elements, *in situ* LA-ICPMS analyses of U and Pb isotopes, U-Pb TIMS analyses and X-ray computed tomography (CT) has allowed: (i) to investigate the U-Pb isotope systematics of wolframite and its suitability for U-Pb dating; and (ii) to determine the timing of W mineralization in the FMC and the temporal relations with the different phases of granitic magmatism and the geodynamic evolution of the Variscan belt. The main results obtained in this study are:

1. Although wolframite is a stable mineral over a large range of P-T conditions in magmatic and hydrothermal settings, the U-Pb isotope system may be disturbed by late fluid-mineral interactions. These fluid events may result in hydrothermal alteration of wolframite and replacement by secondary minerals (e.g., ferberite, scheelite) or may induce recrystallization and redistribution of U and Pb within the crystalline structure of wolframite. Wolframite with such secondary features are not suited for dating as their U-Pb system(s) record several events. Combining BSE imagery and LA-ICPMS analyses allows to identify samples that record only one event and, therefore, are suitable for U-Pb dating.

2. Micro-inclusions within wolframite may be a severe issue, in particular if these minerals are not cogenetic with the host wolframite and carry their own U-Pb system. Such

mixed systems may yield incorrect ages that may reflect the formation of the micro-inclusions rather than the time of host formation. For instance, scheelite, ferberite and sulphides may contain higher U and/or Pb than wolframite. Even if micro-inclusions do not appear important in BSE images, their proportions may be under-estimated at the scale of the grain volume. CT seems to be a powerful method to quantify the relative proportions and to characterize the spatial distribution of micro-inclusions within wolframite. Its use appears as an efficient and timesaving technique in order to select samples without micro-inclusions, which may be suitable for the U-Pb TIMS dating.

3. Uranium content in wolframite from the FMC is variable, both on the scale of individual crystals as well as on the regional scale. Although U may be incorporated in wolframite through several possible mechanisms, the low U content in wolframite from the FMC seems to reflect the limited availability of U in the hydrothermal fluids during the precipitation of W. Thus, whether wolframite has a high $^{238}U/^{204}Pb$ at the time of crystallization and, thus, is suitable for U-Pb dating, may largely depend on the redox conditions of the hydrothermal fluid.

4. The initial Pb isotope composition of vein minerals (quartz, scheelite, pyrite) closely associated with wolframite in the same sample show regional variability reflecting different fluid sources and indicating that Gondwana-derived rocks (high $^{207}Pb/^{204}Pb$ at a given $^{206}Pb/^{204}Pb$) represent an important source of W in the FMC. The Pb isotope compositions of the different deposits are not correlated with the age of wolframite, but reflect the lithological variability of the Pb source materials in the nappe pile of the FMC.

5. The U-Pb ages obtained for wolframite from the FMC fall in three distinct groups in constrating geodynamic settings: (i) Visean to Namurian mineralization (333-327 Ma) is coeval with the syn-orogenic compression and the emplacement of peraluminous Visean to Namurian granites (ca. 335-325 Ma); (ii) Namurian to Westphalian mineralization (317-315 Ma) is synchronous with the onset of late-orogenic extension of the internal zones of the Variscan belt and contemporaneous with the emplacement of late Namurian to Westphalian granites (ca. 315-310 Ma); and (iii) Stephanian to Permian mineralization (ca. 298-274 Ma) formed during a period of post-orogenic extension in the Variscan belt. The youngest ages (ca. 276-274 Ma) reflect likely reopening of the U-Pb isotopic system of wolframite during a late fluid event and may be related to a hydrothermal alteration process, such as ferberitization. Consequently, these results demonstrate that W mineralization in the FMC was polyphase, over a time range of at least 40 Ma, reflecting changes in the tectono-metamorphic evolution of the Variscan belt.

Acknowledgements

This work was supported by the French National Research Agency through the national program "Investissements d'avenir" of the Labex Ressources 21 with the reference ANR-10-LABX-21-RESSOURCES21. The authors would like to thank Dr Michel Cathelineau, Dr Bernard Mouthier, Dr Hossein Ahmadzadeh, and the Musée Minéralogique de l'Ecole des Mines d'Alès (France) for supplying some of the wolframite samples. We would like also to thank Sandrine Mathieu, Dr Andreï Lecomte and Dr Chantal Peiffert (GeoRessources, Vandœuvre-lès-Nancy, France) for technical support in providing analytical data with SEM and LA-ICPMS analyses.

Table 1: Major element composition (wt.%) for selected wolframite from the French Massif Central.

Sample	**Vaulry *(CFM16)***					**St-Goussaud *(BOS3c)***					**Puy-les-Vignes *(PLV-7594)***				
	1	2	3	4	5	1	2	3	4	5	1	2	3	4	5
FeO	16.7	16.4	16.7	16.6	16.1	18.0	18.2	19.2	17.8	18.3	18.6	18.8	18.2	18.3	17.6
MnO	6.99	6.32	6.57	6.46	6.77	5.29	5.07	4.85	5.78	5.59	3.79	3.82	3.67	3.71	3.61
MgO	0.00	0.00	0.00	0.00	0.00	0.00	0.00	0.00	0.00	0.00	0.57	0.73	0.58	0.67	0.61
WO_3	77.6	76.7	77.3	77.8	77.4	77.2	77.9	78.2	77.9	76.8	76.8	76.8	76.6	76.0	75.3
Total	101.3	99.4	100.5	100.9	100.2	100.4	101.1	102.2	101.6	100	99.8	100.1	99.1	98.7	97.2

Sample	**La Bosse *(ECH-X1)***					**Les Montmins *(MTM-1)***					**Leucamp *(LCP-35a)***				
	1	2	3	4	5	1	2	3	4	5	1	2	3	4	5
FeO	17.7	18.4	18.2	18.3	17.8	19.0	18.6	18.2	18.9	18.8	18.5	19.5	18.0	18.9	18.9
MnO	4.82	4.92	4.51	4.73	4.80	4.61	4.46	4.41	4.64	4.61	3.86	3.12	4.65	2.61	2.92
MgO	0.00	0.00	0.00	0.00	0.00	0.00	0.00	0.00	0.00	0.00	0.62	0.54	0.00	0.00	0.56
WO_3	76.2	76.6	74.2	76.7	76.6	77.7	76.4	76.7	76.6	76.0	77.0	77.1	76.0	75.9	75.7
Total	98.7	99.9	96.9	99.8	99.2	101.4	99.4	99.3	100.1	99.4	100.0	100.2	98.6	97.4	98.1

Sample	**Enguialès *(ENG-21b)***					**St-Mélany *(SM-1)***					**Montredon-Labessonnié *(ML-1)***				
	1	2	3	4	5	1	2	3	4	5	1	2	3	4	5
FeO	16.5	16.3	16.1	15.9	16.0	15.1	14.0	15.1	13.8	14.4	13.8	12.8	13.2	14.0	13.3
MnO	6.67	6.96	6.62	6.38	6.23	8.55	9.29	8.45	8.82	9.19	9.37	9.15	9.71	9.16	9.38
MgO	0.00	0.00	0.00	0.00	0.00	0.00	0.00	0.00	0.00	0.00	0.00	0.00	0.00	0.00	0.00
WO_3	76.7	75.8	76.1	75.2	75.5	74.2	75.0	73.9	75.3	74.4	75.0	76.0	75.3	76.3	75.4
Total	99.8	99.0	98.8	97.5	97.8	97.9	98.3	97.4	97.8	98.0	98.2	98.0	98.2	99.5	98.0

Table 2: Lead isotope composition of vein minerals for the selected tungsten deposits from the French Massif Central.

Sample[a]		Pb[b] ppm	U[b] ppm	$^{206}Pb/^{204}Pb$[c]	$^{207}Pb/^{204}Pb$[c]	$^{208}Pb/^{204}Pb$[c]	Initial $^{206}Pb/^{204}Pb$[d]	Initial $^{207}Pb/^{204}Pb$[d]
Vaulry *(CFM-16)*								
1	Quartz	0.12	2.13	20.030	15.702	38.596	19.60	15.68
St-Goussaud *(BOS3c)*								
2	Quartz	0.07	4.90	28.338	16.072	38.567	26.50	15.97
Puy-les-Vignes *(PLV-7594)*								
3	Pyrite	21.9	2.01	18.573	15.671	38.756	18.57	15.67
Echassières *(ECH-X1)*								
4	Quartz	0.18	0.20	17.885	15.571	37.826	17.86	15.57
Leucamp *(LCP-35a)*								
5	Quartz (a)	0.66	1.15	17.987	15.604	37.992	17.89	15.56
6	Quartz (b)	0.34	0.004	18.399	15.621	38.421	18.36	15.62
7	Pyrite	9.33	78.0	18.485	15.681	38.858	18.27	15.67
9	Scheelite	43.9	312	18.375	15.655	38.540	18.22	15.65
Enguialès *(ENG-21b)*								
9	Quartz (a)	0.26	3.38	18.588	15.693	38.549	18.28	15.68
10	Quartz (b)	0.15	0.001	18.139	15.631	38.316	18.12	15.63
11	Scheelite	12.4	127	18.490	15.671	38.410	18.26	15.66
St-Mélany *(SM-1)*								
12	Quartz	0.03	0.09	18.258	15.590	38.037	18.15	15.57
13	Pyrite	41.4	3.58	18.324	15.671	38.535	18.23	15.60
Montredon-Labessonnié *(ML-1)*								
14	Quartz	0.02	0.03	24.049	15.839	38.028	18.56	15.55

[a] All samples are from quartz-wolframite veins.

[b] Concentrations of Pb and U were determined by isotope dilution using a mixed ^{205}Pb-^{235}U tracer.

[c] Lead isotope analyses were performed at GFZ German Research Centre for Geosciences, Potsdam, Germany, using a TRITON multi-collector mass-spectrometer. The lead isotopic composition is corrected for mass discrimination with 0.1%/a.m.u. 2σ reproducibility is better than 0.1%. For details see text.

[d] Determined from $^{206}Pb/^{238}U$ and $^{207}Pb/^{235}U$ values for an age of 300 Ma.

Table 3: U-Pb analytical results for high-radiogenic wolframite from the French Massif Central.

Sample	Weight (mg)	Concentrations[a] (ppm)		Measured ratios[b]				Atomic ratios[c]				Apparent ages (Ma)[d]		
		U	Pb	$^{206}Pb/^{204}Pb$	$^{207}Pb/^{204}Pb$	$^{208}Pb/^{204}Pb$	$^{238}U/^{204}Pb$	$^{206}Pb/^{238}U$	$^{207}Pb/^{235}U$	$^{207}Pb/^{206}Pb$	Rho[d]	$^{206}Pb/^{238}U$	$^{207}Pb/^{235}U$
Vaulry *(CFM-16)*													
CFM-16_a	2.887	1.36	0.29	34.80	16.48	39.55	361	0.04211	0.3088	0.0531	0.15	265.9 ± 3.8	273.3 ± 19.7
CFM-16_b	2.939	1.52	0.26	43.77	16.95	38.88	512	0.04724	0.3436	0.0528	0.29	297.6 ± 3.3	299.9 ± 17.7
CFM-16_c	1.348	1.79	1.27	22.93	15.88	38.90	96	0.03480	0.3043	0.0627	0.38	220.8 ± 14.8	269.8 ± 135
CFM-16_d	1.165	0.88	0.11	58.53	17.83	39.85	818	0.04760	0.3639	0.0554	0.27	299.7 ± 2.3	315.1 ± 28.9
CFM-16_e	0.983	1.54	0.61	29.04	16.15	39.63	186	0.05080	0.3576	0.0510	0.25	319.5 ± 7.1	310.5 ± 46.5
CFM-16_f	1.390	3.92	0.31	96.69	19.66	31.11	1624	0.04748	0.3388	0.0517	0.27	299.0 ± 1.8	296.2 ± 16.0
CFM-16_g	1.027	0.92	0.34	31.22	16.26	57.66	249	0.04665	0.3271	0.0508	0.25	293.9 ± 5.5	287.4 ± 36.5
CFM-16_h	1.243	0.86	0.12	49.60	17.33	39.22	641	0.04681	0.3569	0.0553	0.35	294.9 ± 3.1	309.9 ± 28.0
St-Goussaud *(BOS3c)*													
BOS3c_a	2.340	5.77	1.95	44.10	16.63	38.86	257	0.07094	0.3656	0.0372	0.71	441.8 ± 71.2	316.4 ± 75.6
BOS3c_b	2.607	7.94	2.96	39.50	16.48	38.77	222	0.05914	0.3184	0.0390	0.54	370.4 ± 4.5	280.7 ± 36.7
BOS3c_c	1.245	5.99	1.99	39.66	16.51	38.74	249	0.05337	0.3022	0.0410	0.57	335.2 ± 4.1	268.1 ± 36.9
BOS3c_d	1.221	4.31	2.15	37.25	16.40	38.69	161	0.06744	0.3733	0.0401	0.29	420.7 ± 5.3	322.2 ± 39.4
BOS3c_e	1.319	5.80	1.29	47.54	16.83	38.98	404	0.05244	0.2954	0.0409	0.19	329.5 ± 2.2	262.8 ± 15.4
BOS3c_f	1.199	6.44	1.87	38.16	16.43	38.62	280	0.04206	0.2264	0.0390	0.26	265.6 ± 3.1	207.2 ± 25.1
BOS3c_g	1.845	4.60	1.19	44.02	16.73	38.71	333	0.05299	0.3162	0.0433	0.43	332.9 ± 11.3	278.9 ± 22.8
BOS3c_h	1.390	8.03	3.08	37.23	16.33	38.72	210	0.05160	0.2351	0.0330	0.57	324.4 ± 5.0	214.4 ± 50.0
Puy-les-Vignes *(PLV-7594)*													
PLV-7594_a	1.031	1.70	0.14	109.96	20.43	38.53	1829	0.05010	0.3642	0.0527	0.35	315.2 ± 1.5	315.4 ± 6.1
PLV-7594_b	1.022	1.50	0.17	67.35	18.08	38.10	940	0.05218	0.3633	0.0504	0.21	327.9 ± 6.1	314.7 ± 73.3
PLV-7594_c	1.009	1.77	0.12	154.17	22.87	39.06	2684	0.05057	0.3703	0.0531	0.47	318.0 ± 1.6	319.8 ± 7.6
PLV-7594_d	0.824	1.71	0.13	130.16	21.50	38.52	2194	0.05089	0.3668	0.0523	0.40	320.0 ± 4.1	317.2 ± 12.5
PLV-7594_e	0.919	1.80	0.16	87.12	19.28	38.79	1380	0.04990	0.3680	0.0534	0.29	312.8 ± 1.4	313.3 ± 8.7
PLV-7594_f	0.903	1.78	0.16	91.90	19.52	38.33	1439	0.05090	0.3687	0.0525	0.31	320.1 ± 1.7	318.7 ± 8.1
PLV-7594_g	1.107	1.76	0.13	134.75	21.74	38.29	2301	0.05049	0.3638	0.0523	0.23	317.5 ± 1.0	315.0 ± 3.2
PLV-7594_h	1.333	1.44	0.11	131.50	21.56	38.38	2239	0.05045	0.3629	0.0522	0.48	317.3 ± 1.9	314.3 ± 3.5
PLV-7594_i	0.940	1.69	0.14	103.20	20.10	38.61	1679	0.05041	0.3638	0.0523	0.33	317.0 ± 1.4	315.0 ± 9.4

Table 3: Continued.

La Bosse *(ECH-X1)*												
ECH-X1_a	1.636	36.0	4.20	66.36	18.18	38.51	916	0.05295	0.3937	0.0539	0.43	332.6 ± 1.8	337.0 ± 8.3
ECH-X1_b	1.038	70.6	9.56	56.18	17.67	38.72	723	0.05301	0.4011	0.0549	0.32	332.9 ± 1.7	342.5 ± 9.7
ECH-X1_c	1.709	56.7	20.6	29.38	16.23	38.42	202	0.05487	0.4321	0.0571	0.10	344.4 ± 4.1	364.7 ± 28.3
ECH-X1_d	1.103	69.2	41.1	24.06	15.95	38.39	115	0.04982	0.4172	0.0607	0.06	313.4 ± 5.5	354.1 ± 50.2
ECH-X1_e	1.599	36.2	4.88	56.86	17.70	38.54	729	0.05347	0.4027	0.0546	0.40	335.7 ± 1.9	343.5 ± 10.2
ECH-X1_f	1.215	54.6	24.5	28.40	16.19	38.45	161	0.06244	0.4987	0.0579	0.09	390.4 ± 4.2	410.8 ± 34.1
Les Montmins *(MTM-1)*												
MTM-1_a	2.635	16.6	1.24	132.91	21.73	38.84	2249	0.05096	0.3755	0.0534	0.43	320.4 ± 1.5	323.7 ± 3.5
MTM-1_b	2.516	51.4	6.50	60.16	17.86	38.68	802	0.05277	0.3946	0.0542	0.21	331.5 ± 1.6	337.7 ± 7.9
MTM-1_c	1.202	5.79	0.87	50.76	17.36	38.66	620	0.05311	0.3996	0.0546	0.50	333.6 ± 6.5	341.3 ± 12.6
MTM-1_d	1.557	68.3	7.40	73.83	18.58	38.69	1050	0.05329	0.3956	0.0538	0.27	334.7 ± 1.4	338.4 ± 6.2
MTM-1_e	1.559	5.51	0.87	51.83	17.43	36.66	596	0.05629	0.4234	0.0545	0.17	353.0 ± 1.8	358.5 ± 11.0
MTM-1_f	1.490	8.53	1.06	65.00	18.13	38.76	855	0.05463	0.4085	0.0542	0.34	342.9 ± 1.9	347.8 ± 12.2
MTM-1_g	1.294	12.4	1.30	77.60	18.80	38.78	1115	0.05358	0.3999	0.0541	0.28	336.4 ± 2.0	341.6 ± 12.4
MTM-1_h	1.295	5.79	0.89	49.64	17.32	38.67	593	0.05362	0.4062	0.0549	0.26	336.7 ± 1.9	346.1 ± 14.3
Montredon-Labessonnié *(ML-1)*												
ML-1_a	2.703	3.74	0.41	61.90	17.98	38.85	944	0.04590	0.3549	0.0561	0.21	289.3 ± 1.6	308.4 ± 7.4
ML-1_b	2.519	8.40	0.21	278.17	29.32	38.83	11937	0.02177	0.1585	0.0528	0.63	138.8 ± 9	149.4 ± 1.5
ML-1_c	1.302	3.75	0.26	151.34	22.59	38.77	2644	0.05023	0.3673	0.0530	0.48	315.9 ± 2.3	317.6 ± 4.7
ML-1_d	1.419	4.58	0.38	83.63	19.22	36.73	1466	0.04438	0.3452	0.0564	0.33	279.9 ± 2.5	301.1 ± 14.8
ML-1_e	1.559	5.16	1.20	31.43	16.08	36.18	315	0.04173	0.2117	0.0341	0.75	263.6 ± 18.9	195 ± 281
ML-1_f	1.554	3.40	0.86	31.32	16.29	38.57	298	0.04280	0.3405	0.0577	0.29	270.2 ± 5.1	297.6 ± 31.2
ML-1_g	2.053	3.49	0.25	113.78	20.68	39.04	2031	0.04690	0.3483	0.0539	0.32	295.5 ± 2.1	303.4 ± 9.1
ML-1_h	1.482	2.19	0.33	47.66	17.26	38.88	594	0.04898	0.3955	0.0586	0.38	308.3 ± 1.9	338.4 ± 20.7

[a] Concentrations of Pb and U were determined by isotope dilution using a mixed ^{205}Pb-^{235}U tracer.

[b] Isotope ratios corrected for fractionation and isotopic tracer.

[c] Corrected for fractionation, 15 pg Pb blank, 1 pg U blank, isotopic tracer, and initial lead. The initial lead values were determined from lead isotopes composition of vein minerals (quartz, pyrite or scheelite) associated with the wolframite (see Table 2).

[d] Apparent ages were calculated using the decay constants recommended by IUGS (Steiger and Jäger, 1977). Uncertainties at 2σ level were calculated using Monte-Carlo modeling as described in Schmid et al. (2003). Rho = correlation between errors of $^{206}Pb/^{238}U$ and $^{207}Pb/^{235}U$ values.

Table 4: U-Pb analytical results for low-radiogenic wolframite from the French Massif Central.

Sample	Weight (mg)	Concentrations[a] (ppm)		Measured ratios[b]			
		U	Pb	$^{206}Pb/^{204}Pb$	$^{207}Pb/^{204}Pb$	$^{208}Pb/^{204}Pb$	$^{238}U/^{204}Pb$
Leucamp *(LCP-35a)*							
LCP-35a_a	1.300	1.63	0.57	27.46	16.10	38.33	205
LCP-35a_b	0.846	1.40	1.50	21.06	15.76	38.34	61.2
LCP-35a_c	0.776	1.99	0.91	24.92	16.00	38.48	152
LCP-35a_d	1.400	1.79	0.45	31.52	16.37	38.49	300
LCP-35a_e	2.977	1.28	0.35	26.17	16.00	38.35	259
Enguialès *(ENG-21b)*							
ENG-21b_a	0.817	13.7	3.21	25.18	16.01	38.56	298
ENG-21b_b	1.675	1.62	1.35	21.49	15.81	38.59	80
ENG-21b_c	1.726	1.46	1.16	21.83	15.81	38.54	84
ENG-21b_d	1.181	1.13	0.82	22.53	15.80	38.38	92.5
ENG-21b_e	1.221	1.56	2.06	20.26	15.72	38.50	49.5
ENG-21b_f	2.073	3.03	5.40	19.79	15.71	38.54	36.4
St-Mélany *(SM-1)*							
SM-1_a	2.378	10.4	7.68	22.75	15.90	38.53	91.2
SM-1_b	2.769	5.68	28.3	18.91	15.68	38.46	12.8
SM-1_c	1.507	9.67	12.0	20.79	15.84	38.72	53.2
SM-1_d	1.156	9.90	16.6	20.22	15.76	38.50	39.0
SM-1_e	1.109	7.05	11.7	20.24	15.76	38.44	39.4
SM-1_f	1.367	7.44	15.0	19.93	15.76	38.54	32.2

[a] Concentrations of Pb and U were determined by isotope dilution using a mixed ^{205}Pb-^{235}U tracer.

[b] Isotopic ratios corrected for fractionation, 15 pg Pb blank, 1 pg U blank, isotopic tracer, and initial lead with $^{206}Pb/^{204}Pb$=18.3; $^{207}Pb/^{204}Pb$=15.6 and $^{208}Pb/^{204}Pb$=38.0. Uncertainties at 2σ level were calculated using Monte-Carlo modeling as described in the text. Rho = correlation between errors of $^{206}Pb/^{238}U$ and $^{207}Pb/^{235}U$ values.

Chapter 2: LA-ICPMS analysis of minor and trace elements in wolframite: geochemical fingerprinting of Variscan tungsten deposits from the French Massif Central

Abstract

Wolframite is the main ore mineral in hydrothermal tungsten deposits and may represent a potential carrier of critical high-technology metals, such as Nb, Ta, Sc and REE. Determining the trace elements compositions of wolframite may allow both to establish geochemical fingerprints of tungsten deposits for mineral exploration and to characterize the composition of the mineralizing fluids to better understand the fluid sources. This work focuses on the LA-ICPMS analyses of minor and trace elements in wolframite from several hydrothermal W±Sn deposits located in the French Massif Central (FMC). Preliminary study on homogeneous wolframite crystals from the Maoping deposit (China) allowed demonstrating the absence of significant matrix effects during LA-ICPMS analysis of wolframite. Wolframites from the selected samples revealed intra-crystalline variations in the trace element contents, principally in Nb, Ta and Sn, which reflect growth zoning during the crystallization of wolframite. Trace elements analysis of wolframite from the studied W deposits in the FMC show regional compositional variations characterized by variable enrichments and impoverishments in several elements compared to the upper continental crust. Four main regional groups of wolframite can be distinguished from the studied deposits: (i) Vaulry, St-Goussaud and St-Mélany; (ii) Enguialès, Leucamp and Puy-les-Vignes; (iii) Echassières (La Bosse and Les Montmins); and (iv) Montredon-Labessonnié. These regional geochemical signatures reflect variations in the composition of the hydrothermal fluids, thus suggesting that the trace element contents in wolframite represent direct markers of the source of the fluids. Incorporation of some trace elements, such as the REE, appears strongly controlled at the first order by the crystallochemistry of wolframite. Comparison of the trace elements signatures of the wolframites from the FMC show several similarities with the compositions of evolved granites, suggesting that the wolframites crystallized from hydrothermal fluids equilibrated with evolved granites. However, the incorporation of some elements (e.g., Zn, U, Mo) seem better explained by a contribution from shales. Finally, these results suggest that the wolframite compositions result from mixing sources.

Keywords:

Wolframite; French Massif Central; tungsten deposits; LA-ICPMS; geochemical tracing.

1. Introduction

Since *in situ* micro-analyses are possible, it appears that the analysis of minor and trace elements in ore minerals represents a major challenge in economic geology both to understand metallogenic processes and to develop genetic models (e.g., Mercadier et al., 2011; Belissont et al., 2014) or to define geochemical fingerprinting of mineral deposits for mineral exploration (e.g., Belousova et al., 2002; Dupuis and Beaudoin, 2011; Nadoll et al., 2014) and for metal ores traceability studies (e.g., Gäbler et al., 2013; Melcher et al., 2015). In the case of hydrothermal deposits, determining the trace elements composition of ore minerals is particularly helpful to constrain the nature of the fluids and the source of the metals (e.g., Jiang et al., 2004), to study the partitioning of the metals between co-crystallized mineral phases (e.g., George et al., 2016) or to understand the temporal evolution of an hydrothermal system (e.g., Genna and Gaboury, 2015). Wolframite ([Fe,Mn]WO_4) represents the main ore mineral in hydrothermal tungsten deposits and may be a potential carrier of critical high-technology metals, such as Nb, Ta, Sc and REE. Some minor and trace elements data exist for Sn-W deposits that have been determined on cassiterite (Plimer et al., 1991; Guoliang and Zhixiong, 1994; Jiang et al., 2004; Neiva, 2008; Pavlova et al., 2015) and on wolframite (Tindle and Webb, 1989; Guoliang and Zhixiong, 1992; Kempe and Wolf, 2006; Goldmann et al., 2013). Nevertheless, few data remain currently available for the Variscan W deposits.

The improvement of this knowledge is mainly linked to the development of analytical techniques and reference standards for precise and accurate determination of *in situ* chemical composition of minerals. Most of these data are obtained from laser ablation - inductively coupled plasma - mass spectrometry (LA-ICPMS), which is currently one of the most suitable analytical methods for trace elements analysis due to its high sensitivity, speed and multi-element capabilities (Heinrich et al., 2003). LA-ICPMS analyses require the availability and the use of external standards for calibration in order to overcome matrix effects that may result from elemental fractionation during laser sampling, aerosol transport or plasma ionization (Sylvester, 2008; Günther and Koch, 2008). Non-matrix-matched calibration may seriously compromise quantification of the signals and may result in inaccurate results if there are large differences in the chemical compositions between the sample analysed and the calibration material (Jackson, 2008; Klemme et al., 2008). In this respect, several homogeneous reference materials, mainly synthetic glasses, have been developed to have a matrix matching as close as possible to the sample to be analysed, both chemically and physically (Jochum and Stoll, 2008).

LA-ICPMS analysis of wolframite is currently limited by the lack of available homogeneous matrix-matched tungstate reference standard. Previously published LA-ICPMS studies of tungstate minerals have been done using silicate NIST glasses as external calibration standard and have shown in part the existence of matrix effects (Sylvester and Ghaderi, 1997; Goldmann et al., 2013). Matrix effects in wolframite using a NIST glass as calibration standard are suspected for two reasons: (i) tungsten has the highest melting temperature of all the metals at 3,422°C; (ii) it represents 60% in mass of the wolframite matrix. Consequently, laser ablation of wolframite using commercially available nanosecond pulse laser systems may yield to incomplete melting and vaporization at the ablation site, resulting in different particle size and density distribution and therefore variable count rates compared to the ablation of a NIST glass. Therefore, it is critical to investigate matrix effects during LA-ICPMS analysis of wolframite, which supposes the development of a matrix-matched external standard. There are two possibilities to develop a standard using either a synthesized material (glass, mineral) or a natural sample. Hydrothermal synthesis of wolframite may lead to homogeneous samples in composition, but is limited by the size of the crystals formed and by the technical considerations. Previous studies on hydrothermal synthesis of wolframite did not considered the incorporation of minor or trace elements (Hsu, 1981; Buhl and Willgallis, 1985; Sakharkar et al., 1997). At the opposite, natural crystals of wolframite are commonly large in size but are generally heterogeneous in composition showing most of the time evidence of intra-crystalline zoning and replacement by secondary mineral phases (e.g., Nakashima et al., 1986; Campbell and Petersen, 1988; Polya, 1988; Tindle and Webb, 1989; Pačevski et al., 2007; Ferenc and Uher, 2007; Neiva, 2008; Llorens and Moro, 2012). In both cases, the main difficulty remains to obtain one homogeneous sample containing a wide range of measurable trace elements and with an adequate size for multiple *in situ* analyses.

The aim of this study is to characterize the trace elements composition of wolframite from several hydrothermal tungsten deposits in the French Massif Central (FMC) in order to compare the regional geochemical fingerprints and to trace the potential sources of the metals at the regional scale. In this objective, a natural crystal of wolframite from the Maoping W-Sn deposit (China) has been used as matrix-matched external standard in order to investigate the matrix effects during LA-ICPMS analysis of wolframite by comparing the standardization procedure with a silicate NIST glass standard.

2. Materials and analytical methods

2.1. Wolframite samples

In order to investigate the matrix effects during LA-ICPMS analysis of wolframite, three natural crystals of wolframite (MAO-1, MAO-2, MAO-3) were selected from the world-class Maoping W-Sn deposit (Jiangxi Province, China; detailed description in Feng et al., 2011 and Legros et al., 2016). These wolframite samples were selected because: (i) they show no visible surface alteration or mineral overgrowths; (ii) they show homogeneous internal textures when observed under optical and electron microscope; (iii) they have homogeneous chemical composition for major elements (W, Fe, Mn). Therefore, these samples represent good candidates as reference materials to investigate the matrix effects during LA-ICPMS analysis of wolframite. An individual crystal (MAO-1) of centimetre-size wolframite, that do not show evidence of surface alterations or cracks, was handpicked and cut in two equal parts. The first part was sent for whole-rock bulk analysis of major, minor and trace elements. The second part was mounted in epoxy resin with the other samples (MAO-2, MAO-3) and then polished for mineralogical and geochemical analysis. Wolframite samples from several tungsten deposits from the FMC were also selected for LA-ICPMS analysis. Samples were collected from eight deposits located in different areas: Vaulry (CFM-16), St-Goussaud (BOS3c), Echassières (ECH-X1, MTM-1), Puy-les-Vignes (PLV-7594), Leucamp (LCP-35a), Enguialès (ENG-21a), St-Mélany (SM-1) and Montredon-Labessonnié (ML-1). The regional geology and the description of each deposit are presented in Chapter 1. Besides this regional study, seven wolframite samples coming from the Puy-les-Vignes deposit were also selected. These samples come from several underground levels in the old Puy-les-Vignes mine (now inaccessible) from the surface down to 300 m at depth, allowing to search for a possible depth-composition relationship of the wolframites. Thick sections of wolframite crystals from each deposit were prepared for mineralogical and geochemical analysis in order to characterize the internal texture and the chemistry of wolframites.

2.2. Preliminary SEM and EMPA analysis

Preliminary analyses of the wolframite samples were carried out using a scanning electron microscope (SEM) and an electron microprobe analyzer (EMPA) at the GeoRessources laboratory (Université de Lorraine, Vandœuvre-lès-Nancy, France).

Mineralogical and textural observations were performed using a Jeol J7600F SEM equipped with a SDD-type EDS spectrometer coupled to an Oxford Wave WDS spectrometer. Backscattered electron (BSE) images were obtained on polished thick sections with an acceleration voltage of 15 kV. Internal texture of wolframite crystals was first investigated to identify the eventual presence of internal zoning, micro-inclusions, replacement phases or exsolution evidences and to select homogeneous areas in the samples for further geochemical analysis. Automated X-ray mapping of a wolframite crystal was performed using a FEI QEMSCAN Quanta 650F facility at the Department of Earth and Environment Sciences from the University of Geneva (Switzerland). Measurements were performed on the carbon-coated thick section at high vacuum conditions using an acceleration voltage of 25 kV and probe current of 10 nA. The X-ray acquisition time was 10 ms per pixel with a point-spacing of 2.5 μm.

Major and minor element composition of wolframite was determined using a Cameca SX100 EMPA equipped with five WDS spectrometers. Major elements (W, Fe, Mn) were measured with an acceleration voltage of 20 kV and a beam current of 20 nA with counting times of 10 s on element peak and 5 s on background. Minor elements (Sc, Ti, Nb, Sn, Ta) were measured with an acceleration voltage of 25 kV and a beam current of 100 nA with counting times of 100 s on element peak and 30 s on background. The following elements, monochromators, standards and limits of detection were used for the measurements: W Lα (LIF, $CaWO_4$, 4200 ppm), Fe Kα (LIF, Fe_2O_3, 1200 ppm), Mn Kα (LIF, $MnTiO_3$, 1300 ppm), Sc Kα (PET, Sc, 120 ppm), Ti Kα (LPET, $MnTiO_3$, 40 ppm), Nb Lα (LPET, Nb, 300 ppm), Sn Lα (PET, SnO_2, 330 ppm) and Ta Lα (LIF, Ta, 400 ppm). Analytical error was < 1% for the element measured. Chemical compositions are expressed in weight per cent oxides (wt.%). Structural formulae of wolframite were calculated on the basis of 4 atoms of oxygen.

2.3. Geochemical whole-rock analysis

Bulk composition of wolframite sample MAO-1 was determined at the SARM-CRPG-CNRS (Vandœuvre-lès-Nancy, France). The selected crystal was first crushed in an agate mortar and then grinded to get a powder below 80 μm in size. Samples of 5 to 10 mg were taken and melted with a mixture of lithium metaborate ($LiBO_2$) and boric acid (H_3BO_3). After quenching, samples are dissolved in HNO_3 0.5 M for overnight. Since tungsten may precipitate in solution after the complete dissolution of wolframite, all solutions were systematically checked visually for precipitates. In order to avoid contamination of the

instruments due to the high content of W, the solutions were diluted 10 times for trace elements analysis. Major elements were measured with a Thermo Fisher ICap 6500 ICP-OES and minor and trace elements with a Thermo Fisher X7 Q-ICPMS, following a well-established procedure (Carignan et al., 2001). The reference material IGS 25 (Lister, 1978) was also used as control standard for the analyses.

2.4. LA-ICPMS analysis

LA-ICPMS analyses were carried out at the GeoRessources laboratory (Université de Lorraine, Vandœuvre-lès-Nancy, France) using a Agilent 7500c quadrupole ICPMS coupled with a 193 nm GeoLas ArF Excimer laser (MicroLas, Göttingen, Germany). Analyses were done on homogeneous zones within wolframites, devoid of micro-defects or alteration, spotted after preliminary SEM and EMPA analyses. Laser ablation was performed with a constant 5 Hz pulse frequency and a constant fluence of 6 J/cm^2 by focussing the beam at the sample surface. Helium was used as carrier gas to transport the laser-generated particles from the ablation cell to the ICPMS and argon was added as an auxiliary gas via a flow adapter before the ICP torch. Typical flow rates of 0.5 L/min for He and 1 L/min for Ar were used. The certified reference materials NIST SRM 610, 612 and 614 (concentrations from Jochum et al., 2011) were used as external standards for calibration of all analyses and were analysed twice at the beginning and at the end for each set of samples, following a bracketing standardization procedure. The NIST SRM 610 was used as primary reference material for the quantification, whereas the NIST SRM 612 and 614 were used as control standards. LA-ICPMS calibration was optimized for highest sensitivity on an intermediate m/Q range, while maintaining Th/U ~ 1 and ThO/Th < 0.5%, as determined on NIST SRM 610.

Two analytical sessions of LA-ICPMS measurements were done:

(i) Analyses of the wolframite samples from Maoping (MAO-1, MAO-2, MAO-3) were firstly performed to investigate the matrix effects using the NIST SRM 610 and the sample MAO-1 as external standards. Ablation lines of 200 µm in length were analysed with a constant laser spot diameter of 60 µm and a speed of 2 µm/s. The following 40 isotopes were measured with a dwell time of 10 ms for each: ^{24}Mg, ^{45}Sc, ^{47}Ti, ^{53}Cr, ^{55}Mn, ^{57}Fe, ^{59}Co, ^{60}Ni, ^{63}Cu, ^{66}Zn, ^{69}Ga, ^{72}Ge, ^{89}Y, ^{90}Zr, ^{93}Nb, ^{95}Mo, ^{111}Cd, ^{115}In, ^{118}Sn, ^{139}La, ^{140}Ce, ^{141}Pr, ^{146}Nd, ^{147}Sm, ^{153}Eu, ^{157}Gd, ^{159}Tb, ^{163}Dy, ^{165}Ho, ^{166}Er, ^{169}Tm, ^{172}Yb, ^{175}Lu, ^{178}Hf, ^{181}Ta, ^{182}W, ^{208}Pb, ^{209}Bi, ^{232}Th and ^{238}U.

(ii) Analyses of the wolframite samples from the FMC were then done using the NIST

SRM 610 as external standard. Ablation lines of 120 μm in length were performed with a constant laser spot diameter of 60 μm with a speed of 2 μm/s. The following 45 isotopes were measured with a dwell time of 10 ms for each: ^{7}Li, ^{24}Mg, ^{45}Sc, ^{47}Ti, ^{51}V, ^{53}Cr, ^{55}Mn, ^{57}Fe, ^{59}Co, ^{60}Ni, ^{63}Cu, ^{66}Zn, ^{69}Ga, ^{72}Ge, ^{85}Rb, ^{88}Sr, ^{89}Y, ^{90}Zr, ^{93}Nb, ^{95}Mo, ^{111}Cd, ^{115}In, ^{118}Sn, ^{121}Sb, ^{139}La, ^{140}Ce, ^{141}Pr, ^{146}Nd, ^{147}Sm, ^{153}Eu, ^{157}Gd, ^{159}Tb, ^{163}Dy, ^{165}Ho, ^{166}Er, ^{169}Tm, ^{172}Yb, ^{175}Lu, ^{178}Hf, ^{181}Ta, ^{182}W, ^{208}Pb, ^{209}Bi, ^{232}Th and ^{238}U.

Data reduction and absolute quantification of signals were performed using the software StalQuant, developed at ETH Zürich, Switzerland (see details in Fricker, 2012). For all analyses of wolframite, ^{182}W was used as internal standard and its content was determined from EMPA analyses. Limits of detection (LOD) were calculated using the 2σ criterion detailed in Longerich et al. (1996).

3. Results

3.1. Matrix effects during LA-ICPMS analysis of wolframite

Chemical data for MAO-1 sample from SARM, EMPA and LA-ICPMS analyses are shown in Table 5. MAO-1 is characterized by major element composition close to the hübnerite pole with Fe/(Fe+Mg) values of 0.22 as determined by SARM and EMPA. Due to the dilution factor and the expected low concentrations of trace elements in wolframite, only nine elements have been detected by whole-rock analysis at the SARM. Nb, Sn and Sc are present as minor elements with respective concentrations of 197 ppm, 690 ppm and 426 ppm, whereas Ta and HREE (Dy, Ho, Er, Tm, Yb, Lu) are trace elements with concentrations ranging from 1 to 17 ppm (Table 5). The Nb content, as determined by EMPA analyses, shows large variations of 930 ± 453 ppm, due to the limited precision of the electron microprobe (Table 5). LA-ICPMS ablation lines within wolframite (Fig. 15) reveal no internal variations in major elements (W, Fe, Mn) and small variations in minor and trace elements (e.g., Sc, Nb, Ta, Ti, Sn, Zn). BSE imagery and EMPA profiles revealed homogeneous internal textures without the presence of internal zoning, micro-inclusions, replacement phases or exsolution evidences, indicating that the observed variations in minor and trace elements are likely related to intra-crystalline heterogeneity (e.g., growth zoning) during the crystallization of wolframite.

LA-ICPMS analysis of MAO-1 using the NIST 610 as external standard (Table 5) show that the analysed minor and trace elements are homogeneous within the sample, with

precisions ranging from 3 to 23% for all measured elements, excepted Ce (56%) and Th (47%). The concentrations calculated are in a very good agreement with the whole-rock bulk composition from SARM with accuracies ranging from -13 to 0.8% for Nb and HREE, whereas Sc, Sn and Ta appear largely under-estimated up to two orders of magnitude compared with the SARM values (Table 5, Fig. 16). The discrepancy between the Sc, Sn and Ta concentrations determined from SARM and LA-ICPMS may be due either to sample heterogeneity or to a disturbance during the wolframite dissolution and analysis at the SARM. As shown on LA-ICPMS spectra (Fig. 15), intra-crystalline variations are minor within wolframite and could not explain for differences of two orders of magnitude as for Sn and Sc (Table 5). Moreover, no isobaric interferences in LA-ICPMS may explain for under-estimated concentrations for Sn, Sc and Ta. Therefore, this difference of quantification for Sc and Sn seems better explained by an instrumental artefact during ICPMS measurements at the SARM.

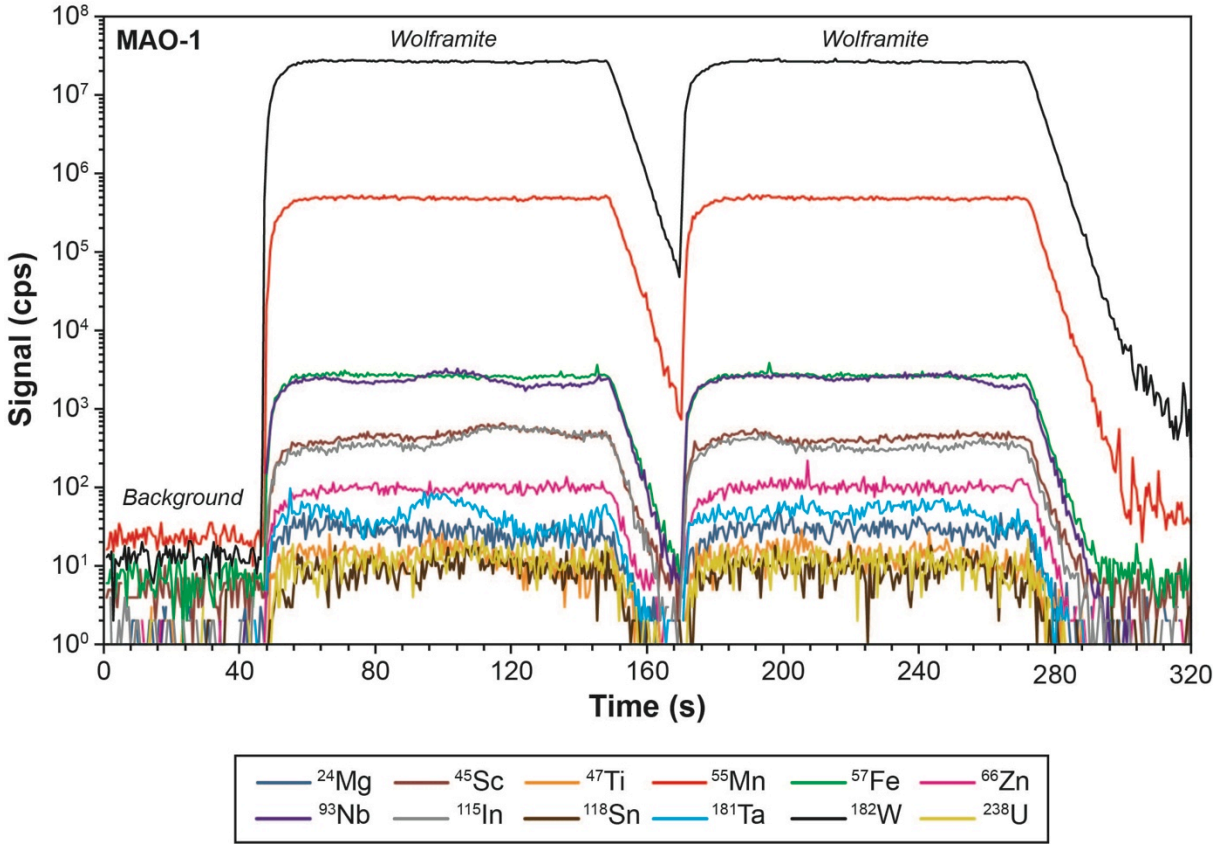

Fig. 15: Typical LA-ICPMS spectra for wolframite MAO-1. The spectra correspond to ablation lines of 200 µm in length using a laser spot diameter of 60 µm and a speed of 2 µm/s.

According from the previous results, the sample MAO-1 appears relatively homogeneous for the elements measured and may represent a suitable external standard to investigate matrix effects during LA-ICPMS of wolframite. In this purpose, two other samples of wolframite from Maoping (MAO-2, MAO-3) were analysed in order to compare the concentrations calculated using the NIST 610 and the sample MAO-1 as external standards. The results show that the concentrations calculated are similar for HREE and Nb, with accuracies ranging from -16 to 0.1% for MAO-2 and from -14 to 0.9% for MAO-3 (Table 6, Fig. 17). Concentrations determined for Sc, Sn and Ta show however large differences (Table 6, Fig. 17), which result from their uncertain reference values in MAO-1. These results indicate therefore that no major matrix effects occur during LA-ICPMS analysis of NIST 610 and MAO samples for the elements measured.

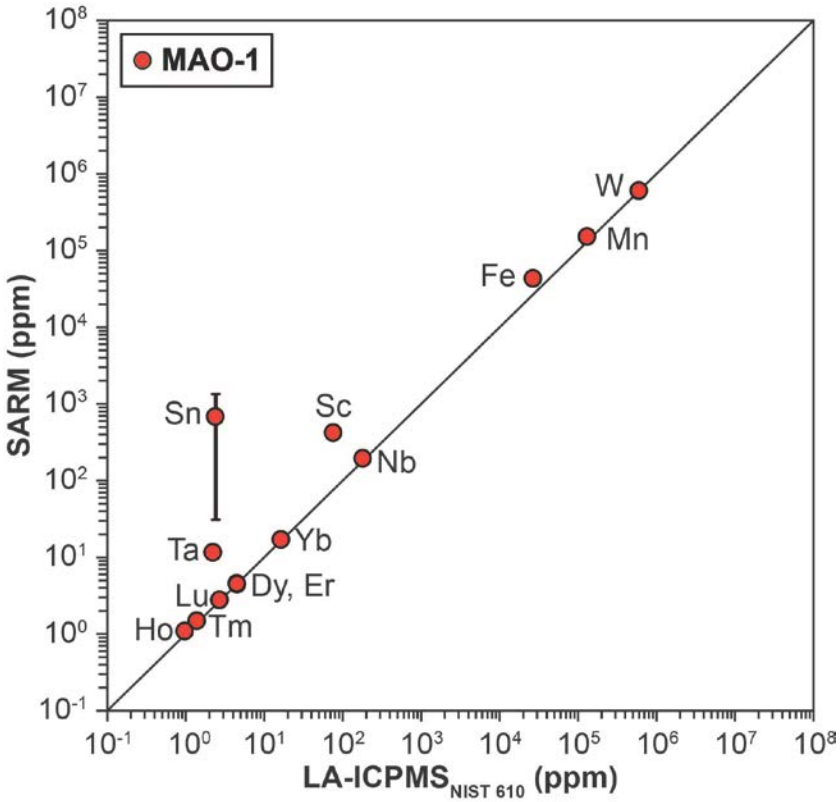

Fig. 16: Average composition of wolframite MAO-1 determined by whole-rock bulk analysis (n=3) versus LA-ICPMS analysis standardized on NIST 610 (n=6). Data are given in Table 5.

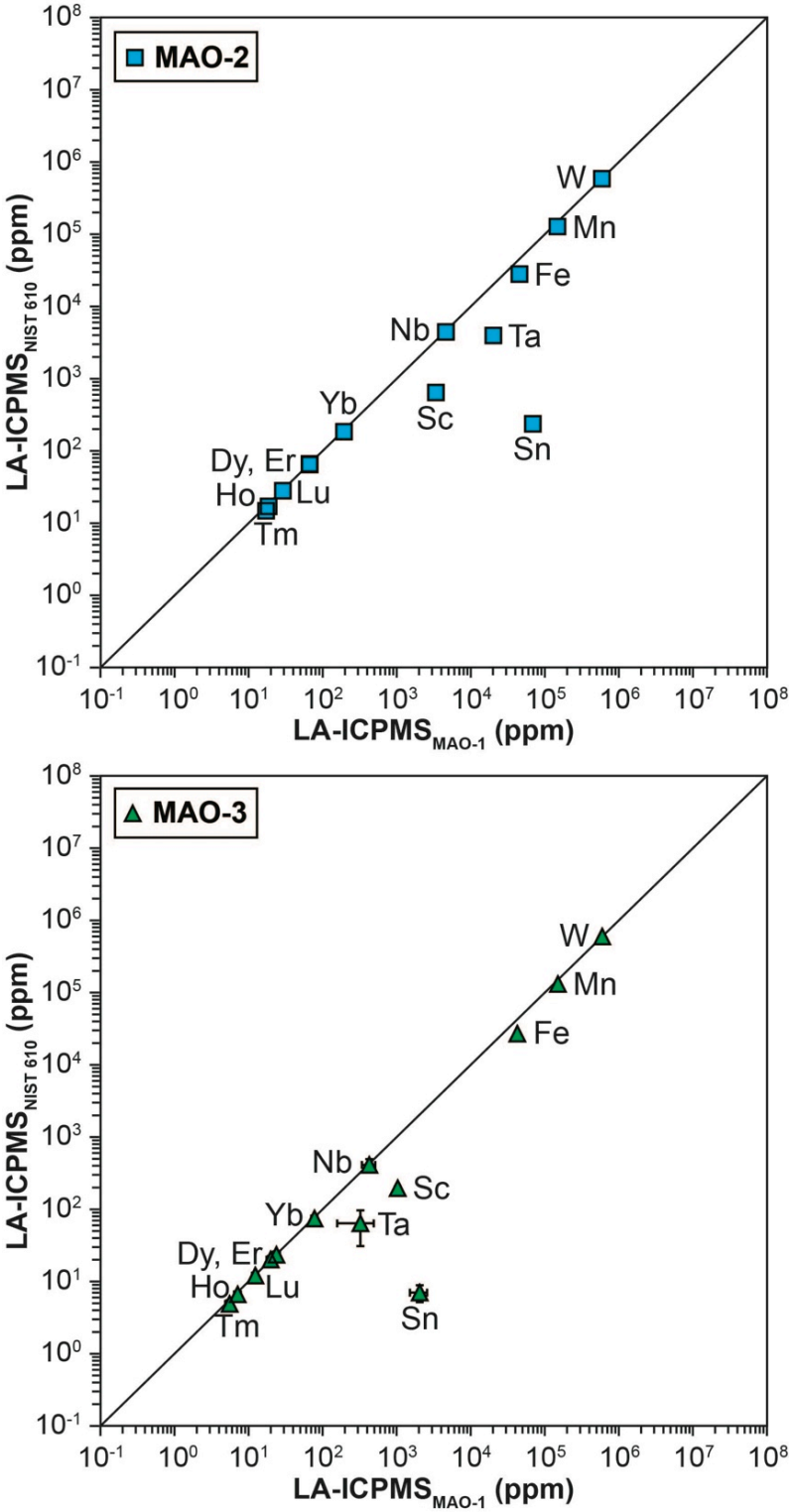

Fig. 17: Average compositions of wolframite MAO-2 and MAO-3 determined by LA-ICPMS standardized on NIST 610 (n=6) versus LA-ICPMS standardized on MAO-1 (n=6). Data are given in Table 6.

3.2. Regional compositional variations in wolframite from the FMC

Compositions of wolframite from the FMC determined by EMPA and LA-ICPMS are given in Table 7 and Table 8, respectively. The major element compositions of wolframite are characterized by variable Fe/(Fe+Mn) values between the deposits, ranging from 0.36 to 0.86, but wolframite from each deposit is characterized by relatively constant Fe/(Fe+Mn) values (Table 7). Most of the wolframites have major element compositions close to the ferberite pole, such as the wolframite from Puy-les-Vignes (0.80-0.81), La Bosse (0.78-0.80), Les Montmins (0.80-0.81), St-Goussaud (0.78-0.80), Leucamp (0.76-0.86), Enguialès (0.69-0.70) and St-Mélany (0.63-0.65) (Fig. 18). Only the wolframite from Montredon-Labessonnié has compositions close to the hübnerite pole (0.36-0.41) (Fig. 18).

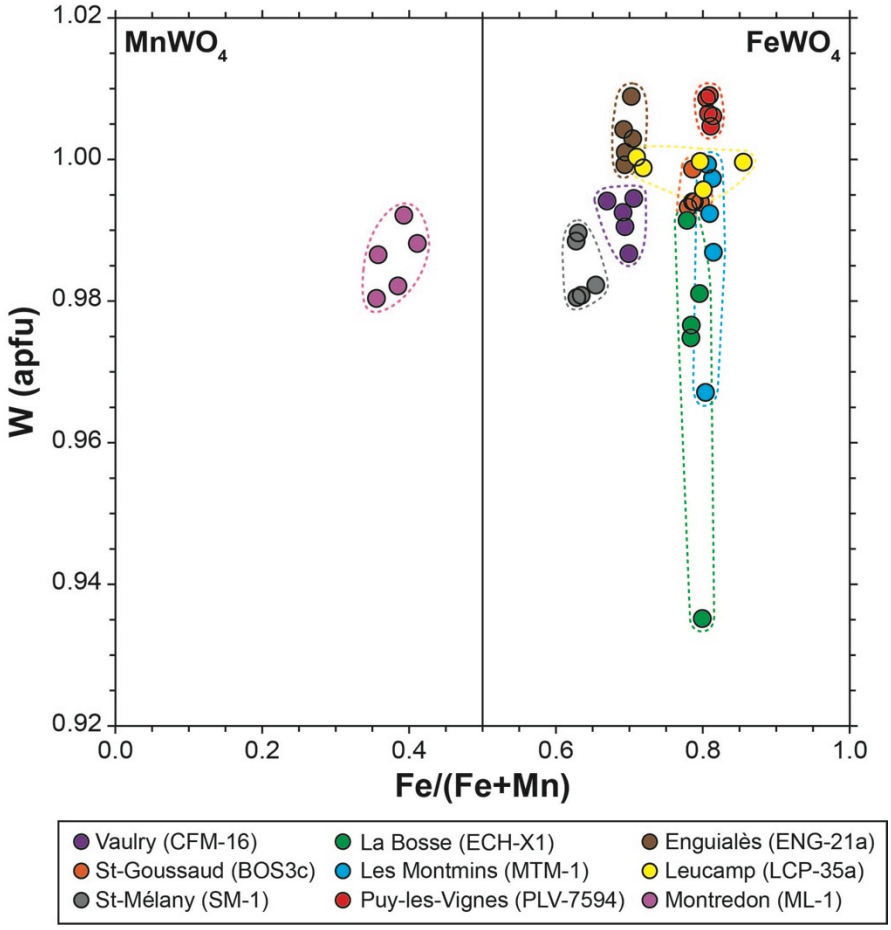

Fig. 18: Compositional variations of wolframites from the FMC in the W vs Fe/(Fe+Mn) diagram.

Most of the wolframite samples from the FMC show homogeneous internal textures when observed in BSE imagery. The presence of mineral micro-inclusions (scheelite,

bismuthinite, pyrite), alteration in ferberite (i.e., ferberitization) or in scheelite (i.e., scheelitization) was punctually detected, as already described in detail in Chapter 1. These zones were evidently avoided for LA-ICPMS analyses and only homogeneous areas within the wolframite crystals were analysed. A cm-size crystal of wolframite was examined by QEMSCAN in order to visualize the variations in major elements at the crystal-scale (Fig. 19).

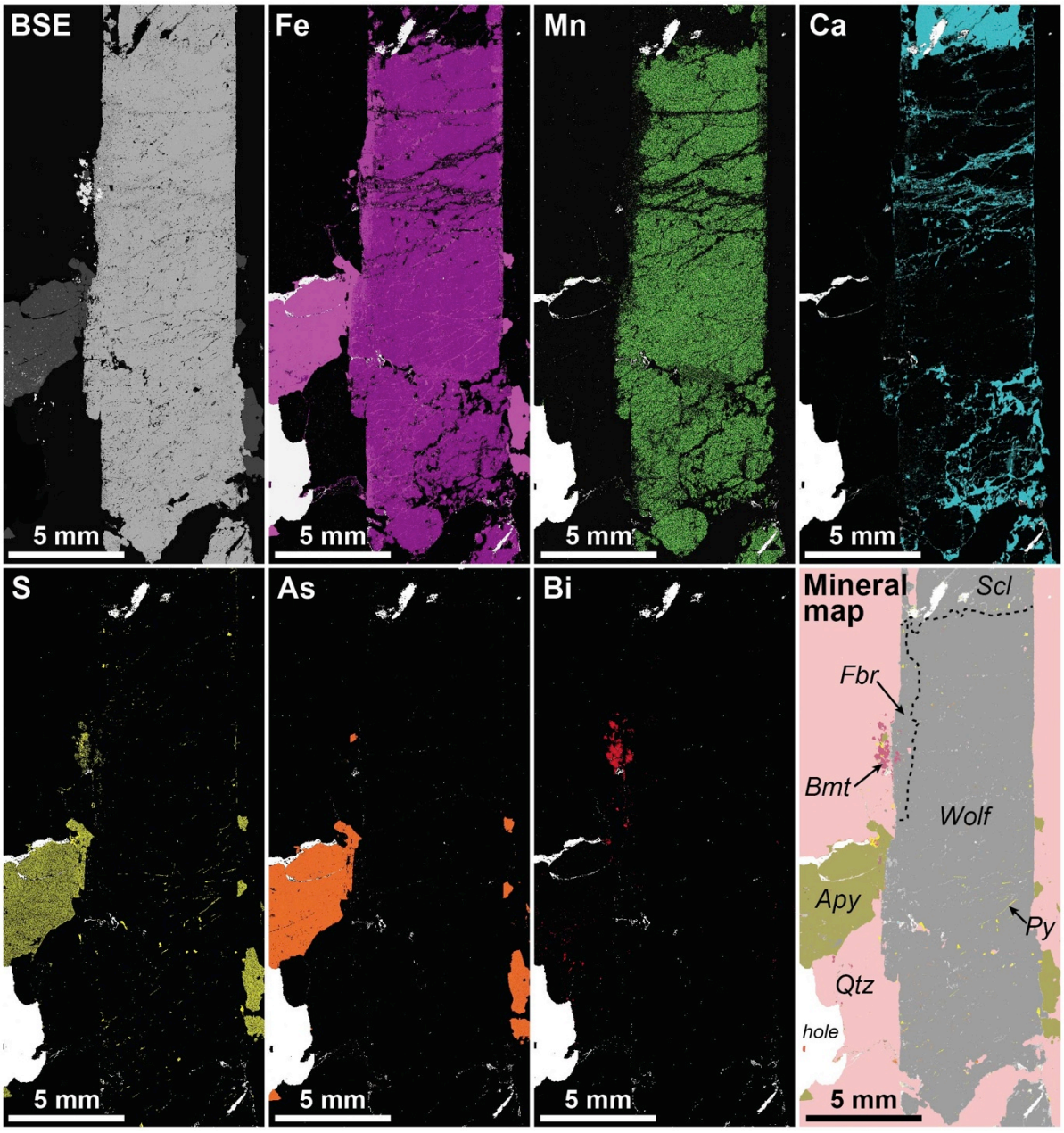

Fig. 19: X-ray element maps obtained by QEMSCAN showing the distribution of Fe, Mn, Ca, S, As and Bi within a wolframite crystal from Puy-les-Vignes (sample PLV-7597a) and automatic mineralogical map generated from the interpretation of the EDS X-ray spectra. Mineral abbreviations: Apy: arsenopyrite; Bmt: bismuthinite; Fbr: ferberite; Py: pyrite; Qtz: quartz; Scl: scheelite; Wolf: Wolframite.

The X-ray element maps show that the ferberitization remains limited to the crystals borders, whereas the scheelitization is more penetrative inside the wolframite crystal (Fig. 19). No primary internal zoning in Fe and Mg was observed, as confirmed also by *in situ* EMPA. Moreover, it can be noted that QEMSCAN allows to visualize easily the presence of arsenopyrite and bismuthinite in overgrowth, as well as pyrite in infillings within the wolframite (Fig. 19).

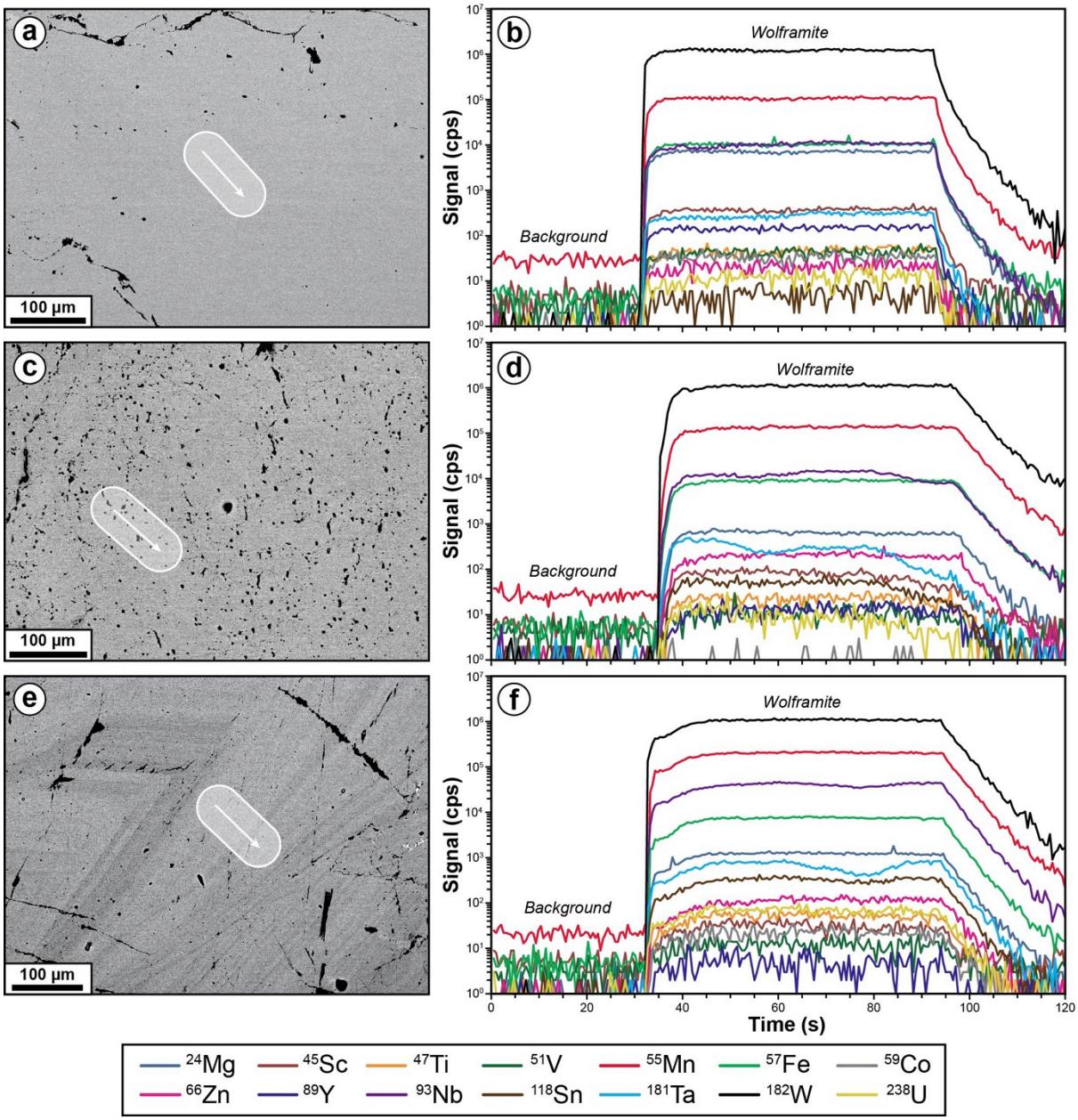

Fig. 20: Representative LA-ICPMS spectra of wolframite from the FMC. (a,b) Homogeneous wolframite crystal in BSE showing homogeneous trace contents in LA-ICPMS (sample PLV-7594). (c,d) Homogeneous wolframite crystal in BSE showing intra-crystalline variations in trace elements (sample BOS3c). (e,f) Zoned wolframite crystal in BSE marked by growth zoning and showing intra-crystalline variations in trace elements (sample SM-1).

Representative LA-ICPMS spectra of wolframite from the FMC are shown in Fig. 20. The majority of the wolframite samples analysed shows homogeneous trace element contents according to the LA-ICPMS spectra (Fig. 20a,b). However, in some samples trace elements showed intra-crystalline variations, especially in Nb, Ta and Sn, although no internal zoning in major elements was observed in BSE imagery (Fig. 20c,d). In the SM-1 wolframite sample showing strong growth zoning on the BSE images, only minor trace elements variations were observed (Fig. 20e,f). Moreover in all the acquired spectra, the Fe/Mn ratios remain constant regardless of the trace elements variations. Therefore, it seems that no correlation can be directly established between the major element variations observed in BSE imagery and the intra-crystalline trace elements variations.

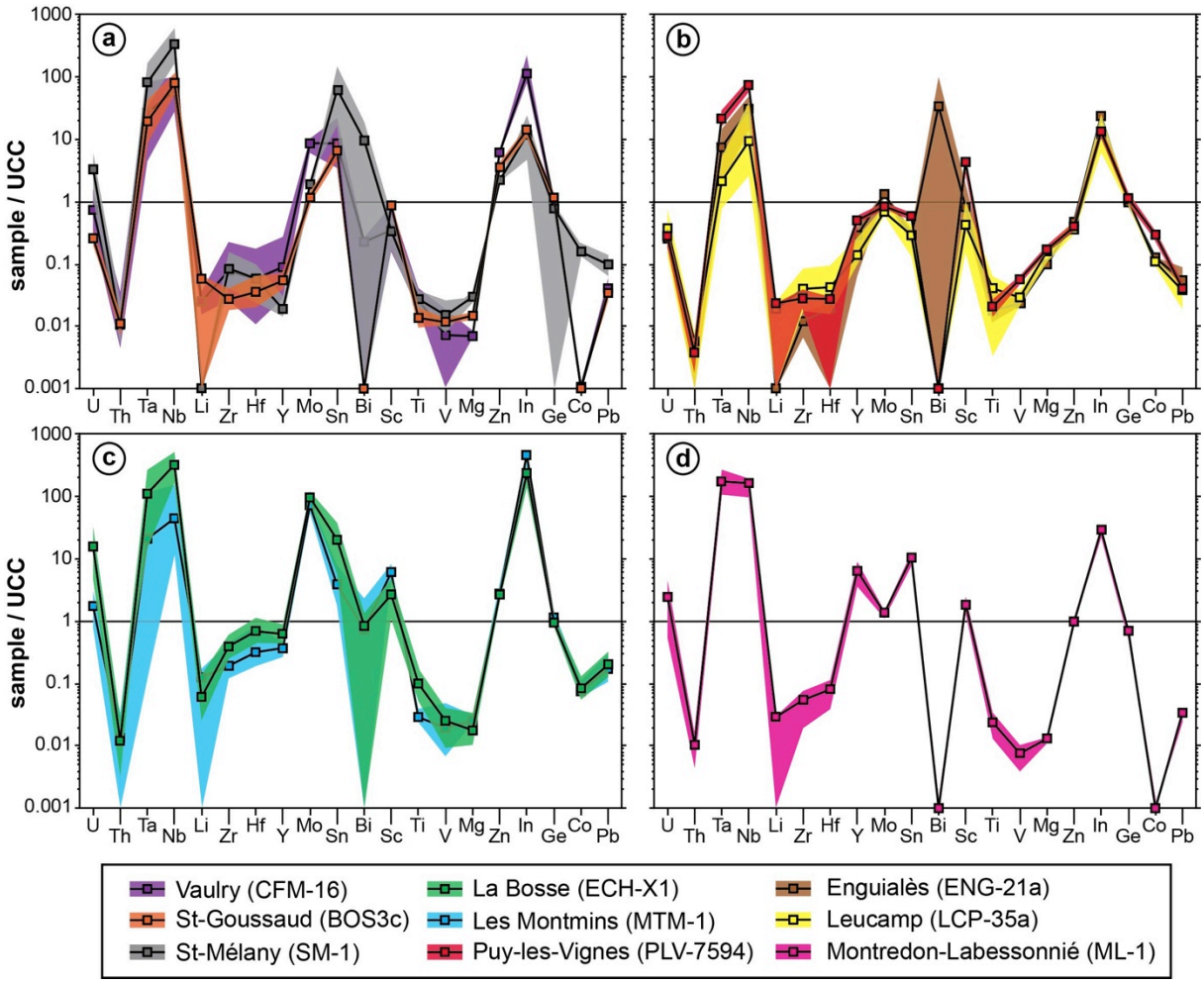

Fig. 21: Trace element compositions of wolframite from the FMC normalized by the upper continental crust (UCC, Rudnick and Gao, 2003). Data are given in Table 8.

Trace element compositions in wolframite determined by LA-ICPMS (Table 8) show regionally variable concentrations mainly in Nb (30-7114 ppm), Ta (0.1-238 ppm), Mg (91-2750 ppm), Ti (13-705 ppm), Sn (0.3-303 ppm), Zn (20-406 ppm), Y (0.3-185 ppm), REE (0.6-395 ppm), Sc (2-113 ppm) and Mo (0.7-130 ppm). Among the REE, the wolframites have a preferential enrichment in HREE (Dy, Ho, Er, Tm, Yb, Lu) compared to LREE, which are below the LOD for some samples. Other trace elements such as Li, V, Ge, In, Hf or Bi are present at low concentrations in the ppm range or are below the LOD (Table 8).

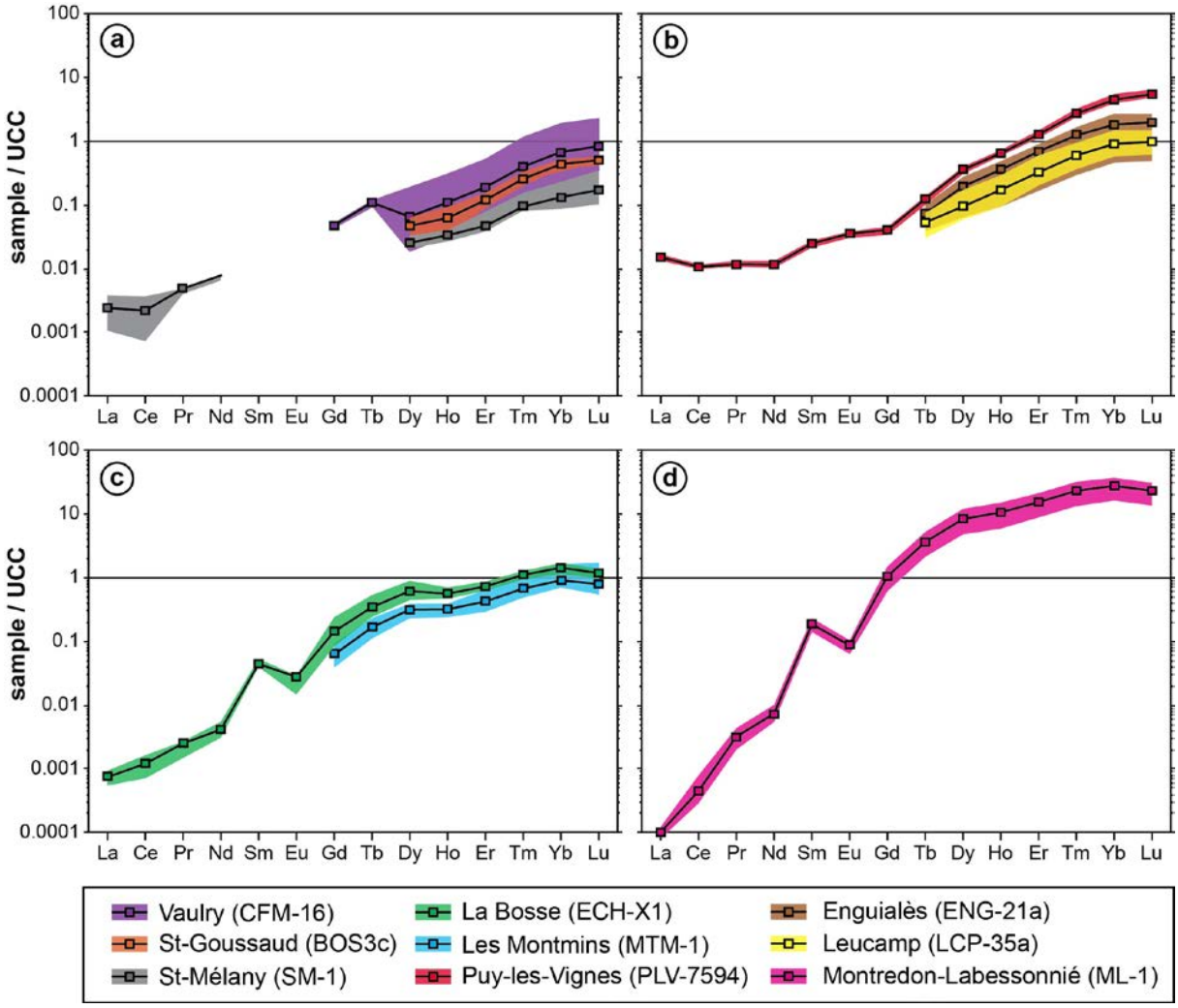

Fig. 22: REE patterns of wolframite from the FMC normalized by the upper continental crust (UCC, Rudnick and Gao, 2003). Data are given in Table 8.

The trace element compositions of wolframite were plotted in multi-element diagrams normalized to the upper continental crust (UCC from Rudnick and Gao, 2003), which is useful to characterize the possible source signatures of the elements in this reservoir, as already discussed by Decrée et al. (2013). The multi-element diagrams allow to distinguish

four main groups of wolframite (Fig. 21):

(i) Samples CFM-16, BOS3c and SM-1 are characterized by high Nb+Ta (319-7260 ppm) and Zn contents (137-406 ppm), and low Mg (91-540 ppm), Y+REE (0.6-13 ppm) and Sc (2-14 ppm) contents (Table 8, Fig. 21a);

(ii) Samples ENG-21a, LCP-35a and PLV-7594 contain low to medium Nb+Ta (31-1101 ppm), Y+REE (3-31 ppm) and Sc (2-69 ppm) contents, low Zn (20-33 ppm) contents, and high Mg (1430-2750 ppm) contents (Table 8, Fig. 21b);

(iii) Samples ECH-X1 and MTM-1 have medium to high Nb+Ta (145-6075 ppm) and Zn (152-200 ppm) contents, low to medium Mg (154-475 ppm) and Sc (16-113 ppm) contents, and low Y+REE (10-30 ppm) contents (Table 8, Fig. 21c);

(iv) Sample ML-1 is characterized by high Y+REE (168-395 ppm) and Nb+Ta (1277-2531 ppm) contents, low Mg (164-211 ppm), Zn (62-69 ppm) and Sc (18-34 ppm) contents (Table 8, Fig. 21d).

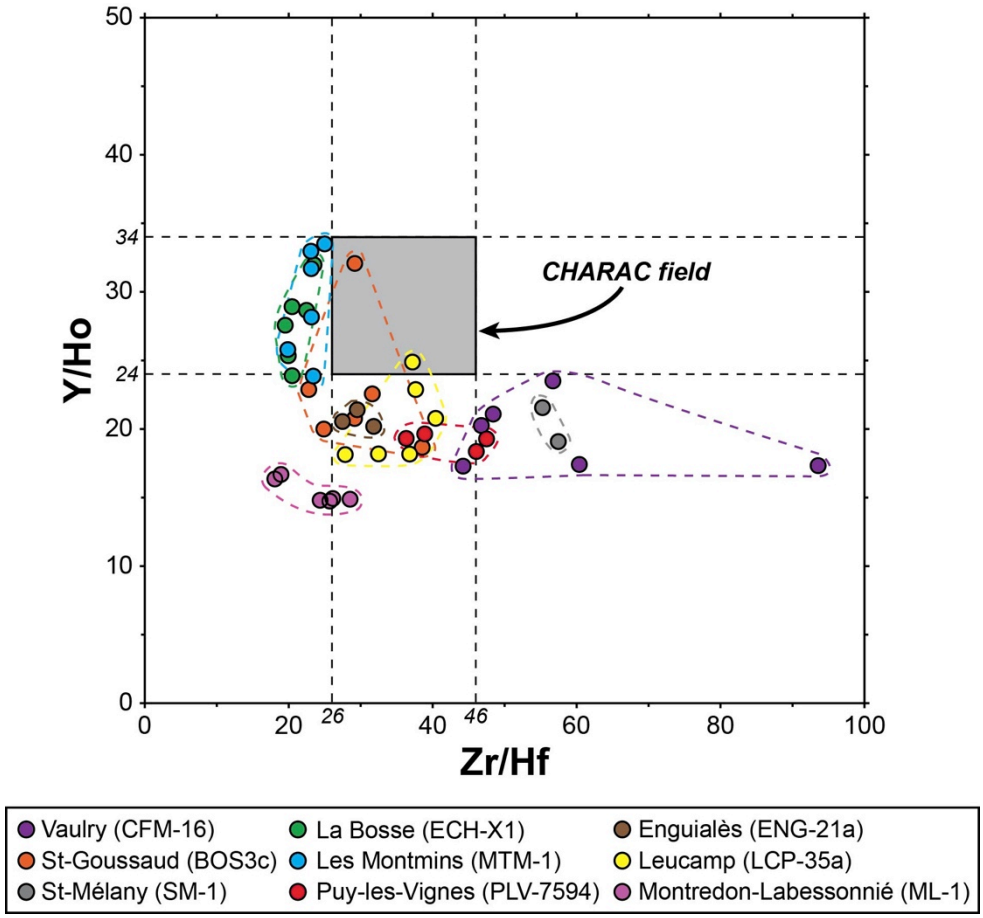

Fig. 23: Plot of Y/Ho ratio versus Zr/Hf ratio for wolframite from the FMC. The CHARAC box is from Bau (1996).

The REE spectra of the wolframites show the same groups discrimination with a common preferential enrichment in HREE compared to LREE (Fig. 22). The REE contents are depleted compared to the UCC for most of the wolframite samples, except for the Puy-les-Vignes and Montredon-Labessonnié deposits, which are enriched up to 6 and 30 times the clarke value, respectively. The REE patterns for the Echassières and Montredon-Labessonnié deposits display a negative Eu anomaly ($0.14<Eu/Eu^*<0.32$) and a M-shape tetrad effect marked by the third (Gd to Ho) and fourth tetrads (Er to Lu). In the Y/Ho vs Zr/Hf plot (Fig. 23), almost all the analyses of wolframites are outside the CHArge-and-Radius-Controlled (CHARAC) box, as defined by Bau (1996).

3.3. Local compositional variations in wolframite from the Echassières deposit

Wolframites from the Echassières deposit distinguish from the other samples from the FMC by their texture and their composition. The structure and the crystal chemistry of the wolframites from Echassières have been previously studied in detail by Aïssa (1987) and Aissa et al. (1987a). In BSE imagery, the wolframites form typically euhedral crystals with elongated shapes, which display internal zoning, marked by the regular succession of micrometric growth bands (Fig. 24a,b). The contrasting colours on the BSE images reflect chemical variations in W (58.8-61.5 wt.%), Fe (14.08-14.99 wt.%) and Mn (3.37-4.04 wt.%), as measured by EDS spectrometry. Locally, the wolframite hosts micrometric-thick Nb-Ta-rich bands (Fig. 24c,d), which are intercalated within the growth bands, suggesting their interpretation as primary. They are characterized by relatively high contents in Nb (up to 3.9 wt.%) and Ta (up to 0.5 wt.%), as indicated by the EDS analyses. Observed at high magnification (Fig. 24e,f), the Nb-Ta-rich bands reveal a granular texture composed by dark rounded aggregates of ca. 50-200 nm in diameter, which are disseminated within a medium-grey matrix. The analytical total shows no significant variations (99.5-100%) between the Nb-Ta-bands and the host-wolframite, which may suggest that the observed dark aggregates correspond to nano-crystals of columbite. This explanation should however be confirmed by high-resolution TEM images and XRD acquisitions. Representative LA-ICPMS spectra acquired in a wolframite crystal from Echassières are shown in Fig. 25. The wolframite is characterized by intra-crystalline variations in the trace contents, particularly in Nb (1960-6060 ppm), Ta (13-235 ppm), U (13-86 ppm), Sn (12-78 ppm) and Sc (16-65 ppm), without variation in the Fe/Mn ratio. For instance, intra-crystalline variations in the Nb/Ta ratio can range from 13 to 240 on a distance less than 1 mm (Fig. 25).

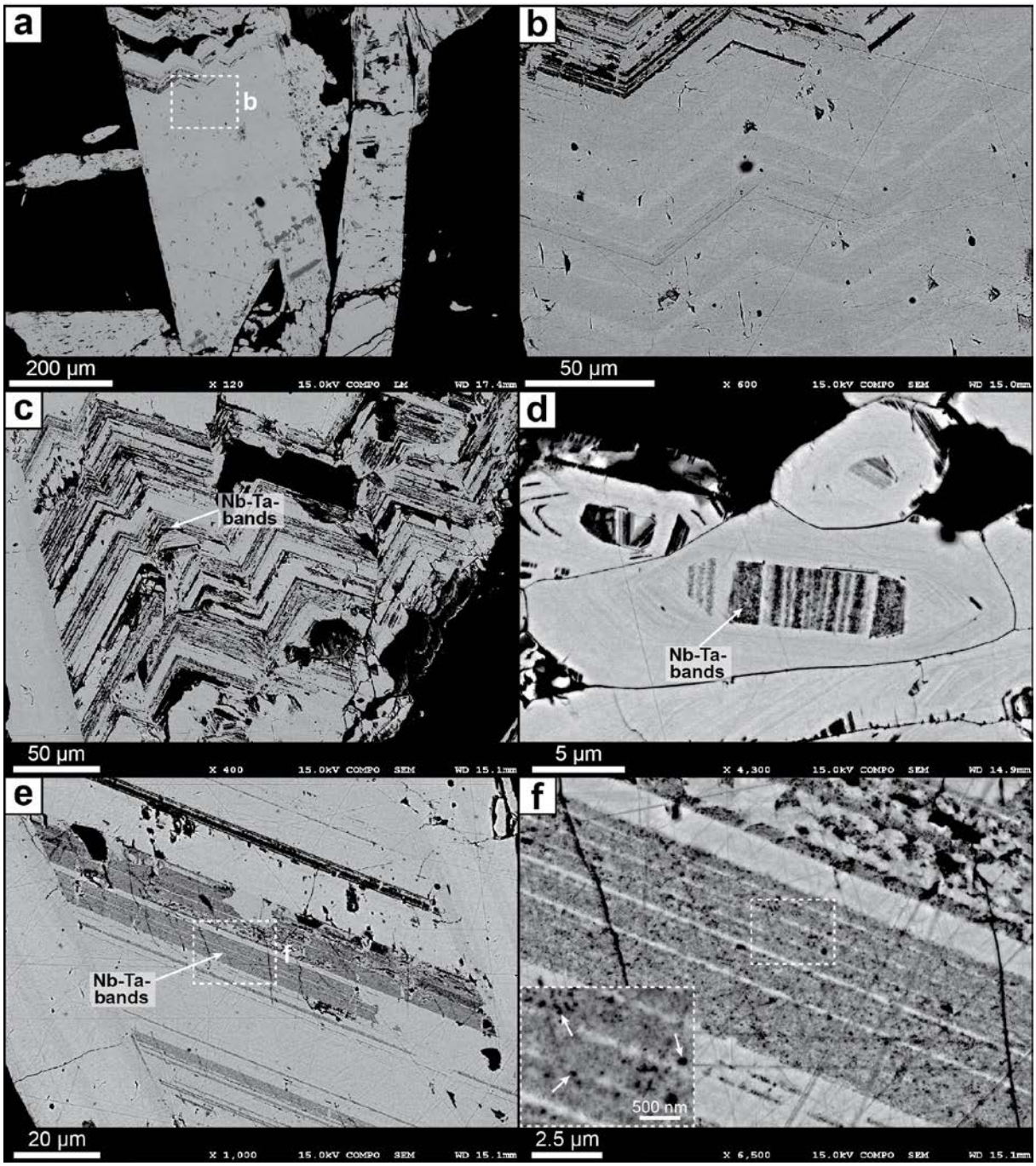

Fig. 24: BSE images of wolframite from the Echassières deposit (sample ECH-X1). (a) Typical elongated shape of the wolframite crystals showing chemical internal zoning (b) marked by regular micrometric growth bands. (c,d) Intra-crystalline Nb-Ta-rich bands correspond to growth bands, more or less regular and continuous. (e,f) Detailed view of the Nb-Ta-rich bands, composed by the aggregation of nano-crystals of columbite-tantalite minerals as observed at high-magnification.

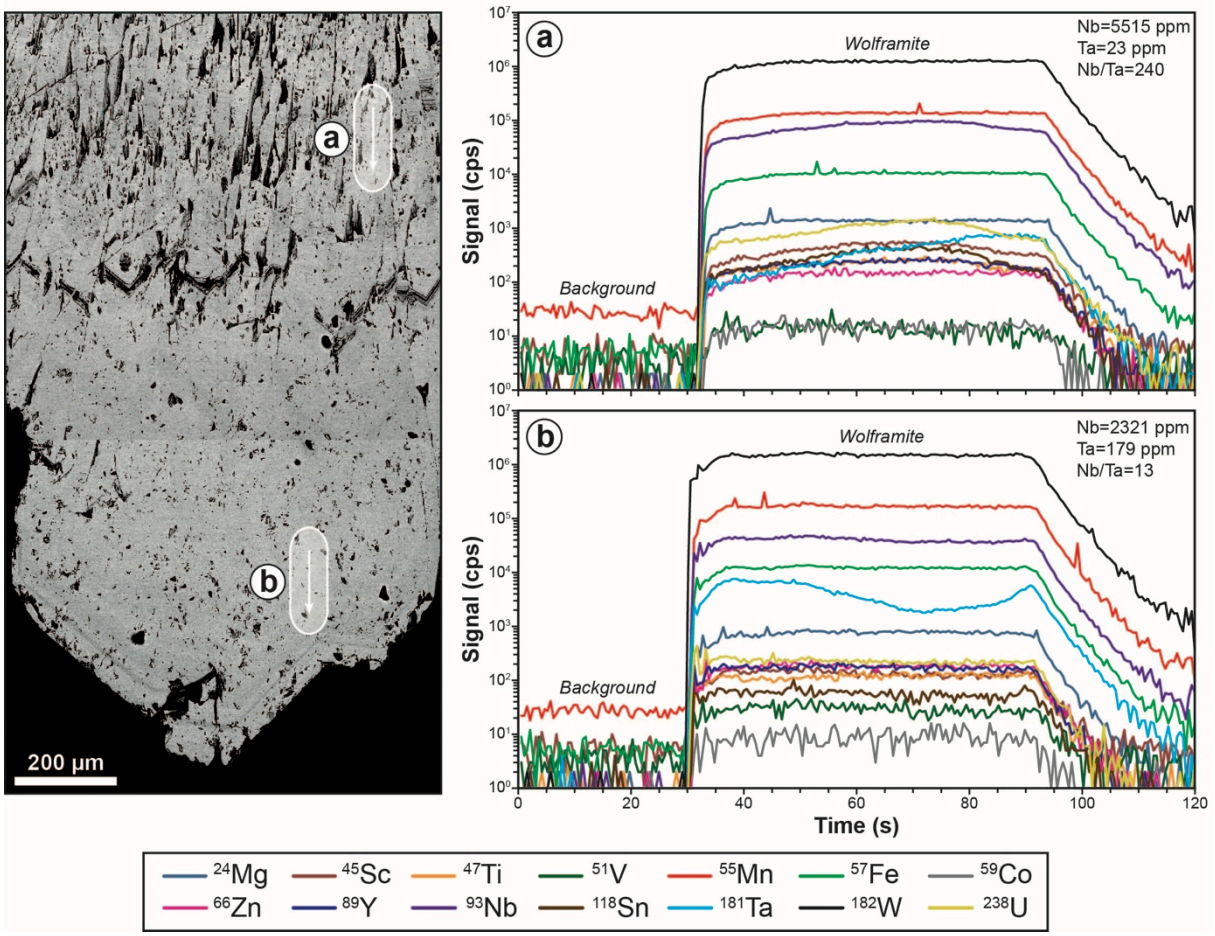

Fig. 25: LA-ICPMS spectra of wolframite from the Echassières deposit showing significant intra-crystalline variations in trace elements.

3.4. Local compositional variations in wolframite from the Puy-les-Vignes deposit

Compositions of seven wolframite samples from the Puy-les-Vignes deposit determined by EMPA and LA-ICPMS are given in Table 9 and Table 10, respectively. The seven samples of wolframite have similar Fe/(Fe+Mn) values ranging from 0.81 to 0.86 (Table 9). The trace elements compositions are characterized by similar geochemical signatures with high contents of Mg (1200-2750 ppm), low to medium contents in Nb+Ta (93-3000 ppm), Y+REE (16-132 ppm) and Sc (1-211 ppm) and low Zn (15-30 ppm) contents (Table 10; Fig. 26a). The REE spectra show smooth patterns with a preferential enrichment in HREE compared to LREE, as observed for the other wolframite from the FMC (Fig. 26b). A slight positive Eu anomaly ($1<Eu/Eu^*<1.36$) is observed for the two samples of wolframites closest to the current surface (samples PLV-14-07 and PV-1), whereas wolframite at higher depth (sample PLV-7594) do not exhibit Eu anomaly (Fig. 26b). This may suggest that the wolframite forming closest to the surface recorded more oxidized conditions. The rare-metals contents in wolframite tend to

increase with depth up to 27 ppm Ta, 2012 ppm Nb, 8 ppm Sn and 22 ppm Li at 300 m under the current surface (Fig. 27). It is interesting to note that the Fe/(Fe+Mn) ratio remains in a limited range (0.81-0.85), without correlation with the other trace elements. Ta, which is one of the less mobile elements in hydrothermal solution, shows the most regular increase with depth, whereas Sn and Li increase abruptly below 270 m.

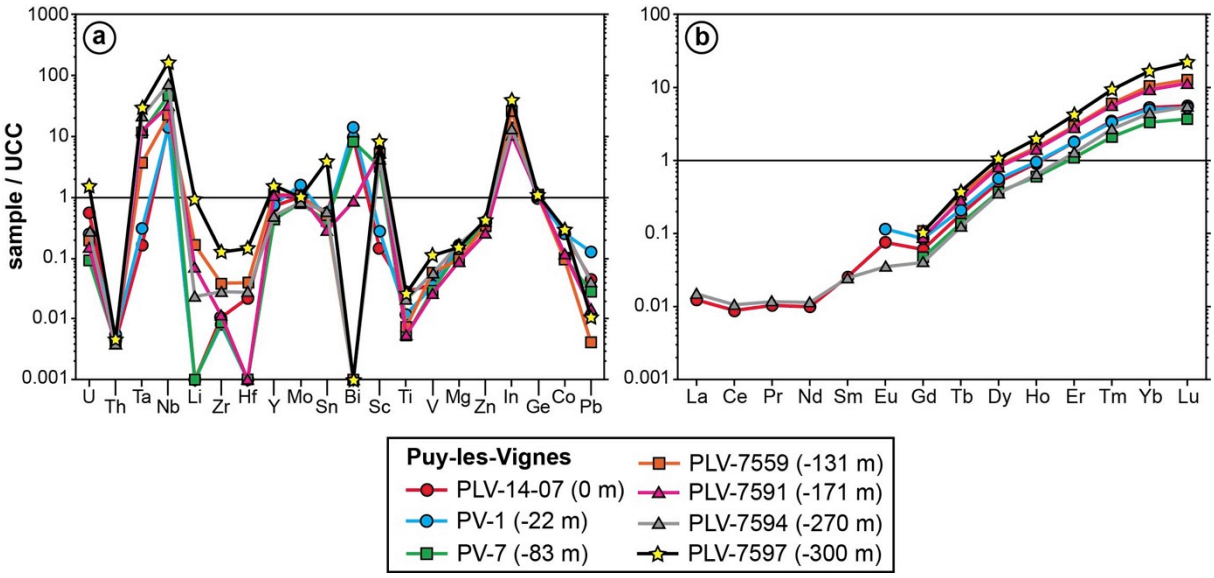

Fig. 26: Trace element compositions and REE patterns of wolframite from the Puy-les-Vignes deposit normalized by the upper continental crust (UCC, Rudnick and Gao, 2003). Data are given in Table 10.

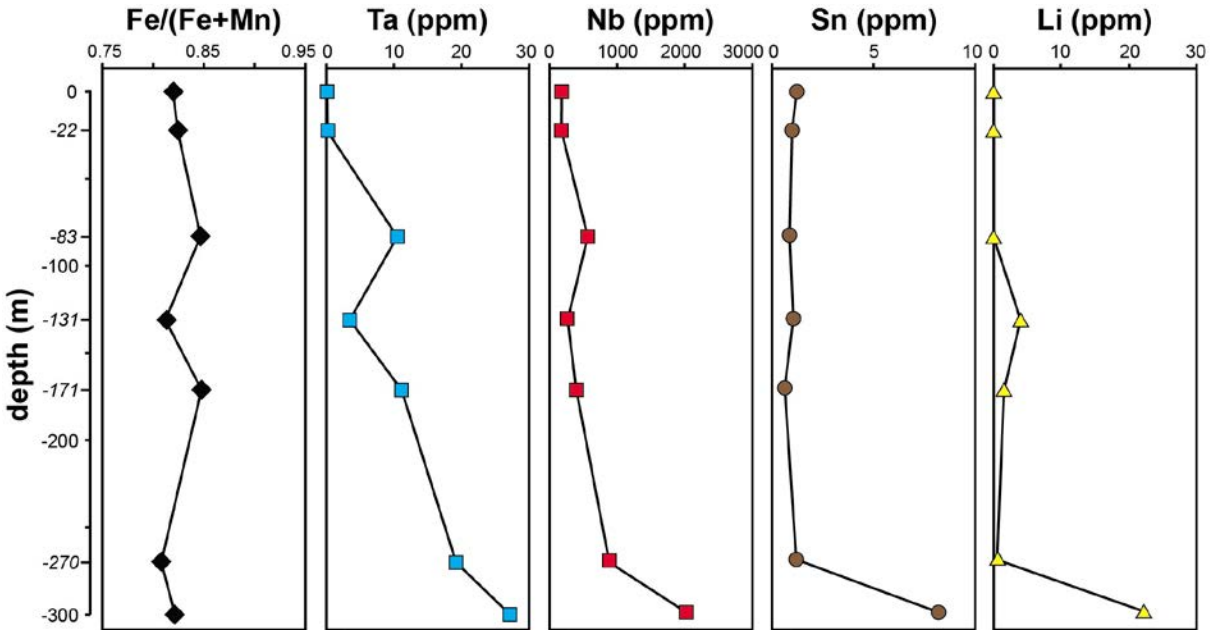

Fig. 27: Geochemical evolution of average compositions of wolframite from the Puy-les-Vignes deposit as function of the depth.

4. Discussion

4.1. Intra-crystalline variations and substitutions mechanisms in wolframite

LA-ICPMS analyses of wolframite have shown intra-crystalline variations in the trace element contents in some samples, principally in Nb, Ta, Sn and secondarily in Ti, Sc or U (Fig. 20 and Fig. 25). These variations show no correlation with the W content or the Fe/(Fe+Mn) values in wolframite. Moreover, they cannot be correlated with internal zoning observed in BSE or the presence of micro-inclusions. Consequently, the observed intra-crystalline variations in the trace elements contents of wolframite reflect more likely a growth zoning linked to the variable incorporation of the trace elements with time during the crystallization of wolframite in the hydrothermal fluid. Chemical variations in major, minor and trace elements in the wolframites from the FMC are shown in Fig. 28. Besides the evident isovalent substitution $Fe^{2+}_{-1}\ Mn^{2+}_{+1}$, it appears that the data points are not perfectly aligned along the substitution line 1:1 and show a slight excess in Fe, thus indicating that a minor amount of iron is present as ferric iron Fe^{3+} (Fig. 28a). This observation has been previously shown in the wolframite from the Echassières deposit (Aïssa et al., 1987a). The W content appears well anti-correlated with the Nb+Ta content with a regression line of slope -1.04 (Fig. 28b). It can be noted however that not all the data points follow this regression line, in particular wolframite from sample ML-1 is approximately aligned along a line of slope -4 (Fig. 28b). Another anti-correlation is observed between W and Fe+Mn content with an average slope of -0.5 (Fig. 28c). Furthermore, an excellent anti-correlation between W+Nb and Fe+Mn showing a low slope of -0.3 is found (Fig. 28d). In the following, the observed chemical variations are discussed formally using convenient exchange vectors, which may represent either true crystallochemical substitutions or syn-crystallization mixing with nano-inclusions. The chemical variations described above may be tentatively explained by the involvement of the exchange vector (1), corresponding to the solid solution $FeWO_4$ - $FeNbO_4$ (Polya, 1988; Tindle and Webb, 1989; Černý and Ercit, 1989).

(1) $\quad {}^{A}(Fe^{2+},Mn^{2+})_{-1}\ {}^{B}W^{6+}_{-1}\ {}^{A}R^{+3}_{+1}\ {}^{B}(Nb^{5+},Ta^{5+})_{+1}$

Where R^{3+} represent the trivalent cations (Fe^{3+}, Sc^{3+}, V^{3+}, In^{3+}, Bi^{3+}, Y^{3+}, REE^{3+}…). Although this exchange vector explains well the observed correlation W-(Nb+Ta) with the slope -1, it doesn't reproduce the expected positive correlation W-(Fe+Mn).

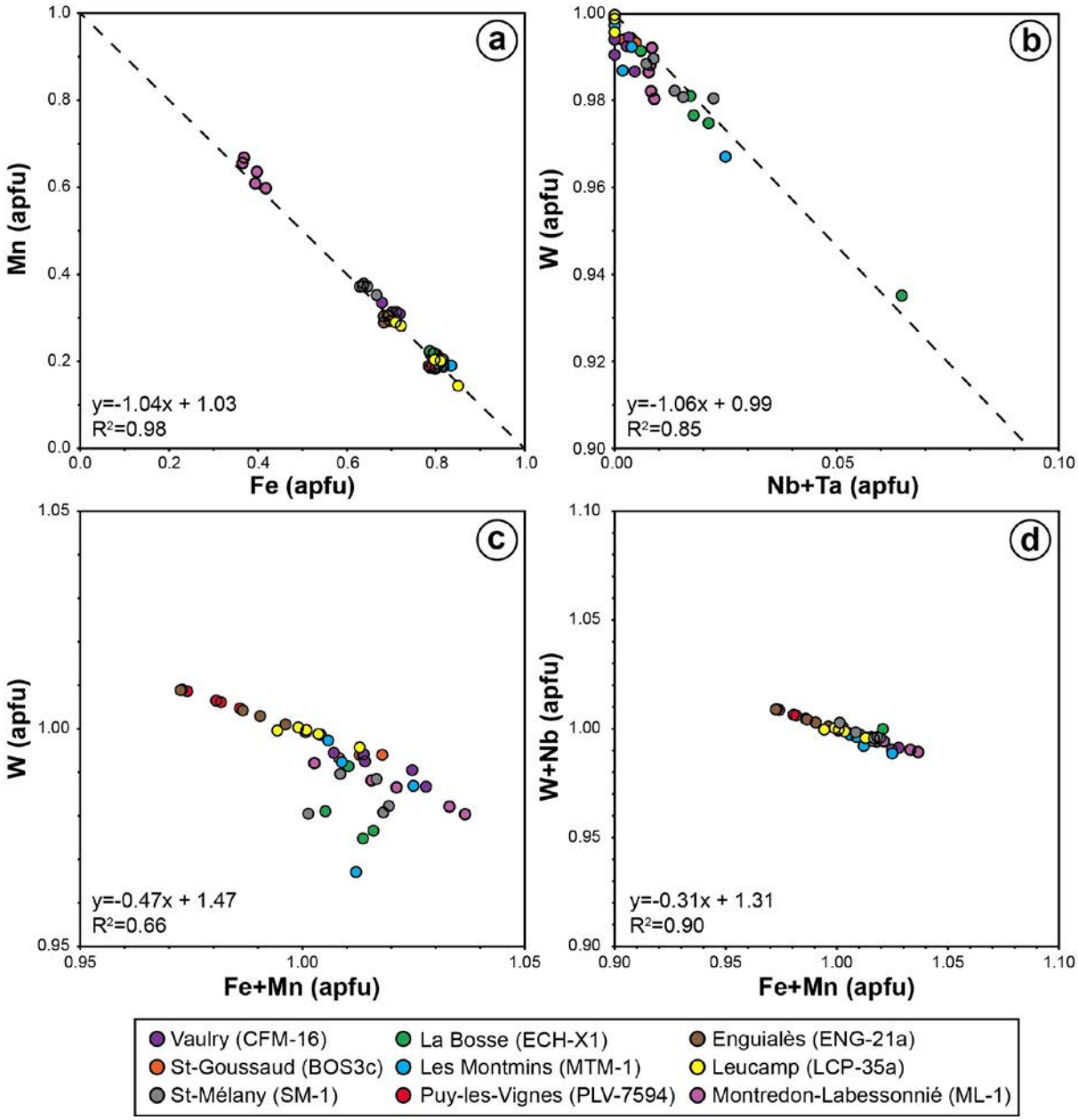

Fig. 28: Main chemical variations in major, minor and trace elements in the wolframites from the FMC.

A second exchange vector (2) corresponding to the solid solution $FeWO_4$ - $FeNb_2O_6$ may also be proposed (Aïssa et al., 1987a; Černý et al., 2007).

(2) $^{A}(Fe^{2+},Mn^{2+})_{-1}\,^{B}\square_{1}\,^{B}W^{6+}_{-3}\,^{A}\square_{+1}\,^{B}(Nb^{5+},Ta^{5+})_{+4}$

This exchange vector supposes however the existence of structural vacancies (□), which may compensate each other.

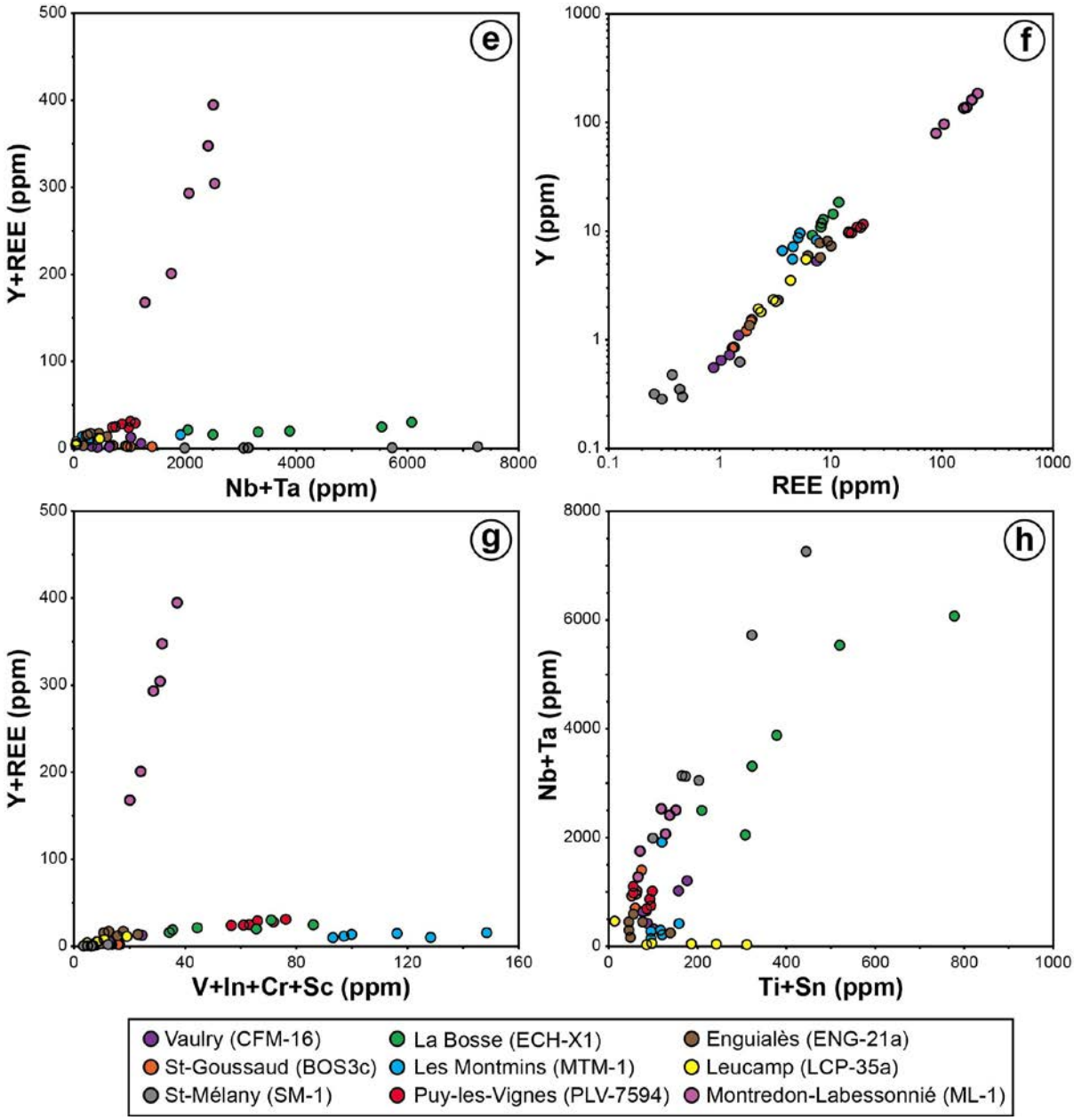

Fig. 28: Continued.

The presence of a relative excess of iron as Fe^{3+} in some of the wolframite suggests substitution mechanisms of types (3) and (4), which suppose also the pre-existence of structural vacancies (Aïssa et al., 1987a).

(3) $^{B}(Nb^{5+},Ta^{5+})_{-1}\ ^{A}\square_{1}\ Fe^{3+}_{+1}\ Fe^{2+}_{+1}$

(4) $^{B}W^{6+}_{-2}\ ^{A}\square_{3}\ Fe^{3+}_{+2}\ Fe^{2+}_{+3}$

The positive correlation between Y+REE and Nb+Ta contents with variable slopes between 0.005 and 0.15 indicates that these elements are incorporated together into the structure of

wolframite (Fig. 28e). This observation does not support the exchange vector (3) and may be better explained by vector (1). Moreover, the anti-correlation W-(Fe+Mn) (Fig. 28c) tends better to favour the exchange vector (4). Among the trivalent cations, Y and REE show a positive correlation along the 1:1 line (Fig. 28f), whereas the Y+REE content is positively correlated with the V+In+Sc+Cr content with variable slopes (Fig. 28g), thus indicating that all the trivalent cations are incorporated via a common mechanism. A positive correlation is also observed between the Ti+Sn and the Nb+Ta content with variable slopes (Fig. 28h) and may be tentatively explained by the exchange vectors (5) and (6) (Aïssa et al., 1987a; Tindle and Webb, 1989).

(5) $^{A}(Fe^{2+},Mn^{2+})_{-2}\ ^{B}W^{6+}{}_{-1}\ ^{A}R^{+3}{}_{+2}\ ^{B}(Ti^{4+},Sn^{4+})_{+1}$

(6) $^{A}\square_{1}\ ^{B}W^{6+}{}_{-1}\ ^{A}(Fe^{2+},Mn^{2+})_{+1}\ ^{B}(Ti^{4+},Sn^{4+})_{+1}$

Small cations like Zn^{2+} and Mg^{2+} enter likely into the wolframite structure through isovalent substitutions with Fe^{2+}, which have similar ionic radii (Shannon, 1976). Finally, the classic isovalent substitutions $Nb^{5+}{}_{-1}Ta^{5+}{}_{+1}$ and $Ti^{4+}{}_{-1}Sn^{4+}{}_{+1}$ complete the crystallochemical description of the wolframite.

4.2. Trace element signatures in wolframite as marker of fluid source reservoirs

Trace elements analysis in wolframite from the studied deposits in the FMC revealed regional compositional variations, which allowed to distinguish four main groups (Fig. 21 and Fig. 22): (i) Vaulry, St-Goussaud and St-Mélany; (ii) Enguialès, Leucamp and Puy-les-Vignes; (iii) Echassières (La Bosse and Les Montmins); and (iv) Montredon-Labessonnié. These regional geochemical signatures show variable enrichments and impoverishments compared to the UCC, which raises therefore the question of the significance of the observed trace elements variations.

4.2.1. Significance of trace element composition in wolframite

The mobility of metallic cations in aqueous solution depend mainly of their speciation, which is a function of the physical fluid properties, such as the temperature and the fluid pressure, but also of the fluid chemical composition, particularly the pH, the fO_2, the fS_2 and the presence of complexing agents (F, Cl, CO_2) able to transport the metals in solution (e.g.,

Yardley and Bodnar, 2014). Fluid inclusions studies from several quartz-wolframite deposits in the FMC indicated that W mineralization formed under similar conditions at temperatures of ca. 300-400°C and pressures of ca. 0.5-2.5 kbar, corresponding to forming depth of around 5-10 km (Ramboz, 1980; Bril, 1982; Noyé, 1985; Ramboz et al., 1985; Aïssa, 1987; Noyé and Weisbrod, 1988; Weisbrod, 1988; Bril and Beaufort, 1989; Alikouss, 1993; Vallance et al., 2001). Empirical and experimental studies showed that the fluids precipitating Sn and W have limited range of pH and fO_2 values, indicating neutral to moderately acid ($4<pH<6$) and relatively oxidized ($-37<fO_2<-22$) conditions (Wood and Samson, 2000 and references therein). The similarities in values of these external parameters may indicate that they do not represent preponderant variables to explain the observed variability in the trace element contents in wolframite. Hence, the latter may rather reflect variations in element concentrations in the fluids and/or crystallochemical effects. In this respect, the preferential enrichment in HREE (Tb to Lu) compared to LREE (La to Gd) observed in the wolframites appears likely controlled by crystallochemical constraints. This behaviour has been already shown in other studies on wolframite (Raimbault, 1984, 1985; Guoliang and Zhixiong, 1992; Goldmann et al., 2013) and appears in good agreement with the partition coefficients calculated by Raimbault (1984) providing enrichment in HREE approximately 85 times greater for Lu than for La, based on the mineral couple apatite/wolframite. This preferential incorporation is likely controlled by the ionic radii of the HREE (Tb^{3+}: 0.92 Å; Lu^{3+}: 0.86 Å), which are close to those of Fe^{2+} (0.78 Å) and Mn^{2+} (0.83 Å) in octahedral coordination in the A-site (Shannon, 1976). The behaviour of the REE in wolframite is opposite to the one in scheelite, which tends rather to incorporate preferentially the LREE (Raimbault, 1985; Raimbault et al., 1993; Ghaderi et al., 1999), which have larger ionic radii (La^{3+}: 1.03 Å; Gd^{3+}: 0.94 Å) close to the one of Ca^{2+} (1.0 Å) in octahedral coordination (Shannon, 1976). Consequently, the incorporation of REE in wolframite seems governed at the first order by crystallochemical controls. Such behaviours have been also observed in other hydrothermal minerals, such as siderite and galena for instance (Morgan and Wandless, 1980). As shown in Fig. 23, the majority of the wolframite analyses fall outside the CHARAC box, which indicates that the ionic radius and the charge valence were not the preponderant parameters controlling the mobility of the REE into the fluids precipitating the wolframites. Thus, the concentration of REE incorporated during the crystallization of wolframite may reflect the chemical composition of the hydrothermal fluid, and particularly the presence of efficient ligands able to complex and to transport the REE in aqueous solution, as indicated by the non-CHARAC behaviour (Fig. 23; Bau, 1996). The significant variations in trace elements

contents observed between the four groups of wolframite may thus be explained by variations in the composition of the hydrothermal fluids, which may suggest that the trace element signatures in wolframite represent direct markers of the source of the fluids. In conclusion, whereas the incorporation or the non-incorporation of some trace elements in wolframite is governed at the first order by its crystal chemistry, the observed regional compositional variations reflect likely variable chemical compositions of the fluids precipitating the wolframites.

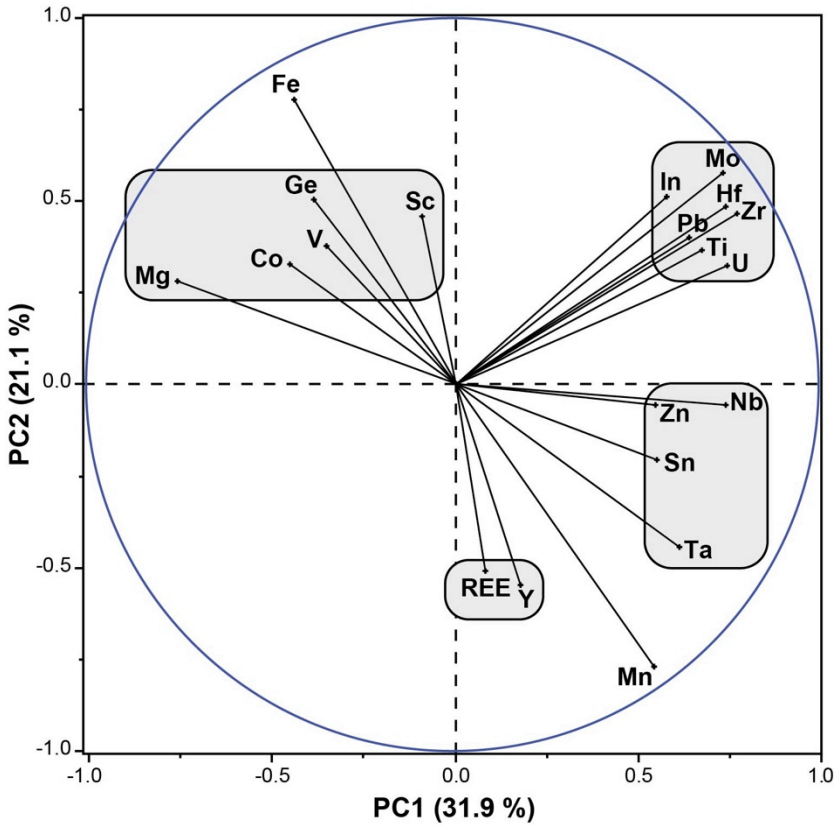

Fig. 29: Principal component analysis (PCA) of LA-ICPMS datasets (n=90) of trace element contents in wolframite from the FMC.

4.2.2. Characterization of trace element signatures in wolframite

Principal component analysis (PCA) has been applied to the LA-ICPMS datasets (n=90) of minor and trace elements in wolframite and the results are shown in Fig. 29. The data for the detected elements in wolframite projected on the PC1 vs PC2 plane account for 53% of the element content variability. The element distribution plotted on the correlation circle shows the evident anti-correlation between Fe and Mn and allows distinguishing four main

groups (Fig. 29). One group is composed of the trace elements Mg, Co, V, Ge and Sc. This first group can actually be subdivided into the Mg and (Co, V, Ge, Sc) sub-groups, the latter consisting in trivalent cations. A second cluster regroups Nb, Zn, Sn and Ta and is located relatively close to a third group composed of REE and Y. The fourth group shows no correlation with the previous ones and is composed of the elements Mo, In, Hf, Zr, Pb, Ti and U, i.e. the main tetravalent cations. It is interesting to note that the PCA separates the different high field strength elements (HFSE) in several groups. PCA was also performed on LA-ICPMS data for each identified group of wolframite and for each deposit and yield to the same group correlations. Correlations matrix shows that Zn is strongly anti-correlated with Mg, Co and V. Nb is well correlated with Sn, but slightly with Ta. U is strongly correlated with Ti, Nb, Zr, Mo and Hf. In appears correlated with Mo and Sc.

The element groups identified from the PCA appear convenient to characterize more easily the differences in trace elements signatures between the four groups of wolframite (Fig. 30):

(i) Wolframite from the Vaulry, St-Goussaud and St-Mélany deposits are characterized by common enrichments in Nb>Ta-Sn-Zn and Mo-In, and impoverishments in Y-REE, Th-Ti-Zr-Hf-Pb, and Sc-V-Co-Mg compared to the UCC (Fig. 30a). They show the highest Sn contents between 6 and 60 times the UCC and highly variable Bi and Co contents;

(ii) Wolframite from the Enguialès, Leucamp and Puy-les-Vignes deposits show only enrichments in Nb>Ta and In with impoverishments in all the other trace elements compared to the UCC (Fig. 30b). They show also highly variable contents in Bi;

(iii) Wolframites from the Echassières deposit (La Bosse and Les Montmins) have enrichments in Nb>Ta-Sn-Zn, U-Mo-In and Sc, with impoverishments in Y-REE, Li, Th-Ti-Zr<Hf-Pb, Bi-V- Co-Mg compared to the UCC (Fig. 30c). They are the only ones characterized by a Mo enrichment close to 100 times the UCC;

(iv) Wolframite from the Montredon-Labessonnié deposit is characterized by enrichments in Y-REE, Ta>Nb-Sn, U-Mo-In and Sc, with impoverishments in Li, Th-Ti-Zr<Hf-Pb, Bi-V-Co-Mg compared to the UCC (Fig. 30d). Y and REE are enriched close to 10 times the UCC, while they are depleted more than 10 to 100 times UCC in all other occurrences. Moreover, it is the only deposit with a normalized Nb/Ta ratio close to 1. In this respect, the wolframite from Montredon-Labessonnié is singular compared to all the other deposits.

Finally, the wolframites from the different deposits show several similarities in their trace element signatures at the first order, which distinguish by minor variations in a limited

number of elements at the second order. In all the wolframites, the Nb, Ta and In contents are high, between 10 and more than 100 times the UCC clarke values, which may indicate that these elements are easily incorporated within wolframite. At the opposite, other elements (Li, Zr, Hf, Ti, V, Mg, Co, Pb) are depleted 10 to 100 times the UCC for all deposits and represent either elements that cannot incorporate easily the wolframite structure (e.g., Li, Rb, Sr) or that are not present in the fluid precipitating wolframite due to low solubility in hydrothermal fluids (e.g., Th, Ti, Zr, Hf).

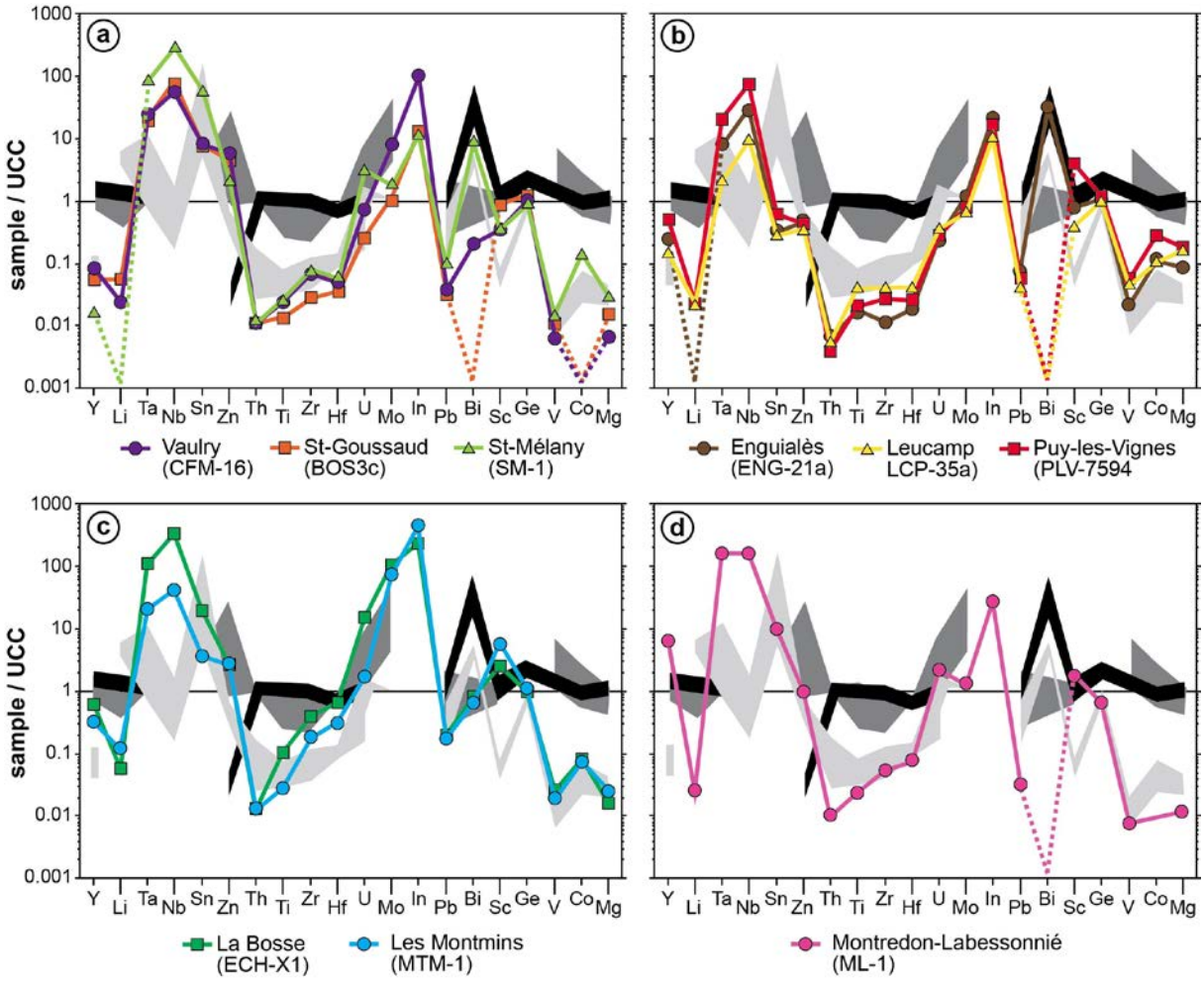

Fig. 30: Comparison of the trace elements signatures in wolframite from the FMC normalized by the upper continental crust (UCC, Rudnick and Gao, 2003) with the composition of evolved granites and shales. The light-grey field represent the average composition of evolved granites from the FMC located in proximity of the studied deposits. The black and dark-grey fields represent respectively the average composition of the North American Shale Composite (NASC, Gromet et al., 1984) and worldwide black shales (Berry et al., 1986; Frost, 1996; Loukola-Ruskeeniemi and Heino, 1996; Hetzel et al., 2009; Mir et al., 2015).

4.2.3. Interpretation of trace element signatures in term of fluid sources

Several authors discussed already the origin of minor elements in wolframite, such as Nb, Ta and Sc, as markers of the geochemistry of their parent environment (e.g., Tindle and Webb, 1989; Černý and Ercit, 1989; Kempe and Wolf, 2006). The geochemical signature of wolframite may be interpreted as reflecting the elemental contributions from various sources, which may range between a pure magmatic pole (i.e., compositions inherited from a granite melt or altered granite) and a pure metamorphic pole (i.e., compositions inherited from the enclosing metamorphic rocks). For instance, mixed signatures have been identified for trace and REE elements in cassiterite from Sn deposits associated with the Mole granite in Australia (Plimer et al., 1991). Comparison of the trace element compositions in wolframite with the average compositions both of regional evolved granites and representative shales from the literature allow to discuss the possible element sources at the regional scale (Fig. 30). The signatures of wolframites from Vaulry, St-Goussaud and St-Mélany (Fig. 30a) show close similarities with the signature of evolved granites for most of the trace elements. Only the normalized Zn content is similar with the signature of black shales. Whereas this finding may not be surprising for the Vaulry and St-Goussaud deposits, both hosted in evolved leucogranites, it is more unexpected for the St-Mélany deposit, which is hosted in metamorphic micaschists and show no evident relationships with a parental granite (see Chapter 6). Wolframites from Enguialès, Leucamp and Puy-les-Vignes (Fig. 30b) show also several similarities with the signatures from evolved granites. At Puy-les-Vignes, the geochemical evolution with depth observed for some trace elements in the wolframite (Fig. 27) may indicate the presence of a hidden highly fractionated granite cupola under the deposit. Similar evolution has been already seen in the scheelite from the Moulin-Barret W±Sn deposit located in the Limousin area at around 50 km in the northwest of Puy-les-Vignes (Raimbault, 1984; Cuney et al., 2002), which showed an increase of the Ta content with depth. At Echassières, a decrease in Nb was observed with depth in the wolframite, which has been interpreted as reflecting the imprint by the magmatic fluids exsolved from the Beauvoir granite (Aïssa et al., 1987b; Cuney et al., 1992). The trace element signatures of wolframites from the Echassières deposit (Fig. 30c) are more difficult to interpret and represent possibly mixing between magmatic and metamorphic sources. The wolframite from the Montredon-Labessonnié deposit has a signature close the one of evolved granite, but show an uncommon geochemical signature compared with the other wolframites, particularly marked by the very high contents in REE. On the whole, it appears that the wolframites from

the FMC have trace element compositions, which are closest to those of evolved granites than to the ones of shales. This result appears in concordance with (i) the non-CHARAC behaviour observed in almost all the wolframites (Fig. 23), which is a common feature of highly evolved magmatic systems (Bau, 1996) and with (ii) the REE patterns of wolframites from Echassières and Montredon-Labessonnié (Fig. 22c,d), which display a negative Eu anomaly and a M-shape tetrad effect marked by the third (Gd to Ho) and fourth tetrads (Er to Lu), which indicates that the wolframites crystallised from hydrothermal fluids, that imprinted their signatures from the interaction with highly evolved granites (e.g., Bau, 1996; Irber, 1999; Monecke et al., 2002). In any case, it remains difficult to explain completely the geochemical signatures of the wolframites from the FMC, in part due to the lack of trace elements data for the regional rocks around the studied deposits and to the possible existence of other potential source rocks at depth, unknown in surface.

5. Conclusions

This work allowed to characterize the trace elements composition of wolframite from several hydrothermal W±Sn deposits located in different areas from the FMC (Vaulry, St-Goussaud, Echassières, Puy-les-Vignes, Leucamp, Enguialès, St-Mélany, Montredon-Labessonnié) in order to compare the regional geochemical fingerprints and to trace the potential metal sources at the regional scale. Preliminary study on homogeneous wolframite crystals from the Maoping deposit allowed demonstrating that no significant matrix effects occur during LA-ICPMS analysis of wolframite for the elements measured. Wolframites from the FMC revealed intra-crystalline variations in the trace element contents in some samples, principally in Nb, Ta, Sn, which are not correlated with internal zoning observed in BSE and reflect more likely growth zoning during the crystallization of wolframite. Trace elements analysis from the studied deposits in the FMC show regional compositional variations, characterized by variable enrichments and impoverishments compared to the UCC, which allowed to distinguish four main groups: (i) Vaulry, St-Goussaud and St-Mélany; (ii) Enguialès, Leucamp and Puy-les-Vignes; (iii) Echassières (La Bosse and Les Montmins); and (iv) Montredon-Labessonnié. These regional geochemical signatures can be explained by variations in the composition of the hydrothermal fluids, thus suggesting that the trace element contents in wolframite represent direct markers of the source of the fluids. Incorporation of some trace elements, such as the REE, appears strongly controlled at the first order by the crystallochemistry of wolframite. Comparison of the trace elements signatures of

the wolframites from the FMC show several similarities with the compositions of evolved granites, which may indicate that the wolframites crystallized from hydrothermal fluids equilibrated, at least partially, with evolved granites. However, some elements (e.g., Zn, U, Mo) seem better explained by a contribution from shales. Finally, these results suggest that the wolframite compositions result from mixing sources.

Table 5: Major and trace element composition of wolframite MAO-1 determined by SARM, EMPA and LA-ICPMS analysis.

	SARM (n=3)			EMPA (n=20)				LA-ICPMS$_{NIST\ 610}$ (n=6)			
	Mean	SD	RSD	Mean	SD	RSD	ACC	Mean	SD	RSD	ACC
Major (wt.%)											
WO_3	77.1	0.88	1.1	74.6	1.18	1.6	-3.3	74.6	1.18	1.1	-3.3
FeO	5.6	0.11	2.0	5.1	0.12	2.4	-9.3	3.4	0.04	0.8	-39
MnO	19.8	0.06	0.3	18.2	0.39	2.1	-8.2	16.7	0.06	0.3	-16
Fe/(Fe+Mn)	0.22	0.003		0.22	0.23			0.17	0.40		
Traces (ppm)											
Bi	bdl			nm				0.04	0.01	21	nc
Cd	bdl			nm				0.45	0.09	20	nc
Co	bdl			nm				0.54	0.02	3.6	nc
Cr	bdl			nm				bdl			nc
Cu	bdl			nm				bdl			nc
Ga	bdl			nm				bdl			nc
Ge	bdl			nm				0.49	0.09	19	nc
Hf	bdl			nm				1.7	0.29	18	nc
In	bdl			nm				26	3.7	14	nc
Mg	bdl			nm				12	0.57	4.8	nc
Mo	bdl			nm				10	0.65	6.2	nc
Nb	197	22.7	11.5	930	453	49	372.01	179	8.9	4.9	-9.0
Ni	bdl			nm				bdl			nc
Pb	bdl			nm				0.71	0.08	11	nc
Sc	426	6.9	1.6	bdl	bdl	bdl	bdl	75	7.8	10	-82
Sn	690	659	95.5	bdl				2.4	0.19	8.0	-100
Ta	12	0.8	6.9	bdl				2.2	0.12	5.4	-81
Th	bdl			nm				0.06	0.03	47	nc
Ti	bdl			bdl				31	2.9	9.4	nc
U	bdl			nm				0.73	0.17	23	nc
Y	bdl			nm				4.3	0.28	6.5	nc
Zn	bdl			nm				134	4.2	3.1	nc
Zr	bdl			nm				12	2.0	16	nc
La	bdl			nm				0.02	0.00	16	nc
Ce	bdl			nm				0.04	0.02	56	nc
Pr	bdl			nm				0.02	0.00	22	nc
Nd	bdl			nm				0.10	0.01	12	nc
Sm	bdl			nm				0.36	0.04	12	nc
Eu	bdl			nm				0.02	0.00	9.2	nc
Gd	bdl			nm				0.68	0.06	8.6	nc
Tb	bdl			nm				0.41	0.03	6.4	nc
Dy	4.5	0.3	7.1	nm				4.5	0.30	6.7	0.8
Ho	1.1	0.1	9.9	nm				0.97	0.07	7.7	-13
Er	4.6	0.1	2.4	nm				4.5	0.24	5.5	-3.1
Tm	1.5	0.04	2.4	nm				1.4	0.10	7.4	-10
Yb	17	0.6	3.5	nm				16	1.0	6.2	-5.0
Lu	2.8	0.02	0.7	nm				2.7	0.19	7.0	-4.3

Table 6: Major and trace element compositions of wolframite MAO-2 and MAO-3 determined by EMPA and LA-ICPMS using the NIST 610 and MAO-1 as external standards.

MAO-2	EPMA (n=20)			LA-ICPMS$_{NIST\ 610}$ (n=6)				LA-ICPMS$_{MAO-1}$ (n=6)				LA-ICPM
	Mean	SD	RSD	Mean	SD	RSD	ACC	Mean	SD	RSD	ACC	ACC
Major (wt.%)												
WO_3	74.13	0.74	1.00	74.13	0.74	1.00	0.00	74.13	0.74	1.00	0.00	0.00
FeO	5.33	0.17	3.19	3.61	0.03	0.74	32.31	5.81	0.05	0.81	-9.06	-61.10
MnO	17.95	0.24	1.34	16.50	0.06	0.38	8.06	19.02	0.07	0.39	-5.97	-15.27
Fe(Fe+Mn)	0.2296	0.4155		0.1799	0.3009			0.2347	0.386			
Traces (ppm)												
Bi	nm			0.2	0.0	17		nc				nc
Cd	nm			0.4	0.1	24		nc				nc
Co	nm			0.1	0.0	16		nc				nc
Cr	nm			bdl				nc				nc
Cu	nm			bdl				nc				nc
Ga	nm			0.14	0.03	18		nc				nc
Ge	nm			0.6	0.04	6		nc				nc
Hf	nm			21	4	18		nc				nc
In	nm			92	8	9		nc				nc
Mg	nm			1.1	0.3	31		nc				nc
Mo	nm			98	6	6		nc				nc
Nb	4980	1270	26	4437	599	14	11	4594	619	13	8	-4
Ni	nm			bdl				nc				nc
Pb	nm			0.5	0.1	16		nc				nc
Sc	485	153	32	643	76	12	-33	3360	391	12	-593	-422
Sn	bdl			237	49	21		68653	14100	21		-28887
Ta	2870	1181	41	3968	677	17	-38	20123	3445	17	-601	-407
Th	nm			1.6	0.5	32		nc				nc
Ti	bdl			16	4	25		nc				nc
U	nm			46	12	26		nc				nc
Y	nm			92	15	16		nc				nc
Zn	nm			116	4	3		nc				nc
Zr	nm			106	20	19		nc				nc
La	nm			0.02	0.01	25		nc				nc
Ce	nm			0.4	0.1	23		nc				nc
Pr	nm			0.2	0.1	23		nc				nc
Nd	nm			2.1	0.5	23		nc				nc
Sm	nm			6.6	1.3	19		nc				nc
Eu	nm			0.01				nc				nc
Gd	nm			12	2	18		nc				nc
Tb	nm			6.3	1.1	17		nc				nc
Dy	nm			66	11	16		66	11	16		0.1
Ho	nm			15	2	16		17	3	16		-16
Er	nm			65	10	15		66	10	15		-3
Tm	nm			17	3	15		19	3	15		-9
Yb	nm			184	27	15		193	29	15		-5
Lu	nm			28	4	14		29	4	14		-3

Table 6: Continued.

MAO-3	EPMA (n=20)			LA-ICPMS$_{NIST\ 610}$ (n=6)				LA-ICPMS$_{MAO-1}$ (n=6)				LA-ICPM
	Mean	SD	RSD	Mean	SD	RSD	ACC	Mean	SD	RSD	ACC	ACC
Major (wt.%)												
WO_3	75.23	0.46	0.61	75.23	0.46	0.61	0.00	75.23	0.46	0.61	0.00	0.00
FeO	4.98	0.23	4.63	3.46	0.03	0.92	30.51	5.48	0.04	0.66	-9.95	-58.23
MnO	18.42	0.35	1.90	16.90	0.05	0.30	8.25	19.41	0.06	0.32	-5.35	-14.82
Fe(Fe+Mn)	0.21	0.40		0.17	0.39			0.22	0.37			
Traces (ppm)												
Bi	nm			0.07	0.02	29		nc				
Cd	nm			0.53	0.06	12		nc				
Co	nm			0.20	0.02	11		nc				
Cr	nm			bdl				nc				
Cu	nm			bdl				nc				
Ga	nm			bdl				nc				
Ge	nm			0.59	0.13	22		nc				
Hf	nm			1.1	0.20	18		nc				
In	nm			62	3	6		nc				
Mg	nm			2.4	0.2	8		nc				
Mo	nm			21	0.6	3		nc				
Nb	1512	1154	76	411	84	20	73	427	87	20	72	-4
Ni	nm			bdl				nc				
Pb	nm			1.1	0.2	17		nc				
Sc	bdl			195	12	6		1032	65	6		-429
Sn	bdl			7	2	26		2041	533	26		-29170
Ta	bdl			64	33	52		323	166	51		-409
Th	nm			0.10	0.03	28		nc				
Ti	bdl			5.5	1.2	22		nc				
U	nm			4.1	0.9	21		nc				
Y	nm			27	4	14		nc				
Zn	nm			130	4	3		nc				
Zr	nm			10	2	20		nc				
La	nm			0.04	0.04	90		nc				
Ce	nm			0.11	0.06	54		nc				
Pr	nm			0.04	0.01	21		nc				
Nd	nm			0.4	0.02	5		nc				
Sm	nm			1.4	0.16	12		nc				
Eu	nm			0.02				nc				
Gd	nm			3	0.3	12		nc				
Tb	nm			1.7	0.19	11		nc				
Dy	nm			20	2	12		20	2	12		0.9
Ho	nm			4.9	0.61	13		6	0.7	13		-14
Er	nm			23	3	11		24	3	11		-2
Tm	nm			6.6	0.7	11		7	0.8	11		-8
Yb	nm			74	7	9		78	7	9		-5
Lu	nm			12.0	1.1	9		12	1	10		-3

Table 7: Representative EMPA compositions of wolframite (wt.%) from the French Massif Central. Analytical conditions, reference standards and limits of detection are given in the text.

Sample	St-Goussaud (*BOS3c*)					Vaulry (*CFM-16*)					Puy-les-Vignes (*PLV-7594*)				
	1	3	5	6	8	1	2	3	4	5	1	2	3	4	5
WO_3	76.2	76.43	75.93	76.17	75.51	75.72	75.94	75.65	75.87	76.06	76.7	77.19	76.41	76.94	77.26
FeO	18.66	18.97	18.63	19.18	18.9	17.09	16.07	16.56	16.88	16.85	18.91	18.66	18.8	18.54	18.84
MnO	5.02	5.1	5.19	4.83	5	7.26	7.83	7.3	7.35	6.93	4.36	4.35	4.25	4.43	4.43
Nb_2O_5	bdl	0.09	0.21	0.08	bdl	0.2	bdl	0.12	bdl	0.14	bdl	bdl	bdl	bdl	bdl
Ta_2O_5	bdl	bdl	bdl	bdl	bdl	bdl	bdl	bdl	bdl	bdl	bdl	bdl	bdl	bdl	bdl
Sc_2O_3	bdl	bdl	bdl	bdl	bdl	bdl	bdl	bdl	bdl	bdl	bdl	bdl	bdl	bdl	bdl
TiO_2	bdl	bdl	bdl	bdl	bdl	0.01	0.05	0.02	0.05	0.02	bdl	bdl	bdl	bdl	bdl
SnO_2	bdl	bdl	bdl	bdl	bdl	bdl	bdl	bdl	bdl	bdl	bdl	bdl	bdl	bdl	bdl
Total	99.88	100.6	99.96	100.3	99.41	100.3	99.89	99.65	100.2	100	99.97	100.2	99.46	99.91	100.53
W	1.00	0.99	0.99	0.99	0.99	0.99	0.99	0.99	0.99	0.99	1.00	1.01	1.01	1.01	1.01
Fe	0.79	0.80	0.79	0.81	0.80	0.72	0.68	0.70	0.71	0.71	0.80	0.79	0.80	0.78	0.79
Mn	0.22	0.22	0.22	0.21	0.22	0.31	0.34	0.31	0.31	0.30	0.19	0.19	0.18	0.19	0.19
Nb	0.00	0.00	0.00	0.00	0.00	0.00	0.00	0.00	0.00	0.00	0.00	0.00	0.00	0.00	0.00
Ta	0.00	0.00	0.00	0.00	0.00	0.00	0.00	0.00	0.00	0.00	0.00	0.00	0.00	0.00	0.00
Sc	0.00	0.00	0.00	0.00	0.00	0.00	0.00	0.00	0.00	0.00	0.00	0.00	0.00	0.00	0.00
Ti	0.00	0.00	0.00	0.00	0.00	0.00	0.00	0.00	0.00	0.00	0.00	0.00	0.00	0.00	0.00
Sn	0.00	0.00	0.00	0.00	0.00	0.00	0.00	0.00	0.00	0.00	0.00	0.00	0.00	0.00	0.00
Fe/(Fe+Mn)	0.79	0.79	0.78	0.80	0.79	0.70	0.67	0.69	0.69	0.71	0.81	0.81	0.81	0.80	0.81

Table 7: Continued.

Sample	Echassières, La Bosse *(ECH-X1)*					Echassières, Les Montmins *(MTM-1)*					Montredon-Labessonnié *(ML-1)*				
	1	2	3	4	5	1	3	4	5	6	4	5	6	7	8
WO_3	75.58	72.35	75.43	75.31	76.3	74.28	77.59	76.3	76.68	75.77	76.06	76.32	75.1	75.13	74.77
FeO	19.11	19.56	19.05	19.02	18.76	19.36	19.42	19.39	19.55	19.86	8.73	9.39	9.42	9.84	8.71
MnO	5.19	4.85	5.19	4.83	5.27	4.67	4.6	4.4	4.55	4.47	15.47	14.33	14.87	13.91	15.59
Nb_2O_5	0.79	2.87	0.94	0.75	0.26	1.1	bdl	bdl	0.17	0.08	0.34	0.37	0.36	0.35	0.39
Ta_2O_5	bdl	bdl	bdl	bdl	bdl	bdl	bdl	bdl	bdl	bdl	bdl	bdl	bdl	bdl	bdl
Sc_2O_3	bdl	bdl	bdl	bdl	bdl	bdl	bdl	bdl	bdl	bdl	bdl	bdl	bdl	bdl	bdl
TiO_2	0.13	0.16	0.12	0.12	0.01	0.32	0.02	0.03	0.06	0.13	bdl	bdl	bdl	bdl	bdl
SnO_2	bdl	bdl	bdl	bdl	bdl	bdl	bdl	bdl	bdl	bdl	bdl	bdl	bdl	bdl	bdl
Total	100.8	99.79	100.7	100.0	100.6	99.73	101.6	100.1	101.0	100.3	100.6	100.4	99.75	99.23	99.46
W	0.98	0.94	0.97	0.98	0.99	0.97	1.00	1.00	0.99	0.99	0.99	0.99	0.98	0.99	0.98
Fe	0.80	0.82	0.79	0.80	0.79	0.81	0.81	0.82	0.82	0.83	0.37	0.39	0.40	0.42	0.37
Mn	0.22	0.20	0.22	0.21	0.22	0.20	0.19	0.19	0.19	0.19	0.66	0.61	0.64	0.60	0.67
Nb	0.02	0.06	0.02	0.02	0.01	0.02	0.00	0.00	0.00	0.00	0.01	0.01	0.01	0.01	0.01
Ta	0.00	0.00	0.00	0.00	0.00	0.00	0.00	0.00	0.00	0.00	0.00	0.00	0.00	0.00	0.00
Sc	0.00	0.00	0.00	0.00	0.00	0.00	0.00	0.00	0.00	0.00	0.00	0.00	0.00	0.00	0.00
Ti	0.00	0.01	0.00	0.00	0.00	0.01	0.00	0.00	0.00	0.00	0.00	0.00	0.00	0.00	0.00
Sn	0.00	0.00	0.00	0.00	0.00	0.00	0.00	0.00	0.00	0.00	0.00	0.00	0.00	0.00	0.00
Fe/(Fe+Mn)	0.78	0.80	0.78	0.80	0.78	0.80	0.81	0.81	0.81	0.81	0.36	0.39	0.38	0.41	0.36

Table 7: Continued.

Sample	Enguialès *(ENG-21a)*					Leucamp *(LCP-35a)*								St-Mélany *(SM-1)*				
	1	2	3	4	5	3	4	6	7	8	1	2	3	4	5
WO_3	76.94	76.73	77.28	77.34	75.85	76.26	76.26	76.27	76.93	75.92	75.26	76.86	76.85	75.97	74.76
FeO	16.59	16.17	16.22	16.56	16.33	18.84	19.25	19.88	18.38	18.16	15.36	15.3	15.37	15.11	15.73
MnO	6.87	7.1	6.78	7.2	7.12	4.76	4.73	3.16	5.46	5.54	8.74	8.86	9.01	8.82	8.21
Nb_2O_5	bdl	bdl	bdl	bdl	bdl	bdl	bdl	bdl	bdl	bdl	0.68	0.39	0.32	0.99	0.59
Ta_2O_5	bdl	bdl	bdl	bdl	bdl	bdl	bdl	bdl	bdl	bdl	bdl	bdl	bdl	bdl	bdl
Sc_2O_3	bdl	bdl	bdl	bdl	bdl	bdl	bdl	bdl	bdl	bdl	bdl	bdl	bdl	bdl	bdl
TiO_2	0.01	0.01	0.01	0.01	0.02	bdl	bdl	0.04	bdl	bdl	0.01	0.01	bdl	0.02	bdl
SnO_2	bdl	bdl	bdl	bdl	bdl	bdl	bdl	bdl	bdl	bdl	bdl	bdl	bdl	bdl	bdl
Total	100.4	100.0	100.3	101.1	99.32	99.86	100.2	99.35	100.8	99.62	100.1	101.4	101.6	100.9	99.29
W	1.00	1.00	1.01	1.00	1.00	1.00	1.00	1.01	1.00	1.00	0.98	0.99	0.99	0.98	0.98
Fe	0.70	0.68	0.68	0.69	0.69	0.80	0.81	0.85	0.77	0.77	0.65	0.64	0.64	0.63	0.67
Mn	0.29	0.30	0.29	0.30	0.31	0.20	0.20	0.14	0.23	0.24	0.37	0.37	0.38	0.37	0.35
Nb	0.00	0.00	0.00	0.00	0.00	0.00	0.00	0.00	0.00	0.00	0.02	0.01	0.01	0.02	0.01
Ta	0.00	0.00	0.00	0.00	0.00	0.00	0.00	0.00	0.00	0.00	0.00	0.00	0.00	0.00	0.00
Sc	0.00	0.00	0.00	0.00	0.00	0.00	0.00	0.00	0.00	0.00	0.00	0.00	0.00	0.00	0.00
Ti	0.00	0.00	0.00	0.00	0.00	0.00	0.00	0.00	0.00	0.00	0.00	0.00	0.00	0.00	0.00
Sn	0.00	0.00	0.00	0.00	0.00	0.00	0.00	0.00	0.00	0.00	0.00	0.00	0.00	0.00	0.00
Fe/(Fe+Mn)	0.70	0.69	0.70	0.69	0.69	0.80	0.80	0.86	0.77	0.76	0.63	0.63	0.63	0.63	0.65

Table 8: Trace element compositions (in ppm) of wolframite from the French Massif Central determined by LA-ICPMS.

	St-Goussaud *(BOS3c)* n=6				Vaulry *(CFM-16)* n=6				Puy-les-Vignes *(PLV-7594)* n=6			
ppm	Mean	SD	Min	Max	Mean	SD	Min	Max	Mean	SD	Min	Max
Li	1.4	-	1.4	1.4	0.6	0.2	0.4	0.8	0.6	-	0.6	0.6
Mg	222	21	195	247	98	11	91	121	2537	113	2441	2749
Sc	12	1.6	11	14	4.6	3.5	2.2	11	60	6.6	52	69
Ti	52	12	37	74	95	31	69	149	79	20	54	97
V	1.1	0.1	1.1	1.3	0.7	0.5	0.3	1.5	5.5	0.6	4.4	6.3
Cr	bdl	-	-	-	bdl	-	-	-	bdl	-	-	-
Co	bdl	-	-	-	bdl	-	-	-	5.1	0.1	4.9	5.2
Ni	bdl	-	-	-	bdl	-	-	-	bdl	-	-	-
Cu	bdl	-	-	-	bdl	-	-	-	bdl	-	-	-
Zn	236	26	214	274	389	12	376	406	26	1.0	25	28
Ga	0.1	-	0.1	0.1	bdl	-	-	-	bdl	-	-	-
Ge	1.6	0.1	1.4	1.8	1.3	0.1	1.3	1.4	1.6	0.1	1.4	1.8
Rb	0.4	-	0.4	0.4	bdl	-	0.0	0.0	bdl	-	-	-
Sr	0.1	-	0.1	0.1	bdl	-	0.0	0.0	0.4	-	0.4	0.4
Y	1.1	0.3	0.8	1.5	1.8	1.9	0.6	5.3	10	0.8	10	12
Zr	5.2	1.7	3.5	7.7	14	15	5	41	5.4	1.4	3.6	7.5
Nb	927	259	643	1366	685	318	314	1136	882	157	678	1080
Mo	1.3	0.1	1.1	1.4	9.0	1.8	6.3	11	0.9	0.1	0.9	1.0
Cd	bdl	-	-	-	bdl	-	-	-	bdl	-	-	-
In	0.8	0.1	0.6	0.9	6.0	2.9	4.2	12	0.7	0.1	0.6	0.8
Sn	14	3.5	10	20	17	15	6.9	43	1.2	0.1	1.1	1.4
Sb	bdl	-	-	-	bdl	-	-	-	bdl	-	-	-
La	bdl	-	-	-	bdl	-	-	-	0.46	-	0.46	0.46
Ce	bdl	-	-	-	bdl	-	-	-	0.67	-	0.67	0.67
Pr	bdl	-	-	-	bdl	-	-	-	0.08	-	0.08	0.08
Nd	bdl	-	-	-	bdl	-	-	-	0.31	-	0.31	0.31
Sm	bdl	-	-	-	bdl	-	-	-	0.12	-	0.12	0.12
Eu	bdl	-	-	-	bdl	-	-	-	0.04	-	0.04	0.04
Gd	bdl	-	-	-	0.19	-	0.19	0.19	0.16	0.02	0.13	0.18
Tb	bdl	-	-	-	0.08	-	0.08	0.08	0.09	0.01	0.07	0.10
Dy	0.18	0.05	0.12	0.25	0.26	0.25	0.07	0.75	1.4	0.13	1.2	1.5
Ho	0.05	0.02	0.03	0.08	0.09	0.09	0.03	0.26	0.53	0.05	0.49	0.60
Er	0.27	0.07	0.20	0.35	0.44	0.42	0.14	1.2	2.9	0.30	2.6	3.4
Tm	0.08	0.02	0.06	0.10	0.12	0.12	0.04	0.36	0.81	0.10	0.71	0.97
Yb	0.86	0.14	0.67	1.0	1.3	1.3	0.46	3.9	8.7	1.2	7.6	11
Lu	0.16	0.03	0.13	0.18	0.26	0.25	0.11	0.74	1.68	0.22	1.5	2.0
Hf	0.19	0.09	0.11	0.34	0.29	0.33	0.05	0.88	0.14	0.02	0.13	0.16
Ta	17	11	8.0	37	22	27	3.8	70	19	4.2	14	26
Pb	0.57	0.11	0.44	0.73	0.65	0.16	0.46	0.94	0.69	0.09	0.60	0.85
Bi	bdl	-	-	-	0.03	0.01	0.03	0.04	bdl	-	-	-
Th	0.11	0.04	0.07	0.16	0.11	0.12	0.05	0.35	0.04	0.02	0.02	0.06
U	0.70	0.16	0.55	0.97	1.9	1.4	0.80	4.0	0.75	0.18	0.50	1.0

Table 8: Continued.

	Echassières, La Bosse *(ECH-X1)* n=6				Echassières, Les Montmins *(MTM-1)* n=6				Montredon-Labessonnié *(ML-1)* n=6			
ppm	Mean	SD	Min	Max	Mean	SD	Min	Max	Mean	SD	Min	Max
Li	1.4	1.0	0.6	3.2	3.0	0.9	1.5	4.1	0.7	-	0.7	0.7
Mg	264	132	154	475	373	43	325	438	194	18	164	211
Sc	37	21	16	65	83	18	64	113	26	5.6	18	34
Ti	377	179	198	705	109	22	88	149	90	32	50	127
V	2.4	1.2	0.9	3.9	1.9	1.6	0.7	4.6	0.7	0.3	0.4	1.0
Cr	4.7	1.9	2.4	7.0	3.5	1.3	2.2	5.3	bdl	-	-	-
Co	1.4	0.5	0.9	2.2	1.3	0.3	1.1	1.9	bdl	-	-	-
Ni	bdl	-	-	-	bdl	-	-	-	bdl	-	-	-
Cu	1.9	1.3	0.6	3.3	bdl	-	-	-	bdl	-	-	-
Zn	177	13	152	192	182	14	165	200	65	3	62	69
Ga	0.6	0.3	0.3	1.1	0.3	0.3	0.1	0.9	0.3	-	0.3	0.3
Ge	1.3	0.1	1.2	1.5	1.6	0.1	1.4	1.7	1.0	0.1	0.7	1.1
Rb	0.5	0.3	0.2	0.8	0.2	0.1	0.2	0.3	bdl	-	-	-
Sr	0.2	0.1	0.1	0.3	0.2	0.2	0.1	0.3	0.8	1.3	0.0	2.3
Y	13	3.2	9.2	18	7.7	1.5	5.5	10	133	39	80	185
Zr	75	25	48	115	36	24	23	86	10	4.6	3.7	15
Nb	3794	1683	1958	6062	526	637	145	1814	1936	471	1150	2343
Mo	104	14	88	131	78	3.2	73	83	1.5	0.1	1.2	1.6
Cd	bdl	-	-	-	bdl	-	-	-	bdl	-	-	-
In	13	4.0	7.7	18	25	4.0	21	31	1.6	0.2	1.3	1.9
Sn	42	29	12	78	8.0	4.5	3.7	16.2	22	4.3	16	26
Sb	bdl	-	-	-	bdl	-	-	-	bdl	-	-	-
La	0.02	0.01	0.02	0.03	0.02	-	0.02	0.02	bdl	-	-	-
Ce	0.07	0.03	0.04	0.10	0.09	0.06	0.04	0.17	0.03	0.01	0.02	0.05
Pr	0.02	0.00	0.02	0.02	bdl	-	-	-	0.02	0.01	0.01	0.03
Nd	0.11	0.03	0.08	0.15	bdl	-	-	-	0.20	0.05	0.15	0.27
Sm	0.21	0.04	0.18	0.25	bdl	-	-	-	0.87	0.15	0.66	1.08
Eu	0.03	0.00	0.03	0.03	bdl	-	-	-	0.09	0.01	0.06	0.10
Gd	0.57	0.21	0.33	0.95	0.25	0.07	0.15	0.37	4.2	1.3	2.4	5.9
Tb	0.24	0.07	0.17	0.37	0.12	0.03	0.08	0.16	2.5	0.8	1.5	3.6
Dy	2.4	0.6	1.7	3.5	1.22	0.21	0.90	1.51	32	11	19	47
Ho	0.5	0.1	0.4	0.6	0.26	0.04	0.20	0.32	8.7	2.9	4.9	12
Er	1.7	0.2	1.4	2.0	0.97	0.28	0.66	1.48	35	11	20	48
Tm	0.3	0.0	0.3	0.4	0.20	0.06	0.14	0.32	6.9	2.2	4.0	9.5
Yb	2.8	0.4	2.2	3.3	1.77	0.70	1.32	3.16	54	16	32	72
Lu	0.4	0.0	0.3	0.4	0.24	0.14	0.17	0.53	7.1	2.1	4.2	9.5
Hf	3.6	1.3	2.3	5.9	1.7	1.3	1.0	4.3	0.42	0.15	0.21	0.60
Ta	99	90	13	236	19	41	0.1	102	155	49	95	238
Pb	3.4	1.3	2.1	5.4	2.8	1.1	1.8	5.0	0.6	0.1	0.4	0.7
Bi	0.13	0.06	0.09	0.20	0.12	0.14	0.04	0.36	bdl	-	-	-
Th	0.13	0.10	0.03	0.26	0.14	0.14	0.06	0.35	0.11	0.04	0.05	0.16
U	42	29	13	86	4.6	2.3	2.1	8.0	6.4	4.1	1.4	12

Table 8: Continued

	Enguialès *(ENG-21a)* n=6				Leucamp *(LCP-35a)* n=6				St-Mélany *(SM-1)* n=6			
ppm	Mean	SD	Min	Max	Mean	SD	Min	Max	Mean	SD	Min	Max
Li	bdl	-	-	-	0.5	0.2	0.3	0.6	bdl	-	-	-
Mg	1471	37	1430	1530	2367	394	1589	2619	441	58	360	540
Sc	11	4.6	6.5	19	5.9	4.3	2.2	14	4.6	2.1	2.4	8.4
Ti	68	36	44	138	155	110	13	310	104	29	63	141
V	2.3	0.3	2.0	2.8	2.8	0.7	2.1	3.7	1.4	0.6	0.8	2.5
Cr	bdl	-	-	-	bdl	-	-	-	bdl	-	-	-
Co	2.2	0.1	2.1	2.2	1.9	0.2	1.6	2.0	2.7	0.6	2.1	3.6
Ni	bdl	-	-	-	bdl	-	-	-	bdl	-	-	-
Cu	bdl	-	-	-	bdl	-	-	-	bdl	-	-	-
Zn	32	1.7	29	33	23	5	20	32	147	6	137	153
Ga	bdl	-	-	-	0.1	-	0.1	0.1	0.2	0.1	0.1	0.3
Ge	1.4	0.2	1.2	1.6	1.5	0.2	1.2	1.7	1.1	0.1	0.9	1.2
Rb	bdl	-	-	-	0.1	0.0	0.1	0.2	bdl	-	-	-
Sr	bdl	-	-	-	0.2	0.0	0.2	0.2	0.1	-	0.1	0.1
Y	6.0	2.5	1.4	8.1	2.9	1.4	1.8	5.5	0.4	0.1	0.3	0.6
Zr	2.3	0.8	1.3	3.3	7.6	4.9	3.4	16	16	8.6	7.9	30
Nb	361	154	165	581	111	171	30	459	3977	1959	1962	7114
Mo	1.4	0.1	1.3	1.6	0.7	0.1	0.7	0.9	2.1	0.3	1.7	2.6
Cd	bdl	-	-	-	bdl	-	-	-	1.1	0.3	0.9	1.3
In	1.3	0.1	1.1	1.5	0.7	0.4	0.3	1.4	0.7	0.4	0.3	1.3
Sn	0.6	0.1	0.4	0.7	0.6	0.2	0.3	0.9	130	100	36	303
Sb	bdl	-	-	-	bdl	-	-	-	bdl	-	-	-
La	bdl	-	-	-	bdl	-	-	-	0.07	0.06	0.03	0.12
Ce	0.1	-	0.1	0.1	bdl	-	-	-	0.14	0.13	0.05	0.23
Pr	bdl	-	-	-	bdl	-	-	-	0.03	-	0.03	0.03
Nd	bdl	-	-	-	bdl	-	-	-	0.21	-	0.21	0.21
Sm	bdl	-	-	-	bdl	-	-	-	bdl	-	-	-
Eu	bdl	-	-	-	bdl	-	-	-	bdl	-	-	-
Gd	bdl	-	-	-	bdl	-	-	-	bdl	-	-	-
Tb	0.1	0.01	0.04	0.07	0.04	0.02	0.02	0.05	bdl	-	-	-
Dy	0.8	0.30	0.25	1.07	0.37	0.17	0.23	0.67	0.10	0.04	0.07	0.13
Ho	0.3	0.12	0.08	0.40	0.14	0.06	0.08	0.24	0.03	0.01	0.02	0.03
Er	1.6	0.62	0.39	2.04	0.74	0.34	0.46	1.37	0.11	0.05	0.08	0.18
Tm	0.4	0.15	0.09	0.50	0.18	0.06	0.11	0.28	0.03	0.01	0.02	0.05
Yb	3.6	1.5	0.9	5.3	1.8	0.7	1.1	2.9	0.26	0.09	0.17	0.43
Lu	0.61	0.27	0.15	0.85	0.30	0.10	0.19	0.46	0.05	0.03	0.03	0.11
Hf	0.10	0.02	0.08	0.12	0.22	0.15	0.08	0.50	0.31	0.15	0.12	0.52
Ta	6.7	4.0	1.7	13	1.9	1.5	0.7	4.7	72	44	30	148
Pb	0.9	0.29	0.71	1.50	0.64	0.18	0.32	0.78	1.6	0.5	1.1	2.3
Bi	5.4	6.8	0.09	16	bdl	-	-	-	1.5	2.1	0.0	3.0
Th	0.05	0.01	0.04	0.06	0.06	0.01	0.05	0.08	0.11	0.07	0.05	0.25
U	0.7	0.22	0.48	1.06	1.00	0.67	0.36	2.02	8.7	5.6	3.0	16

Table 9: Representative EMPA compositions (wt.%) of wolframite from the Puy-les-Vignes deposit coming from different depths. Analytical conditions, reference standards and limits of detection are given in the text.

	0 m (Filon 2, PLV-14-07)					-22 m (Filon T18, PV-1)					-83 m (Filon T18, PV-7)						-131 m (Croiseur 1, PLV-7559)					
	1	2	3	4	5	1	2	3	4	5	1	2	3	4	5	11	2	3	4	7	8	
WO_3	76.54	76.23	76.63	75.54	75.97	76.48	75.65	76.66	76.92	76.72	76.5	75.29	76.31	76.18	76.31		76.3	76.71	77.07	76.99	76.23	
FeO	18.65	18.93	18.84	19.01	19.13	19	19.31	19.06	19.02	19.23	18.62	18.74	18.65	19.07	19.34		18.69	18.87	18.61	19.11	18.64	
MnO	4.23	4.08	4.08	4.17	3.96	4.02	3.88	4.05	4.13	3.86	4.22	4.24	4.29	4.1	3.86		4.32	4.18	4.35	4.19	4.35	
Nb_2O_5	bdl	bdl	bdl	bdl	bdl	bdl	bdl	bdl	bdl	bdl	0.09	0.1	bdl	bdl	0.13		bdl	0.08	bdl	0.09	bdl	
Ta_2O_5	bdl	bdl	bdl	bdl	bdl	bdl	bdl	bdl	bdl	bdl	bdl	bdl	bdl	bdl	bdl		bdl	bdl	bdl	bdl	bdl	
Sc_2O_3	bdl	bdl	bdl	bdl	bdl	bdl	bdl	bdl	bdl	bdl	bdl	bdl	bdl	bdl	bdl		bdl	bdl	bdl	bdl	bdl	
TiO_2	0.01	0.03	0.01	0.03	0.01	bdl	bdl	bdl	0.01	bdl	0.01	0.01	bdl	bdl	bdl		0.01	bdl	bdl	bdl	bdl	
SnO_2	bdl	bdl	bdl	bdl	bdl	bdl	bdl	bdl	bdl	bdl	bdl	bdl	bdl	bdl	bdl		bdl	bdl	bdl	bdl	bdl	
Total	99.43	99.27	99.56	98.75	99.07	99.5	98.84	99.77	100.1	99.81	99.44	98.38	99.25	99.35	99.64		99.32	99.84	100	100.4	99.22	
W	1.01	1.01	1.01	1.00	1.00	1.01	1.00	1.01	1.01	1.01	1.01	1.00	1.01	1.00	1.00		1.01	1.01	1.01	1.00	1.01	
Fe	0.79	0.81	0.80	0.81	0.82	0.81	0.83	0.81	0.80	0.81	0.79	0.80	0.79	0.81	0.82		0.80	0.80	0.79	0.80	0.79	
Mn	0.18	0.18	0.18	0.18	0.17	0.17	0.17	0.17	0.18	0.17	0.18	0.18	0.19	0.18	0.17		0.19	0.18	0.19	0.18	0.19	
Nb	0.00	0.00	0.00	0.00	0.00	0.00	0.00	0.00	0.00	0.00	0.00	0.00	0.00	0.00	0.00		0.00	0.00	0.00	0.00	0.00	
Ta	0.00	0.00	0.00	0.00	0.00	0.00	0.00	0.00	0.00	0.00	0.00	0.00	0.00	0.00	0.00		0.00	0.00	0.00	0.00	0.00	
Sc	0.00	0.00	0.00	0.00	0.00	0.00	0.00	0.00	0.00	0.00	0.00	0.00	0.00	0.00	0.00		0.00	0.00	0.00	0.00	0.00	
Ti	0.00	0.00	0.00	0.00	0.00	0.00	0.00	0.00	0.00	0.00	0.00	0.00	0.00	0.00	0.00		0.00	0.00	0.00	0.00	0.00	
Sn	0.00	0.00	0.00	0.00	0.00	0.00	0.00	0.00	0.00	0.00	0.00	0.00	0.00	0.00	0.00		0.00	0.00	0.00	0.00	0.00	
Fe/(Fe+Mn)	0.81	0.82	0.82	0.82	0.83	0.82	0.83	0.82	0.82	0.83	0.81	0.81	0.81	0.82	0.83		0.81	0.82	0.81	0.82	0.81	

Table 9: Continued.

	-171 m (Croiseur 1, PLV-7591)					-270 m (Filon A, PLV-7594)					-300 m (Croiseur 1, PLV-7597a)				
	1	2	3	4	5	1	2	3	4	5	1	2	3	4	5
WO_3	75.69	75.92	76.68	76.19	75.91	76.7	77.19	76.41	76.94	77.26	76.09	76.54	76.7	76.51	76.21
FeO	20.14	19.72	19.99	19.84	20.4	18.91	18.66	18.8	18.54	18.84	19.41	19.13	19.1	18.88	19.12
MnO	3.36	3.51	3.18	3.55	3.37	4.36	4.35	4.25	4.43	4.43	3.9	4.11	4.09	4.27	4.11
Nb_2O_5	0.09	bdl	bdl	0.09	bdl	bdl	bdl	bdl	bdl	bdl	0.48	0.5	0.45	0.41	0.46
Ta_2O_5	bdl	bdl	bdl	bdl	bdl	bdl	bdl	bdl	bdl	bdl	bdl	bdl	bdl	bdl	bdl
Sc_2O_3	bdl	bdl	bdl	bdl	bdl	bdl	bdl	bdl	bdl	bdl	bdl	bdl	bdl	bdl	bdl
TiO_2	bdl	bdl	bdl	bdl	bdl	bdl	bdl	bdl	bdl	bdl	0.01	0.01	0.01	0.02	0.02
SnO_2	bdl	bdl	bdl	bdl	bdl	bdl	bdl	bdl	bdl	bdl	bdl	bdl	bdl	bdl	bdl
Total	99.28	99.15	99.85	99.67	99.68	99.97	100.2	99.46	99.91	100.5	99.89	100.3	100.4	100.1	99.92
W	1.00	1.00	1.01	1.00	1.00	1.00	1.01	1.01	1.01	1.01	1.00	1.00	1.00	1.00	1.00
Fe	0.86	0.84	0.85	0.84	0.86	0.80	0.79	0.80	0.78	0.79	0.82	0.80	0.80	0.80	0.81
Mn	0.14	0.15	0.14	0.15	0.14	0.19	0.19	0.18	0.19	0.19	0.17	0.18	0.17	0.18	0.18
Nb	0.00	0.00	0.00	0.00	0.00	0.00	0.00	0.00	0.00	0.00	0.01	0.01	0.01	0.01	0.01
Ta	0.00	0.00	0.00	0.00	0.00	0.00	0.00	0.00	0.00	0.00	0.00	0.00	0.00	0.00	0.00
Sc	0.00	0.00	0.00	0.00	0.00	0.00	0.00	0.00	0.00	0.00	0.00	0.00	0.00	0.00	0.00
Ti	0.00	0.00	0.00	0.00	0.00	0.00	0.00	0.00	0.00	0.00	0.00	0.00	0.00	0.00	0.00
Sn	0.00	0.00	0.00	0.00	0.00	0.00	0.00	0.00	0.00	0.00	0.00	0.00	0.00	0.00	0.00
Fe/(Fe+Mn)	0.86	0.85	0.86	0.85	0.86	0.81	0.81	0.81	0.81	0.81	0.83	0.82	0.82	0.81	0.82

Table 10: Trace element compositions (in ppm) of wolframite from the Puy-les-Vignes deposit determined by LA-ICPMS.

	0 m (Filon 2, PLV-14-07) n=6				-22 m (Filon T18, PV-1) n=6				-83 m (Filon T18, PV-7) n=6				-131 m (Croiseur 1, PLV-7559) n=6			
	Mean	SD	Min	Max	Mean	SD	Min	Max	Mean	SD	Min	Max	Mean	SD	Min	Max
Li	bdl	-	-	-	bdl	-	-	-	bdl	-	-	-	4.0	0.5	3.3	4.4
Mg	2427	59	2380	2529	2303	27	2275	2349	1990	235	1698	2257	1428	38	1393	1496
Sc	2.0	0.7	1.1	3.1	3.8	0.8	2.9	5.1	44	8.8	35	59	74	20	39	97
Ti	107	48	58	168	46	5.0	39	54	20	14	10	46	28	21	17	71
V	3.6	0.6	2.8	4.4	3.3	1.3	2.6	6.0	2.9	0.7	2.2	3.7	5.6	1.3	3.1	6.8
Cr	bdl	-	-	-	bdl	-	-	-	bdl	-	-	-	bdl	-	-	-
Co	4.4	0.1	4.2	4.5	4.4	0.2	4.2	4.6	1.7	1.6	0.3	3.8	1.6	0.1	1.5	1.8
Ni	bdl	-	-	-	bdl	-	-	-	bdl	-	-	-	bdl	-	-	-
Cu	bdl	-	-	-	bdl	-	-	-	bdl	-	-	-	bdl	-	-	-
Zn	26	1.0	25	27	27	0.4	26	27	22	5.5	17	30	23	1.1	21	25
Ga	bdl	-	-	-	bdl	-	-	-	bdl	-	-	-	bdl	-	-	-
Ge	1.4	0.2	1.3	1.7	1.3	0.1	1.1	1.4	1.6	0.2	1.4	1.8	1.4	0.2	1.2	1.7
Rb	bdl	-	-	-	bdl	-	-	-	bdl	-	-	-	bdl	-	-	-
Sr	0.15	0.03	0.10	0.19	bdl	-	-	-	0.09	0.03	0.04	0.13	bdl	-	-	-
Y	15	4.5	10	21	16	15	8.4	47	9.1	2.3	6.2	12	24	6.7	10	28
Zr	2.0	1.0	1.1	3.9	1.6	0.6	1.1	2.3	1.7	0.5	1.3	2.7	7.5	2.2	3.6	10
Nb	185	94	93	336	170	42	124	228	566	35	497	588	268	178	161	629
Mo	1.1	0.1	1.0	1.2	1.8	1.8	0.9	5.3	0.9	0.1	0.7	1.0	1.2	0.1	1.1	1.4
Cd	bdl	-	-	-	bdl	-	-	-	bdl	-	-	-	bdl	-	-	-
In	0.8	0.1	0.7	0.9	0.8	0.3	0.6	1.4	0.6	0.3	0.4	1.0	1.5	0.4	0.6	1.8
Sn	1.2	0.4	0.7	1.9	0.9	0.6	0.6	2.1	0.8	0.3	0.5	1.2	1.0	0.1	0.9	1.2
Sb	bdl	-	-	-	bdl	-	-	-	bdl	-	-	-	bdl	-	-	-
La	0.4	-	0.4	0.4	bdl	-	-	-	bdl	-	-	-	bdl	-	-	-
Ce	0.6	-	0.6	0.6	bdl	-	-	-	bdl	-	-	-	bdl	-	-	-
Pr	0.1	-	0.1	0.1	bdl	-	-	-	bdl	-	-	-	bdl	-	-	-
Nd	0.3	-	0.3	0.3	bdl	-	-	-	bdl	-	-	-	bdl	-	-	-
Sm	0.1	-	0.1	0.1	bdl	-	-	-	bdl	-	-	-	bdl	-	-	-
Eu	0.1	-	0.1	0.1	0.1	-	0.1	0.1	bdl	-	-	-	bdl	-	-	-
Gd	0.2	0.1	0.2	0.3	0.3	0.4	0.1	0.9	0.2	0.1	0.1	0.2	0.4	0.1	0.2	0.6
Tb	0.1	0.0	0.1	0.2	0.1	0.2	0.1	0.4	0.1	0.0	0.1	0.1	0.2	0.1	0.1	0.3
Dy	2.0	0.6	1.3	2.8	2.2	2.1	1.0	6.5	1.5	0.4	1.0	2.0	3.4	0.9	1.5	4.1
Ho	0.8	0.2	0.5	1.1	0.8	0.7	0.4	2.3	0.5	0.1	0.3	0.6	1.3	0.4	0.6	1.5
Er	4.1	1.2	2.5	5.9	4.1	3.7	2.2	12	2.5	0.6	1.8	3.4	6.8	1.9	3.1	8.0
Tm	1.0	0.3	0.7	1.5	1.0	0.9	0.6	2.8	0.6	0.1	0.5	0.9	1.8	0.5	0.8	2.2
Yb	10	2.8	6.7	15	10	7.8	5.7	26	6.6	1.3	5.4	8.8	21	6	9	24
Lu	1.7	0.4	1.2	2.4	1.6	1.2	1.0	4.1	1.1	0.2	0.9	1.5	3.9	1.2	1.6	4.6
Hf	0.1	-	0.1	0.1	bdl	-	-	-	bdl	-	-	-	0.2	0.1	0.1	0.3
Ta	0.1	0.1	0.1	0.3	0.3	0.1	0.2	0.4	10	2.1	7.7	13	3.3	3.2	1.3	10
Pb	0.8	0.2	0.6	1.1	2.2	1.0	1.4	3.9	0.5	0.1	0.4	0.7	0.07	0.01	0.06	0.08
Bi	1.5	0.7	0.8	2.1	2.2	3.6	0.1	6.4	1.3	1.6	0.2	2.5	bdl	-	-	-
Th	0.0	0.0	0.0	0.1	0.1	0.0	0.0	0.1	0.0	0.0	0.0	0.0	0.05	0.01	0.04	0.06
U	1.5	0.7	0.8	2.6	0.7	0.6	0.3	2.0	0.2	0.1	0.2	0.5	0.5	0.1	0.4	0.6

Table 10: Continued.

	-171 m (Croiseur 1, PLV-7591) n=6				-270 m (Filon A, PLV-7594) n=6				-300 m (Croiseur 1, PLV-7597a) n=6			
	Mean	SD	Min	Max	Mean	SD	Min	Max	Mean	SD	Min	Max
Li	1.7	0.6	0.9	2.2	0.6	-	0.6	0.6	22	-	22	22
Mg	1316	109	1197	1451	2537	113	2441	2749	2249	78	2155	2362
Sc	75	21	48	99	60	6.6	52	69	115	52	69	211
Ti	21	13	11	40	79	20	54	97	100	44	51	163
V	2.5	0.7	1.5	3.4	5.5	0.6	4.4	6.3	11	5.2	4.7	17
Cr	bdl	-	-	-	bdl	-	-	-	2.1	0.4	1.7	2.7
Co	2.0	0.4	1.5	2.5	5.1	0.1	4.9	5.2	5.2	0.1	5.1	5.3
Ni	bdl	-	-	-	bdl	-	-	-	bdl	-	-	-
Cu	bdl	-	-	-	bdl	-	-	-	bdl	-	-	-
Zn	17	1.7	15	19	26	1.0	25	28	29	0.7	28	29
Ga	bdl	-	-	-	bdl	-	-	-	0.1	0.0	0.1	0.1
Ge	1.5	0.2	1.1	1.7	1.6	0.1	1.4	1.8	1.5	0.2	1.1	1.7
Rb	bdl	-	-	-	bdl	-	-	-	1.2	-	1.2	1.2
Sr	0	-	-	-	0.4	-	0.4	0.4	0.1	-	0.1	0.1
Y	22	11	7.4	34	10	0.8	10	12	33	12	18	45
Zr	2.2	0.6	1.7	3.2	5.4	1.4	3.6	7.5	24	15	7.3	45
Nb	386	146	243	562	882	157	678	1080	2012	642	1012	2977
Mo	1.2	0.1	1.1	1.3	0.9	0.1	0.9	1.0	1.1	0.1	1.0	1.2
Cd	bdl	-	-	-	bdl	-	-	-	bdl	-	-	-
In	0.6	0.2	0.4	0.8	0.7	0.1	0.6	0.8	2.2	1.0	1.2	3.6
Sn	0.6	0.2	0.5	0.8	1.2	0.1	1.1	1.4	8.2	4.1	3.6	14
Sb	bdl	-	-	-	bdl	-	-	-	bdl	-	-	-
La	0.1	-	0.1	0.1	0.5	-	0.5	0.5	bdl	-	-	-
Ce	0.1	-	0.1	0.1	0.7	-	0.7	0.7	bdl	-	-	-
Pr	bdl	-	-	-	0.1	-	0.1	0.1	bdl	-	-	-
Nd	bdl	-	-	-	0.3	-	0.3	0.3	bdl	-	-	-
Sm	bdl	-	-	-	0.1	-	0.1	0.1	bdl	-	-	-
Eu	bdl	-	-	-	0.0	-	0.0	0.0	bdl	-	-	-
Gd	0.4	0.2	0.1	0.6	0.2	0.0	0.1	0.2	0.4	0.2	0.2	0.6
Tb	0.2	0.1	0.1	0.3	0.1	0.0	0.1	0.1	0.3	0.1	0.2	0.4
Dy	3.2	1.6	1.0	5.2	1.4	0.1	1.2	1.5	4.2	1.5	2.3	5.5
Ho	1.2	0.6	0.4	1.8	0.5	0.1	0.5	0.6	1.6	0.6	0.9	2.3
Er	6.5	3.2	2.2	10	2.9	0.3	2.6	3.4	10	3.7	5.0	14
Tm	1.7	0.8	0.6	2.5	0.8	0.1	0.7	1.0	2.8	1.1	1.4	4.1
Yb	18	8.3	7.0	26	8.7	1.2	7.6	11	33	13	17	50
Lu	3.5	1.6	1.4	5.1	1.7	0.2	1.5	2.0	6.9	2.9	3.4	11
Hf	bdl	-	-	-	0.1	0.0	0.1	0.2	0.8	0.5	0.2	1.4
Ta	11	7.4	4.3	23	19	4.2	14	26	27	16	5.2	50
Pb	0.25	0.05	0.20	0.33	0.7	0.1	0.6	0.9	0.2	0.0	0.2	0.3
Bi	0.14	0.03	0.09	0.19	bdl	-	-	-	bdl	-	-	-
Th	0.04	0.01	0.03	0.05	0.0	0.0	0.0	0.1	0.0	0.0	0.0	0.1
U	0.40	0.09	0.27	0.54	0.8	0.2	0.5	1.0	4.1	2.3	1.4	7.0

Chapter 3: Capabilities of sequential and quasi-simultaneous LA-ICPMS for the multi-element analysis of small quantity of liquids (pl to nl): insights from fluid inclusion analysis

Matthieu Harlaux[1], Olga Borovinskaya[2,3], Daniel A. Frick[2,4], Daniel Tabersky[2], Sabrina Gschwind[2], Antonin Richard[1], Detlef Günther[2] and Julien Mercadier[1]

Article published in *Journal of Analytical Atomic Spectrometry* (2015, 30, 1945-1969)

1: Université de Lorraine, CNRS, CREGU, GeoRessources, F-54506 Vandœuvre-lès-Nancy, France.
2: ETH Zurich, Department of Chemistry and Applied Biosciences, Laboratory of Inorganic Chemistry, Vladimir-Prelog-Weg 1, CH-8093 Zürich, Switzerland.
3: Present address: Tofwerk AG, Uttigenstrasse 22, CH-3600 Thun, Switzerland.
4: Present address: GFZ German Research Centre for Geosciences, Section 3.4 Earth Surface Geochemistry, Telegrafenberg, D-14473 Potsdam, Germany.

Abstract

Three configurations of inductively coupled plasma mass spectrometers (ICPMS), namely: a quadrupole (QMS) and a sector-field (SFMS), both equipped with a standard cylindrical ablation cell, and an orthogonal time-of-flight (TOFMS), equipped with a fast washout ablation cell, were coupled with the same 193 nm Excimer laser ablation system in order to evaluate their capabilities for measurement of multiple minor and trace elements in small quantities of liquids (pl to nl), such as fluid inclusions. Analyses were performed with different objects: (i) multi-element solutions sealed in silica capillaries of internal diameter of 20 µm serving as synthetic analogues of natural fluid inclusions; (ii) natural two-phase (liquid + vapour) fluid inclusions with low salinity (ca. 4.8 wt% NaCl eq) and homogeneous compositions, trapped in quartz crystals from the Alps; (iii) natural multi-phase (liquid + vapour + multiple solids) fluid inclusions with high salinity (ca. 13-15 wt% NaCl eq) and homogeneous compositions, trapped in quartz crystals from the Zambian Copperbelt. This study demonstrates that the SFMS and TOFMS provide improvements, particularly in term of

limits of detection (LODs) and precision, compared to the QMS traditionally used for the measurement of fluid inclusions. SFMS leads on average to lower LODs within one order of magnitude compared to QMS and TOFMS, but precision and accuracy are lower due to longer acquisition cycle times. TOFMS presents both advantages of having rapid and quasi-simultaneous acquisition for all isotopes from ^{6}Li to ^{238}U in a very short cycle time down to 30 μs, with higher precisions and lower LODs than for QMS for isotopes with m/Q > 11. Its use, coupled to a fast washout cell, leads to (i) the improvement in the analysis of small-size (< 10 μm) and multi-phase fluid inclusions and (ii) detection of higher number of isotopes compared to QMS and SFMS, which are both limited by the number of measured isotopes from short transient signals of fluid inclusions. Consequently, the tested TOFMS, coupled with a fast washout ablation cell, appears to be a promising instrument for the analysis of natural fluid inclusions by LA-ICPMS, especially for small, multi-phase and/or low salinity fluid inclusions.

Keywords:
LA-ICPMS; Quadrupole; Sector-field; Time-of-flight; fluid inclusions; capillaries.

1. Introduction

The multi-element quantification of minor and trace elements, typically present in concentrations from the ng l^{-1} to g l^{-1} range, in small quantities of liquids (pl to nl) is of a major analytical interest for a large variety of applied fields, for instance in chemistry (e.g., Gschwind et al., 2011; 2013), geology (e.g., Günther et al., 1998; Heinrich et al., 2003; Allan et al., 2005; Pettke et al., 2012; Rauchenstein-Martinek et al., 2014; Albrecht et al., 2014), biology (e.g., Kutscher et al., 2011), medicine (e.g., Hsieh et al., 2011; Kumtabtim et al., 2011), climatology (e.g., Krachler et al., 2005) or environmental sciences (e.g., Ciceri et al., 2008). One current analytical challenge is to improve and to develop strategies for analyses of such small quantities of liquid, whether by: (1) reducing the detectable fluid volume; (2) increasing the number of detectable elements; (3) increasing the sensitivity of the instruments and/or (4) increasing the precision and accuracy of the measurements. For example, a recent research field has been developed on the detection and quantification of nanoparticles carried by liquid microdroplets, in order to study the risks of nanoparticles for the environment and the human health (Gschwind et al., 2011; Borovinskaya et al., 2013). Such microdroplets have a typical diameter of 30-40 µm and generate very short transient signals when analysed by inductively coupled mass spectrometry, and remain a challenging analytical issue (Gschwind et al., 2011; Borovinskaya et al., 2013).

One of the most challenging case studies are the geological fluids trapped in natural fluid inclusions. The latter represent droplets of fluids, ranging from pl to nl in volume, and trapped in tiny cavities of typically tens of µm in diameter during the crystallization of minerals. Natural fluid inclusions can consequently provide direct information about the composition of fluids from which minerals have precipitated and represent therefore invaluable tool for the reconstruction of the geological fluids, which have circulated in the Earth's interior for ca. 4.6 billions years (Roedder, 1984). They are of primary interest for a large set of geological research fields, in particular for the study of diagenesis (e.g., Goldstein, 2001), metamorphism (e.g., Touret, 2001; Scambelluri and Philippot, 2001), geothermal systems (e.g., Smith et al., 1998; Simmons et al., 2007), oil and gas deposits (e.g., Munz, 2001; Burruss et al., 1998) and mineral deposits (e.g., Ulrich et al., 1999; Wilkinson et al., 2009; Richard et al., 2012; Stepherd et al., 1995). Natural geological fluids are characterized by an extremely wide variety of chemical elements, potentially from Li to U, with varying concentration ranges from percent to below µg g^{-1}, and their analysis represents consequently high analytical challenge.

Due to its high sensitivity, speed and multi-element capabilities, laser ablation coupled to inductively coupled plasma quadrupole mass spectrometers (LA-ICPQMS, hereafter called QMS) has proven (Günther et al., 1997) to be one of the most suitable techniques for the analysis of geological fluids trapped in natural crystals (see review in Pettke et al., 2012). This technique offers several advantages compared to other instrumentations (LIBS, synchrotron-XRF or PIXE for example), like well-controlled ablation of quartz using UV lasers (Longerich et al., 1996), the large concentration dynamic range (10^9 to 10^{11}), the relatively low limits of detection (down to 0.01 μg g^{-1}; Pettke et al., 2012) and fast acquisition times (in the ms range per isotope). At the present time, sequential scanning QMS typically allows registering 20 isotope signals with m/Q from 7 to 238 in less than 260 ms in a single mass scan (Pettke et al., 2012). The development of specific quantification strategies to evaluate the elemental concentrations by QMS was also a major cause of the increasing acceptance of LA-ICPMS in fluid inclusion research (e.g., Günther et al., 1998; Heinrich et al., 2003; Allan et al., 2005; Schlegel et al., 2012; Wälle et al., 2014).

The signals generated in QMS from this type of tiny samples are usually of relatively low intensity for minor to trace elements and last only for several seconds due to the rapid release of the fluid during the ablation process (Longerich et al., 1996). Unambiguous multi-element detection of such transient signals is not a trivial task when sequential quadrupole mass spectrometers are used and often requires a compromise between the signal duration, acquisition parameters of the mass spectrometer and the number of isotopes to be monitored (Heinrich et al., 2003; Allan et al., 2005; Pettke et al., 2012; 2000). The current use of QMS is consequently restricted to relatively large-size (> 30 μm) and moderate- to high-salinity (> 5 wt% NaCl eq) fluid inclusions, which contain detectable concentrations of the analytes (Heinrich et al., 2003; Allan et al., 2005; Pettke et al., 2012). However, this type of fluid inclusions represents a rather limited proportion of the fluid inclusions present in natural samples and are potentially more affected by post-crystallization modifications (e.g., leaking, cracks and/or deformation) than smaller ones. Moreover, even for such samples, the number of isotopes that can be monitored rarely exceeds 20, including majors, minors and trace elements. This can consequently makes a global and representative understanding of the chemical composition of paleofluids difficult. Furthermore, analytical limitations are encountered for small-size (< 10 μm) fluid inclusions as well as for those containing low trace element contents (< 1 μg g^{-1}), thus constraining the interpretation of several geological processes related to paleofluids circulations.

Other types of mass spectrometers coupled to laser ablation systems have been tested

during the last years, with the aim of improving the quantification of elemental and even isotopic compositions of geological fluids (see review of Pettke et al., 2012). Single-collector sector-field mass spectrometers coupled to laser ablation (LA-ICPSFMS, hereafter called SFMS) have achieved about ten times higher sensitivities compared to QMS instrumentation for natural fluid inclusions (Wälle and Heinrich, 2014). However, QMS and SFMS are both limited by sequential detection, which can deteriorate accuracy and precision of the analysis due to signal aliasing (Borovinskaya et al., 2013; Pettke et al., 2000). Moreover, SFMS are also limited by the multiple magnet jumps required to cover the entire mass range from Li to U, which results in longer cycle times compared to QMS, with around 20% longer cycle for 20 isotopes measured. This temporal limitation could appear as a main drawback especially for small fluid inclusions (< 20 μm), but the recent study by Wälle and Heinrich (2014) concluded that SF expands the accessible fluid inclusion size range to 2 or 3 times smaller volumes or 10 times lower concentrations in larger inclusions.

One application of multi-collector mass spectrometers coupled to laser ablation (LA-MC-ICPMS) was recently successfully proposed for the determination of Pb isotopic ratios in natural fluid inclusions (Pettke et al., 2011). However, the small volume of fluid trapped is a major limitation for the precise measurement of isotopic ratios. Even with a multi-collection and high sensitivity, the extremely limited duration of the signal and the relatively low concentration allow successful results only for exceptional geological conditions, for example for the Bingham Cu-Mo-Au deposit (Pettke et al., 2010). Even if LA-MC-ICPMS present far lower limits of detection than QMS, they do not allow the acquisition of the whole mass spectra, which is a strong limitation for fluid inclusion studies, especially with the need to measure an internal standard (mainly ^{23}Na) for the quantification of the fluid compositions (Heinrich et al., 2003).

Detection based on time-of-flight mass spectrometers coupled to laser ablation (LA-ICPTOFMS, hereafter called TOFMS) has been considered highly promising for multi-element analysis of very short transient signals, because it allows quasi-simultaneous measurements of all isotopes (Myers and Hieftje, 2010). This configuration of a mass spectrometer allows overcoming the problem of aliasing for short transient signals and could consequently improve the quantification of fluids trapped in natural minerals (Borovinskaya et al., 2013; Tanner and Günther, 2008; 2009). First generations of TOFMS with an axial configuration applied to natural fluid inclusions had lower sensitivities, low signal to noise ratio, low dynamic range and higher limits of detection compared to QMS (Heinrich et al., 2003; Chen et al., 2011). Nevertheless, previous study on multiphase fluid inclusions from the

Mole granite (Bleiner et al., 2000) demonstrated the abilities of axial TOFMS for the detection of up to 42 isotopes above the LODs, as well as the discrimination of signals of elements contained in fluid or in solid matrices. Recently, a new prototype of TOFMS with an orthogonal configuration has been developed (Borovinskaya et al., 2013; Tanner and Günther, 2008), which allows quasi-simultaneous detection of the whole mass range, with a high temporal resolution of 30 µs, a mass resolving power > 1200, a dynamic range of 10^6 and abundance sensitivity of 10^{-5}. This instrument was shown to be of particular use for extremely short transient signals (tens of µs up to ms range) generated by nanoparticles and microdroplets. Coupling this new TOFMS with laser ablation systems providing low signal dispersion (Wang et al., 2013) can lead to increased signal to noise ratios. Other types of simultaneous and quasi-simultaneous mass analysers exist, such as the Mattauch-Herzog sector-field mass spectrometer (MHMS) (Schilling et al., 2007; Resano et al., 2012) or the ICPTOFMS Optimass (Sturgeon et al., 2000), respectively. However, no data are currently available from these instruments for the analysis of minor and trace elements in small quantity of liquids.

The aim of the present study is to describe and determine the capabilities of SFMS and TOFMS for the analysis of fluid inclusions and to compare them to QMS, which is the state-of-the-art and the most frequently used instrument for the measurements of fluid inclusions by LA-ICPMS. In this objective, two types of samples have been analysed and the three instruments were evaluated and compared in terms of signal duration, intensity, precision, accuracy (when possible) and limits of detection (LODs). The first set of objects was consisting of sealed 20 µm inner diameter silica capillaries, containing multi-element (33 to 37) solutions with different set of concentrations (0.1, 1, 10 and 50 µg g^{-1}) and with Na fixed at a concentration of ca. 1000 µg g^{-1}. These capillaries mimic the configurations of small volumes of liquid trapped in a solid matrix, such as natural fluid inclusions, and have already been applied successfully to standardize the fluid inclusion analysis by LA-ICPMS (Stoffell et al., 2008; Leisen et al., 2012). They allow determining the achievable accuracy of the measurements for different concentrations of trace elements, as they are filled with solutions of known elemental concentrations. They moreover exhibit a much higher reproducibility compared to natural fluid inclusions, due to their fixed geometry and to their constant behaviour during laser ablation. A second set of objects are natural fluid inclusions selected from two origins and trapped within quartz crystals: (i) the first sample (BP-66-210, Alps) contains numerous two-phase (liquid + vapour) and low salinity fluid inclusions, with a homogeneous composition and variable diameters (from 5 to 100 µm), allowing to test

precision and LODs of the three LA-ICPMS configurations for a wide range of fluid volumes; (ii) the second sample (7703-25, Zambia) contains multi-phase (liquid + vapour + solids) and high salinity fluid inclusions, but with a smaller range of diameters (10 to 30 μm). The presence of several phases, including precipitates, makes the interpretation of the signals obtained for these inclusions with sequential ICPMS more challenging. In this respect, the capabilities of the TOFMS have been tested compared with QMS for the distinction between elements contained in fluid and solids and consequently for a better multi-elemental quantification of complex fluid inclusions.

2. Experimental

2.1. Instrumentation, operating conditions and data processing

All analyses were carried out at the Laboratory of Inorganic Chemistry at ETH Zürich (Switzerland). Three different configurations of LA-ICPMS were used for this study: a quadrupole (QMS) (Elan DRC Plus, PerkinElmer Inc., Ontario, Canada), a sector-field (SFMS) (Element 2, ThermoScientific, Bremen, Germany) and a prototype of time-of-flight (TOFMS) (Tofwerk AG, Thun, Switzerland). This prototype had been developed, by coupling an orthogonal TOF mass analyser (Tofwerk AG, Thun, Switzerland) with the ICP and vacuum interface of a commercial quadrupole-based ICPMS (Elan 6000, PerkinElmer/Sciex, Ontario, Canada) (see Borovinskaya et al., 2013 for details). The same laser ablation system, namely a 193 nm GeoLas ArF Excimer (MicroLas, Göttingen, Germany), was coupled to the three ICPMS systems. A standard cylindrical ablation cell with relatively large internal volume was used for both QMS and SFMS configurations, as traditionally used for the analysis of fluid inclusions by sequential instruments (Heinrich et al., 2003; Pettke et al., 2012; Günther et al., 1997; Wälle and Heinrich, 2014). For the TOFMS, a low dispersion tube cell, developed by Wang et al. (2013), was used, which provides a higher signal to noise ratio per single laser pulse and can reduce the signal duration to less than 30 ms. Its use with a sequential mass spectrometer instrument, like QMS and SFMS, is problematic because signal aliasing will strongly deteriorate the attainable precision (Pettke et al., 2000). However, it is particularly beneficial in the case of TOFMS, by strongly increasing the signal/noise ratio, as shown in recent studies (Wang et al., 2013; Giesen et al., 2014). The cycle time in this paper is resembling the time necessary to produce a single data point in the transient signal. For sequential instruments, such as QMS and SFMS, the cycle time is given by the number of

measured isotopes and by the time necessary for the analysis of each isotope (dwell time), plus the time necessary for the change of scanning mass windows (settling time). The Element 2 was configured to achieve lowest possible magnet settling times, reducing the cycle time by about a factor of two compared to the manufacturer technical recommendations. For the configuration of TOFMS used, the quasi-simultaneous acquisition of all isotope signals is performed in 30 μs (cycle time). In our experiments, 1000 of these extractions were integrated before every data point was read out to reduce the total amount of data generated (Borovinskaya et al., 2013). For simplicity, the cycle time for TOFMS in the text will be considered as 30 ms. The reader should, however, keep in mind that every cycle is an average of 1000 TOF extractions. The standard reference material NIST SRM 610 (reference values from Jochum et al., 2011) was used as external standard for the calibration of all analyses, and was analysed twice at the beginning and at the end for each set of samples to establish elemental sensitivity and to correct for instrumental drift (Longerich et al., 1996).

Operating conditions are given in Table 11, and are different between the measurement of multi-element solution in silica capillaries and the two types of natural fluid inclusions analysed (see 2.2 for sample description). Laser ablation of silica capillaries (see 3.1.) was realised with a frequency of 10 Hz, a laser spot diameter fixed at 32 μm and a theoretical fluence of 124 J cm^{-2} per pulse. Laser ablation of fluid inclusions (see 3.2. and 3.3.) was realised with a frequency of 10 Hz and using a stepwise opening procedure, as described in Günther et al. (1998), starting the ablation with a laser spot diameter of 2 μm and stepwise increasing the spot diameter to the size of the fluid inclusion (from 5 to 90 μm), with a theoretical fluence between 16 and 500 J cm^{-2} per pulse. This procedure allows a controlled ablation by reducing the mechanical stress on the quartz surface, which limits the risk of splashing of the fluid (Günther et al., 1998). LA-ICPMS were optimized for highest sensitivity for an intermediate m/Q range, while maintaining a ThO/Th < 0.5%, U/Th ~ 1 and Ba^{2+}/Ba^{+} < 3%, as determined on NIST SRM 610. Instrumental background signals (only from the gas blank) were measured for 20 s before each ablation for background correction and calculation of the limits of detection (Longerich et al., 1996). Helium was used as the carrier gas to transport the ablated material from the ablation cell to the ICPMS and argon was added via a laminar flow adapter before the ICP torch (Eggins et al., 1998). For the fast washout cell, a combination of argon and helium is used directly in the cell and so no additional make-up gas was used (Wang et al., 2013). To increase the apparent magnet settling time on the Element 2, without increasing the actual magnet settling time, ^{22}Ne was introduced as a support mass. The earlier magnet settling together with the measurement time

spent on ^{22}Ne helped to stabilise the magnet and improved the precision of the ^{23}Na intensity (measured using a E-Scan). For consistency, the support mass ^{22}Ne was also measured on the QMS. Due to a very high background, originating from previous experiments, the quantification of ^{11}B was compromised with the SFMS. Operating conditions for the TOFMS were chosen to maximize the transmission of high m/Q trace element isotopes thus compromising the transmission of ions below m/Q = 9 within the notch filter upstream the TOFMS. Therefore, the sensitivity of these ions (including ^{7}Li) was insufficient for their detection at the concentrations used. Signal integration and absolute quantification were performed using the software StalQuant, developed at ETH Zürich (see details in Fricker, 2012). The LODs were calculated according to the equation of Longerich et al. (1996), since it is the most frequently method used in publications dealing with natural and synthetic fluid inclusions. For all analyses of silica capillaries and fluid inclusions, ^{23}Na was used as the internal standard for the quantification. For fluid inclusions, the Na content was estimated from the wt.% equivalent NaCl as determined by microthermometry (Bodnar, 2003). Signal integration for capillaries and fluid inclusions was set on the basis of the Na total signal duration.

2.2. Materials

Three in-house multi-element solutions containing 33 elements (Li, B, Na, Mg, Al, K, Ca, Cr, Mn, Fe, Co, Ni, Cu, Zn, Ga, Ge, Sr, Nb, Ag, Cd, In, Sn, Ba, La, Tb, Hf, Ta, W, Pt, Tl, Pb, Bi, U) at concentrations of ca. 0.1, 1 and 10 µg g^{-1} each (except Na fixed at ca. 1000 µg g^{-1}) were prepared in 1% HNO_3 from single- and multi-element standard solutions (Inorganic Ventures, Merck). An in-house multi-element solution containing 37 elements (the 33 elements cited above + Rb, Cs, Ba and Sb) at a concentration of ca. 50 µg g^{-1} (except Na which was fixed at ca. 1000 µg g^{-1}) was also prepared. Silica capillaries (Photon Lines SAS, St-Germain-en-Laye, France) with an internal and external diameter of 20 µm and 150 µm respectively, and of ca. 1 cm length were filled with the solutions by capillarity and the ends were tipped with paraffin wax for sealing. An internal diameter of 20 µm was selected to mimic the typical size of natural fluid inclusions analysed by LA-ICPMS.

Two types of natural fluid inclusions were selected from two different quartz samples for this study:

(i) Two-phase (liquid + vapour) fluid inclusions from a quartz crystal from the French Alps (sample BP-66-210, Mont Blanc Massif, Pointe des Améthystes, see Fabre, 2000 for

description). This sample contains numerous fluid inclusions, which are considered to be homogeneous in composition, as already shown by previous studies (Leisen et al., 2012; Fabre, 2000; Fabre et al., 1999; Fabre et al., 2002) of fluid inclusions in similar quartz crystals from the Mont Blanc Massif. These fluid inclusions have irregular shape and range from a few microns to 100 µm in diameter (Fig. 31a) and consequently from a few hundred pl to tens of nl in volume. At room temperature they are characterized by a dominant liquid aqueous phase with dissolved salts and a vapour phase of H_2O-CO_2-N_2 as determined by Raman spectroscopy, and no daughter minerals (Fabre, 2000). All fluid inclusions have a relatively homogeneous salinity of 4.8 ± 0.5 wt% NaCl equivalent as determined by microthermometry prior to LA-ICPMS analysis. The characteristics of its fluid inclusions (homogeneity in chemical composition and variability in size) make this sample a perfect experimental case study for the analytical comparison of the three LA-ICPMS setups;

(ii) Multi-phase (liquid + vapour + multiple solids) fluid inclusions were selected from a quartz crystal from the western Zambian Copperbelt (sample 7703-25, Kabompo domes, Lolwa occurrence, see Eglinger et al., 2014 for description). These fluid inclusions show irregular shape and range from 10 to 30 µm in diameter (Fig. 31b). They contain a dominant aqueous phase with dissolved salts, a vapour phase of H_2O-N_2-H_2 determined by Raman spectroscopy and numerous solids previously identified by Raman spectroscopy as calcium chloride hydrates, halite (NaCl), hematite (Fe_2O_3) and calcite ($CaCO_3$), plus other unidentified solids (Fig. 31b). All fluid inclusions have a high, relatively homogeneous salinity of 53-59 wt% $CaCl_2$ and 13-15 wt% NaCl equivalent as determined by microthermometry and their detailed composition, as determined by LA-ICPQMS, is given by Eglinger et al. (2014). This sample was used in order to test the capabilities of the TOFMS for analysing complex, multi-phase and high-salinity fluid inclusions compared with the QMS. No analyses were performed with SFMS on this sample.

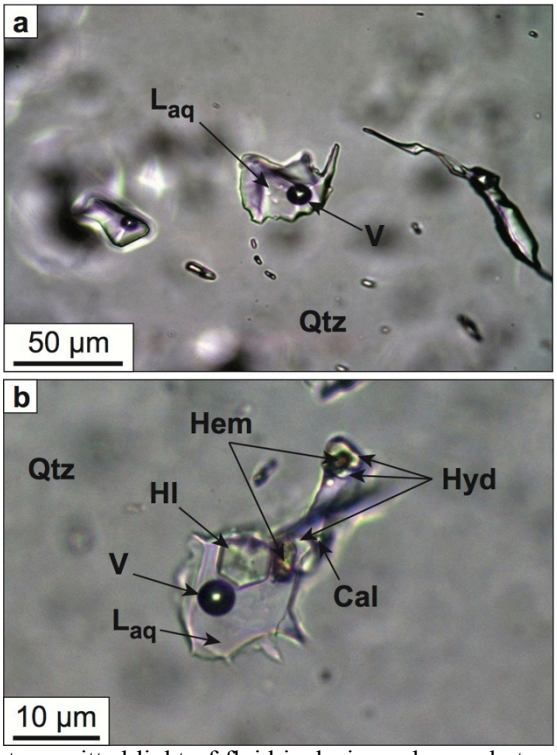

Fig. 31: Microphotographs in transmitted light of fluid inclusions observed at room temperature from selected quartz (Qtz) samples. (a) Two-phase fluid inclusions (sample BP-66-210, Mont Blanc Massif, Pointe des Amethystes, French Alps) containing a dominant aqueous phase with dissolved salts (L_{aq}) and a vapour phase (V). This sample contains numerous 5 to 100 µm fluid inclusions of this type with high compositional homogeneity. (b) Multi-phase fluid inclusion (sample 7703-25, Kabompo domes, Lolwa occurence, Zambia) containing a dominant aqueous phase with dissolved salts (L_{aq}), a vapour phase (V) and various solids: calcium chloride hydrates (Hyd), halite (Hl), hematite (Hem) and calcite (Cal).

3. Results and discussion

3.1. Silica capillaries

3.1.1. Signals

Typical transient LA-ICPMS signals obtained from silica capillaries containing multi-element solutions of ca. 10 µg g^{-1} concentration are shown in Fig. 32. The oscillations observed in the transient signals from the TOFMS acquisition (Fig. 32c) corresponds to the 10 Hz frequency of the laser and demonstrates the low aerosol dispersion of the transport system employed with the short cycle time used (30 ms). The signal durations for the capillaries (determined based on the ^{23}Na signal) are typically longer than 20 s for the high dispersion transport system used for QMS and SFMS, while this is reduced to about 4 s for the tube cell

used for TOFMS. With a cycle time of 468 ms for QMS, 887 ms for SFMS and 30 ms for TOFMS, the signal durations correspond to ca. 47, 27 and 133 data points respectively. Peak signal/background ratios for ^{23}Na are similar for the three setups, with ca. 5×10^3 for QMS, 6×10^2 for SFMS and 10^3 for TOFMS. For the four tested solutions, the lighter isotopes (^{7}Li and ^{11}B) are barely detected by TOFMS due to the optimization setting used for these experiments (see 2.1.). At high concentrations (ca. 50 µg g^{-1}), all elements added to the solutions are detected by QMS, SFMS and TOFMS, except for ^{11}B by SFMS and ^{7}Li by TOFMS (due to elevated backgrounds). At low concentrations (ca. 0.1 µg g^{-1}), only isotopes with m/Q > 88 are detected on average by QMS and SFMS, whereas TOFMS detects only isotopes with m/Q > 139.

3.1.2. Precision and accuracy

The precision and accuracy were calculated from means and standard deviations for a series of measurements of different silica capillaries (n = 4 to 7) for each solution (0.1, 1, 10, 50 µg g^{-1}) and for all the isotopes listed in Table 12. The precision is represented by the relative standard deviation (RSD) expressed in % for a series of measurements and is defined by equation (1).

(1) $$RSD_i = \frac{s_i}{m_i} \times 100\%$$

where s_i and m_i are respectively the standard deviation (1σ) and the mean of the measurements (n = 4 to 7) for one isotope i.

The accuracy is represented by the relative error (RE) expressed in % between the expected concentration of one isotope i in each selected solution (C_i) and the mean concentration calculated from the LA-ICPMS analyses (C_m) of the same solution trapped in different silica capillaries (n = 4 to 7) as defined by equation (2).

(2) $$RE_i = \frac{(C_m - C_i)}{C_i} \times 100\%$$

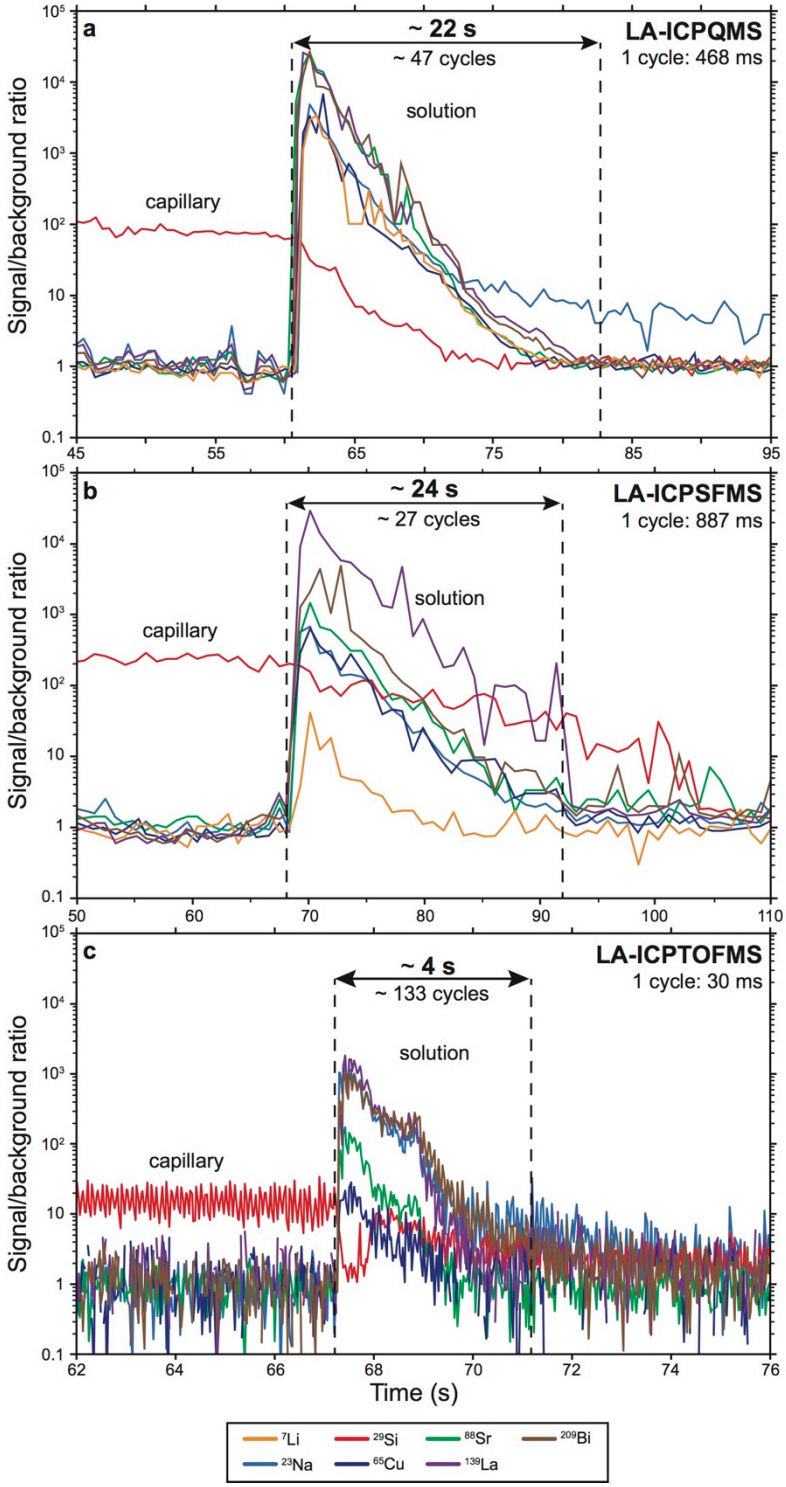

Fig. 32: Typical transient signals for silica capillaries with internal diameter of 20 µm containing multi-element solutions at concentration of 10 µg g^{-1} (except Na with 1000 µg g^{-1}) analysed by LA-ICPQMS (a), LA-ICPSFMS (b) and LA-ICPTOFMS (c). Seven representative isotopes (^{7}Li, ^{23}Na, ^{29}Si, ^{65}Cu, ^{88}Sr, ^{139}La, ^{209}Bi) are shown here, but the dataset for all isotopes is given in Table 12. For QMS and SFMS, 35 isotopes were measured, whereas all isotopes are measured with the TOFMS (see Table 11). Signal duration (based on ^{23}Na), number of cycles and cycle times for each setup are indicated. Analytical conditions for the three setups are given in Table 11.

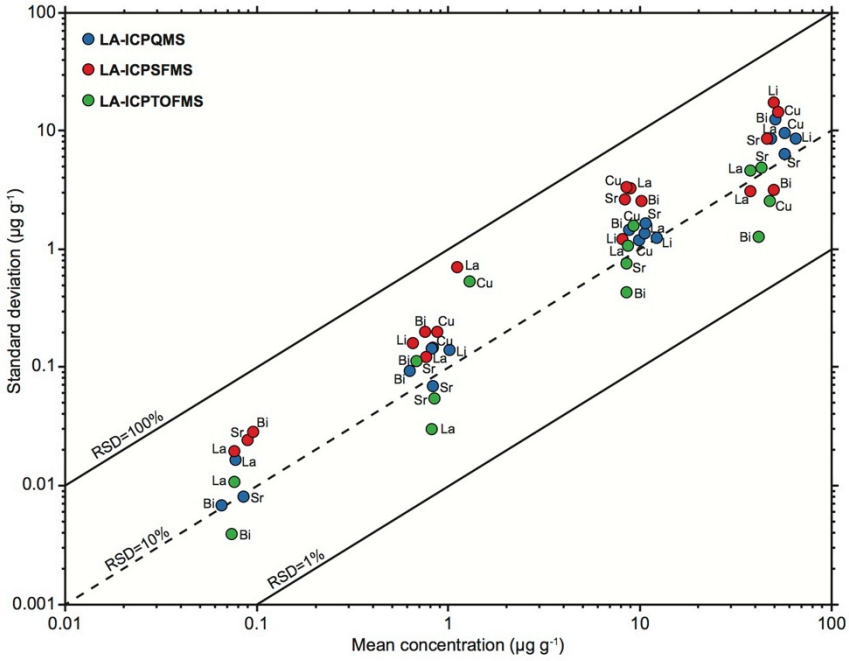

Fig. 33: Standard deviation versus mean concentration (n=4 to 7) for five selected isotopes (^{7}Li, ^{65}Cu, ^{88}Sr, ^{139}La, ^{209}Bi) from silica capillaries with internal diameter of 20 µm containing four different multi-element solutions at concentration of 0.1, 1, 10 and 50 µg g^{-1} (except for ^{23}Na with 1000 µg g^{-1}) analysed by LA-ICPQMS, LA-ICPSFMS and LA-ICPTOFMS. The precision is represented by the RSD (relative standard deviation). Dataset for all measured isotopes is given in Table 12. Elements with concentration below limit of detection are not represented. Analytical conditions for the three setups are given in Table 11.

The value of accuracy is therefore negative if the calculated mean concentration from LA-ICPMS analyses is underestimated and positive if it is overestimated. The precision and accuracy values obtained for the four solutions and for five isotopes (^{7}Li, ^{65}Cu, ^{88}Sr, ^{139}La, ^{209}Bi), selected from the low to high atomic masses, are presented in Fig. 33 and Fig. 34 respectively. The full dataset for solutions with 33 elements (at ca. 0.1, 1 and 10 µg g^{-1}) or 37 elements (at ca. 50 µg g^{-1}) is given in Table 12. RSD values are typically within 9 to 30% for QMS and 6 to 60% for SFMS, using the same cylindrical ablation cell, and within 3 to 40% for TOFMS (except ^{7}Li) using the fast washout cell, depending on concentrations and detected isotopes (Fig. 33, Table 12). The RSD values of the measured isotopes are not depending on the concentration of the different solutions for the three investigated setups and are not directly correlated with the signal intensity. These findings indicate that the analytical precision is likely dominated by the laser ablation behaviour (non-continuous ablation of liquid) and not by counting statistics. RE values are typically within -40 to 40% for QMS, -50 to 50% for SFMS and -30 to 30% for TOFMS, for all concentrations and isotopes when detected (Fig. 34, Table 12), and generally tend to be higher at low concentration.

Anomalously high RSD and RE values are occasionally found for some isotopes such as ^{57}Fe (RSD up to 125%, RE up to 170%), ^{118}Sn (RSD up to 122%, RE up to 47%) or ^{205}Tl (RSD up to 67%, RE down to -74%). For isotopes such as ^{57}Fe, this can be related to polyatomic interferences of $^{40}Ar^{16}O^{1}H$. For other isotopes such as ^{118}Sn, ^{181}Ta or ^{205}Tl, these variabilities could be either due to a problem of stability of these elements in solution or to a problem during solution preparation. The fact that Ba in the 50 µg g^{-1} solution is consistently found at twice the reference values is most likely explained by an error in sample preparation. Consequently, these five elements are not considered in the final evaluation.

3.1.3. Limits of detection

LODs calculated from means of the individual acquisitions (n = 5 to 6) for the QMS, SFMS and TOFMS are presented in Fig. 35 for the solutions at concentration of ca. 10 µg g^{-1} and the dataset for all the tested solutions is given in Table 12. The LODs do not depend of the concentration of the different solutions for a same instrument. The observed differences reflect only the variations in fillings of the capillary or the quantity of fluid removed during laser ablation. For the three instruments, LODs decrease of ca. two to three orders of magnitude from low to high atomic mass. The highest LODs are typically within 5 to 30 µg g^{-1} for light isotopes (m/Q < 57) for the QMS and SFMS (except for ^{11}B) and within 10 to 20 µg g^{-1} for the TOFMS (except for ^{7}Li). The lowest LODs are typically within 0.01 and 0.1 µg g^{-1} for heavy isotopes (m/Q > 139) for the SFMS and TOFMS and between 0.1 to 1 µg g^{-1} for the QMS. For intermediate isotopes with 57 ≤ m/Q ≤ 139, SFMS shows systematically lower LODs than the QMS and SFMS within up to one order of magnitude of ca. 0.05 µg g^{-1} for m/Q < 88. QMS and TOFMS have similar LODs within the same order of magnitude of ca. 0.5-3 µg g^{-1} and 0.01-0.5 µg g^{-1} for light and heavy isotopes respectively, but TOFMS tends to have slightly lower LODs than QMS for isotopes with m/Q > 111 (Fig. 35, Table 12). Compared to the QMS, LODs are lower for SFMS and TOFMS, and are in the same order of magnitude of ca. 0.01 µg g^{-1} for m/Q > 159 for both SFMS and TOFMS.

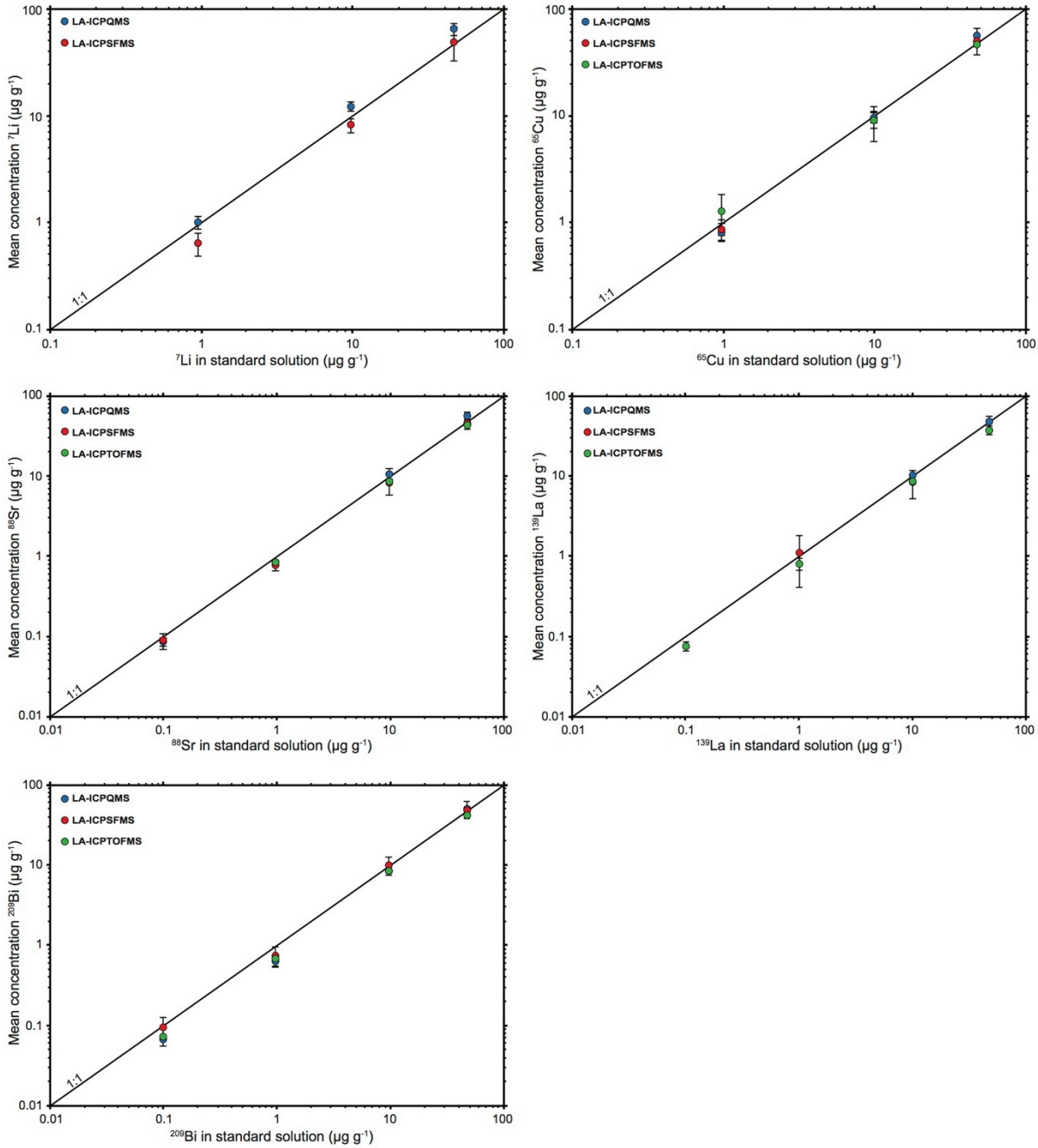

Fig. 34: Mean and standard deviation (1σ) of concentrations measured by LA-ICPMS (LA-ICPQMS, LA-ICPSFMS and LA-ICPTOFMS) versus nominal concentration in standard solution for five selected isotopes (^{7}Li, ^{65}Cu, ^{88}Sr, ^{139}La, ^{209}Bi) from silica capillaries with internal diameter of 20 µm containing multi-element solutions. The accuracy is a function of the length of the orthogonal projection of the data points on the 1:1 slope. Circles and error bars stand for mean (n=4 to 7) and standard deviation (1σ) values respectively (see Table 12). Dataset for all measured isotopes is given in Table 12. Analytical conditions for the three setups are given in Table 11.

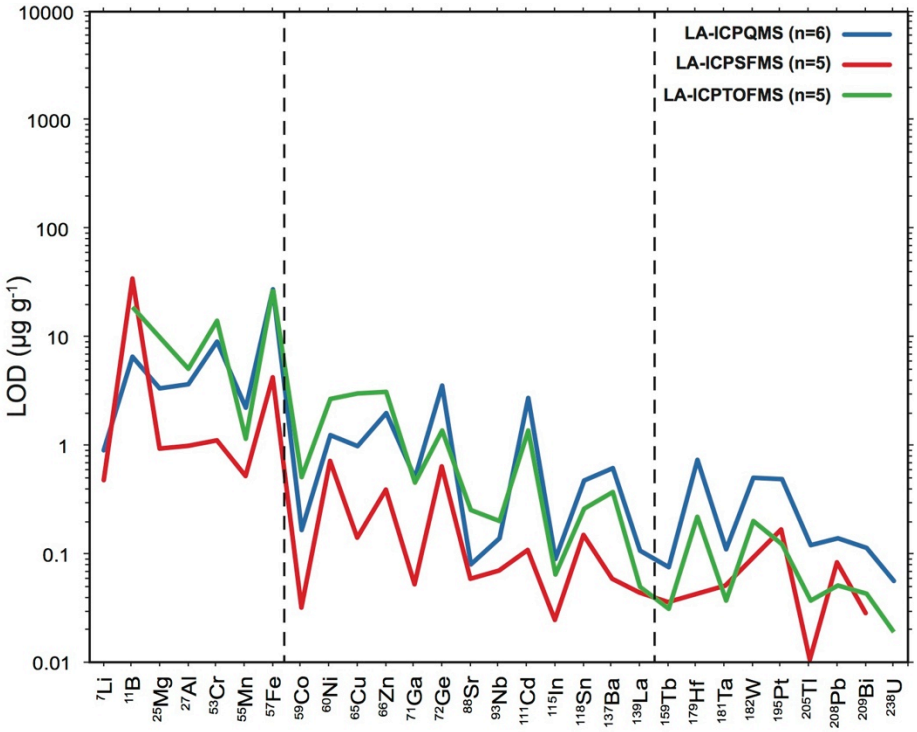

Fig. 35: Mean value for limits of detection (LOD) calculated for silica capillaries with internal diameter of 20 µm containing multi-element solutions at concentration of 10 µg g^{-1}, and analysed by LA-ICPQMS, LA-ICPSFMS and LA-ICPTOFMS. Analytical conditions for the three setups are given in Table 11.

3.2. Two-phase fluid inclusions

3.2.1. Signals

Typical transient LA-ICPMS signals for 25 µm two-phase fluid inclusions from sample BP-66-210 (Mont Blanc Massif, French Alps) are shown in Fig. 36. The signal durations after opening the fluid inclusions mainly depend on the inclusion size (Fig. 37), the salinity being identical for all fluid inclusions. For inclusions of 25 µm in size, the cylindrical ablation cell led to signal durations typically of ca. 26 s with the QMS and 22 s with the SFMS, while the fast washout tube cell reduced the signal length to ca. 9 s. With a cycle time of 273 ms for QMS, 560 ms for SFMS and 30 ms for TOFMS (Table 11), the signal durations correspond to ca. 95, 39 and 300 data points respectively. Within the two-phase fluid inclusions, 9 isotopes (^{7}Li, ^{11}B, ^{23}Na, ^{25}Mg, ^{35}Cl, ^{85}Rb, ^{88}Sr, ^{133}Cs and ^{137}Ba) could be detected with the QMS, 10 isotopes (^{7}Li, ^{23}Na, ^{35}Cl, ^{44}Ca, ^{85}Rb, ^{88}Sr, ^{133}Cs, ^{137}Ba, ^{182}W and ^{208}Pb) with the SFMS, whereas 14 isotopes (^{11}B, ^{23}Na, ^{25}Mg, ^{35}Cl, ^{39}K, ^{55}Mn, ^{75}As, ^{85}Rb, ^{88}Sr, ^{121}Sb, ^{133}Cs, ^{137}Ba, ^{182}W and ^{208}Pb) were detected using the TOFMS. Considering the ratios normalized to ^{23}Na, only the first seconds of the fluid inclusions signals show constant values (5 s for QMS, 9 s

for SFMS and 1.5 s for TOFMS). This corresponds to ca. 96 to 98% of the integrated ^{23}Na intensity of the fluid inclusions signals and ca. 18, 16 and 52 data points for QMS, SFMS and TOFMS respectively (Fig. 36). Peak signal/background ratios for ^{23}Na are ca. 10^4 for QMS, 2×10^3 for SFMS and 9×10^3 for TOFMS respectively. Peak signal/background ratios for minor and trace elements are in the same order of magnitudes for the three configurations (Fig. 36).

3.2.2. Concentration, standard deviation and precision

The concentrations for the two-phase fluid inclusions analysed (sample BP-66-210, Alps) are presented for the three instruments (QMS, SFMS and TOFMS) and as function of their diameter (in ranges of < 10 µm, 10-25 µm and > 25 µm) in Fig. 38. The calculated mean concentrations, standard deviations (1σ) and precisions (RSD) for all fluid inclusions are given in Table 13. The isotopes ^{35}Cl, ^{85}Rb, ^{88}Sr and ^{133}Cs, ^{137}Ba were systematically detected by the three LA-ICPMS configurations and for fluid inclusions > 10 µm, with a good reproducibility of the measurements. The mean concentrations and standard deviations for the QMS, SFMS and TOFMS are respectively of 4110 ± 7640, 1100 ± 710 and 19000 ± 5140 µg g^{-1} for ^{35}Cl, 210 ± 80, 155 ± 127 and 113 ± 37 µg g^{-1} for ^{85}Rb, 55 ± 30, 49 ± 36 and 36 ± 10 µg g^{-1} for ^{88}Sr, 70 ± 35, 62 ± 65 and 35 ± 13 µg g^{-1} for ^{133}Cs and 10 ± 20, 6.5 ± 8 and 7.4 ± 5 µg g^{-1} for ^{137}Ba (Table 13). The RSD calculated for all fluid inclusions vary considerably and range within 33 to 200% for QMS (n=35), 10 to 182% for SFMS (n=24) and 23 to 167% for TOFMS (n=40) respectively. For the detected elements, RSDs calculated appear lower for the TOFMS compared to QMS and SFMS respectively, suggesting an improvement in terms of precision achieved by the quasi-simultaneous detection. In all cases, however, the calculated RSDs for fluid inclusions are higher compared to silica capillaries due to their variability in size, shape and depth. Other isotopes are detected sporadically by the three instruments, such as ^{25}Mg, ^{137}Ba or ^{182}W, and are characterized by higher standard deviations (Table 13). ^{79}Br was detected in the fluid inclusions by the three instruments, but was not quantified because of the uncertain reference value for NIST SRM 610 used for calibration (Jochum et al., 2011). Additional isotopes, detected by the TOFMS in fluid inclusions > 10 µm, are ^{39}K, ^{55}Mn, ^{75}As and ^{121}Sb, which were not included in the isotope selection for the QMS and SFMS. On the other hand, the isotopes ^{59}Co, ^{65}Cu or ^{66}Zn were not detected by the three instruments due to concentrations below LODs (Table 13).

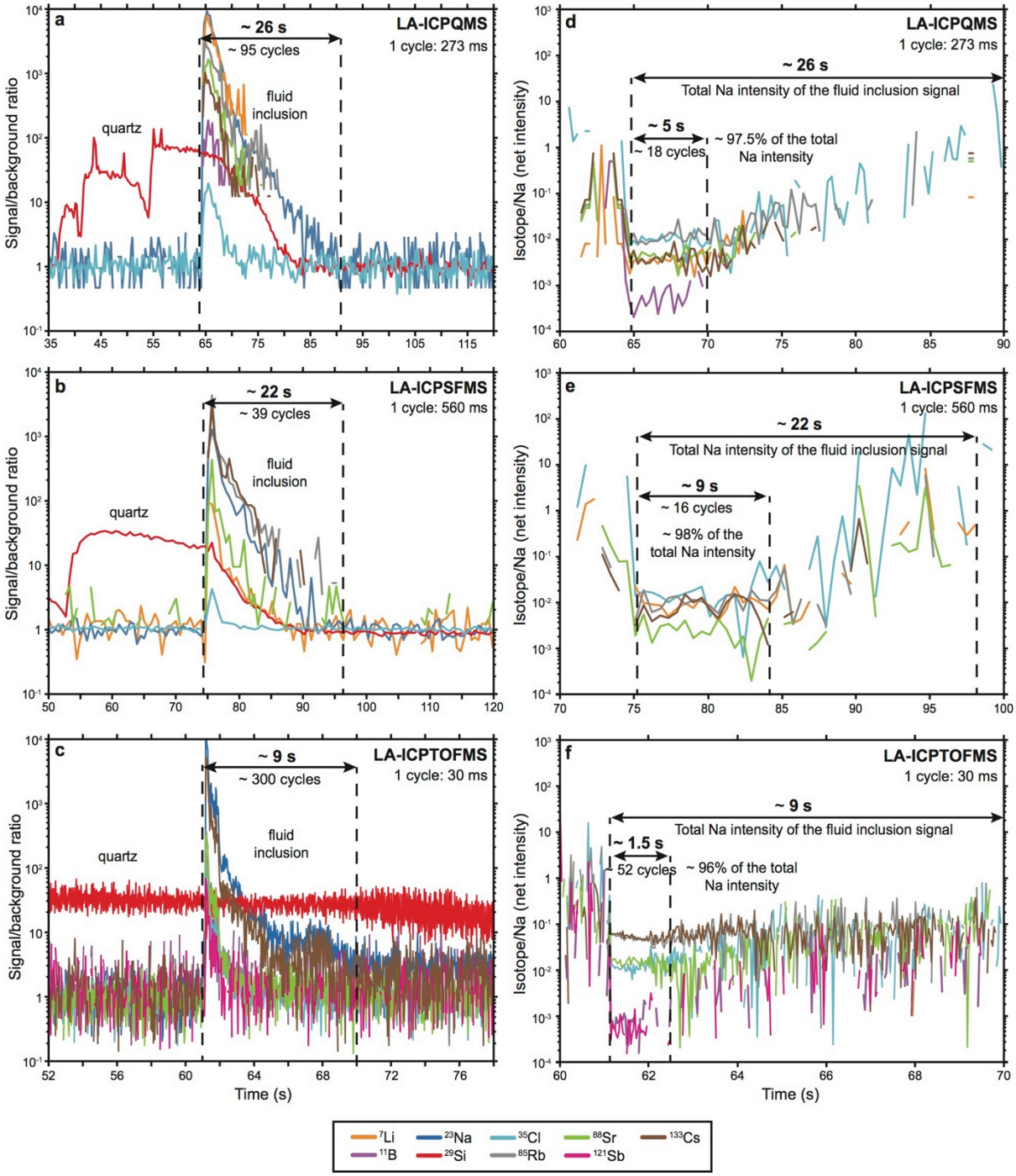

Fig. 36: Typical transient signals for 25 µm two-phase fluid inclusions (sample BP-66-210, Alps) analysed by LA-ICPQMS (a), LA-ICPSFMS (b) and LA-ICPTOFMS (c). Corresponding signal/background ratios of analysed isotopes normalised to ^{23}Na (internal standard) are presented for LA-ICPQMS (d), LA-ICPSFMS (e) and LA-ICPTOFMS (f). Nine selected isotopes (^{7}Li, ^{11}B, ^{23}Na, ^{29}Si, ^{35}Cl, ^{85}Rb, ^{88}Sr, ^{121}Sb, ^{133}Cs) are shown here, but the dataset for all isotopes is given in Table 12.Analytical conditions for the three setups are given in Table 11.

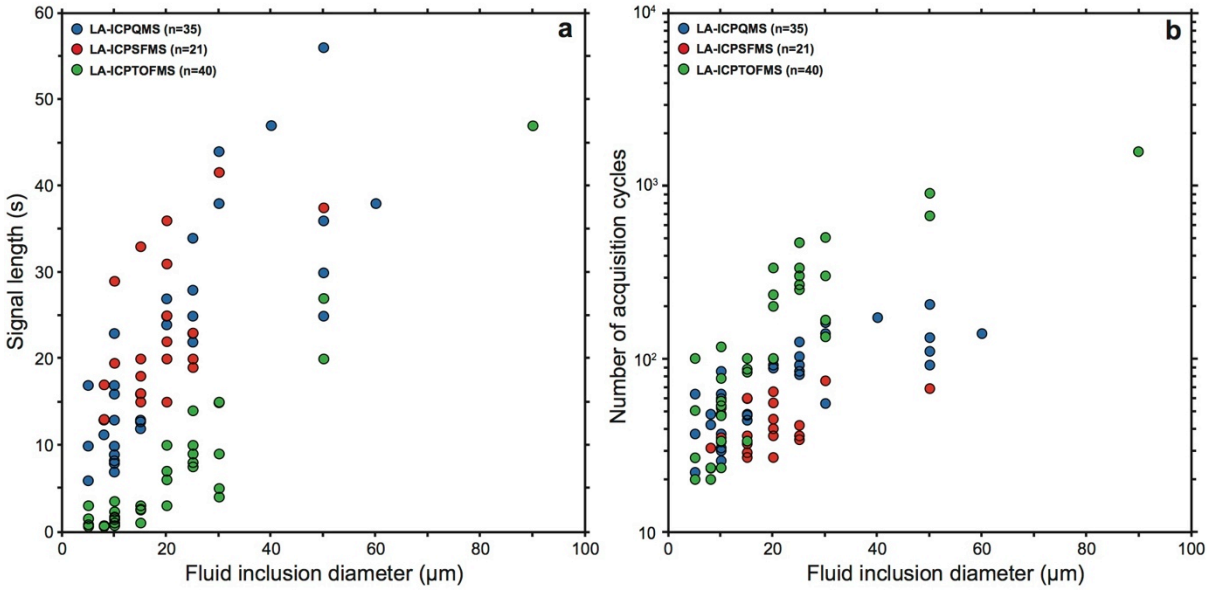

Fig. 37: Total signal duration (a) and number of acquisition cycles (b) as function of fluid inclusion diameter for individual two-phase fluid inclusions measurement (sample BP-66-210, Alps) analysed by LA-ICPQMS, LA-ICPSFMS and LA-ICPTOFMS. The number of acquisition cycles is function of the cycle time for each configuration of LA-ICPMS (273 ms for QMS, 560 ms for SFMS and 30 ms for TOFMS). Analytical conditions for the three setups are given in Table 11. n: number of fluid inclusions analysed.

Small fluid inclusions (< 10 µm) were also measured with the three instruments, but relatively few data were obtained for this sample set. Nevertheless, results obtained show that TOFMS still detects five isotopes (^{35}Cl, ^{85}Rb, ^{88}Sr, ^{133}Cs and ^{208}Pb) in addition to ^{23}Na, whereas QMS and SFMS detect only one to two isotopes (^{85}Rb and/or ^{133}Cs). As shown in Fig. 39, the analysis of a 5 µm fluid inclusion by QMS allows only the detection of the ^{23}Na signal, present as the major isotope. Minor isotopes such as ^{85}Rb, ^{88}Sr and ^{133}Cs cannot be detected by QMS, but were detected using the TOFMS. Detection of ^{35}Cl signal is improved with the TOFMS, which represents a major benefit for the quantification of fluid inclusions based on their chlorinity (Wilkinson et al., 2009). Considering signal to background ratios of different isotopes as function of ^{23}Na signal to background ratio for a 25 µm fluid inclusion analysed by TOFMS (Fig. 40), it appears that all isotopes show a linear positive correlation with the ^{23}Na used as internal standard. The correlation is particularly strong for the first 1.3 s of the signal, which represents 95% of the total ^{23}Na intensity and corresponds to ca. 44 measurements cycles. About 90% of fluid inclusions total ^{23}Na intensity is contained in the first 0.7 s, which corresponds to ca. 24 measurements cycles (Fig. 40). Due to its quasi-simultaneous detection, quantification of two-phase fluid inclusions with the TOFMS could

be consequently realised on one data point at the maximum peak intensity of the ^{23}Na signal, corresponding to the first 30 ms of the signal.

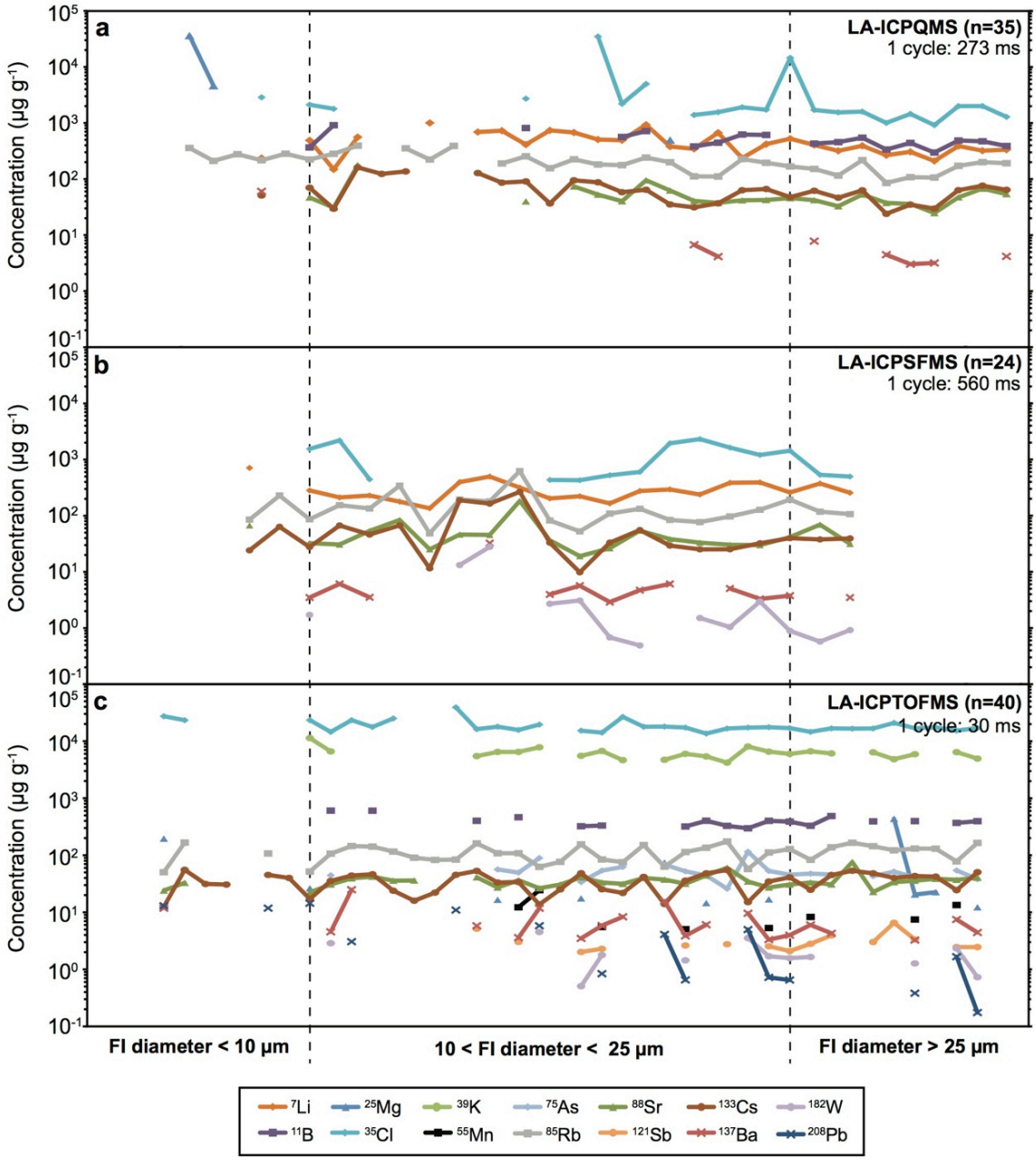

Fig. 38: Composition of two-phase fluid inclusions (sample BP-66-210, Alps) with different diameters (< 10 µm, 10-25 µm, > 25 µm) analysed by LA-ICPQMS (a), LA-ICPSFMS (b) and LA-ICPTOFMS (c). Dataset for all fluid inclusions is given in Table 13. Analytical conditions for the three setups are given in Table 11. n= number of fluid inclusions analysed.

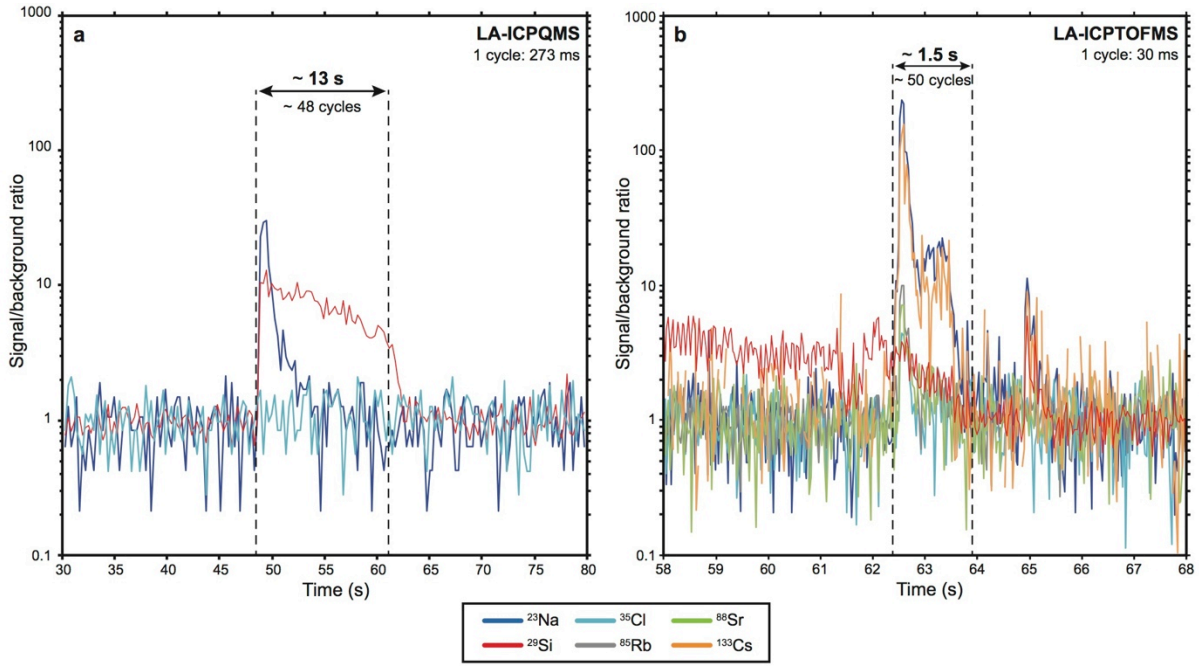

Fig. 39: Typical transient signals for 5 µm two-phase fluid inclusions (sample BP-66-210, Alps) analysed by LA-ICPQMS (a) and LA-ICPTOFMS (b).

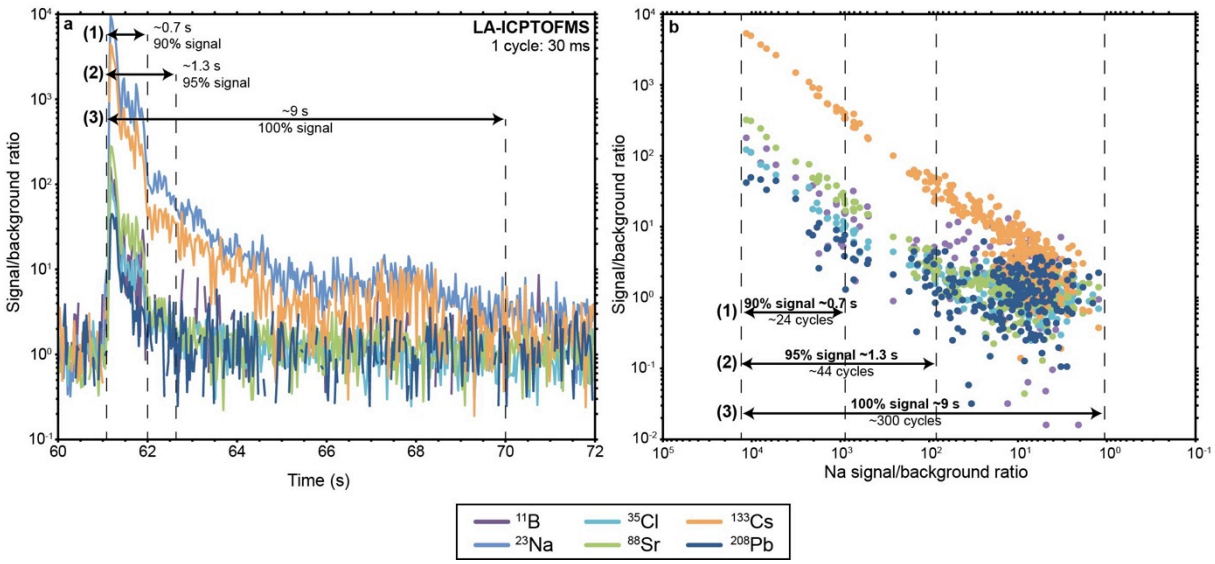

Fig. 40: Representation of different integration windows for a transient LA-ICPTOFMS signal from a 25 µm fluid inclusion (sample BP-66-210, Alps). (a) Na signal/background ratio as a function of time for 90, 95 and 100% of the total fluid inclusion Na signal. (b) Signal/background ratios for different isotopes as a function of Na signal/background ratio.

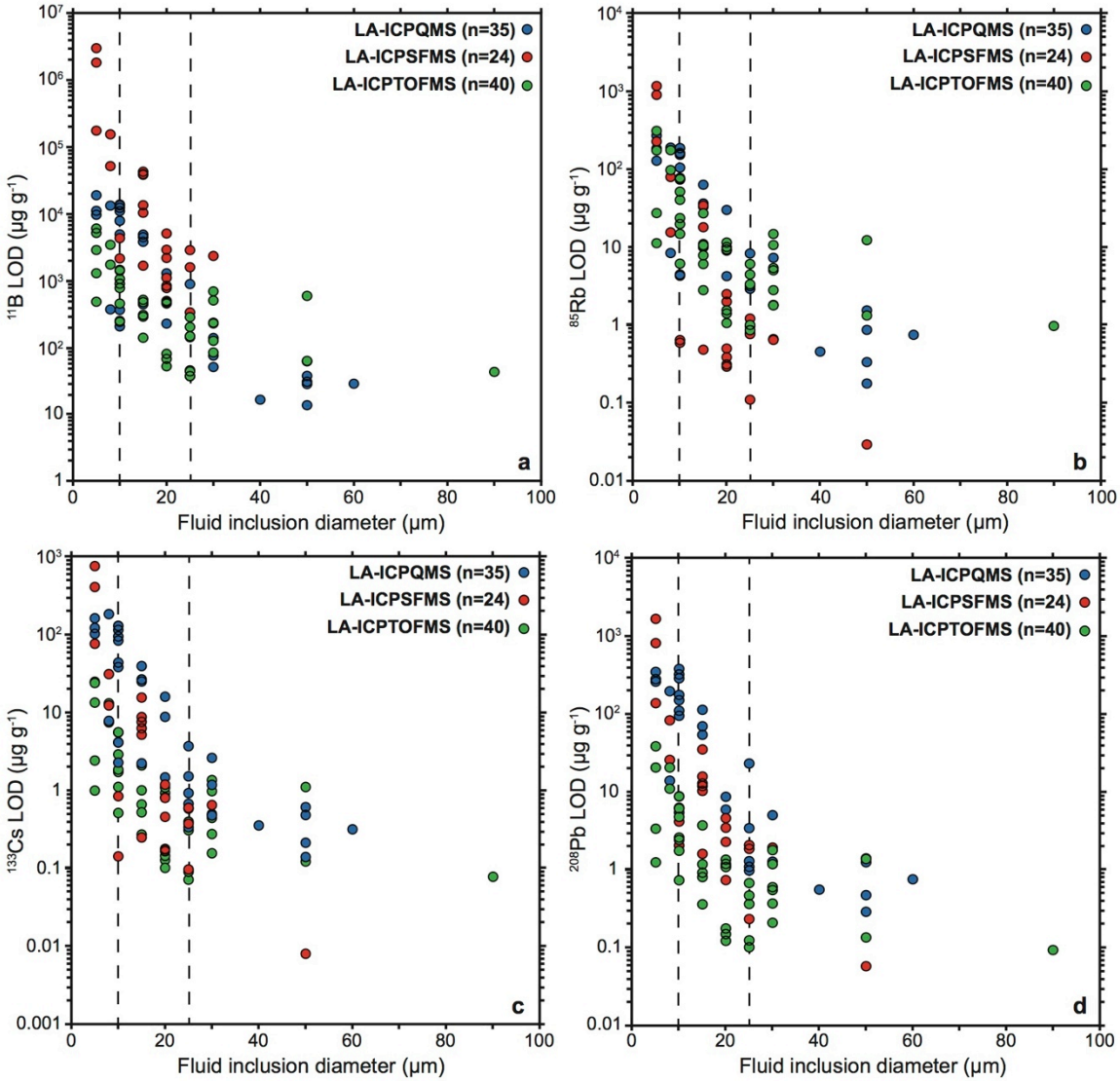

Fig. 41: Limits of detection (LODs) for LA-ICPQMS, LA-ICPSFMS and LA-ICPTOFMS as a function of two-phase fluid inclusion diameter (sample BP-66-210, Alps) for ^{11}B (a), ^{85}Rb (b), ^{133}Cs (c) and ^{208}Pb (d). The values are reported in Table 13. Analytical conditions for the three setups are given in Table 11. n= number of fluid inclusions analysed.

3.2.3. Limits of detection

LODs calculated for fluid inclusions from means of individual acquisitions (n=24 to 40) for the QMS, SFMS and TOFMS are given in Table 13. As shown in Fig. 41, the LODs are inversely correlated to the inclusion diameter with a parabolic decrease, regardless of the element considered. LODs calculated for isotopes analysed by QMS, SFMS and TOFMS and variable diameters of fluid inclusions (< 10 µm, 10-25 µm and > 25 µm) are shown in Fig. 42.

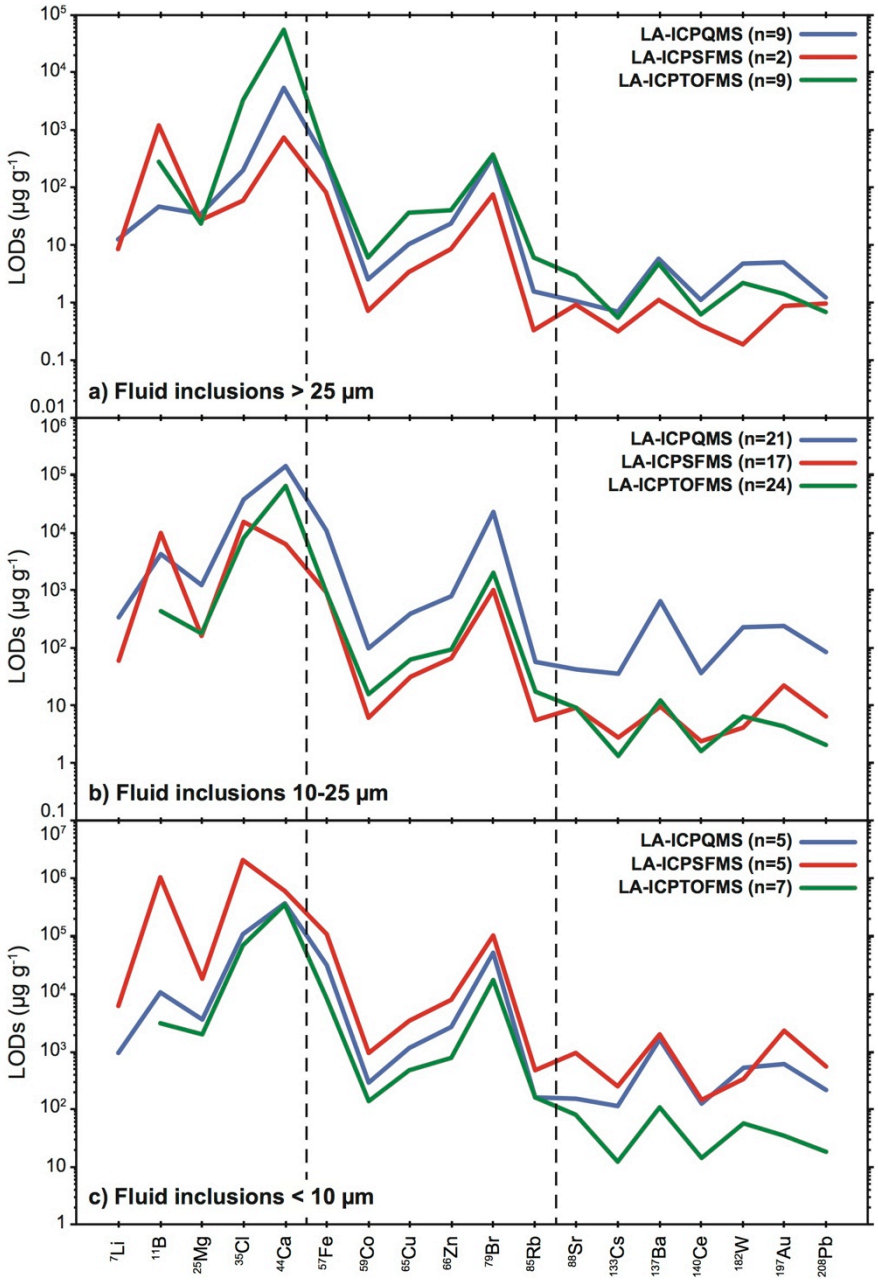

Fig. 42: Mean limits of detection (LODs) calculated for a series of individual fluid inclusions (sample BP-66-210, Alps) of diameter < 10 µm (a), 10-25 µm (b) and > 25 µm (c), analysed by LA-ICPQMS, LA-ICPSFMS and LA-ICPTOFMS. The values are reported in Table 13. Analytical conditions for the three setups are given in Table 11.

For fluid inclusions > 25 µm, LODs for QMS and TOFMS are within the same order of magnitude, varying typically within 10^1 to 10^4 µg g^{-1} for light isotopes ($m/Q \leq 57$) and within 10^{-1} to 10^1 µg g^{-1} for heavy isotopes ($m/Q \geq 85$), whereas SFMS shows the lowest LODs, generally within one to two orders of magnitude below QMS and TOFMS. For fluid inclusions between 10 and 25 µm in diameter, LODs for SFMS and TOFMS are within the same order of magnitude, varying between 10^2 to 10^5 µg g^{-1} for light isotopes ($m/Q \leq 57$) and

between 1 to 10^3 µg g^{-1} for heavier isotopes. LODs for QMS tend to be higher by ca. one order of magnitude compared to TOFMS and SFMS. For fluid inclusions < 10 µm, the lowest LODs are achieved by TOFMS, varying within 10^2 to 10^5 µg g^{-1} for m/Q < 85 and within 10^1 to 10^2 µg g^{-1} for m/Q > 85, for which they are lower by ca. one order of magnitude compared to those of QMS and SFMS. Thus, the size of fluid inclusions strongly constrains the achievable LODs of each instrument and the results show particularly that TOFMS provide the lowest LODs for fluid inclusions with diameter ≤ 10 µm.

3.3. Multi-phase fluid inclusions

3.3.1. Signal structure

Typical transient signals from QMS and TOFMS acquisition of 15 µm multi-phase (liquid + vapour + solids) fluid inclusions from sample 7703-25 (Kabompo domes, Zambia) are shown in Fig. 43. The signal durations (based on ^{23}Na) obtained for such fluid inclusions are longer than those obtained for fluid inclusions of similar size from the Alps (sample BP-66-210) due to their higher salinities and last for ca. 60 s for QMS and ca. 20 s for TOFMS. With a cycle time of 195 ms for QMS and 30 ms for TOFMS (Table 11), this corresponds to ca. 307 and 667 acquisitions cycles respectively. Peak signal/background ratios for ^{23}Na are ca. 10^3 for QMS and 2×10^2 for TOFMS. The QMS allows the detection of 13 isotopes (^{23}Na, ^{25}Mg, ^{39}K, ^{44}Ca, ^{47}Ti, ^{57}Fe, ^{65}Cu, ^{85}Rb, ^{88}Sr, ^{95}Mo, ^{137}Ba, ^{208}Pb and ^{238}U) on the 15 measured, whereas TOFMS detects 38 isotopes (^{23}Na, ^{24}Mg, ^{25}Mg, ^{26}Mg, ^{27}Al, ^{35}Cl, ^{39}K, ^{55}Mn, ^{57}Fe, ^{59}Co, ^{64}Zn, ^{65}Cu, ^{66}Zn, ^{67}Zn, ^{68}Zn, ^{85}Rb, ^{86}Sr, ^{88}Sr, ^{95}Mo, ^{96}Mo, ^{97}Mo, ^{98}Mo, ^{130}Te, ^{133}Cs, ^{135}Ba, ^{136}Ba, ^{137}Ba, ^{138}Ba, ^{139}La, ^{140}Ce, ^{141}Pr, ^{143}Nd, ^{205}Tl, ^{206}Pb, ^{207}Pb, ^{208}Pb, ^{209}Bi and ^{238}U) on the whole analysed mass range.

The signals obtained for QMS for all detected isotopes have all the same shape and are correlated in time, as observed in Fig. 43 by constant ratios normalized to ^{23}Na. The different solids (halite, calcite, hydrates, hematite) observed in the fluid inclusions by optical microscopy and determined by Raman spectroscopy are consequently not individualized with QMS.[54] For a similar 15 µm multi-phase fluid inclusion, the liquid and solid phases are properly discriminated during TOFMS measurement, with the signals of the majority of the detected isotopes displaying specific shapes during acquisition. This confirms that elements or groups of elements are present in different physical phases within the fluid inclusions, as

previously observed by microscopy and Raman spectroscopy. The observed elemental discrimination, shown here for the first time using TOFMS, is possible only due to the fast washout of the ablation cell used in combination with the quasi-simultaneous detection of the TOF mass analyser. The different phases present within the fluid inclusion are thus not dispersed significantly within the ablation cell and are transported separately during laser ablation to the MS. As a result, the signals of Rb-Sr-Cu-Al-Pb-Ba-Cs, Na-Mg-K-Cl and Fe-Mn-Ti could be interpreted respectively as those of the aqueous phase, hydroxides and hematite crystals, as previously identified by Raman spectroscopy (Eglinger et al., 2014). However, some signals are mixed and could indicate a partitioning of the elements between different phases. The ^{23}Na signal is not completely correlated to the signal of ^{35}Cl, which is probably due to quasi-simultaneous ablation of NaCl solid and liquid phase in which Na and Cl are major solutes but present in different proportions to NaCl. The same observation is made with the Ba isotopes, which show a common signal shape compared to those of Rb and Sr isotopes, but with minor differences, suggesting that Ba could be present both in the aqueous phase and in a solid phase (e.g., barite, $BaSO_4$) not identified previously by Raman spectroscopy. The signal of ^{65}Cu is partially correlated with those of ^{64}Zn, ^{66}Zn, ^{67}Zn and ^{68}Zn, suggesting that these elements are likely associated within a single phase. Finally, the signal of U shows a peak clearly distinct from the other signals, and correlated with the one of Mo (not shown), indicating that these two elements are present in an independent phase and not as a solute in the aqueous phase. However, the presence of a U-bearing mineral is not common in these fluid inclusions, since its signal has not been detected systematically here.

Discrimination between elements in fluid phase and daughter minerals has been previously observed by LA-ICPMS (Günther et al., 1998 for the first occurrence), but this was obtained for large-size (> 40 μm in diameter) and high-salinity fluid inclusions (Günther et al., 1998; Heinrich et al., 2003; Bleiner et al., 2000), and could not be reached for the tested small fluid inclusions, as demonstrated by the QMS results (Fig. 43). These previous observations suggest that the aerosol dispersion in the large volume ablation cells does not allow distinguishing the different phases at such extent. This preliminary result requires an extensive investigation, in particular, by testing the capabilities and the limits on synthetic fluid inclusions in comparison with natural multi-phase fluid inclusions from different geological contexts. Nevertheless, this result opens interesting perspectives, for instance to allow: (i) identification of solids difficult to analyse by Raman spectroscopy (small size and/or transparent solids) and (ii) detailed analysis of minor to trace elements concentrations within solids.

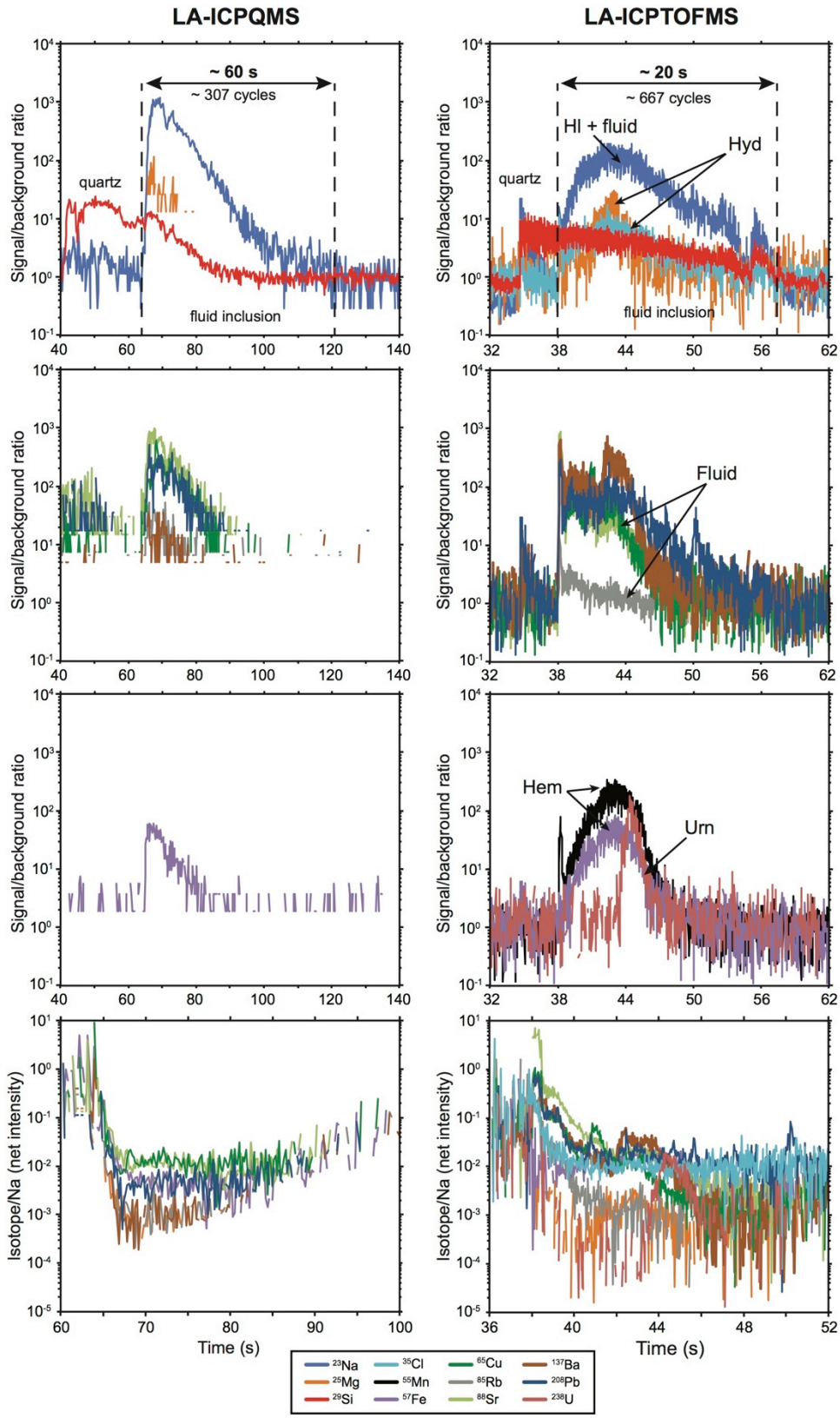

Fig. 43: Typical transient signals for 15 µm multi-phase fluid inclusions (sample 7703-25, Zambia) analysed by LA-ICPQMS and LA-ICPTOFMS. The signals for detected elements obtained by QMS with the standard ablation cell have all the same shape and are correlated in time (top left to middle left), as observed by constant ratios normalised to Na (bottom left). The signals obtained by TOFMS with the fast washout cell differ from one group of isotopes to another, as shown by variable ratios normalised to Na (bottom right), allowing to

distinguish the signals of the aqueous phase, halite (Hl) and magnesium hydroxides (Hyd) (top right), and hematite (Hem) and uraninite crystals (Urn) (middle right). Analytical conditions for the three setups are given in Table 11.

3.3.2. Concentrations, standard deviations, precisions and limits of detection

The calculated mean concentrations, standard deviations (1σ) and precisions (RSD) for multi-phase fluid inclusions from sample 7703-25 for QMS and TOFMS are presented in Table 14. The major input of TOFMS is the detection of 38 isotopes on the whole mass range, with particularly the discrimination of several isotopes of a same element, such as Mg, Zn, Mo, Ba and Pb isotopes (Table 14), with a good reproducibility. Concentrations are variable among the analysed fluid inclusions, in particular for isotopes such as ^{39}K, ^{65}Cu or ^{57}Fe for instance, resulting in relatively high RSD. For isotopes detected both by QMS and TOFMS, the calculated RSD are lower on average for TOFMS, as already shown for two-phase fluid inclusions, and range within 39 to 154% and 6 to 100% for QMS and TOFMS, respectively. Considering that these fluid inclusions have approximately the same dimension (10 to 25 µm), these variations are likely related to a heterogeneous trapping of the fluid during the quartz crystallization. The calculated LODs for QMS and TOFMS show the same results as for the two-phase fluid inclusions, that is similar LODs for QMS and TOFMS for $m/Q < 57$ and lower LODs for TOFMS for heavy isotopes ($m/Q > 95$).

4. Summary and conclusions

Three different configurations of LA-ICPMS, namely a quadrupole (QMS), a sector-field (SFMS) and an orthogonal time-of-flight (TOFMS), were tested in this study in order to address their respective capabilities for sequential (QMS, SFMS) and quasi-simultaneous (TOFMS) multi-element analysis of small quantities of liquids (pl to nl) contained in silica capillaries and in natural fluid inclusions.

The two sets of objects studied, namely multi-element solutions in silica capillaries and natural fluid inclusions, allowed to evaluate the capabilities of SFMS and TOFMS and to compare them to QMS, which is currently the traditionally used and state-of-the-art instrument for the measurements of fluid inclusions by LA-ICPMS. The main results obtained in this study are: (i) QMS, SFMS and TOFMS have similar signal to background ratios for ^{23}Na within the same order of magnitude of ca. 10^3 to 10^4, those of QMS being slightly higher

to the other ones; (ii) Signals durations are similar (20-30 s) for silica capillaries and two-phase fluid inclusions using a standard cylindrical ablation cell with QMS and SFMS, but are 2 to 30 times shorter (1-15 s) using the fast washout tube cell in combination with the TOFMS. In the case of high-salinity and multi-phase fluid inclusions, the signals durations are longer and last for ca. 60 s and 20 s for QMS and TOFMS, respectively; (iii) Cycle times for covering the range of measured masses with QMS and SFMS are ca. 10 to 30 longer compared to those of TOFMS, where cycle time is only 30 ms for quasi-simultaneous measurement of the entire mass range, resulting in a number of cycles of ca. 2 to 5 times higher compared to QMS and SFMS and compensating for the multiplicative noise in the ICPMS; (iv) RSD calculated are on average lower for TOFMS compared to QMS and SFMS, for all measured isotopes, indicating better precision achievable by TOFMS; (v) LODs for silica capillaries are approximately 10 times lower for SFMS compared to QMS and TOFMS for isotopes with m/Q < 137 (except ^{11}B) and almost equivalent for SFMS and TOFMS for heavier isotopes and ca. 3 times lower than for QMS. For fluid inclusions, LODs are inversely correlated to the inclusion diameter with a parabolic decrease. SFMS presents lower LODs of ca. one order of magnitude compared to QMS and TOFMS for diameter > 25 µm, whereas TOFMS achieve the lower LODs for inclusions < 10 µm, with one order of magnitude below SFMS and QMS for isotopes with m/Q > 85.

Consequently, the present study demonstrates that SFMS and TOFMS provide improvements, particularly in terms of precision and LODs, compared to the QMS instrumentation tested, and leads to the following conclusions:

1. QMS is a very efficient instrument for the multi-element analysis of fluid inclusions, with good reproducibility, precisions and accuracies, but is limited by relatively high LODs compared to SFMS and TOFMS, in particular for heavy isotopes, and by a limited set of measureable elements (generally less than 20) due to a compromise between signal duration and cycle time.
2. SFMS has the great advantage to reduce LODs within one order of magnitude compared to QMS and TOFMS, especially for light isotopes, but has longer acquisition times, due to the necessary magnet jumps, which limits the number of measureable elements and the attainable precision. It is consequently a well-adapted instrument for the precise measurement of a few isotopes (< 5) present at low concentrations in fluid inclusions.
3. TOFMS presents both advantages to have rapid, quasi-simultaneous data acquisition for all isotopes from ^{6}Li to ^{238}U in a cycle time of 30 µs. The precisions were found to

be better than for QMS and SFMS and LODs are slightly higher or even similar than SFMS for heavy isotopes and lower for small fluid inclusions. Using TOFMS coupled to the fast washout ablation cell, which improves considerably the signal to noise ratio by decreasing the aerosol dispersion, allows detection of small-size (< 10 μm) and low-salinity fluid inclusions. Its application to complex multi-phase and high-salinity fluid inclusions allows discrimination of signals of the different phases (liquid and solids), as well as the detection of a higher number of isotopes, even for a same element. Moreover, detection of ^{35}Cl is improved with the TOFMS, which could represent a major benefit for the quantification of fluid inclusions based on their chlorinity.

In conclusion, the orthogonal TOFMS reveals to be a highly promising instrument for the multi-element analysis of fluid inclusions, particularly since it provides fast and relatively complete information on fluid inclusions composition. Its use is consequently of high interest for the study of geological fluids, which are characterized by an extremely wide variety of chemical elements, potentially from Li to U, with a very variable range of concentrations, from a few parts per billions (ppb) to tens of percents. Future applications could be considered in particular for the analysis of melt inclusions by TOFMS (e.g., Pettke et al., 2006), but also for the measurement of isotopic ratios in fluid inclusions (e.g., Pettke et al., 2011). By extension, these results demonstrate the analytical potential of the TOFMS for the determination of minor and trace elements in small volumes of liquids (pl to nl) trapped in various solid matrices.

Acknowledgements

This work was supported by the CNRS through the national call CESSUR (INSU) with a financial grant given to Dr. Julien Mercadier in 2014 and by the Labex Ressources 21 through the national program "Investissements d'avenir" with the reference ANR-10-LABEX-21-RESSOURCES21. The authors are highly thankful to Dr. Marie-Christine Boiron and Dr. Aurélien Eglinger for supplying the quartz samples. We would like also to thank Dr. Bodo Hattendorf for the helpful discussions and comments. Two anonymous reviewers are also thanked for their constructive comments that helped to improve the manuscript.

Table 11: Operating conditions and acquisition parameters used for this study.

	LA-ICPQMS	**LA-ICPSFMS**	**LA-ICPTOFMS**
Model	Elan DRC Plus (PerkinElmer Inc.)	Element 2 (ThermoScientific)	Prototype (Tofwerk AG)
Laser	GeoLas ArF Excimer 193 nm (MicroLas)		
Ablation cell	Standard cylindrical cell		Fast washout tube cell
ICP-MS			
Plasma RF power	1380 W	1280 W	1300 W
Cooling gas (Ar)	17.5 L min^{-1}	16 L min^{-1}	16.5 L min^{-1}
Carrier gas (He)	1.2 L min^{-1}	1.1 L min^{-1}	0.6 L min^{-1}
Nebulizer gas (Ar)	0.72 L min^{-1}	0.84 L min^{-1}	1.2 L min^{-1}
Auxiliary gas (Ar)	0.8 L min^{-1}	0.66 L min^{-1}	1.2 L min^{-1}
Intensities (cps) on NIST SRM 610 for a low, mid and heavy isotope			
^{23}Na	1.6×10^7	1.2×10^8	5.3×10^5
^{140}Ce	1.5×10^5	1.7×10^6	4.7×10^4
^{209}Bi	1.0×10^5	1.7×10^6	7.0×10^4
Acquisition parameters for multi-element solutions in silica capillaries			
Cycle time	468 ms	887 ms	30 ms
Isotopes measured	^7Li, ^{11}B, ^{22}Ne, ^{23}Na, ^{25}Mg, ^{27}Al, ^{29}Si, ^{53}Cr, ^{55}Mn, ^{57}Fe, ^{59}Co, ^{60}Ni, ^{65}Cu, ^{66}Zn, ^{71}Ga, ^{72}Ge, ^{85}Rb, ^{88}Sr, ^{93}Nb, ^{111}Cd, ^{115}In, ^{118}Sn, ^{121}Sb, ^{133}Cs, ^{137}Ba, ^{139}La, ^{140}Ce, ^{159}Tb, ^{179}Hf, ^{181}Ta, ^{182}W, ^{195}Pt, ^{205}Tl, ^{208}Pb, ^{209}Bi, ^{238}U (U not measured with SFMS)		^6Li to ^{238}U
Acquisition parameters for two-phase fluid inclusions (sample BP-66-210, Alps)			
Cycle time	273 ms	560 ms	30 ms
Isotopes measured	^7Li, ^{11}B, ^{22}Ne, ^{23}Na, ^{25}Mg, ^{29}Si, ^{35}Cl, ^{44}Ca, ^{57}Fe, ^{59}Co, ^{65}Cu, ^{66}Zn, ^{79}Br, ^{85}Rb, ^{88}Sr, ^{133}Cs, ^{137}Ba, ^{140}Ce, ^{182}W, ^{197}Au, ^{208}Pb		^6Li to ^{238}U
Acquisition parameters for multi-phase fluid inclusions (sample 7703-25, Zambia)			
Cycle time	195 ms		30 ms
Isotopes measured	^{23}Na, ^{25}Mg, ^{29}Si, ^{34}S, ^{39}K, ^{44}Ca, ^{47}Ti, ^{57}Fe, ^{65}Cu, ^{85}Rb, ^{88}Sr, ^{95}Mo, ^{137}Ba, ^{208}Pb, ^{238}U		^6Li to ^{238}U

Table 12: Nominal and measured compositions of silica capillaries with internal diameter of 20 µm containing multi-element solutions at concentration of ca. 0.1, 1, 10 and 50 µg g^{-1} analysed by LA-ICPQMS, LA-ICPSFMS and LA-ICPTOFMS. The analytical conditions are given in Table 11. SD: standard deviation; LOD: limit of detection; n.m.: not measured; n: number of analyses.

		Concentration at ca. 50 µg g^{-1}															
	Solution	**LA-ICPQMS**					**LA-ICPSFMS**					**LA-ICPTOFMS**					
Isotopes	Concentration	Mean (n=5)	SD	LOD	Precision	Accuracy	Mean (n=6)	SD	LOD	Precision	Accuracy	Mean (n=7)	SD	LOD	Precision	Accuracy
	µg g^{-1}	µg g^{-1}	µg g^{-1}	µg g^{-1}	%	%	µg g^{-1}	µg g^{-1}	µg g^{-1}	%	%	µg g^{-1}	µg g^{-1}	µg g^{-1}	%	%
^{7}**Li**	46.9	64.7	8.6	0.6	13	38	49.5	17.2	1	35	6	n.m.	n.m.			
^{11}**B**	47.7	59.1	23.1	4	39	24	< LOD		130			41.8	4.0	2	9	-12
^{25}**Mg**	47.5	48.1	3.6	1	7	1	40.8	7.7	2	19	-14	31.9	2.8	1	9	-33
^{27}**Al**	46.7	47.2	4.1	2	9	1	53.6	14.9	3	28	15	46.5	6.8	0.4	15	-0.5
^{53}**Cr**	47.3	51.9	5.7	5	11	10	48.8	13.1	3	27	3	44.0	1.6	1	4	-7
^{55}**Mn**	47.5	53.5	7.5	1	14	13	47.0	7.6	1	16	-1	47.3	2.4	0.1	5	-0.4
^{57}**Fe**	47.1	58.6	15.3	16	26	24	49.7	12.2	9	24	5	54.1	10.1	2.5	19	15
^{59}**Co**	46.8	58.0	3.8	0.2	7	24	42.4	5.4	0.1	13	-9	45.8	1.3	0.05	3	-2
^{60}**Ni**	47.4	58.8	8.8	0.9	15	24	49.2	11.7	2	24	4	47.2	2.0	0.3	4	-0.5
^{65}**Cu**	47.4	57.0	9.4	0.7	17	20	52.0	14.4	0.3	28	10	47.4	2.5	0.3	5	0
^{66}**Zn**	47.0	51.1	10.5	1.2	21	9	47.0	11.4	1	24	0.1	40.5	2.3	0.3	6	-14
^{71}**Ga**	47.1	51.2	9.1	0.4	18	9	43.3	7.4	0.2	17	-8	41.3	2.3	0.04	6	-12
^{72}**Ge**	47.4	49.9	9.2	2	18	5	47.5	12.3	2	26	0.1	41.0	2.5	0.3	6	-13
^{88}**Sr**	47.4	56.9	6.4	0.04	11	20	46.3	8.5	0.1	18	-2	43.1	4.9	0.03	11	-9
^{93}**Nb**	47.5	50.1	5.8	0.06	12	6	42.2	8.3	0.1	20	-11	41.5	5.1	0.02	12	-13
^{111}**Cd**	47.3	48.5	13.0	1.5	27	3	49.2	7.1	0.3	14	4	41.5	2.6	0.15	6	-12
^{115}**In**	47.5	54.2	15.3	0.05	28	14	46.8	5.6	0.06	12	-1	44.7	1.4	0.01	3	-6
^{118}**Sn**	47.5	49.3	8.8	0.2	18	4	42.7	8.6	0.3	20	-10	42.2	1.7	0.03	4	-11
^{137}**Ba**	47.2	109.6	11.3	0.4	10	132	92.2	13.7	0.1	15	95	86.8	10.2	0.04	12	84
^{139}**La**	47.8	47.9	8.5	0.07	18	0	37.9	3.1	0.04	8	-21	37.5	4.6	0.004	12	-21
^{159}**Tb**	47.2	53.0	5.1	0.05	10	12	38.2	4.2	0.05	11	-19	39.0	4.7	0.003	12	-17
^{179}**Hf**	47.2	51.7	7.1	0.3	14	10	43.3	10.0	0.09	23	-8	38.9	5.6	0.02	14	-17
^{181}**Ta**	47.3	21.2	4.2	0.05	20	-55	19.2	2.8	0.05	15	-59	13.5	4.0	0.004	30	-72
^{182}**W**	47.5	51.9	7.6	0.4	15	9	48.7	11.5	0.09	24	3	37.9	5.7	0.02	15	-20
^{195}**Pt**	47.5	55.0	22.9	0.5	42	16	48.6	14.1	0.4	29	2	20.0	4.8	0.01	24	-58
^{205}**Tl**	47.4	48.6	32.6	0.07	67	2	37.0	12.9	0.01	35	-22	19.6	3.4	0.005	17	-59
^{208}**Pb**	47.6	57.5	18.4	0.1	32	21	52.2	7.4	0.2	14	10	45.2	1.1	0.01	3	-5
^{209}**Bi**	47.3	50.6	12.4	0.06	25	7	49.4	3.1	0.05	6	4	41.7	1.3	0.01	3	-12
^{238}**U**	46.6	52.6	6.3	0.03	12	13	n.m.	n.m.				46.8	1.8	0.003	4	0.4

Table 12: Continued.

Isotopes	Solution Concentration µg g^{-1}	LA-ICPQMS Mean (n=6) µg g^{-1}	SD µg g^{-1}	LOD µg g^{-1}	Precision %	Accuracy %	Concentration at ca. 10 µg g^{-1} LA-ICPSFMS Mean (n=5) µg g^{-1}	SD µg g^{-1}	LOD µg g^{-1}	Precision %	Accuracy %	LA-ICPTOFMS Mean (n=5) µg g^{-1}	SD µg g^{-1}	LOD µg g^{-1}	Precision %	Accuracy %
^{7}Li	9.7	12.2	1.2	0.9	10	26	8.1	1.2	0.5	15	-16	n.m.	n.m.			
^{11}B	9.9	13.9	4.3	7	31	40	< LOD		35			< LOD		19		
^{25}Mg	9.9	10.4	1.7	3	16	6	11.0	5.3	0.9	49	11	8.7	1.0	10	11	-11
^{27}Al	9.7	9.2	2.6	4	29	-5	10.2	2.3	1.0	23	5	12.9	2.1	5	17	33
^{53}Cr	9.8	17.1	10.4	9	61	74	9.8	3.1	1	31	-0.5	< LOD		14		
^{55}Mn	9.9	10.2	1.2	2	11	4	9.0	2.3	0.5	25	-8	9.1	0.8	1	8	-8
^{57}Fe	9.8	26.5	9.4	27	35	170	17.4	8.3	4	48	77	< LOD		27		
^{59}Co	9.7	9.9	1.4	0.2	15	2	9.0	2.5	0.03	28	-7	8.7	0.4	0.5	5	-11
^{60}Ni	9.9	11.4	2.6	1	23	16	12.5	6.2	0.7	49	27	10.2	1.4	3	14	4
^{65}Cu	9.9	9.9	1.2	1	12	0.2	9.0	3.2	0.1	36	-9	9.3	1.6	3	17	-6
^{66}Zn	9.8	5.7	1.7	2	30	-42	8.2	1.8	0.4	22	-16	6.7	0.3	3	5	-31
^{71}Ga	9.8	9.8	2.0	0.5	21	0	8.1	2.1	0.05	26	-17	8.3	0.5	0.5	6	-16
^{72}Ge	9.9	10.2	2.4	4	23	3	8.6	1.9	0.6	22	-13	10.2	1.8	1	18	4
^{88}Sr	9.9	10.8	1.6	0.1	15	9	8.4	2.6	0.06	31	-15	8.5	0.8	0.3	9	-14
^{93}Nb	9.9	10.5	2.0	0.1	19	7	8.7	3.5	0.07	40	-12	8.6	1.1	0.2	13	-13
^{111}Cd	9.8	5.8	1.4	3	24	-41	10.1	2.6	0.11	26	2	8.0	0.5	1	7	-18
^{115}In	9.9	9.2	1.7	0.1	18	-7	8.3	2.0	0.02	24	-16	8.9	0.3	0.1	3	-10
^{118}Sn	10.1	9.2	1.5	0.5	16	-9	7.3	1.6	0.15	21	-28	8.4	0.5	0.3	6	-17
^{137}Ba	9.9	10.5	1.9	0.6	18	6	9.8	6.4	0.06	65	-1	8.8	0.7	0.4	8	-11
^{139}La	10.2	10.5	1.4	0.1	13	3	8.5	3.3	0.04	39	-16	8.6	1.1	0.05	12	-15
^{159}Tb	9.7	9.5	1.0	0.1	11	-2	8.1	2.1	0.04	26	-17	8.0	1.1	0.03	13	-18
^{179}Hf	9.8	10.0	1.0	0.7	10	2	8.4	2.0	0.04	24	-14	8.7	0.9	0.2	11	-11
^{181}Ta	9.8	6.6	0.7	0.1	10	-33	5.5	1.6	0.05	30	-44	5.3	0.8	0.04	16	-46
^{182}W	10.1	10.5	1.7	0.5	16	4	7.7	2.4	0.09	31	-24	9.1	0.7	0.2	8	-10
^{195}Pt	10.1	7.3	1.1	0.5	15	-28	6.5	1.2	0.17	19	-36	4.5	0.6	0.1	13	-55
^{205}Tl	9.9	3.6	1.2	0.1	34	-63	2.5	1.1	0.01	42	-74	2.9	0.4	0.04	13	-70
^{208}Pb	9.9	9.9	1.6	0.1	16	0.4	9.8	3.4	0.08	35	-1	9.1	0.3	0.05	3	-8
^{209}Bi	9.8	8.8	1.4	0.1	16	-11	10.1	2.6	0.03	25	3	8.4	0.4	0.04	5	-14
^{238}U	10.0	10.7	0.5	0.1	5	7	n.m.	n.m.				8.8	0.6	0.02	7	-12

Table 12: Continued.

Isotopes	Solution Concentration µg g^{-1}	Concentration at ca. 1 µg g^{-1} LA-ICPQMS Mean (n=5) µg g^{-1}	SD µg g^{-1}	LOD µg g^{-1}	Precision %	Accuracy %	LA-ICPSFMS Mean (n=5) µg g^{-1}	SD µg g^{-1}	LOD µg g^{-1}	Precision %	Accuracy %	LA-ICPTOFMS Mean (n=6) µg g^{-1}	SD µg g^{-1}	LOD µg g^{-1}	Precision %	Accuracy %
^{7}Li	0.96	1.01	0.1	0.3	14	6	0.64	0.2	0.5	25	-33	n.m.	n.m.			
^{11}B	0.98	< LOD		2			< LOD		52			< LOD		7		
^{25}Mg	0.98	0.87	0.2	1	18	-11	< LOD		2			< LOD		3		
^{27}Al	0.96	< LOD		0.8			1.15	0.3	0.9	26	20	< LOD		2		
^{53}Cr	0.97	< LOD		2			1.78	0.5	1	29	84	< LOD		5		
^{55}Mn	0.98	0.84	0.1	0.5	15	-15	0.88	0.2	0.5	20	-10	1.07	0.3	0.4	26	9
^{57}Fe	0.97	< LOD		6			9.68	4.9	4	50		< LOD		9		
^{59}Co	0.96	0.81	0.1	0.06	13	-16	0.69	0.1	0.03	13	-29	0.84	0.1	0.2	8	-12
^{60}Ni	0.97	0.98	0.2	0.3	16	1	2.06	1.6	0.7	79	113	1.81	0.7	0.9	41	87
^{65}Cu	0.97	0.83	0.1	0.2	18	-14	0.87	0.2	0.1	23	-10	1.29	0.5	1	41	33
^{66}Zn	0.97	0.59	0.4	0.5	60	-39	0.78	0.3	0.3	40	-19	1.27	0.5	1	39	31
^{71}Ga	0.97	0.70	0.1	0.1	11	-28	0.63	0.1	0.1	18	-36	0.73	0.03	0.2	5	-24
^{72}Ge	0.97	0.87	0.2	0.8	23	-10	1.11	0.3	0.6	31	14	0.89	0.1	0.5	10	-9
^{88}Sr	0.97	0.82	0.1	0.02	8	-15	0.77	0.1	0.03	16	-21	0.84	0.1	0.08	6	-14
^{93}Nb	0.98	0.58	0.1	0.03	15	-41	0.51	0.1	0.02	21	-48	0.43	0.1	0.07	15	-56
^{111}Cd	0.97	0.82	0.5	0.4	60	-16	0.92	0.2	0.06	23	-6	0.71	0.1	0.5	14	-27
^{115}In	0.98	0.73	0.1	0.02	16	-25	0.68	0.1	0.01	13	-30	0.76	0.1	0.02	8	-23
^{118}Sn	1.00	0.42	0.1	0.1	17	-58	0.54	0.2	0.1	29	-46	0.41	0.04	0.1	10	-59
^{137}Ba	0.98	0.90	0.1	0.2	10	-9	0.86	0.1	0.05	15	-12	0.79	0.1	0.1	17	-19
^{139}La	1.00	0.81	0.1	0.02	18	-19	1.11	0.7	0.01	63	11	0.81	0.03	0.02	4	-19
^{159}Tb	0.96	0.78	0.1	0.02	14	-19	0.83	0.2	0.01	27	-14	0.74	0.04	0.01	5	-23
^{179}Hf	0.97	0.86	0.2	0.1	27	-12	0.80	0.2	0.01	23	-18	0.74	0.1	0.07	9	-24
^{181}Ta	0.97	0.62	0.2	0.03	33	-37	0.72	0.3	0.01	35	-26	0.46	0.1	0.01	17	-52
^{182}W	1.00	0.92	0.2	0.2	27	-8	0.74	0.1	0.01	19	-26	0.78	0.1	0.06	8	-22
^{195}Pt	1.00	0.91	0.2	0.2	20	-9	0.97	0.3	0.2	32	-3	0.62	0.03	0.04	5	-38
^{205}Tl	0.97	0.93	0.1	0.03	16	-4	0.78	0.3	0.01	33	-20	0.80	0.1	0.01	16	-17
^{208}Pb	0.98	0.70	0.1	0.03	10	-29	0.83	0.2	0.05	18	-16	0.79	0.1	0.02	13	-19
^{209}Bi	0.97	0.62	0.1	0.03	15	-36	0.75	0.2	0.01	26	-22	0.68	0.1	0.02	17	-29
^{238}U	0.99	0.82	0.1	0.01	14	-17	n.m.	n.m.				0.78	0.03	0.01	4	-21

Table 12: Continued.

							Concentration at ca. 0.1 µg g^{-1}											
	Solution	**LA-ICPQMS**					**LA-ICPSFMS**						**LA-ICPTOFMS**					
Isotopes	Concentration	Mean (n=5)	SD	LOD	Precision	Accuracy	Mean (n=5)	SD	LOD	Precision	Accuracy	Mean (n=4)	SD	LOD	Precision	Accuracy
	µg g^{-1}	µg g^{-1}	µg g^{-1}	µg g^{-1}	%	%	µg g^{-1}	µg g^{-1}	µg g^{-1}	%	%	µg g^{-1}	µg g^{-1}	µg g^{-1}	%	%
^{7}Li	0.10	< LOD		0.2			< LOD		0.7			n.m.	n.m.			
^{11}B	0.10	< LOD		1			< LOD		70			< LOD		6		
^{25}Mg	0.10	< LOD		0.6			0.9	0.9	0.8	104		< LOD		3		
^{27}Al	0.10	< LOD		0.7			1.7		1			< LOD		2		
^{53}Cr	0.10	< LOD		2			1.8	1.3	1	76		< LOD		5		
^{55}Mn	0.10	< LOD		0.4			< LOD		0.6			< LOD		0.4		
^{57}Fe	0.10	< LOD		5			12.8	16.0	5	125		< LOD		10		
^{59}Co	0.10	0.08	0.01	0.04	6	-18	0.09	0.03	0.05	30	-8	< LOD		0.2		
^{60}Ni	0.10	0.6	0.2	0.2	27		< LOD	0.4	0.8			< LOD		1		
^{65}Cu	0.10	< LOD		0.2			< LOD	0.1	0.2			< LOD		1		
^{66}Zn	0.10	< LOD		0.4			0.5	0.6	0.5	122		< LOD		1		
^{71}Ga	0.10	< LOD		0.1			0.12	0.1	0.06	73	23	< LOD		0.2		
^{72}Ge	0.10	< LOD		0.6			< LOD		0.7			< LOD		0.6		
^{88}Sr	0.10	0.09	0.01	0.01	9	-14	0.09	0.02	0.04	27	-11	< LOD		0.1		
^{93}Nb	0.10	0.04	0.01	0.02	26	-58	0.05	0.02	0.03	50	-52	< LOD		0.1		
^{111}Cd	0.10	< LOD		0.3			0.2	0.1	0.08	91	53	< LOD		0.6		
^{115}In	0.10	0.08	0.01	0.01	9	-21	0.08	0.04	0.02	51	-20	0.08	0.02	0.03	18	-16
^{118}Sn	0.10	0.13	0.1	0.08	113	26	0.15	0.2	0.1	122	47	< LOD		0.1		
^{137}Ba	0.10	0.103	0.02	0.08	19	3	0.104	0.04	0.08	37	4	< LOD		0.1		
^{139}La	0.10	0.08	0.02	0.01	22	-23	0.08	0.02	0.01	26	-24	0.08	0.01	0.02	14	-24
^{159}Tb	0.10	0.07	0.01	0.01	16	-28	0.07	0.01	0.02	16	-31	0.07	0.004	0.01	6	-30
^{179}Hf	0.10	< LOD		0.10			0.05	0.04	0.03	73	-48	0.06	0.01	0.1	17	-42
^{181}Ta	0.10	0.06	0.02	0.01	38	-39	0.06	0.03	0.02	58	-43	0.05	0.02	0.02	36	-53
^{182}W	0.10	< LOD		0.13			0.2	0.2	0.03	111	114	< LOD	0.00	0.08		
^{195}Pt	0.10	< LOD		0.10			0.2	0.2	0.2	84	97	0.06	0.01	0.06	19	-36
^{205}Tl	0.10	0.07	0.003	0.03	4	-26	0.098	0.04	0.01	40	-2	0.09	0.01	0.02	17	-12
^{208}Pb	0.10	0.14	0.12	0.03	88	39	0.14	0.04	0.06	29	43	0.08	0.01	0.02	14	-18
^{209}Bi	0.10	0.07	0.01	0.02	10	-34	0.096	0.03	0.02	29	-4	0.07	0.00	0.02	5	-26
^{238}U	0.10	0.08	0.02	0.004	23	-17	n.m.	n.m.				0.08	0.01	0.01	8	-23

Table 13: Chemical compositions of two-phase fluid inclusions from sample BP-66-210 (Mont Blanc Massif, French Alps) analysed by LA-ICPQMS, LA-ICPSFMS and LA-ICPTOFMS. See Table 11 for the analytical conditions. The limits of detections (LOD) are reported as a function of the fluid inclusions diameter (< 10 µm, 10-25 µm and > 25 µm respectively). FI: fluid inclusion; n: number of fluid inclusions analysed; SD: standard deviation; RSD: relative standard deviation; n.m.: not measured.

LA-ICPQMS

Isotopes	All FI n=35			FI diameter < 10 µm n=5			10 µm < FI diameter < 25 µm n=21			FI diameter > 25 µm n=9		
	Mean concentration µg g^{-1}	SD µg g^{-1}	RSD %	Mean LOD µg g^{-1}	Range µg g^{-1}	RSD %	Mean LOD µg g^{-1}	Range µg g^{-1}	RSD %	Mean LOD µg g^{-1}	Range µg g^{-1}	RSD %
^{7}Li	470	210	45	930	43 - 1265	57	333	5 - 1550	126	12	2 - 50	133
^{11}B	520	170	33	10700	370 - 19000	63	4200	45 - 14000	117	47	14 - 140	84
^{25}Mg	13900	19600	141	3500	290 - 6600	70	1250	23 - 5250	116	34	4 - 130	120
^{35}Cl	4110	7640	186	105000	1750 - 155000	61	37000	120 - 165000	130	199	30 - 705	109
^{44}Ca	< LOD			375000	36500 - 530000	55	142000	3050 - 450000	110	5450	1200 - 17000	118
^{57}Fe	< LOD			31000	2100 - 50000	58	11000	185 - 44000	118	290	42 - 1200	122
^{59}Co	< LOD			300	24 - 430	54	100	1.5 - 350	116	3	0.5 - 8	100
^{65}Cu	< LOD			1150	100 - 1600	53	400	6 - 1550	120	10	2 - 40	125
^{66}Zn	< LOD			2600	130 - 4000	60	800	8 - 2800	123	24	3 - 115	147
^{85}Rb	210	80	38	150	9 - 270	62	60	0.8 - 190	116	2	0.2 - 7	144
^{88}Sr	55	30	55	150	4 - 260	65	42	0.6 - 210	134	1	0.1 - 5	147
^{133}Cs	70	35	50	110	8 - 180	59	36	0.3 - 130	124	1	0.1 - 2.5	109
^{137}Ba	10	20	200	1610	23 - 2500	63	670	3 - 2700	128	6	0.7 - 15	84
^{140}Ce	< LOD			125	3 - 220	63	36	0.8 - 160	121	1	0.1 - 5	150
^{182}W	< LOD			515	31 - 825	58	235	3.5 - 1040	123	5	1 - 13	91
^{197}Au	< LOD			615	36 - 990	62	240	2.5 - 1050	129	5	0.8 - 23	135
^{208}Pb	< LOD			220	14 - 345	58	85	1 - 375	135	1	0.3 - 5	123

Table 13: Continued.

	LA-ICPSFMS											
	All FI			**FI diameter < 10 µm**			**10 µm < FI diameter < 25 µm**			**FI diameter > 25 µm**		
	n=24			**n=5**			**n=17**			**n=2**		
Isotopes	Mean concentration	SD	RSD	Mean LOD	Range	RSD	Mean LOD	Range	RSD	Mean LOD	Range	RSD
	µg g^{-1}	µg g^{-1}	%	µg g^{-1}	µg g^{-1}	%	µg g^{-1}	µg g^{-1}	%	µg g^{-1}	µg g^{-1}	%
^{7}Li	300	130	43	6100	290 - 18000	126	60	3 - 254	134	8.5	0.4 - 17	135
^{11}B	< LOD			1040000	51700 - 3000000	127	10000	337 - 42600	148	1200.0	62 - 2345	134
^{25}Mg	< LOD			18000	750 - 56100	132	164	6 - 700	139	27.0	1.2 - 54	135
^{35}Cl	1100	710	65	2050000	101700 - 5930000	128	15335	32 - 79000	173	60.0	3.5 - 115	133
^{44}Ca	1430	610	43	600000	31500 - 1570000	123	6350	163 - 29000	143	750	37 - 1460	134
^{57}Fe	< LOD			106000	4700 - 300000	126	913	23 - 4150	147	84	4.5 - 164	134
^{59}Co	< LOD			950	33 - 2725	127	6	0.2 - 36	160	0.7	0.03 - 1.4	136
^{65}Cu	< LOD			3420	200 - 10000	120	32	1 - 170	153	3	0.2 - 6	135
^{66}Zn	< LOD			7700	250 - 23110	127	67	2 - 314	156	8	0.3 - 17	137
^{85}Rb	155	127	82	480	15 - 1170	109	5	0.1 - 34	166	0.3	0.03 - 0.6	129
^{88}Sr	49	36	73	950	53 - 2160	115	9	0.3 - 36	142	0.9	0.05 - 1.8	133
^{133}Cs	62	65	105	250	12 - 740	126	3	0.1 - 15	153	0.3	0.01 - 0.6	138
^{137}Ba	6.5	8	123	1950	124 - 5000	123	10	0.8 - 40	140	1.1	0.01 - 2.2	141
^{140}Ce	< LOD			143	7 - 390	124	2	0.1 - 11	142	0.4	0.26 - 0.6	52
^{182}W	4.4	8	182	334	27 - 1270	186	4	0.3 - 22	174	0.2	0.02 - 0.4	129
^{197}Au	< LOD			2300	106 - 6000	118	22	0.4 - 110	165	0.9	0.05 - 1.7	134
^{208}Pb	2	0.2	10	540	25 - 1650	129	6	0.2 - 35	135	1.0	0.06 - 1.9	133

Table 13: Continued.

	LA-ICPTOFMS											
	All FI			**FI diameter < 10 µm**			**10 µm < FI diameter < 25 µm**			**FI diameter > 25 µm**		
	n=40			**n=7**			**n=24**			**n=9**		
Isotopes	Mean concentration	SD	RSD	Mean LOD	Range	RSD	Mean LOD	Range	RSD	Mean LOD	Range	RSD
	µg g^{-1}	µg g^{-1}	%	µg g^{-1}	µg g^{-1}	%	µg g^{-1}	µg g^{-1}	%	µg g^{-1}	µg g^{-1}	%
^{7}Li	n.m.	n.m.										
^{11}B	400	90	23	3010	485 - 6040	68	443	38 - 1455	92	290	43 - 700	86
^{25}Mg	78	130	167	1935	43 - 4130	81	180	3 - 1000	163	24	3 - 58	86
^{35}Cl	19000	5140	27	68200	6210 - 136500	72	8130	490 - 33650	115	3384	490 - 8200	86
^{39}K	6225	1461	23	109547	4410 - 233270	84	11320	316 - 59770	153	2450	365 - 6120	86
^{44}Ca	< LOD			355730	91340 - 630000	56	65700	7400 - 184500	74	56500	8160 - 136700	84
^{55}Mn	10	7	66	327	24 - 660	77	35	1.8 - 155	124	13	1.9 - 32	85
^{57}Fe	< LOD			8250	618 - 17050	77	917	47 - 4000	125	350	48 - 890	88
^{59}Co	< LOD			137	11 - 290	76	16	0.8 - 67	122	6	0.8 - 15	86
^{65}Cu	< LOD			463	66 - 884	68	64	5 - 205	90	37	6 - 92	88
^{66}Zn	< LOD			771	77 - 1520	73	94	4 - 377	114	40	6 - 92	84
^{75}As	53	19	36	495	47 - 1035	76	70	3.4 - 263	113	25	4 - 58	84
^{85}Rb	113	37	33	155	11 - 311	76	17	0.9 - 77	129	6	1 - 15	85
^{88}Sr	36	10	28	81	6 - 162	75	9	0.4 - 41	130	3	0.5 - 8	87
^{121}Sb	3.1	1.2	39	68	5 - 135	76	8	0.1 - 31	120	3	0.4 - 8	86
^{133}Cs	35	13	37	12	1 - 24	77	1.3	0.1 - 5	120	0.5	0.1 - 1.3	85
^{137}Ba	7.4	5	72	109	10	73	12	0.6 - 55	123	5	0.7 - 11	86
^{140}Ce	< LOD			14	1 - 26	71	1.6	0.1 - 6	117	0.6	0.1 - 1.5	84
^{182}W	2	1	60	56	4 - 115	78	6	0.3 - 28	125	2.2	0.3 - 5	84
^{197}Au	< LOD			34	2.5 - 70	77	4.3	0.2 - 17	117	1.4	0.2 - 3.5	86
^{208}Pb	4.9	5	104	18	1.2 - 38	78	2.0	0.1 - 9	127	0.7	0.1 - 1.8	87

Table 14: Chemical compositions of multi-phase fluid inclusions from sample 7703-25 (Kabompo domes, Zambia) analysed by LA-ICPQMS and LA-ICPTOFMS. See Table 11 for the analytical conditions. SD: standard deviation; LOD: limit of detection; n: number of analyses.

	LA-ICPQMS (n=10)						LA-ICPTOFMS (n=5)					
	Concentration			LOD			Concentration			LOD		
Isotopes	Mean µg g^{-1}	SD µg g^{-1}	RSD %	Mean µg g^{-1}	Range µg g^{-1}	RSD %	Mean µg g^{-1}	SD µg g^{-1}	RSD %	Mean µg g^{-1}	Range µg g^{-1}	RSD %
^{24}Mg	n.m.	n.m.					384	168	44	39	10 - 76	75
^{25}Mg	600	628	105	142	14 - 710	140	470	126	27	238	54 - 510	83
^{26}Mg	n.m.	n.m.					625	35	6	325	74 - 660	78
^{27}Al	n.m.	n.m.					518	117	23	87	20 - 170	78
^{34}S	< LOD			11400	1325 - 51300	125	< LOD			14410	3800 - 30000	76
^{35}Cl	n.m.	n.m.					60350	18800	31	6000	1640 - 10650	71
^{39}K	6090	7135	117	360	40 - 1500	115	7700	3578	46	3350	900 - 6150	74
^{44}Ca	19670	14502	74	12600	1400 - 55300	122	< LOD			176000	40200 - 350000	78
^{47}Ti	55	37	68	123	15 - 470	112	< LOD			930	222 - 1900	80
^{55}Mn	n.m.	n.m.					3750	1870	50	30	7 - 60	76
^{57}Fe	15300	6040	39	1015	115 - 4250	117	15000	5065	34	850	220 - 1600	73
^{59}Co	n.m.	n.m.					22	10	47	12	3 - 25	75
^{64}Zn	n.m.	n.m.					313	295	94	52	12 - 105	76
^{65}Cu	1800	1459	81	40	5 - 200	138	2100	362	17	96	20 - 250	99
^{66}Zn	n.m.	n.m.					346	271	78	77	18 - 160	77
^{67}Zn	n.m.	n.m.					457	395	86	410	100 - 825	77
^{68}Zn	n.m.	n.m.					475	461	97	310	80 - 640	77
^{85}Rb	61	80	133	6	0.6 - 27	122	52	45	86	11	3 -21	71
^{86}Sr	n.m.	n.m.					639	346	54	81	22 - 150	71
^{88}Sr	818	1259	154	3	0.4 - 12	122	510	360	70	6	2 -10	69
^{95}Mo	16	13	79	32	4.5 - 150	128	33	23	71	26	7 - 50	74
^{96}Mo	n.m.	n.m.					20	12	61	17	5 - 32	72
^{97}Mo	n.m.	n.m.					18			36	10 - 67	72
^{98}Mo	n.m.	n.m.					16	4	24	14	4 - 27	75
^{130}Te	n.m.	n.m.					23			22	6 - 45	78
^{133}Cs	n.m.	n.m.					14	14	95	1.1	0.3 - 2	77
^{135}Ba	n.m.	n.m.					1128	569	50	18	5 - 35	76
^{136}Ba	n.m.	n.m.					1123	553	49	39	12 - 71	70
^{137}Ba	1700	2217	130	45	7 - 180	111	1143	570	50	10	3 - 20	77
^{138}Ba	n.m.	n.m.					1119	565	51	1.4	0.3 - 3	74
^{139}La	n.m.	n.m.					2.1	0.8	40	1.2	0.3 - 2	75
^{140}Ce	n.m.	n.m.					1.5	0.7	46	1.1	0.3 - 2	73
^{141}Pr	n.m.	n.m.					0.8	0.6	70	0.9	0.2 - 1.8	75
^{143}Nd	n.m.	n.m.					9			8.5	2 - 17	74
^{205}Tl	n.m.	n.m.					1	1	77	1.5	0.4 - 3	76
^{206}Pb	n.m.	n.m.					387	380	98	4.2	1.1 - 9	79
^{207}Pb	n.m.	n.m.					328	326	99	5.0	1.3 - 10	78
^{208}Pb	390	512	131	6	0.8 - 21	103	321	322	100	2.0	0.5 - 4	77
^{209}Bi	n.m.	n.m.					2.5	0.9	37	1.5	0.3 - 3	82
^{238}U	4	2	39	1.7	0.1 - 7	107	3.3	1.6	48	0.8	0.2 - 2	79

PART II: Case studies of hydrothermal W deposits: Insights into mineralization processes

Chapter 4: The Puy-les-Vignes W±Nb-Ta deposit (Massif Central, France): petrological, geochemical and geochronological constraints on the emplacement of an atypical case of W-mineralized hydrothermal breccia pipe in the Variscan belt

Abstract

The Puy-les-Vignes deposit, located in the Limousin area (NW French Massif Central), represents a rare occurrence of quartz-wolframite-tourmaline breccia pipe in the West European Variscan belt. The formation of the deposit results from successive hydrothermal fluid circulations events, which resulted in the final breccia pipe structure. An integrated petrographic, geochemical and geochronological study of this atypical deposit allowed to propose a detailed chronology divided into five main stages:

(i) Early hydrothermal alteration (greisenization and tourmalinization) of the host-rocks, dated at ca. 327-325 Ma, was followed by a main brecciation episode dated at ca. 323-321 Ma, which led to the breccia pipe structure composed by heterometric clasts of the altered enclosing rocks (mainly gneisses and granites). The greisenization episode fall in the same time interval than a leucogranite dyke dated at 324.7 ± 4.2 Ma, whose the whole-rock geochemistry is typical of an evolved Limousin-type granite, and may thus indicate that a hidden leucogranite cupola is located under the Puy-les-Vignes deposit;

(ii) W-As-Nb-Ta mineralization associated with the formation of quartz-wolframite-arsenopyrite veins, during a second stage brecciation, which crosscut the breccia pipe. The W episode is dated independently by U-Pb on wolframite at ca. 317 Ma (see Chapter 1), thus indicating that the main mineralization episode is clearly disconnected temporally from the early hydrothermal alteration and brecciation stages. A Nb-Ta mineralization, associated with rare-metals oxide minerals, emplaced after the wolframite may result from a magmatic-hydrothermal fluid derived from a rare-metal granite at depth. The presence of a rare-metal granitic cupola is indirectly inferred from a sample of rare-metal aplo-pegmatite, which exhibit the all mineralogical, textural and geochemical features of a rare-metal granitic dyke derived from a highly evolved granite cupola. This sample has been dated at 314 ± 5.2 Ma by Ar-Ar on muscovite, which is consistent with the time interval of the other rare-metal granites and pegmatites emplaced in the Limousin area at ca. 315-310 Ma.

(iii) Minor Fe-Cu-Zn mineralization composed mainly by pyrite, chalcopyrite and sphalerite, which crosscut the minerals from the previous stages;

(iv) A late hydrothermal Nb-Ti-Y-HREE mineralization corresponds to the formation of a crackle-breccia with a matrix of tourmaline, adularia and vermicular chlorite, which cuts the mineralized quartz veins after the main ductile deformation episode. The breccia contains several disseminated accessory minerals within the adularia matrix, which consist in monazite, xenotime, zircon, Nb-Fe-W-rich rutile and Nb-Ti-Y-HREE-W-U oxides. This stage is characterized by a P, Y, HREE, Nb, Ti, Zr, U geochemical signature and has been interpreted as the contribution of a peralkaline magmatic source at depth (see Chapter 5).

(v) A discrete mineralization of Bi±Au-Ag fills microcavities and microcracks within the minerals from the previous stages and appears similar to those found in the mesothermal gold deposits from the FMC and particularly from the Limousin area. An Ar-Ar age of 301.3 ± 3 Ma obtained on adularia from the late hydrothermal crackle-breccia (stage IV) represents the youngest age obtained in this study and may record this last hydrothermal episode known regionally in the Limousin area.

Keywords:

Puy-les-Vignes; breccia pipe; tungsten mineralization; rare-metal granite; U-Pb and Ar-Ar dating.

1. Introduction

Sn-W mineralization are generally spatially associated with felsic plutons forming a large variety of magmatic and hydrothermal deposits types, including greisen, quartz veins, pegmatites, skarn and porphyry, which are also known to contain significant amounts of rare-metals (Nb, Ta, Li, Be, Sc) of economic importance (e.g., Černý et al., 2005; Černý and Ercit, 2005; Linnen and Cuney, 2005; Linnen et al., 2012). In Western Europe, the Variscan belt represents a more than 2000 km large Sn-W-rich metallogenic province, which is the host for many important deposits in Cornwall, the Iberian Massif, the Bohemian Massif, the Armorican Massif and the French Massif Central (FMC). Most of these Sn-W occurrences form peribatholitic vein-type deposits, in close proximity with syn- to late-orogenic peraluminous granites, and typically occur as quartz-wolframite-cassiterite stockwork systems hosted either in enclosing metasedimentary rocks ("exo-granitic") or in evolved granites ("endo-granitic") (Stussi, 1989). At the continental scale, the spatial distribution of these Sn-W deposits results from the partial melting and metal mobilization from pre-enriched metasedimentary rocks during the tectono-metamorphic evolution of the Variscan belt through the Upper Paleozoic (Romer and Kroner, 2015, 2016).

The Puy-les-Vignes deposit, located in the northwestern part of the FMC in the Limousin area, represents a rare occurrence of hydrothermal W mineralization associated with a breccia pipe structure in the West European Variscan belt. This atypical quartz-wolframite-tourmaline deposit has been initially studied by Weppe (1951, 1958), who was the first to describe the geology of the deposit and to identify the breccia pipe structure. A genetic interpretation of the Puy-les-Vignes breccia pipe was later proposed by Alikouss (1993) on the basis of detailed petrographic and fluid inclusions studies. A second example of W-mineralized breccia pipe in the West European Variscan belt is known at Borralha in Portugal (Noronha, 1983). Intrusive breccia pipes are found worldwide mainly in association with porphyry-type deposits and with a large variety of mineralization, for instance with Cu deposits (e.g., Sillitoe and Sawkins, 1971; Jacobsen et al., 1976; Skewes et al., 2003; Anderson et al., 2009), Cu-W deposits (e.g., Fletcher, 1977; Yang and Bodnar, 2004), Au deposits (e.g., Baker and Andrew, 1991; Chen et al., 2009) or Mo-W-Sn deposits (e.g., Plimer, 1974; Ren et al., 1995; Somarin and Ashley, 2004; Solomovich et al., 2012). Tourmaline-rich breccia pipes have been generally interpreted as resulting from a magmatic-hydrothermal origin in link with an underlying granitic cupola (e.g., Allman-Ward et al., 1982; Pollard et al., 1987; Sillitoe, 1985; Skewes et al., 2003; Yang and Bodnar, 2004; Gawęda et al., 2013).

This chapter aims to give new petrological, geochemical and geochronological constraints on the emplacement of the Puy-les-Vignes deposit and to propose a genetic model for the formation of this atypical tourmaline-rich hydrothermal breccia pipe.

2. Geological setting

2.1. Regional geology

The Puy-les-Vignes deposit is located in the Limousin area (Fig. 44), which belongs to the internal part of the West European Variscan belt, formed during the continental collision between Gondwana and Laurussia through the Upper Paleozoic (Faure et al., 2009 and references therein). The geological structure of the FMC has been classically described as a stack of metamorphic nappes that from the north to the south define three major tectonic units (Ledru et al., 1989; Faure et al., 2009): (i) the Upper Gneiss Unit (UGU), which is composed of migmatitic ortho- and paragneisses and contains the so-called "leptynite-amphibolite complex", formed by the bimodal association of mafic/ultramafic rocks with acidic rocks; (ii) the Lower Gneiss Unit (LGU) which consists of ortho- and paragneisses similar to those of the UGU; and (iii) the Para-Autochtonous Unit (PAU), dominated by metasedimentary units (micaschists, metagrauwackes and quartzites) that generally experienced Variscan low-grade metamorphism. To the south, these metamorphic units are overthrusted onto the non-metamorphic rocks of the external zone with its fold-and-thrust belt and its foreland basin. This three nappes pile is overthrusted by local allochtonous low-grade units, corresponding to the Brévenne and Somme units and the Tuffs anthracifères series to the ENE and the Thiviers-Payzac and Génis units in the WSW. The Puy-les-Vignes deposit is located 20 km south of the St-Sylvestre leucogranitic complex dated at 324 ± 4 Ma (U-Pb on monazite and zircon; Holliger et al., 1986) and 15 km west of the Millevaches leucogranitic complex dated between 337 ± 4 Ma and 323 ± 4 Ma (^{40}Ar-^{39}Ar on muscovite; Rolin et al., 2014), both Limousin-type peraluminous granites (AKL type of Stussi, 1989). The St-Sylvestre granite is delimited at its northern boundary by the Arrênes-Ouzilly strike-slip fault at the contact with the Guéret granite dated at 356 ± 10 Ma (Rb-Sr on whole rock; Berthier et al., 1979) and at its western boundary by the Nantiat ductile fault active during the emplacement of the Brame leucogranite (Fig. 44). The Argentat normal fault in the east delimits the western border of the Millevaches granitic complex and is coeval with its syn-tectonic emplacement during the Visean at ca. 335-325 Ma (Faure, 1995; Roig et al., 2002). Ar-Ar thermo-geochronology on

muscovite along profiles through the St-Sylvestre leucogranitic complex and its enclosing metamorphic rocks showed that the metamorphic pile south of the leucogranite has been down warped of several kilometres with respect to the leucogranite (Le Carlier de Veslud et al., 2013).

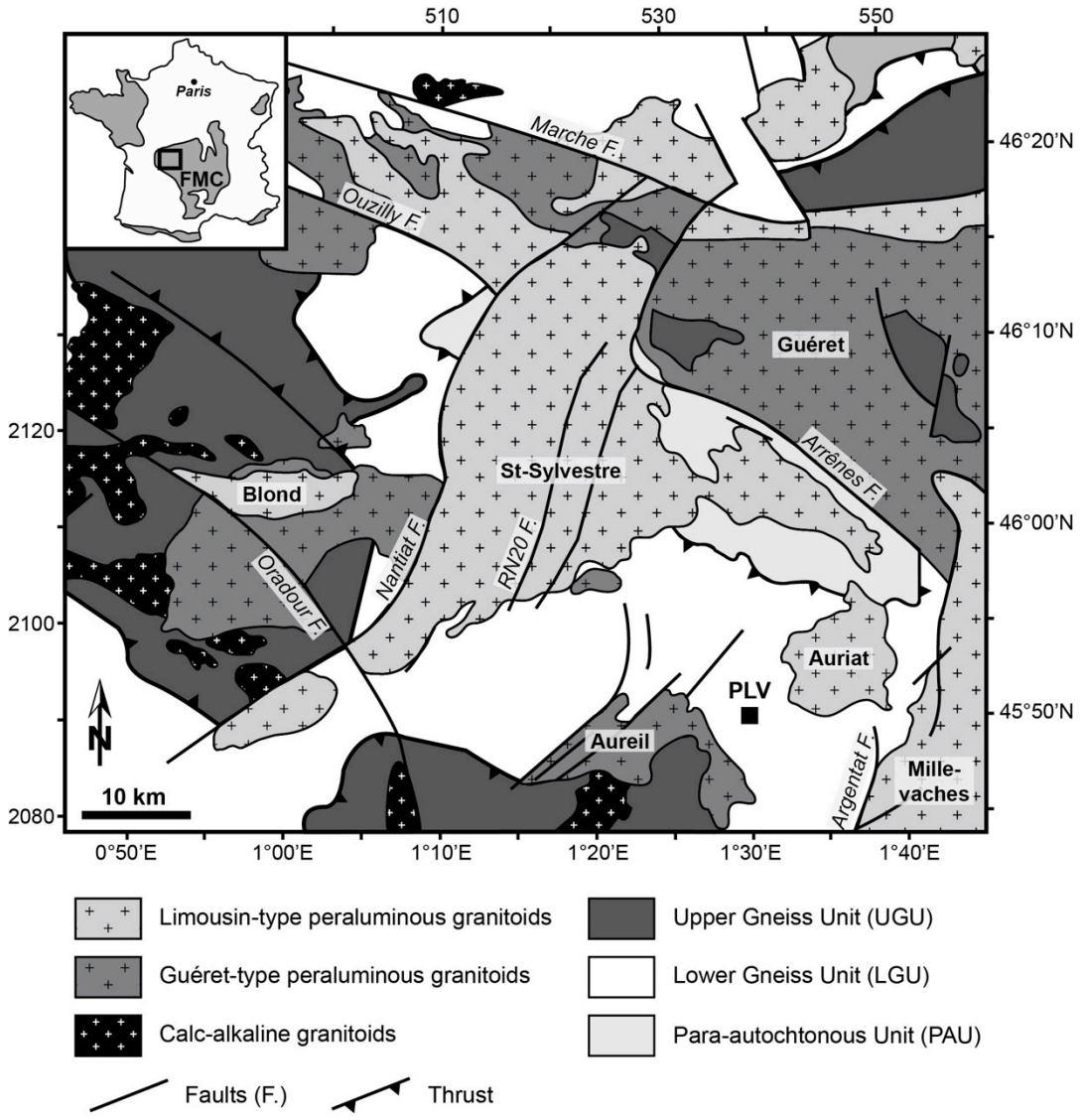

Fig. 44: Location and geological setting of the Puy-les-Vignes (PLV) deposit in the Limousin area, French Massif Central (FMC).

The breccia pipe is hosted in the biotite-sillimanite gneisses of the LGU in the close vicinity of the Auriat granite dated at 324 ± 1 Ma (U-Pb on zircon; Gebauer et al., 1981) and the Aureil granite dated at 346 ± 14 Ma (Rb-Sr on whole rock; Duthou, 1978), which are peraluminous granites of Limousin-type and Guéret-type, respectively (Stussi, 1989) (Fig. 45a). In this respect, Puy-les-Vignes represents the only known W deposit hosted in high-grade metamorphic terranes ("catazone") in the FMC. A set of NE-trending microgranites

dykes is known regionally to crosscut the Aureil granite in the southwest of Puy-les-Vignes (Weppe, 1951). The breccia pipe is located at the intersection of two NE-trending dykes of leucogranites and lamprophyres, respectively oriented N40°E and N20°E (Fig. 45b), which are known to cut the enclosing gneisses and are found fragmented within the breccia (Weppe, 1951, 1958). At depth, a lamprophyre dyke with the same orientation crosscuts the entire breccia pipe (Weppe, 1958), thus suggesting the existence of several generations of lamprophyres. Lamprophyre dykes are known regionally in the Limousin area crosscutting the St-Sylvestre and Millevaches leucogranitic complexes (Leroy, 1978; Chenevoy et al., 1984; Chalier and Sabourdy, 1987) and are thought to be emplaced during the Permian between 285 ± 10 Ma (Rb-Sr on whole rock; Leroy and Sonet, 1976) and 290 ± 5 Ma (Rb-Sr on whole rock; Chalier et al., 1994).

2.2. Structure of the deposit

The Puy-les-Vignes deposit represents a rare case of hydrothermal tungsten mineralization associated with a breccia pipe structure in the Variscan belt. The deposit was mined underground until 1957, producing around 4,000 t WO_3 at an average grade of 0.5% WO_3 and was the second ranking tungsten mine in France during the XX^{th} century. Tungsten resources may be still significant since only half of the pipe was mined and the breccia itself represents a potential low-grade tungsten ore (Mouthier, 2005). In addition, several mineralized tungsten showings are known in the surroundings of Puy-les-Vignes (Fig. 45a), such as quartz-wolframite vein deposits (Lifarnet, Le Moulard, Les Clauds, Etivaud, Chassagnat, Beynat), as well as a second similar breccia pipe at Les Caillaudoux, possibly also mineralized (Weppe, 1958). The deposit is centred on a large extended W-As geochemical anomaly, associated with two other regional Sn-As anomalies at Le Couret and Conjat, respectively located at ca. 15 km in the northwest and 10 km in the southeast of Puy-les-Vignes (Bertrand et al., 2015). The pipe has an oval shape with dimensions 80 x 340 m at surface (Fig. 45b) and is cut in two parts by a N30°E sinistral strike-slip fault (“faille limite”) with a 120 m horizontal displacement (Weppe, 1951, 1958). Only the eastern part was mined down to ca. 200 m in depth, whereas the western part was barely explored (Weppe, 1958).

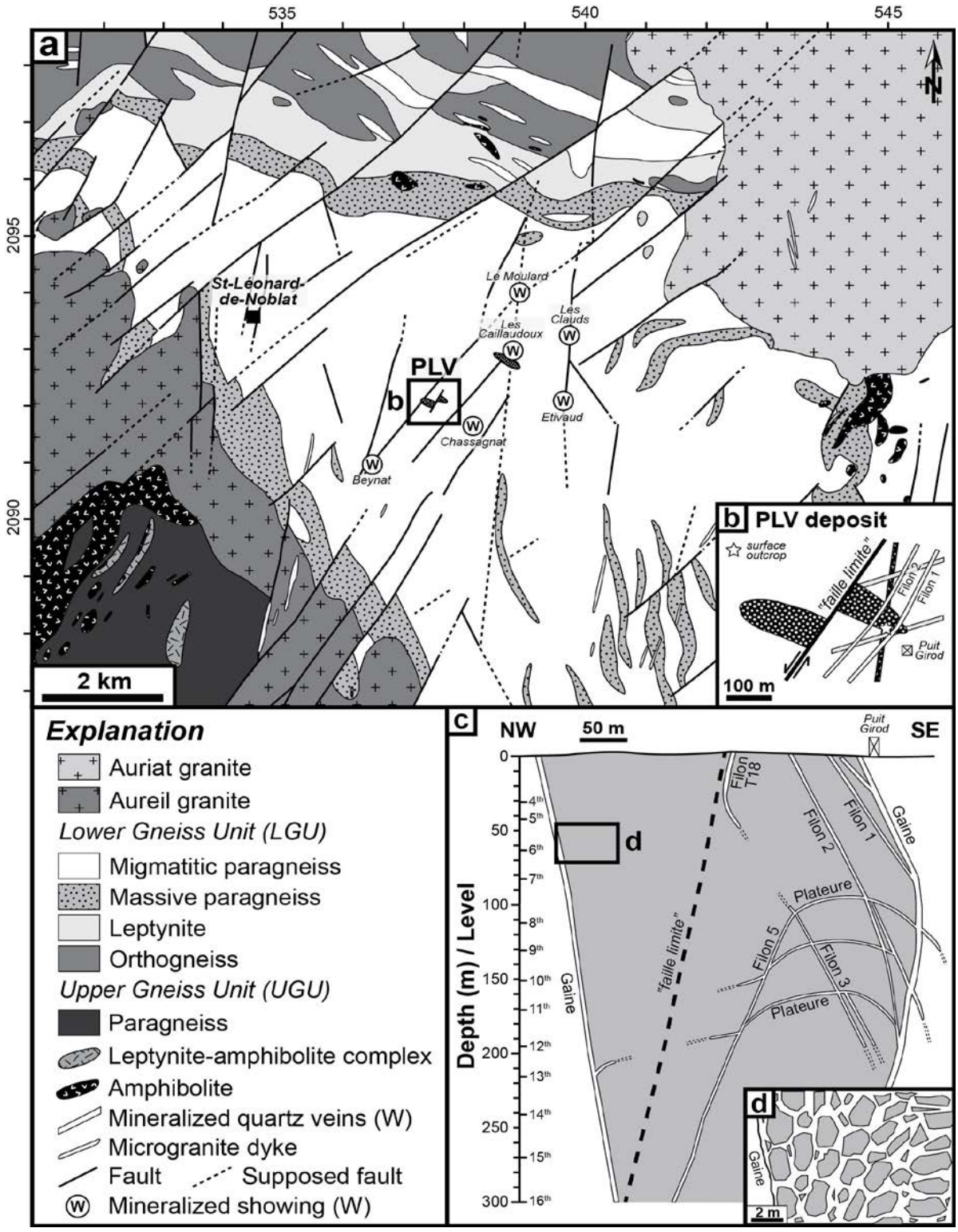

Fig. 45: Local geology of the Puy-les-Vignes (PLV) deposit. (a) Geological map in the surroundings of Puy-les-Vignes (PLV) and localization of the other W showings (modified after Chenevoy et al., 1984). (b) Detailed view of the structure of the breccia pipe in surface (from Weppe, 1951). (c) Interpretative cross-section through the Puy-les-Vignes breccia pipe projected along the major axis (modified after Weppe, 1951, 1958). (d) Illustrative sketch showing the internal structure of the breccia and the apparent rotational movement of the clasts, from the wall-rocks toward the center of the pipe, according to the descriptions of Weppe (1951, 1958).

The breccia pipe likely emplaced at the intersection of several faults. The "faille limite" fault has similar direction than the regional faults in the surroundings of Puy-les-Vignes (Fig. 45a), as well as the faults located at the northern border of the Aureil granite and the RN20 fault within the St-Sylvestre leucogranite (Fig. 44). The Puy-les-Vignes deposit was recognized down to 300 m in depth (Fig. 45c) and is possibly located at the apex of a hidden granite, as already described for other breccia pipes by Sillitoe (1985).

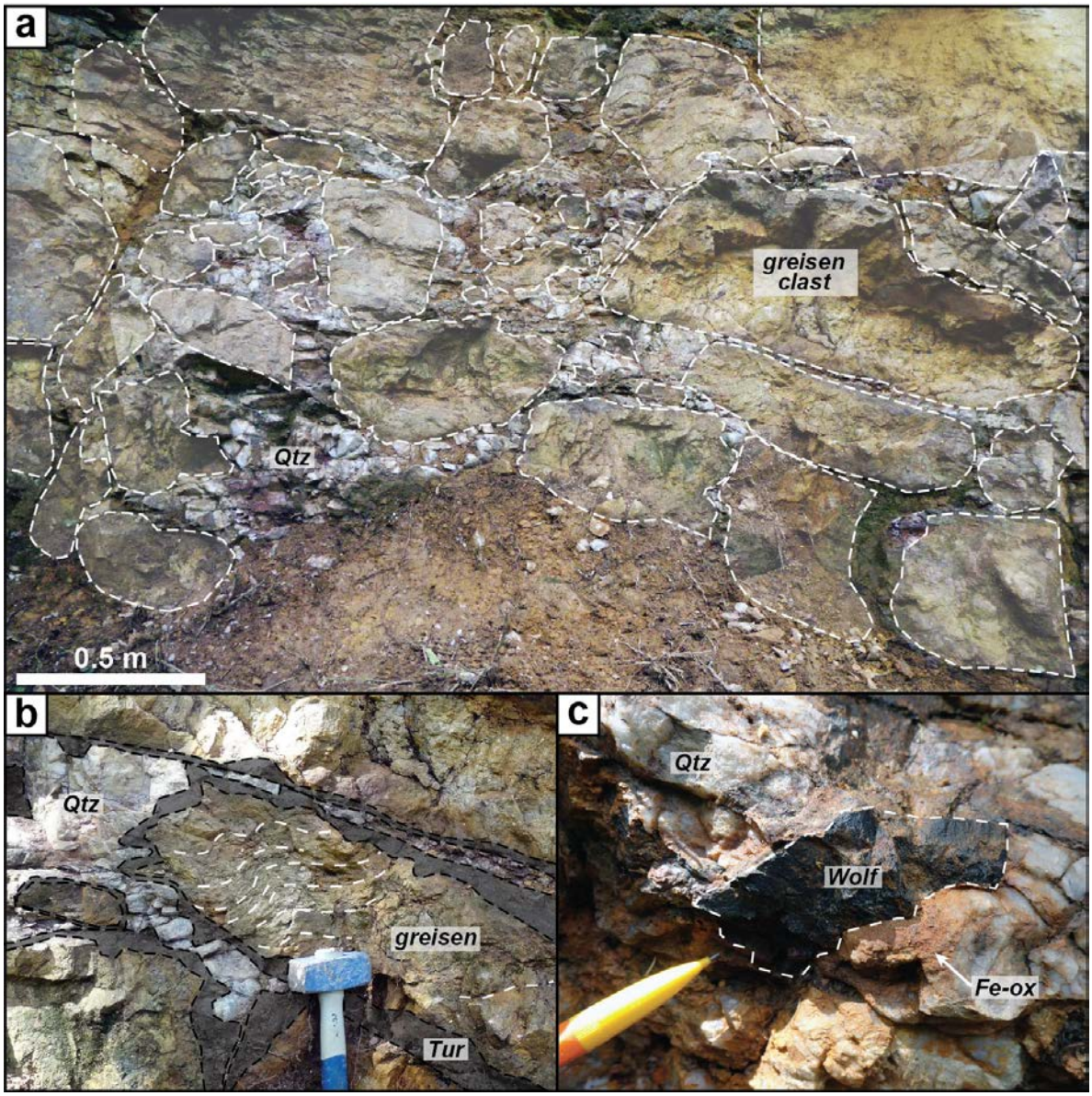

Fig. 46: Photographs of the Puy-les-Vignes breccia at surface outcrop. (a) Overview of the polygenic breccia composed by decimetric to metric clasts of altered gneisses and granites (greisens) cemented within a quartz (Qtz) matrix. (b) Detail view of a greisenized gneissic clast showing a preserved foliation (white dashed lines) and surrounded by an irregular tourmalinite rim (Tur). (c) Wolframite (Wolf) crystal disseminated within the quartz matrix of the breccia and partially altered in Fe-oxides (Fe-ox).

According to Weppe (1951, 1958), the formation of the Puy-les-Vignes breccia pipe resulted from two main successive stages: (i) a first stage of gravitational collapse leading to a quartz-matrix supported heterolithic and heterometric breccia of the country rocks (mainly gneisses and granites). Within the breccia, the metric blocks show an apparent rotational movement characterized by vertical clasts at the country rocks-breccia boundary progressively falling to horizontal clasts in the centre of the breccia (Fig. 45d). The clasts are angular to sub-angular and centimetric to metric in size and do not show any granulometric classification (Fig. 46a). They are cemented within the quartz matrix and are systematically rimmed by an aureole of tourmalinite, of which the thickness varies from a few millimeters to ten centimeters, up to the complete tourmalinization of the fragments (Fig. 46b); (ii) a second stage of "mass collapse" underlined by planar-curved quartz veins ("plateures" and "filons") crosscutting the breccia and quartz-filled decollements ("gaine") that delineate the contacts between breccia and country rocks (Fig. 45c). The mineralization formed during this stage and is hosted in 0.5 to 1 m wide quartz-wolframite-sulphides veins with grades ranging from 0.2 to 2% WO_3 (Mouthier, 2005), as well as disseminated wolframite within the quartz matrix of the breccia itself (Fig. 46c). ^{40}Ar-^{39}Ar dating on muscovite closely associated with wolframite yielded to a plateau age of 323 ± 0.9 Ma (Cuney et al., 2002), suggesting a Namurian emplacement age of the tungsten mineralization. At depth, a quartz-galena vein crosscuts the breccia pipe (Weppe, 1958) and likely formed between the Trias and the Cretaceous, as for other Pb±Zn deposits in the FMC (Marignac and Cuney, 1999; Cathelineau et al., 2012).

The Puy-les-Vignes mine is closed since 1957 and the underground workings are no more accessible. Nevertheless, old samples collections coming directly from the mine when it was still operating (Musée Minéralogique de l'Ecole des Mines d'Alès, France, and old miner collection recovered by B. Mouthier) were completed by a sampling of the mining dumps (PhD thesis from S. Alikouss, 1993). In addition, a small outcrop of the breccia (Fig. 46) was also studied allowing to get access to surface samples. This outcrop is located at the margin of the breccia pipe (Fig. 45b), close to an old mined quartz-wolframite vein ("Filon 1") in the proximity of the old mining headframe ("Puit Girod"). This diversified sampling gives us a large set of representative samples from the Puy-les-Vignes deposit, both of the ore body and the host-rock (Fig. 47).

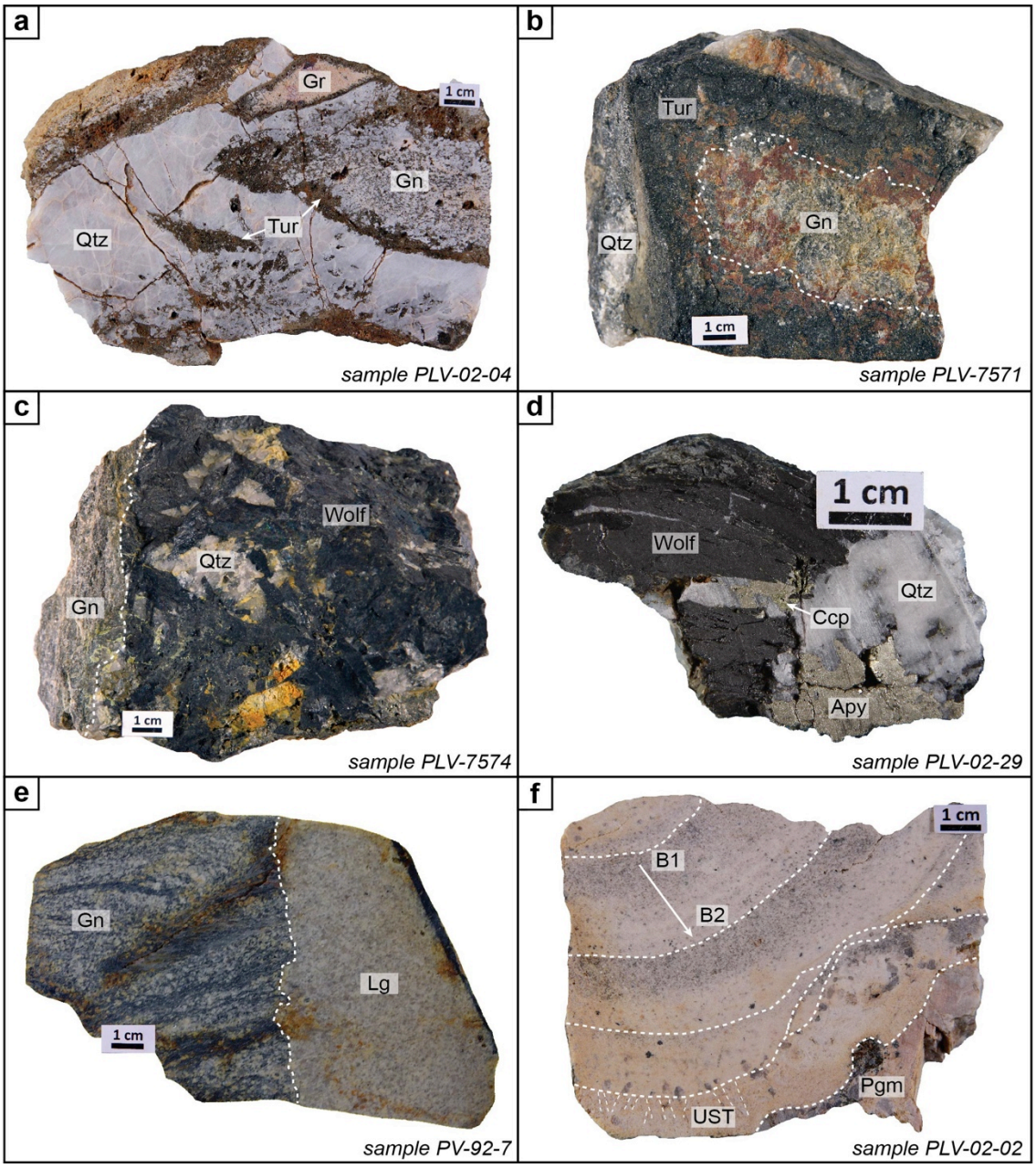

Fig. 47: Photographs of representative samples from the Puy-les-Vignes deposit. (a) Polygenic breccia (sample PLV-02-04) composed of clasts of greisenized gneisses (Gn) and granites (Gr) rimmed by an aureole of tourmalinite (Tur) and cemented by a milky quartz (Qtz) matrix. The breccia constitutes the main body of the pipe. (b) Fragment of greisenized gneiss rimmed by a cm-thick aureole of tourmalinite (sample PLV-7571). (c) Massive mineralized vein composed of centimetric crystals of wolframite (Wolf) in a quartz matrix, hosted in the enclosing gneiss (sample PLV-7574). (d) Typical quartz vein containing an association of wolframite and arsenopyrite (Apy) with minor chalcopyrite (Ccp) (sample PLV-02-29). (e) Discordant dyke of leucogranite (Lg) crosscutting the foliation of the enclosing gneisses (sample PV-92-7). (f) Rare-metal aplo-pegmatite (sample PLV-02-02) showing a magmatic layering composed by the repetitive sequence of quartz-albite-phengite bands (B1) at the bottom passing to albite-quartz bands (B2) at the top. The last albite-quartz band in the lower part of the sample is marked by the beginning of an unidirectional solidification texture (UST), which precede the transition with a granitic pegmatite (Pgm).

3. Analytical methods

3.1. Petrography and geochemistry

Petrographic studies and geochemical analyses were performed at GeoRessources Laboratory (Université de Lorraine, Vandœuvre-lès-Nancy, France). Mineralogical and textural observations were carried out using a Jeol J7600F scanning electron microscope equipped with a SDD-type EDS spectrometer coupled to an Oxford Wave WDS spectrometer. Backscattered electron (BSE) images were obtained on polished thin sections with an acceleration voltage of 15 kV. Chemical analyses were obtained by an electron microprobe analyser (EMPA) Cameca SX100 with acceleration voltage and beam current of 20 kV and 20 nA respectively and with a beam diameter of 1 µm. The following elements and standards were measured: Fe (*Kα*, Fe_2O_3), Mn, Ti (*Kα*, $MnTiO_3$), Mg (*Kα*, $[Mg,Fe]_2SiO_4$), Al (*Kα*, Al_2O_3), Si, Na (*Kα*, $NaAlSi_3O_8$), Sc (*Kα*, Sc metal), Cr (*Kα*, Cr_2O_3), Nb (*Lα*, $LiNbO_3$), Ta (*Lα*, $LiTaO_3$), W (*Lα*, $CaWO_4$), Sn (*Lα*, SnO_2), U (*Mα*, UO_2) and Pb (*Mα*, PbS). Element peaks and backgrounds were measured with counting times of 10 s and 5 s respectively. Major and minor elements are expressed in weight per cent (wt.%) oxides. Whole-rock bulk compositions of samples from various lithologies were determined at the Service d'Analyse des Roches et des Minéraux (SARM-CRPG-CNRS, Vandoeuvre-lès-Nancy, France) using a Thermo Fisher ICap 6500 ICP-OES for major and minor elements and a Thermo Fisher X7 Q-ICPMS for trace elements. Sample preparation, analytical conditions and limits of detection are detailed in Carignan et al. (2001).

3.2. LA-ICPMS analyses of rutile

Trace element compositions in rutile were measured by LA-ICPMS at the GeoRessources laboratory (Université de Lorraine, Vandœuvre-lès-Nancy, France) using a Agilent 7500c quadrupole ICPMS coupled with a 193 nm GeoLas ArF Excimer laser (MicroLas, Göttingen, Germany). Laser ablation was performed with a constant 5 Hz pulse frequency and a fluence of 7 J/cm^2 by focussing the beam at the sample surface using variable laser spot diameters between 32 and 60 µm. Helium was used as carrier gas to transport the laser-generated particles from the ablation cell to the ICPMS and argon was added as an auxiliary gas via a flow adapter before the ICP torch. Typical flow rates of 0.5 L/min for He and 0.9 L/min for Ar were used. The certified reference material NIST SRM 610

(concentrations from Jochum et al., 2011) was used as external standard for calibration of all analyses and was analysed twice at the beginning and at the end for each set of samples, following a bracketing standardization procedure. The reference material NIST SRM 612 was also used as control standard for the standardization. LA-ICPMS calibration was optimized for highest sensitivity on an intermediate m/Q range, while maintaining Th/U ~ 1 and ThO/Th < 0.5%, as determined on NIST SRM 610. The following isotopes were measured with a dwell time of 20 ms for each: ^{29}Si, ^{45}Sc, ^{47}Ti, ^{51}V, ^{53}Cr, ^{57}Fe, ^{60}Ni, ^{63}Cu, ^{66}Zn, ^{90}Zr, ^{93}Nb, ^{95}Mo, ^{118}Sn, ^{181}Ta and ^{182}W. Data reduction and absolute quantification of signals were performed using the software StalQuant, developed at ETH Zürich, Switzerland (see details in Fricker, 2012). For all analyses, the content of ^{47}Ti determined from EMPA analyses was used as internal standard. Limits of detection (LOD) were calculated using the 2σ criterion detailed in Longerich et al. (1996). Zr-in-rutile temperatures were calculated using the thermometer defined by Watson et al. (2006) based on the coexistence of zircon, rutile and quartz phases with a temperature uncertainty of ±20°C.

3.3. U-Pb and ^{40}Ar-^{39}Ar geochronology

U-Pb dating of rutiles have been realized at Géosciences Rennes laboratory (Université Rennes 1, France) using a ESI NWR193UC 193 nm excimer laser coupled to a quadrupole Agilent 7700x ICPMS equipped with a dual pumping system to enhance sensitivity. Laser ablation was performed with a constant 5 Hz frequency and a constant fluence of 8.6 J/cm^2 by focussing the beam at the sample surface. The ablated material was carried by a helium flow and then mixed with nitrogen and argon before injection into the ICP torch. Typical gas flows of 0.8 L/min for He, 4 mL/min for N_2 and 0.85 L/min for Ar were used. Mass calibration was performed before each analytical session using the NIST SRM 612 reference material (Jochum et al., 2011) maintaining Th/U~1 and minimizing ThO/Th < 0.5%. Ablation spot diameters of 40, 50 and 80 μm were used depending of the size of the crystals analysed. The isotopes ^{204}Pb, ^{206}Pb, ^{207}Pb, ^{208}Pb, ^{232}Th and ^{238}U were measured with a dwell time of 10 ms. Data were corrected for U-Pb fractionation and for the mass bias by standard bracketing with repeated measurements of the GJ-1 zircon (Jackson et al., 2004) and of the R10 rutile (Luvizotto et al., 2009) reference standards. The R19 rutile reference material (Luvizotto et al., 2009) was also analysed as secondary standard to control the reproducibility and accuracy of the corrections. Data reduction was carried out with the GLITTER software package (Jackson et al., 2004). Data were plotted using ISOPLOT v.3.75 (Ludwig, 1993).

Uncertainties in tables and text are given at the 2σ level.

$^{40}Ar/^{39}Ar$ analytical work was performed at the University of Manitoba (Canada) using a multi-collector Thermo Fisher Scientific ARGUS VI mass spectrometer, linked to a stainless steel Thermo Fisher Scientific extraction/purification line, Photon Machines (55 W) Fusions 10.6 CO_2 laser, and Photon Machines (Analyte Excite) 193 nm laser. Argon isotopes (from mass 40 to 37) were measured using Faraday detectors with low noise 1 x 10^{12} Ω resistors and mass 36 was measured using a compact discrete dynode (CDD) detector. The sensitivity for argon measurements is ~6.312 x 10^{17} moles/fA as determined from measured aliquots of Fish Canyon Sanidine (Dazé et al., 2003; Kuiper et al., 2008). Standards and samples were placed in 2 mm deep wells in 18 mm diameter aluminium disks, with standards placed strategically so that the lateral neutron flux gradients across the disk could be evaluated. Planar regressions were fit to the standard data, and the $^{40}Ar/^{39}Ar$ neutron fluence parameter (J) interpolated for the unknowns. Uncertainties in J are estimated at 0.1 - 0.2% (1σ), based on Monte Carlo error analysis of the planar regressions (Best et al., 1995). All specimens were irradiated in the Cadmium-lined, in-core CLICIT facility of the TRIGA reactor at the Oregon State University (USA). The duration of irradiation was 17 hours and using the Fish Canyon sanidine (Kuiper et al., 2008) and GA1550 biotite (Spell and McDougall, 2003) standards. Standards for $^{40}Ar/^{39}Ar$ measurements were placed in a Cu sample tray, with a KBr cover slip, in a stainless steel chamber with a differentially pumped ZnS viewport attached to a Thermo Fisher Scientific extraction/purification line and baked with an infrared lamp for 24 hours. Single crystals were fused using the CO_2 laser. The samples selected for the $^{40}Ar/^{39}Ar$ dating were previously investigated by optical microscopy and SEM, in order to spot homogeneous areas within the analysed minerals (mica or adularia) devoid of alteration, micro-inclusions or internal zoning. Discs of 5 mm in diameter and ~150 μm thick were cut from the same polished thick section (150 - 200 μm thick). The discs were mounted using a ceramic adhesive (PELCO) on a quartz slide placed in a stainless steel chamber with a sapphire viewport attached to the same stainless steel high vacuum extraction system as the CO_2 laser, and baked with an infrared lamp for 48 hours. For this study, a raster size of about 100 x 100 μm was used and ablation pits were excavated to an estimated depth of 50 μm. Reactive gases were removed for both the standard and unknown, after 3 minutes, by three GP-50 SAES getters (two at room temperature and one at 450 °C) prior to being admitted to an ARGUS VI mass spectrometer by expansion. Five argon isotopes were measured simultaneously over a period of 6 minutes. Measured isotope abundances were corrected for extraction-line blanks, which were determined before every sample analysis. Line blanks in both the Excimer and

CO_2 system averaged ~3 fA for mass 40 and ~0.013 fA for mass 36. Mass discrimination was monitored by online analysis of air pipettes based on a power law relationship (Renne et al., 2009), which gave D = 1.0081 ± 0.0002 per amu, based on 71 aliquots interspersed with the unknowns. A value of 295.5 was used for the atmospheric $^{40}Ar/^{36}Ar$ ratio (Steiger and Jäger, 1977) for the purposes of routine measurement of mass spectrometer discrimination using air aliquots, and correction for atmospheric argon in the $^{40}Ar/^{39}Ar$ age calculation. Corrections are made for neutron-induced ^{40}Ar from potassium, ^{39}Ar and ^{36}Ar from calcium, and ^{36}Ar from chlorine (Roddick, 1983; Renne et al., 1998; Renne and Norman, 2001). Data were plotted using DensityPlotter (Vermeesch, 2012).

4. Paragenetic sequence of the Puy-les-Vignes deposit

Petrographic observations and geochemical analyses of the studied samples, from the outcrop-scale to the micrometre-scale, completed by the descriptions from Weppe (1951, 1958) and Alikouss (1993) allow to propose a detailed paragenetic sequence of the Puy-les-Vignes deposit, which can be divided into six main stages (Fig. 48).

4.1. Stage I: Early hydrothermal alteration and brecciation

The country rocks are affected by a pervasive greisenization, destabilizing the primary feldspars and biotites and forming a secondary quartz-muscovite±tourmaline assemblage (Fig. 49a). Quartz textures are characterized by ductile deformation (undulose extinction) and dynamic recrystallization. The foliation is partly preserved within the gneissic clasts (Fig. 46b; Fig. 49a) and relicts of biotites and feldspars remain in unaltered parts of the clasts, suggesting that the greisenization is diffuse within the country rocks and likely limited to early fissural discontinuities. Fluid overpressures lead to the hydraulic brecciation and collapse of the enclosing rocks, forming the quartz-matrix supported breccia.

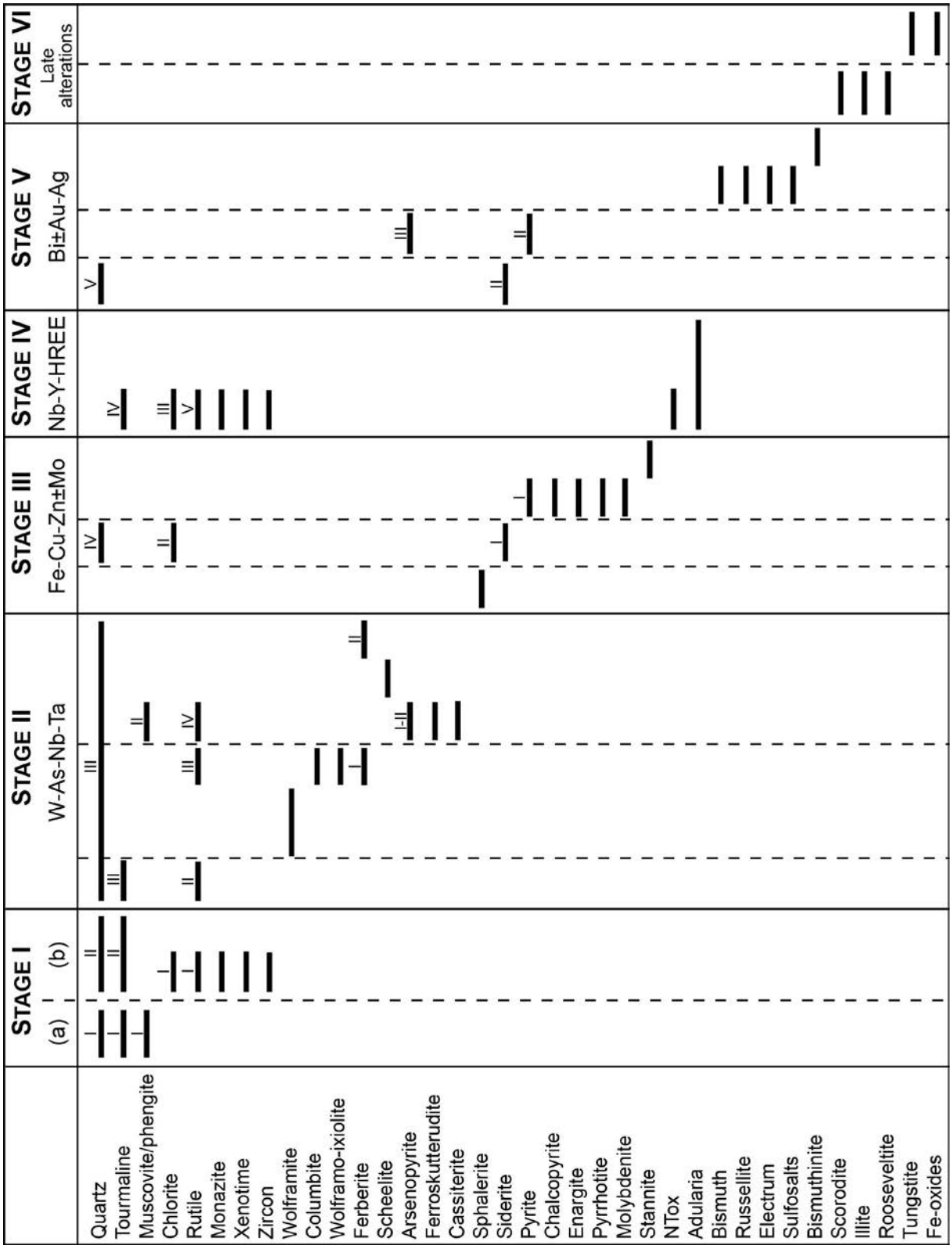

Fig. 48: Paragenetic sequence of the Puy-les-Vignes deposit. Dash lines represent minor episodes of hydraulic fracturing.

At the outcrop-scale, the breccia is composed by polygenic clasts of altered gneisses and granites, which are decimetric to metric in size with a sub-angular shape (Fig. 46a). The clast rims have highly irregular borders and are intensely tourmalinized regardless of their lithology (gneisses or granites) forming a recrystallization front (boron metasomatism), of which the thickness varies from a few millimeters to centimeters (Fig. 47a,b), until up to the complete tourmalinization of the fragments. It can be noted that the tourmalinite rims are generally thicker and more developed on the gneissic clasts compared to the granitic clasts, which reflects possibly differences in rock permeability. Moreover, lateral variations in the thickness of the tourmalinite rims are observed on some clasts at the outcrop-scale (Fig. 46b). There were two successive steps in the alteration of the clasts: (i) chloritization of the residual biotites, with the formation of secondary anhedral crystals (50-100 μm) of W-bearing rutiles (type-1) (Fig. 50a) coeval with the crystallization of monazite, xenotime and zircon, followed by tourmalinization of the greisen, resulting in a quartz-tourmaline assemblage; (ii) massive tourmalinization of the clasts rims, forming a tourmalinite aggregate composed of elongated prisms of tourmalines imbricated with limpid quartz (Fig. 49b).

4.2. Stage II: W-As-Nb-Ta mineralization

Second stage brecciation leads to the infilling by milky quartz according to a hydraulic fracturing mechanism, forming the matrix of the breccia and cutting the tourmalinite rims (Fig. 46a,b). At the microscopic scale, the quartz matrix is commonly formed by polycrystalline quartz aggregates, millimetric in size, which show evidence of intracrystalline plastic deformation (undulose extinction, lamellar deformation) and dynamic recrystallization (bulging and subgrain rotation). However, it should be noted that the intensity of the quartz deformation is variable between different quartz-wolframite samples, thus suggesting that the plastic deformation is spatially partitioned within the breccia. The mineralogy of the quartz veins consists in the main association of wolframite and arsenopyrite, together with minor disseminated crystals of acicular tourmalines and muscovites. The muscovite forms large laths (millimetric in size) in the quartz matrix, which are found either as isolated fan-like crystals or as crystals in overgrowth on the wolframite and showing evidence of kink-bands plastic deformation (Fig. 49c). The muscovite appears therefore after the wolframite in the vein, possibly synchronous with the quartz crystallization.

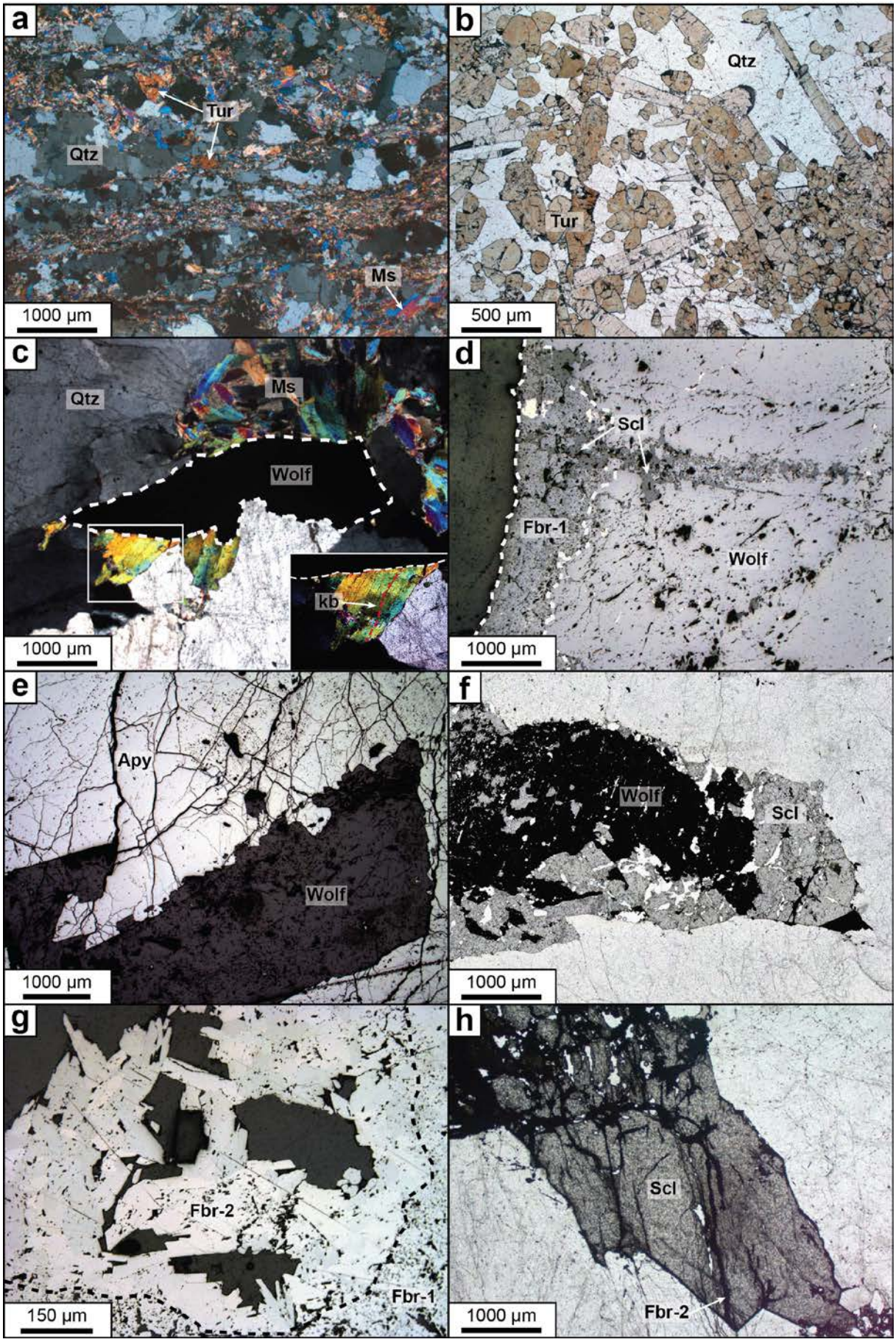
a
Tur
Qtz
Ms
1000 µm
b
Qtz
Tur
500 µm
c
Qtz
Ms
Wolf
kb
1000 µm
d
Scl
Fbr-1
Wolf
1000 µm
e
Apy
Wolf
1000 µm
f
Wolf
Scl
1000 µm
g
Fbr-2
Fbr-1
150 µm
h
Scl
Fbr-2
1000 µm

Fig. 49

Fig. 49: Thin sections microphotographs of the different paragenetic stages of the Puy-les-Vignes deposit (1). (a) Greisenized gneiss observed in cross-polarized transmitted light composed by an assemblage of secondary quartz, muscovite and tourmaline within preserved foliation (sample PLV-02-01a). (b) Tourmalinite rim on a gneissic clast observed in plane-polarized transmitted light composed of prismatic crystals of tourmaline within a quartz matrix (sample PLV-02-01a). (c) Quartz-wolframite-muscovite vein observed in cross-polarized transmitted light. Muscovite crystals are in overgrowth on the wolframite and show evidence of kink-band (kb) deformation (sample PLV-02-03). (d) Wolframite partially replaced by ferberite-1 along crystalline borders and cut by late scheelite, observed in reflected light (sample PLV-7597a). (e) Sub-euhedral crystal of wolframite partially corroded by massive crystal of arsenopyrite, observed in reflected light (sample PLV-02-28b). (f) Scheelite replacing partially a large crystal of wolframite observed in plane-polarized transmitted light (sample PLV-7597b). (g) Polycrystalline aggregates of randomly oriented fibrous ferberite-2 crystals within ferberite-1, observed in reflected light (sample PLV-02-11). (h) Scheelite partially replaced by ferberite-2 ("reinite") in plane-polarized transmitted light (sample PLV-02-26). Mineral abbreviations: Apy: arsenopyrite; Fbr: ferberite; Ms: muscovite; Qtz: quartz; Scl: scheelite; Tur: tourmaline; Wolf: wolframite.

Fig. 50: BSE images the different paragenetic stages of the Puy-les-Vignes deposit (1). (a) Sub-euhedral crystal of W-bearing rutile (type-1) associated with the tourmalinite rim on a greisen clast (sample PLV-02-04a). (b) Wolframite partially altered by ferberite-1 showing a complex patchy texture (sample PLV-7597a). (c) Strongly zoned Ta-Nb-rich ferberite associated within the ferberite-1 and showing Ta-Nb-rich growing bands (dark grey) composed by nanocrystal aggregates of ferberite with high Ta and Nb contents (sample PV-3). (d) Sub-euhedral crystals of W-bearing rutile (type-2) disseminated within the quartz-wolframite vein. The rutiles are composed of a homogeneous core (dark grey) with a sector zoning marked by W-rich growing bands (medium grey) and external overgrowths of Nb±Ta-rich rutiles (bright grey) with a patchy texture (sample PLV-7574a). (e) Sub-euhedral crystal of Nb-Ta-rich rutile (type-3) within the ferberite-1 showing an internal growth zoning (sample PLV-02-17). (f) Wolframoixiolite in overgrowth on a wolframite crystal (sample PV-5a). (g) Wolframoixiolite crystal surrounded by an overgrowth of ferberite-1 within the scheelite (sample PLV-02-13b). (h) Sub-euhedral crystals of Cr-Nb-W-bearing rutiles (type-4) within the arsenopyrite from stage II and showing a strong internal growth zoning (PLV-02-28b). Mineral abbreviations: Apy: arsenopyrite; Fbr: ferberite; Qtz: quartz; Rt: rutile; Scd: scorodite; Scl: scheelite; Tur: tourmaline; Wix: wolframoixiolite; Wolf: wolframite.

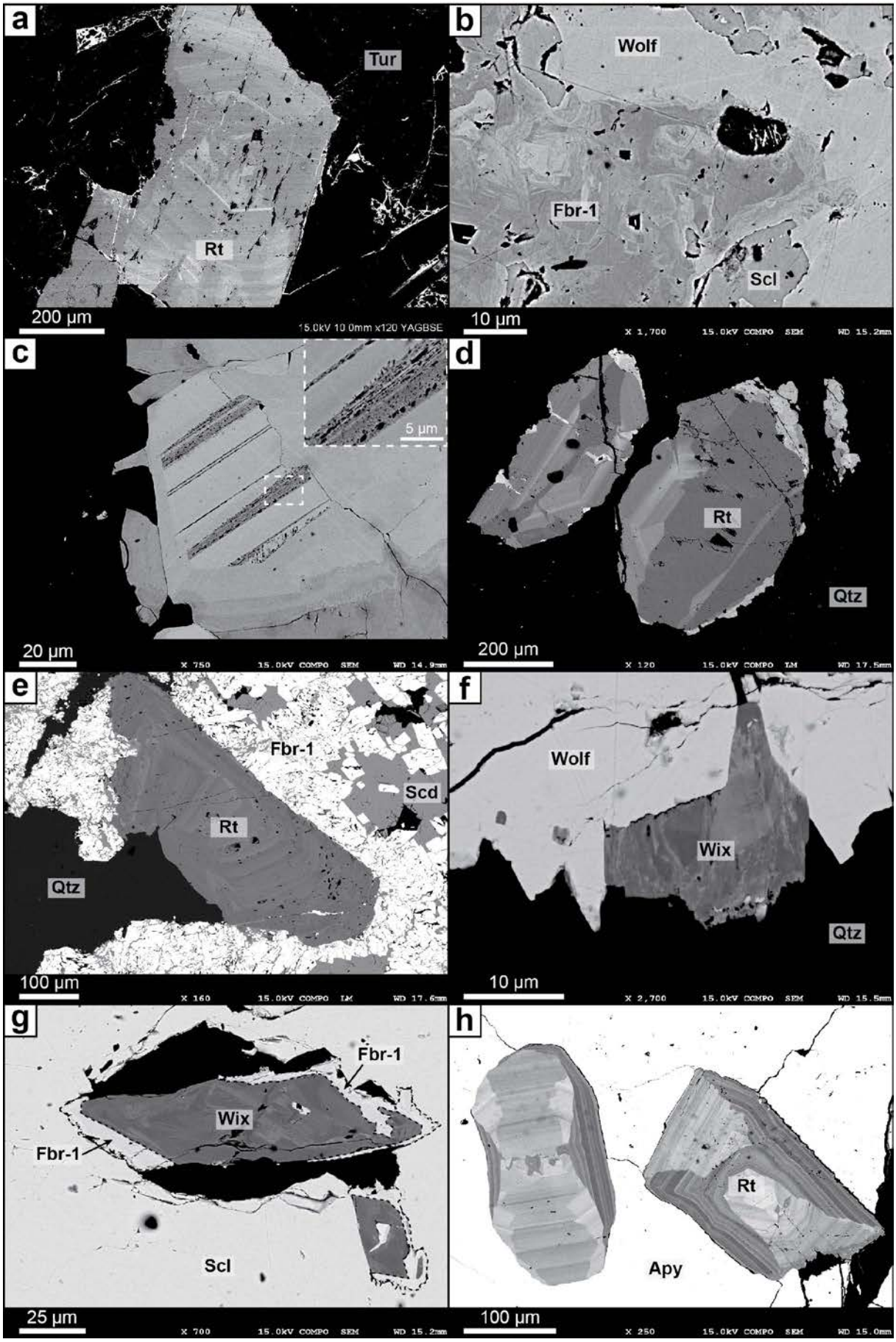
a
Tur
Rt
200 µm
15.0kV 10.0mm x120 YAGBSE
b
Wolf
Fbr-1
Scl
10 µm
X 1,700 15.0kV COMPO SEM WD 15.2mm
c
5 µm
20 µm
X 750 15.0kV COMPO SEM WD 14.9mm
d
Rt
Qtz
200 µm
X 120 15.0kV COMPO LM WD 17.5mm
e
Fbr-1
Scd
Rt
Qtz
100 µm
X 160 15.0kV COMPO LM WD 17.6mm
f
Wolf
Wix
Qtz
10 µm
X 2,700 15.0kV COMPO SEM WD 15.5mm
g
Fbr-1
Wix
Fbr-1
Scl
25 µm
X 700 15.0kV COMPO SEM WD 15.2mm
h
Rt
Apy
100 µm
X 250 15.0kV COMPO SEM WD 15.0mm

Fig. 50

The wolframite forms euhedral prismatic crystals, millimetric to centimetric in size, growing locally onto the tourmalinite, but forming mostly disseminated and fragmented crystals within the quartz vein. The primary wolframite has homogeneous composition ($0.80<Fe/(Fe+Mn)<0.86$) and is partially replaced by ferberite-1 ($0.95<Fe/(Fe+Mn)<1.0$) along cracks or crystal borders (Fig. 49d). Ferberitization appears as a discontinuous process, which replaces progressively the wolframite with a patchy texture and forming successive growing bands on the crystals borders (Fig. 50b). Locally, ferberite-1 is associated with the crystallization of a strongly zoned Ta-Nb-rich ferberite (Fig. 50c). At high magnification in BSE imagery, the zoning appears composed by nanocrystal aggregates of ferberite with Ta and Nb contents up to 1.6 wt.% and 0.4 wt.% respectively, accompanied by minor P content (0.4-0.8 wt.% P). Several Nb-Ta oxides are also associated with the stage II: (i) euhedral to sub-euhedral crystals (100-500 μm) of W-bearing rutiles (type-2) disseminated in the quartz, which are similar to type-1 rutiles, but showing Nb±Ta-rich rutiles overgrowths with a patchy texture (Fig. 50d); (ii) sub-euhedral crystals (500 μm) of Nb-Ta-rutiles (type-3), which are disseminated within the ferberitized wolframite (Fig. 50e); (iii) sub-euhedral crystals (200-500 μm) of wolframoixiolite, which are present either in microcavities infillings within the wolframite, or in overgrowths on the quartz-cemented wolframite boundaries (Fig. 50f) or as partially replaced crystals disseminated within the late scheelite and showing ferberite-1 overgrowths (Fig. 50g).

The arsenopyrite constitutes the main sulphide mineral in the quartz vein and forms sub-euhedral crystals, which partially crosscuts and corrodes the wolframite (Fig. 49e). Even though the wolframite and arsenopyrite are commonly found together within most of the mineralized samples, the arsenopyrite forms clearly after the wolframite during a temporally distinct fluid episode. In BSE imagery, the arsenopyrite shows an internal zoning corresponding to two different types of arsenopyrite (Fig. 52a): (i) arsenopyrite-1 is characterized by a ratio As/S~3 and contains ca. 4.5 wt.% Co and ca. 1 wt.% Ni. Mineral inclusions of Fe-skutterudite are present within arsenopyrite-1, together associated with minor wolframite, xenotime, monazite and Cr-Nb-W-bearing rutiles (type-4) (Fig. 50h); (ii) arsenopyrite-2 cuts and grows over the arsenopyrite-1 and is characterized by a ratio As/S~2.5 and show no detectable Co-Ni content by EDS spectrometry. The deposition of arsenopyrite seems also coeval with the crystallization of minor cassiterite (Fig. 52b). Rare Cr-rich phengites (so-called “mariposite”) have also been found in association with arsenopyrite.

Scheelite occurs lately by replacement of the wolframite and ferberite-1 along crystalline borders or in micro-cracks (Fig. 49f) and crosscuts the arsenopyrite within veins,

locally associated with minor stolzite ($PbWO_4$). One large crystal of scheelite containing relics of partially replaced wolframite showed textural evidence of plastic deformation (undulose extinction). A second generation of late ferberite occurs as partial pseudomorphs after ferberite-1 and scheelite, forming polycrystalline aggregates of randomly oriented fibrous ferberite crystals (Fig. 49g,h). This ferberite-2 may correspond to an incomplete crystalline form of the so-called "reinite", described by Weppe (1958).

4.3. Stage III: Fe-Cu-Zn±Mo mineralization

An association of base metals (Fe-Cu-Zn±Mo) sulphides composed mainly by pyrite, chalcopyrite and sphalerite, with minor pyrrhotite, enargite, stannite and molybdenite, fills the microcracks and microcavities within the tourmalinite from the stage I and ore minerals from the stage II (Fig. 51a,b,c). Pyrite and chalcopyrite form generally large sub-euhedral crystals, cm in size, in overgrowth onto the primary wolframite and arsenopyrite and are coeval with the deposition of quartz, siderite and chlorite (Fig. 52c). Enargite and molybdenite appear coeval with chalcopyrite, whereas sphalerite is early (Fig. 51d). Sphalerite can contain up to 2 wt.% Cd. Stannite is late and form exsolution phases within chalcopyrite (Fig. 52d). Sulphide deposition is accompanied by the recrystallization of the milky quartz into limpid quartz along the wolframite and arsenopyrite boundaries.

4.4. Stage IV: Nb-Y-HREE mineralization

A late hydrothermal stage corresponds to the formation of a crackle-breccia with a matrix of tourmaline, adularia and vermicular chlorite, which cuts the deformed quartz-wolframite-scheelite vein (Fig. 51e). The breccia is not deformed, thus indicating that it forms after the main ductile deformation episode. The crystals of tourmaline and chlorite are fragmented within the adularia matrix, which may indicate that the adularia itself is late. This stage is coeval with the crystallization of a series of accessory minerals disseminated within the adularia matrix, which consist in monazite, xenotime, zircon, Nb-Fe-W-rich rutile (type-5) and Nb-Ti-Y-HREE-W-U oxides, referred to as NTox (Fig. 51f). The latter form large sub-euhedral crystals (10-400 μm), which are characterized by uncommon chemical compositions and complex internal textures. A complete description of the NTox is given in the Chapter 5.

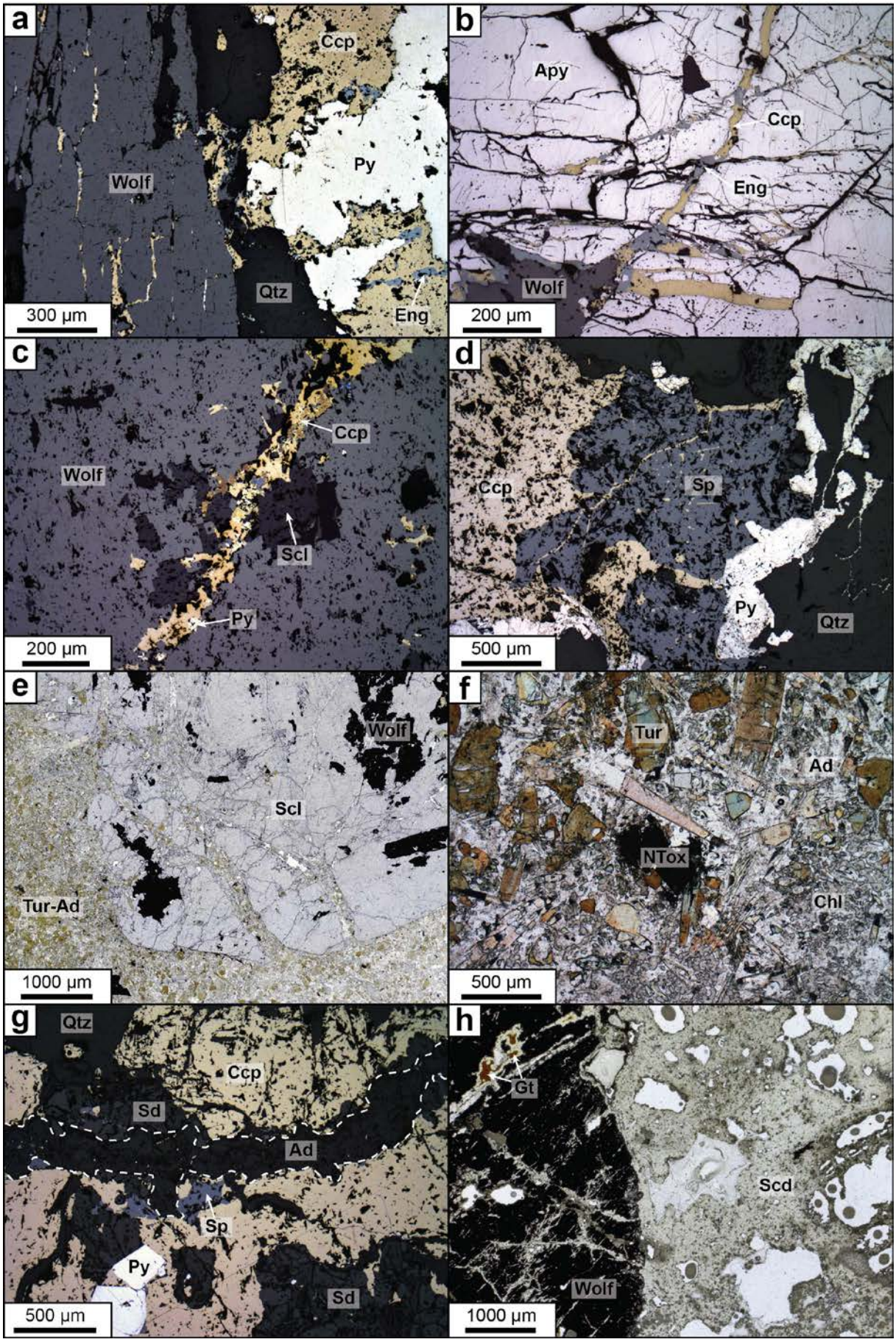
a
Ccp
Py
Wolf
Qtz
Eng
300 µm
b
Apy
Ccp
Eng
Wolf
200 µm
c
Ccp
Wolf
Scl
Py
200 µm
d
Ccp
Sp
Py
Qtz
500 µm
e
Wolf
Scl
Tur-Ad
1000 µm
f
Tur
Ad
NTox
Chl
500 µm
g
Qtz
Ccp
Sd
Ad
Sp
Py
Sd
500 µm
h
Gt
Scd
Wolf
1000 µm

Fig. 51

Fig. 51: Thin sections microphotographs of the different paragenetic stages of the Puy-les-Vignes deposit (2). (a) Association of pyrite, chalcopyrite and enargite in overgrowths and infillings into a quartz-wolframite vein observed in reflected light (sample PLV-02-29). (b) Massive crystal of arsenopyrite cut by a chalcopyrite-enargite vein, observed in reflected light (sample PLV-7574a). (c) Sphalerite cut by chalcopyrite and pyrite association, observed in reflected light (sample PV-2a). (d) Vein of pyrite-chalcopyrite crosscutting wolframite and scheelite, observed in reflected light (sample PV-3). (e) Large crystal of scheelite containing relicts of partially replaced wolframite cut by a tourmaline-adularia breccia, observed in plane-polarized transmitted light (sample PLV-02-13a). (f) Detail of the breccia composed by fragmented crystals of tourmaline, vermicular chlorite and Nb-Ti-Y-HREE-W-U oxides within an adularia matrix (sample PLV-02-13a). (g) Adularia vein crosscutting quartz, siderite and chalcopyrite association, observed in reflected light (sample PV-2b). (h) Arsenopyrite completely altered in scorodite associated with goethite, observed in plane-polarized transmitted light (sample PLV-02-17). Mineral abbreviations: Ad: adularia; Apy: arsenopyrite; Ccp: chalcopyrite; Chl: chlorite; Eng: enargite; Gt: goethite; NTox: Nb-Ti-Y-HREE-W-U oxides; Py: pyrite; Qtz: quartz; Scd: scorodite; Scl: scheelite; Sd: siderite; Sp: sphalerite; Tur: tourmaline; Wolf: wolframite.

Fig. 52: BSE images the different paragenetic stages of the Puy-les-Vignes deposit (2). (a) Arsenopyrite-1 with numerous small inclusions of native bismuth cut by arsenopyrite-2 in veins and overgrowth (sample PLV-7597a). (b) Cassiterite crystal within arsenopyrite (stage II) cut by veins of chalcopyrite (stage III) (sample PV-2a). (c) Arsenopyrite cut by chalcopyrite-pyrite-chlorite veins (stage III) and with disseminated inclusions of native Bi (sample PV-3). (d) Exsolution of stannite within chalcopyrite (sample PV-2a). (e) Association of native Bi and electrum (Au-Ag) in microcavities infilling within the arsenopyrite-1 and Fe-skutterudite (sample PLV-7597a). (f) Overgrowth of collomorph As-rich pyrite on euhedral arsenopyrite-3 and chalcopyrite (sample PV-2b). (g) As-rich pyrite and siderite (stage V) in overgrowth on sphalerite and chalcopyrite from stage III (sample PV-2b). (h) As-rich pyrite and siderite crosscutting adularia vein (sample PV-2b). Mineral abbreviations: Ad: adularia; Apy: arsenopyrite; As-Py: As-rich pyrite; Bi: native bismuth; Ccp: chalcopyrite; Chl: chlorite; Cst: cassiterite; El: electrum; Fsk: Fe-skutterudite; Py: pyrite; Sd: siderite; Sp: sphalerite; Stn: stannite.

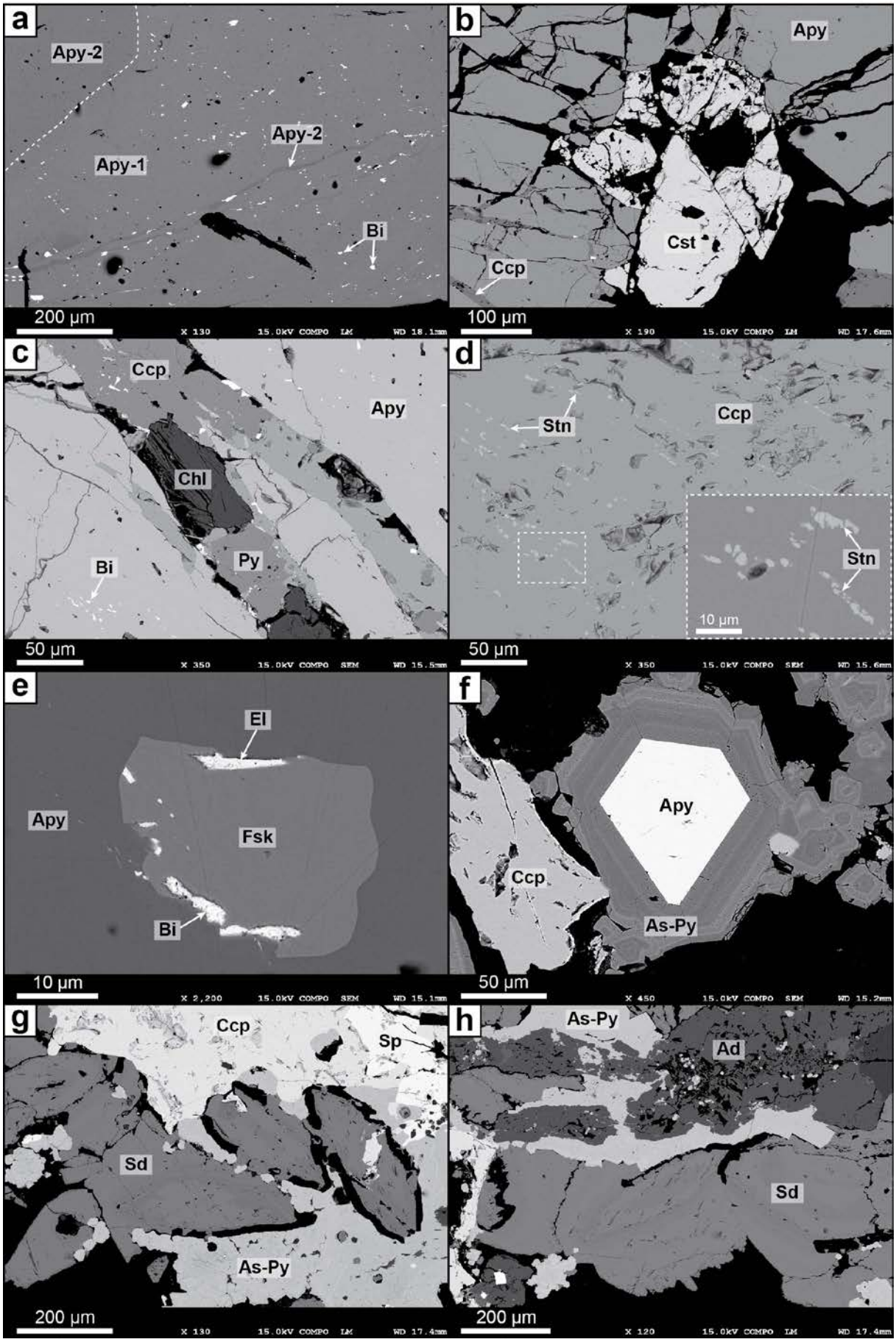
a
Apy-2
Apy-2
Apy-1
Bi
200 µm
b
Apy
Cst
Ccp
100 µm
c
Ccp
Apy
Chl
Py
Bi
50 µm
d
Stn
Ccp
Stn
10 µm
50 µm
e
El
Apy
Fsk
Bi
10 µm
f
Apy
Ccp
As-Py
50 µm
g
Ccp
Sp
Sd
As-Py
200 µm
h
As-Py
Ad
Sd
200 µm

Fig. 52

4.5. Stage V: Bi±Au-Ag mineralization

A discrete mineralization of native bismuth, bismuthinite, Bi-Ag-Se-Te sulphosalts and electrum (ca. 78 wt.% Au and 22 wt.% Ag) fills microcavities and microcracks within the quartz, wolframite and arsenopyrite from the stage II and the base metal sulphides from the stage III (Fig. 51g; Fig. 52e). Bi-minerals are also found crosscutting adularia from the stage IV. They show variable compositions in Bi (70-78 wt.%), Te (5-20 wt.%), S (5-18 wt.%), Se (up to 0.8 wt.%), Sb (1-5 wt.%), Fe (1-3 wt.%) and Ag (up to 7 wt.%). An association of quartz, siderite, arsenopyrite-3 and collomorph As-rich pyrite (1-10 wt.% As) precedes the deposition of the Bi-phases (Fig. 52f,g,h). Native bismuth is occasionally surrounded by a rim of bismuthinite, indicating a progressive sulphidation (increase in f_{S2}) of the fluids, as already observed in other W-Sn deposits (Nicolas, 1985; Aïssa et al., 1987a; Gama, 2000) and Au deposits (Demange et al., 2006) from the FMC. Russellite (Bi_2WO_6) occurs in pseudomorph after ferberite at the contact with native bismuth. This Bi±Au-Ag paragenesis is similar to those found in Variscan orogenic gold deposits (e.g., Noronha et al., 2000; Boiron et al., 2003; Zachariáš et al., 2004; Cepedal et al., 2008).

4.6. Stage VI: Late hydrothermal and supergene alterations

Late hydrothermal circulations are responsible for alteration of arsenopyrite in scorodite ($FeAsO_4.2H_2O$) and in other arsenate phases such as pharmacosiderite, carminite and beudantite. Scorodite forms greenish minerals with a skeletal and porous texture, which occurs in pseudomorph after arsenopyrite or in vein infillings within wolframite and chalcopyrite, locally in association with illite (Fig. 51h). Scorodite veins contain in particular mineral inclusions of rooseveltite ($BiAsO_4$), indicating the remobilisation of bismuth during the alteration of arsenopyrite. The formation of scorodite reflects a change to more oxidizing and acid conditions allowing arsenopyrite oxidation (Dove and Rimstidt, 1985). Finally, supergene alteration affects the ore body, destabilizing the ferberite, scorodite and residual sulphides and forming secondary minerals, such as tungstite ($WO_3.H_2O$), collomorph goethite and other Fe-hydroxides.

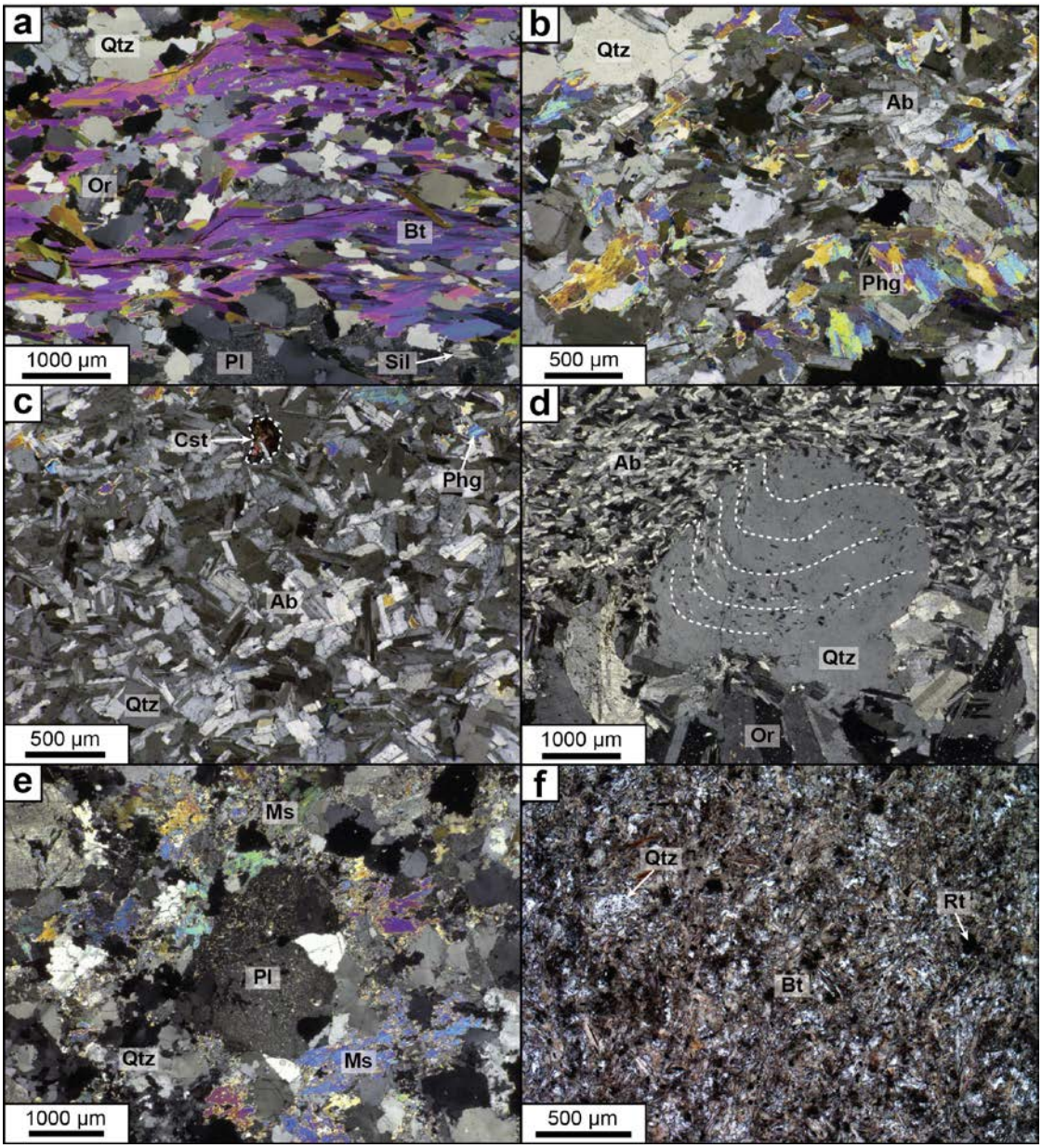

Fig. 53: Thin sections microphotographs of host-rocks from the Puy-les-Vignes deposit. (a) Enclosing gneiss composed of quartz, K-feldspar and plagioclase feldspar intercalated in the foliation underlined by biotite and sillimanite, observed in cross-polarized transmitted light (sample PV-92-20). (b) Quartz-albite-phengite band within the rare-metal aplo-pegmatite, observed in cross-polarized transmitted light (sample PLV-02-02). (c) Albite-quartz±phengite band with minor cassiterite in the rare-metal aplo-pegmatite, observed in cross-polarized transmitted light (sample PLV-02-02). (d) Globular quartz phenocryst with poikilitic inclusions of rotated albite laths (dashed lines) in a typical "snowball" texture, disseminated within the rare-metal aplo-pegmatite, observed in cross-polarized transmitted light (sample PLV-02-02). (e) Leucogranite dyke composed of quartz, plagioclase feldspar and muscovite, showing evidence of ductile deformation and minor alteration, observed in cross-polarized transmitted light (sample PV-92-7). (f) Typical microcrystalline texture in the lamprophyre composed of biotite and xenomorphic quartz with minor rutile, observed in plane-polarized transmitted light (sample PV-92-17). Mineral abbreviations: Ab: albite; Bt: biotite; Cst: cassiterite; Or: orthoclase; Phg: phengite; Pl: plagioclase; Qtz: quartz; Rt: rutile; Sil: sillimanite.

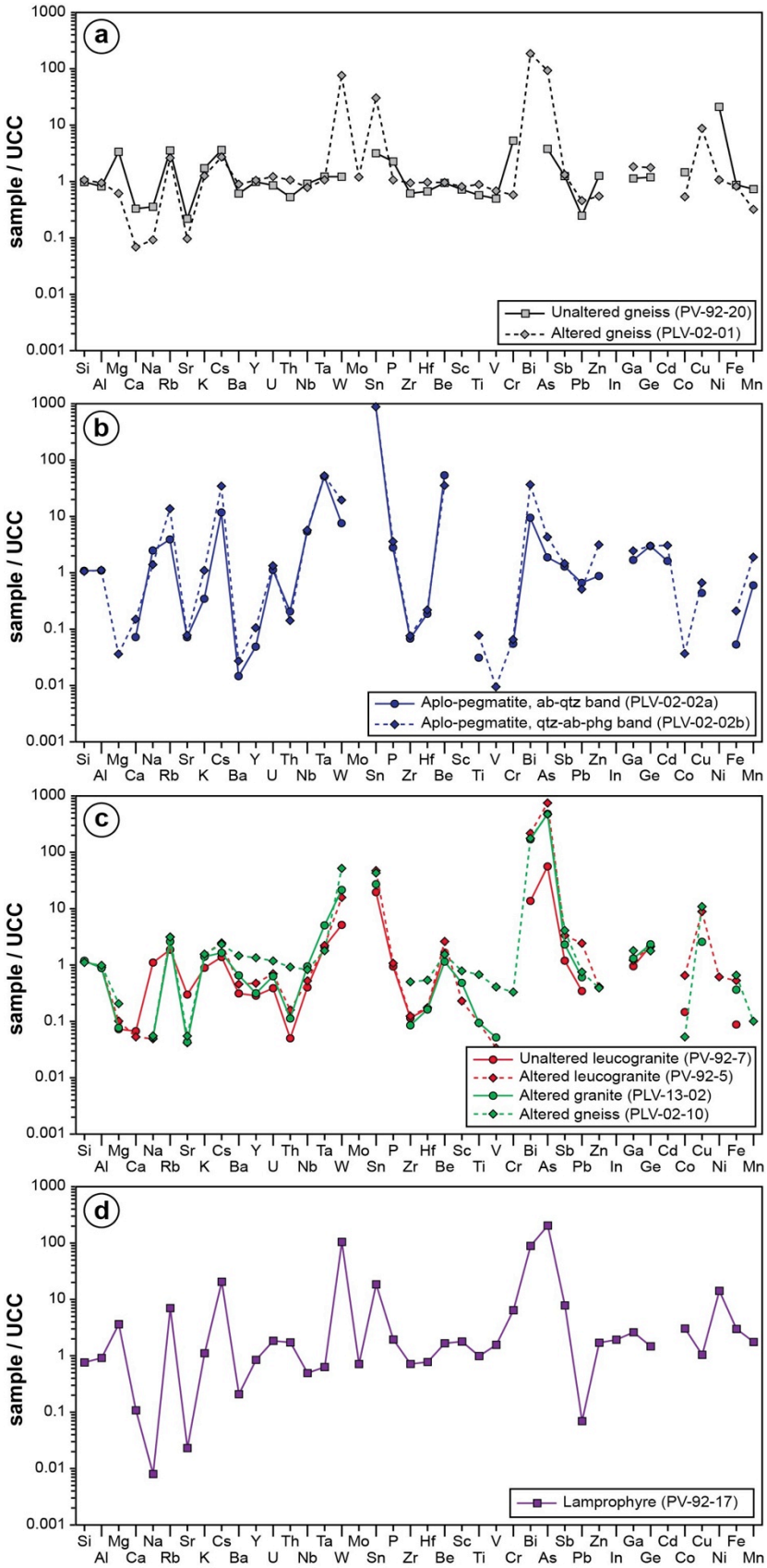

Fig. 54: Whole-rock geochemical compositions of host-rocks from the Puy-les-Vignes deposit normalized by the upper continental crust (UCC, Rudnick and Gao, 2003). Data are given in Table 15.

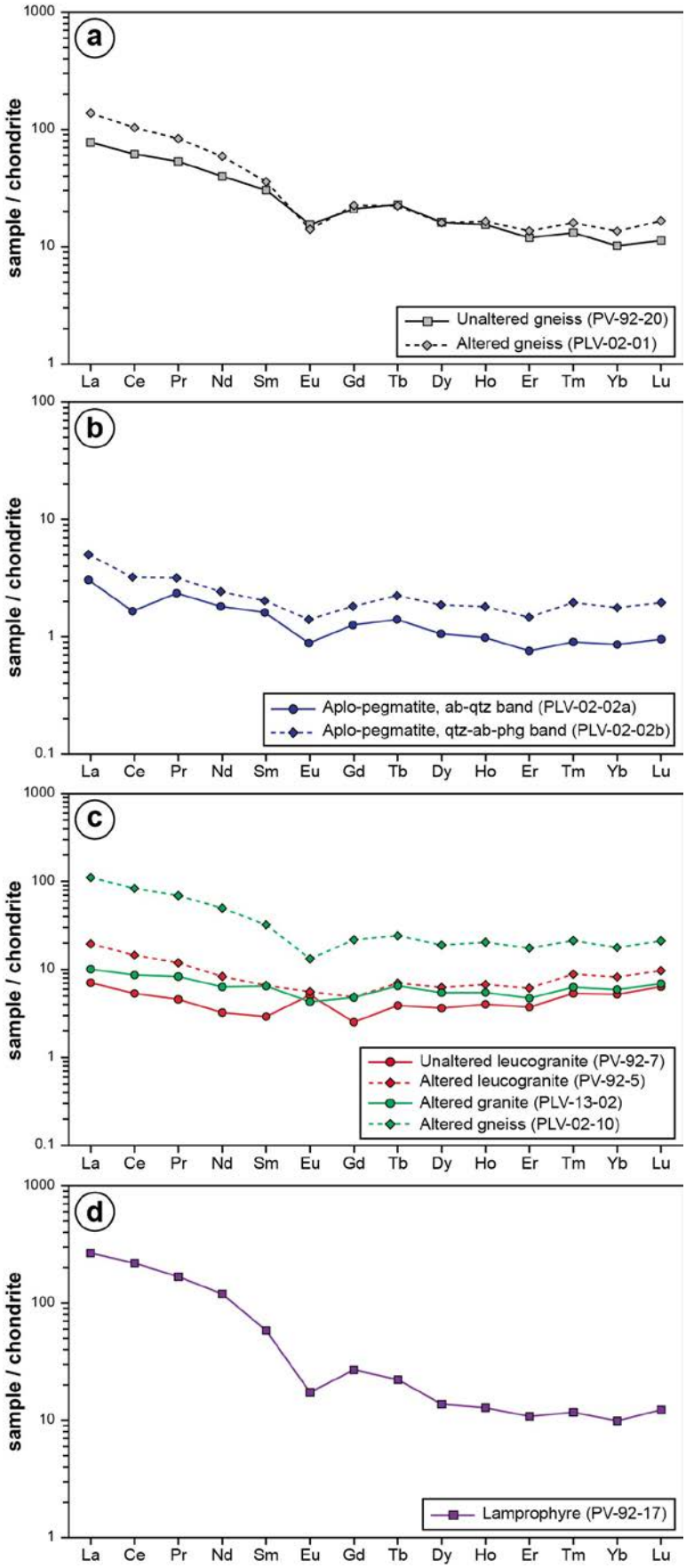

Fig. 55: Chondrite-normalized REE patterns of host-rocks from the Puy-les-Vignes deposit. Data for chondrite are from Palme and O'Neill (2014). Data are given in Table 15.

5. Petrography and geochemistry of the host-rocks

5.1. Enclosing gneiss

The enclosing rocks of the Puy-les-Vignes deposit consist of relatively homogeneous schistose gneisses with undulated foliation, forming the St-Léonard-de-Noblat unit, which are composed by a mineralogical association of quartz, biotite, K-feldspar and sillimanite with a fine- to medium-grained texture (Fig. 53a). Locally, the gneisses alternate with lenses of massive quartz-K-feldspar-biotite gneisses and with migmatitic sillimanite±cordierite gneisses (Chenevoy et al., 1984). Whole-rock geochemistry of an unaltered gneiss sample taken in the mining dumps (sample PV-92-20) is characterized by a metapelitic composition (Table 15), indicating a metasedimentary origin. The trace elements contents indicate compositions close to the values of the upper continental crust, with relative depletion in Ca, Na, Sr, Ba, U, Th, Zr, Hf, Sc, Ti, V, Pb and enrichment in Mg, Rb, K, Cs, Sn, P, Cr and As (Fig. 54a). No particular enrichment in rare-metals is observed. The REE pattern show enrichment in LREE compared to HREE (La/Yb=7.62) with a negative Eu anomaly (Eu/Eu*=0.61) (Fig. 55a), typical of a metasedimentary rock. Altered gneiss samples taken within the breccia pipe (sample PLV-02-01; Fig. 54a) show very high concentrations in W (145 ppm), Sn (64 ppm), Bi (30 ppm), As (448 ppm) and Cu (246 ppm), thus indicating that the gneiss was altered by the mineralizing fluids during the formation of the breccia pipe.

5.2. Granitic rocks

Several samples of granitic rocks found in the Puy-les-Vignes deposit have been studied. An unique sample of rare-metal aplo-pegmatite (sample PLV-02-02; Fig. 47f), coming directly from the old underground workings at the time where the mine was still operating, has been studied. Although the precise location of this sample within the deposit as well as the relationships with the breccia pipe remain unknown, it comes very likely from an intrusive granitic body at depth. A sample of unaltered leucogranite dyke crosscutting the enclosing gneisses (sample PV-92-7; Fig. 47e) was taken in the mining dumps. According to the descriptions of Weppe (1951, 1958), leucogranite dykes are known in the surroundings of the deposit and are found fragmented within the breccia. This indicates that the leucogranite dyke was emplaced before the main hydrothermal alteration and brecciation and that a hidden leucogranite intrusion is likely present at depth. Other samples of altered granitic rocks were

taken from the mining dumps (sample PV-92-5 and PLV-02-10) and from the breccia outcrop in surface (sample PLV-13-02).

5.2.1. Rare-metal aplo-pegmatite

The sample of rare-metal aplo-pegmatite (PLV-02-02; Fig. 47f) is characterized by a magmatic layering corresponding to a repetitive sequence of quartz-albite-phengite bands at the bottom (Fig. 53b) passing to albite-quartz bands at the top with a fine-grained texture (Fig. 53c). The transition between the two bands is marked by a progressive grain size decrease from 500-1000 μm in average in the lower quartz-albite-phengite bands down to 100-200 μm in the upper albite-quartz bands. The albite crystals are imbricated with a cumulative texture, whereas the quartz form xenomorphic globular phenocryst with poikilitic inclusions of albite laths in a typical "snowball" helicitic texture (Fig. 53d). This rotational texture within the albitic cumulate can be interpreted as resulting from a syn-magmatic flattening. Phengites contain relatively high contents in F (2.3-8.5 wt.%) with an average concentration of 4.2 wt.% F, as determined by EMPA. Accessory minerals consist in disseminated crystals of apatite, cassiterite and columbite-tantalite. Cassiterite form sub-euhedral crystals, 100-500 μm in size, which are disseminated or in clusters within the albite-quartz bands (Fig. 53c). The cassiterite crystals show a discrete internal zoning in BSE imagery and contain small inclusions (5 to 20 μm) of columbite-tantalite (Fig. 56a,b). These crystals are anhedral with irregular borders (Fig. 56b), excluding their interpretation as exsolution products (Neiva, 1996). Their textures suggest that they formed early in the aplo-pegmatite and were trapped during the crystallization of cassiterite. Occasionally, internal zoning is observed in columbite-tantalite crystal (Fig. 56c), which may be interpreted texturally as growth zoning. Larger crystals (100-200 μm) of columbite-tantalite are also found disseminated within the albite-quartz bands. In BSE imagery, the columbite-tantalite minerals exhibit a strong internal zoning composed of five constituents (Fig. 56d,e): (i) dark grey zones forming the cores of the crystals with small dimensions (ca. 15-20 μm) and with oval shapes. They likely represent initial nuclei corresponding to the early crystallization; (ii) a patchy complex with irregular shapes which are closely associated with the dark cores; (iii) a cortex-I with a medium grey colour surrounding the dark core and patchy complex with a regular growth zoning and forming the main part of the crystals; (iv) a cortex-II with a light grey colour which is in continuity of the cortex-I; and (v) a bright external overgrowth, rarely exceeding 10 μm in thickness, forming a late phase in corrosive overgrowth on the cortex. The last albite-quartz band in the lower part

of the sample is marked by the beginning of an unidirectional solidification texture (UST), formed by perpendicularly oriented phenocryst of K-feldspars ("stockscheider"), which precede the transition with a granitic pegmatite (Fig. 47f). These mineralogical and textural features are characteristics of a rare-metal granitic dyke derived from a highly evolved granite cupola (Zhu et al., 2001; Breiter et al., 2005).

The two zones within the aplo-pegmatite, i.e. the albite-quartz band (sample PLV-02-02a) and the quartz-albite-phengite band (sample PLV-02-02b), have been analysed for whole-rock geochemistry. The aplo-pegmatite shows a peraluminous composition (A/CNK=1.13-1.45) with low concentrations in Fe, Mg, Ca, Sr, Ba, Y, Th, Zr, Hf, Ti and high concentrations in Na, Rb, Cs, Nb, Ta, W, Sn, P, Be compared to the upper continental crust (Fig. 54b, Table 15). The REE contents are low (∑REE=4.0-6.5 ppm) and exhibit a negative Eu anomaly (Eu/Eu*=0.62-0.73) (Fig. 55b). The rare-metals contents are particularly high in Sn (1853-3044 ppm), Nb (65-69 ppm), Ta (46-47.5 ppm) and W (14-37 ppm) (Table 15). This geochemical composition is typical of the peraluminous intermediate phosphorus (0.42-0.54 wt.% P_2O_5) rare-metal granites (Linnen and Cuney, 2005 and references therein), which belong to the PIP-RMG fractionation trend. In the A-B diagram (Fig. 57a), the two samples of rare-metal aplo-pegmatite define a segment in the lower left part of the plot, which intercept the fractionation trends of the Beauvoir and Blond granites. The albite-quartz band (sample PLV-02-02a) corresponds to a fractionation of albitite cumulate, whereas the quartz-albite-phengite band (sample PLV-02-02b) corresponds to a fractionation of mica layer. The same conclusion can be made in the (QBF)3 diagram (Fig. 58).

5.2.2. Leucogranite

The mineralogy of the leucogranite is composed of quartz, plagioclase feldspar and muscovite with a medium-grained texture (Fig. 53e). The quartz crystals show intra-crystalline deformation marked by undulose extinction, whereas the feldspars and muscovites are partially altered within the leucogranite. Whole-rock geochemistry of the slightly altered leucogranite (sample PV-92-7) shows a peraluminous composition (A/CNK=1.54) corresponding to the Beauvoir-type fractionation trend in the A-B diagram (Fig. 57). The trace elements composition is characterized by low concentrations in Sr, Ba, U, Th, Sc, Zr, Hf, Y, Pb and by high concentrations in Rb, Cs, W, Sn, Bi, As compared to the crust with Ta/Nb=0.39 (Fig. 54c; Table 15). The REE contents are low and show a flat pattern (La/Yb=1.36) with a positive Eu anomaly (Eu/Eu*=1.89) (Fig. 55c). In the A-B diagram (Fig.

57a), the leucogranite falls close to the rare-metal aplo-pegmatite and the fractionation trends of the Beauvoir and Blond granites. As the analysed sample is slightly altered, its composition may have been a little bit shifted from a Limousin-type fractionation trend toward a greisen-type composition. This evolution is more easily visible in the (QBF)3 diagram (Fig. 58). Compared to the Aureil and Auriat granites (Fig. 57a,b), the leucogranite sample differs significantly and may represent an evolved member of the St-Sylvestre granite, which is located close to Puy-les-Vignes. The altered sample of leucogranite within the breccia pipe (sample PV-92-5) has higher contents in Fe, K and lower contents in Si, Na (Table 15; Fig. 57 and Fig. 58), corresponding to a greisen-type composition reflecting the dissolution of the feldspars and the crystallization of secondary phengites. The trace elements composition reveals very high contents in W (30 ppm), Sn (98 ppm), Bi (34 ppm), As (3540 ppm) and Cu (246 ppm), thus indicating that the leucogranite fragmented in the breccia pipe was altered by the mineralizing fluids.

5.2.3. Granites

Two other samples of more altered granites (samples PLV-02-10 and PLV-13-02) have been also analysed (Table 15). These samples are composed of quartz, secondary phengites and Fe-rich phyllosilicates with a medium-grained texture, which replace the destabilized primary feldspars. They are characterized by high A parameter (Fig. 57a) because of clay and/or greisen-type alteration, similar to the altered leucogranite (sample PV-92-5). The greisenization trends observed in the A-B and Q-P diagrams (Fig. 57), as well as in the (QBF)3 diagram (Fig. 58), may indicate that the granites come from a Guéret-type granite (AKG type of Stussi, 1989), such as the Aureil granite (or equivalent) at depth.

5.3. Lamprophyre

The lamprophyre forms melanocrate dykes, typically 1 to 3 m thick, which crosscut the enclosing gneisses and locally the breccia pipe (Weppe, 1958). They are also found fragmented within the quartz of the breccia. One sample of unaltered lamprophyre (sample PV-92-17) was taken from the mining dumps. The mineralogy of the lamprophyre is composed of biotite, xenomorphic quartz and minor plagioclase with a microcrystalline texture (Fig. 53f). Accessory minerals consist in rutile, monazite, fluoro-apatite, skutterudite and pyrite. The whole-rock geochemistry of the lamprophyre (sample PV-92-17) shows Mg-

K rich mafic composition with low concentrations in Ca, Na, Sr, Nb, Ta, Pb and high concentrations in As, Cr, Rb, Ni, W, V, Zr, Ba, Zn, Cs, Co, Ga, Sn and Cu (Fig. 53d). The REE pattern shows high enrichment in LREE (La/Yb=27) with a negative Eu anomaly (Eu/Eu*=0.44) (Fig. 55d). The high contents in W (198 ppm), Sn (39 ppm) and As (974 ppm) indicate that the W-mineralizing fluids overprinted the composition of the lamprophyre during the breccia pipe formation.

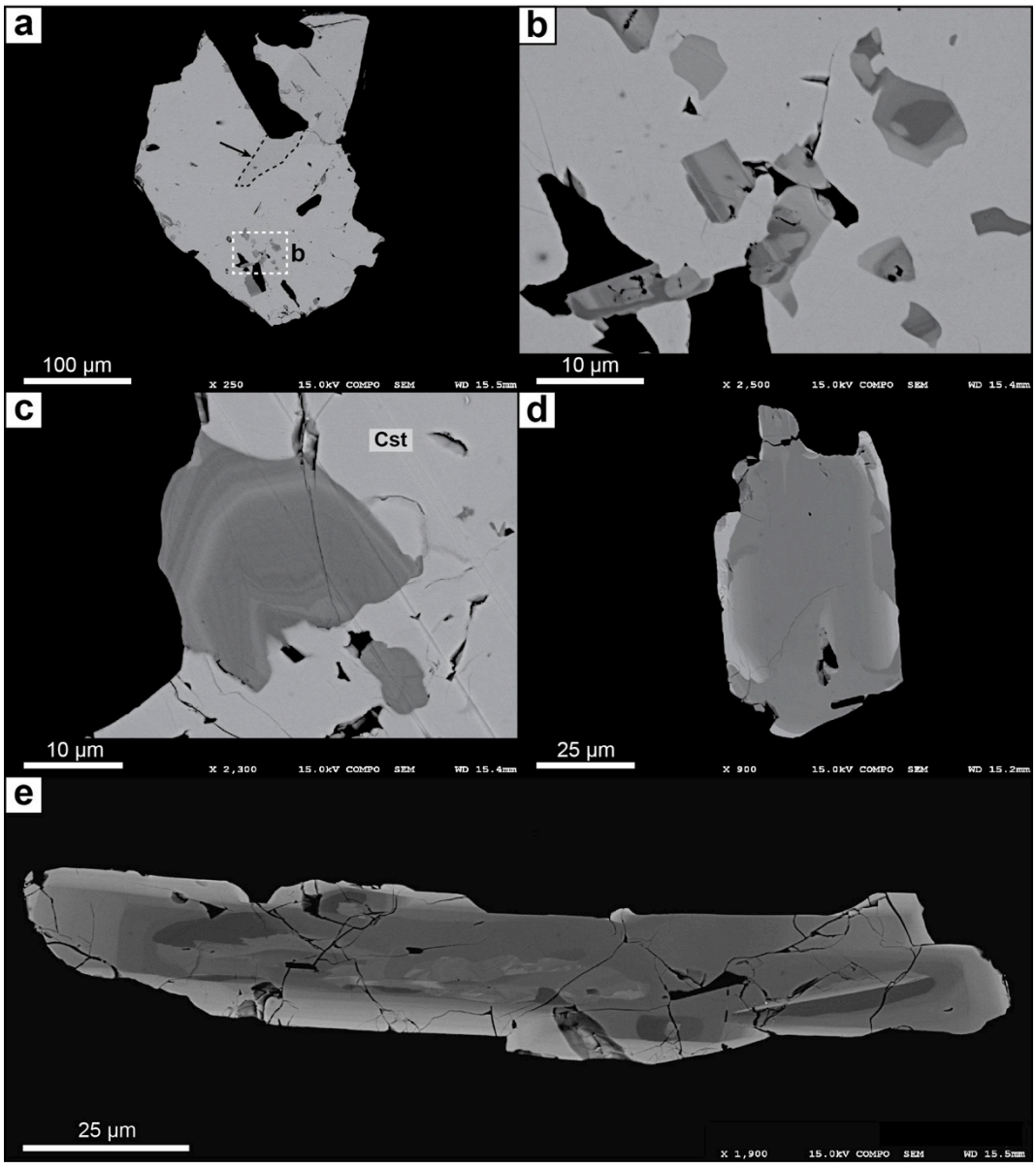

Fig. 56: BSE images of cassiterite and columbite-tantalite minerals in the rare-metal aplo-pegmatite (sample PLV-02-02). (a) Cassiterite crystal showing intra-crystalline zoning (arrow) and containing mineral inclusions of columbite-tantalite. (b) Detail view of columbite-tantalite crystals in inclusion within the cassiterite. (c) Columbite-tantalite crystal in cassiterite showing a growth zoning. (d, e) Columbite-tantalite crystals showing internal zoning composed by a dark columbite core (dark grey) surrounded by a zoned rim (medium grey) and late external tantalite overgrowths (bright grey).

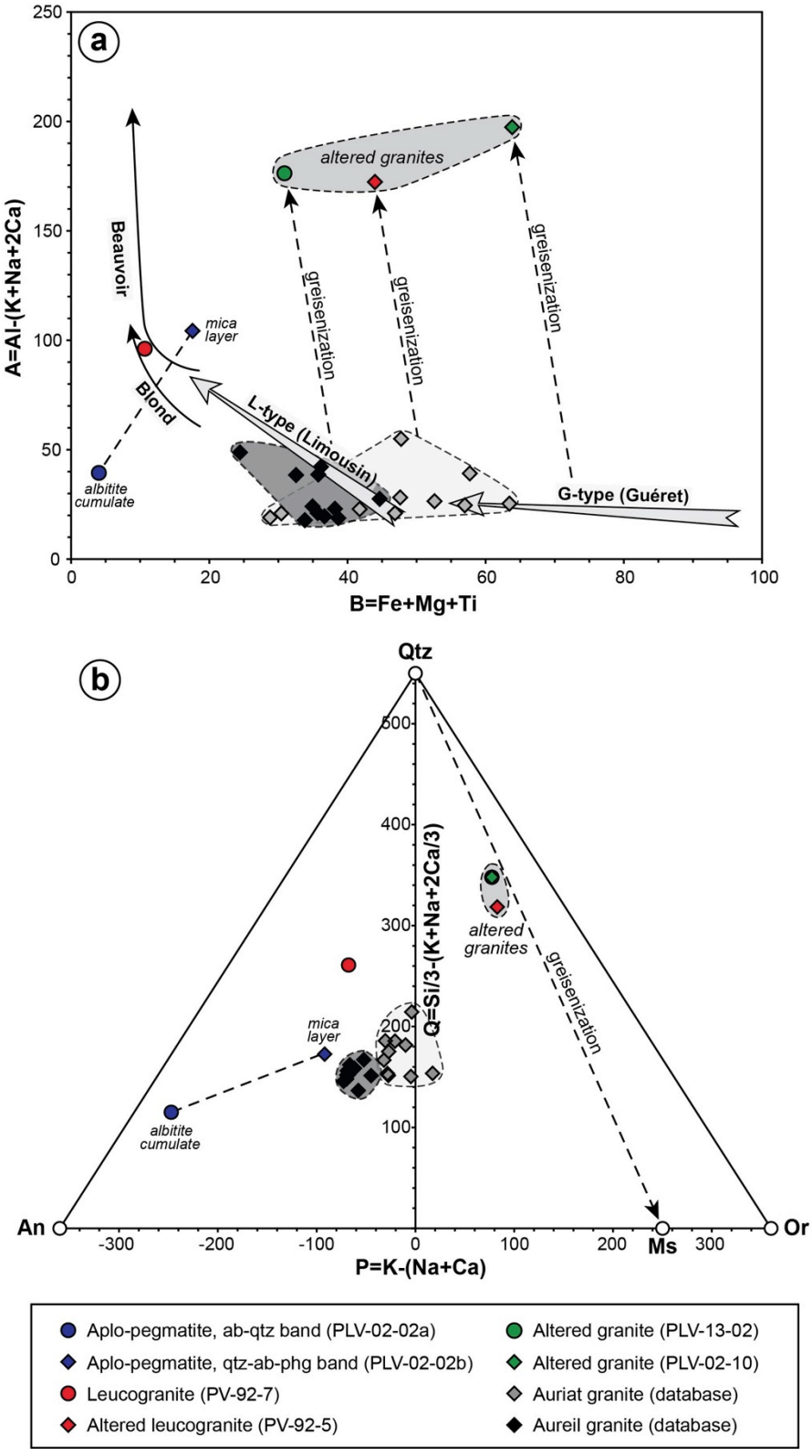

Fig. 57: Major element compositions of the granitic rocks from the Puy-les-Vignes deposit. (a) A-B diagram representing the peraluminous index A=Al-(Na+K+2Ca) as function of the differentiation index B=Fe+Mg+Ti (after Debon and Lefort, 1988). The main fractionation trends of the granitic rocks from the Limousin are shown for comparison. (b) Q-P diagram representing the quartz content Q=Si/3-(K+Na+2Ca/3) as function of the relative proportion of feldspars P=K-(Na+Ca) (after Debon and Lefort, 1988). Composition from the Auriat granite (Arniaud et al., 1984) and the Aureil granite (Artemise database) are plotted for comparison.

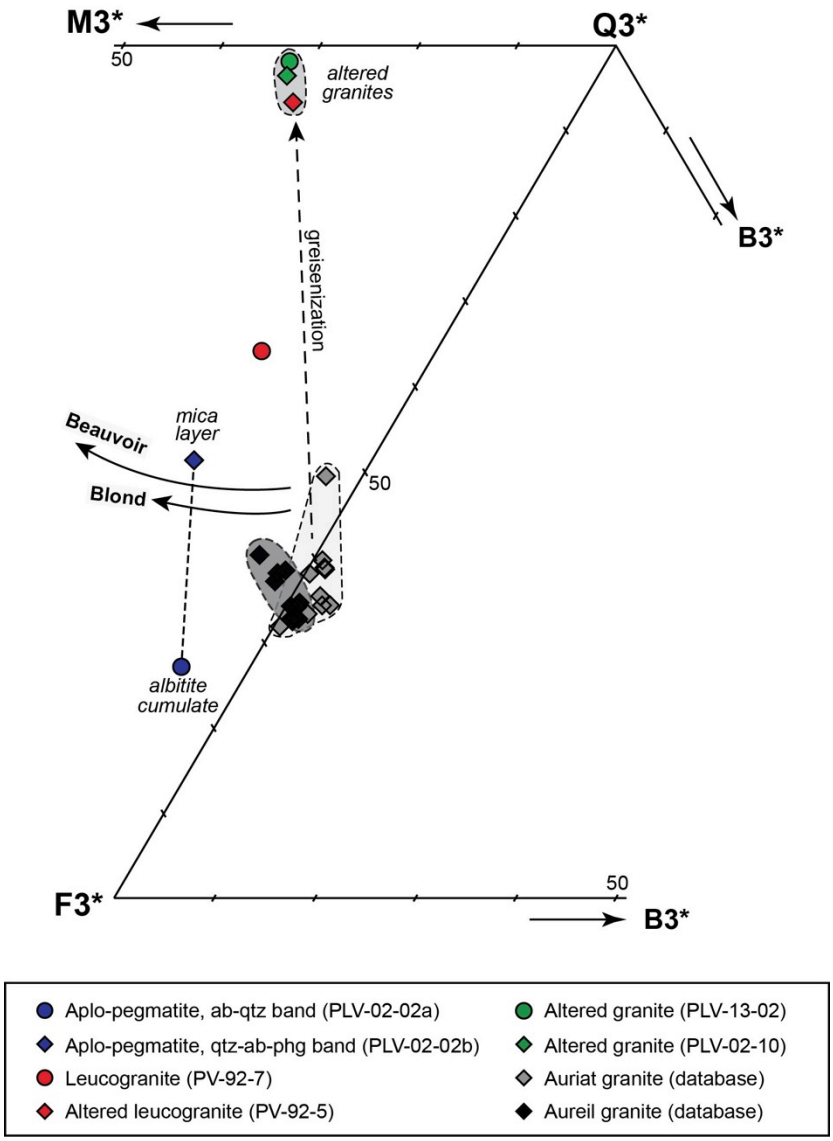

Fig. 58: Evolutionary trends of the granitic rocks from Puy-les-Vignes projected in the (QBF)3 diagram (after Debon and Lefort, 1988), where Q3=Si+7Al/2-5Ca-13(Na+K)/2, B3=-7Al/2+7Ca+7(Na+K)/2+8(Fe+Mg+Ti)/3 and F3=Al+3Ca+4(Na+K)-5(Fe+Mg+Ti)/3. The normalization of these parameters to the Q3+B3+F3 sum yield to the (Q3*B3*F3*) diagram, where Q3* represents the quartz pole, B3* the biotite pole and F3* the feldspar pole. A fourth summit M3*, symmetrical to B3* relatively to the Q3*-F3* segment and corresponding to the muscovite pole can be also projected.

6. Chemistry of the Nb-Ta-W-Ti-Sn oxide minerals

6.1. Rutile

Representative EPMA compositions of rutile are given in Table 16. The type-1 rutiles associated with the tourmalinization from the stage I (samples PLV-02-01a and PLV-02-04a) have compositions close to the ideal formula for the dark cores (96.5-99.6 wt.% TiO_2),

whereas the light rims have minor contents in Fe (up to 1.62 wt.% FeO), Sn (up to 0.55 wt.% SnO_2) and W (up to 5 wt.% WO_3). The rutiles associated within tourmalinite from a granitic clast (sample PLV-02-04a) show additionally significant concentrations in Cr (up to 2.78 wt.% Cr_2O_3). The type-2 rutiles disseminated in the quartz-wolframite veins from the stage II (samples PLV-7574a and PLV-02-13b) have similar compositions for the dark cores and light rims, but differ by external overgrowths showing high contents in Nb (up to 12 wt.% Nb_2O_5), Ta (up to 5.1 wt.% Ta_2O_5) and Fe (up to 4.8 wt.% FeO). The type-3 rutile associated within the ferberitized wolframite from the stage II (sample PLV-02-17) is characterized by elevated concentrations in Nb (up to 14.15 wt.% Nb_2O_5), Ta (up to 1.29 wt.% Ta_2O_5) and Fe (up to 4.49 wt.% FeO), with only minor amounts of W (up to 0.88 wt.% WO_3) and Sn (0.6 wt.% SnO_2). The type-4 rutiles disseminated in the arsenopyrite (sample PLV-02-28b) have high contents in Nb (up to 14.22 wt.% Nb_2O_5), Ta (up to 2.31 wt.% Ta_2O_5), W (up to 12.13 wt.% WO_3) and Cr (up to 9.28 wt.% Cr_2O_3). In the ternary diagram (Nb+Ta)-(Sn+Ti+W)-(Fe+Mn), the compositions of the type-1 and type-2 rutiles (dark cores and light rims) plot along the TiO_2 – $(Fe,Mn)WO_4$ vector involving the substitution mechanism $Ti^{4+}_{-2}Fe^{2+}_{+1}W^{6+}_{+1}$ (Fig. 59a,b). The compositions of Nb-Ta-bearing overgrowths from type-2 rutiles and the type-3 rutiles plot however along the TiO_2 – $(Fe,Mn)Nb_2O_6$ solid solution line, which implies the contribution of the exchange vector $Ti^{4+}_{-3}Fe^{2+}_{+1}(Nb,Ta)^{5+}_{+2}$ (Fig. 59b,c). Finally, the compositions of type-4 rutiles show a different trend through the TiO_2 – $FeNbO_4$ solid solution, thus involving the participation of the $Ti^{4+}_{-2}(Fe,Cr)^{3+}_{+1}(Nb,Ta)^{5+}_{+1}$ exchange vector (Černý et al., 2000), plus the previous substitution mechanisms in order to explain the incorporation of W^{6+}, Nb^{5+} and Ta^{5+} through the observed trend (Fig. 59d). Trace elements compositions determined for type-1 and type-2 rutile (Table 17) show higher contents in W (up to 5.2%), Fe (up to 11.7%) and Sc (up to 150 ppm) for type-2 rutiles associated with the main W stage. Zr-in-rutile temperatures were calculated based on the thermometer from Watson et al. (2006) for rutiles coexisting with zircon and quartz, which concern only type-1 and type-2 rutiles. The calculated temperatures show a range from 472°C to 598°C, with a mode around 540-560°C (Table 17, Fig. 60). The temperatures appear similar within the incertitude between the two generations of rutiles, with slightly lower temperatures for the type-1 rutiles from sample PLV-02-01a.

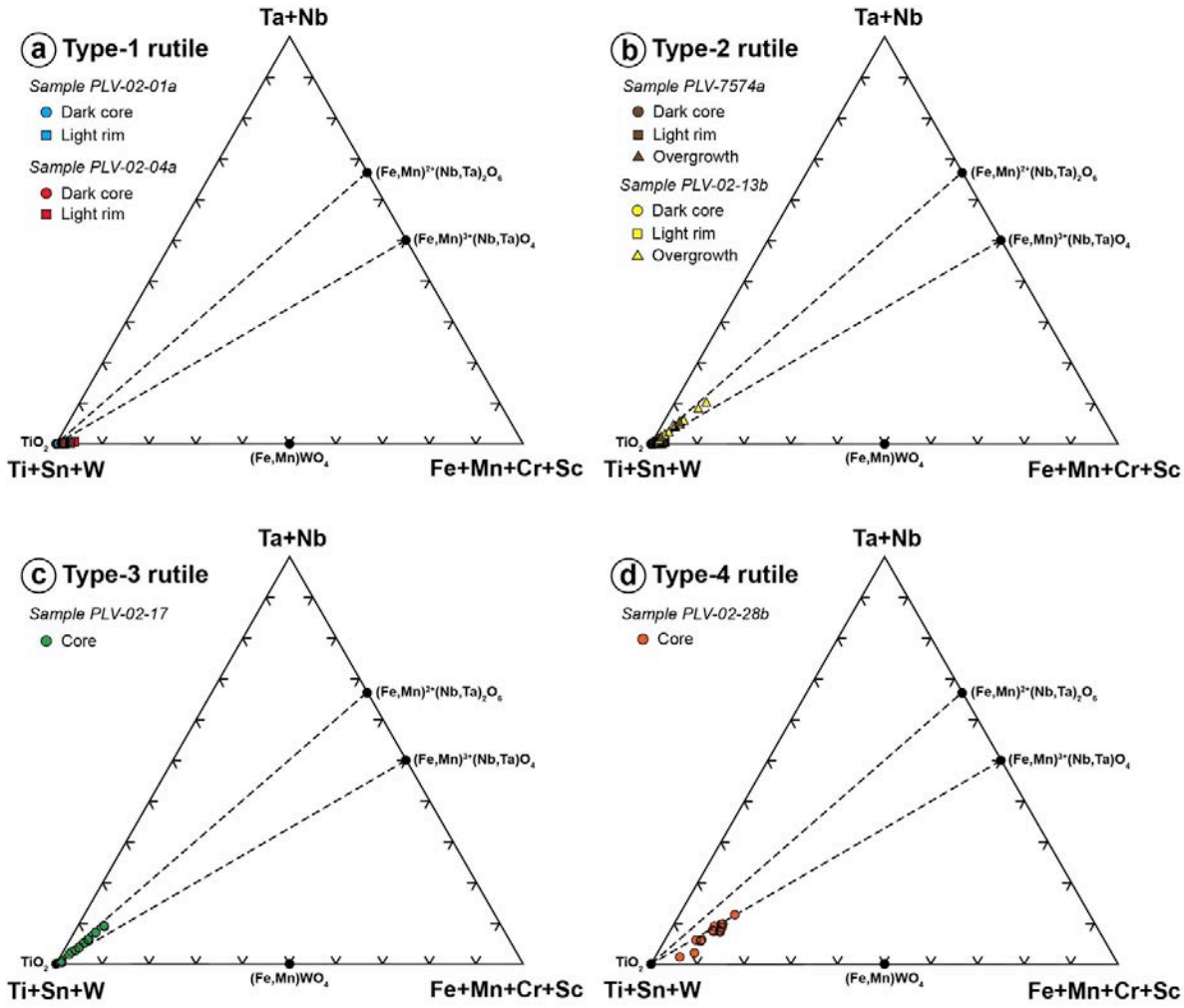

Fig. 59: Compositions of rutile from Puy-les-Vignes in the ternary diagram (Nb+Ta)-(Sn+Ti+W)-(Fe+Mn). Data are given in Table 16.

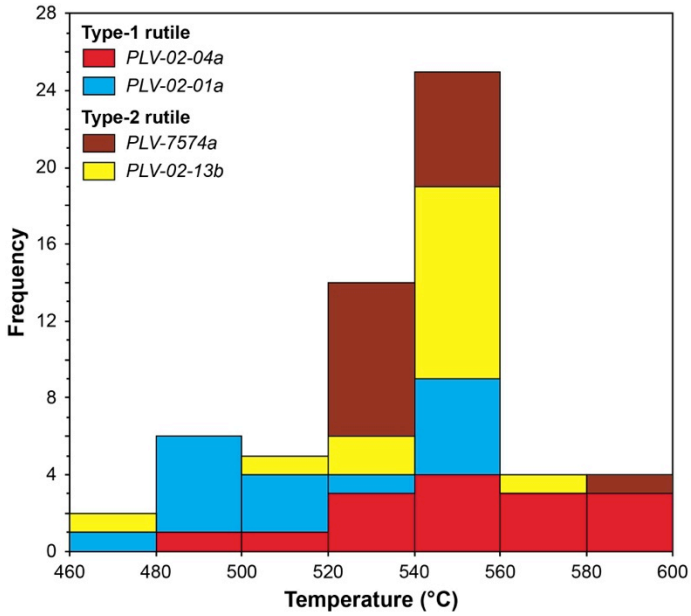

Fig. 60: Frequency histogram for Zr-in-rutile temperatures calculated using the thermometer defined by Watson et al. (2006). Data are given in Table 17.

6.2. Cassiterite

Compositions for cassiterite are given in Table 18. Cassiterite from a quartz-wolframite vein (sample PV-2) is homogeneous and do not show evidence of internal zoning. The chemical composition is close to the ideal formula with SnO_2 content ranging from 97.22 to 100 wt.%, with minor contents in W (up to 1.71 wt.% WO_3), Fe (up to 1.46 wt.% FeO) and trace contents in Nb (up to 0.71 wt.% Nb_2O_5), Ta (up to 0.33 wt.% Ta_2O_5) and Ti (bdl). Cassiterite from the rare-metal aplo-pegmatite (sample PLV-02-02) has conversely higher content in Nb (up to 2.82 wt.% Nb_2O_5), Ti (up to 1.58 wt.% TiO_2) and lower content in Fe (up to 0.69 wt.% FeO) and W (bdl). No significant compositional differences have been found between the lighter and darker zones observed on the contrasted BSE images. In the ternary diagram (Nb+Ta)-(Sn+Ti+W)-(Fe+Mn) (Fig. 61), the data for cassiterite from the quartz-wolframite vein plot along the vector SnO_2 - $FeWO_4$ indicating a substitution mechanism according to $(Sn,Ti)^{4+}_{-2}(Fe,Mn)^{2+}_{+1}W^{6+}_{+1}$, whereas cassiterite data from the rare-metal aplo-pegmatite plot along the vector SnO_2 - $FeNb_2O_6$ according to the substitution mechanism $(Sn,Ti)^{4+}_{-3}(Fe,Mn)^{2+}_{+1}(Nb,Ta)^{5+}_{+2}$ (Möller et al., 1988).

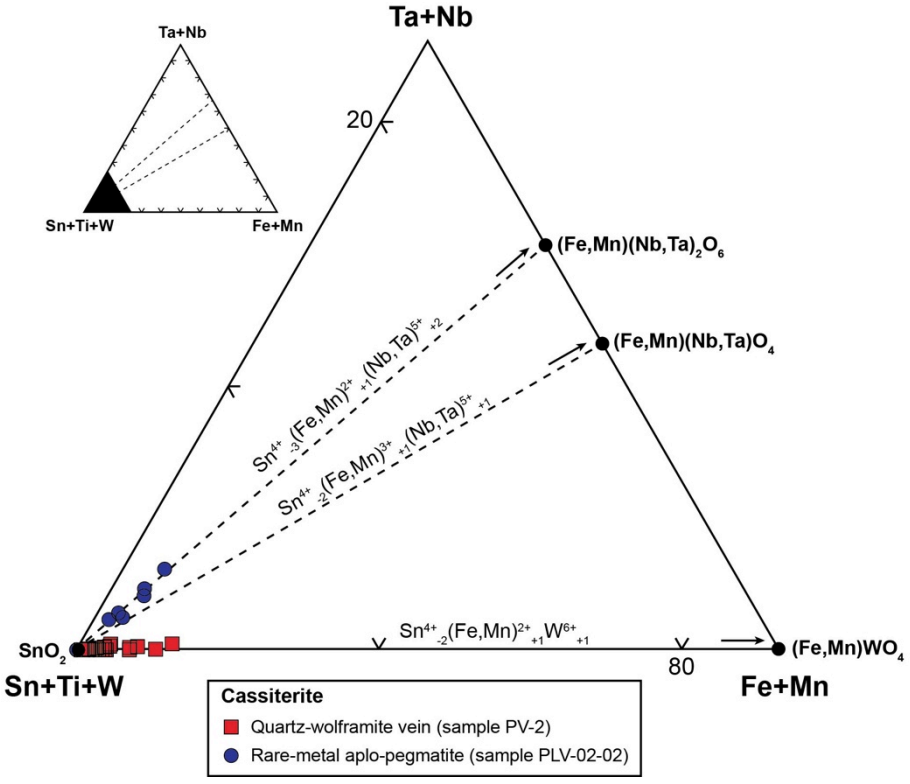

Fig. 61: Compositions of cassiterite from Puy-les-Vignes in the ternary diagram (Nb+Ta)-(Sn+Ti+W)-(Fe+Mn). Data are given in Table 18.

6.3. Wolframoixiolite

The wolframoixiolites associated with the quartz-wolframite-scheelite veins (samples PV-5a and PLV-02-13b) are composed by a core with an internal zoning composed of dark and light zones in BSE imagery, surrounded by an invasive overgrowth. The dark cores have in average higher contents in Nb (60.5-66.6 wt.% Nb_2O_5), Fe (13.6-17.1 wt.% FeO), Mn (2.5-4.6 wt.% MnO) and lower contents in W (7-13.7 wt.% WO_3) and Ti (2.4-9.8 wt.% TiO_2) compared to the light cores, which have reversely lower contents in Nb (52.7-64.5 wt.% Nb_2O_5), Fe (13.8-15.2 wt.% FeO), Mn (2.7-3.9 wt.% MnO) and higher contents in W (8.7-23.1 wt.% WO_3) and Ti (3.2-8.5 wt.% TiO_2) (Table 19). The external overgrowth is characterized by low contents in Nb (40.4-49.7 wt.% Nb_2O_5) and high contents in W (21.9-33.4 wt.% WO_3) (Table 19). In the ternary diagram (Nb+Ta)-(Sn+Ti+W)-(Fe+Mn) (Fig. 62), the composition of wolframoixiolite fall along a line parallel to the vector $FeNb_2O_6 – FeWO_4$ corresponding to the coupled substitution $(Nb,Ta)^{5+}_{-4}(Fe,Mn)^{2+}_{+1}W^{6+}_{+3}$ (Černý et al., 2007). Some of the data points are also aligned along the $FeNb_2O_6 – TiO_2$ vector involving the substitution mechanism $(Fe,Mn)^{2+}_{-1}(Nb,Ta)^{5+}_{-2}(Ti,Sn)^{4+}_{+3}$ (Černý et al., 1998). A third solid solution $FeNb_2O_6 – FeNbO_4$ is necessary to explain the observed trend through the exchange vector $(Nb,Ta)^{5+}_{-1}(Fe,Mn)^{2+}_{-2}(Fe,Sc)^{3+}_{+3}$ (Černý et al., 2007).

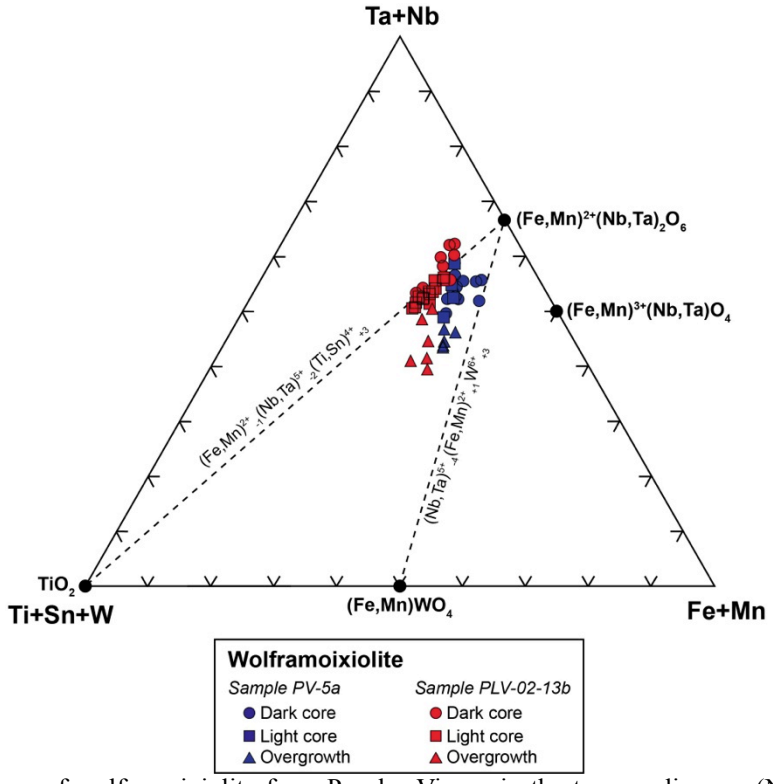

Fig. 62: Compositions of wolframoixiolite from Puy-les-Vignes in the ternary diagram (Nb+Ta)-(Sn+Ti+W)-(Fe+Mn). Data are given in Table 19.

6.4. Columbite-tantalite

Representative chemical compositions of columbite-tantalite minerals from the rare-metal aplo-pegmatite (sample PLV-02-02) are given in Table 20. The dark cores have the higher contents in Fe (up to 11.58 wt.% FeO) and Nb (up to 65.63 wt.% Nb_2O_5) and the lower contents in Mn (up to 9.20 wt.% MnO) and Ta (up to 19.65 wt.% Ta_2O_5), whereas the external overgrowths have conversely the higher contents in Ta (up to 48.05 wt.% Ta_2O_5) and Mn (up to 10.19 wt.% MnO) and the lower contents in Fe (up to 7.68 wt.% FeO) and Nb (up to 36.73 wt.% Nb_2O_5). The cortex–I and –II have intermediate compositions in Nb (39.57-62.54 wt.% Nb_2O_5), Ta (10.05-37.92 wt.% Ta_2O_5), Fe (6.69-11.63 wt.% FeO) and Mn (8.45-13.19 wt.% MnO), but are characterized by high contents in Sn (up to 2.74 wt.% SnO_2), W (up to 3.5 wt.% WO_3) and Ti (up to 5.38 wt.% TiO_2). The electrostatic charge balance calculated assuming $Fe_{tot}=Fe^{2+}$ is respected indicating that Fe is only present as Fe^{2+}.

In the columbite quadrilateral (Fig. 63a), the composition of the crystals vary from ferrocolumbite for the dark cores to manganotantalite for the external overgrowth with Mn/(Mn+Fe) and Ta/(Ta+Nb) ratios ranging from 0.42 to 0.67 and 0.07 to 0.51, respectively. This geochemical evolution from the core to the rim is typical of the magmatic fractionation trend observed in columbite-tantalite from rare-metal granites and pegmatites (e.g., Černý et al., 1986; Belkasmi et al., 2000; Van Lichtervelde et al., 2007; René and Škoda, 2011) and reflects the higher solubility of the columbite relatively to the tantalite in peraluminous melts (Linnen and Cuney, 2005). In the ternary diagram (Nb+Ta)-(Sn+Ti+W)-(Fe+Mn) (Fig. 63b), the data fall along the vector $FeNb_2O_6$ – $FeTiWO_6$ indicating the participation of the substitution mechanism $(Nb,Ta)^{5+}_{-2}(Ti,Sn)^{4+}_{+1}W^{6+}_{+1}$ (Johan and Johan, 1994), which is also supported by the negative correlation between (Nb+Ta) vs (Ti+Sn+W) (Fig. 64a). The incorporation of W^{6+} through the solid solution $FeNb_2O_6$ – $FeWO_4$ involving the substitution mechanism $(Nb,Ta)^{5+}_{-4}(Fe,Mn)^{2+}_{+1}W^{6+}_{+3}$ is negated by the poor correlation between (Nb+Ta) vs (Fe+Mn+W) (not shown). The entrance of Ti^{4+} and Sn^{4+} can be explained by the solid solution $FeNb_2O_6$ – TiO_2 according to the substitution mechanism $(Fe,Mn)^{2+}_{-1}(Nb,Ta)^{5+}_{-2}(Ti,Sn)^{4+}_{+3}$ (Fig. 64b). These exchange vectors are simultaneous with the isovalent substitutions $Nb^{5+}_{-1}Ta^{5+}_{+1}$ and $Fe^{2+}_{-1}Mn^{2+}_{+1}$ (Fig. 64c,d).

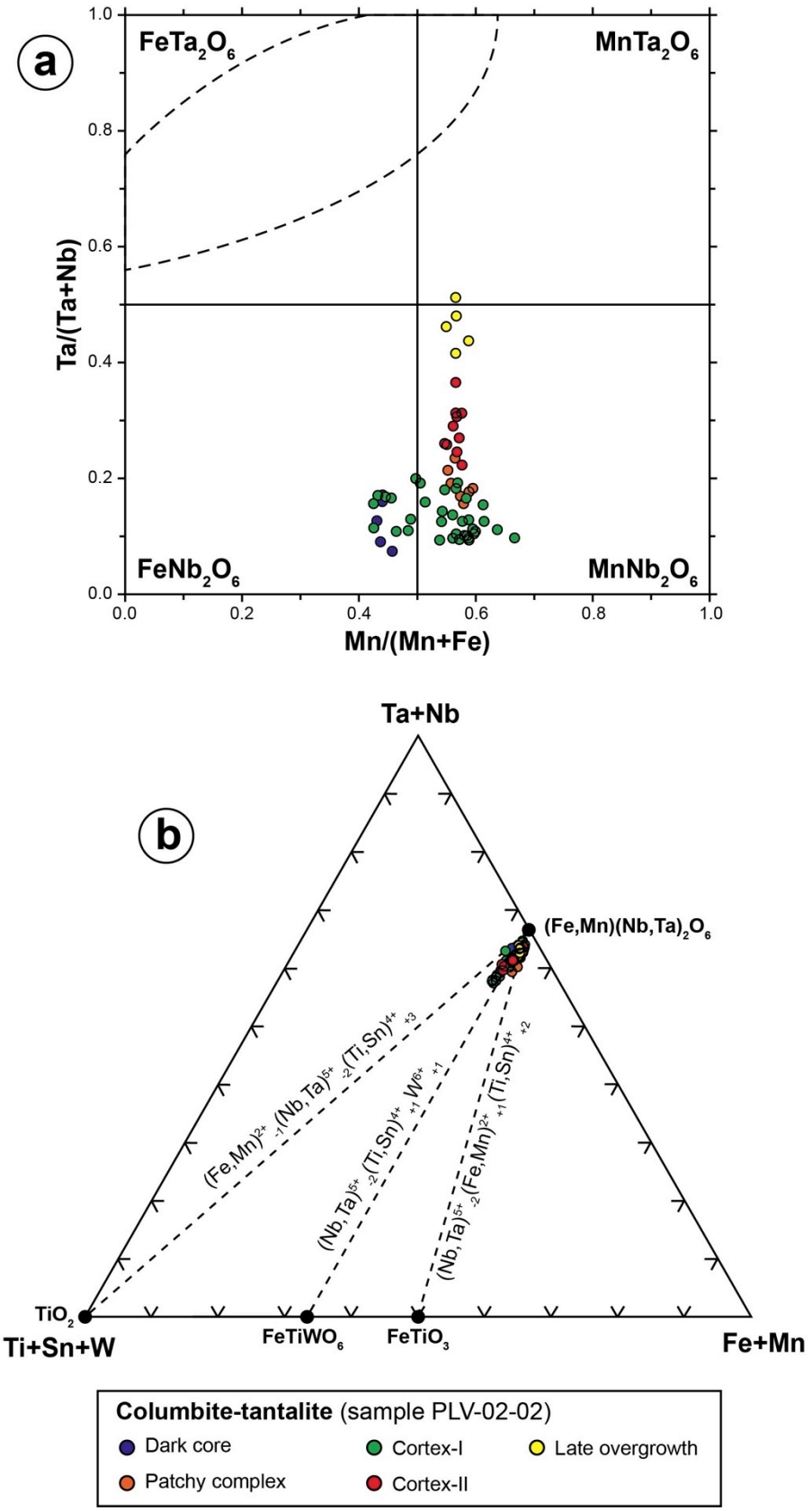

Fig. 63: Compositions of the columbite-tantalite minerals from the rare-metal aplo-pegmatite (sample PLV-02-02) in the columbite quadrilateral diagram (a) and in the ternary diagram (Nb+Ta)-(Sn+Ti+W)-(Fe+Mn) (b). The dash lines corresponds to the compositional gap of Černý et al. (1992). Data are given in Table 20.

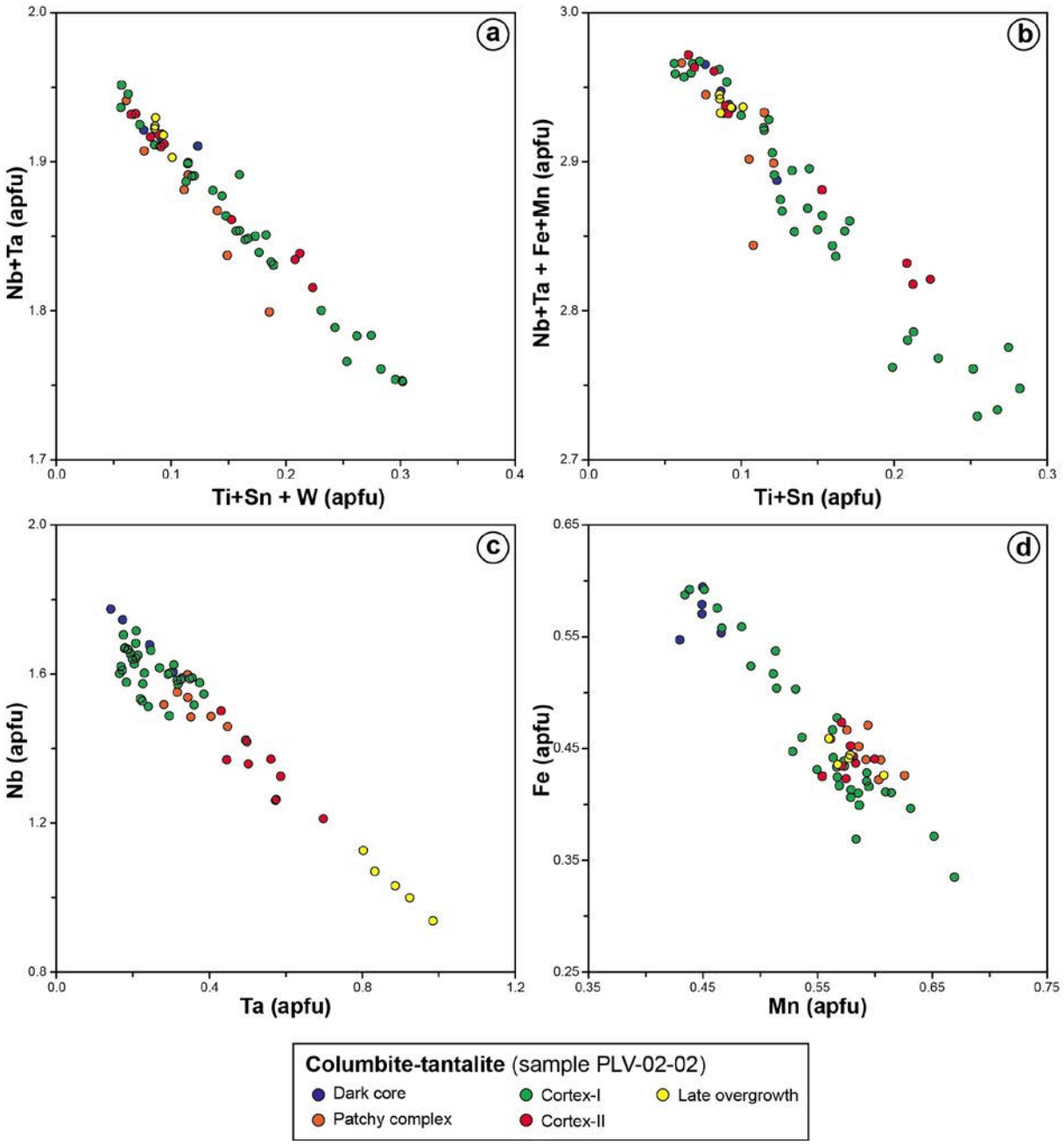

Fig. 64: Main chemical variations and substitution vectors for the columbite-tantalite from the rare-metal aplo-pegmatite (sample PLV-02-02). Data are given in Table 20.

7. Geochronology

7.1. U-Pb dating of rutile

Four samples of rutile from different paragenetic stages have been selected for the U-Pb dating. The rutile crystals were previously analysed by SEM and EMPA in order to select

areas, which are relatively homogeneous in composition and do not show textural evidence of exsolution, micro-inclusions or alteration. In total 59 analyses were carried out on 10 rutile grains. Analyses showing anomalous isotopic ratios have not been included in the final age calculation. The rutile samples are characterized by variable contents of U ranging from 0.51 to 32.69 ppm and very low Pb contents ranging from 0.001 to 0.67 ppm. They show variable isotopic compositions with $^{238}U/^{206}Pb$ values ranging from 0.12 to 18.63 and $^{207}Pb/^{206}Pb$ values ranging from 0.09 to 0.85 (Table 21). All the rutile data are discordant in the Tera-Wasserburg diagram, which is a common feature for hydrothermal rutiles (e.g., Wong et al., 1991; Davis et al., 1994).

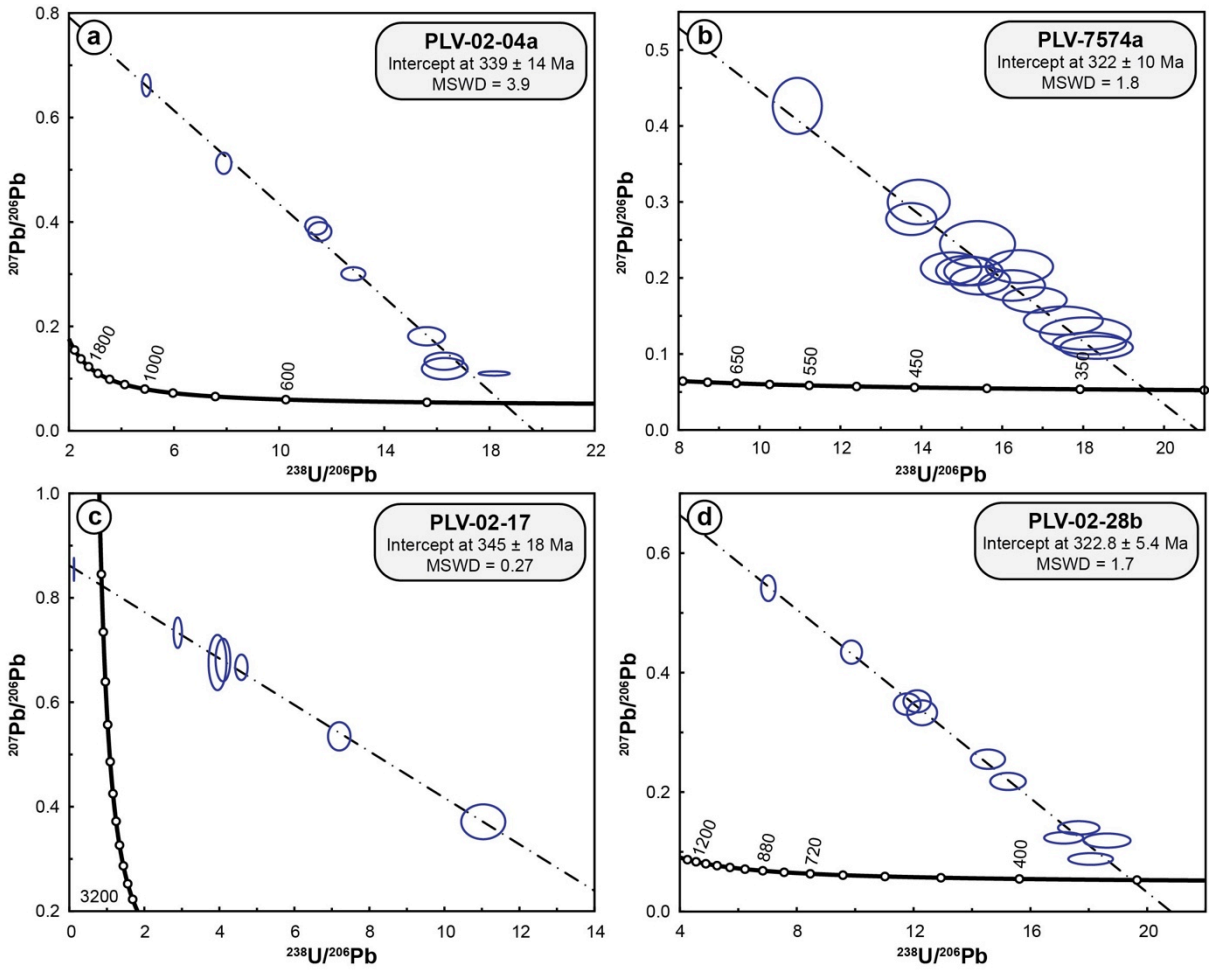

Fig. 65: Tera-Wasserburg diagrams for rutiles from the Puy-les-Vignes deposit. (a) Type-1 rutile (sample PLV-02-04a); (b) Type-2 rutile (sample PLV-7574a); (c) Type-3 rutile (sample PLV-02-17); (d) Type-4 rutile (sample PLV-02-28b). Error ellipses are plotted at 2σ level. U-Pb isotopic data are given in Table 21.

7.1.1. Type-1 rutile (sample PLV-02-04a)

Rutile from sample PLV-02-04a is associated with the tourmalinite (type-1 rutile) and formed during the early hydrothermal alteration (stage I) of the breccia pipe. The rutile has variable U and Pb contents ranging from 1.42 to 32.69 ppm and 0.001 to 0.042 ppm, respectively (Table 21). In the Tera-Wasserburg diagram, regression line of the data (n=9) gives a lower intercept age of 339 ± 14 Ma (2σ, MSWD=3.9; Fig. 65a).

7.1.2. Type-2 rutile (sample PLV-7574a)

Rutile from sample PLV-7574a are found within the quartz-wolframite vein (type-2 rutile) and were likely formed during the quartz deposition (stage II). The U and Pb contents range respectively from 1.39 to 2.75 ppm and 0.001 to 0.004 ppm. The rutiles have relatively high radiogenic composition with $^{238}U/^{206}Pb$ values ranging from 10.93 to 18.33 and $^{238}U/^{206}Pb$ values from 0.11 to 0.43 (Table 21). The data (n=15) define a discordia line with a lower intercept age of 322 ± 10 Ma (2σ, MSWD=1.8; Fig. 65b).

7.1.3. Type-3 rutile (sample PLV-02-17)

Rutiles from sample PLV-02-17 are associated within the ferberite-1 (type-3 rutile) and coeval with the main W mineralization (stage II). The rutiles contain low U and Pb contents ranging from 0.51 to 2.18 ppm and 0.003 to 0.67 ppm, respectively. They have low radiogenic composition with $^{238}U/^{206}Pb$ values from 0.12 to 11.04 (Table 7). Linear regression of the data (n=7) defines a discordia with a lower intercept age of 345 ± 18 Ma (2σ, MSWD=0.27; Fig. 65c). The large uncertainty of this age is mainly due to the low radiogenic Pb content of the rutile, which yields an apparent old age.

7.1.4. Type-4 rutile (sample PLV-02-28b)

Rutile from sample PLV-02-28b (type-4 rutile) is associated with the arsenopyrite (stage II) and is interpreted to represent a co-crystallized phase. Rutiles have low U and Pb contents ranging from 5.25 to 8.64 ppm and 0.005 to 0.034 ppm respectively (Table 21). In the Tera-Wasserburg diagram regression line of the data (n=11) yields to a lower intercept age of 322.8 ± 5.4 Ma (2σ, MSWD=1.7; Fig. 65d).

7.2. ^{40}Ar-^{39}Ar dating of micas and adularia

Seven samples of micas and one sample of adularia were selected from different paragenetic stages for ^{40}Ar-^{39}Ar dating. The selected minerals were preliminary analysed by SEM in order to spot homogeneous areas devoid of internal zoning or micro-inclusions. The results of the $^{40}Ar/^{39}Ar$ analyses are shown in Fig. 66 and are summarized in Table 22. Errors associated with reported ages are quoted at the 1σ level.

7.2.1. Muscovite from greisenized gneiss (sample PLV-02-01a)

Muscovites from sample PLV-02-01a correspond to large laths, which are associated with the neoformed quartz in the greisenized gneiss. The calculated apparent ages range from 308.2 to 326.3 Ma. Integration of the concordant data (n=5) yields an age of 321.1 ± 2.8 Ma (1σ, MSWD=0.67; Fig. 66a).

7.2.2. Muscovite from greisenized granite (sample PLV-02-10)

Muscovites from sample PLV-02-10 correspond to disseminated laths in the greisenized granite, interpreted as formed during the early hydrothermal alteration. The apparent ages fall between 304.1 and 337.7 Ma. The integrated age calculated on concordant data (n=5) gives 327.5 ± 2.4 Ma (1σ, MSWD=1.12; Fig. 66b).

7.2.3. Muscovite from quartz-wolframite veins (sample PV1)

Muscovites from sample PV1 correspond to large crystals, which are disseminated within the quartz of the mineralized veins. The apparent ages range from 310.3 to 338.4 Ma. The oldest ages likely correspond to two-component mixing with interstitial chlorites. Integration of the concordant data (n=6) yields an age of 320 ± 2.7 Ma (1σ, MSWD=1.10; Fig. 66c).

7.2.4. Muscovite selvage from quartz vein (sample PV2c)

Sample PV2c correspond to a quartz vein with selvage muscovite, which is lately fractured by chlorite. The calculated apparent ages range from 326.4 to 342.4 Ma. An age of

335 ± 3 Ma (1σ, MSWD=0.60; Fig. 66d) was calculated from the concordant data (n=6). This old age may actually result from the mixing with interstitial chlorite sampled during the laser ablation.

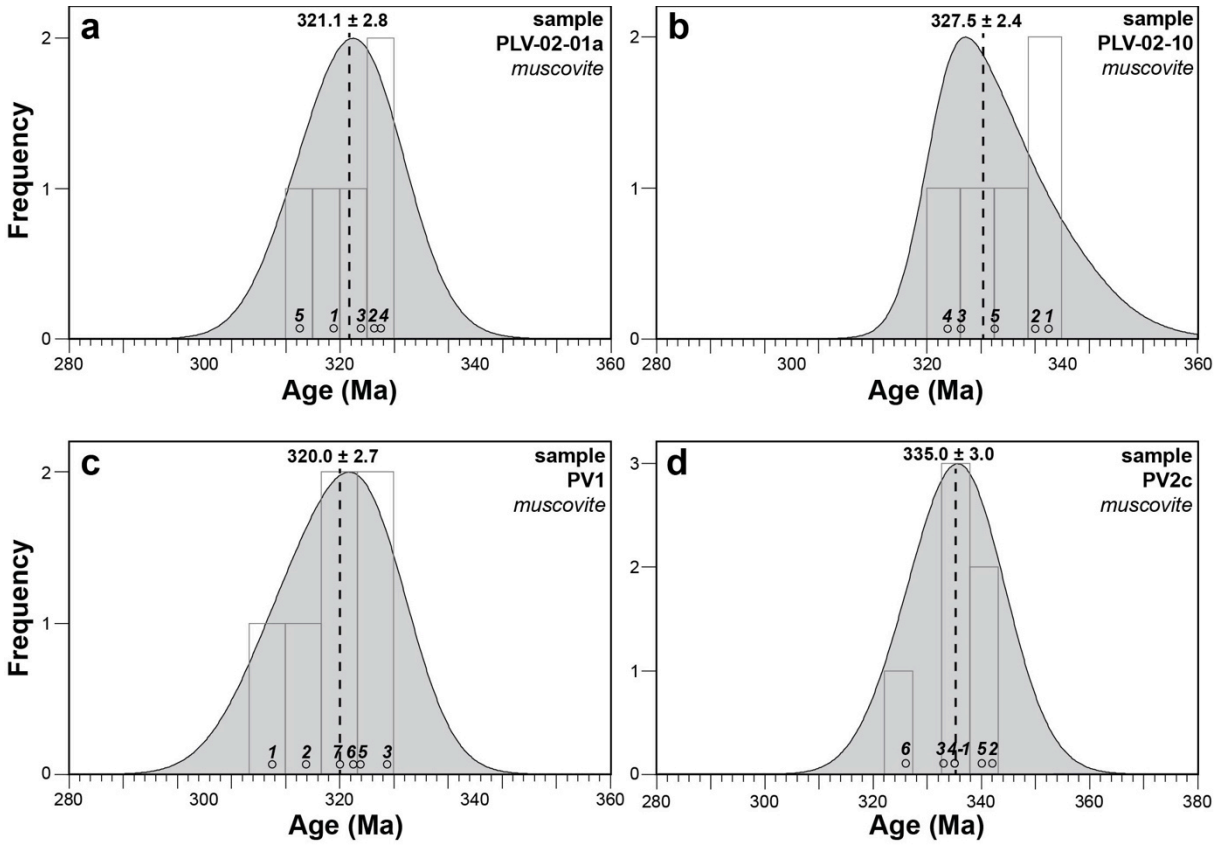

Fig. 66: $^{40}Ar/^{39}Ar$ ages obtained on micas and adularia from the Puy-les-Vignes deposit. $^{40}Ar/^{39}Ar$ isotopic data are given in Table 22.

7.2.5. Muscovite from the rare-metal aplo-pegmatite (sample PLV-02-02b)

Muscovites in the rare-metal aplo-pegmatite (sample PLV-02-02b) gave apparent ages comprised between 292.7 and 323.4 Ma. Integration of the concordant data (n=6) yields an age of 314 ± 2.6 Ma (1σ, MSWD=1.28; Fig. 66e), interpreted as the crystallization age of muscovites.

7.2.6. Muscovite from the leucogranite (sample PV-92-7)

Muscovites from the leucogranite (sample PV-92-7) gives apparent ages ranging from 306.3 to 335.8 Ma. Almost all the data are concordant (n=11), yielding to an age of 324.7 ± 2.1 (1σ, MSWD=1.10; Fig. 66f).

7.2.7. Biotite from lamprophyre (sample PV-92-17)

A few crystals of biotite disseminated within a lamprophyre sample (PV-92-17) were analysed. The obtained apparent ages range from 324.8 to 347.4 Ma and are concordant within uncertainty. An integrated age of the data (n=3) yields 331.1 ± 7 Ma (1σ, MSWD=0.74; Fig. 66g), interpreted as the crystallization age of the lamprophyre.

7.2.8. Adularia from late hydrothermal breccia (sample PLV-02-13b)

Adularia forming the matrix of the late hydrothermal crackle-breccia (stage IV) was analysed. It gave apparent ages comprised between 296.3 and 309.9 Ma. Integration of the concordant data (n=6) yields an age of 301.3 ± 1.5 Ma (1σ, MSWD=2.02; Fig. 66h), corresponding to the youngest age obtained in this study.

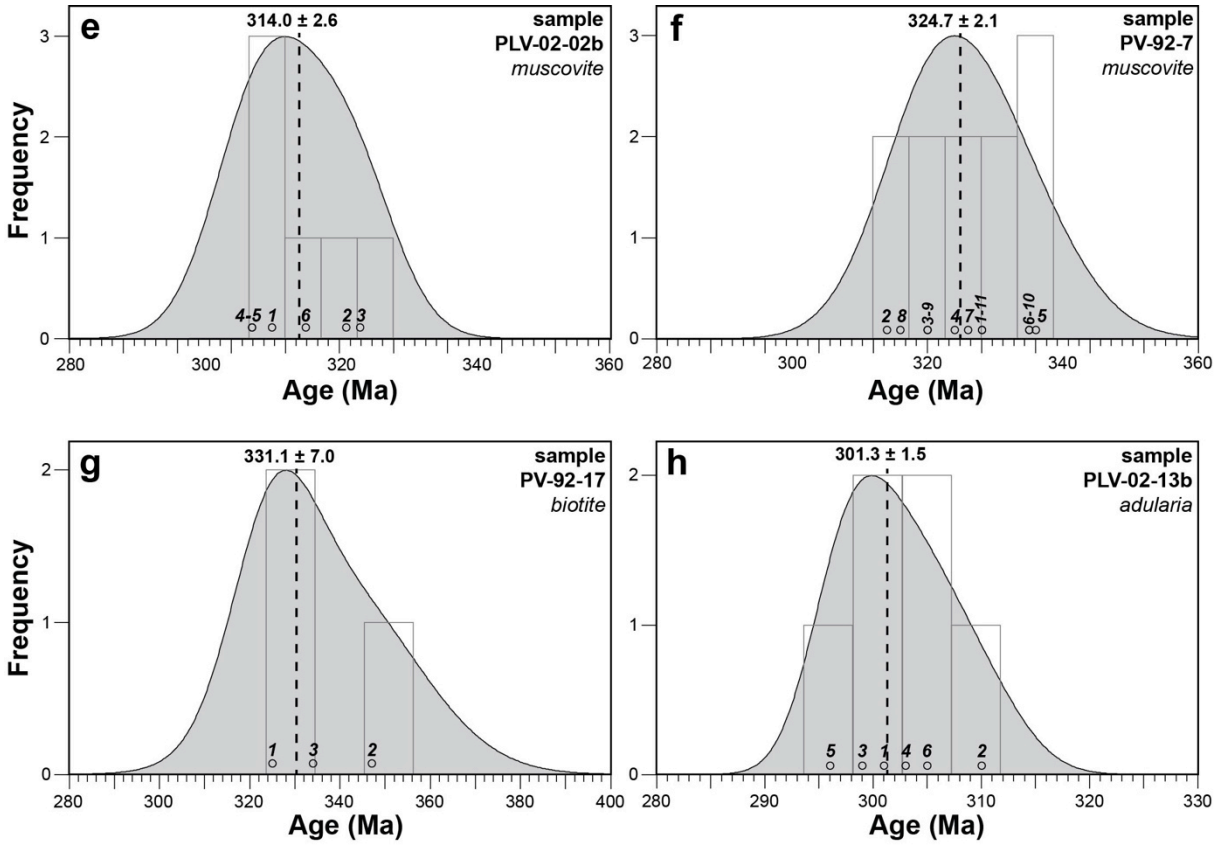

Fig. 66: Continued.

8. Discussion

8.1. Timing of the magmatic and hydrothermal episodes in the Puy-les-Vignes deposit

The detailed paragenetic sequence combined with the isotopic dating of the different stages allows to propose a chronology of the successive magmatic and hydrothermal events in the Puy-les-Vignes deposit. A synthesis of the geochronological data is given in Fig. 67. The earliest magmatic event recorded at Puy-les-Vignes is related to the intrusion of a lamprophyre dyke dated at 331.1 ± 14 Ma (2σ) on biotite. Although its relative large uncertainty, the lower limit of this age can be constrained by the age of the leucogranite dyke, dated at 324.7 ± 4.2 Ma (2σ), which is known to cut the lamprophyre. Considering this relative chronology, an interval age of ca. 345-330 Ma may be proposed for the emplacement of the lamprophyre. The age of the leucogranite is consistent with the age of the St-Sylvestre leucogranitic complex dated at 324 ± 4 Ma (U-Pb on monazite and zircon; Holliger et al., 1986), which is also compatible with the whole-rock geochemical composition typical of an evolved granite (see 5.2.2). The U-Pb age obtained on a rutile associated with the selvage tourmalinite at 339 ± 14 Ma (2σ), combined with the Ar-Ar ages on muscovites from greisenized gneiss and granite clasts, respectively at 321.1 ± 5.6 Ma and 327.5 ± 4.8 Ma (2σ), allows to constrain the early hydrothermal alteration episode at ca. 327-325 Ma. This age falls in the same temporal interval than the emplacement of the leucogranite dyke and may thus indicates that the greisenization alteration resulted from the interaction of magmatic fluids derived from an evolved granite at depth. The age of the main brecciation event, responsible for the formation of the breccia pipe, can be constrained by the U-Pb age obtained on a W-bearing rutile preceding the wolframite at 322 ± 10 Ma (2σ) and by the Ar-Ar ages on an intra-quartz muscovite dated at 320 ± 5.4 Ma (2σ) and the one obtained by Cuney et al. (2002) at 323.4 ± 1.8 Ma (2σ). Interpolation of these ages yields a temporal interval of ca. 323-321 Ma for the main brecciation event. U-Pb dating of the wolframite from Puy-les-Vignes (see Chapter 1) yielded an age of 317.7 ± 0.7 Ma (2σ), allowing to constrain very precisely the W mineralization episode. The U-Pb age of 322.8 ± 5.4 Ma (2σ) obtained on a Cr-Nb-W-rutile within the arsenopyrite appears however problematic since the arsenopyrite formed clearly after the wolframite during a distinct hydrothermal episode. The lower limit of this age is compatible with the U-Pb age of wolframite, which would indicate that the arsenopyrite episode is relatively close in time, less than 1 Ma, than the W event. Another possible interpretation is that the dated rutile does not represent a co-crystallized mineral with

the arsenopyrite, but was inherited from the main hydrothermal stage at ca. 323-321 Ma. The sample of rare-metal aplo-pegmatite yielded an Ar-Ar age on muscovite of 314 ± 5.2 Ma (2σ), which is within the same temporal interval of 315-310 Ma than the other rare-metal granites and pegmatites known regionally in the Limousin area (Cuney et al., 2002; Melleton et al., 2015). Finally, the Ar-Ar age of 301.3 ± 3 Ma (2σ) on adularia from the late hydrothermal crackle-breccia (stage IV) represents the youngest age obtained in this study and corresponds temporally to the age interval of the mesothermal gold deposits in the FMC (Bouchot et al., 2000, 2005; Boiron et al., 2003).

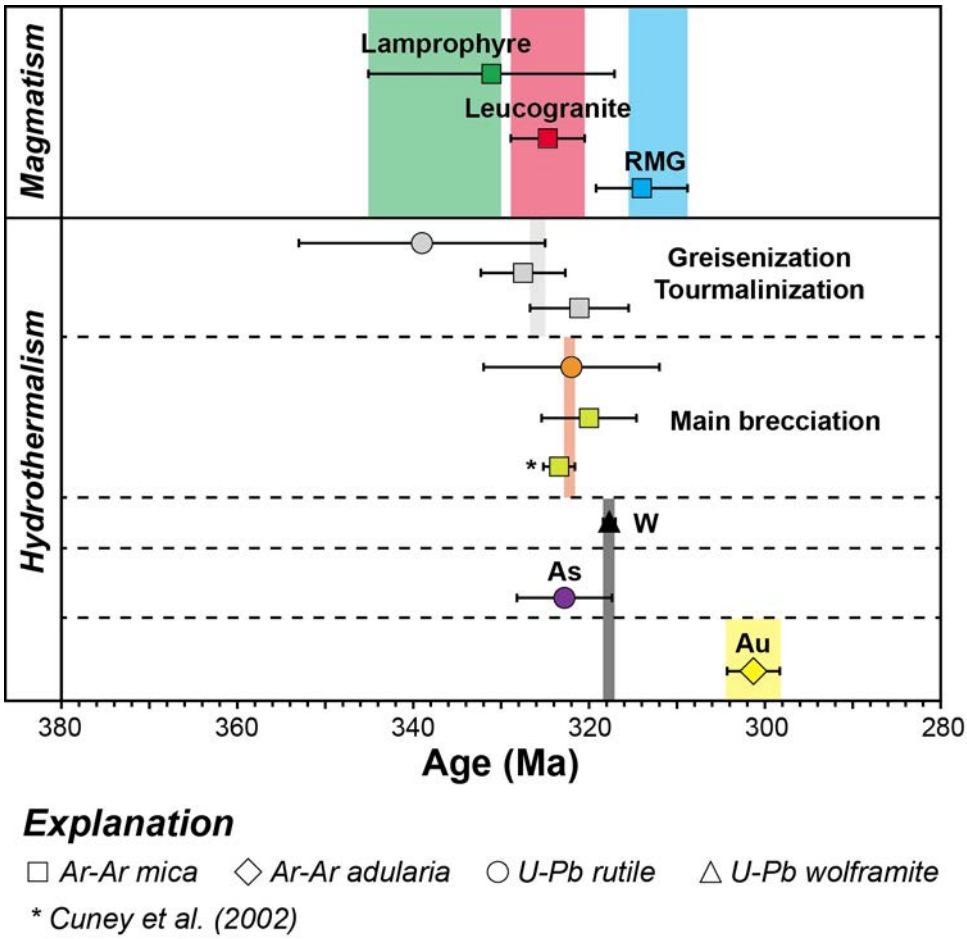

Fig. 67: Synthesis of the geochronological ages obtained for the Puy-les-Vignes deposit. Errors associated with reported ages are quoted at the 2σ level.

8.2. Relationships with the regional magmatic episodes in the Limousin area

The previous geochronological results indicate that the Puy-les-Vignes deposit results from a multistage history involving successive hydrothermal episodes during a time lapse of at least 25 Ma, between 325 Ma (Namurian) and 300 Ma (Stephanian).

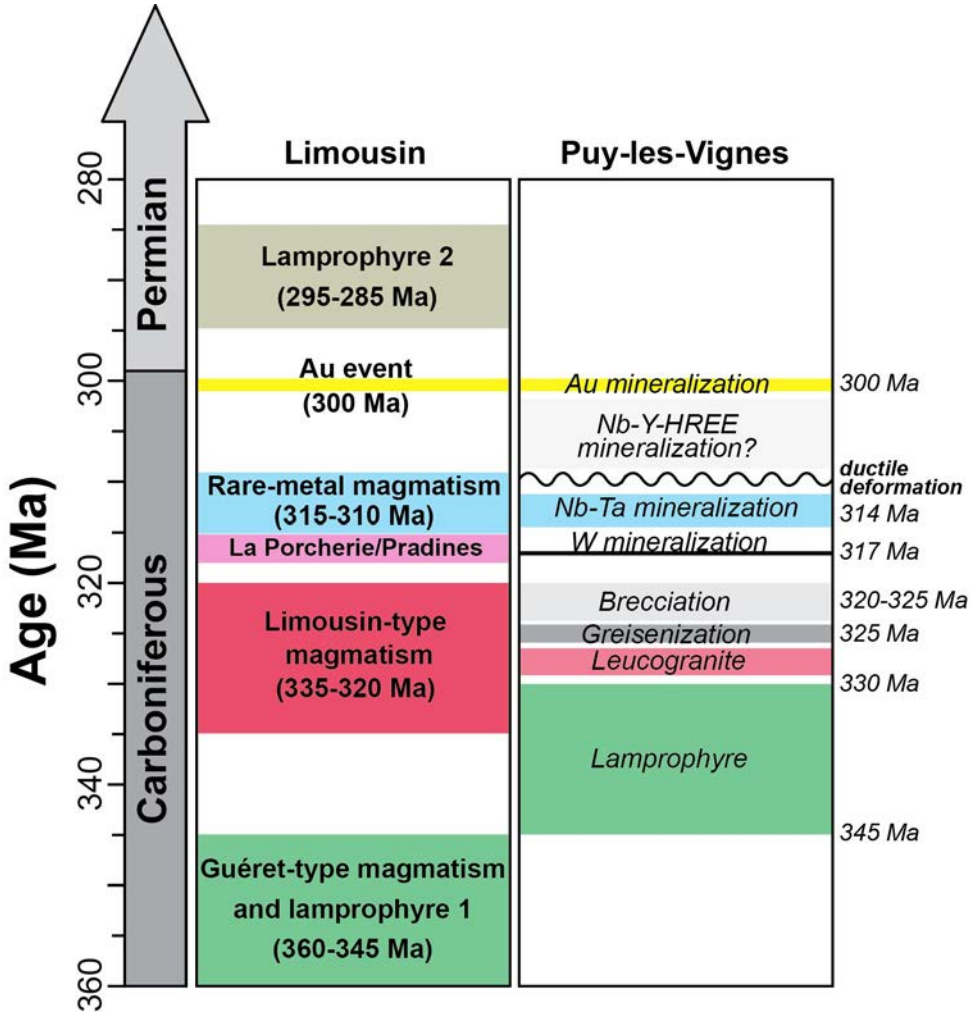

Fig. 68: Chronological sequence of the successive magmatic and hydrothermal events in the Limousin area and in the Puy-les-Vignes deposit.

A synthetic chronological sequence of the successive episodes at Puy-les-Vignes and a comparison with the main magmatic events in the Limousin area is shown in Fig. 68. The early hydrothermal alteration (ca. 327-325 Ma), the brecciation stage (ca. 323-321 Ma) and the W mineralization (ca. 317 Ma) are clearly disconnected in time and relatively well constrained temporally. These successive hydrothermal events occur during a period of intense granitic magmatism in the Limousin area during the Visean-Namurian at ca. 335-320 Ma, which led to the emplacement of large peraluminous leucogranitic complexes (AKL type of Stussi, 1989). The most prominent intrusions of this type are those of St-Sylvestre, Millevaches and St-Mathieu (e.g., Holliger et al., 1986; Scaillet et al., 1996; Rolin et al., 2014). Moreover, a later episode of peraluminous magmatism at ca. 317-315 Ma is known in the Limousin as indicated both by the La Porcherie granite dated at 317 ± 3 Ma (U-Pb on

zircon; Lafon and Respaut, 1988) and by a syntectonic two-mica leucogranite, along the Pradines shear zone in the Millevaches complex, dated at 313 ± 4 Ma (U-Pb on zircon and monazite; Gébelin et al., 2009). This peraluminous magmatism is then followed by a regional rare-metal magmatism at ca. 315-310 Ma (Cuney et al., 2002; Melleton et al., 2015), which is associated with the emplacement of small and highly fractionated rare-metal granites (RMG) such as Beauvoir, Blond, Montebras and Chavence (Aubert, 1969; Mourey, 1985; Soufi, 1988; Cuney et al., 1992; Raimbault et al., 1995; Belkasmi and Cuney, 1998), LCT-type pegmatites such as Chèdeville (Raimbault, 1998; Deveaud et al., 2013, 2015) and rhyolites such as Richemont (Ebougué, 1995; Raimbault and Burnol, 1998). This continuum of magmatism during the late-Carboniferous in a complicated setting characterized by coeval compressive and extensive conditions raises the question of the role of granites for the formation of the Puy-les-Vignes deposit, both for the source of fluids and metals. Hence, the formation of the Puy-les-Vignes breccia pipe may result of the exceptional superposition at the local-scale of several distinct magmatic and hydrothermal events at the regional-scale.

8.3. Interpretation of the paragenetic stages from Puy-les-Vignes as metallogenic events

The petrographic characterization and the geochemical analyses of the studied samples allowed to propose a detailed paragenetic sequence of the Puy-les-Vignes deposit (Fig. 48), which distinguish four main metallogenic stages separated by hydraulic fracturing episodes. Interpretation of the mineral paragenesis and the geochemical compositions of the main stages may allow to characterize the temporal evolution of the hydrothermal system and possibly to determine the possible source reservoirs of fluids and metals.

8.3.1. Early W-As±Nb-Ta mineralization (stage II)

This stage corresponds to the main W mineralization event forming the formerly mined economic mineralization at Puy-les-Vignes. It follows the early greisen-type hydrothermal alteration and hydraulic brecciation (stage I) yielding to the breccia pipe structure. Deposition of wolframite and arsenopyrite in the mineralized quartz-veins are clearly separated in time, as commonly observed for other Variscan W deposits (e.g., Kelly and Rye, 1979; Derré, 1983; Nicolas, 1985; Noronha et al., 1999). Wolframite is lately replaced by ferberite-1 and associated with several W-Nb-Ta oxide minerals (wolframioixiolite, Nb-Ta-ferberite, rutile). Several observations suggest a genetic link between the deposition of Nb-Ta minerals and the

ferberitization: (i) Wolframoixiolite minerals were found in overgrowth on wolframite or in close association with ferberite-1 crystals disseminated within the late scheelite; (ii) Ferberite-1 showing intracrystalline Nb-Ta growth zoning, similar to the one described at the Echassières W deposit (Aïssa et al., 1987a), has been observed locally in overgrowth on the wolframite; (iii) Nb-Ta-rich rutiles were observed disseminated within the ferberitized wolframite. These Nb-Ta oxide minerals were therefore not coeval with the wolframite crystallization and were rather superposed on the primary W mineralization during a later fluid episode. The associations of Nb-Ta-ferberite with wolframoixiolite have been previously considered as strong mineralogical markers of the magmatic-hydrothermal transition from rare-metal granites (e.g., Marignac et al., 2001; Breiter et al., 2007; Alekseev et al., 2011). Hence, the Nb-Ta oxide minerals associated with the ferberite-1 from the stage II may have crystallized from a rare-metal-rich hydrothermal fluid after the deposition of wolframite and may reflect the overprint by magmatic fluids derived from a rare-metal granitic cupola at depth. The presence of a rare-metal granite under Puy-les-Vignes is indirectly inferred from the sample of rare-metal aplo-pegmatite dyke, which has a whole-rock composition close to those of the Beauvoir granite (Cuney et al., 1992; Raimbault et al., 1995) and the Blond granite (Soufi, 1988). Moreover, the $^{40}Ar/^{39}Ar$ age of 314 ± 2.6 Ma obtained on muscovite from the aplo-pegmatite fall in the same age interval of 315-310 Ma than the other rare-metal granites and pegmatites known regionally in the Limousin area (Cuney et al., 2002; Melleton et al., 2015). Arsenopyrite contrasts clearly with the wolframite by its mineral associations and its geochemical signature. The crosscut relationships and corrosion textures observed in wolframite suggests that arsenopyrite formed during a distinct fluid event after the wolframite deposition, characterized by a significantly different fluid composition. The mineral association of arsenopyrite and Fe-skutterudite indicates a crystallization temperature > 300°C in the Fe-Co-Ni(AsS) system (Hem and Marovicky, 2004). The high content of siderophile elements (Fe, Co, Ni, Cr) in the primary arsenopyrite, together with the presence of accessory minerals of Fe-skutterudite and Cr-Nb-W-rich rutile, may suggest the contribution of mafic/ultramafic rocks as sources of these elements. In this regard, amphibolite massifs are known in a radius < 10 km in the surroundings of Puy-les-Vignes at the north, the east and the southwest of the deposit (Fig. 45a). Furthermore, the leptynite-amphibolite complex outcrops in the paragneiss from the UGU at ca. 12 km southwest of Puy-les-Vignes (Fig. 45a) and may represent a potential source of siderophile elements.

8.3.2. Late Nb-Y-HREE mineralization (stage IV)

The stage IV is characterized by a mineral association of tourmaline, chlorite and adularia composing the matrix of the late hydrothermal breccia formed after the main ductile deformation episode. It contains several accessory minerals such as monazite, xenotime, zircon, Nb-Fe-W-rich rutile and NTox. The latter represent excellent mineralogical markers of the fluid composition and are described in detail in Chapter 5. This mineral paragenesis is characterized by a P, Y, HREE, Nb, Ti, Zr, U geochemical signature, which is typical of the rare-metal peralkaline magmatism (Černý et al., 2005), and contrasts clearly with the peraluminous signature of the early W-As-Nb-Ta mineralization. This contrasting geochemical signature may reflect a change with time in the source of the fluids, which may be linked with the presence of a peralkaline magmatic source at depth. In this respect, it can be noted that a small peralkaline syenite is known at Ecubillou (Chèvremont et al., 1996) at approximately 50 km to the west of Puy-les-Vignes. This suggests that similar peralkaline plutonic bodies may be present at depth in the proximity of the Puy-les-Vignes deposit and may represent a potential source of metals.

9. Conclusions

The Puy-les-Vignes deposit, located in the Limousin area, represents a rare occurrence of quartz-wolframite-tourmaline breccia pipe in the West European Variscan belt. The integrated petrographic, geochemical and geochronological study of this atypical deposit allowed to propose a detailed paragenetic sequence divided into five main stages:

(i) Early hydrothermal alteration (greisenization and tourmalinization) of the host-rocks, dated at ca. 327-325 Ma, was followed by a main brecciation episode dated at ca. 323-321 Ma, which led to the breccia pipe structure composed by heterometric clasts of the altered enclosing rocks (mainly gneisses and granites). The greisenization episode fall in the same time interval than a leucogranite dyke dated at 324.7 ± 4.2 Ma, whose the whole-rock geochemistry is typical of an evolved Limousin-type granite, and may thus indicate that a hidden leucogranite cupola is located under the Puy-les-Vignes deposit;

(ii) W-As-Nb-Ta mineralization associated with the formation of quartz-wolframite-arsenopyrite veins, during a second stage brecciation, which crosscut the breccia pipe. The W episode is dated independently by U-Pb on wolframite at ca. 317 Ma (see Chapter 1), thus indicating that the main mineralization episode is clearly disconnected temporally from the

early hydrothermal alteration and brecciation stages. This episode corresponds to a succession of wolframite, ferberite-1, arsenopyrite, scheelite and ferberite-2 during crack-seal reopenings. Several W-Nb-Ta oxide minerals are associated temporally with the ferberite-1 and are interpreted to have crystallized from a magmatic-hydrothermal fluid derived from a rare-metal granite at depth. The presence of a rare-metal granitic cupola is indirectly inferred from a sample of rare-metal aplo-pegmatite, which exhibit the all mineralogical, textural and geochemical features of a rare-metal granitic dyke derived from a highly evolved granite cupola. This sample has been dated at 314 ± 5.2 Ma by Ar-Ar on muscovite, which is consistent with the time interval of the other rare-metal granites and pegmatites emplaced in the Limousin area at ca. 315-310 Ma.

(iii) Minor Fe-Cu-Zn mineralization composed mainly by pyrite, chalcopyrite and sphalerite, which crosscut the minerals from the previous stages;

(iv) A late hydrothermal Nb-Ti-Y-HREE mineralization corresponds to the formation of a crackle-breccia with a matrix of tourmaline, adularia and vermicular chlorite, which cuts the mineralized quartz veins after the main ductile deformation episode. The breccia contains several disseminated accessory minerals within the adularia matrix, which consist in monazite, xenotime, zircon, Nb-Fe-W-rich rutile and Nb-Ti-Y-HREE-W-U oxides. This stage is characterized by a P, Y, HREE, Nb, Ti, Zr, U geochemical signature and has been interpreted as the contribution of a peralkaline magmatic source at depth (see Chapter 5).

(v) A discrete mineralization of Bi±Au-Ag fills microcavities and microcracks within the minerals from the previous stages and appears similar to those found in the mesothermal gold deposits from the FMC and particularly from the Limousin area. An Ar-Ar age of 301.3 ± 3 Ma obtained on adularia from the late hydrothermal crackle-breccia (stage IV) represents the youngest age obtained in this study and may record this last hydrothermal episode known regionally in the Limousin area.

To summary, the Puy-les-Vignes deposit represents an exceptional case of hydrothermal W mineralization associated with a breccia pipe structure, which results from multistage successive hydrothermal episodes during a time lapse of at least 25 Ma between 325 Ma (Namurian) and 300 Ma (Stephanian). This temporal interval is synchronous with an intense period of granitic magmatism in a complicated setting characterized by coeval compressive and extensive conditions in the internal zones of the Variscan belt. Hence, the formation of the Puy-les-Vignes breccia pipe may result of the exceptional superposition at the local-scale of several distinct magmatic and hydrothermal events at the regional-scale.

Table 15: Whole-rock chemical compositions of rocks from the Puy-les-Vignes deposit. bdl: below detection limit.

Sample	PV-92-20 *Unaltered gneiss*	PLV-02-01 *Altered gneiss*	PV-92-7 *Unaltered leucogranite*	PV-92-5 *Altered leucogranite*	PLV-13-02 *Altered granite*	PLV-02-10 *Altered granite*	PLV-02-02a *Rare-metal granite*	PLV-02-02b *Rare-metal granite*	PV-92-17 *Lamprophyre*
wt.%									
SiO_2	65.31	70.90	77.94	75.19	78.63	73.34	72.43	70.77	50.55
Al_2O_3	12.63	14.60	13.94	14.05	13.49	15.05	16.94	17.19	14.06
Fe_2O_3	4.90	4.61	0.49	2.95	2.03	3.67	0.30	1.18	16.70
MnO	0.07	0.03	0.00	0.00	0.00	0.01	0.06	0.19	0.17
MgO	8.37	1.53	0.18	0.25	0.19	0.51	bdl	0.09	8.97
CaO	1.19	0.25	0.24	0.19	bdl	bdl	0.26	0.54	0.39
Na_2O	1.17	0.30	3.59	0.16	0.17	0.18	8.15	4.58	0.03
K_2O	4.82	3.53	2.48	4.30	3.90	4.33	0.97	3.09	3.09
TiO_2	0.37	0.57	bdl	0.06	0.06	0.43	0.02	0.05	0.63
P_2O_5	0.34	0.16	0.14	0.16	bdl	bdl	0.42	0.54	0.29
LOI	2.10	3.17	1.30	3.51	2.58	3.07	0.93	1.82	5.00
Total	101.26	99.65	100.31	100.82	101.06	100.57	100.48	100.05	99.87
ppm									
As	18.2	448	266	3540	2275	2235	9.0	20.7	974
Ba	385	564	195	285	409	911	9.2	17.2	130
Be	2.0	2.0	3.5	5.5	2.4	3.2	113.0	74.3	3.5
Bi	bdl	29.7	2.2	34.2	26.8	27.9	1.5	5.9	14.2
Cd	bdl	bdl	bdl	bdl	bdl	bdl	0.1	0.3	bdl
Co	25.3	9.3	2.5	11.2	bdl	0.9	bdl	0.6	52.2
Cr	488	53.2	bdl	bdl	bdl	30.2	5.1	6.0	589
Cs	17.8	13.4	6.7	12.0	8.0	11.3	57.8	170	100
Cu	bdl	246	bdl	246	71.5	301	12.3	18.7	29.0
Ga	19.9	32.1	16.5	21.1	22.7	31.3	29.6	43.0	45.5
Ge	1.7	2.5	3.0	3.0	3.2	2.5	4.2	4.2	2.0
Hf	3.6	5.1	0.9	0.9	0.9	2.8	1.0	1.2	4.1
In	bdl	bdl	bdl	bdl	bdl	bdl	bdl	bdl	0.1
Mo	bdl	1.3	bdl	bdl	bdl	bdl	bdl	bdl	0.8
Nb	11.0	9.4	4.8	6.2	11.3	9.9	64.9	68.7	5.9
Ni	365	18.5	bdl	10.6	bdl	bdl	bdl	bdl	244
Pb	4.2	7.8	5.8	41.0	10.2	12.7	11.3	8.7	1.2
Rb	299	220	156	263	218	261	329	1151	586
Sc	10.1	11.4	bdl	3.2	6.7	10.9	bdl	bdl	24.9
Sb	0.5	0.5	0.5	1.3	0.9	1.6	0.5	0.6	3.1
Sn	6.7	63.9	40.6	98.1	56.3	89.3	3044	1853	38.6
Sr	69.9	31.0	95.2	13.3	13.7	17.6	23.1	25.0	7.4
Ta	1.1	1.0	1.9	2.0	4.5	1.6	46.0	47.5	0.6
Th	5.6	11.2	0.5	1.7	1.2	9.6	2.2	1.5	18.0
U	2.3	3.3	1.0	1.9	1.7	3.2	3.0	3.6	4.9
V	48.4	66.3	2.8	3.3	5.0	39.4	bdl	0.9	151
W	2.3	145	9.7	29.7	40.4	97.2	14.4	37.2	198
Y	20.7	22.0	6.0	9.9	6.6	28.0	1.0	2.2	17.7
Zn	84.7	36.8	bdl	27.3	bdl	26.1	58.8	212	114
Zr	119	182	22.1	23.9	16.4	96.5	13.2	14.7	137
La	18.6	33.0	1.7	4.7	2.4	26.6	0.7	1.2	64.0
Ce	37.6	63.1	3.3	8.9	5.3	50.9	1.0	2.0	133
Pr	4.8	7.5	0.4	1.1	0.7	6.2	0.2	0.3	15.1
Nd	18.7	27.7	1.5	3.9	3.0	23.4	0.9	1.1	56.1
Sm	4.6	5.4	0.4	1.0	1.0	4.8	0.2	0.3	8.7
Eu	0.8	0.7	0.3	0.3	0.2	0.7	0.0	0.1	0.9
Gd	4.2	4.5	0.5	1.0	1.0	4.4	0.3	0.4	5.4
Tb	0.7	0.7	0.1	0.2	0.2	0.7	0.0	0.1	0.7
Dy	4.0	4.0	0.9	1.6	1.4	4.7	0.3	0.5	3.4
Ho	0.8	0.8	0.2	0.3	0.3	1.0	0.0	0.1	0.6
Er	1.9	2.2	0.6	1.0	0.8	2.8	0.1	0.2	1.7
Tm	0.3	0.3	0.1	0.2	0.1	0.4	0.0	0.0	0.2
Yb	1.6	2.2	0.8	1.3	0.9	2.8	0.1	0.3	1.6
Lu	0.2	0.3	0.1	0.2	0.1	0.4	0.0	0.0	0.2

Table 16: Representative EMPA data of rutile from Puy-les-Vignes.

	Type-1 rutile in tourmalinite from gneissic clast (PLV-02-01a)									Type-1 rutile in tourmalinite from granitic clast (PLV-02-04)									Type-2 rutile in quartz-wolframite vein (PLV-7574a)								
	Dark core			*Light rim*						*Dark core*					*Light rim*				*Dark core*			*Light rim*				*Overgrowth*	
	1	2	3	4	6	7	8	9	35	1	5	11	16	2	4	7	8	12	7	13	8	9	10	12	11	14
FeO	0.29	0.43	0.28	0.38	1.62	1.40	1.38	1.18	bdl	bdl	bdl	bdl	bdl	0.85	0.49	0.54	1.33	bdl	0.56	0.51	1.38	1.98	1.10	1.14	2.76	1.06
MnO	bdl	bdl	bdl	bdl	bdl	bdl	bdl	bdl	bdl	bdl	bdl	bdl	bdl	bdl	bdl	bdl	bdl	bdl	bdl	bdl	bdl	bdl	bdl	bdl	bdl	bdl	bdl
Cr_2O_3	bdl	bdl	bdl	bdl	bdl	bdl	bdl	bdl	bdl	1.42	1.00	1.70	1.50	0.91	0.68	2.78	1.16	bdl	bdl	bdl	bdl	bdl	bdl	bdl	bdl	bdl	bdl
Sc_2O_3	bdl	bdl	bdl	bdl	bdl	bdl	bdl	bdl	bdl	bdl	bdl	bdl	bdl	bdl	bdl	bdl	bdl	bdl	bdl	bdl	bdl	bdl	bdl	bdl	bdl	bdl	bdl
TiO_2	99.22	98.61	99.61	98.88	94.90	95.75	96.31	96.29	97.60	97.05	97.60	96.66	96.52	94.55	95.75	90.58	91.55	96.67	96.56	94.16	91.90	94.98	94.81	85.33	92.94
SnO_2	bdl	0.66	bdl	0.34	0.34	0.55	0.43	0.35	0.27	0.24	0.44	0.28	0.39	0.42	0.49	0.25	0.35	0.32	bdl	bdl	0.31	0.34	0.26	0.26	0.38	0.24
Nb_2O_5	bdl	bdl	bdl	bdl	bdl	bdl	0.43	bdl	bdl	bdl	bdl	bdl	0.20	0.22	0.23	0.72	0.22	bdl	bdl	bdl	bdl	bdl	bdl	bdl	5.20	1.13
Ta_2O_5	bdl	bdl	bdl	bdl	bdl	bdl	bdl	bdl	bdl	bdl	bdl	bdl	bdl	bdl	bdl	bdl	bdl	bdl	bdl	bdl	bdl	bdl	bdl	bdl	5.10	2.58
WO_3	bdl	bdl	bdl	bdl	4.05	2.61	2.37	1.96	0.06	0.03	0.28	0.70	2.76	1.75	4.48	5.07	0.71	0.75	2.56	4.15	1.87	1.96	0.00	0.00	0.00	0.00
Total	99.51	99.70	99.89	99.60	100.91	100.31	100.92	99.78	98.80	98.87	99.08	99.20	99.68	99.32	99.59	99.58	98.29	98.14	98.41	98.37	98.21	98.17	98.77	97.95		
Fe	0.00	0.00	0.00	0.00	0.02	0.02	0.02	0.01	0.00	0.00	0.00	0.00	0.00	0.01	0.01	0.01	0.02	0.01	0.01	0.01	0.02	0.02	0.01	0.01	0.03	0.01
Mn	0.00	0.00	0.00	0.00	0.00	0.00	0.00	0.00	0.00	0.00	0.00	0.00	0.00	0.00	0.00	0.00	0.00	0.00	0.00	0.00	0.00	0.00	0.00	0.00	0.00	0.00
Cr	0.00	0.00	0.00	0.00	0.00	0.00	0.00	0.00	0.00	0.02	0.01	0.02	0.02	0.01	0.01	0.03	0.01	0.00	0.00	0.00	0.00	0.00	0.00	0.00	0.00	0.00
Sc	0.00	0.00	0.00	0.00	0.00	0.00	0.00	0.00	0.00	0.00	0.00	0.00	0.00	0.00	0.00	0.00	0.00	0.00	0.00	0.00	0.00	0.00	0.00	0.00	0.00	0.00
Ti	1.00	0.99	1.00	1.00	0.97	0.98	0.97	0.98	0.99	0.99	0.99	0.98	0.98	0.97	0.98	0.94	0.95	0.99	0.99	0.98	0.96	0.98	0.98	0.98	0.92	0.97
Sn	0.00	0.00	0.00	0.00	0.00	0.00	0.00	0.00	0.00	0.00	0.00	0.00	0.00	0.00	0.00	0.00	0.00	0.00	0.00	0.00	0.00	0.00	0.00	0.00	0.00	0.00
Nb	0.00	0.00	0.00	0.00	0.00	0.00	0.00	0.00	0.00	0.00	0.00	0.00	0.00	0.00	0.00	0.00	0.00	0.00	0.00	0.00	0.00	0.00	0.00	0.00	0.03	0.01
Ta	0.00	0.00	0.00	0.00	0.00	0.00	0.00	0.00	0.00	0.00	0.00	0.00	0.00	0.00	0.00	0.00	0.00	0.00	0.00	0.00	0.00	0.00	0.00	0.00	0.02	0.01
W	0.00	0.00	0.00	0.00	0.01	0.01	0.01	0.01	0.00	0.00	0.00	0.00	0.00	0.01	0.01	0.02	0.02	0.00	0.00	0.00	0.01	0.02	0.01	0.01	0.00	0.00

	Type-2 rutile in quartz-scheelite vein (PLV-02-13b)									Type-3 rutile in ferberite (PLV-02-17)									Type-4 rutile in arsenopyrite (PLV-02-28b)							
	Dark core				*Light rim*				*Overgrowth*	*Core*									*Core*							
	1	5	6	14	2	4	28	35	7	8	11	12	1	2	3	4	5	6	1	3	4	5	7	8		
FeO	0.54	0.65	0.73	0.60	1.82	1.38	2.13	2.29	2.99	4.80	2.51	2.55	4.49	3.07	2.19	2.92	3.57	1.84	0.64	0.39	2.54	0.29	0.33	0.79		
MnO	bdl	bdl	bdl	bdl	bdl	bdl	bdl	bdl	bdl	bdl	bdl	bdl	0.06	0.07	0.08	0.03	0.00	0.00	0.00	0.08	0.00	0.08	0.04	0.06		
Cr_2O_3	bdl	bdl	bdl	bdl	bdl	bdl	bdl	bdl	bdl	bdl	bdl	bdl	0.06	0.18	0.21	0.22	0.26	0.26	9.25	9.48	7.17	8.39	7.32	7.61		
Sc_2O_3	bdl	bdl	bdl	bdl	bdl	bdl	bdl	bdl	bdl	bdl	bdl	bdl	0.09	0.09	0.03	0.08	0.12	0.02	0.02	0.02	0.06	0.00	0.00	0.05		
TiO_2	97.19	96.91	96.50	96.52	92.84	94.14	91.89	90.98	88.44	79.91	88.08	88.47	80.97	87.25	91.17	88.27	84.93	93.21	73.67	75.84	73.09	79.65	83.12	77.84		
SnO_2	0.35	0.33	0.30	0.30	0.32	0.20	0.32	0.29	0.24	0.20	0.21	0.31	0.34	0.31	0.53	0.51	0.37	0.52	0.38	0.28	0.32	0.15	0.53	0.32		
Nb_2O_5	0.22	0.67	0.19	0.24	0.30	0.47	0.80	0.50	7.18	12.15	5.86	5.40	14.15	9.74	6.41	9.67	11.87	5.16	11.81	13.09	12.58	12.75	9.30	14.22		
Ta_2O_5	bdl	bdl	bdl	bdl	bdl	bdl	bdl	bdl	1.06	2.61	1.72	2.01	1.29	0.00	0.17	0.00	0.87	0.42	0.58	0.00	2.31	1.12	0.69	1.05		
WO_3	0.72	0.79	1.03	1.03	4.03	3.00	4.60	5.23	0.27	0.13	0.21	0.07	0.67	0.00	0.73	0.36	0.00	0.02	2.94	2.41	4.23	0.84	0.51	0.00		
Total	98.48	98.70	98.02	98.09	97.49	97.81	97.61	97.00	97.19	95.00	96.08	96.26	102.12	100.71	101.52	102.06	101.99	101.45	99.29	101.59	102.30	103.27	101.84	101.94		
Fe	0.01	0.01	0.01	0.01	0.02	0.02	0.03	0.03	0.04	0.06	0.03	0.03	0.05	0.04	0.02	0.03	0.04	0.02	0.01	0.00	0.03	0.00	0.00	0.01		
Mn	0.00	0.00	0.00	0.00	0.00	0.00	0.00	0.00	0.00	0.00	0.00	0.00	0.00	0.00	0.00	0.00	0.00	0.00	0.00	0.00	0.00	0.00	0.00	0.00		
Cr	0.00	0.00	0.00	0.00	0.00	0.00	0.00	0.00	0.00	0.00	0.00	0.00	0.00	0.00	0.00	0.00	0.00	0.00	0.11	0.11	0.08	0.09	0.08	0.08		
Sc	0.00	0.00	0.00	0.00	0.00	0.00	0.00	0.00	0.00	0.00	0.00	0.00	0.00	0.00	0.00	0.00	0.00	0.00	0.00	0.00	0.00	0.00	0.00	0.00		
Ti	0.99	0.99	0.99	0.99	0.96	0.97	0.96	0.95	0.92	0.86	0.93	0.93	0.85	0.90	0.93	0.90	0.88	0.94	0.80	0.80	0.79	0.82	0.86	0.81		
Sn	0.00	0.00	0.00	0.00	0.00	0.00	0.00	0.00	0.00	0.00	0.00	0.00	0.00	0.00	0.00	0.00	0.00	0.00	0.00	0.00	0.00	0.00	0.00	0.00		
Nb	0.00	0.00	0.00	0.00	0.00	0.00	0.01	0.00	0.05	0.08	0.04	0.03	0.09	0.06	0.04	0.06	0.07	0.03	0.08	0.08	0.08	0.08	0.06	0.09		
Ta	0.00	0.00	0.00	0.00	0.00	0.00	0.00	0.00	0.00	0.00	0.01	0.01	0.00	0.00	0.00	0.00	0.00	0.00	0.00	0.00	0.01	0.00	0.00	0.00		
W	0.00	0.00	0.00	0.00	0.01	0.01	0.02	0.02	0.00	0.00	0.00	0.00	0.00	0.00	0.00	0.00	0.00	0.00	0.01	0.01	0.02	0.00	0.00	0.00		

Structural formulae were calculated on the basis of 2 atoms of oxygen.
bdl: below detection limit

Table 17: Trace element concentrations (in ppm) for type-1 and type-2 rutiles from Puy-les-Vignes.

	Type-1 rutile in tourmalinite from a gneissic clast (sample PLV-02-01a)																
	1	2	3	4	5	6	7	8	9	10	11	12	13	14	15	Mean	SD
^{45}Sc	22	22	23	28	29	23	22	17	19	27	19	20	26	13	8	21	6
^{51}V	321	263	280	256	339	446	60	110	82	70	72	78	89	62	105	176	128
^{53}Cr	41	46	23	120	48	380	12	17	17	22	17	20	10	8	23	54	94
^{57}Fe	5258	4245	5316	5974	3448	5339	1884	5082	4406	2810	3402	2518	2131	4102	5422	4089	1325
^{60}Ni	1.97	1.16	4.03	3.10	3.21	18.39	1.05	bdl	1.51	bdl	bdl	bdl	bdl	bdl	1.70	4	5
^{63}Cu	6.76	4.25	10.62	6.99	6.96	40.30	3.83	3.22	6.59	8.11	5.63	3.75	3.53	3.59	4.70	8	9
^{66}Zn	14	14	15	16	15	21	14	12	13	13	15	13	13	13	13	14	2
^{90}Zr	78	46	58	73	97	93	30	38	39	79	39	29	29	27	24	52	26
^{93}Nb	1260	1219	1060	635	595	1019	576	1718	1058	703	851	1214	651	1231	1292	1005	331
^{95}Mo	1.85	0.73	2.23	2.34	2.77	9.99	0.61	0.13	2.50	3.24	2.46	1.04			1.43	2	2
^{118}Sn	3760	3219	3329	2676	3702	2522	2170	1819	2619	1933	2189	1376	2207	2418	2501	2563	685
^{181}Ta	187	183	141	94	79	145	81	154	132	100	134	120	104	151	194	133	37
^{182}W	16583	12752	15823	7559	6868	4889	1685	17708	12887	5086	7975	5408	2749	13362	18746	10005	5690
T (°C)	545	512	526	540	559	556	486	500	501	546	501	485	485	481	475	513	29

	Type-1 rutile in tourmalinite from a granitic clast (sample PLV-02-04a)																
	1	2	3	4	5	6	7	8	9	10	11	12	13	14	15	Mean	SD
^{45}Sc	11	5	6	14	13	12	9	13	10	14	13	12	16	17	19	12	4
^{51}V	823	286	342	751	717	689	369	421	554	785	1074	1356	1175	1573	1673	839	443
^{53}Cr	4013	13928	9283	5734	5928	6626	7551	5864	6923	5716	3071	3874	2366	2542	1644	5671	3128
^{57}Fe	2924	281	331	1250	1911	1497	1945	1893	1075	1460	1135	7115	46736	8608	6120	5619	11653
^{60}Ni	1.08	1.04	0.49		0.54	0.66	1.12	0.72	0.84	1.14	1.17	0.87	5.76	0.75	0.90	1	1
^{63}Cu	7.30	4.87	4.50	3.97	7.12	4.19	18	19	3.96	13.71	6.97	18.07	369	13.20	4.40	33	93
^{66}Zn	17	17	15	17	16	15	15	15	12	16	14	17	63	14	12	18	12
^{90}Zr	157	41	35	129	113	83	68	79	70	74	61	119	150	170	86	96	42
^{93}Nb	2108	1230	1089	1695	1579	1508	1236	795	1323	858	770	2147	2463	2016	1450	1484	522
^{95}Mo	bdl	bdl	bdl	bdl	0.12	bdl	0.76	0.49	bdl	0.90	0.19	0.33	15.58	1.22	bdl	2	5
^{118}Sn	2460	3227	2443	2743	2960	3014	2421	2811	3146	3803	2920	3256	3575	3540	2913	3015	419
^{181}Ta	93	41	41	71	79	75	46	51	61	58	58	154	211	250	146	96	65
^{182}W	15502	6387	5672	12823	16572	16281	5543	3098	11042	4206	4053	31420	36981	42940	29930	16163	13064
T (°C)	593	504	496	578	569	548	536	545	538	541	529	573	589	598	551	553	31

Table 17: Continued.

	Type-2 rutile in quartz-wolframite vein (sample PLV-7574a)																
	1	2	3	4	5	6	7	8	9	10	11	12	13	14	15	Mean	SD
^{45}Sc	31	32	29	46	29	30	27	31	39	24	19	20	18	31	31	29	7
^{51}V	281	240	294	304	255	265	395	492	348	370	235	241	205	300	291	301	74
^{53}Cr	29	19	23	33	14	11	18	22	29	15	14	13	12	22	32	20	8
^{57}Fe	3005	3375	3150	2831	8865	9290	3184	3334	2970	7940	6869	6824	6257	10916	11767	6038	3162
^{60}Ni	bdl	bdl	bdl	bdl	bdl	bdl	bdl	bdl	bdl	bdl	1.36	1.08	bdl	bdl	bdl	1	0
^{63}Cu	4.16	2.74	2.48	2.90	2.94	2.88	3.78	13.23	3.42	31.38	4.21	4.44	6.64	4.56	3.33	6	7
^{66}Zn	13	11	10	10	10	11	14	13	12	12	13	12	12	11	10	12	1
^{90}Zr	54	66	67	78	86	85	59	68	69	74	68	69	66	90	83	72	10
^{93}Nb	454	539	609	555	1134	1765	464	403	435	1124	1144	1060	1250	1437	1187	904	432
^{95}Mo	bdl	bdl	bdl	bdl	bdl	0.17	bdl	bdl	0.13	0.12	bdl	bdl	bdl	0.14	bdl	0	0
^{118}Sn	2130	2118	2060	2371	2370	2437	2342	2857	2782	2485	2306	2169	2142	2277	2196	2336	233
^{181}Ta	36	49	56	48	123	177	41	47	35	205	161	118	141	62	23	88	60
^{182}W	7227	7346	6608	5678	36331	37906	7252	7501	5977	30967	24350	22973	20207	45866	52053	21216	16108
T (°C)	522	533	535	545	551	550	527	536	536	541	536	536	534	554	549	539	9

	Type-2 rutile in quartz-scheelite vein (sample PLV-02-13b)																
	1	2	3	4	5	6	7	8	9	10	11	12	13	14	15	Mean	SD
^{45}Sc	49	40	33	27	32	31	39	31	34	37	32	32	32	35	150	42	30
^{51}V	534	585	510	461	412	756	802	781	609	586	596	525	617	867	118	584	184
^{53}Cr	65	50	152	53	156	51	82	75	57	40	39	43	47	133	59	73	40
^{57}Fe	2841	8044	6259	4209	2535	11602	2800	4006	5851	9215	8746	9652	10409	10537	3616	6688	3217
^{60}Ni	bdl	bdl	1.45	bdl	bdl	bdl	bdl	bdl	bdl	bdl	bdl	bdl	bdl	4.96	bdl	3	2
^{63}Cu	3.47	3.37	8.89	4.26	2.66	4.21	3.59	2.83	3.40	3.55	2.88	3.81	4.01	7.91	3.33	4	2
^{66}Zn	13	12	22	15	11	13	12	11	12	11	13	12	16	17	14	14	3
^{90}Zr	76	95	76	68	23	95	74	74	94	88	90	88	100	64	49	77	20
^{93}Nb	1076	2306	3571	2179	3473	4135	1253	2006	2489	4116	3038	2939	3891	3935	1468	2792	1056
^{95}Mo	bdl	bdl	bdl	bdl	bdl	bdl	bdl	bdl	bdl	bdl	0.26	bdl	bdl	bdl	bdl	0	
^{118}Sn	2229	2308	1893	1870	2117	2243	2152	2053	2106	2025	2043	2069	2234	2023	1767	2075	151
^{181}Ta	85	136	123	61	188	207	60	65	79	142	103	154	210	117	87	121	51
^{182}W	4932	33275	20229	11047	1688	52357	6580	12347	20115	35017	34191	38093	40102	42478	9051	24100	16115
T (°C)	543	557	542	536	472	558	541	541	557	553	554	552	561	532	515	541	23

Table 18: Representative EMPA data of cassiterite from Puy-les-Vignes.

	Quartz-wolframite±cassiterite veins (sample PV-2)										Rarc-metal aplo-pegmatite (sample PLV-02-02)									
	95	96	97	100	101b	104c	105c	106c	108c	111b	1a	2a	3a	4a	6a	7a	8a	2b	3b	4b
SnO_2	99.68	99.07	99.77	97.31	97.74	99.00	98.96	99.89	97.34	97.22	99.42	97.93	98.96	99.51	96.72	99.23	98.05	98.72	99.80	99.05
WO_3	bdl	0.40	bdl	1.53	1.65	bdl	bdl	bdl	bdl	1.26	bdl	bdl	bdl	bdl	bdl	bdl	bdl	bdl	bdl	bdl
Nb_2O_5	bdl	0.06	bdl	bdl	0.19	0.11	0.08	0.03	0.20	bdl	bdl	1.24	bdl	bdl	1.82	bdl	1.03	2.82	1.12	2.12
Ta_2O_5	bdl	bdl	bdl	bdl	bdl	bdl	bdl	bdl	0.33	bdl	bdl	bdl	bdl	bdl	bdl	bdl	bdl	bdl	bdl	bdl
TiO_2	bdl	bdl	bdl	bdl	bdl	bdl	bdl	bdl	bdl	bdl	1.58	0.35	1.12	1.29	0.51	1.16	1.20	0.73	0.85	0.77
FeO	0.07	0.30	0.08	0.46	0.48	0.94	0.82	0.19	1.46	0.34	bdl	0.33	0.20	bdl	0.58	bdl	0.24	0.69	0.45	0.54
MnO	bdl	bdl	bdl	bdl	bdl	bdl	bdl	bdl	bdl	bdl	bdl	bdl	bdl	bdl	bdl	bdl	bdl	bdl	bdl	bdl
Total	99.79	99.83	99.85	99.31	100.06	100.05	99.86	100.11	99.34	98.82	101.00	99.85	100.28	100.80	99.63	100.39	100.52	102.96	102.22	102.48
Sn	1.00	0.99	1.00	0.98	0.98	0.99	0.99	1.00	0.98	0.98	0.97	0.97	0.98	0.98	0.96	0.98	0.96	0.94	0.96	0.95
W	0.00	0.00	0.00	0.00	0.00	0.00	0.00	0.00	0.00	0.00	0.00	0.00	0.00	0.00	0.00	0.00	0.00	0.00	0.00	0.00
Nb	0.00	0.00	0.00	0.00	0.00	0.00	0.00	0.00	0.00	0.00	0.00	0.01	0.00	0.00	0.02	0.00	0.01	0.03	0.01	0.02
Ta	0.00	0.00	0.00	0.00	0.00	0.00	0.00	0.00	0.00	0.00	0.00	0.00	0.00	0.00	0.00	0.00	0.00	0.00	0.00	0.00
Ti	0.00	0.00	0.00	0.00	0.00	0.00	0.00	0.00	0.00	0.00	0.03	0.01	0.02	0.02	0.01	0.02	0.02	0.01	0.02	0.01
Fe	0.00	0.01	0.00	0.01	0.01	0.02	0.02	0.00	0.03	0.01	0.00	0.01	0.00	0.00	0.01	0.00	0.00	0.01	0.01	0.01
Mn	0.00	0.00	0.00	0.00	0.00	0.00	0.00	0.00	0.00	0.00	0.00	0.00	0.00	0.00	0.00	0.00	0.00	0.00	0.00	0.00

Structural formulae were calculated on the basis of 2 atoms of oxygen.
bdl: below detection limit

Table 19: Representative EMPA data of wolframoixiolite from Puy-les-Vignes.

	Quartz-wolframite vein (sample PV-5a)													Quartz-scheelite-wolframite vein (sample PLV-02-13b)										
	Dark core				*Light core*			*Overgrowth*						*Dark core*				*Light core*				*Overgrowth*		
	5	6	7	9	19	21	22	23	1	2	3	4	2	6	16	26	23	24	27	29	7	8	14	17
Nb_2O_5	63.70	60.48	60.54	63.82	52.70	64.47	56.24	59.62	49.67	49.59	45.54	46.72	65.51	61.85	61.07	66.65	62.16	61.42	61.23	61.82	40.38	44.07	46.32	45.19
Ta_2O_5	bdl	bdl	1.00	bdl	bdl	1.10	bdl	bdl	bdl	bdl	bdl	bdl	bdl	bdl	bdl	bdl	bdl	bdl	bdl	bdl	bdl	bdl	bdl	bdl
FeO	14.46	14.46	15.28	17.10	14.99	13.85	15.42	14.65	15.49	14.48	15.93	15.38	13.80	15.24	13.65	13.60	14.64	14.07	14.08	13.87	17.47	17.43	15.13	16.06
MnO	4.06	4.57	3.92	4.61	3.90	3.73	3.28	3.44	3.82	6.19	3.70	4.30	3.04	2.84	2.47	3.42	3.18	3.01	3.16	2.77	1.68	1.83	2.93	2.52
WO_3	10.14	13.32	13.77	11.40	23.14	8.75	19.00	15.56	24.17	21.87	26.74	26.87	7.07	10.72	9.40	7.76	11.68	12.79	12.10	11.23	33.37	31.30	25.71	29.47
TiO_2	5.29	4.60	3.32	2.40	4.06	4.97	3.16	4.03	4.02	3.97	4.04	3.79	7.06	5.72	9.76	4.65	8.52	5.42	5.92	7.12	4.43	5.16	5.62	8.26
SnO_2	bdl	bdl	bdl	bdl	bdl	bdl	0.25	bdl	0.31	0.31	bdl	bdl	bdl	bdl	bdl	0.28	bdl	bdl	bdl	0.24	bdl	bdl	bdl	bdl
UO_2	bdl	bdl	bdl	bdl	bdl	bdl	bdl	bdl	bdl	bdl	bdl	bdl	bdl	bdl	bdl	bdl	bdl	bdl	bdl	bdl	bdl	bdl	bdl	bdl
PbO	bdl	bdl	bdl	bdl	bdl	bdl	bdl	bdl	bdl	bdl	bdl	bdl	bdl	bdl	bdl	bdl	bdl	bdl	bdl	bdl	bdl	bdl	bdl	bdl
Total	97.65	97.43	97.83	99.33	98.79	96.87	97.35	97.30	97.48	96.41	95.95	97.06	96.48	96.37	96.35	96.36	100.2	96.71	96.49	97.05	97.33	99.79	95.71	101.5
Nb	1.67	1.61	1.63	1.68	1.44	1.70	1.54	1.61	1.38	1.39	1.30	1.32	1.70	1.64	1.58	1.76	1.57	1.64	1.63	1.62	1.16	1.22	1.31	1.20
Ta	0.00	0.00	0.02	0.00	0.00	0.02	0.00	0.00	0.00	0.00	0.00	0.00	0.00	0.00	0.00	0.00	0.00	0.00	0.00	0.00	0.00	0.00	0.00	0.00
Fe	0.70	0.71	0.76	0.83	0.76	0.68	0.78	0.73	0.80	0.75	0.84	0.80	0.66	0.75	0.66	0.66	0.69	0.69	0.69	0.67	0.93	0.89	0.79	0.79
Mn	0.20	0.23	0.20	0.23	0.20	0.18	0.17	0.17	0.20	0.33	0.20	0.23	0.15	0.14	0.12	0.17	0.15	0.15	0.16	0.14	0.09	0.09	0.16	0.13
W	0.15	0.20	0.21	0.17	0.36	0.13	0.30	0.24	0.39	0.35	0.44	0.44	0.11	0.16	0.14	0.12	0.17	0.20	0.18	0.17	0.55	0.50	0.42	0.45
Ti	0.23	0.20	0.15	0.11	0.18	0.22	0.14	0.18	0.19	0.19	0.19	0.18	0.31	0.25	0.42	0.20	0.36	0.24	0.26	0.31	0.21	0.24	0.26	0.37
Sn	0.00	0.00	0.00	0.00	0.00	0.00	0.01	0.00	0.01	0.01	0.00	0.00	0.00	0.00	0.00	0.01	0.00	0.00	0.00	0.01	0.00	0.00	0.00	0.00
U	0.00	0.00	0.00	0.00	0.00	0.00	0.00	0.00	0.00	0.00	0.00	0.00	0.00	0.00	0.00	0.00	0.00	0.00	0.00	0.00	0.00	0.00	0.00	0.00
Pb	0.00	0.00	0.00	0.00	0.00	0.00	0.00	0.00	0.00	0.00	0.00	0.00	0.00	0.00	0.00	0.00	0.00	0.00	0.00	0.00	0.00	0.00	0.00	0.00
Ta/(Ta+Nb)	0.00	0.00	0.01	0.00	0.00	0.01	0.00	0.00	0.00	0.00	0.00	0.00	0.00	0.00	0.00	0.00	0.00	0.00	0.00	0.00	0.00	0.00	0.00	0.00
Mn/(Mn+Fe)	0.22	0.24	0.21	0.21	0.21	0.21	0.18	0.19	0.20	0.30	0.19	0.22	0.18	0.16	0.15	0.20	0.18	0.18	0.19	0.17	0.09	0.10	0.16	0.14

Structural formulae were calculated on the basis of 6 atoms of oxygen.
bdl: below detection limit

Table 20: Representative EMPA data of columbite-tantalite from Puy-les-Vignes.

Rare-metal aplo-pegmatite (sample PLV-02-02)																									
	Dark core					*Patchy complex*					*Cortex-I*				*Cortex-II*							*External overgrowth*			
	13	18	30	3	16	22	23	24	25	26	10	15	19	32	33	11	35	5	7	30	20	29	36	4	8
Nb_2O_5	64.58	57.16	65.63	59.89	60.31	53.82	51.04	53.14	56.58	49.99	56.20	62.42	59.39	55.94	56.28	48.21	43.84	46.92	42.26	45.50	36.73	27.52	33.64	30.26	28.57
Ta_2O_5	10.69	19.65	8.75	18.96	14.56	16.59	20.12	19.76	20.21	25.52	18.89	12.63	14.69	19.12	18.64	28.19	32.24	25.40	31.98	27.96	43.49	48.05	43.49	46.49	40.78
FeO	11.58	11.09	11.07	11.04	11.55	8.43	8.75	7.96	8.08	8.37	11.12	10.99	10.37	11.30	10.72	8.70	7.92	8.05	7.69	7.91	7.68	7.05	7.24	7.22	6.87
MnO	8.87	8.62	9.20	8.56	8.63	11.45	10.89	11.54	11.40	10.71	8.82	9.39	9.78	8.50	8.85	10.36	10.26	10.44	9.89	10.42	9.87	9.06	10.19	9.32	8.27
WO_3	bdl	bdl	bdl	bdl	bdl	4.82	2.64	1.37	bdl	bdl	bdl	bdl	bdl	bdl	bdl	bdl	bdl	bdl	bdl	bdl	bdl	bdl	bdl	bdl	bdl
TiO_2	1.93	1.82	2.03	2.54	1.65	2.08	1.77	1.70	1.30	1.58	2.40	1.59	1.71	1.75	2.28	1.68	1.87	4.08	3.63	2.73	1.52	1.35	1.74	1.38	1.38
SnO_2	bdl	0.32	bdl	0.43	bdl	0.41	0.76	0.27	bdl	bdl	0.26	bdl	0.24	0.32	0.32	bdl	bdl	0.99	1.20	0.65	0.33	0.31	0.32	0.35	0.33
UO_2	bdl	bdl	bdl	bdl	bdl	bdl	bdl	bdl	bdl	bdl	bdl	bdl	bdl	bdl	bdl	bdl	bdl	bdl	bdl	bdl	bdl	bdl	bdl	bdl	bdl
PbO	bdl	bdl	0.46	bdl	bdl	0.46	bdl	bdl	bdl	2.34	bdl	bdl	bdl	bdl	bdl	bdl	0.46	0.48	bdl	1.23	bdl	bdl	0.36	bdl	bdl
Total	97.65	98.66	97.14	101.4	96.70	98.06	95.97	95.74	97.57	98.51	97.69	97.02	96.18	96.93	97.09	97.14	96.59	96.36	96.65	96.40	99.62	93.34	96.98	95.02	86.20
Nb	1.75	1.59	1.77	1.60	1.68	1.52	1.49	1.54	1.60	1.46	1.57	1.72	1.66	1.58	1.58	1.42	1.33	1.37	1.26	1.36	1.13	0.94	1.07	1.00	1.03
Ta	0.17	0.33	0.14	0.31	0.24	0.28	0.35	0.34	0.34	0.45	0.32	0.21	0.25	0.33	0.32	0.50	0.59	0.45	0.58	0.50	0.80	0.98	0.83	0.92	0.89
Fe	0.58	0.57	0.55	0.55	0.59	0.44	0.47	0.43	0.42	0.45	0.58	0.56	0.54	0.59	0.56	0.47	0.44	0.43	0.43	0.44	0.44	0.44	0.43	0.44	0.46
Mn	0.45	0.45	0.47	0.43	0.45	0.60	0.59	0.63	0.60	0.59	0.46	0.48	0.51	0.45	0.47	0.57	0.58	0.57	0.55	0.58	0.57	0.58	0.61	0.58	0.56
W	0.00	0.00	0.00	0.00	0.00	0.08	0.04	0.02	0.00	0.00	0.00	0.00	0.00	0.00	0.00	0.00	0.00	0.00	0.00	0.00	0.00	0.00	0.00	0.00	0.00
Ti	0.09	0.08	0.09	0.11	0.08	0.10	0.09	0.08	0.06	0.08	0.11	0.07	0.08	0.08	0.11	0.08	0.09	0.20	0.18	0.14	0.08	0.08	0.09	0.08	0.08
Sn	0.00	0.01	0.00	0.01	0.00	0.01	0.02	0.01	0.00	0.00	0.01	0.00	0.01	0.01	0.01	0.00	0.00	0.03	0.03	0.02	0.01	0.01	0.01	0.01	0.01
U	0.00	0.00	0.00	0.00	0.00	0.00	0.00	0.00	0.00	0.00	0.00	0.00	0.00	0.00	0.00	0.00	0.00	0.00	0.00	0.00	0.00	0.00	0.00	0.00	0.00
Pb	0.00	0.00	0.01	0.00	0.00	0.01	0.00	0.00	0.00	0.04	0.00	0.00	0.00	0.00	0.00	0.00	0.01	0.01	0.00	0.02	0.00	0.00	0.01	0.00	0.00
Ta/(Ta+Nb)	0.09	0.17	0.07	0.16	0.13	0.16	0.19	0.18	0.18	0.23	0.17	0.11	0.13	0.17	0.17	0.26	0.31	0.25	0.31	0.27	0.42	0.51	0.44	0.48	0.46
Mn/(Mn+Fe)	0.44	0.44	0.46	0.44	0.43	0.58	0.56	0.59	0.59	0.56	0.45	0.46	0.49	0.43	0.46	0.55	0.57	0.57	0.57	0.572	0.57	0.57	0.59	0.57	0.55

Structural formulae were calculated on the basis of 6 atoms of oxygen.
bdl: below detection limit

Table 21: U-Pb analytical data for rutile from the Puy-les-Vignes deposit.

	Concentration (ppm)			Isotope ratios			Apparent ages (Ma)							
	Pb	Th	U	$^{238}U/^{206}Pb$	err%	$^{207}Pb/^{206}Pb$	err%	$^{207}Pb/^{206}Pb$	±	$^{206}Pb/^{238}U$	±	$^{207}Pb/^{235}U$	±
Sample PLV-02-04a (type-1 rutile)													
PLV-02-04a-A-1	0.00	0.14	2.21	15.61	1.84	0.18	3.95	2664	64	400	7	970	24
PLV-02-04a-C-2	0.00	0.01	1.42	16.30	2.18	0.12	7.05	1942	121	384	8	707	35
PLV-02-04a-D-1	0.00	0.71	2.28	16.27	1.85	0.13	5.07	2145	86	385	7	769	27
PLV-02-04a-A-5	0.00	0.05	1.91	11.55	1.56	0.38	1.94	3839	29	536	8	1742	16
PLV-02-04a-C-3	0.01	1.27	3.83	12.82	1.46	0.30	1.72	3474	26	484	7	1465	14
PLV-02-04a-C-4	0.04	136.43	32.69	18.18	1.33	0.11	1.51	1798	27	345	4	616	8
PLV-02-04a-C-5	0.01	0.21	2.19	4.95	1.39	0.66	1.31	4649	19	1187	15	3013	14
PLV-02-04a-D-5	0.01	0.23	2.33	7.89	1.50	0.51	1.63	4277	24	769	11	2333	15
PLV-02-04a-D-6	0.00	0.13	2.07	11.41	1.49	0.39	1.76	3881	26	542	8	1775	15
Sample PLV-7574a (type-2 rutile)													
PLV-7574a-A-1	0.00	0.00	2.22	18.33	2.00	0.11	5.62	1775	99	342	7	606	25
PLV-7574a-A-2	0.00	0.00	2.11	18.16	2.03	0.11	5.14	1862	90	346	7	633	23
PLV-7574a-A-4	0.00	0.01	2.38	16.80	1.92	0.17	3.97	2569	65	373	7	891	22
PLV-7574a-A-5	0.00	0.00	2.03	16.24	2.06	0.19	4.30	2743	69	385	8	976	25
PLV-7574a-A-6	0.00	0.01	2.19	15.45	1.96	0.20	3.80	2797	61	404	8	1028	23
PLV-7574a-C-1	0.00	0.00	1.42	18.05	2.55	0.13	6.83	2055	116	348	9	688	33
PLV-7574a-C-2	0.00	0.00	1.39	15.39	2.46	0.24	5.02	3151	77	406	10	1179	32
PLV-7574a-C-3	0.00	0.00	1.52	13.94	2.24	0.30	4.00	3469	61	447	10	1399	28
PLV-7574a-C-4	0.00	0.01	2.76	15.09	1.96	0.21	3.77	2902	60	414	8	1086	24
PLV-7574a-C-5	0.00	0.00	2.68	16.42	2.07	0.21	4.10	2943	65	381	8	1047	25
PLV-7574a-C-6	0.00	0.01	2.68	13.75	1.84	0.28	3.09	3349	48	453	8	1351	22
PLV-7574a-C-8	0.00	0.00	1.87	17.51	2.28	0.14	5.27	2274	88	358	8	769	27
PLV-7574a-C-9	0.00	0.00	2.41	15.29	1.93	0.21	3.61	2896	57	408	8	1075	23
PLV-7574a-C-10	0.00	0.00	2.55	14.74	2.08	0.21	4.02	2926	64	423	9	1112	26
PLV-7574a-C-11	0.00	0.02	1.39	10.93	2.26	0.43	3.54	4005	52	564	12	1881	27

Table 21: Continued.

	Concentration (ppm)			Isotope ratios				Apparent ages (Ma)					
	Pb	Th	U	$^{238}U/^{206}Pb$	err%	$^{207}Pb/^{206}Pb$	err%	$^{207}Pb/^{206}Pb$	±	$^{206}Pb/^{238}U$	±	$^{207}Pb/^{235}U$	±
Sample PLV-02-17 (type-3 rutile)													
PLV-02-17-A-1	0.00	0.07	1.05	11.04	2.17	0.37	3.68	3796	55	559	12	1756	28
PLV-02-17-A-2	0.01	0.24	0.51	4.10	1.95	0.68	2.46	4691	35	1408	25	3224	21
PLV-02-17-A-3	0.00	0.10	0.96	7.20	1.70	0.53	2.07	4340	30	839	13	2457	18
PLV-02-17-A-4	0.01	0.25	1.05	2.89	1.58	0.73	1.63	4797	23	1915	26	3638	16
PLV-02-17-A-5	0.01	0.17	1.12	4.59	1.48	0.67	1.50	4661	21	1271	17	3094	15
PLV-02-17-A-6	0.01	0.07	1.57	3.95	2.46	0.68	3.20	4681	45	1455	32	3252	27
PLV-02-17-A-7	0.67	0.56	2.18	0.12	1.35	0.85	1.05	5016	15		77	6971	14
PLV-02-28b (type-4 rutile)													
PLV-02-28b-A-1	0.00	0.26	6.28	18.06	1.73	0.09	4.55	1384	85	347	6	522	18
PLV-02-28b-B-1	0.02	0.62	6.87	9.87	1.49	0.43	1.83	4032	27	622	9	1985	15
PLV-02-28b-C-1	0.01	0.02	5.96	14.55	1.64	0.26	2.59	3217	40	429	7	1248	18
PLV-02-28b-A-2	0.00	0.02	6.74	18.63	1.77	0.12	4.07	1940	71	337	6	641	19
PLV-02-28b-A-3	0.01	0.03	8.01	17.66	1.64	0.14	3.28	2229	56	355	6	751	17
PLV-02-28b-A-4	0.01	0.25	7.74	15.23	1.63	0.22	2.69	2965	43	410	6	1106	17
PLV-02-28b-B-2	0.03	0.54	8.64	7.03	1.45	0.54	1.63	4358	24	858	12	2491	15
PLV-02-28b-B-3	0.01	0.38	5.25	12.29	1.71	0.33	2.56	3630	39	504	8	1578	19
PLV-02-28b-B-4	0.01	0.35	7.88	12.12	1.58	0.35	2.15	3716	32	511	8	1635	17
PLV-02-28b-A-5	0.01	0.24	6.68	11.78	1.59	0.35	2.12	3695	32	525	8	1647	17
PLV-02-28b-C-3	0.00	0.03	5.85	17.14	1.59	0.12	3.16	2007	55	366	6	700	16

Table 22: $^{40}Ar/^{39}Ar$ analytical data for micas and adularia from the Puy-les-Vignes deposit.

Samples	Relative isotopic abundances (fAmps)* ^{40}Ar	± (1σ)	^{39}Ar	± (1σ)	^{38}Ar	± (1σ)	^{37}Ar	± (1σ)	^{36}Ar	± (1σ)	Ca/K	± (1σ)	Cl/K	± (1σ)	$^{40}Ar^*/^{39}Ar_{(K)}$	± (1σ)	$^{40}Ar^*$ (%)	Apparent age Age (Ma)	± (1σ)	MSWD
PLV-02-01a: muscovite from greisenized gneiss																				
Spot 1	119.293	0.074	2.718	0.056	0.043	0.029	-0.014	0.026	0.001	0.001	-0.067	0.124	0.010	0.032	43.710	0.922	99.65	318.5	6.2	
Spot 2	130.569	0.075	2.924	0.062	0.048	0.032	0.068	0.027	0.000	0.001	0.298	0.119	0.013	0.033	44.627	0.974	100.01	324.6	6.5	
Spot 3	139.169	0.079	3.117	0.063	0.071	0.030	-0.037	0.028	0.003	0.001	-0.153	0.115	0.030	0.028	44.341	0.917	99.39	322.7	6.1	
Spot 4	113.688	0.067	2.502	0.061	0.061	0.031	0.039	0.024	0.004	0.001	0.199	0.125	0.034	0.036	44.884	1.126	98.86	326.3	7.5	
Spot 5	134.910	0.073	3.133	0.065	0.001	0.032	0.069	0.025	0.000	0.001	0.284	0.105	-0.034	0.030	43.055	0.910	100.05	314.1	6.1	
Spot 6	128.858	0.072	3.044	0.063	0.050	0.033	0.023	0.029	0.001	0.001	0.097	0.124	0.012	0.031	42.166	0.901	99.69	308.2	6.1	
							Fluence J: 0.0044174 ± 2.45E-6								**Integrated age (spots 1-5):**			**321.1**	**2.8**	**0.67**
PLV-02-10: muscovite from greisenized granite																				
Spot 1	93.078	0.071	1.994	0.066	0.000	0.029	-0.052	0.030	0.001	0.001	-0.338	0.198	-0.036	0.043	46.508	1.579	99.70	337.7	10.5	
Spot 2	127.351	0.078	2.747	0.058	-0.043	0.030	-0.020	0.027	0.000	0.001	-0.095	0.128	-0.080	0.032	46.276	1.007	99.91	336.1	6.7	
Spot 3	188.942	0.077	4.146	0.061	0.079	0.031	-0.049	0.027	0.013	0.001	-0.156	0.086	0.018	0.022	44.620	0.676	97.99	325.1	4.5	
Spot 4	194.979	0.087	4.314	0.063	0.080	0.032	0.050	0.027	0.013	0.001	0.151	0.081	0.017	0.022	44.251	0.667	97.98	322.7	4.5	
Spot 5	178.944	0.085	3.869	0.062	0.013	0.031	-0.049	0.028	0.011	0.001	-0.168	0.097	-0.027	0.023	45.402	0.745	98.24	330.3	5.0	
Spot 6	99.288	0.077	2.201	0.059	0.009	0.028	-0.005	0.028	0.027	0.001	-0.031	0.167	-0.030	0.037	41.486	1.157	92.02	304.1	7.8	
							Fluence J: 0.0044259 ± 1.99E-6								**Integrated age (spots 1-5):**			**327.5**	**2.4**	**1.12**
PV1: muscovite from quartz-wolframite veins																				
Spot 1	110.547	0.078	2.602	0.065	0.033	0.029	0.002	0.028	0.001	0.001	0.006	0.111	0.001	0.033	42.325	1.090	99.66	310.3	7.3	
Spot 2	127.717	0.078	2.947	0.064	0.102	0.031	-0.014	0.026	0.003	0.001	-0.048	0.092	0.064	0.031	42.971	0.969	99.22	314.6	6.5	
Spot 3	131.603	0.078	2.926	0.056	0.041	0.029	-0.042	0.028	0.001	0.001	-0.158	0.105	0.005	0.029	44.880	0.882	99.84	327.4	5.9	
Spot 4	136.508	0.081	2.925	0.061	0.033	0.029	-0.058	0.026	0.001	0.001	-0.218	0.100	-0.003	0.029	46.535	0.995	99.80	338.4	6.6	
Spot 5	138.278	0.072	3.127	0.065	0.067	0.032	-0.028	0.027	-0.001	0.001	-0.097	0.096	0.026	0.030	44.254	0.940	100.15	323.2	6.3	
Spot 6	120.527	0.074	2.718	0.069	-0.008	0.031	-0.051	0.028	0.002	0.001	-0.207	0.114	-0.044	0.034	44.131	1.152	99.60	322.4	7.7	
Spot 7	130.326	0.077	2.935	0.066	0.093	0.032	-0.015	0.030	0.005	0.001	-0.055	0.111	0.055	0.032	43.827	1.009	98.75	320.4	6.8	
Spot 8	130.522	0.089	2.864	0.066	0.034	0.034	0.014	0.027	0.002	0.001	0.052	0.103	-0.001	0.035	45.374	1.070	99.62	330.7	7.1	
							Fluence J: 0.0044338 ± 1.54E-6								**Integrated age (spots 1-3;5-7):**			**320.0**	**2.7**	**1.10**
PV2c: muscovite selvage from quartz vein																				
Spot 1	132.381	0.076	2.885	0.060	0.021	0.029	0.040	0.028	-0.001	0.001	0.152	0.107	-0.014	0.030	46.021	0.992	100.34	335.0	6.6	
Spot 2	122.231	0.082	2.598	0.063	0.040	0.031	0.005	0.026	-0.001	0.001	0.019	0.114	0.009	0.035	47.133	1.168	100.26	342.4	7.7	
Spot 3	119.104	0.077	2.605	0.063	0.127	0.029	-0.010	0.029	0.000	0.001	-0.044	0.125	0.106	0.033	45.667	1.134	99.93	332.6	7.5	
Spot 4	119.433	0.077	2.596	0.058	-0.004	0.028	0.009	0.028	0.000	0.001	0.038	0.119	-0.040	0.032	45.983	1.048	100.01	334.7	7.0	
Spot 5	138.385	0.084	2.912	0.061	0.044	0.030	-0.017	0.027	0.007	0.001	-0.065	0.106	0.007	0.030	46.749	1.008	98.44	339.8	6.7	
Spot 6	126.196	0.077	2.815	0.064	0.046	0.032	-0.037	0.027	0.001	0.001	-0.146	0.109	0.012	0.033	44.738	1.046	99.87	326.4	7.0	
							Fluence J: 0.0044336 ± 1.530E-6								**Integrated age (spots 1-6):**			**335.0**	**3.0**	**0.60**

* Corrected for blank, mass discrimination, and radioactive decay
Sensitivity: 6.312E-17 ± 1.047E-18 (mol/fAmp)

Table 22: Continued.

Samples	Relative isotopic abundances (fAmps)* ^{40}Ar	± (1σ)	^{39}Ar	± (1σ)	^{38}Ar	± (1σ)	^{37}Ar	± (1σ)	^{36}Ar	± (1σ)	Ca/K	± (1σ)	Cl/K	± (1σ)	$^{40}Ar^*/^{39}Ar_{(K)}$	± (1σ)	$^{40}Ar^*$ (%)	Apparent age Age (Ma)	± (1σ)	MSWD
PLV-02-02b: muscovite from rare-metal aplo-pegmatite																				
Spot 1	122.597	0.074	2.891	0.067	0.046	0.030	0.040	0.026	0.001	0.001	0.184	0.123	0.011	0.031	42.284	1.010	99.77	309.7	6.8	
Spot 2	124.771	0.083	2.821	0.065	0.047	0.032	-0.057	0.030	0.002	0.001	-0.272	0.142	0.012	0.034	43.950	1.046	99.45	320.8	7.0	
Spot 3	127.648	0.072	2.870	0.059	0.049	0.029	-0.014	0.028	0.001	0.001	-0.064	0.129	0.013	0.030	44.331	0.934	99.74	323.4	6.2	
Spot 4	121.773	0.077	2.890	0.067	-0.019	0.028	0.010	0.028	0.002	0.001	0.050	0.140	-0.054	0.028	41.931	1.005	99.60	307.3	6.8	
Spot 5	120.231	0.070	2.811	0.058	0.005	0.029	0.030	0.028	0.009	0.001	0.152	0.144	-0.032	0.030	41.816	0.886	97.84	306.5	6.0	
Spot 6	124.828	0.082	2.904	0.063	-0.003	0.028	0.052	0.027	-0.001	0.001	0.263	0.139	-0.038	0.029	43.057	0.957	100.24	314.9	6.4	
Spot 7	122.917	0.072	3.067	0.069	0.029	0.032	-0.026	0.027	0.003	0.001	-0.124	0.130	-0.008	0.030	39.769	0.922	99.32	292.7	6.3	
							Fluence J: 0.0044286 ± 1.65E-6								**Integrated age (spots 1-6):**			**314.0**	**2.6**	**1.28**
PV-92-7: muscovite from leucogranite																				
Spot 1	118.123	0.080	2.583	0.060	0.044	0.034	-0.065	0.027	0.005	0.001	-0.287	0.120	0.013	0.039	45.110	1.074	98.70	328.0	7.1	
Spot 2	120.757	0.073	2.769	0.062	0.066	0.032	-0.013	0.027	0.005	0.001	-0.052	0.111	0.033	0.034	43.078	0.991	98.85	314.4	6.6	
Spot 3	124.290	0.078	2.825	0.061	0.028	0.031	0.001	0.026	0.001	0.001	0.004	0.104	-0.007	0.032	43.861	0.969	99.75	319.7	6.5	
Spot 4	125.860	0.075	2.779	0.061	0.085	0.030	0.034	0.027	0.007	0.001	0.140	0.114	0.052	0.032	44.559	1.005	98.46	324.3	6.7	
Spot 5	124.579	0.079	2.680	0.060	0.037	0.029	0.038	0.027	0.002	0.001	0.164	0.117	0.004	0.032	46.283	1.070	99.63	335.8	7.1	
Spot 6	114.466	0.072	2.462	0.064	0.165	0.031	-0.036	0.028	0.002	0.001	-0.167	0.133	0.158	0.037	46.228	1.229	99.50	335.4	8.1	
Spot 7	140.712	0.077	2.822	0.062	0.029	0.030	-0.053	0.026	0.048	0.001	-0.219	0.109	-0.015	0.031	44.783	1.020	89.88	325.8	6.8	
Spot 8	128.764	0.078	2.955	0.067	-0.025	0.029	0.027	0.023	0.003	0.001	0.108	0.092	-0.060	0.029	43.286	1.006	99.40	315.8	6.7	
Spot 9	121.731	0.082	2.757	0.058	0.088	0.030	0.025	0.029	0.002	0.001	0.106	0.123	0.057	0.033	43.928	0.955	99.54	320.1	6.4	
Spot 10	90.648	0.078	1.943	0.065	0.121	0.028	-0.012	0.027	0.003	0.001	-0.091	0.206	0.144	0.043	46.182	1.582	99.08	335.1	10.5	
Spot 11	141.845	0.074	3.131	0.065	0.087	0.030	0.024	0.028	0.002	0.001	0.110	0.131	0.045	0.028	45.134	0.963	99.68	328.1	6.4	
Spot 12	117.096	0.081	2.783	0.062	-0.004	0.030	-0.069	0.028	0.001	0.001	-0.364	0.147	-0.039	0.032	41.871	0.958	99.59	306.3	6.4	
							Fluence J: 0.0044198 ± 1.38E-6								**Integrated age (spots 1-11):**			**324.7**	**2.1**	**1.10**
PV-92-17: biotite from lamprophyre																				
Spot 1	93.822	0.074	2.084	0.063	0.012	0.032	-0.017	0.030	0.005	0.001	-0.117	0.206	-0.020	0.046	44.283	1.374	98.46	324.8	9.2	
Spot 2	61.277	0.071	1.276	0.061	-0.047	0.031	0.058	0.026	0.001	0.001	0.659	0.301	-0.143	0.072	47.673	2.358	99.34	347.4	15.6	
Spot 3	60.043	0.069	1.306	0.061	0.071	0.029	-0.052	0.027	0.001	0.001	-0.574	0.307	0.121	0.066	45.652	2.192	99.39	333.9	14.6	
							Fluence J: 0.0044538 ± 1.25E-6								**Integrated age (spots 1-3):**			**331.1**	**7.0**	**0.74**
PLV-02-13b: adularia from late hydrothermal breccia																				
Spot 1	238.730	0.085	4.923	0.061	0.063	0.028	0.009	0.028	0.122	0.002	0.022	0.072	-0.012	0.017	41.163	0.532	84.95	301.4	3.6	
Spot 2	198.688	0.079	4.522	0.064	0.019	0.031	-0.056	0.027	0.023	0.001	-0.156	0.074	-0.026	0.020	42.423	0.622	96.63	309.9	4.2	
Spot 3	262.817	0.083	5.307	0.060	0.110	0.029	-0.015	0.026	0.157	0.002	-0.037	0.063	0.009	0.016	40.742	0.484	82.33	298.6	3.3	
Spot 4	220.511	0.083	4.853	0.062	0.066	0.030	-0.047	0.027	0.065	0.001	-0.122	0.071	-0.003	0.018	41.454	0.549	91.29	303.4	3.7	
Spot 5	240.797	0.083	5.253	0.060	0.155	0.030	0.029	0.027	0.096	0.002	0.069	0.064	0.040	0.017	40.409	0.478	88.21	296.3	3.2	
Spot 6	244.212	0.093	5.099	0.065	0.091	0.032	-0.002	0.027	0.106	0.002	-0.006	0.066	0.005	0.018	41.746	0.552	87.22	305.4	3.7	
							Fluence J: 0.0044178 ± 2.40E-6								**Integrated age (spots 1-6):**			**301.3**	**1.5**	**2.02**

* Corrected for blank, mass discrimination, and radioactive decay
Sensitivity: 6.312E-17 ± 1.047E-18 (mol/fAmp)

Chapter 5: Nb-Ti-Y-HREE-W-U oxides with uncommon composition associated with the tungsten mineralization in the Puy-les-Vignes deposit (Massif Central, France): evidence for rare-metal mobilization by late hydrothermal fluids with a peralkaline signature

Matthieu Harlaux[1*], Christian Marignac[1], Michel Cuney[1], Rémi Magott[2] and Julien Mercadier[1]

Article published in *The Canadian Mineralogist,* 53, 653-672.

1: Université de Lorraine, CNRS, CREGU, GeoRessources, 54506 Vandœuvre-lès-Nancy, France.

2: Université de Franche-Comté, CNRS, Chrono-environnement, 25000 Besançon, France.

* Corresponding author: matthieu.harlaux@univ-lorraine.fr

Abstract

The Puy-les-Vignes deposit, located in the northwestern part of the French Massif Central, is an original occurrence in the West European Variscan belt of a hydrothermal tungsten mineralization associated with a breccia pipe structure. The late stage of the mineralization consists of a mineral paragenesis composed of zircon, xenotime, monazite, Nb-Fe-W rutile and Nb-Ti-Y-HREE-W-U oxides (hereafter referred to as NTox) within an adularia-tourmaline-chlorite matrix. This study is focused on these rare-metal oxides, which display complex internal textures and uncommon chemical compositions with variable concentrations in Nb, Ti, Y, HREE and W, not described until now. They are also characterized by low microprobe totals (76 to 95%), together with the presence of OH^- groups within the crystallographic structure as detected by FTIR spectroscopy, which is interpreted as the result from alteration, such as hydratation and/or metamictization. The crystallochemical study shows that these crystals appear as a complex multi-polar solid solution, involving a chemical mixing between two groups of binary solid solutions: a first group of anatase - columbite solid solution and a second group of euxenite-(Y) - columbite solid solution. Interpretation of their internal texture and their chemistry suggest that the NTox were formed during a multi-

phase crystallization in an open system by the mixing between two different hydrothermal fluids: a first fluid L_1 enriched in Ti>Nb, Fe, W, with the same geochemical signature as the main mineralization, and a second fluid L_2 enriched in Nb>Ti, Fe, Y, REE, W, with a geochemical signature clearly contrasting with the former and coeval with the crystallization of adularia, xenotime, monazite, zircon and rutile. This mineral paragenesis is characterized by a P, Y, HREE, Nb>Ta, Ti, Zr, U geochemical signature, typical of the rare-metal peralkaline magmatism, thus suggesting the rare-metal mobilization by late hydrothermal fluids with a peralkaline signature, likely derived from an unknown source at depth (e.g. NYF pegmatites or related granite), during the late metallogenic stages at Puy-les-Vignes.

Keywords:

Nb-Ti-Y-HREE-W-U oxides; rare-metals; tungsten mineralization; hydrothermal fluids; Puy-les-Vignes; French Massif Central; Variscan belt.

1. Introduction

The oxides of Nb-Ta-Ti-Y-REE-W have drawn considerable attention since several years because of their importance in retracing the geochemical evolution of rare-metal magmas (e.g., Johan and Johan, 1994; Belkasmi et al., 2000; Aurisicchio et al., 2001, 2002; Breiter et al., 2007; Škoda and Novák, 2007; Pieczka, 2010). These oxides are generally found in rare-metal granites or pegmatites and consist of many mineral groups with high concentrations of high-field-strength elements (HFSE) of which the principals belong to the columbite-tantalite, euxenite, aeschynite, pyrochlore, samarskite and fergusonite groups (Černý and Ercit, 1989; Ercit, 2005). They are generally characterized by complex crystal chemistry and often display metamictization due to high U and/or Th contents, which complicates their study and their identification (e.g., Graham and Thornber, 1974; Ewing 1975a,b; Bonazzi and Menchetti, 1999; Tomašić et al., 2004).

The vast majority of the worldwide occurrences of Nb-Ta-Ti-Y-REE-W oxides are of magmatic origin, either in evolved granites and pegmatites (e.g., Wang et al., 1997; Aurisicchio et al., 2001, 2002; Černý and Ercit, 2005; De Vito et al., 2006; Škoda and Novák, 2007; Van Lichtervelde et al., 2007; Pieczka, 2010; Llorens and Moro, 2012), or in carbonatites (e.g., Nasraoui and Bilal, 2000; Bermanec et al., 2008; Cordeiro et al., 2011; Melgarejo et al., 2012; Chakhmouradian et al., 2015), or in alkaline to peralkaline granites and syenites (e.g., Salvy and Williams-Jones, 2005; Estrade et al., 2014) or even in kimberlites (e.g., Sharygin et al., 2009). Hydrothermal occurrences of these oxides are rare and mainly found in tourmaline-quartz veins and/or breccias (e.g., Rice et al., 1998; Gama 2000; Müller and Halls, 2005; Lerouge et al., 2007) or in altered peralkaline granites and syenites (e.g., Salvi and Williams-Jones, 2006).

A new hydrothermal occurrence has been discovered in the Puy-les-Vignes deposit (Massif Central, France), where Nb-Ti-Y-HREE-W-U oxides are associated with a tungsten mineralization related to a breccia pipe structure. These oxides are late minerals in the paragenetic sequence and display uncommon chemical compositions, which do not correspond to any known mineral until now. This paper aims to provide petrographic and geochemical data on these uncommon Nb-Ti-Y-HREE-W oxides (hereafter referred to as NTox) in the Puy-les-Vignes tungsten deposit.

2. Geological setting

The Puy-les-Vignes deposit is located in the northwestern part of the French Massif Central (FMC) in the Limousin area, which consists of a stack of metamorphic nappes emplaced during the continental collision between Gondwana and Laurussia through the Upper Paleozoic (Faure et al., 2009 and references therein). In France, the FMC is the largest area where Variscan terranes are exposed and has an important economic potential for the W-Sn and rare-metal deposits (Marignac and Cuney, 1999; Cuney et al., 2002; Bouchot et al., 2005). The Puy-les-Vignes deposit represents an original occurrence in the West European Variscan belt of a hydrothermal tungsten mineralization associated with a breccia pipe structure, characterized by the polymetallic W-Bi-Cu-Fe-As-(Au) association. The deposit was mined underground until 1957; it produced around 4,000 t WO_3 with an average grade at 0.5% WO_3 and was the second ranking tungsten mine in France during the XX^{th} century. Only half the breccia pipe was mined, where the workings went down to 300 m depth, but the total vertical and lateral extension of the deposit has never been recognized and it is likely that an economic potential for tungsten is still present (Mouthier, 2005).

The tungsten mineralization at Puy-les-Vignes is contained in a hydrothermal breccia pipe-type deposit, hosted in the biotite-sillimanite gneisses of the Lower Gneiss Unit, the intermediate nappe in the three nappes pile of the FMC (Ledru et al., 1989). The deposit is located 20 km south of the St-Sylvestre leucogranitic complex (324±4 Ma, Holliger et al., 1986) and 15 km west of the Millevaches leucogranitic complex (337±4 Ma to 323±4 Ma, Rolin et al., 2014), both Limousin-type peraluminous granites (AKL type of Stussi, 1989). It is in the close vicinity of the Auriat granite (324±1 Ma, Gebauer et al., 1981) and the Aureil granite (346±14 Ma, Duthou, 1978), which are respectively Limousin-type peraluminous (AKL type) and Guéret-type peraluminous (AKG type) granites (Stussi, 1989) (Fig. 69). The breccia pipe has an oval shape with dimensions 80 x 340 m at surface and is cut in two parts by a N130°E sinistral strike-slip fault with a 120 m horizontal displacement (Weppe, 1951). It is possibly located at the apex of a hidden granite, as already described for other breccia pipes by Sillitoe (1985). The country rocks are mainly migmatitic gneisses, but the pipe is known to overprint two NE-trending dykes of leucogranite and lamprophyre. The pipe has been interpreted by Weppe (1951, 1958) as a collapse breccia, which has evolved in several steps. In a first step, collapsing leads to a matrix-supported heterolithic and heterometric breccia, with metric to centimetric clasts of the enclosing gneisses and granites in a quartz matrix. The clasts are angular to sub-angular; they are greisenized and are systematically rimmed by an

aureole of tourmalinization (tourmaline ± quartz), of which the thickness varies from a few millimeters to ten centimeters, until up to the complete tourmalinization of the fragments. The following steps lead to the formation of quartz-wolframite-sulphides veins, some delineating the breccia to country rocks boundaries ("gaine"), the others forming planar-curved veins ("plateures") within the former breccia. The economic mineralization was hosted in these veins with grades ranging from 0.2 to 2% WO_3, but the whole breccia is a low-grade potential ore for tungsten since mining tests led to average grade at 0.5% WO_3 (Mouthier, 2005). The mineralization was dated at 323±0.9 Ma by $^{40}Ar/^{39}Ar$ on a muscovite associated with the wolframite (Cuney et al., 2002) and would therefore be coeval with the AKL-type leucogranites.

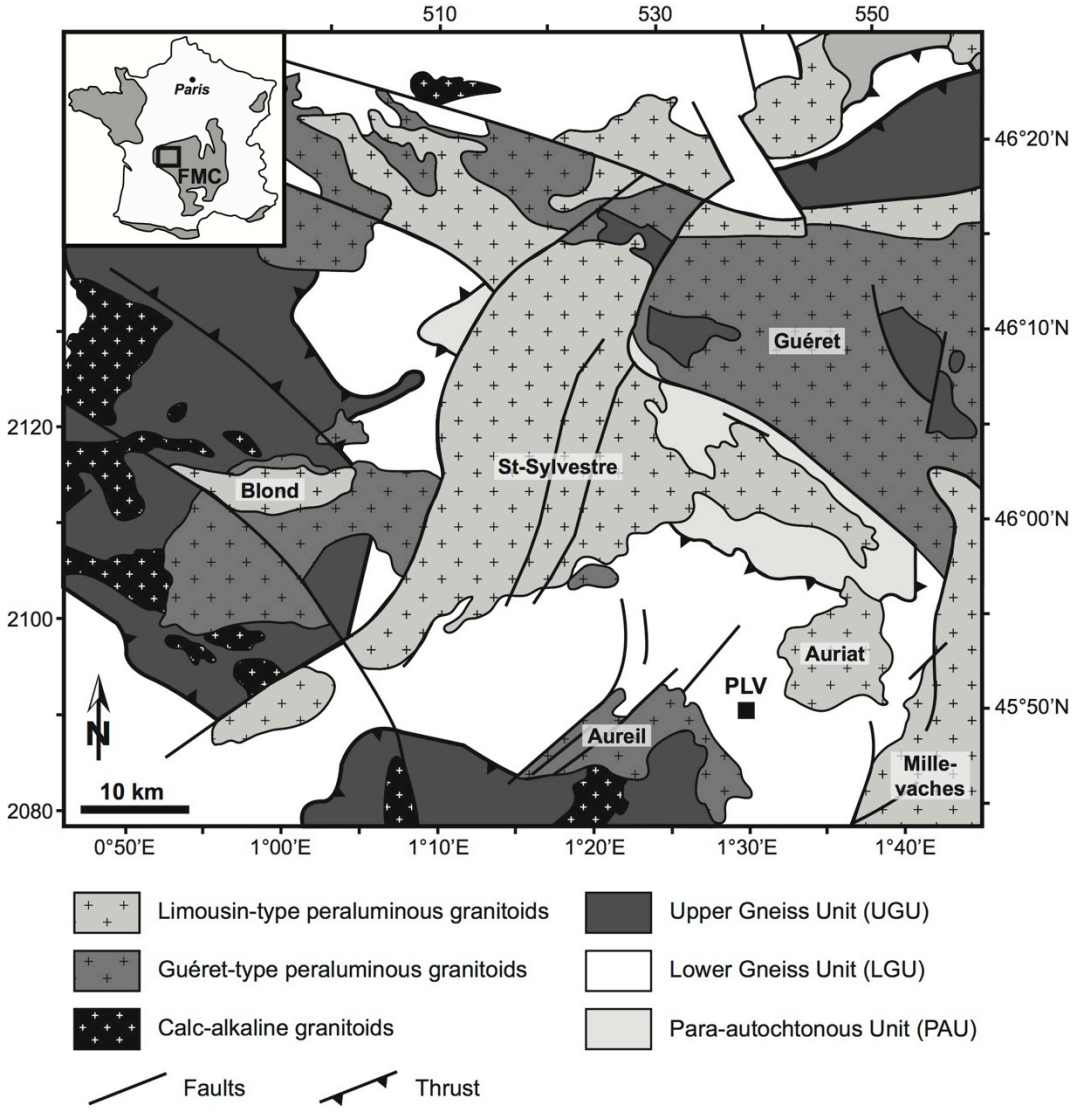

Fig. 69: Location and geological setting of the Puy-les-Vignes (PLV) deposit in the Limousin area, French Massif Central (FMC).

According to Alikouss (1993) and to new petrographic observations, the primary paragenetic sequence of the Puy-les-Vignes deposit can be divided into six main stages: (i) brecciation and early hydrothermal alteration of the country rocks characterized by a first step of pervasive greisenization, forming a quartz-muscovite assemblage, followed by an intense diffuse tourmalinization of the breccia fragments; (ii) tungsten mineralization stage associated with hydraulic fracturing and formation of quartz-wolframite-arsenopyrite veins; the wolframite forms euhedral prismatic crystals, millimetric to centimetric in size, which are partially replaced by ferberite 1 along cracks or crystal borders; scheelite occurs lately by replacement of the ferberitised wolframite and is itself replaced by ferberite 2 (so-called "reinite"); (iii) base metals sulphides (mainly pyrite, chalcopyrite, enargite and sphalerite) stage; (iv) a late hydrothermal stage, associated with the formation of a crackle-breccia with a tourmalinite-adularia-chlorite matrix, together with a series of accessory minerals comprising zircon, xenotime, monazite, Nb-Fe-W-rich rutile and the NTox (Fig. 70); (v) minor and discrete Bi-Au stage associated with the deposition of native bismuth and bismuthinite, with electrum and Bi-Ag-Se-Te sulphosalts in microcavity and microcrack fillings; (vi) a scorodite-illite association likely represent low temperature alteration of the early sulphides. Finally, supergene alteration affects the deposit forming secondary minerals, such as tungstite and Fe-oxides.

3. Materials and analytic methods

The Puy-les-Vignes mine is closed since 1957 and the underground workings are no more accessible. Nevertheless, access to old samples collections coming directly from the mine when it was still operating, completed by a sampling of surface outcrop and mining dumps, gives us a large set of representative samples, both of the ore body and the host-rock. We present here the results obtained on the NTox associated with the stage (iv) of the paragenetic sequence of the deposit (Fig. 70). All analyses were performed at the GeoRessources laboratory (Université de Lorraine, Vandœuvre-lès-Nancy, France).

Mineralogical and textural observations were carried out using a Hitachi S-4800 scanning electron microscope (SEM) equipped with an EDS spectrometer and a Jeol J7600F scanning electron microscope equipped with a SDD-type EDS spectrometer coupled to an Oxford Wave WDS spectrometer. Backscattered electron (BSE) images were obtained on polished thin sections with an acceleration voltage of 15 kV.

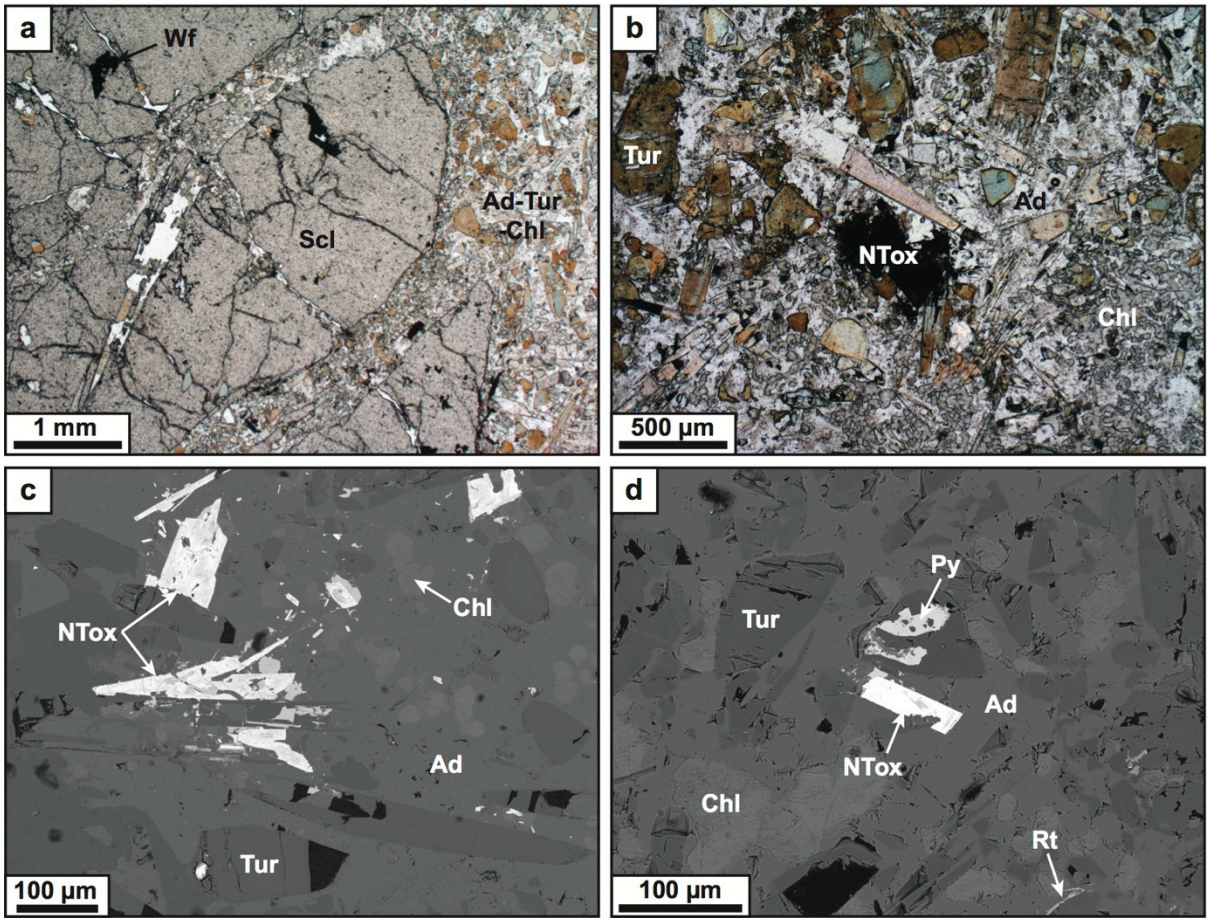

Fig. 70: Microphotographs in transmitted light (a, b) and BSE images (c, d) of the late hydrothermal paragenesis (stage (iv)) of the Puy-les-Vignes deposit. (a) Scheelite (Scl) replacing primary wolframite (Wf) and brecciated by a tourmaline (Tur), adularia (Ad) and chlorite (Chl) matrix. (b) Nb-Ti-Y-HREE-W-U oxide (NTox) associated with the brecciated tourmaline within the matrix of adularia and chlorite. (c) Fractured NTox crystals within the adularia, tourmaline and chlorite matrix. (d) Late pyrite (Py) and Nb-Fe-W-rich rutile (Rt) associated with the NTox.

Chemical analyses were obtained by an electron microprobe (EMP) Cameca SX100 with acceleration voltage and beam current of 20 kV and 20 nA respectively and with a beam diameter of 1 µm. The following elements were analyzed using WDS spectrometers: MnKα, FeKα, WLα, NdLα, GdLβ, TbLα, DyLα, HoLα, ErLα and YbLα on LiF; SiKα, FKα, YLα and NbLα on TAP; CaKα and CeLα on PET; TiKα, TaMα, ThMα and UMα on LPET. The elements Sn, La, Pr, Sm, Eu, Tm and Lu were not analyzed since preliminary checks showed undetectable concentrations. Element peaks and backgrounds were measured with counting times of 10 s each. Reference standards used are: $MnTiO_3$ for Mn and Ti, Fe_2O_3 for Fe, metallic W for W, monazite for Nd and Ce, $GdRu_2Ge_2$ for Gd, TbTiGe for Tb, $DyRu_2Ge_2$ for Dy, $HoRu_2Ge_2$ for Ho, $ErNi_2Si_2$ for Er, Yb_2S_3 for Yb, albite for Si, topaze for F, YPO_4 for Y, $LiNbO_3$ for Nb, andradite for Ca, $LiTaO_3$ for Ta, ThO_2 for Th and UO_2 for U. Detection limits

calculated are: 1040 ppm for Mn, 1035 ppm for Fe, 3660 ppm for W, 2780 ppm for Nd, 5850 ppm for Gd, 2370 ppm for Tb, 7400 ppm for Dy, 2620 ppm for Ho, 2600 ppm for Er, 2600 ppm for Yb, 400 ppm for Si, 10300 ppm for F, 1100 ppm for Y, 1650 ppm for Nb, 520 ppm for Ca, 1860 ppm for Ce, 320 ppm for Ti, 2500 ppm for Ta, 1400 ppm for Th and 1540 ppm for U. We present here the results of around 120 in situ EMP analyses obtained on different single crystals. Major and minor elements are expressed in weight per cent oxides (wt.%).

The Raman spectra were recorded on polished thin sections using a Horiba Jobin-Yvon LabRAM HR spectrometer equipped with a 600 $gr.mm^{-1}$ grating and an Edge filter. The confocal hole aperture is of 500 µm, the slit aperture is of 100 µm. The excitation beam is provided by a Stabilite 2017 Ar^{+} laser (Spectra Physics, Newport Corporation) at 514.53 nm and a power of 200 mW, focused on the sample using x20 and x100 objectives equipped on an Olympus BX40 microscope. The laser beam diameter is around 1 µm. Acquisition time and numbers of accumulation are chosen in a way to optimize the signal-to-noise ratio (S/N), ideally lower than 1 %.

The infrared spectra were recorded on polished thin sections in transmission mode using a Bruker Equinox 55 Fourier transform infrared (FTIR) spectrometer coupled to a Bruker A590 microscope. The microscope is equipped with a MCT (mercury cadmium telluride) detector with a 100 µm diameter window cooled at 77 K. The FTIR spectra were obtained in the mid-infrared region with a 2 cm^{-1} spectral resolution. The beam diameter was fixed at 30 µm with X15 objective magnification. All FTIR spectra were corrected for the glass and resin background signals.

4. Results

4.1. Morphology and internal textures

The NTox form sub-euhedral crystals disseminated within the adularia-chlorite-tourmaline association and range from 10 µm to 400 µm in size with a medium size around 100 µm. They are light to dark brown in plane polarized transmitted light and light to medium grey in reflected light. The crystals display a complex internal texture in BSE imagery, characterized at first glance by a strong zoning at the micrometre scale. The largest crystals are complex, displaying growth twins and synneusis, with the development of new growth zones around the clusters (Fig. 71a,b). Micrometre-scale growth bands are grouped in sequences (mesobands), from a few to several tens of micrometers in width, showing intense

oscillatory zoning (Fig. 71c) and locally sector zoning (Fig. 71f). A general organization scheme of these crystals may be proposed using five components:

(i) dark grey zones or bands, often forming the core of the crystals (Fig. 71a), but recurrently occurring in the growth process;

(ii) medium grey mesobands, which surround the dark cores when they exist, or follow the dark mesobands, and constitute the main growth stage of the crystals (Fig. 71c); microprobe analysis reveals the existence of two group of such mesobands (type I and II), that alternate during the crystal growth;

(iii) bright interstitial platelets, discontinuous and micrometric in width, are pseudo-periodically intercalated within the growth bands; observed at high magnification, they tend to display a granular texture, indicating that they in fact consist in nanocrystal aggregates (Fig. 71d); they locally tend to overprint the regular zoning;

(iv) bright external overgrowths, of which the thickness exceeds rarely 10 μm, succeed to a strong corrosion episode, which is sometimes related to fracturation with infilling by a late anhedral pyrite (Fig. 71a,e);

(v) medium grey invasive phases, with clear-cut boundaries, but apparently anhedral, and devoid of internal structures, overprint the zoning in many places inside the crystals; they seem to grow either along interfaces between growth bands or along twin plans or starting from intracrystalline microcracks (Fig. 71f,g) that never reach the external crystal boundaries; they are never observed on the crystal peripheries; they may be interpreted as "primary alteration" phases sensu Lumpkin and Ewing (1992, 1995, 1996).

In addition, small inclusions (< 10 μm) of a W-rich Fe-columbite ($FeNb_2O_6$) are often present within the NTox structure (Fig. 71h); they are highly anhedral, with very ragged contours, excluding their interpretation as exsolution products (Okrusch et al., 2003, Klementová and Rieder, 2004). The texture could suggest that they are secondary, but owing to the fact that these phases are never observed outside the NTox, neither to distinctly invade them from the outside, they are better seen as inherited crystals. They would have been trapped during the early crystallization, and highly instable at that time, being close to full dissolution (Fig. 71h). To summarize, the NTox have a very complex internal texture resulting from multiple episodes of crystallization, marked by an initial nucleation followed by rhythmic growth stages, which alternate with corrosion stages during crystallization breaks and ends with late overgrowths.

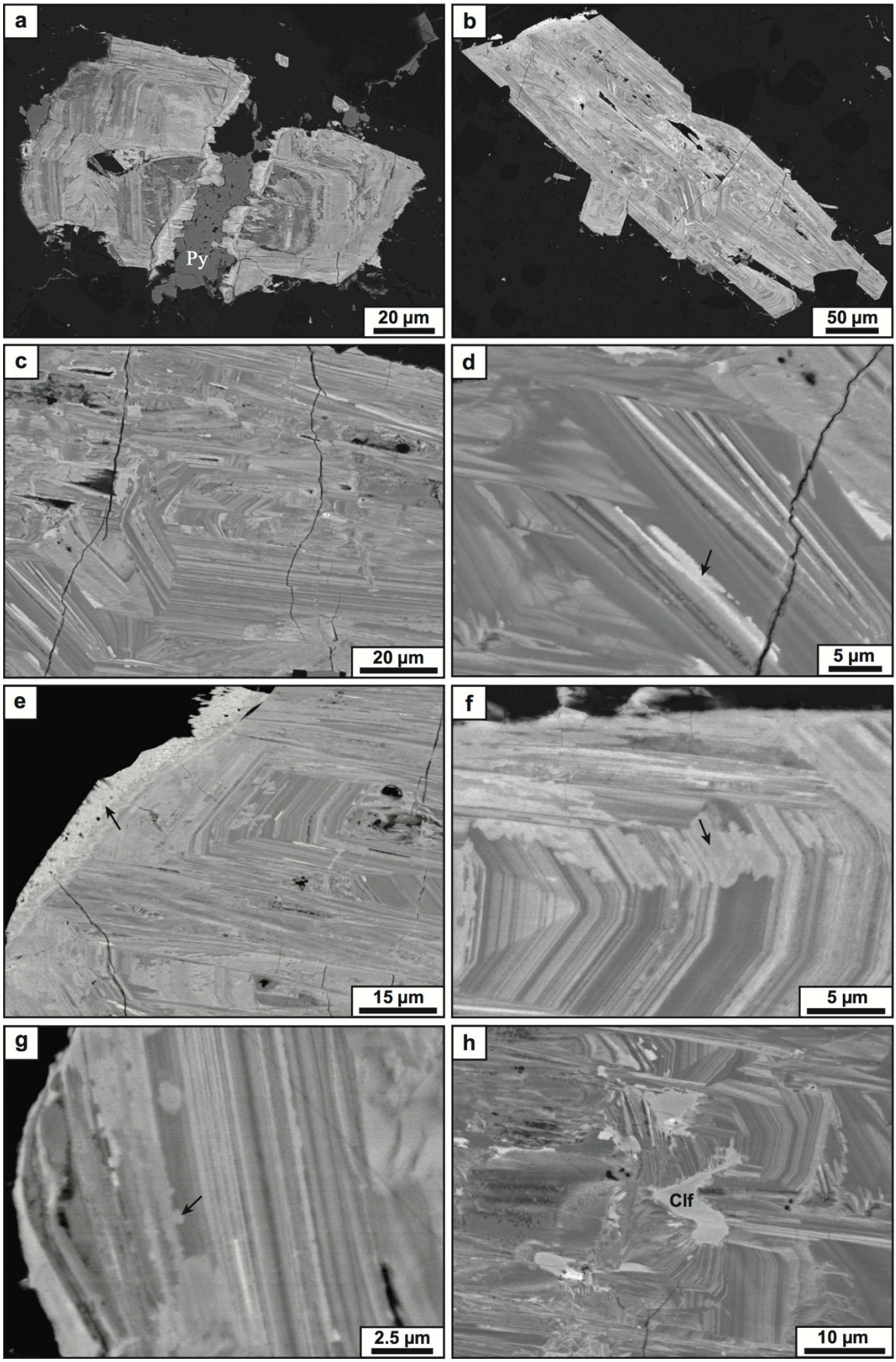

Fig. 71

Fig. 71: BSE images of the Nb-Ti-Y-HREE-W-U oxides (NTox) from Puy-les-Vignes. (a): Crystal cut by late anhedral pyrite (Py) showing a dark core (dark grey) surrounded by a zoned cortex of mesobands (medium grey) and a late external overgrowth (bright grey). The crystal shows a twinning plane in the upper part of the image. (b) Complex crystal formed by the aggregation of smaller crystals with dissolution patterns on periphery and corrosion texture within the crystalline structure. (c) Detail view of the complex internal texture marked by intense oscillatory zoning with variable crystallographic orientations. (d) Interstitial platelets (arrow) composed of nanocrystals aggregates intercalated periodically between the rhythmic growth bands. They differ from the micro-invasive phases by a brighter colour in BSE and a granular texture. (e) Late external overgrowth (arrow) developed in unconformity on the crystalline borders. (f) Invasive phase (arrow) corroding diffusely the oscillatory and sectorial zoning in the type II mesobands (observed in plane view). (g) Invasive phase (arrow) with corrosion patterns developed diffusely and irregularly between the growth planes of the type II mesobands (observed in section view). (h) Crystal of W-rich ferro-columbite (Clf) trapped within the NTox structure and surrounded by mesobands with oscillatory zoning.

4.2. Physical properties

Raman and FTIR spectra of the NTox are shown in Fig. 72 The NTox are fluorescent at all the laser wavelengths available in the laboratory (from 457 nm to 785 nm). The minimum of fluorescence is observed using the Ar^+ laser at 514.5 nm. The observed fluorescence limits the spectrum quality because of an intense background and prevents the acquisition of Raman spectra in the high wavenumber region (> 2000 cm^{-1}). Consequently, only spectra in the low wavenumber region (100-900 cm^{-1}) have been acquired. Raman spectra have been obtained for the dark cores, type I and II mesobands and external overgrowths (Fig. 72a). The Raman spectra of the previous units are poorly defined due to fluorescence but show distinct patterns, thus suggesting varying degrees of crystallinity within the NTox. The dark cores and the mesobands are characterized by a narrow peak at 150 cm^{-1} and by a broad peak at 650 cm^{-1}, which corresponds to the Ti-O bonds of anatase. The dark cores are distinguished by higher intensities compared to mesobands, indicating that their structure is likely better organised. The type I and II mesobands have both similar Raman spectra, however type II has a higher intensity peak at 150 cm^{-1} and type I presents a shoulder peak at 135 cm^{-1}, suggesting that type I and II differ by their crystallinity degree. The external overgrowths have clearly a different Raman spectral signature, characterized by the absence of the 150 cm^{-1} peak and by the presence of three broad peaks at 215, 300 and 675 cm^{-1}. The latter are not well defined, indicating that these phases are poorly organised, and do not correspond to any identified mineral phase. These differences between Raman spectra reflect variations of matter organization within the crystallographic structure of the NTox, which are likely due to

alteration, i.e. metamictization and/or hydratation. The FTIR spectra obtained do not allow distinguishing precisely the previous units, due to the larger spot size (30 µm for FTIR instead of 1 µm for Raman), and cannot consequently be correlated properly with the Raman data acquired at the growth band scale. However, all the obtained FTIR spectra exhibit systematically a broad peak in the 3700-2800 cm^{-1} region, which corresponds to the O-H bonds stretching, thus nevertheless indicating the presence of OH^- groups in the crystallographic structure of the NTox (Fig. 72b).

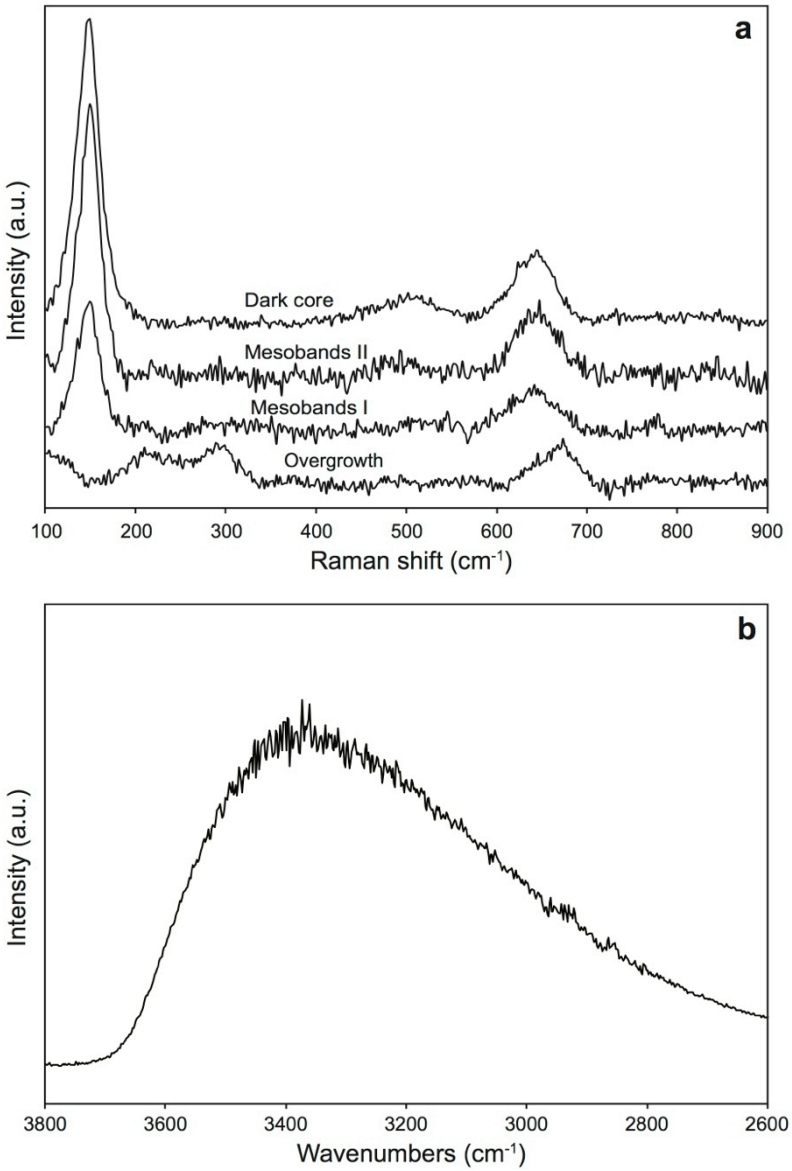

Fig. 72: (a) Raman and (b) FTIR spectra of the Nb-Ti-Y-HREE-W-U oxides (NTox).

4.3. Chemical composition

Representative EMP analyses of the NTox are given in Table 23. Analytic totals range

from 76.12 to 95.24 wt.%, thus suggesting either significant alteration (metamictization and/or hydratation) or relative high concentrations of another elements not measured. EMP preliminary checks were realized previously to the analysis and revealed only the presence of the measured elements. Other elements not measurable by EMP such as Li, Be or B are unlikely in this type of oxides and moreover should be present at high concentrations to explain the low total. F was systematically detected below the detection limit of 1% and could therefore not contribute significantly for the low probe total. Consequently, the total deficient is better interpreted as reflecting the presence of significant amount of OH and/or H_2O in the structure, as discussed above. The global chemical composition of the NTox is characterized by major contents of Nb_2O_5 and TiO_2, minor contents of Y_2O_3, REE_2O_3, FeO, SiO_2, WO_3, UO_2 and CaO and trace contents of Ta_2O_5, MnO and ThO_2. Among the REE, there is a preferential enrichment in HREE, particularly for Gd, Ho, Er and Yb. The cores have a higher content of TiO_2 (up to 43.42 wt.%) compared to Nb_2O_5 (up to 34.48 wt.%) and are rich in FeO (up to 13.39 wt.%), but are poor in Y_2O_3 (up to 2.31 wt.%), REE_2O_3 (up to 2.31 wt.%), CaO (up to 0.74 wt.%) and UO_2 (up to 1.8 wt.%), which explains their dark grey colour on BSE images. The composition of the mesobands forming the peripheral cortex can be divided in two types (Table 23): a type I relatively rich in Y_2O_3 (up to 6.83 wt.%), REE_2O_3 (up to 6.65 wt.%), UO_2 (up to 3.17 wt.%) and CaO (up to 2.52 wt.%), relatively poor in FeO (up to 5.13 wt.%) and with a lower content of TiO_2 (up to 20.9 wt.%) compared to Nb_2O_5 (up to 33.66 wt.%); a type II relatively poorer in Y_2O_3 (up to 5.27 wt.%), REE_2O_3 (up to 3.60 wt.%), UO_2 (up to 1.97 wt.%) and CaO (up to 1.46 wt.%), relatively richer in FeO (up to 9.82 wt.%) and with a lower content of TiO_2 (up to 33.42 wt.%) compared to Nb_2O_5 (up to 37.27 wt.%). The interstitial platelets are characterized by a very high content of Y_2O_3 (up to 12.90 wt.%) and REE_2O_3 (up to 7.68 wt.%), which explains their bright colour on BSE images. They have a higher content of Nb_2O_5 (up to 38.46 wt.%) compared to TiO_2 (up to 27.01 wt.%) and are relatively poorer in FeO (up to 5.36 wt.%), CaO (up to 1.83 wt.%) and UO_2 (up to 1.96 wt.%). The invasive phases are relatively richer in FeO (up to 14.95 wt.%), but relatively poorer in Y_2O_3 (up to 4.78 wt.%), REE_2O_3 (up to 2.48 wt.%), CaO (up to 0.96 wt.%), UO_2 (up to 1.23 wt.%) and have a higher content of Nb_2O_5 (up to 42.84 wt.%) compared to TiO_2 (up to 33.43 wt.%). Finally, the external overgrowths are richer in Y_2O_3 (up to 16.87 wt.%), REE_2O_3 (up to 11.06 wt.%), FeO (up to 10.26 wt.%) and CaO (up to 2.58 wt.%) and poorer in UO_2 (up to 1.67 wt.%), with higher contents of Nb_2O_5 (up to 40.43 wt.%) compared to TiO_2 (up to 25.76 wt.%).

4.4. Crystal chemistry

The chemical data for the NTox suggest that their structural formula is of the general form AB_2O_6, where the A-site is occupied by Fe^{2+}, Mn^{2+}, Y^{3+}, REE^{3+}, Ca^{2+}, U^{4+}, Th^{4+} and the B-site is occupied by Nb^{5+}, Ta^{5+}, Ti^{4+}, Si^{4+} and W^{6+} (Černý and Ercit, 1989; Ercit, 2005; Škoda and Novák, 2007). However, incorporation of hydroxyl groups in the structure is considered by Ewing (1975a,b and references therein) as the result of low temperature alterations, either "primary" (hydrothermal alteration of preexisting minerals) or "secondary" (heralding metamictization), with concomitant leaching in the A-site and creation of structural vacancies. This feature has already been shown for other U-rich Nb-Ta-Ti-Y-REE oxides, for instance for aeschynite-(Y), which is a mineral commonly hydrated or metamict (Bonazzi and Menchetti, 1999; Bonazzi et al., 2002; Tomašić et al., 2004). On the one hand, as clearly seen in Fig. 70, the NTox evidently retain their primary structure and do not present net evidence of metamictization (e.g., Nasdala et al., 2001; Anderson et al., 2008). On the other hand, primary alteration proceeds from "intracrystalline diffusion and fluid transport through preexisting cracks and voids" (Lumpkin and Ewing, 1992) and results in microfracture overprinting and diffusion or patchy zoning, all features that are clearly absent in the NTox (except the "invasive" phase) (Fig. 71). To the contrary, the existence of the generally not disturbed micrometre-scale zoning points to a primary incorporation of the OH^- ions in the crystal structure. Finally, stoichiometry was assumed and the structural formula of the NTox was calculated on the basis of 3 cations, assuming $Fe_{tot}=Fe^{2+}$, $Mn_{tot}=Mn^{2+}$ and $U_{tot}=U^{4+}$ (Table 23).

The crystal chemistry of our NTox is characterized by a cationic deficiency in the A-site with $\sum A<1$ ranging from 0.44 to 0.96 apfu and by a cationic excess in the B-site with $\sum B>2$ ranging from 2.04 to 2.56 apfu (Table 23). The structural formula of our NTox must consequently be written $A_{1-x}B_{2+x}O_6$, with x the number of vacancies in the A-site, ranging from 0.04 to 0.56 apfu. According to Bonazzi and Menchetti (1999), the mineral stoichiometry for this kind of oxides is realized by the partial filling of a third C-site, which incorporates in priority the smallest B-site cations, and in particular W^{6+}. The formula would be then strictly speaking of the form $A_{1-x}B_2C_xO_6$ (Bonazzi and Menchetti, 1999), but since there is no way to partition the cations between the B- and C-sites, we prefer the $A_{1-x}B_{2+x}O_6$ formulation.

Finally, taking into account the presence of some O^{2-} to OH^- substitutions, proved both by the FTIR spectra (Fig. 72b) and the non-respect of the electrostatic charge balance (Table

23), the general formula of our NTox would be of the form:

$$A_{1-x}B_{2+x}(O,OH)_6$$

Where:
A is occupied by Fe^{2+}, Mn^{2+}, Y^{3+}, REE^{3+}, Ca^{2+}, U^{4+}, Th^{4+}
B is occupied by Nb^{5+}, Ta^{5+}, Ti^{4+}, Si^{4+}, W^{6+}
x corresponds to the A-site vacancies

In the A-site, there is a competition between the trivalent cations, mainly Y^{3+} (up to 0.51 apfu) and minor $HREE^{3+}$ (up to 0.24 apfu), and the divalent cations, mainly Fe^{2+} (up to 0.7 apfu) and very minor Mn^{2+}, but Ca^{2+} (up to 0.19 apfu) and also U^{4+} (up to 0.05 apfu) are systematically present (Fig. 73a). In the B-site, there is a competition between Nb^{5+} (up to 1.09 apfu) with very minor Ta^{5+}, and Ti^{4+} (up to 1.74 apfu) with very minor Si^{4+}, but W^{6+} is systematically present as a minor cation (from 0.02 to 0.1 apfu) (Fig. 73b).

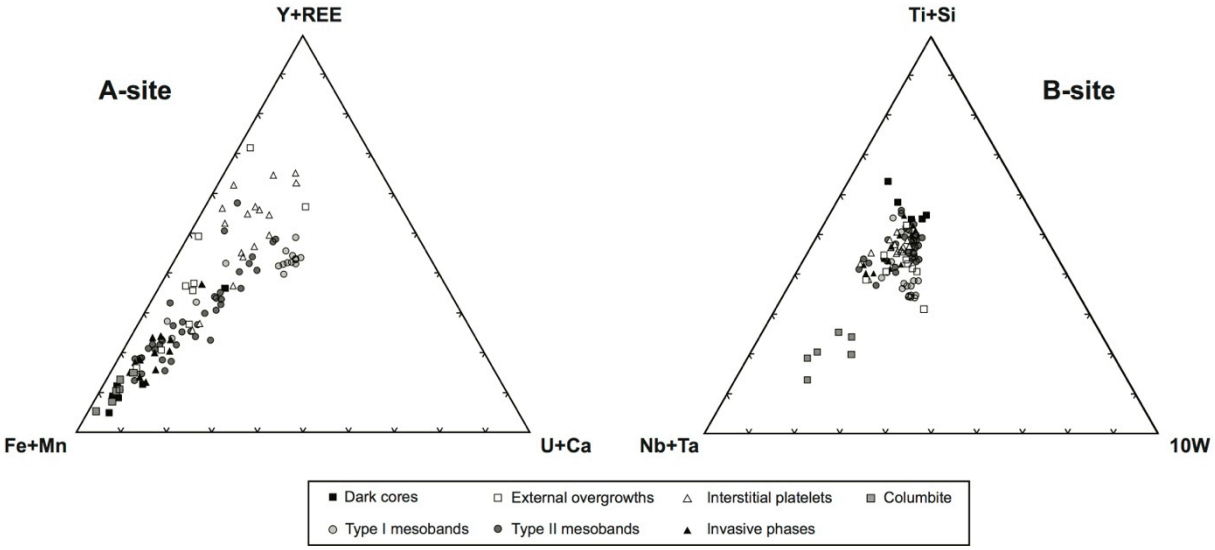

Fig. 73: A-site and B-site occupancy (at. %) of the Nb-Ti-Y-HREE-W-U oxides (NTox).

5. Discussion

5.1. Substitution vectors

When plotted in the (W+Nb+Ta)-(Ti+Si)-∑A triangular diagram (Fig. 74), our NTox appears as an unknown complex multi-polar solid solution, which may be described at the

first order, and neglecting the OH^- components, as the mixing between two groups of binary solid solutions: a first group of anatase (TiO_2) - columbite ($FeNb_2O_6$) solid solution (to which also belong the Fe-columbite crystals enclosed within the NTox) and a second group of euxenite-(Y) ($YTiNbO_6$)-columbite ($FeNb_2O_6$) solid solution (in fact, a ternary solid solution involving a W end-member, see below). In this respect, our NTox appears unique and until now never described.

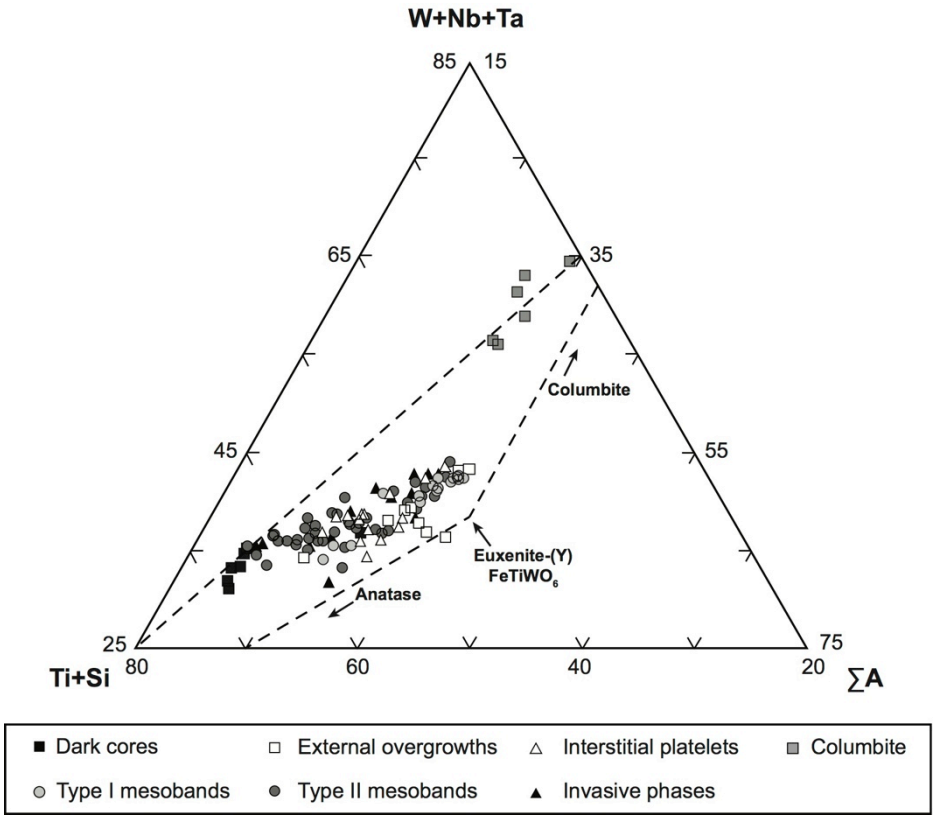

Fig. 74: Ternary diagram (W+Nb+Ta)-(Ti+Si)-∑A (at. %) representing the chemical composition of the Nb-Ti-Y-HREE-W-U oxides (NTox).

Conveniently writing anatase as $TiTi_2O_6$, the first group of solid solution between $TiTi_2O_6$ and $FeNb_2O_6$ may be described by the vector [1] (Fig. 75a):

[1] $(Ti^{4+},Si^{4+})_{-3}\ ^{A}(Fe^{2+},Mn^{2+})_{+1}\ ^{B}(Nb^{5+},Ta^{5+})_{+2}$

The second group of solid solution between $YTiNbO_6$ and $FeNb_2O_6$ may be described by the vector [2] (Fig. 75b):

[2] $^{A}(Y^{3+},REE^{3+})_{-1}\ ^{B}(Ti^{4+},Si^{4+})_{-1}\ ^{A}(Fe^{2+},Mn^{2+})_{+1}\ ^{B}(Nb^{5+},Ta^{5+})_{+1}$

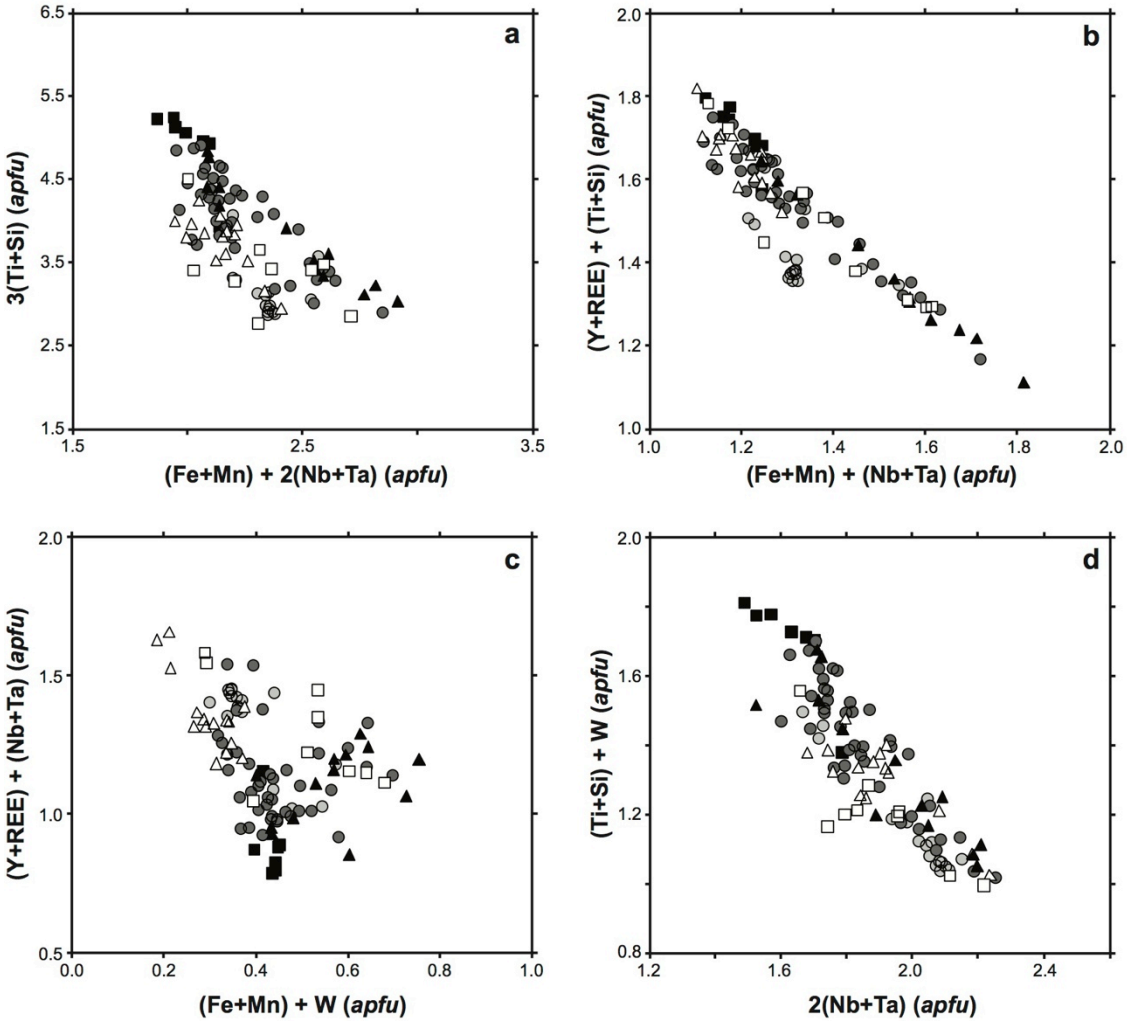

Fig. 75: Main chemical correlations and substitution vectors for the Nb-Ti-Y-HREE-W oxides (NTox). The legend is the same as Fig. 73 and Fig. 74.

To explain the incorporation of W^{6+} in the B-site, it is convenient to introduce the theoretical end-member $FeTiWO_6$, which may be derived from the euxenite-(Y) by the vector [3] (Fig. 75c):

[3] $^{A}(Y^{3+},REE^{3+})_{-1}\ ^{B}(Nb^{5+},Ta^{5+})_{-1}\ ^{A}(Fe^{2+},Mn^{2+})_{+1}\ ^{B}W^{6+}_{+1}$

A solid solution between $FeTiWO_6$ and $FeNb_2O_6$ must also be considered and is described by the vector [4] (Aurisicchio et al., 2001) (Fig. 75d):

[4] $^{B}(Ti^{4+},Si^{4+})_{-1}\ ^{B}W^{6+}_{-1}\ ^{B}(Nb^{5+},Ta^{5+})_{+2}$

Whereas the preceding vectors explain well the main correlations in the crystal compositions,

the entrance of U^{4+} and Ca^{2+} in the structure is more problematic. The simple substitution vector $\square_1U^{4+}_{-1}Ca^{2+}_{+2}$ in the A-site (Ewing, 1975b) is negated by the U-Ca positive correlation (Fig. 76a) and the equally possible $\square_1(Y, REE)^{3+}_{-2}Ca^{2+}_{+1}U^{4+}_{+1}$ vector is not consistent with either the slope of the Ca-U correlation (Ca ~ 4U: Fig. 76a) or the positive correlation between both U^{4+} and Ca^{2+} with Y and REE (not shown). The classical substitution models equally involve a negative correlation, between either U^{4+} and Ca^{2+}, or these elements and Y^{3+} or REE^{3+}. According to Černý and Ercit (1989), U^{4+} entrance in the AB_2O_6 structure can be explained by a solid solution between euxenite-(Y) and an uranopolycrase end-member (UTi_2O_6), which involves the vector [5]:

[5] $^{A}(Y^{3+},REE^{3+})_{-1}\ ^{B}(Nb^{5+},Ta^{5+})_{-1}\ ^{A}U^{4+}_{+1}\ ^{B}(Ti^{4+},Si^{4+})_{+1}$

This vector seems to work (Fig. 76b), but given the very low content in U^{4+}, this would as well be a mere reflection of the valid vectors [3] and [4]. In the same way, Černý and Ercit (1989) proposed that Ca^{2+} entrance in the structure is conditioned by a solid solution between euxenite-(Y) and a vigezzite end-member ($CaNb_2O_6$), according to the vector [6]:

[6] $^{A}(Y^{3+},REE^{3+})_{-1}\ ^{B}(Ti^{4+},Si^{4+})_{-1}\ ^{A}Ca^{2+}_{+1}\ ^{B}(Nb^{5+},Ta^{5+})_{+1}$

However, the scatterplot (Y+REE)+(Ti+Si) vs Ca+(Nb+Ta) is poorly organized (not shown), indicating that this vector is probably poorly involved. Yet, as already suggested by Aurisicchio et al. (2001), the Ca^{2+} entrance could be explained calling for the solid solution between uranopolycrase and vigezzite, described by vector [7], which is a linear combination of vectors [5] and [6].

[7] $^{A}U^{4+}_{-1}\ ^{B}(Ti^{4+},Si^{4+})_{-2}\ ^{A}Ca^{2+}_{+1}\ ^{B}(Nb^{5+},Ta^{5+})_{+2}$

This vector would result in a negative correlation between U^{4+} and Ca^{2+}, contrary to the evidence in Fig. 76a. Although vector [7] seems to work (Fig. 76c), this is again likely a reflection of the vectors governing the substitutions between the major elements Ti and Nb. Finally, as shown in Fig. 76d, there is a positive correlation between Ca+U and (100-Total), the latter being a loose proxy for the otherwise unknown OH^- content. This suggests that metamictization could at least partially explain the low probe total, in combination with the hydratation of the NTox.

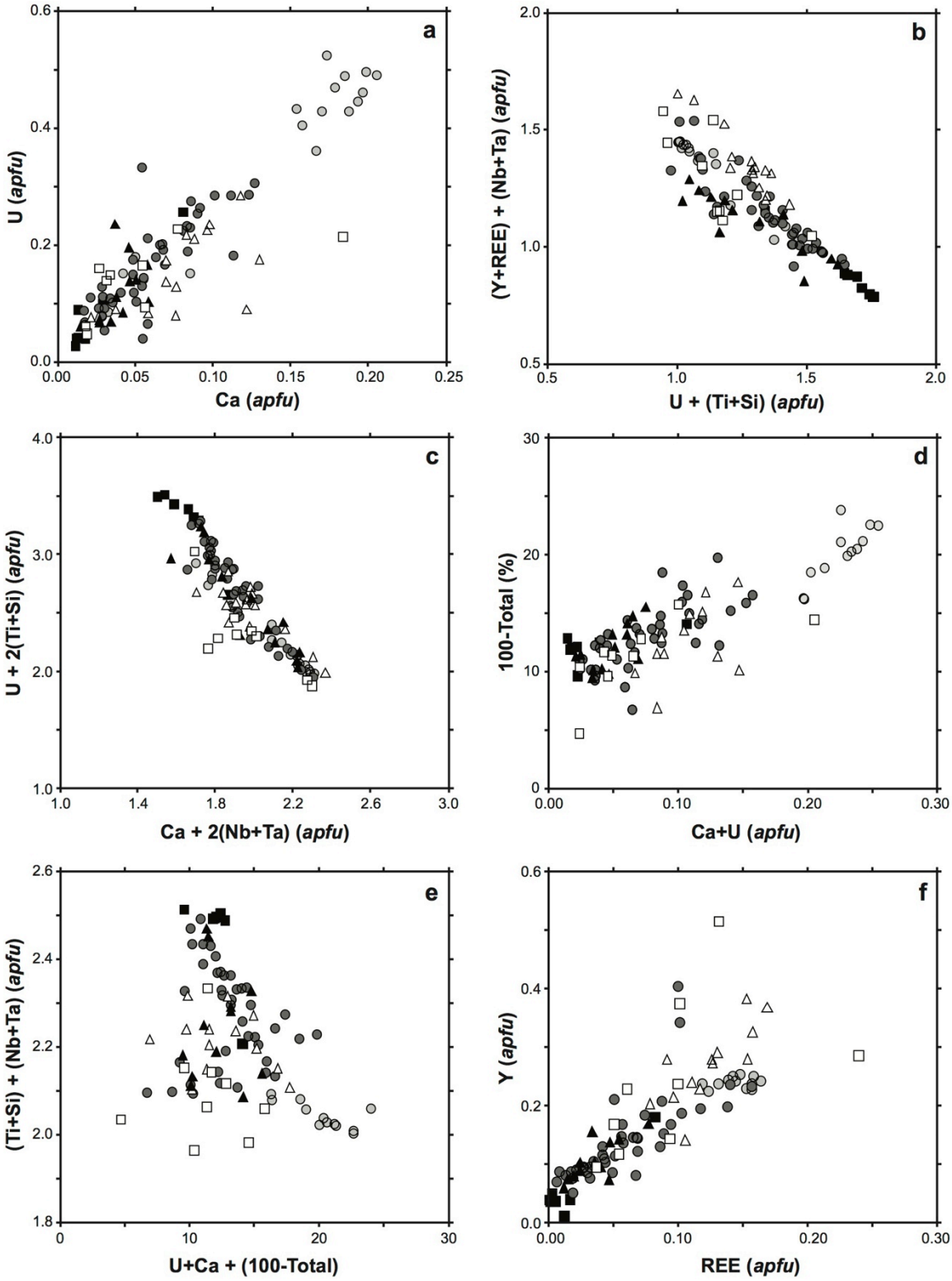

Fig. 76: Chemical variations and substitution vectors in the A-site of the Nb-Ti-Y-HREE-W-U oxides (NTox). The legend is the same as Fig. 73 and Fig. 74.

From the observed correlations, it may be suspected that the Ca^{2+} and/or U^{4+} entrance and the OH^- or H_2O incorporation are coupled in the NTox. It may tentatively be proposed the operation of the vectors [8] and [9]:

[8] $^{A}\square_{1}\ ^{B}(Ti^{4+},Si^{4+})_{-1}\ O^{2-}{}_{-2}\ ^{A}Ca^{2+}{}_{+1}\ ^{B}\square_{+1}\ OH^{-}{}_{+2}$

[9] $^{A}\square_{1}\ ^{B}(Nb^{5+},Ta^{5+})_{-1}\ O^{2-}{}_{-1}\ ^{A}U^{4+}{}_{+1}\ ^{B}\square_{+1}\ OH^{-}{}_{+1}$

However, these vectors present the difficulty of creating vacancies in the B site, but are nevertheless not too bad verified, if only the dark cores and type I and II mesobands are considered (Fig. 76e). To conclude, although the mechanism of Ca^{2+} and U^{4+} entrance in the crystals remains obscure, it seems nevertheless clear that it is mainly linked with the hydration of the NTox, in what case the U-Ca correlation would be imposed by external conditions (i.e. a fluid with a definite Ca/U ratio) rather than by crystallochemical constraints.

5.2. Significance of the zoning

Beyond the crystal chemistry constraints, the amplitude of the chemical variations seen in Fig. 75 to Fig. 76 may testify for significant variations in fluid composition when the chemical trends visible in the diagrams are correlated with the main features of the crystal zoning. For instance, as shown in Fig. 76f, there is a positive correlation between Y^{3+} and REE^{3+}, meaning that there is no Y-REE substitution, which would imply a negative correlation according to the vector $Y^{3+}{}_{-1}REE^{3+}{}_{+1}$. More precisely, there are three linear arrays in Fig. 76f, characterising the two styles of mesobands and an interstitial+overgrowth group. Thus, Y^{3+} and REE^{3+} entered simultaneously in the crystal structure, and the linear arrays in Fig. 76f may be interpreted as the record of three ore-forming fluids, each characterised by its own constant Y/REE ratio. Using this approach, it is possible to infer some general characteristics of the ore-forming fluids at the mesoband scale.

(i) The dark cores and bands have compositions dominated by the solid solution $TiTi_2O_6$ - $FeNb_2O_6$ (vector [1]) with Ti>Nb and with a minor but constant component of the vector [4], testifying for a fluid enriched in Ti, Nb, (Ta), Fe and W.

(ii) The type I and II mesobands are both characterized by a multicomponent solid solution, plotting in Fig. 74 along the mixing line between a Nb-rutile end-member (corresponding to the dark core compositions) and a solid solution between euxenite (and the W equivalent $FeTiWO_6$) and columbite, involving vectors [2] and [4]. In other terms, they may be seen at the first order as deposited from fluids sharing the characteristics of the preceding with Y and REE in addition. The two types of mesobands differ mainly by the ratio

between the two end-members. Type I mesobands are characterized by the predominance of the euxenite/columbite end-member, as shown by their higher contents in Y, REE, Nb>>Ti and lower contents in Fe. In addition, they display elevated Ca+U content, contrasting with all other zone types in the NTox, and they show lower Y/REE ratios. To the contrary, type II mesobands display lower contents of Y and REE and higher contents of Ti ¬Nb and Fe, being therefore closer to the Nb-rutile end-member. They are poorer in Ca+U, but show distinctly higher Y/REE ratios. These differences are modulated at the micrometre-scale in the individual growth bands, where continuous (and recurrent) variations of composition are observed for some elements: Y enrichments in type I mesobands, Nb and Y enrichments correlated to Ti decrease in type II mesobands.

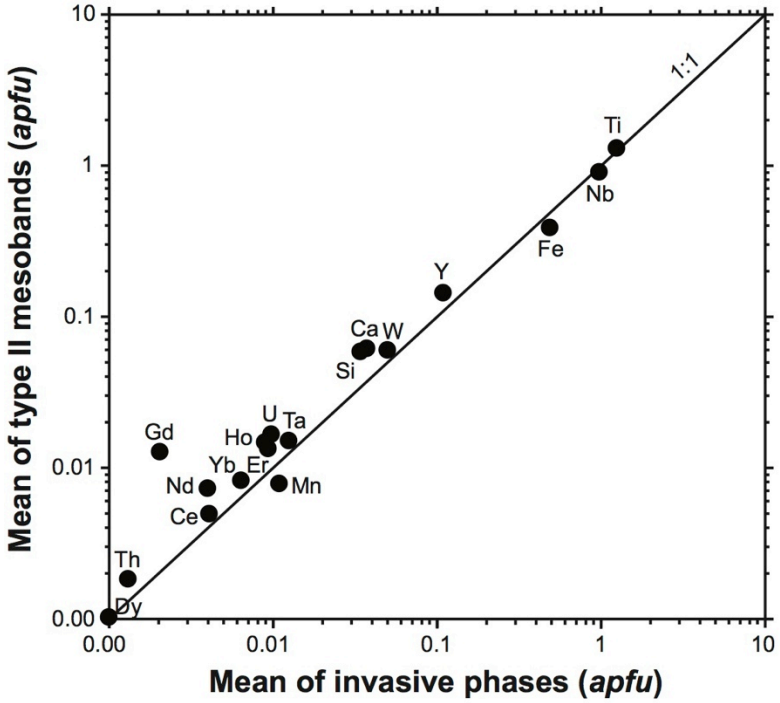

Fig. 77: Average composition of invasive phases (n=11) vs average composition of type II mesobands (n=40) calculated for the Nb-Ti-Y-HREE-W-U oxides (NTox).

(iii) The interstitial platelets and the overgrowths have both very different compositions characterized by elevated Y and REE contents with however a tendency of the interstitial platelets to display lower contents of (Fe+Mn) and higher contents of (Ti+Si). Compared with the preceding types of zones, they correspond to a predominance of the euxenite-$FeTiWO_6$ end-members. These phases were evidently deposited from a very different fluid, rich in Y and REE, with an elevated Y/REE ratio.

(iv) The analysed invasive phases are all contained in type II mesobands, and their

average compositions are close (but not identical) to the average composition of the type II mesobands: Ti and Nb are invariant, whereas Y and mostly the REE, U, Ca and W are slightly depleted, Fe and Mn are slightly enriched (Fig. 77). They are interpreted as the result of an alteration process, which, given these data, could have consisted in dissolution followed by in situ re-precipitation involving a third fluid, able to corrode the NTox and to partially leach the more soluble rare elements.

5.3. Fractionation versus fluid mixing

All these variations must be related to some evolution of the hydrothermal fluid(s) compositions over time, and the question arises about the driving mechanism for the observed changes. Long-term fractionation trends in the growth medium (= closed system), from a Ti-rich composition towards a Y-REE-rich composition, for instance, may be discarded, for the following reasons: (i) abrupt changes characterize the transition from dark cores (or bands) toward the type I or II mesobands; (ii) there are no continuous trends at the scale of the mesobands and (iii) the potentially most fractionated phases (interstitial platelets and overgrowths) equally appear without transition, being to the contrary often associated with a discontinuity in the growth process. Such characteristic would be better explained by a fluid mixing process (= open system), involving two main end-members: a {Ti, Fe, Nb, W} L_1 fluid (as the one responsible for the dark cores) and a {Nb, Fe, Y, REE, W} L_2 fluid (similar to the one involved in the formation of the interstitial platelets and the overgrowths). The question of U and Ca being also present in the L_2 fluid, or being independently brought into the system must be kept open. Nevertheless, at the growth band scale, fractionation effects better explain the observed variations, with Ti-rich phases precipitating before Y- and REE-rich phases. At this specific time-space scale, the system must be therefore considered as closed. Consequently, two time scales of mixing must be called for. At the growth band (short time) scale, (pseudo)-periodic replenishing in L_1 fluid is required to explain the oscillatory zoning. At the mesoband (long time) scale, the oscillatory zoning within the type I and II mesobands may be explained by alternative inputs of L_2 and L_1 fluids over time in an open system, although a high crystal growth rate could also play a role by exhausting rare-metals in the fluid. Temporary and short time flushing by a L_2 fluid would explain the formation of the interstitial platelets and the final overgrowth. In addition, the frequency of fluid inputs in the growth medium of the NTox must have been sufficient to prevent significant fractionation at the time-scale of the mesobands. This type of behaviour suggests that the hydrothermal

system was a succession of opening/closing over time. It remains to be explained such features as the variable enrichment in Ca+U, or the variable Y/REE ratios in the mesobands and interstitial platelets/overgrowth zones. The latter may record fractionation effects in the source of the L_2 fluid(s), related for instance to crystallization of xenotime and monazite in the (unknown) source area. The former could imply a distinct source of the U-Ca component, characterized nevertheless by a constant U/Ca ratio.

5.4. Nature of the fluids

The composition of the L_1 fluid, enriched in Ti>Nb, Fe, W, is in continuity with the mineralogical composition of the hydrothermal veins crosscutting the breccia pipe, which are composed of wolframite, scheelite, Nb-Fe-W-rich rutile and sulphides (mainly arsenopyrite and pyrite). The dark cores and the columbite crystals trapped inside may thus represent direct witnesses of these primary fluid circulations. However, the composition of the L_2 fluid, enriched in Nb>Ti, Fe, Y and HREE, shows a contrasting signature compared to the one of the L_1 fluid. The NTox represent direct evidence of hydrothermal fluids enriched in HFSE, from which they have precipitated and which led to the crystallization of zircon, xenotime, monazite and Nb-Fe-W-rutile, all associated with the NTox in an adularia matrix. This mineral paragenesis is characterized by a P, Y, HREE, Nb>Ta, Ti, Zr and U geochemical signature, which is typical of the rare-metal peralkaline magmatism (Černý and Ercit, 2005; Černý et al., 2005). The L_2 fluid may thus represent a hydrothermal fluid derived from an unknown peralkaline source at depth, for instance from NYF pegmatites or related granites, during the late stages of mineralization in the Puy-les-Vignes deposit. Previous studies on accessory minerals associated with W-Sn and rare-metals deposits from the FMC have never highlighted this type of mineral paragenesis (e.g., Béziat et al., 1980; Aïssa, 1987; Cuney et al., 1992; Ohnenstetter and Piantone, 1992; Wang et al., 1992; Belkasmi and Cuney, 1998; Raimbault, 1998; Raimbault and Burnol, 1998; Belkasmi et al., 2000; Gama, 2000; Vallance et al., 2001; Lerouge et al., 2007), which is shown here for the first time. Consequently, this discovery could likely represent the first indirect evidence in the FMC for a contribution of peralkaline magmatism in a regional context dominated by peraluminous magmatism.

6. Conclusion

The textural observations of the NTox from the Puy-les-Vignes deposit reveal a complex internal texture, resulting from multiple episodes of crystallization, marked by an initial nucleation followed by rhythmic growth stages, which alternate with corrosion stages during crystallization breaks and ends with late overgrowths. Their chemical compositions are characterized by variable concentrations in rare-metals and by structural hydratation, but by a common crystal chemistry according to a structural formula of the form $A_{1-x}B_{2+x}(O,OH)_6$, where A is occupied by Fe^{2+}, Mn^{2+}, Y^{3+}, REE^{3+}, Ca^{2+}, U^{4+}, Th^{4+}, B is occupied by Nb^{5+}, Ta^{5+}, Ti^{4+}, Si^{4+}, W^{6+} and x corresponds to the A-site vacancies. The NTox appear as a complex multi-polar solid solution, described here for the first time, involving a chemical mixing between two groups of binary solid solutions: a first group of anatase - columbite solid solution and a second group of euxenite-(Y) - columbite solid solution. The abrupt changes between the internal zones of the NTox and the contrasting variable contents in rare-metals suggest that these oxides crystallized in an open system and result from the mixing between two different hydrothermal fluids: a first fluid L_1 enriched in Ti>Nb, Fe, W, with the same geochemical signature as the main mineralization; a second fluid L_2 enriched in Nb>Ti, Fe, Y, REE, W, with a signature contrasting with the first one and which is associated with the crystallization of adularia, xenotime, monazite and zircon. We propose that this hydrothermal paragenesis, characterized by a P, Y, HREE, Nb>Ta, Ti, Zr, U signature, typical of the rare-metal peralkaline magmatism, represents the contribution of rare-metal enriched peralkaline hydrothermal fluids derived from an unknown source at depth (e.g. NYF pegmatites or related granite) during the late metallogenic stages in the Puy-les-Vignes deposit. This result represents a new evidence for rare-metal mobilization during hydrothermal processes and could be likely the first indirect evidence for peralkaline magmatism in the French Massif Central. This opens consequently new perspectives, both for the understanding of the rare-metal metallogenesis in this Variscan crustal segment and for the exploration of the rare-metal economic potential at Puy-les-Vignes and more widely in the Limousin area.

Acknowledgements

This work was supported by the French National Research Agency through the national program "Investissements d'avenir" of the Labex Ressources 21 with the reference ANR-10-LABX-21-RESSOURCES21. The authors are highly thankful to Bernard Mouthier for access to the samples and to the field. We would like also to thank Sandrine Mathieu, Lise Salsi, Olivier Rouer, Marie-Camille Caumon and Odile Barrès (GeoRessources, Vandœuvre-lès-Nancy, France) for technical support in providing analytical data on SEM, EMP, Raman and FTIR spectroscopy. The authors are also grateful to Dr. Robert Linnen and Dr. Marieke Van Lichtervelde for their constructive comments and suggestions, and to Dr. Daniel Ohnenstetter for editorial work.

Table 23: Representative EMP analyses of the Nb-Ti-Y-HREE-W-U oxides (NTox) from Puy-les-Vignes. Analytical conditions, reference standards and limits of detection are given in the text. bdl: below detection limit.

	Dark cores					*Type I mesobands*					*Type II mesobands*				
Oxide (*wt. %*)	12	13	81	84	103	15	16	17	18	19	29	30	31	35	41
FeO	7.94	8.19	9.40	13.39	11.36	4.83	4.67	4.90	4.54	5.13	7.17	9.22	9.82	6.96	5.91
MnO	0.22	0.27	bdl	bdl	bdl	bdl	bdl	bdl	bdl	bdl	0.23	0.27	0.28	bdl	bdl
CaO	0.20	0.23	0.24	0.59	0.74	2.32	2.49	2.35	2.52	2.33	1.09	0.44	0.57	1.26	1.46
Y_2O_3	1.68	1.21	0.38	2.31	2.12	5.83	6.60	6.56	6.83	6.68	3.19	2.22	2.74	4.36	5.27
Ce_2O_3	bdl	bdl	0.42	0.94	0.27	bdl	bdl	bdl	bdl	bdl	bdl	bdl	bdl	bdl	bdl
Nd_2O_3	bdl	bdl	ndl	0.47	bdl	bdl	bdl	bdl	bdl	bdl	bdl	bdl	bdl	bdl	bdl
Gd_2O_3	bdl	bdl	bdl	bdl	bdl	2.48	2.58	2.74	2.57	2.48	1.03	bdl	bdl	1.05	1.34
Dy_2O_3	bdl	bdl	bdl	bdl	bdl	bdl	bdl	bdl	bdl	bdl	bdl	bdl	bdl	bdl	bdl
Ho_2O_3	bdl	bdl	bdl	0.40	0.29	1.31	1.44	1.48	1.80	1.44	0.68	0.37	0.45	0.90	0.80
Er_2O_3	bdl	bdl	bdl	bdl	bdl	0.93	1.43	1.20	1.32	1.09	0.60	bdl	bdl	0.87	0.80
Yb_2O_3	bdl	bdl	bdl	bdl	bdl	0.62	0.80	0.62	0.96	0.53	bdl	bdl	bdl	0.64	0.66
ThO_2	bdl	bdl	0.39	0.41	0.39	bdl	bdl	bdl	bdl	bdl	bdl	bdl	bdl	bdl	bdl
UO_2	0.23	0.34	0.77	1.80	1.51	2.93	3.17	2.85	2.77	2.43	1.27	0.73	0.79	1.69	1.97
TiO_2	41.93	39.39	43.42	24.12	29.63	19.14	19.08	20.55	18.56	20.90	31.96	33.42	29.63	28.45	26.67
SiO_2	bdl	bdl	0.73	1.20	2.94	bdl	bdl	bdl	bdl	bdl	bdl	bdl	bdl	bdl	bdl
Nb_2O_5	29.33	33.46	31.60	34.88	28.20	30.77	32.61	32.40	32.71	33.66	33.31	35.83	37.27	31.93	30.92
Ta_2O_5	0.81	0.74	1.03	0.90	1.20	1.05	0.95	1.01	1.19	0.80	1.02	0.78	0.61	0.95	0.72
WO_3	4.72	4.08	1.76	3.86	2.93	3.91	3.88	4.36	4.32	4.03	4.51	4.56	4.70	4.29	3.78
F	bdl	bdl	bdl	bdl	bdl	bdl	bdl	bdl	bdl	bdl	bdl	bdl	bdl	bdl	bdl
Total	87.06	87.91	90.14	85.27	81.58	76.12	79.70	81.02	80.09	81.50	86.06	87.84	86.86	83.35	80.30
A-site (apfu)															
Fe^{2+}	0.37	0.38	0.41	0.66	0.55	0.29	0.27	0.28	0.26	0.29	0.36	0.44	0.48	0.36	0.32
Mn^{2+}	0.01	0.01	0.00	0.00	0.00	0.00	0.00	0.00	0.00	0.00	0.01	0.01	0.01	0.00	0.00
Ca^{2+}	0.01	0.01	0.01	0.04	0.05	0.18	0.19	0.17	0.19	0.17	0.07	0.03	0.04	0.08	0.10
Y^{3+}	0.05	0.04	0.01	0.07	0.07	0.22	0.24	0.24	0.25	0.24	0.10	0.07	0.09	0.14	0.18
Ce^{3+}	0.00	0.00	0.01	0.02	0.01	0.00	0.00	0.00	0.00	0.00	0.00	0.00	0.00	0.00	0.00
Nd^{3+}	0.00	0.00	0.00	0.01	0.00	0.00	0.00	0.00	0.00	0.00	0.00	0.00	0.00	0.00	0.00
Gd^{3+}	0.00	0.00	0.00	0.00	0.00	0.06	0.06	0.06	0.06	0.05	0.02	0.00	0.00	0.02	0.03
Dy^{3+}	0.00	0.00	0.00	0.00	0.00	0.00	0.00	0.00	0.00	0.00	0.00	0.00	0.00	0.00	0.00
Ho^{3+}	0.00	0.00	0.00	0.01	0.01	0.03	0.03	0.03	0.04	0.03	0.01	0.01	0.01	0.02	0.02
Er^{3+}	0.00	0.00	0.00	0.00	0.00	0.02	0.03	0.03	0.03	0.02	0.01	0.00	0.00	0.02	0.02
Yb^{3+}	0.00	0.00	0.00	0.00	0.00	0.01	0.02	0.01	0.02	0.01	0.00	0.00	0.00	0.01	0.01
Th^{4+}	0.00	0.00	0.00	0.01	0.01	0.00	0.00	0.00	0.00	0.00	0.00	0.00	0.00	0.00	0.00
U^{4+}	0.00	0.00	0.01	0.02	0.02	0.05	0.05	0.04	0.04	0.04	0.02	0.01	0.01	0.02	0.03
∑A	0.44	0.45	0.46	0.84	0.71	0.86	0.89	0.86	0.90	0.85	0.60	0.56	0.63	0.68	0.71
B-site (apfu)															
Ti^{4+}	1.74	1.64	1.71	1.07	1.30	1.04	1.00	1.05	0.97	1.05	1.42	1.43	1.30	1.33	1.31
Si^{4+}	0.00	0.00	0.04	0.07	0.17	0.00	0.00	0.00	0.00	0.00	0.00	0.00	0.00	0.00	0.00
Nb^{5+}	0.73	0.84	0.75	0.93	0.74	1.00	1.02	0.99	1.03	1.02	0.89	0.92	0.98	0.90	0.91
Ta^{5+}	0.01	0.01	0.01	0.01	0.02	0.02	0.02	0.02	0.02	0.01	0.02	0.01	0.01	0.02	0.01
W^{6+}	0.07	0.06	0.02	0.06	0.04	0.07	0.07	0.08	0.08	0.07	0.07	0.07	0.07	0.07	0.06
∑B	2.56	2.55	2.54	2.15	2.28	2.13	2.11	2.13	2.10	2.15	2.40	2.44	2.37	2.31	2.29
∑ charge	12.05	12.12	11.94	11.53	11.55	11.87	11.87	11.88	11.89	11.90	12.03	12.04	11.98	11.93	11.95

Table 23: Continued.

	Interstitial platelets					*Invasive phases*					*External overgrowths*				
Oxide (*wt. %*)	6	46	106	114	120	33	34	37	38	123	66	67	85	96	99
FeO	2.96	4.79	5.36	5.24	4.66	10.46	8.42	10.73	14.95	10.51	3.41	9.45	4.74	10.26	9.31
MnO	bdl	bdl	0.23	bdl	bdl	0.18	0.21	0.19	0.27	0.18	bdl	0.41	bdl	bdl	bdl
CaO	1.83	1.68	0.36	1.46	1.09	0.89	0.81	0.96	0.45	0.68	2.58	0.88	0.31	1.18	0.29
Y_2O_3	11.59	8.01	12.90	6.99	9.13	4.78	3.26	2.86	2.62	4.41	8.03	7.41	16.87	4.36	11.90
Ce_2O_3	bdl	0.25	0.24	0.40	0.31	bdl	bdl	bdl	bdl	0.43	0.22	0.32	0.39	0.34	0.27
Nd_2O_3	bdl	0.65	0.36	0.93	0.91	bdl	bdl	bdl	bdl	0.32	1.17	0.74	0.57	0.58	0.53
Gd_2O_3	3.52	1.82	1.16	1.52	1.88	bdl	bdl	bdl	bdl	bdl	3.68	1.37	1.90	0.92	0.88
Dy_2O_3	bdl	bdl	bdl	bdl	bdl	bdl	bdl	bdl	bdl	bdl	bdl	bdl	bdl	bdl	bdl
Ho_2O_3	1.57	1.20	1.07	1.16	1.53	0.65	0.48	0.70	0.35	0.64	2.45	1.22	1.32	1.21	1.39
Er_2O_3	1.30	1.10	1.37	1.02	1.23	0.75	0.50	0.39	0.49	0.60	1.82	0.88	1.60	1.04	1.15
Yb_2O_3	0.59	0.92	1.23	0.76	0.83	0.37	0.35	bdl	bdl	0.46	1.06	0.57	1.31	0.61	1.11
ThO_2	bdl	0.38	0.23	0.23	0.27	bdl	bdl	bdl	bdl	0.33	bdl	bdl	0.24	0.22	0.22
UO_2	0.66	1.96	0.62	1.65	1.04	1.23	1.09	0.81	0.58	0.66	1.45	0.70	0.38	1.67	0.46
TiO_2	22.67	21.66	23.37	26.54	27.01	24.32	33.43	28.00	23.93	25.51	16.33	19.70	25.76	22.07	23.49
SiO_2	bdl	1.71	6.10	1.55	1.18	bdl	bdl	bdl	bdl	1.01	1.63	1.12	0.46	2.02	0.86
Nb_2O_5	38.46	30.79	32.57	30.99	33.61	36.74	32.04	39.95	42.84	38.06	34.77	40.43	33.86	32.58	32.17
Ta_2O_5	0.91	1.17	0.73	0.58	0.61	0.71	0.75	0.85	0.52	0.79	0.68	0.88	1.31	0.77	0.91
WO_3	2.00	4.26	3.08	3.81	3.18	3.43	3.98	3.25	2.63	3.37	5.60	2.58	4.22	4.35	4.65
F	bdl	bdl	bdl	bdl	bdl	bdl	bdl	bdl	bdl	bdl	bdl	bdl	bdl	bdl	bdl
Total	88.06	82.35	90.98	84.83	88.47	84.51	85.32	88.69	89.63	87.96	84.88	88.66	95.24	84.18	89.59
A-site (apfu)															
Fe^{2+}	0.15	0.26	0.25	0.27	0.23	0.53	0.41	0.51	0.70	0.51	0.19	0.47	0.23	0.53	0.46
Mn^{2+}	0.00	0.00	0.01	0.00	0.00	0.01	0.01	0.01	0.01	0.01	0.00	0.02	0.00	0.00	0.00
Ca^{2+}	0.12	0.12	0.02	0.10	0.07	0.06	0.05	0.06	0.03	0.04	0.18	0.06	0.02	0.08	0.02
Y^{3+}	0.38	0.28	0.39	0.23	0.29	0.16	0.10	0.09	0.08	0.14	0.28	0.24	0.51	0.14	0.37
Ce^{3+}	0.00	0.01	0.00	0.01	0.01	0.00	0.00	0.00	0.00	0.01	0.01	0.01	0.01	0.01	0.01
Nd^{3+}	0.00	0.02	0.01	0.02	0.02	0.00	0.00	0.00	0.00	0.01	0.03	0.02	0.01	0.01	0.01
Gd^{3+}	0.07	0.04	0.02	0.03	0.04	0.00	0.00	0.00	0.00	0.00	0.08	0.03	0.04	0.02	0.02
Dy^{3+}	0.00	0.00	0.00	0.00	0.00	0.00	0.00	0.00	0.00	0.00	0.00	0.00	0.00	0.00	0.00
Ho^{3+}	0.03	0.02	0.02	0.02	0.03	0.01	0.01	0.01	0.01	0.01	0.05	0.02	0.02	0.02	0.03
Er^{3+}	0.03	0.02	0.02	0.02	0.02	0.01	0.01	0.01	0.01	0.01	0.04	0.02	0.03	0.02	0.02
Yb^{3+}	0.01	0.02	0.02	0.01	0.02	0.01	0.01	0.00	0.00	0.01	0.02	0.01	0.02	0.01	0.02
Th^{4+}	0.00	0.01	0.00	0.00	0.00	0.00	0.00	0.00	0.00	0.00	0.00	0.00	0.00	0.00	0.00
U^{4+}	0.01	0.03	0.01	0.02	0.01	0.02	0.01	0.01	0.01	0.01	0.02	0.01	0.00	0.02	0.01
∑A	0.81	0.82	0.78	0.74	0.74	0.81	0.61	0.70	0.85	0.76	0.90	0.90	0.90	0.87	0.96
B-site (apfu)															
Ti^{4+}	1.06	1.06	0.99	1.23	1.22	1.12	1.47	1.20	1.01	1.12	0.82	0.89	1.11	1.02	1.04
Si^{4+}	0.00	0.11	0.34	0.10	0.07	0.00	0.00	0.00	0.00	0.06	0.11	0.07	0.03	0.12	0.05
Nb^{5+}	1.08	0.91	0.83	0.86	0.91	1.01	0.85	1.03	1.09	1.00	1.04	1.09	0.88	0.90	0.86
Ta^{5+}	0.02	0.02	0.01	0.01	0.01	0.01	0.01	0.01	0.01	0.01	0.01	0.01	0.02	0.01	0.01
W^{6+}	0.03	0.07	0.04	0.06	0.05	0.05	0.06	0.05	0.04	0.05	0.10	0.04	0.06	0.07	0.07
∑B	2.18	2.18	2.22	2.26	2.25	2.19	2.39	2.30	2.15	2.24	2.08	2.10	2.10	2.13	2.04
∑ charge	12.07	11.91	11.88	11.91	11.98	11.74	11.91	11.87	11.59	11.81	11.97	11.75	11.88	11.6	11.58

Chapter 6: Mobilization of W during the late-Variscan metamorphism: example of the St-Mélany Sn-W deposit (Cévennes, French Massif Central)

Abstract

The St-Mélany Sn-W deposit, located in the Cévennes area (SE French Massif Central), represents an interesting case of hydrothermal quartz-cassiterite-wolframite vein system hosted in mesozonal micaschists in the vicinity of two heterochronous granites emplaced in a polyphase tectono-metamorphic regional setting. Structural and petrographic study of the mineralized veins showed that the hydrothermal system formed during a polyphase vein opening, according to a hydraulic fracturing mode, and was lately affected by a plastic deformation in compressive conditions consistent with the regional LP-HT metamorphism (M3) at ca. 315 Ma, coeval with the emplacement of the Rocles granite in the north. Geochemical analyses of the main regional magmatic rocks revealed the existence of two potential rare-metal sources in the region of St-Mélany: (i) the muscovite-facies of the Rocles granite, which corresponds to an evolved granite emplaced at ca. 315 Ma; (ii) rare-metal aplites and pegmatites cross-cutting the St-Mélany deposit and emplaced at ca. 305 Ma. Whereas the latter were clearly temporally disconnected from the Sn-W mineralization, the former was however emplaced during the M3 prograde metamorphism and could represent a potential source of Sn-W for the St-Mélany deposit. Whole-rock geochemistry of the Cévenol micaschists revealed a W anomaly in the surroundings of St-Mélany. A transect realized along the Beaume valley in the prograde micaschists toward the contact with the Rocles granite revealed a progressive decrease in W and Sn from the epizone to the mesozone-catazone transition, thus reflecting a depletion during the prograde metamorphism. The detailed mineralogical and geochemical study of the Ti-oxides contained in the micaschists from the Beaume valley showed a progressive dissolution of the initial ilmenite and the crystallization of anatase and rutile during the M3 prograde metamorphism, releasing significant amounts of W. Local enrichments in rare-metals (W, Nb, Sn, Ta) have been recorded in anatase crystals from the enclosing micaschists at St-Mélany, suggesting the local interaction with a rare-metal-rich hydrothermal fluid during the M3 metamorphism. By integrating these results, we propose that the St-Mélany deposit formed during the regional LP-HT metamorphism through a two-stage model: (i) a preconcentration stage by magmatic-hydrothermal fluids derived

from the evolved Rocles muscovite-granite and resulting in a regional W anomaly stocked in the Ti-oxides; and (ii) a remobilization stage consisting in the partial leaching of this W stock by the regional metamorphic fluids during the M3 prograde metamorphism and yielding to their progressive concentration at St-Mélany forming the mineralized vein system. This work highlights the important role played by metamorphic fluids in a polyphase tectono-metamorphic setting for the formation of peri-batholitic Sn-W mineralization and opens new perspectives for the understanding of these complex hydrothermal systems at the crustal scale.

Keywords:
W mineralization; rare-metals; prograde metamorphism; Ti-oxides; Cévennes area; French Massif Central.

1. Introduction

The French Massif Central (FMC), located in the internal zone of the West European Variscan belt, hosts several W-Sn and rare-metals deposits, which are associated with hydrothermal peri-batholitic quartz-wolframite-cassiterite veins and with specialized granites and pegmatites (e.g., Marignac and Cuney, 1999; Bouchot et al., 2005). Most of these mineralization are spatially associated with large peraluminous granitic bodies emplaced during the Carboniferous (Stussi, 1989). Despite the large number of studies, the spatio-temporal framework for this type of mineralization, typically considered as "magmatic-hydrothermal", remains unclear and the genetic models are still debated, in particular concerning the source(s) of the fluids and the metals. Orthomagmatic models involving an underlying granite as direct source of the fluids and metals have been generally proposed (e.g., Webster et al., 2004; Rickers et al., 2006; Dewaele et al., 2016). Other genetic models exist, in which the granite plays only a role as thermal source driving metamorphic fluid circulations and mobilizing the metals from the surrounding country rocks (e.g., So et al., 1991; Vindel et al., 1995; Vallance et al., 2001). Recently, Marignac and Cathelineau (2010) proposed a critical review and a classification of the ore-forming fluids in peri-batholitic Sn-W deposits.

In the Cévennes area, located in the southeastern part of the FMC, are observed both syn-metamorphic W concentrations associated with scheelite-bearing calc-silicate gneisses and wolframite-bearing quartz veins. In the Drobie valley are known several showings of quartz-wolframite veins, such as Serrecourte (Ramboz et al., 1985) and St-Mélany (Noyé, 1985; Noyé and Weisbrod, 1988), whose the genetic relationships with a parental granite are not obvious. The small St-Mélany deposit represents an interesting case study of hydrothermal Sn-W mineralization, which is hosted in the mesozonal micaschists and located in the close vicinity of two heterochronous granites in a polyphase tectono-metamorphic regional context. The spatial and temporal relationships between the Sn-W mineralization and the regional metamorphic and magmatic events raises therefore the question of the possible role played by the late-Variscan metamorphism on the mobilization of the fluids and the metals in this part of the FMC. In this regard, a preliminary work (Mangin et al., 1994) suggested that W could be mobilized during the prograde metamorphism from Ti-oxides in the metasediments.

The objectives of this chapter are: (i) to determine the temporal framework for the emplacement of the St-Mélany Sn-W deposit and its relation with the regional metamorphism

and the spatially associated granites; (ii) to characterize the regional geochemical variations in tungsten and associated rare-metals in the granites and in the metamorphic rocks surrounding the St-Mélany deposit; (iii) to study the mineralogical and geochemical evolution of Ti-oxides in the metasedimentary rocks during the prograde metamorphism and their possible role as source of W. In this chapter, the different grades of the regional metamorphism are referred to the epizone-mesozone-catazone nomenclature, defined as followed: epizone for the low-grade metamorphic rocks, characterized by the chlorite+muscovite±biotite assemblage, equivalent to the greenschist facies; mesozone for the medium-grade metamorphic rocks, characterized by the muscovite+biotite assemblage (chlorite$^-$ isograde), equivalent to the lower amphibolite facies; catazone for the high-grade metamorphic rocks, characterized by the biotite±aluminosilicate assemblage (muscovite$^-$ isograde), equivalent to the upper amphibolite to granulite facies (migmatites).

2. Geological setting

2.1. Regional geology of the North Cévennes area

The North Cévennes area (Fig. 78) is located in the southeastern part of the FMC, at the southern boundary of the Velay dome, and belongs structurally to the Para-Autochtonous Unit (PAU) (Ledru et al., 2001). This unit overthrusts southward over the Cambrian series of the Viganais and is overlaid to the north by the Lower Gneiss Unit (LGU) and to the east by the Mesozoic sedimentary cover (Faure et al., 1999, 2001). Three main lithological units are distinguished in the Cévennes para-autochtonous domain (Fig. 78) (Thierry et al., 2014; Barbey et al., 2015; and references therein) from top to bottom: (i) the "Série de Joyeuse", in continuity with the Cézarenque series in the southwest and considered equivalent to the LGU, consists in low-grade orthogneisses and micaschists; (ii) the "Série Cévenole", composed by micaschists (metapelites, metagreywackes), quartzites and calc-silicate gneisses, is thought to represent the lower part of the Cévennes schists, which to the south are stacked in a middle Carboniferous nappe pile (Arnaud et al., 2004). This series is supposed to be of Neoproterozoic (Ediacarian) to Cambrian in age; and (iii) the "Série Ardéchoise", composed by augen gneisses, undifferentiated orthogneisses and leucogneisses (leptynites). The three series are affected by a late-Carboniferous LP-HT metamorphism, which increases from the south (low-grade) to the north (high-grade) (Fig. 78).

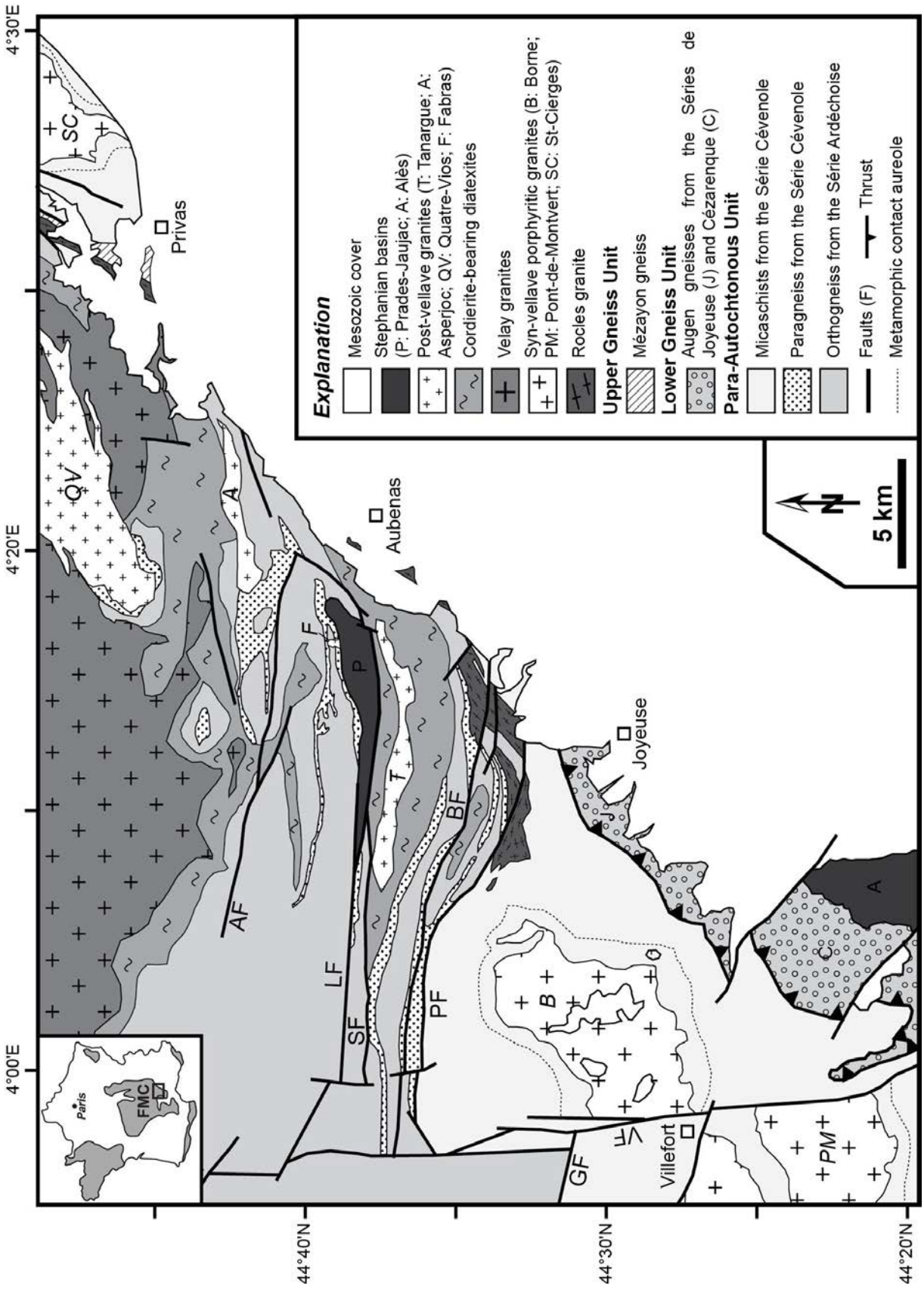

Fig. 78: Geological setting of the North Cévennes area (modified after Thierry et al., 2014) located in the southeastern part of the French Massif Central (FMC). Faults names: AF: Ardèche fault; BF: Beaume fault; GF: Goulet fault; LF: Lignon fault; PF: Pioule fault; SF: La Souche fault; VF: Villefort fault.

The geological setting and the tectono-metamorphic evolution of the Cévennes area have been studied for many years (e.g., Marignac et al., 1980; Weisbrod et al., 1980; Weber and Barbey, 1986; Macaudière et al., 1987; Laumonier et al., 1991; Montel et al., 1992; Faure et al., 1999, 2001; Ledru et al., 2001; Barbey et al., 2005; Bouilhol et al., 2006; Brichau et al., 2008; Couzinié et al., 2014) and a comprehensive synthesis has been proposed recently by Thierry et al. (2014) and Barbey et al. (2015). The structure of the studied area is complex and results from a polyphase evolution during the Variscan orogeny. In their recent synthesis, Thierry et al. (2014) and Barbey et al. (2015) describe the succession of five main tectono-metamorphic and magmatic events. As shown in Table 24, correlations of this succession with the events at the whole-FMC scale as proposed by Bouchot et al. (2005) and Faure et al. (2009) remain problematic, whereas many similarities are fortunately observed with other schemes proposed at the Cévennes-scale by Ledru et al. (2001), Faure et al. (2001), Bouilhol et al. (2006) and Brichau et al. (2008). The discrepancies between these various models are discussed in detail in Thierry et al. (2014), to which we therefore refer in the following.

There is no field evidence in the studied area of the earliest HP metamorphic episode D1 (Faure et al., 2009), which is widespread known in the FMC as exhumed granulites or lherzolites and dated at ca. 430-410 Ma during the Silurian (Lardeaux et al., 2001; Berger et al., 2010).

(i) The first event recorded in the studied area (D2) is marked by a penetrative regional schistosity S2 associated with F2 folds (Macaudière et al., 1987) and occurred under MP-MT Barrovian metamorphic conditions (Toteu, 1981; Toteu and Macaudière, 1984). This event represents likely the N-S compression and the main nappe stacking at ca. 340-330 Ma in the Cévennes schists to the south (Arnaud et al., 2004 and references therein).

(ii) Following D2, the D3 episode is characterized by mid-crustal water-assisted partial melting enhanced by coeval lamprophyric magmas (vaugnerites I) and formation of kilometer-scale northward-vergent syn-migmatitic folds (F3a) in the catazone (Laumonier et al., 1991). The migmatites are “lit par lit” metatexites with biotite melanosomes and tonalitic leucosomes (in the paragneiss). This M3 LP-HT metamorphism peaked at T~720°C and P~500-600 MPa (Montel et al., 1992; Barbey et al., 2005). Based on converging U-Pb dating of monazite in an orthogneiss metatexite leucosome at 314 ± 5 Ma (Mougeot et al., 1997) and U-Pb zircon dating of vaugnerite I at 314 ± 5 and 310 ± 4 Ma (Ait Malek, 1997), a Namuro-Westphalian age (ca. 315 Ma) is adopted by Barbey et al. (2015) for the M3 event and adopted here. Conflicting ages were however proposed on the basis of less robust U-Th-Pb chemical dating of monazite from biotite melanosomes in paragneiss metatexite, found either

slightly younger (311 ± 2 Ma; Bouilhol et al., 2006) or distinctly older (329 ± 5 and 323 ± 3 Ma; Be Mezeme et al., 2006). U-Pb dating of the syn-D3 Rocles granite (Fig. 78) yielded ages varying from 325 ± 4 to 318 ± 3 Ma (U-Th-Pb on monazite; Be Mezeme et al., 2007), the latter being consistent with the Namuro-Westphalian age. The D3 event is variously interpreted. It has been considered as purely NW-SE extension at ca. 330-320 Ma (Faure et al., 2001). Adopting the "crustal fluage" model of Jamieson et al. (2011), Thierry et al. (2014) propose that the M3 migmatite sheet represents a fluage corridor of the middle-crust, at the top of a deep northward-verging ductile shear zone (i.e., overall compressive conditions). At the hanging-wall of the sheet, injections of thick vaugnerites sills and a syn-kinematic granite sheet (Rocles granite) allows mechanical decoupling, at the level of the sillimanite-muscovite zone ("lower" mesozone), with the upper plate, which is subjected to extension (southwest verging F3b fold and C-S structures) in the so-called Mylonitic Metamorphic Vellave Zone (MMVZ) of Bouilhol et al. (2006).

(iii) While the M3 metamorphic pile started exhumation and experienced the beginning of a retrograde path, the North Cévennes area was subjected to a N-S compressive D4 event resulting in kilometric-scale F4 folds and the formation of an overall antiformal structure heralding the Velay dome. Towards the end of this event were emplaced granite plutons (Borne-Pont-de-Montvert, Largentière; Fig. 78) and lamprophyre dykes in the epizone (synform), and vaugnerite II bodies in the catazonal areas. According to Talbot et al. (2004), the Borne-Pont-de-Montvert massif was emplaced under extensional conditions. This late-D4 magmatic event is well dated at the Westphalian-Stephanian boundary (ca. 305 Ma) on both granites and vaugnerites at 304 ± 6 Ma (U-Pb on zircon; Couzinié et al., 2014), and 303 ± 3 Ma (U-Pb on monazite; Brichau et al., 2008) and on the Mayras vaugnerite II at 308 ± 5 Ma (U-Pb on zircon; Ait Malek, 1997) and 305.8 ± 2.3 (U-Pb on zircon; Couzinié et al., 2014). Assimilation of hosting rocks (roof-pendants) is typical of the Velay contacts, and in this connexion it is significant that most zircons from the Velay granite have inherited cores clustering around 315 Ma (Couzinié et al., 2014). This age corresponds to the estimated age of the M3 migmatites, which are the protoliths of the M4 diatexites (Barbey et al., 2005).

(iv) Immediately following D4, a second metamorphic event (M4) culminating at T≥800°C and P~300-400 MPa (Montel et al., 1992, Barbey et al., 2005) was associated with the emplacement of the large cordierite-bearing peraluminous Velay granite pluton, and the development of a pervasive aureole of cordierite-bearing diatexites (dehydration melting) (Fig. 78). This event is considered to be representative of a D4 extensional event at the scale of the FMC by Faure et al. (2009). The Velay granite yielded ages of 301 ± 5 Ma (U-Pb on

monazite; Mougeot et al., 1997) and 305.9 ± 1.4 Ma (U-Pb on monazite; Couzinié et al., 2014), which indicates an emplacement age at ca. 305-300 Ma.

(v) Finally, the D5 episode is related to the E-W to NW-SE ductile strike-slip faulting during the generalized extension and collapse of the FMC at ca. 300-290 Ma, which led to the formation of intra-montane coal basins, to which belongs the Prades-Jaujac basin (Fig. 78) of late Stephanian age dated at 296 ± 7 Ma (U-Pb on zircons from intercalated tuffs; Bruguier et al., 2003). This event is associated in the North Cévennes area with late intrusions of peraluminous granites (Tanargue, Quatre-Vios, Fabras; Fig. 78) and microgranites dykes that crosscut the Velay granites and were recently dated at 303.9 ± 6.5 Ma (U-Pb on zircon from Tanargue granite; Couzinié et al., 2014), and 297 ± 4 Ma (U-Th-Pb on monazite; Didier et al., 2013). The great brittle E-W faults that run across the metamorphic pile are thought to be Permian.

2.2. Regional evidences of hydrothermal fluid circulations

2.2.1. Quartz veins

Late metamorphic quartz veins are frequently observed in the micaschists of the Série Cévenole and are particularly well exposed in the Beaume and Drobie valleys (Fig. 79). Two types of veins can be distinguished structurally: (i) concordant quartz lenses (type 1) elongated in the schistosity plane S2, which show locally boudinage and syn-schistose (F2) folding (Fig. 79a,b). These lenses are typically a few millimeters to centimeters thick and are of limited lateral extension in the micaschists. This type of quartz lenses is found regionally in the Cévennes area and were formed during shearing deformation by dissolution-crystallization mechanism and fluid overpressure (“exudation quartz”) under P-T metamorphic conditions of ca. 450 MPa and 500°C (Arnaud et al., 2004); (ii) concordant to discordant quartz lenses (type 2), which are secant on the schistosity S2 and deformed by asymmetric F3 folds (Fig. 79c,d). They form discontinuous lenses in the micaschists, which are typically several centimeters to pluri-decimeters in thickness. They contain K-feldspars, biotite and eventually tourmaline crystals, which allows distinguishing them easily from the syn-folial quartz lenses. In the Beaume valley, this second type of quartz lens forms locally interconnected vein system with an apparent inverse movement (Fig. 79d) during the D3 compression. Whereas the quartz lenses of type 1 are found regionally, the type 2 occurs only in the surroundings of the St-Mélany deposit at the epizone-mesozone transition. At St-

Mélany, the two types of veins are superposed (Fig. 79e) and large quartz lenses are observed in the direct surroundings of the deposit (Fig. 79f).

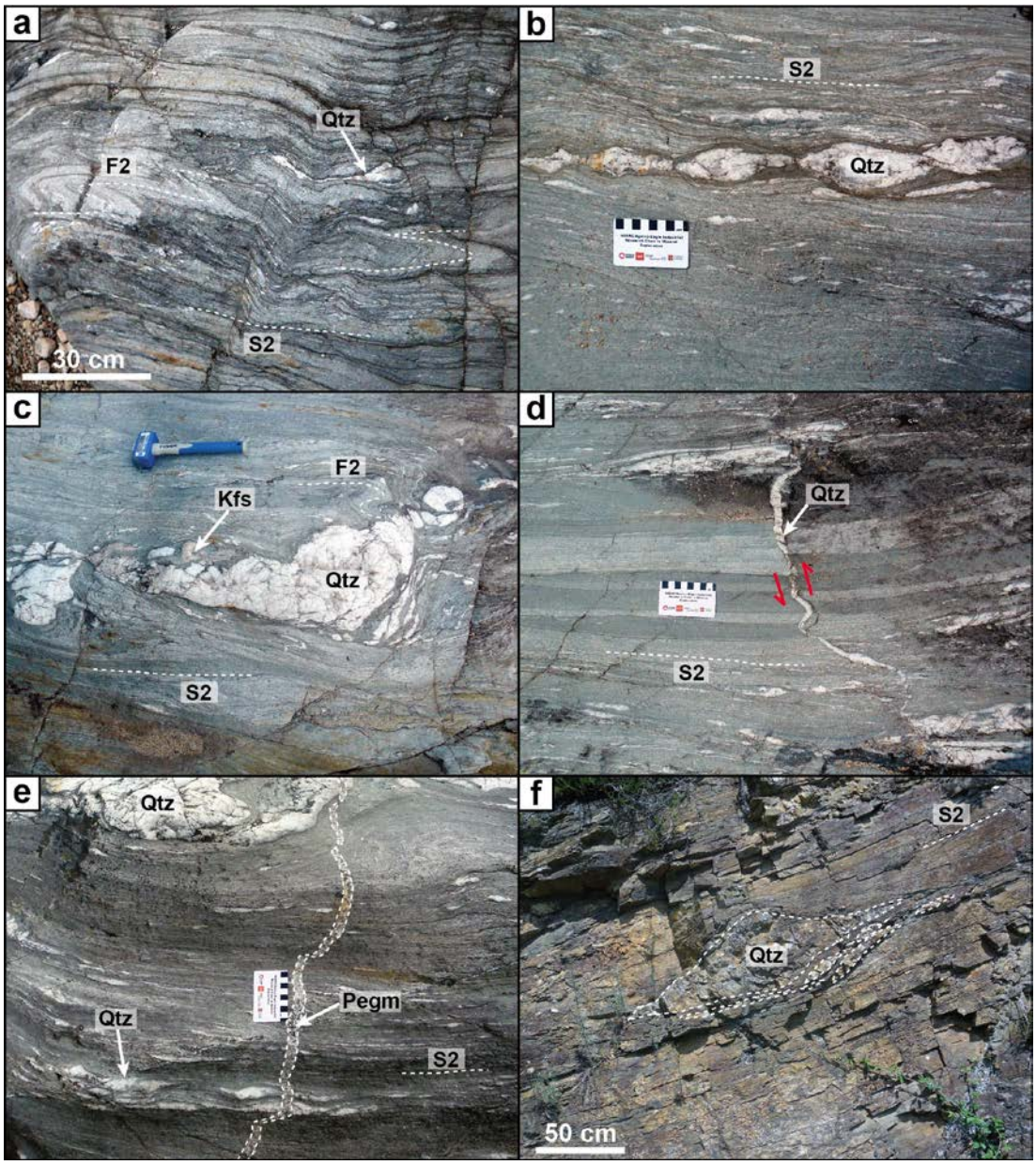

Fig. 79: Quartz lenses observed in the micaschists from the Beaume and Drobie valleys. (a) Concordant quartz (Qtz) lens (type 1) deformed in the schistosity S2 and the syn-schistose folds F2 within epizonal micaschists from the Beaume valley. (b) Concordant quartz lens (type 1) showing boudinage deformation within the schistosity plane S2 in epizonal micaschists from the Beaume valley. (c) Sub-concordant quartz-K-feldspar (Kfs) lens (type 2) non-deformed by the F2 folds in epizonal micaschists from the Beaume valley. (d) Discordant quartz lens (type 2) on the schistosity S2 showing an apparent inverse movement within epizonal micaschists from the Beaume valley. (e) Early quartz lenses (type 1) in the mesozonal micaschists enclosing the St-Mélany deposit (Drobie valley) and cut by a late pegmatite dyke (Pegm). (f) Large quartz lenses (type 2) flattened in the S2 schistosity in the mesozonal micaschists from the Drobie valley, close to St-Mélany (D220 Road in direction of Sablières).

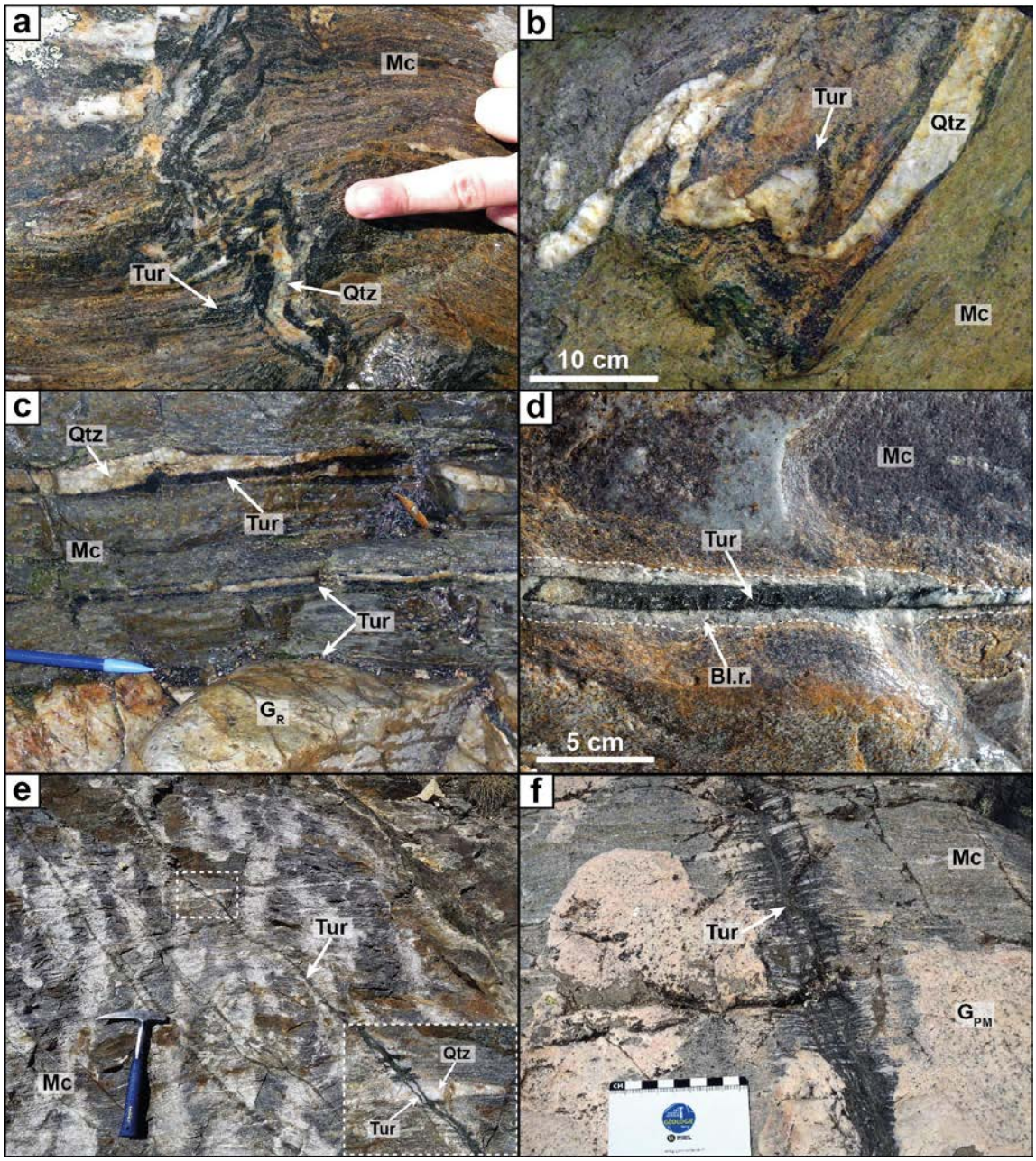

Fig. 80: Representative examples of tourmalinization in the North Cévennes area. (a) Tourmalinite (Tur) at the selvage of a secant quartz vein (Qtz) crosscutting mesozonal micaschists (Mc) (St-Mélany, Drobie valley). (b) Diffuse tourmalinite surrounding a deformed quartz vein in proximity of the Rocles granite (Pont du Gua, Beaume valley). (c) Tourmalinite at the selvages of quartz veins and leucogranitic dykes (G_R) in proximity of the Rocles granite (Pont du Gua, Beaume valley). (d) Tourmalinite vein surrounded by cm-thick bleached rims (Bl.r.) corresponding to the leaching and silicification of the enclosing micaschists (St-Mélany, Drobie valley). (e) Tourmalinite veins crosscutting the micaschists and the hosted quartz lenses (inset) in the metamorphic contact aureole of the Pont-de-Montvert granite (Le Travers cross-section). (f) Tourmalinite vein with bleached rims crosscutting the Pont-de-Montvert granite (G_{PM}).

2.2.2. Tourmalinization

Tourmalinization represents a common hydrothermal alteration in the Cévenol micaschists, which is pervasive and of regional extension (Fig. 80). Two main types of tourmalinization can be distinguished in the Cévennes area: (i) a first type ("Rocles-style") affecting the Cévenol micaschists in the proximity of the Rocles granite and characterized by a diffuse tourmalinization in the micaschists, forming cm-thick tourmalinite at the selvage of quartz veins or leucogranitic dykes (Fig. 80a,b,c); (ii) a second type ("Borne-Pont-de-Montvert-style") characterized by cm-thick tourmalinite veins with bleached selvages, that crosscut both the Borne granite in the north and the Pont-de-Montvert granite in the south, as well as their enclosing micaschists (Fig. 80d,e,f). Tourmalinites veins found in the surroundings of the Pont-de-Montvert granite were emplaced in shear-zones during the late-D4 extension and contain disseminated Au-bearing sulphides (arsenopyrite, pyrite), which were interpreted as formed during the regional Au mineralization event at ca. 300 Ma (Charonnat et al., 1999; Chauvet et al., 2012). Finally, tourmalines are also found associated with leucogranitic dykes crosscutting the Borne granite, in which they constitute post-solidus accessory minerals replacing plagioclase feldspars (Mialhe, 1980).

2.3 The St-Mélany Sn-W deposit

The St-Mélany Sn-W deposit (Fig. 81) is one of several tungsten occurrences in the North Cévennes area, which includes also disseminated scheelite in calc-silicate rocks from the Série Cévenole ("St-Mélany quartzites", "Loubaresse skarn") (Samama, 1971; Noyé, 1985) and wolframite-scheelite-bearing muscovite episyenite at St-Cierge-la-Serre (Ramboz, 1980). Close to St-Mélany, a small showing of quartz-wolframite vein was also described at Serrecourte (Fig. 81) by Ramboz et al. (1985). The St-Mélany Sn-W deposit is located in the Drobie valley, at around 10 km to the southern boundary of the Velay migmatitic dome and around 5 km to the west of the Mesozoic Largentière basin (Fig. 81). It was formerly studied by Noyé (1985) and Noyé and Weisbrod (1988). The deposit is hosted in the mesozonal cordierite-biotite-bearing micaschists of the Série Cévenole, close to the chlorite$^-$ isograde, at less than 3 km from the Rocles granite in the northeast and the Borne granite in the west. The deposit consists in a network of up to 40 cm wide N110-N140°E striking flat quartz-cassiterite±wolframite veins, which cut the regional schistosity (Fig. 83a). Cross-sections perpendicular to the regional structures are shown in Fig. 82.

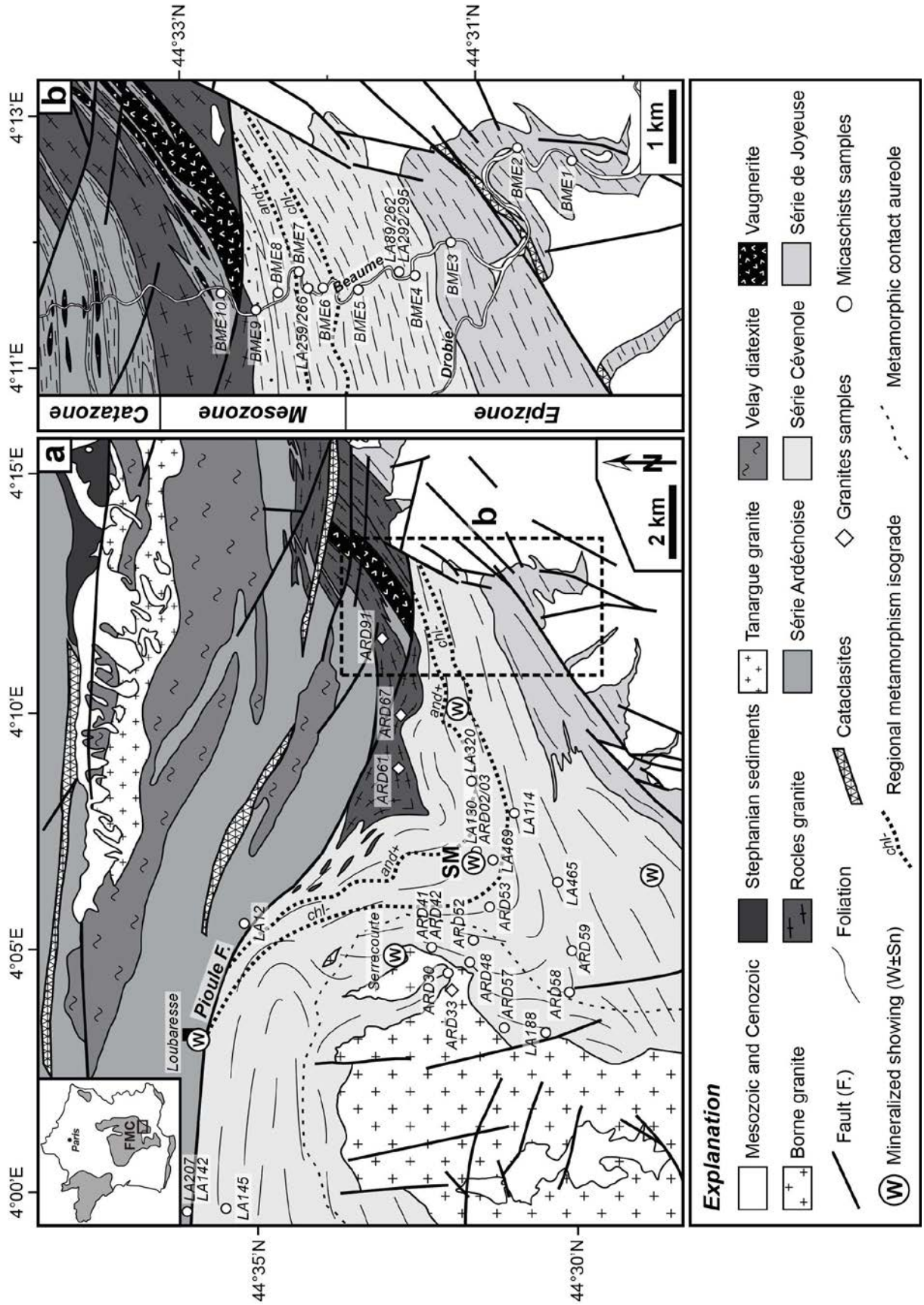

Fig. 81: (a) Location and geological setting of the St-Mélany (SM) deposit in the North Cévennes area (modified after Weisbrod et al., 1974). Regional W occurrences are also reported (Noyé, 1985). (b) Detailed view of the Beaume valley. The position of the samples collected for this study is indicated.

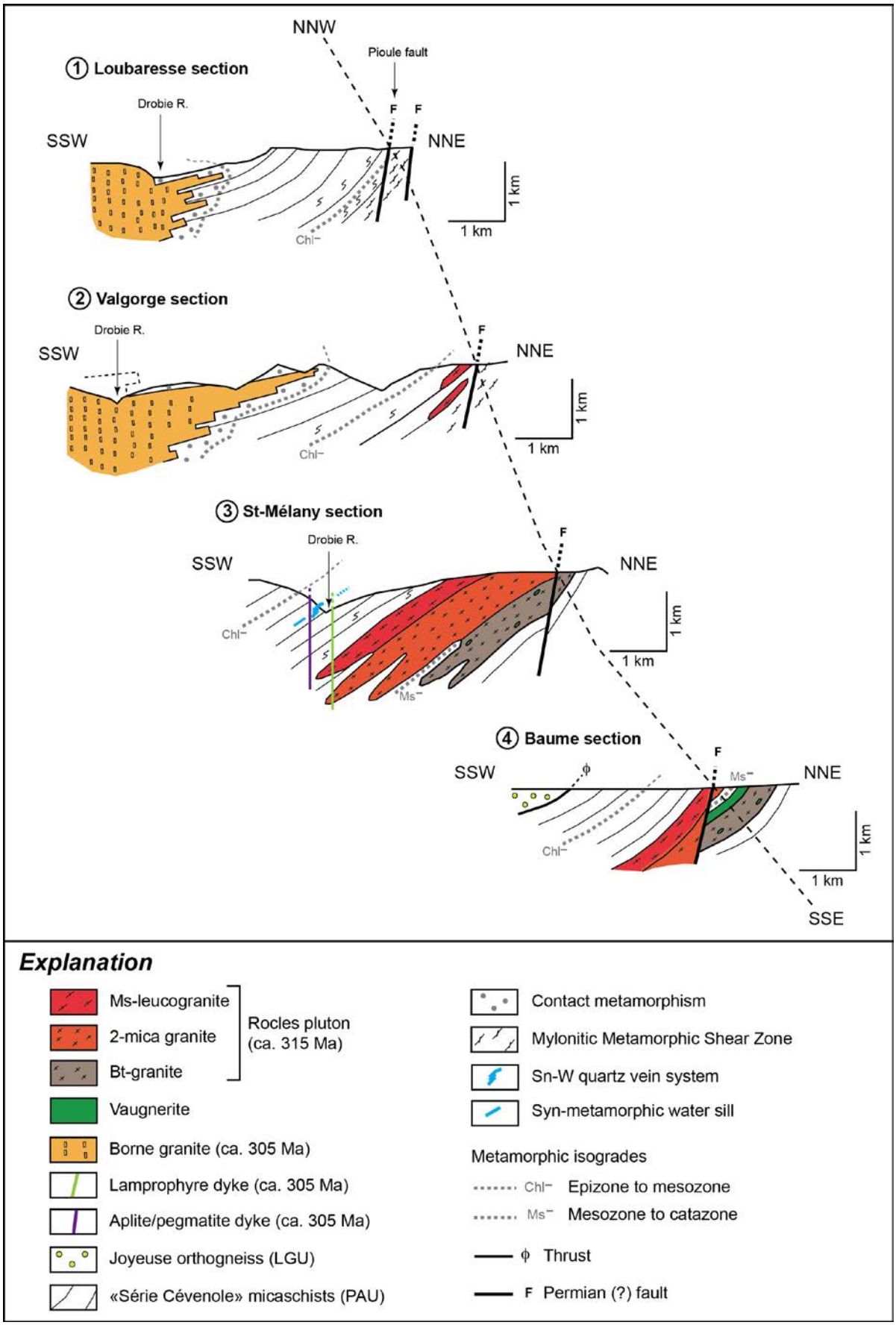

Fig. 82: Cross-sections in the region of the St-Mélany Sn-W deposit showing the spatial relationships between the regional metamorphism, granitic magmatism and hydrothermal veins.

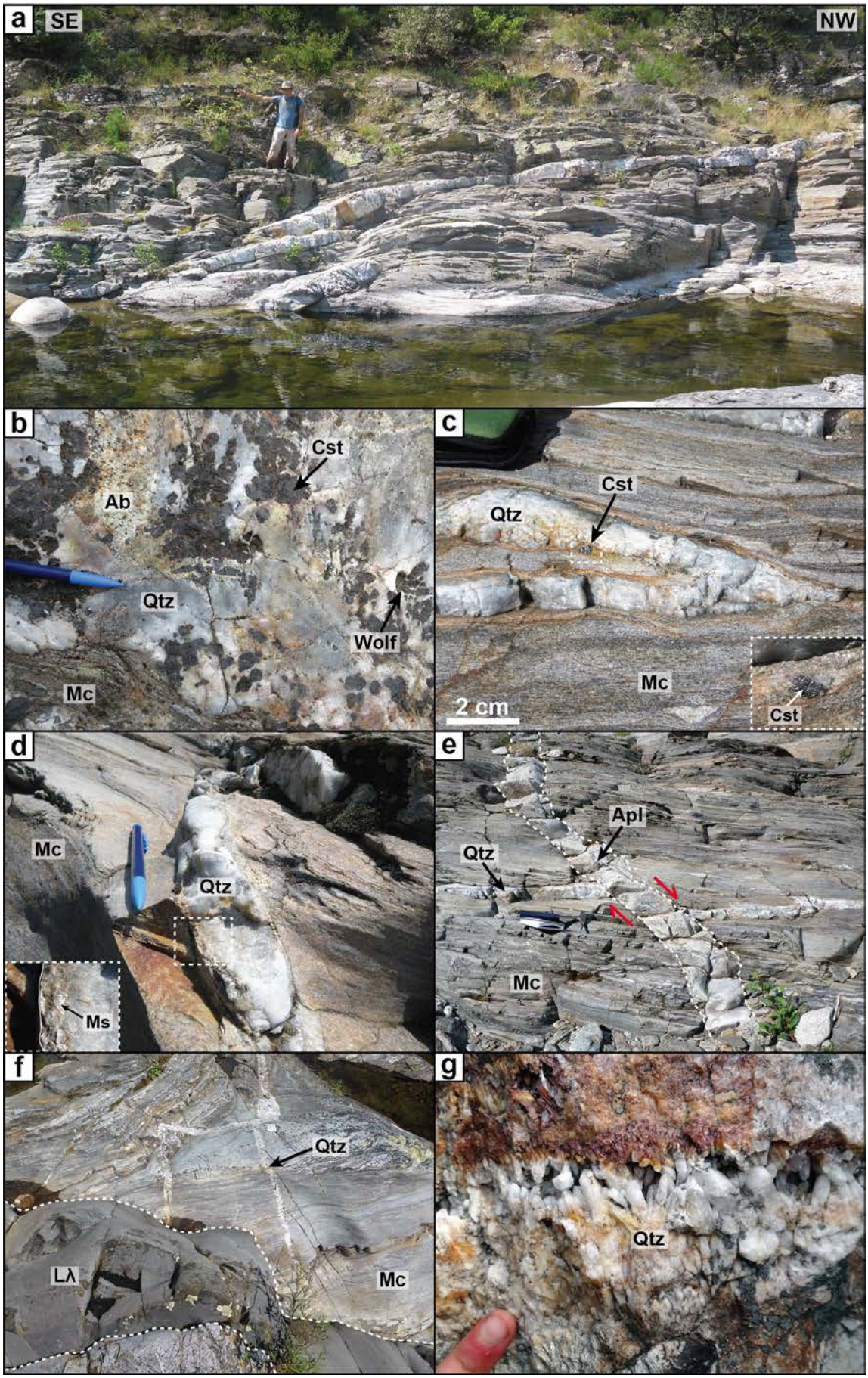
a
SE
NW
b
Cst
Ab
Qtz
Wolf
Mc
c
Cst
Qtz
Mc
2 cm
Cst
d
Mc
Qtz
Ms
e
Apl
Qtz
Mc
f
Qtz
Lλ
Mc
g
Qtz

Fig. 83

Fig. 83: Photographs of the St-Mélany Sn-W deposit. (a) General view of the quartz-cassiterite±wolframite vein system, crosscutting the mesozonal micaschists. (b) Detail of the cassiterite-wolframite mineralization at the hanging wall of a quartz vein. (c) Cassiterite crystal in the micaschist at the selvage of a quartz vein. (d) Muscovite crystals developed at the selvages of a mineralized quartz vein. (e) Aplite dyke crosscutting a mineralized quartz vein and the micaschists with an apparent normal movement. (f) Late intrusion of lamprophyre cutting the micaschists and quartz veins. (g) Detail view of a quartz-barite vein with crack-seal and geodic textures. Abbreviations: Ab: albite; Apl: aplite; Cst: cassiterite; Lλ: lamprophyre; Mc: micaschist; Ms: muscovite; Qtz: quartz; Wolf: wolframite.

The mineralization is located at the hanging wall and footwall of the quartz veins (Fig. 83b) and is composed by millimeter to centimeters euhedral crystals of cassiterite and wolframite in association with minor albite, apatite and beryl (Noyé, 1985). One crystal of cassiterite has been observed in the micaschists at the selvage of a quartz vein (Fig. 83c). The quartz veins are frequently surrounded by a mm-thick muscovite selvage (Fig. 83d), which appear late compared with the main mineralization. The mineralized system is cut by late N20°-60°E-striking aplite and pegmatite veins, dated at 306.5 ± 3.1 Ma (^{40}Ar-^{39}Ar on muscovite; Chauvet et al., 2012), which emplaced in brittle conditions during late extension, as indicated by an apparent normal movement (Fig. 83e). A swarm of lamprophyre dykes overprint the vein system (Fig. 83f) and is representative of the late-D4 mafic magmatism heralding the Velay emplacement (Barbey et al., 2015). Finally, late N100-N120°E striking quartz-barite±galena-sphalerite veins cut the St-Mélany vein network. These veins are locally associated with silicified breccias and show typically crack-seal textures with geodic quartz infilling (Fig. 83g). These Ba-Pb-Zn occurrences are known regionally and are interpreted as post-Variscan fluid circulations during the Trias-Lias extension (Mialhe, 1980; Noyé, 1985).

3. Materials and analytical methods

3.1. Sampling

Regional sampling of the micaschists and the granites was performed in the area of St-Mélany in order to analyse the spatial geochemical variations in tungsten and associated rare-metals. The location of the samples is indicated in Fig. 81. Whole-rock bulk compositions of the samples collected were determined at the SARM-CRPG-CNRS (Vandœuvre-lès-Nancy, France). Major elements were measured with a Thermo Fisher ICap 6500 ICPOES and minor and trace elements with a Thermo Fisher X7 Q-ICPMS. Sample preparation, analytical

conditions and limits of detection are detailed in Carignan et al. (2001). All the mineralogical and geochemical analyses were performed at the GeoRessources laboratory (Université de Lorraine, Vandœuvre-lès-Nancy, France).

3.2. Scanning electron microscope and electron microprobe

Mineralogical and textural observations were carried out using a Jeol J7600F scanning electron microscope (SEM) equipped with a SDD-type EDS spectrometer coupled to an Oxford Wave WDS spectrometer. Backscattered electron (BSE) images were obtained on polished thin sections with an acceleration voltage of 15 kV adjusting the electronic contrast to reveal the internal zoning within the observed crystals. Punctual EDS analyses were calibrated using both natural and synthetic standards. Geochemical analyses of the Ti-oxides were done using a Cameca SX100 electron microprobe analyzer (EMPA) equipped with five WDS spectrometers. Major elements (Ti, Fe) were measured with an acceleration voltage of 15 kV and a beam current of 12 nA, with counting times of 10 s on element peak and 5 s on background. Minor elements (V, Sn, Si, Mn, Ta, Nb, Zr, Cr, W) were measured with an acceleration voltage of 25 kV and a beam current of 100 nA, with counting times of 100 s on element peak and 50 s on background. The following elements, monochromators, standards and limits of detection were used for the measurements: Ti Kα (LPET, $MnTiO_3$, 700 ppm), Fe Kα (LIF, Fe_2O_3, 1920 ppm), V Kβ (PET, V metal, 440 ppm), Sn Lα (PET, SnO_2, 130 ppm), Si Kα (TAP, albite, 50 ppm), Mn Kα (LIF, $MnTiO_3$, 90 ppm), Ta Lα (LIF, Ta metal, 275 ppm), Nb Lα (PET, $LiNbO_3$, 200 ppm), Zr Lα (PET, ZrO_2, 200 ppm), Cr Kα (LLIF, Cr_2O_3, 60 ppm) and W Lα (LLIF, $CaWO_4$, 150 ppm). Analytical error was < 1% for the element measured. Chemical compositions are expressed in weight percent oxides (wt.%). Structural formulae were calculated on the basis of 2 atoms of oxygen for TiO_2 and 3 atoms of oxygen for ilmenite.

3.3. Raman spectrometry

Raman spectrometry was used to identify the TiO_2 polymorphs (rutile, anatase, brookite) based on the Raman bands compilation from Meinhold (2010). Raman spectra were recorded on polished thin sections using a Horiba Jobin-Yvon LabRAM spectrometer equipped with a 1800 $gr.mm^{-1}$ grating and an Edge filter. The confocal hole aperture is of 500 µm, the slit aperture is of 100 µm. The excitation beam is provided by a Stabilite 2017 Ar^+

laser (Spectra Physics, Newport Corporation) at 514.53 nm and a power of 200 mW, focused on the sample using x20 and x100 objectives equipped on an Olympus BX40 microscope. The laser beam diameter is around 1 µm. Acquisition time and numbers of accumulation are chosen in a way to optimize the signal-to-noise ratio, ideally lower than 1%.

3.4. Laser ablation ICPMS

Trace element compositions in Ti-oxides were measured by LA-ICPMS using a Agilent 7500c quadrupole ICPMS coupled with a 193 nm GeoLas ArF Excimer laser (MicroLas, Göttingen, Germany). Laser ablation was performed with a constant 5 Hz pulse frequency and a fluence of 7 J/cm^2 by focusing the beam at the sample surface using variable laser spot diameters between 24 and 44 µm. Helium was used as carrier gas to transport the laser-generated particles from the ablation cell to the ICPMS and argon was added as an auxiliary gas via a flow adapter before the ICP torch. Typical flow rates of 0.5 L/min for He and 0.9 L/min for Ar were used. The certified reference material NIST SRM 610 (concentrations from Jochum et al., 2011) was used as external standard for calibration of all analyses and was analysed twice at the beginning and at the end for each set of samples, following a bracketing standardization procedure. The reference material NIST SRM 612 was also used as control standard for the standardization. LA-ICPMS calibration was optimized for highest sensitivity on an intermediate m/Q range, while maintaining Th/U ~ 1 and ThO/Th < 0.5%, as determined on NIST SRM 610. The following isotopes were measured with a dwell time of 20 ms for each: ^{29}Si, ^{45}Sc, ^{47}Ti, ^{51}V, ^{53}Cr, ^{57}Fe, ^{60}Ni, ^{63}Cu, ^{66}Zn, ^{90}Zr, ^{93}Nb, ^{95}Mo, ^{118}Sn, ^{181}Ta and ^{182}W. Data reduction and absolute quantification of signals were performed using the software StalQuant, developed at ETH Zürich, Switzerland (see details in Fricker, 2012). For all analyses, the content of ^{47}Ti determined from EMPA analyses was used as internal standard. Limits of detection (LOD) were calculated using the 2σ criterion detailed in Longerich et al. (1996). Zr-in-rutile temperatures were calculated using the thermometer defined by Watson et al. (2006) based on the coexistence of zircon, rutile and quartz phases with a temperature uncertainty of ±20°C.

3.5. ^{40}Ar-^{39}Ar geochronology

^{40}Ar/^{39}Ar analytical work was performed at the University of Manitoba (Canada) using a multi-collector Thermo Fisher Scientific ARGUS VI mass spectrometer, linked to a stainless

steel Thermo Fisher Scientific extraction/purification line, Photon Machines (55 W) Fusions 10.6 CO_2 laser, and Photon Machines (Analyte Excite) 193 nm laser. Argon isotopes (from mass 40 to 37) were measured using Faraday detectors with low noise 1 x 10^{12} Ω resistors and mass 36 was measured using a compact discrete dynode (CDD) detector. The sensitivity for argon measurements is ~6.312 x 10^{17} moles/fA as determined from measured aliquots of Fish Canyon Sanidine (Dazé et al., 2003; Kuiper et al., 2008). Standards and sample were placed in 2 mm deep wells in 18 mm diameter aluminium disks, with standards placed strategically so that the lateral neutron flux gradients across the disk could be evaluated. Planar regressions were fit to the standard data, and the $^{40}Ar/^{39}Ar$ neutron fluence parameter (J) interpolated for the unknowns. Uncertainties in J are estimated at 0.1 - 0.2% (1σ), based on Monte Carlo error analysis of the planar regressions (Best et al., 1995). All specimens were irradiated in the Cadmium-lined, in-core CLICIT facility of the TRIGA reactor at the Oregon State University (USA). The duration of irradiation was 17 hours and using the Fish Canyon sanidine (Kuiper et al., 2008) and GA1550 biotite (Spell and McDougall, 2003) standards. Standards for $^{40}Ar/^{39}Ar$ measurements were placed in a Cu sample tray, with a KBr cover slip, in a stainless steel chamber with a differentially pumped ZnS viewport attached to a Thermo Fisher Scientific extraction/purification line and baked with an infrared lamp for 24 hours. Single crystals were fused using the CO_2 laser. The sample selected for the $^{40}Ar/^{39}Ar$ dating has been previously investigated by optical microscopy and SEM in order to spot homogeneous areas devoid of alteration, micro-inclusions or internal zoning. Discs of 5 mm in diameter and ~150 µm thick were cut from the same polished thick section (150 - 200 µm thick). The discs were mounted using a ceramic adhesive (PELCO) on a quartz slide placed in a stainless steel chamber with a sapphire viewport attached to the same stainless steel high vacuum extraction system as the CO_2 laser, and baked with an infrared lamp for 48 hours. For this study, a raster size of about 100 x 100 µm was used and ablation pits were excavated to an estimated depth of 50 µm. Reactive gases were removed for both the standard and unknown, after 3 minutes, by three GP-50 SAES getters (two at room temperature and one at 450 °C) prior to being admitted to an ARGUS VI mass spectrometer by expansion. Five argon isotopes were measured simultaneously over a period of 6 minutes. Measured isotope abundances were corrected for extraction-line blanks, which were determined before every sample analysis. Line blanks in both the Excimer and CO_2 system averaged ~3 fA for mass 40 and ~0.013 fA for mass 36. Mass discrimination was monitored by online analysis of air pipettes based on a power law relationship (Renne et al., 2009), which gave D = 1.0081 ± 0.0002 per amu, based on 71 aliquots interspersed with the unknowns. A value of 295.5 was used for the atmospheric

$^{40}Ar/^{36}Ar$ ratio (Steiger and Jäger, 1977) for the purposes of routine measurement of mass spectrometer discrimination using air aliquots, and correction for atmospheric argon in the $^{40}Ar/^{39}Ar$ age calculation. Corrections are made for neutron-induced ^{40}Ar from potassium, ^{39}Ar and ^{36}Ar from calcium, and ^{36}Ar from chlorine (Roddick, 1983; Renne et al., 1998; Renne and Norman, 2001). Data were plotted using DensityPlotter (Vermeesch, 2012).

4. The St-Mélany Sn-W deposit

4.1. The mineralized quartz vein system

At the outcrop scale, two sets of mineralized quartz veins are found at St-Mélany:

(i) flat-lying veins which are secant at low-angle and almost concordant to the regional schistosity S2 (Fig. 84a), with general orientations of N100-140°E and N00-40°W with a mean dip of 20° (Fig. 85a). They form lenticular veins, 10-50 cm thick and 5-25 m long, and show typically boudinage deformation (Fig. 84b). The extremities of the veins exhibit irregular boundaries with quartz digitations into the micaschist, both affected by flattening (Fig. 84c).

(ii) steep veins which are discordant to the regional schistosity (Fig. 84d) with variable orientations of N40-170° and variable dip of 45-90° (Fig. 85b). They are 2-15 cm thick and are deformed by asymmetric folds with axial planes sub-parallel to the schistosity (Fig. 84e,f).

These two types of quartz veins are spatially interconnected laterally. At the contact, the milky quartz of the veins is sealed continuously forming one interconnected vein system.

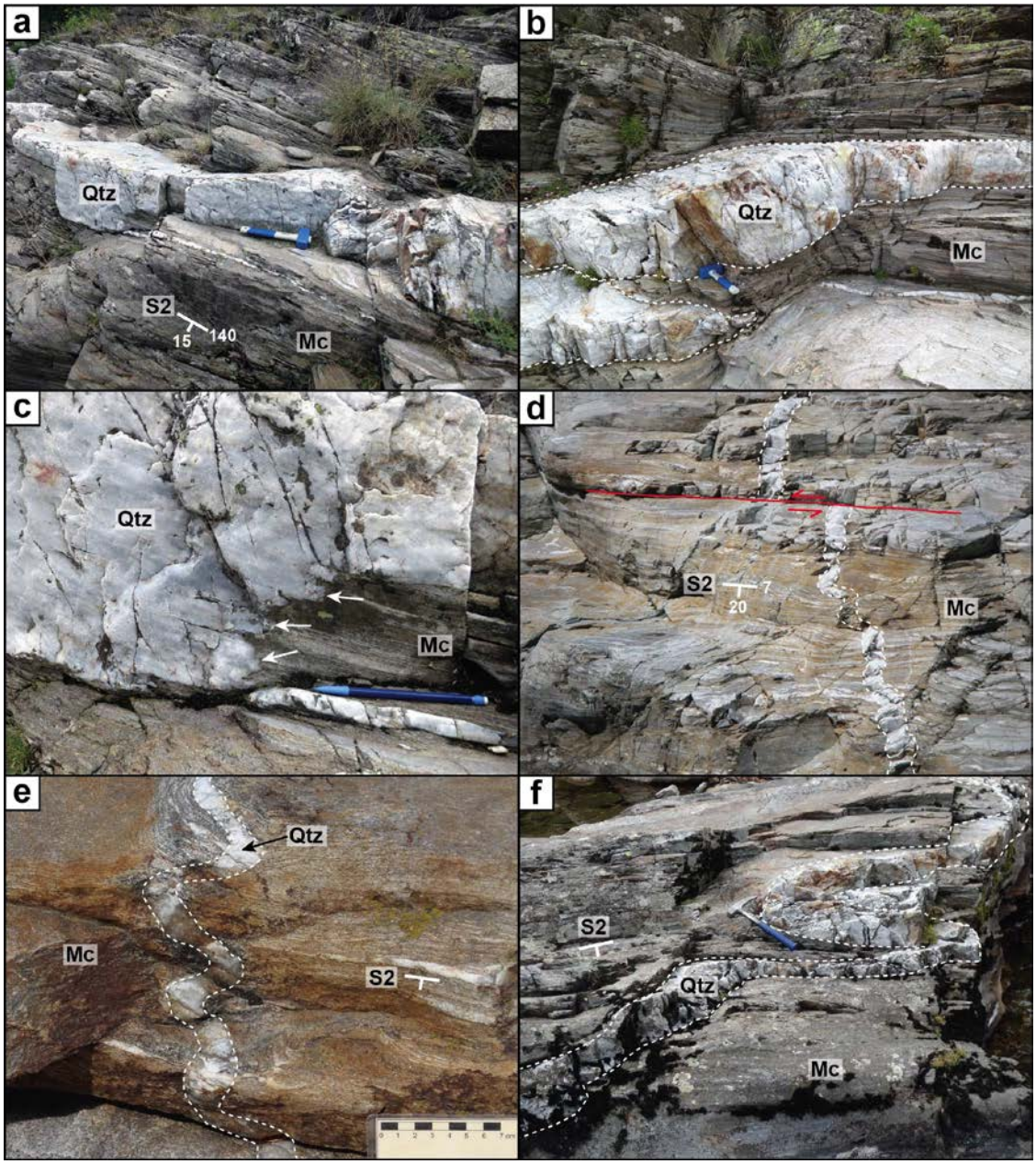

Fig. 84: Ductile deformation in the mineralized quartz veins from the St-Mélany Sn-W deposit. (a) Sub-concordant flat lying quartz vein crosscutting the micaschist. (b) Flat laying quartz vein showing boudinage deformation in the micaschist. (c) Detailed view of the quartz digitations into the micaschist (white arrows). (d) Oblique discordant quartz vein crosscutting the schistosity S2. (e,f) Oblique quartz veins deformed by asymmetric folds with axial planes sub-parallel to the schistosity.

At the thin section scale, the quartz veins are formed by polycrystalline quartz aggregates exhibiting textural evidences of intracrystalline deformation and dynamic recrystallization (Fig. 86a). The quartz grains range from a few cm down to 100 µm in size. The largest grains show undulose extinction and elongate subgrains with deformation bands, which are delimited by smaller grains with regular shapes likely formed by subgrain rotation

recrystallization. The smallest grains have irregular and interlobate boundaries, which suggest grain boundary migration. These microstructural features are typical of ductile deformation at high temperature (500-700°C) (e.g., Stipp et al., 2002; Passchier and Trouw, 2005). The narrow muscovite fringe, observed locally at the selvages of the mineralized quartz veins, shows also microscopic evidences of plastic deformation (Fig. 86b). The muscovite form comb-like crystals, millimetres in size, which crystallize on the schistosity of the micaschist and are slightly kinked with an apparent shearing movement at the contact with the quartz vein (Fig. 86b). Cassiterite growth directly on the selvage muscovite (Fig. 86c) and is lately deformed in the quartz vein. The cassiterite and wolframite form mostly euhedral crystals, millimetres to centimetres in size, which are corroded within the deformed quartz (Fig. 86d). They are fractured by micro-cracks infilled by recrystallized quartz, which may be interpreted as tension gashs (Fig. 86d). The temporal relationship between cassiterite and wolframite was not observed. However, since cassiterite is frequently observed on the selvage of the veins and wolframite mostly disseminated within the quartz, this may indicate than cassiterite form earlier than wolframite. In this respect, it can be noted that one crystal of cassiterite was observed directly in the micaschist at the selvage of a quartz vein (Fig. 83c), thus indicating that cassiterite crystallization is early during the vein opening. Scheelite forms after wolframite and shows also evidence of undulose extinction (Fig. 86e). Finally, pyrite associated with minor arsenopyrite forms lately in overgrowth or in vein infilling within the wolframite and scheelite (Fig. 86f). In summary, the mineralized vein system from St-Mélany formed during a polyphase vein opening, likely according to a crack-seal mechanism typical of the hydraulic fracturing, and was lately affected by a plastic deformation.

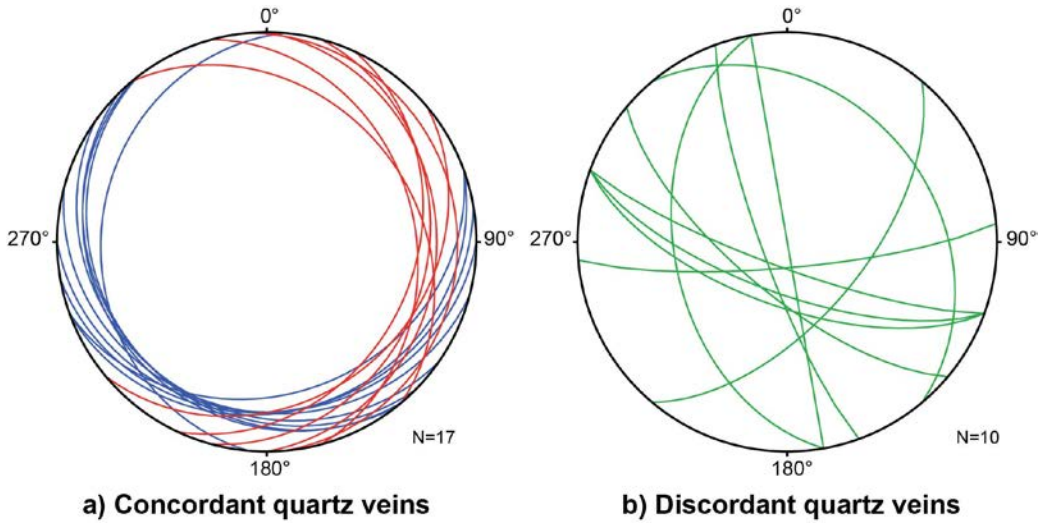

Fig. 85: Lower hemisphere equal-area projection showing the orientation of the measured concordant (a) and discordant (b) quartz veins from St-Mélany.

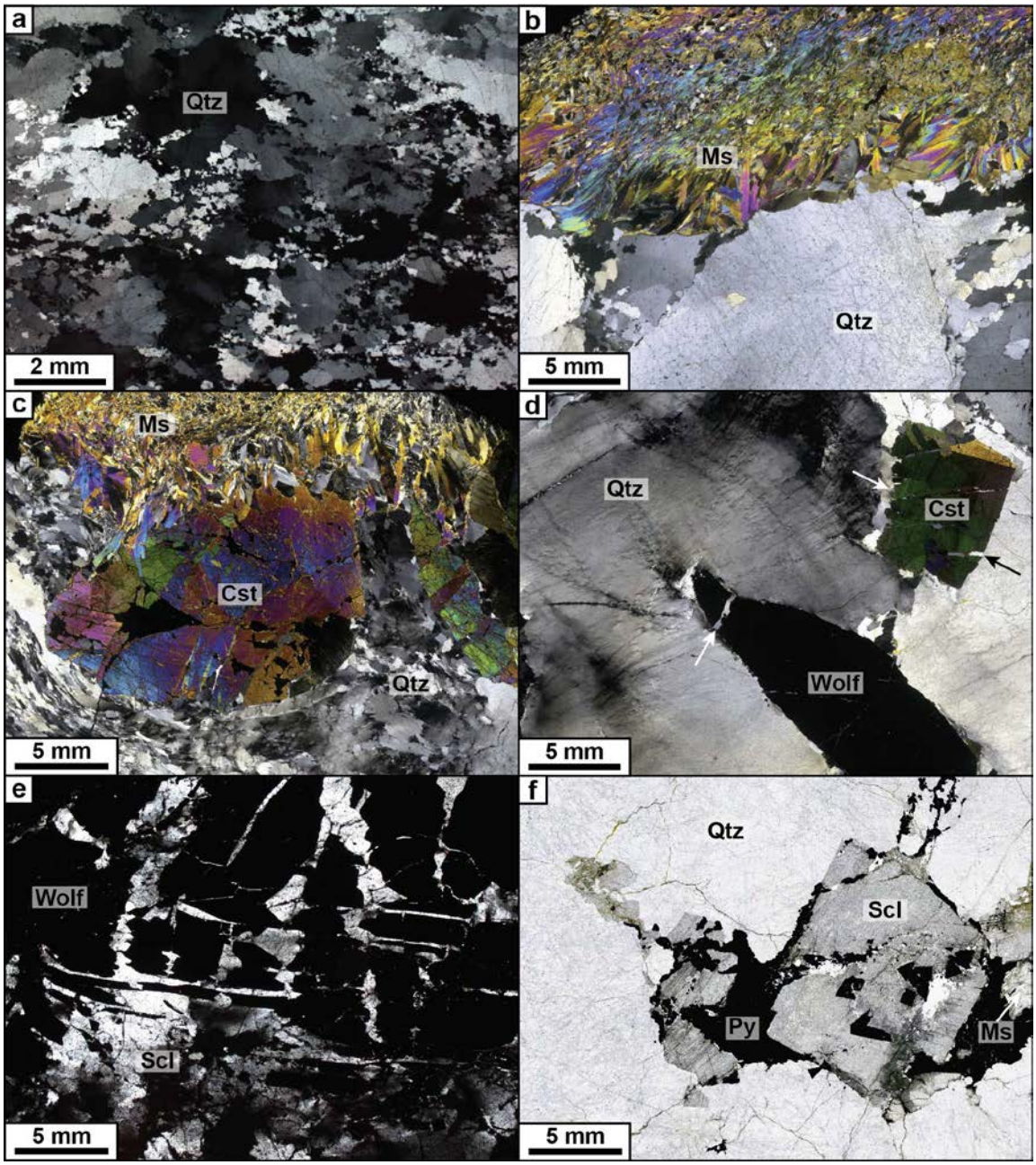

Fig. 86: Microphotographs in transmitted light of the mineralized quartz veins from St-Mélany. (a) Typical microtexture of the quartz in the mineralized veins forming polycrystalline aggregates and showing textural evidences of intracrystalline deformation and dynamic recrystallization (sample 14-ARD03). (b) Muscovite fringe at the selvage of a mineralized quartz vein (sample ARD-13-12). (c) Large cassiterite crystal growing on the muscovite fringe and partially corroded by the quartz of the vein (sample ARD-13-77a). Note the cataclastic texture of the quartz toward the center of the vein. (d) Crystals of cassiterite and wolframite partially cut and corroded within the deformed quartz of the vein (arrows), observed in cross-polarized light (sample 14-ARD01). (e) Scheelite replacing wolframite, observed in cross-polarized light, and showing undulose extinction (sample 14-ARD-06). (f) Subeuhedral scheelite crystal formed after wolframite and partially corroded and cut by late pyrite in the mineralized quartz vein (sample ARD-13-18b). Mineral abbreviations: Cst: cassiterite; Ms: muscovite; Py: pyrite; Qtz: quartz; Scl: scheelite; Wolf: wolframite.

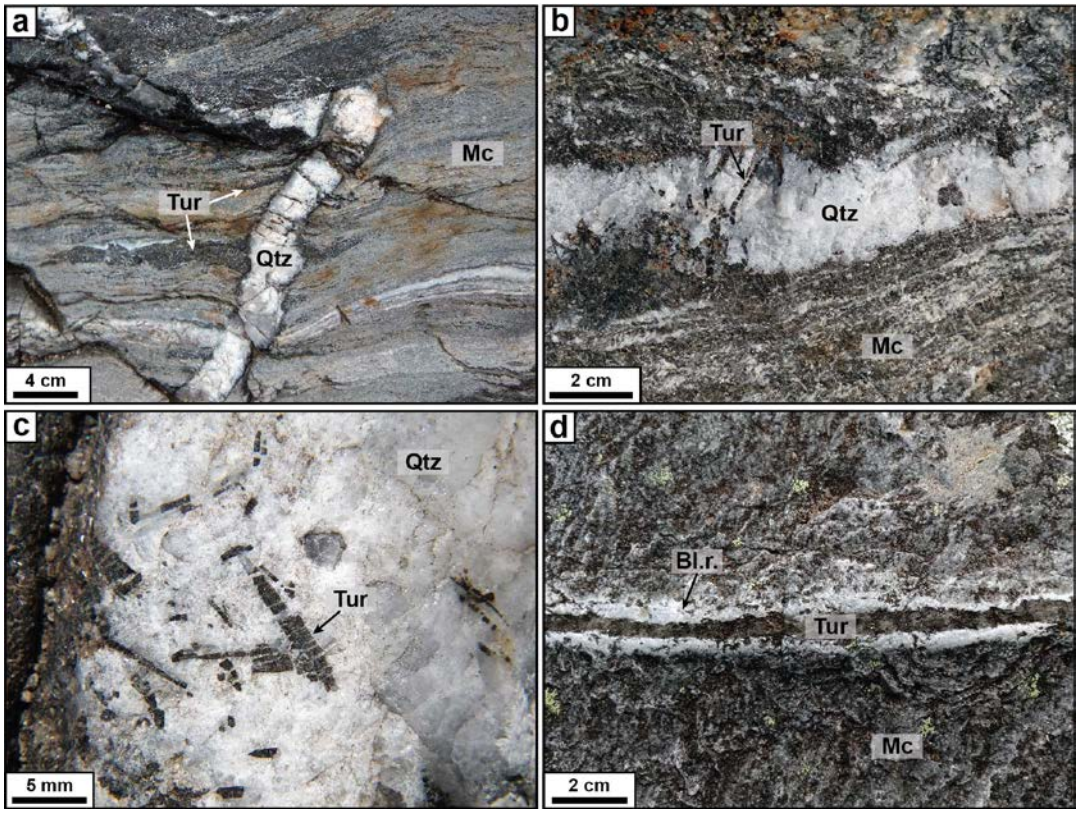

Fig. 87: Photographs of tourmalines from the St-Mélany deposit. (a) Tourmalinite (Tur) at the selvage of mineralized quartz (Qtz) veins crosscutting the micaschists (Mc). Note the sharp contact between the quartz and the tourmalinite. (b) Acicular tourmaline in quartz-cassiterite (Cst) veins, crosscutting the micaschist. (c) Detailed view of tourmaline crystals segmented in the quartz of the veins. (d) Black tourmalinite vein crosscutting the micaschist and rimmed by a bleached rim (Bl.r.) corresponding to the leaching and silicification of the enclosing schist.

4.2. Tourmalinization

Tourmalinization in the St-Mélany deposit represents a major hydrothermal alteration affecting the enclosing micaschists. Pervasive tourmalinization is known regionally and appears without relationships with the Sn-W mineralization (Noyé and Weisbrod, 1988). At St-Mélany, the tourmalinization is multi-stage and at least three main generations of tourmaline can be distinguished (see Chapter 7 for details): (i) diffuse tourmaline developed at the selvage of the quartz veins and progressively diffusing in to the micaschist along schistosity planes by replacement of the phyllosilicates. Observed on the schistosity plane, the tourmalines are segmented along a direction N-S, indicating an extension E-W. This first tourmalinization stage occurs before the emplacement of the Sn-W mineralization and the quartz crystallization; (ii) acicular tourmalines found in the mineralized quartz veins, which formed during vein opening by crystallizing on the tourmalinite selvages. They are lately

fragmented within the quartz according to a crack-seal mechanism; (iii) black tourmalinite veins surrounded by cm-thick bleached rims, which crosscut the micaschists. They are formed by brecciated crystals of tourmaline cemented by an association of chlorite with minor muscovite and K-feldspar.

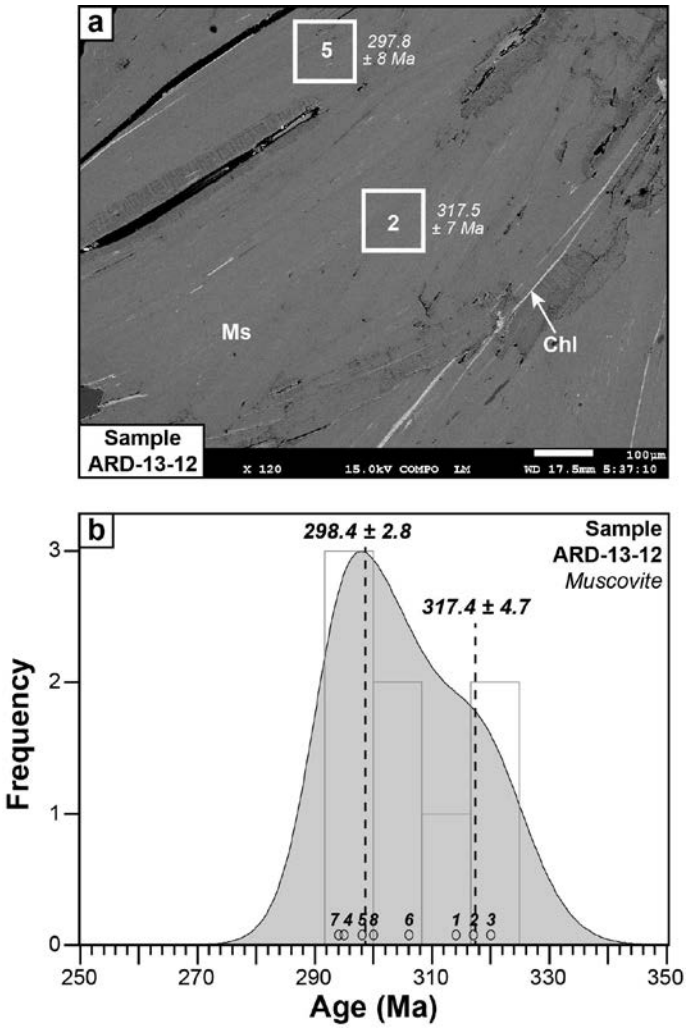

Fig. 88: Results of the $^{40}Ar/^{39}Ar$ dating for the selvage muscovite from the St-Mélany deposit (sample ARD-13-12). (a) BSE image of the dated muscovite (Ms) showing homogeneous internal texture, with minor interstitial chlorite (Chl). The location of two ablation spots (100 x 100 µm) is indicated on the BSE image with the corresponding obtained ages. (b) Frequency histogram of the $^{40}Ar/^{39}Ar$ ages obtained on muscovite and identification of the two age modes. Data are given in Table 25.

4.3. ^{40}Ar-^{39}Ar dating of selvage muscovite

One representative sample of muscovite (sample ARD-13-12) located at the selvages of a mineralized quartz vein was collected in the St-Mélany deposit. This sample was preliminary investigated by SEM in order to investigate the presence of internal zoning or

micro-inclusions. As seen in Fig. 88a, the muscovite is characterized by homogeneous internal texture in BSE imagery and exhibit minor chlorite in interstitial infilling. Results of the $^{40}Ar/^{39}Ar$ dating of muscovite are shown in Fig. 88b and isotopic data are given in Table 25. Two geochronological groups appear from the frequency histogram of the $^{40}Ar/^{39}Ar$ isotopic ages: (i) a younger group yielding an age of 298.4 ± 2.8 Ma; and (ii) an older group yielding an age of 317.4 ± 4.7 Ma. The former correspond to the ablation spots located closer to the external crystal borders, whereas the latter correspond to those closer to the internal part of the muscovite crystals. The apparent old age may be interpreted as the crystallization age of the muscovite, whereas the younger age may reflect recrystallization on the crystal boundaries during later fluid circulations.

5. Petrography and geochemistry of the regional magmatic rocks

The objective of this section is to evaluate the potential of the regional magmatic rocks as source for tungsten and associated rare metals ("source fingerprinting"). A series of 11 samples of the main magmatic rocks were collected during this study and were analysed for major, minor and trace elements. These data were completed with old unpublished database (years 70-80's), for which only major element analyses were available.

5.1. Rocles granite

The Rocles granite is located at the mesozone-epizone boundary and is in overall interstratified in the micaschists. In detail, it is made of coalescing granitic sheets with interleaved panels of the Cévenole series and/or co-magmatic vaugnerite I sills, ranging from metric to hectometric in size. The Rocles granite was emplaced during the D3 event and exhibits typically a syn-magmatic S3 foliation, which is parallel to the granite contact. The granite is clearly zoned, composed at the footwall by a coarse-grained porphyritic biotite-syenogranite and passing upwards to a two-mica medium-grained syenogranite. At the hanging wall, a third granitic unit is represented by a fine-grained muscovite-bearing leucogranite, which outcrops mainly to the west of the body (Fig. 78). A swarm of thin (10-50 cm) leucogranitic dykes occurs on several tens of meters outside the pluton and may serve as channel for the "Rocles-type" tourmalinization, as observed at Pont-du-Gua in the Beaume valley (Fig. 80c).

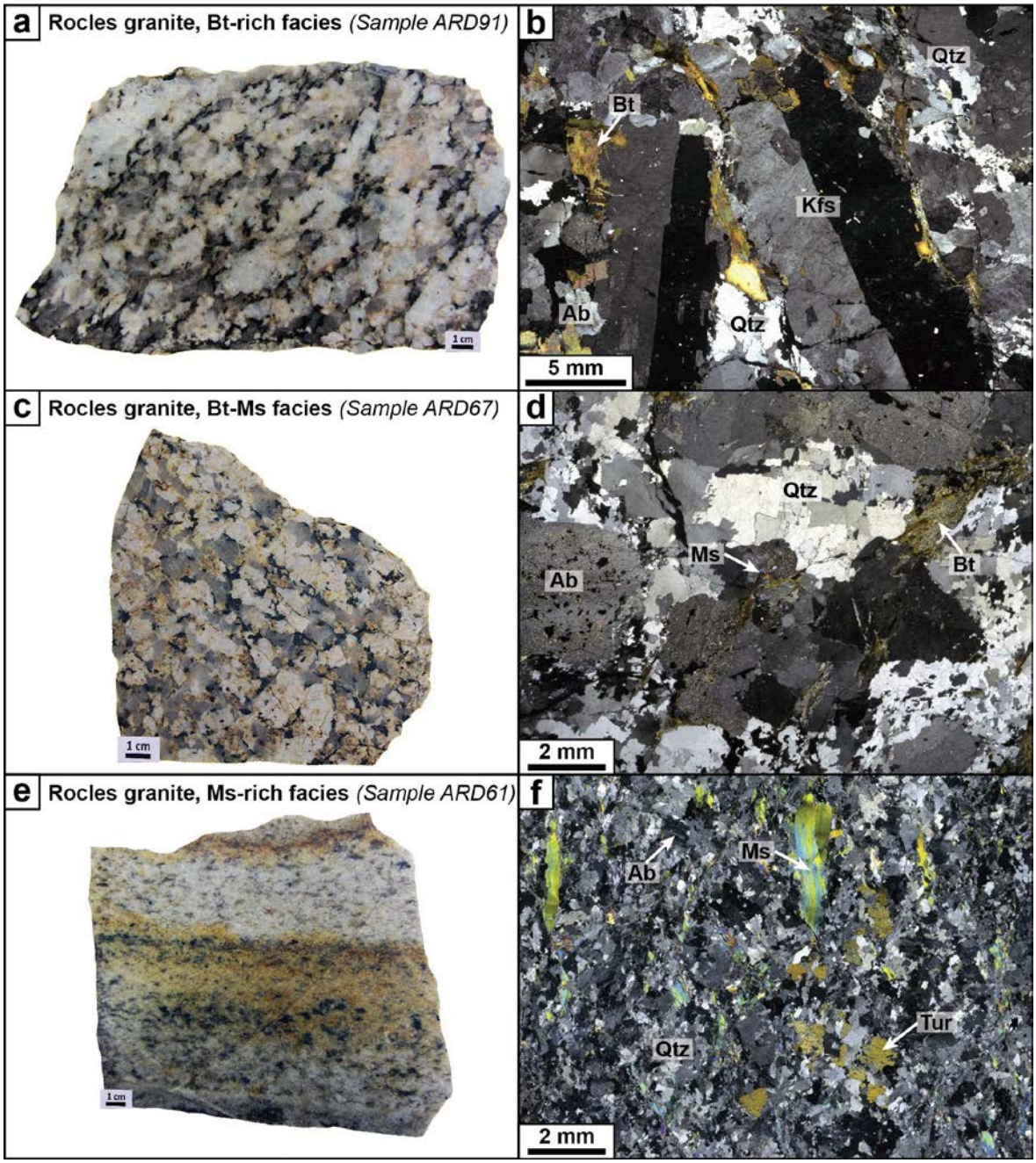

Fig. 89: Photographs of the studied samples from the Rocles granite. (a,b) Biotite-rich facies (sample ARD91). (c,d) Biotite-muscovite facies (sample ARD67). (e,f) Muscovite-rich facies (sample ARD61). Mineral abbreviations: Ab: albite; Bt: biotite; Kfs: K-feldspar; Ms: muscovite; Qtz: quartz; Tur: tourmaline.

Three representative samples corresponding to these three different petrological facies were collected (Fig. 81): (i) the biotite-rich facies (sample ARD91; Fig. 89a) consists in a porphyritic granite containing centimetric euhedral crystals of K-feldspars within a millimetric quartz-biotite matrix (Fig. 89b); (ii) the biotite-muscovite facies (sample ARD67; Fig. 89c) corresponds to a leucocratic medium-grained granite composed by centimetric

euhedral crystals of K-feldspars within a biotite+muscovite+quartz matrix (Fig. 89d); and (iii) the muscovite-rich facies (sample ARD61; Fig. 89e) is composed by a fine-grained muscovite-tourmaline leucogranite with minor amounts of biotite (Fig. 89f).

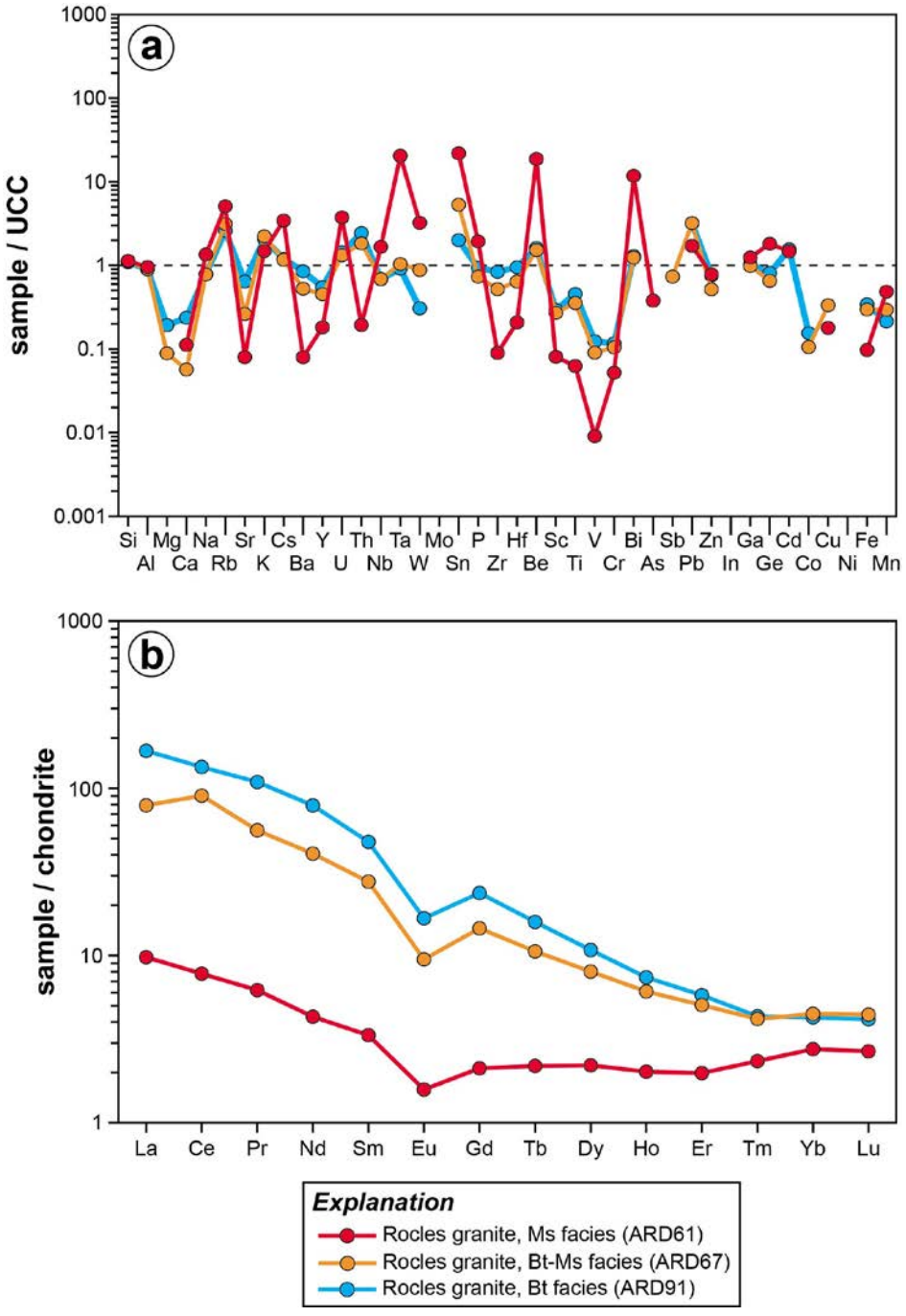

Fig. 90: Whole-rock geochemical composition of the Rocles granite. (a) Multi-element diagram normalized by the upper continental crust (UCC, Rudnick and Gao, 2003). (b) REE pattern normalized to the chondrite (CI, Palme and O'Neill, 2014). Whole-rock data are given in Table 26.

Whole-rock geochemistry of the three facies is characterized by their common peraluminous compositions (Al/CNK=1.15-1.22), but differ by their major and trace element compositions (Table 26). The biotite-rich and biotite-muscovite facies have similar major and trace element compositions (Fig. 90a) with relatively high contents in Rb, K, Th and Pb and lower contents in Mg, Ca, Sr, Ba, Y, Sc, Ti, V, Cr, Co, Fe and Mn compared to the upper continental crust (UCC from Rudnick and Gao, 2003). Their REE patterns (Fig. 90b) are characterized by enrichment in LREE (La/Yb=17.6-39.2) with a negative Eu anomaly (Eu/Eu*=0.47-0.50) and a slightly positive Ce anomaly (Ce/Ce*=1.0-1.36) marked for the two-mica facies.

At the opposite, the muscovite-rich facies has a distinct composition, which distinguish by significant enrichments in Rb, Cs, U, Ta, W, Sn, P, Be, Bi and depletion in Mg, Ca, Sr, Ba, Y, Th, Zr, Hf, Sc, Ti, V, Cr, As, Fe and Mn compared to the UCC (Fig. 90a). In particular, the muscovite-rich facies contains the highest concentrations in rare-metals, such as Sn (46 ppm), W (6.1 ppm), Nb (20 ppm), Ta (18 ppm) and Be (39 ppm) (Table 26). Its REE pattern (Fig. 90b) is less fractionated with a slight enrichment in LREE compared to the HREE (La/Yb=3.5) and a negative Eu anomaly (Eu/Eu*=0.59). In the A-B and Q-P classification diagrams (Fig. 91), the data from the Rocles granite plot in the peraluminous field and are characterized by an enrichment in quartz and albite with a fractionation of the ferromagnesian minerals, from the biotite facies toward the muscovite facies, the latter being the most evolved. In the A-B diagram (Fig. 91a) and the (QBF)3 diagram (Fig. 92), the Rocles granite show a mixing trend with the syn-M3 vaugnerite sills.

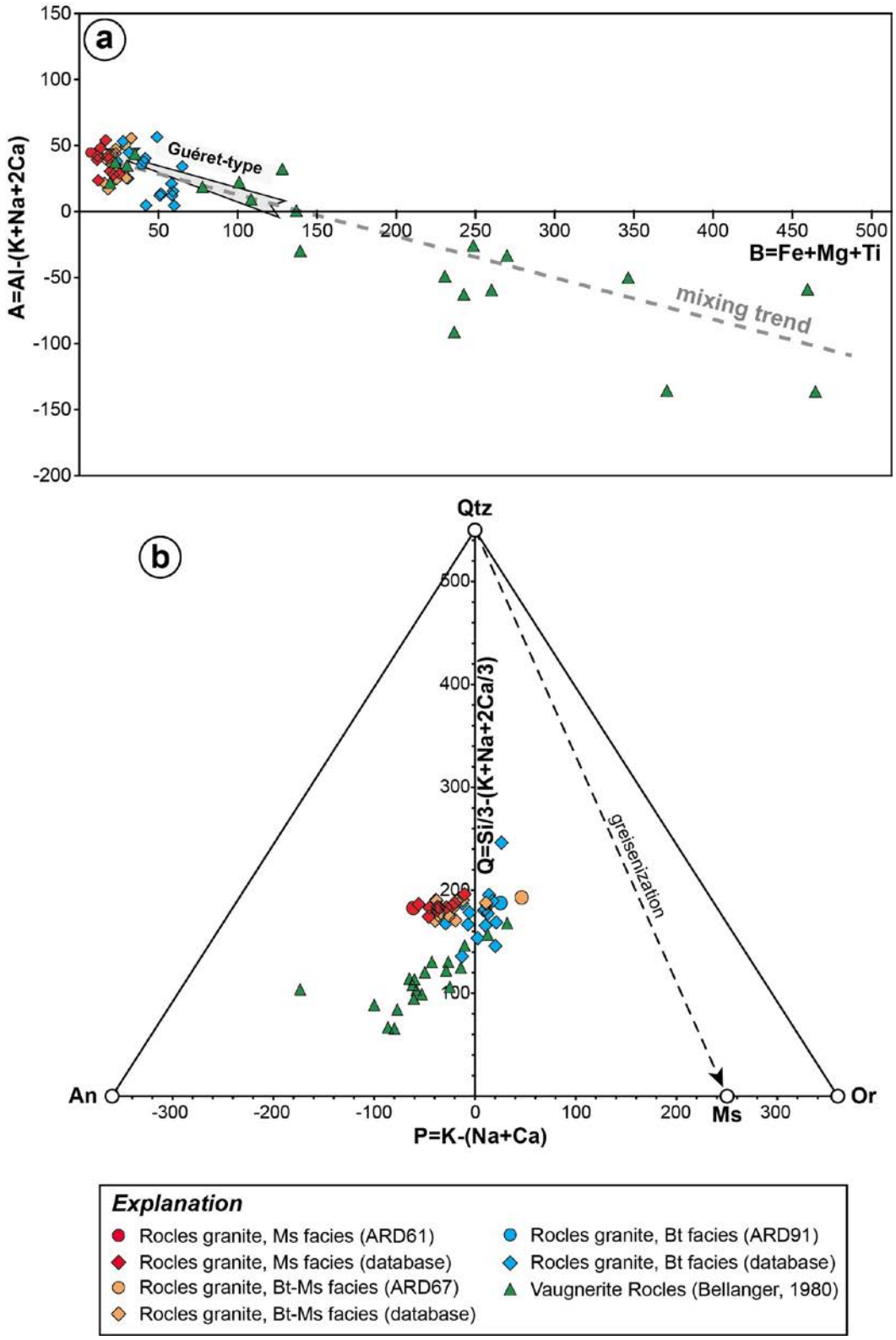

Fig. 91: Major element compositions of the Rocles granite projected in (a) the A-B diagram representing the peraluminous index A=Al-(Na+K+2Ca) as function of the differentiation index B=Fe+Mg+Ti (after Debon and Lefort, 1988) and in (b) the Q-P diagram representing the quartz content Q=Si/3-(K+Na+2Ca/3) as function of the relative proportions of feldspars P=K-(Na+Ca) (after Debon and Lefort, 1988). The data are plotted together with unpublished data from the Rocles granite (Artemise database) and vaugnerite sills within the Rocles granite (Bellanger, 1980). Whole-rock data are given in Table 26.

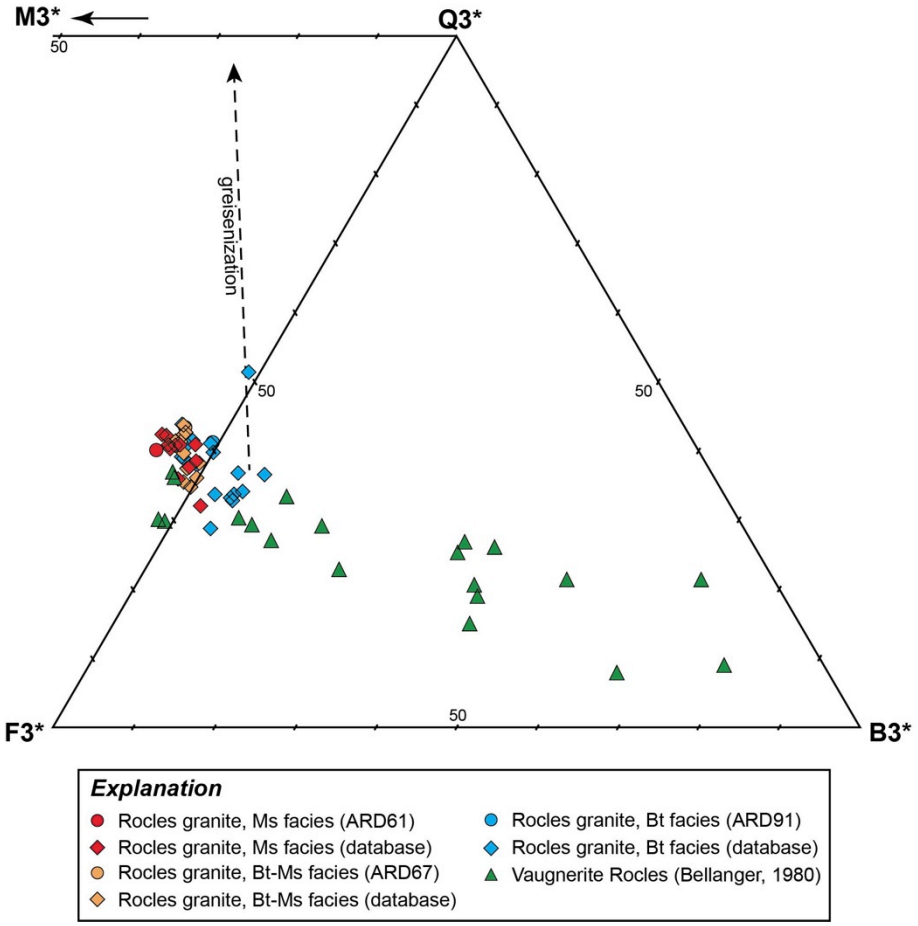

Fig. 92: Major element compositions of the Rocles granite projected in the (QBF)3 diagram (after Debon and Lefort, 1988), where Q3=Si+7Al/2-5Ca-13(Na+K)/2, B3=-7Al/2+7Ca+7(Na+K)/2+8(Fe+Mg+Ti)/3 and F3=Al+3Ca+4(Na+K)-5(Fe+Mg+Ti)/3. The normalization of these parameters to the Q3+B3+F3 sum yield to the (Q3*B3*F3*) diagram, where Q3* represents the quartz pole, B3* the biotite pole and F3* the feldspar pole. A fourth summit M3*, symmetrical to B3* relatively to the Q3*-F3* segment and corresponding to the muscovite pole can be also projected. The data are plotted together with unpublished data from the Rocles granite (Artemise database) and vaugnerite sills within the Rocles granite (Bellanger, 1980). Whole-rock data are given in Table 26.

5.1. Borne granite

The Borne pluton is composed by a medium-grained porphyritic biotite±amphibole monzogranite. It was emplaced as a sill and exhibits an overall E-W subvertical magmatic foliation marked by the K-feldspar megacrysts (Mialhe, 1980). It contains rare subhorizontal biotite schlieren (more frequent close to the hanging-wall) and is rich in decametric microgranular mafic enclaves (MME), which show clear textural evidences of a co-magmatic emplacement (ovoid morphology, chilled rims, incorporation of K-feldspar from the hosting granite). Towards the centre of the pluton exists a small area of a leucocratic non-porphyritic

biotite-granite (Mialhe, 1980). A series of N-S-striking leucogranites and variably oriented aplite dykes crosscut the Borne foliation and develop in the contact metamorphism aureole (easily observed in the Borne River valley). Similarly to the Rocles pluton, they may serve as channels for the "Borne-type" (bleaching) tourmalinisation event, which is regionally observed (Fig. 91d-f).

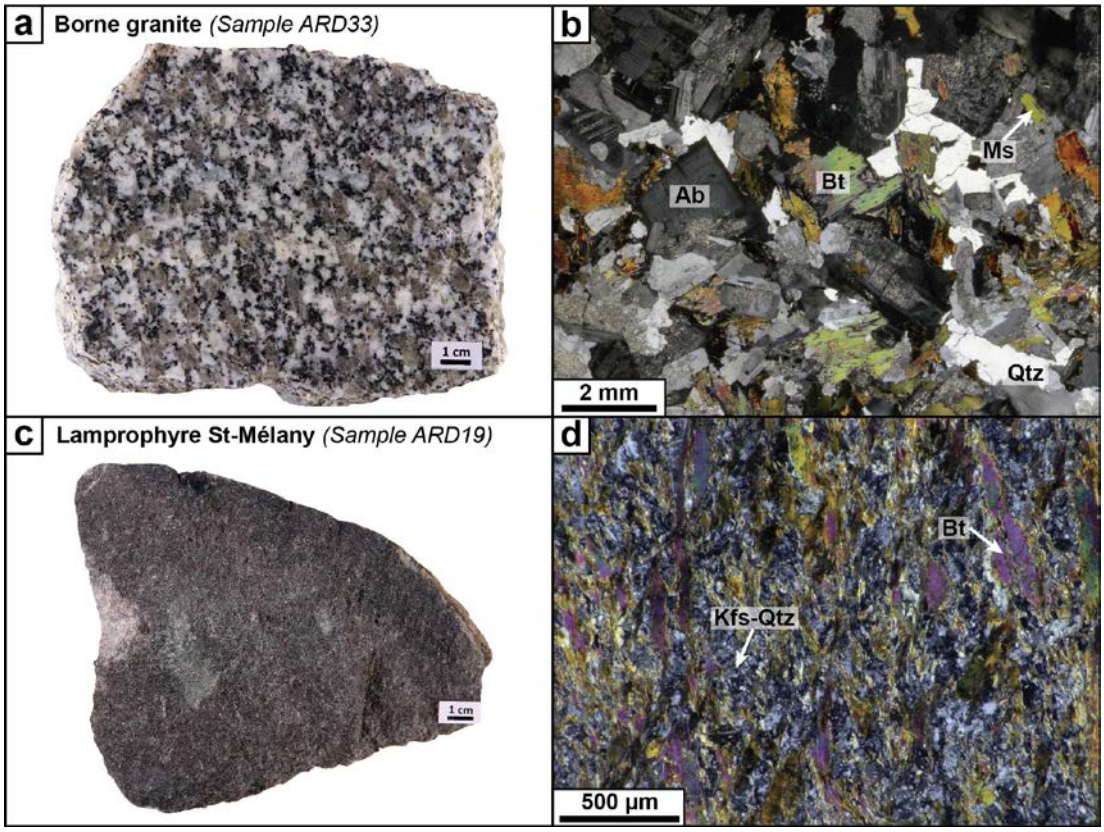

Fig. 93: Photographs of the studied samples from the Borne granite (a,b; sample ARD33) and the lamprophyre from St-Mélany (c,d; sample ARD19). Mineral abbreviations: Ab: albite; Bt: biotite; Kfs: K-feldspar; Ms: muscovite; Qtz: quartz.

One representative sample of the Borne granite has been collected at its eastern termination close to the contact with the enclosing micaschists (Fig. 81). This sample (ARD33; Fig. 93a) corresponds to a homogeneous biotite-muscovite porphyritic monzogranite (Fig. 93b). Whole-rock geochemistry of the Borne granite is characterized by a peraluminous composition (Al/CNK=1.10) with major and trace elements contents close to the values of the average UCC (Fig. 94a). The REE pattern shows an enrichment in LREE (La/Yb=20.4) with a negative Eu anomaly (Eu/Eu*=0.65) (Fig. 94b). No particular enrichment in rare-metals is observed (Table 26). In the A-B diagram (Fig. 95a), the data from the Borne granite exhibit negative values of the A peraluminous index, indicating a two-component mixing with metaluminous magmas. Data scattering toward high values of the A

parameter correspond to greisenization trends. In the Q-P diagram (Fig. 95b), the global trend corresponds to an enrichment in quartz and albite with fractionation of biotite and K-feldspar. Data projection from the MME, the syn-M4 vaugnerites (Roubreaud, Largentière) and the lamprophyres from St-Mélany show a mixing trend with the Borne granite (Fig. 95 and Fig. 96). Finally, it can be noted that the non-porphyritic facies described by Mialhe (1980) has evolved composition toward high peraluminous index values, which may be explained by greisenization trend (Fig. 95 and Fig. 96).

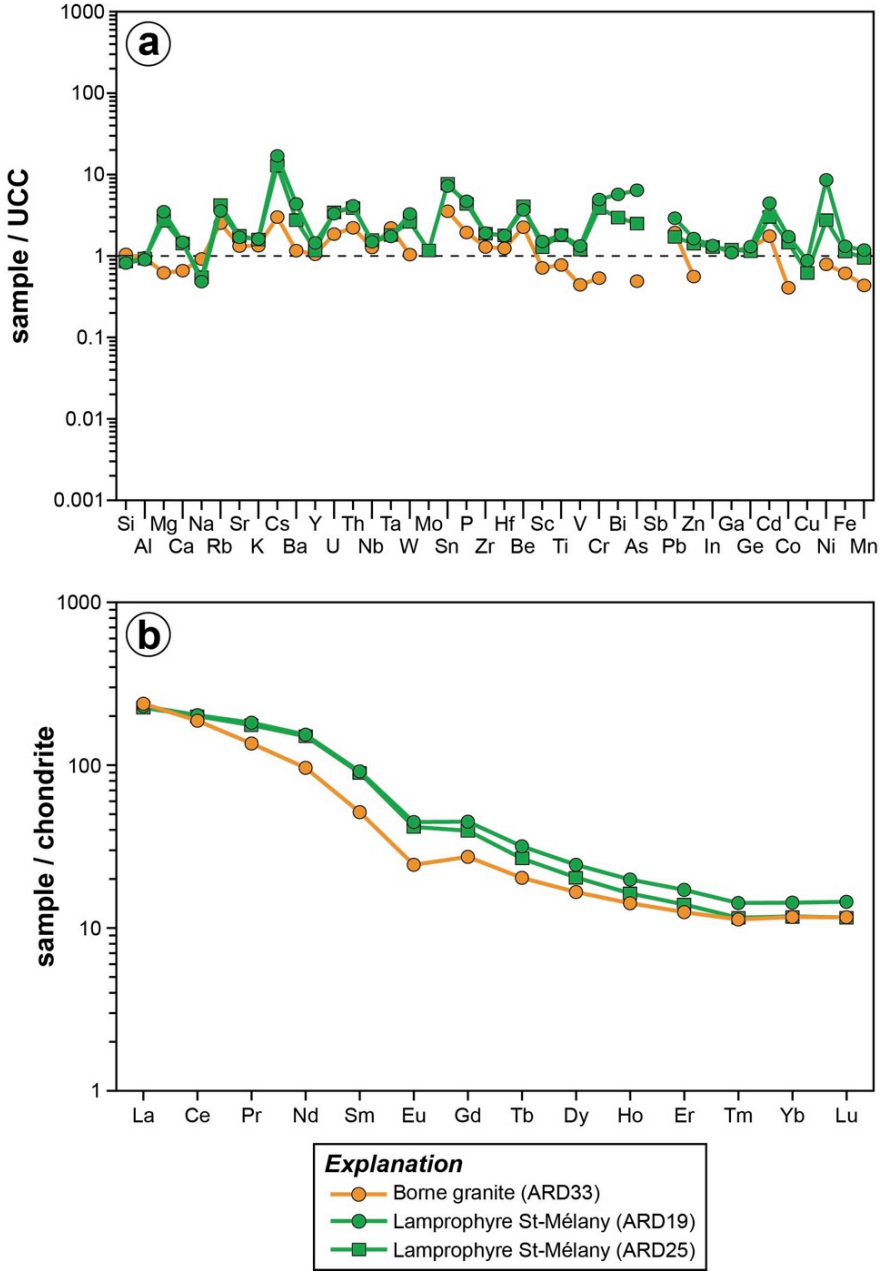

Fig. 94: Whole-rock geochemical compositions of the Borne granite and the lamprophyres from St-Mélany. (a) Multi-element diagram normalized by the upper continental crust (UCC, Rudnick and Gao, 2003). (b) REE pattern normalized to the chondrite (CI, Palme and O'Neill, 2014). Whole-rock data are given in Table 26.

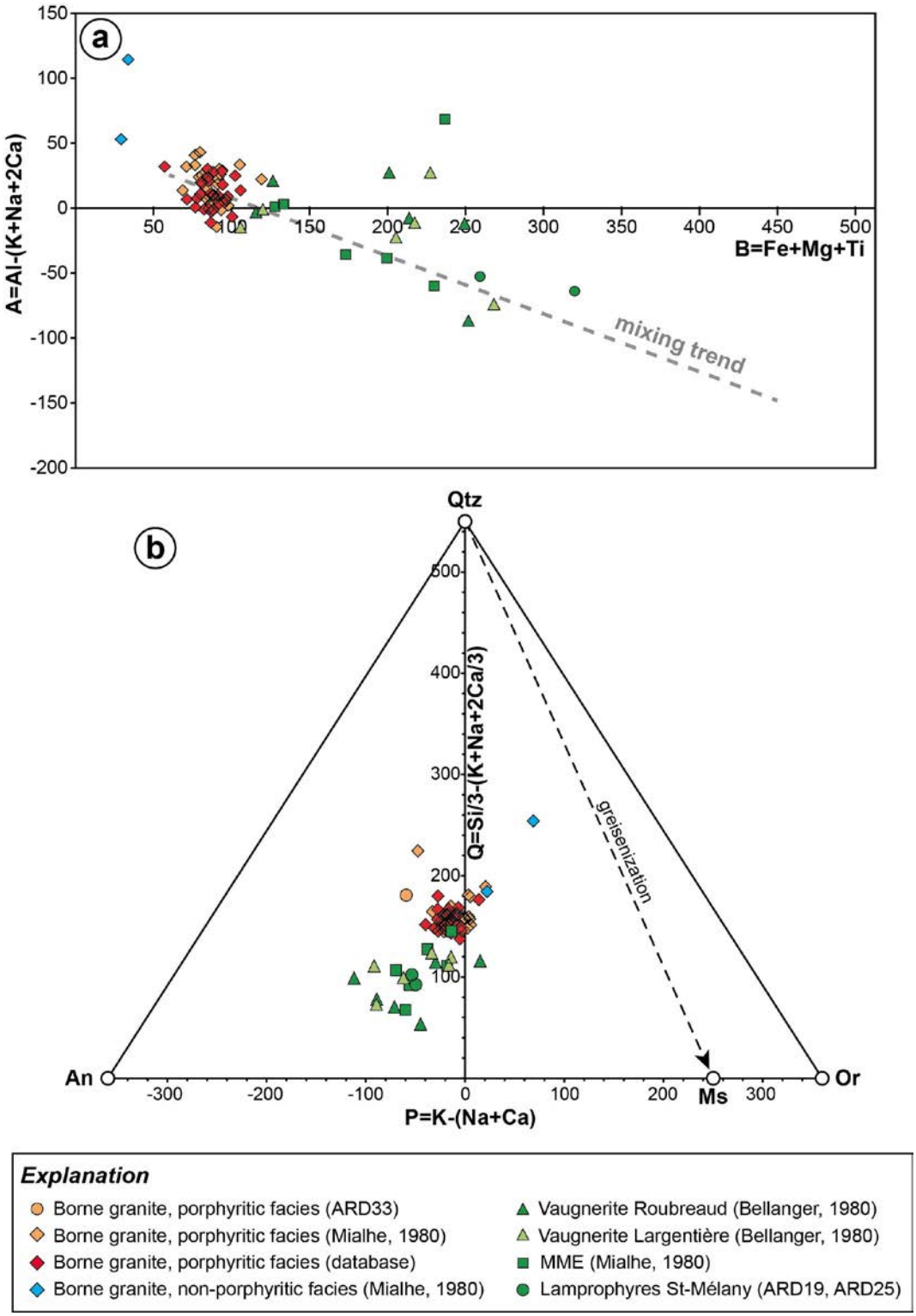

Fig. 95: Major element compositions of the Borne granite projected in (a) the A-B diagram representing the peraluminous index A=Al-(Na+K+2Ca) as function of the differentiation index B=Fe+Mg+Ti (after Debon and Lefort, 1988) and in (b) the Q-P diagram representing the quartz content Q=Si/3-(K+Na+2Ca/3) as function of the relative proportions of feldspars P=K-(Na+Ca) (after Debon and Lefort, 1988). The data are plotted together with old data from the Borne granite (Artemise database; Mialhe, 1980), microgranular mafic enclaves (MME) within the Borne granite (Mialhe, 1980) and catazonal vaugnerites II (Bellanger, 1980). Whole-rock data are given in Table 26.

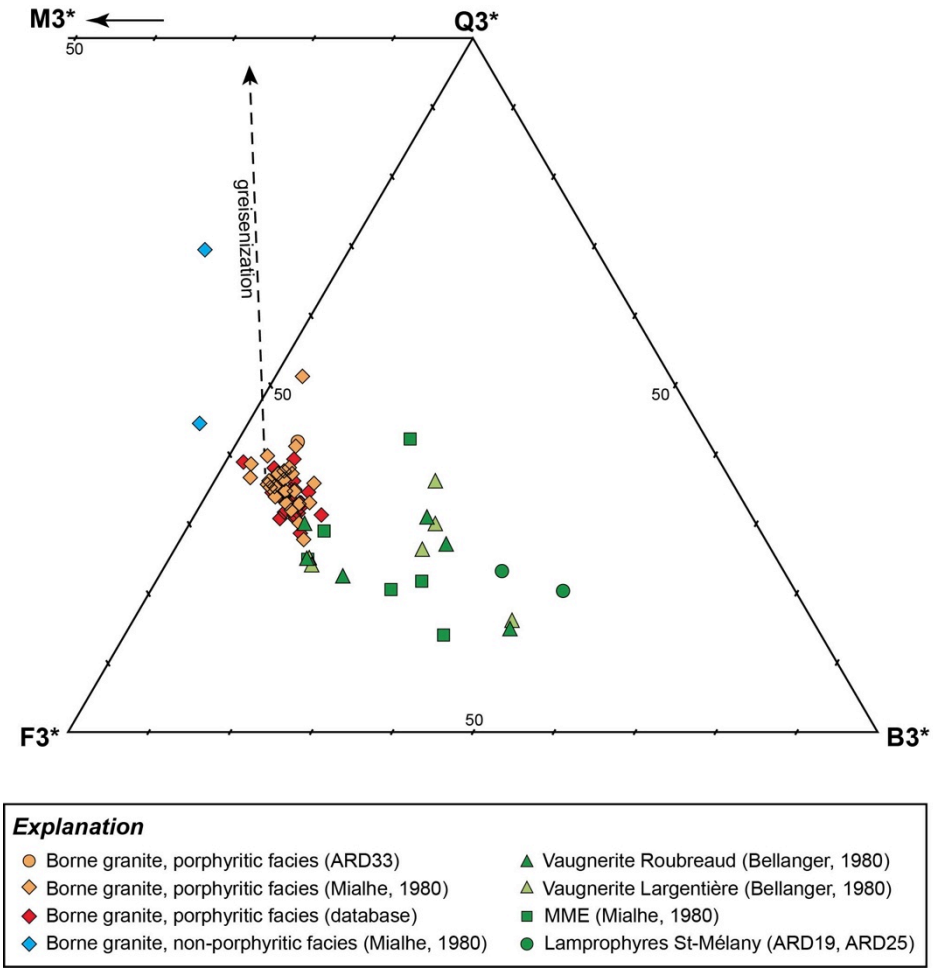

Fig. 96: Major element compositions of the Borne granite projected in the (QBF)3 diagram (after Debon and Lefort, 1988), where Q3=Si+7Al/2-5Ca-13(Na+K)/2, B3=-7Al/2+7Ca+7(Na+K)/2+8(Fe+Mg+Ti)/3 and F3=Al+3Ca+4(Na+K)-5(Fe+Mg+Ti)/3. The normalization of these parameters to the Q3+B3+F3 sum yield to the (Q3*B3*F3*) diagram, where Q3* represents the quartz pole, B3* the biotite pole and F3* the feldspar pole. A fourth summit M3*, symmetrical to B3* relatively to the Q3*-F3* segment and corresponding to the muscovite pole can be also projected. The data are plotted together with old data from the Borne granite (Artemise database; Mialhe, 1980), microgranular mafic enclaves (MME) within the Borne granite (Mialhe, 1980) and catazonal vaugnerites II (Bellanger, 1980). Whole-rock data are given in Table 26.

5.2. Lamprophyres from St-Mélany

A swarm of four NNE-SSW-striking lamprophyres crosscut the St-Mélany deposit and its enclosing micaschists. They form highly irregular melanocratic intrusions, 5-15 m in length and 1-2 m in width, which are surrounded by aphyric chilled rims of variable thickness (cm-dm) at the contact with the micaschists. They display an internal foliation marked by millimetre elongated quartz inclusions, which is sub-parallel to the host-rock contact. Two samples of lamprophyres were collected (ARD19 and ARD25). They are composed by an

association of biotite in a microcrystalline quartzo-feldspathic matrix (Fig. 93c,d) and contain accessory minerals of apatite and pyrite. Whole-rock geochemistry of the lamprophyres is characterized by Mg-K rich composition with enrichments in Ca, Rb, Sr, Cs, Ba, U, Th, W, Sn, P, Cr, Bi, As, Cd and Ni and impoverishments in Si, Al, Na and Cu compared to the UCC (Fig. 94a). The REE pattern shows a high enrichment in LREE (La/Yb=16-19) with a negative Eu anomaly (Eu/Eu*=0.70) (Fig. 94b). The lamprophyres contain in particular high concentrations of Sn (15-16 ppm) and W (4.9-6.2 ppm) (Table 26), which may have been inherited from the enclosing micaschists during their emplacement. In the A-B diagram (Fig. 95a), the lamprophyres define a mixing trend with the Borne granite (see 5.2.).

5.3. Fabras granite

The small Fabras pluton consists in a small Li-muscovite-topaze-albite granitic body, located close to the northern boundary of the Prades-Jaujac coal basin, to the north-east of the studied area (Fig. 78). It was clearly intruded at a mesozonal level, with a distinct fine-grained border, and development of retromorphic muscovite in the hosting migmatites. It is thus one of the youngest known granites in the Cévennes area, intrusive during the exhumation of the Velay dome (Barbey et al., 2015). It was included in the present study because of its possible relationships with the rare-metal aplites and pegmatites from St-Mélany. One sample (ARD92; Fig. 97a) of the Fabras granite was collected. This sample is composed by a quartz, albite and muscovite assemblage, with minor topaze, and characterized by an equigranular fine-grained texture (Fig. 97b). The whole-rock geochemistry of the Fabras granite is characterized by a peraluminous composition (Al/CNK=1.18; Table 26) with high contents in Rb, Cs, U, Ta, W, Sn, P, Be and Bi and low contents in Mg, Ca, Sr, Ba, Y, Th, Zr, Hf, Sc, Ti, V, Cr, Fe and Mn compared to the UCC (Fig. 98a). The REE pattern shows an enrichment in LREE (La/Yb=2.76) with a strongly negative Eu anomaly (Eu/Eu*=0.49) (Fig. 98b). It contains in particular enrichments in rare-metals, such as Ta (7 ppm), Nb (18 ppm), W (10 ppm) and Sn (48 ppm), similarly to the muscovite-facies of the Rocles granite (Table 26). In the A-B diagram (Fig. 99a), the Fabras granite defines a Taourirt fractionation trend typical of the A-type granites (Marignac et al., 2016).

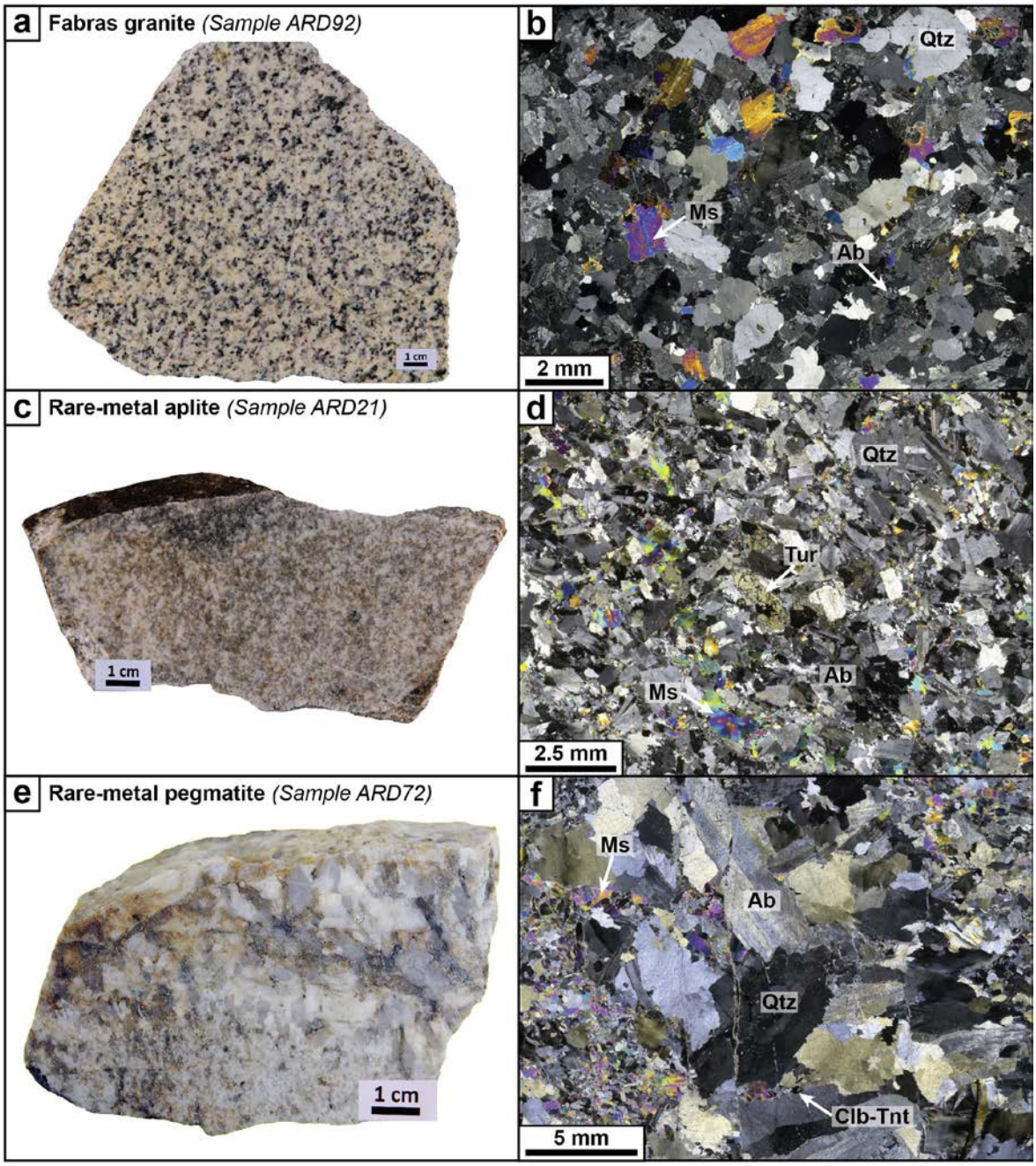

Fig. 97: Photographs of the studied samples from the Fabras granite (a,b; sample ARD92), and rare-metal aplite (c,d; sample ARD21) and pegmatite (e,f; ARD72) from St-Mélany. Mineral abbreviations: Ab: albite; Clb-Tnt: columbite-tantalite; Ms: muscovite; Qtz: quartz; Tur: tourmaline.

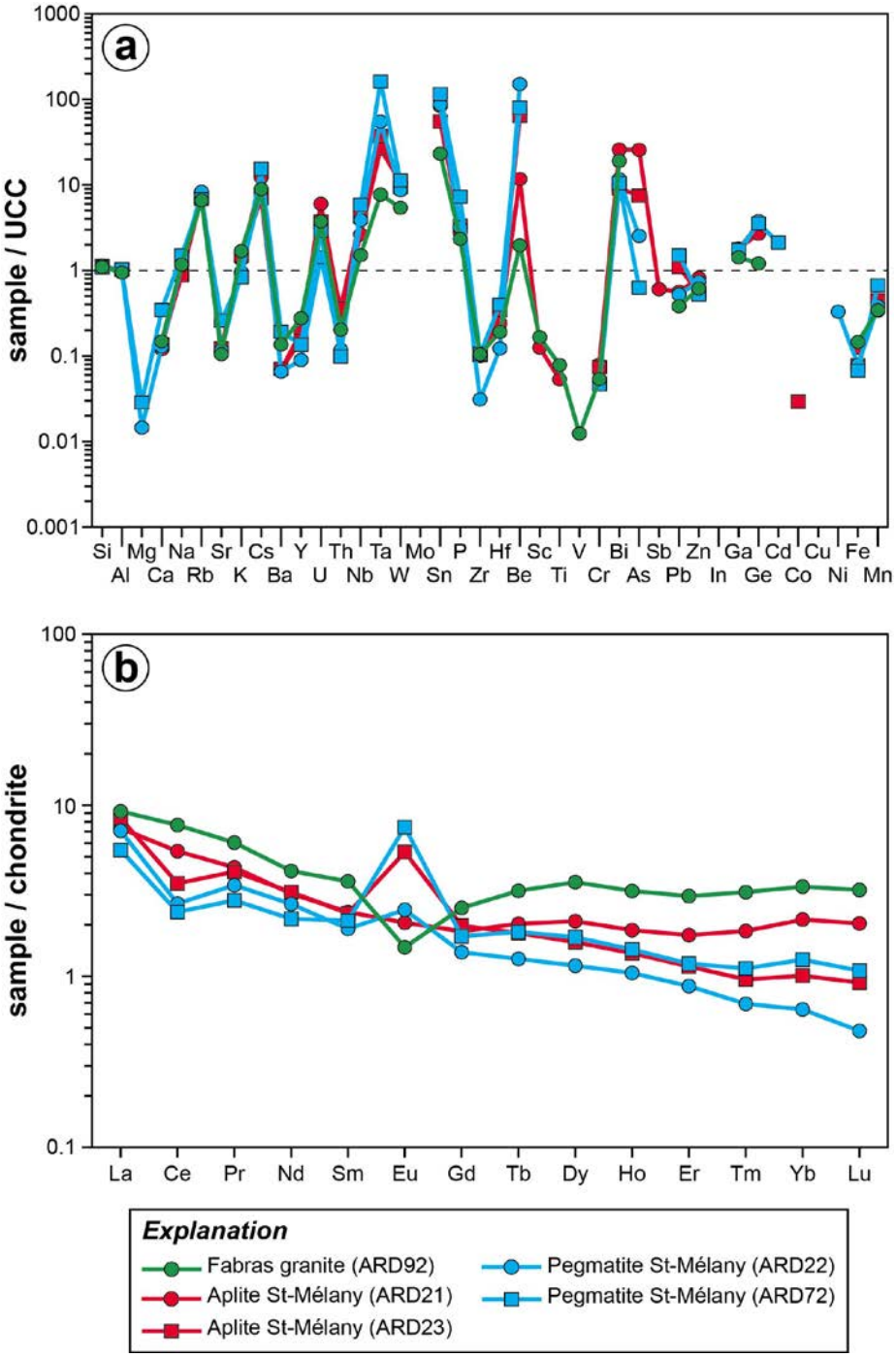

Fig. 98: Whole-rock geochemical compositions of the Fabras granite and the rare-metal aplites-pegmatites from St-Mélany. (a) Multi-element diagram normalized by the upper continental crust (UCC, Rudnick and Gao, 2003). (b) REE pattern normalized to the chondrite (CI, Palme and O'Neill, 2014). Whole-rock data are given in Table 26.

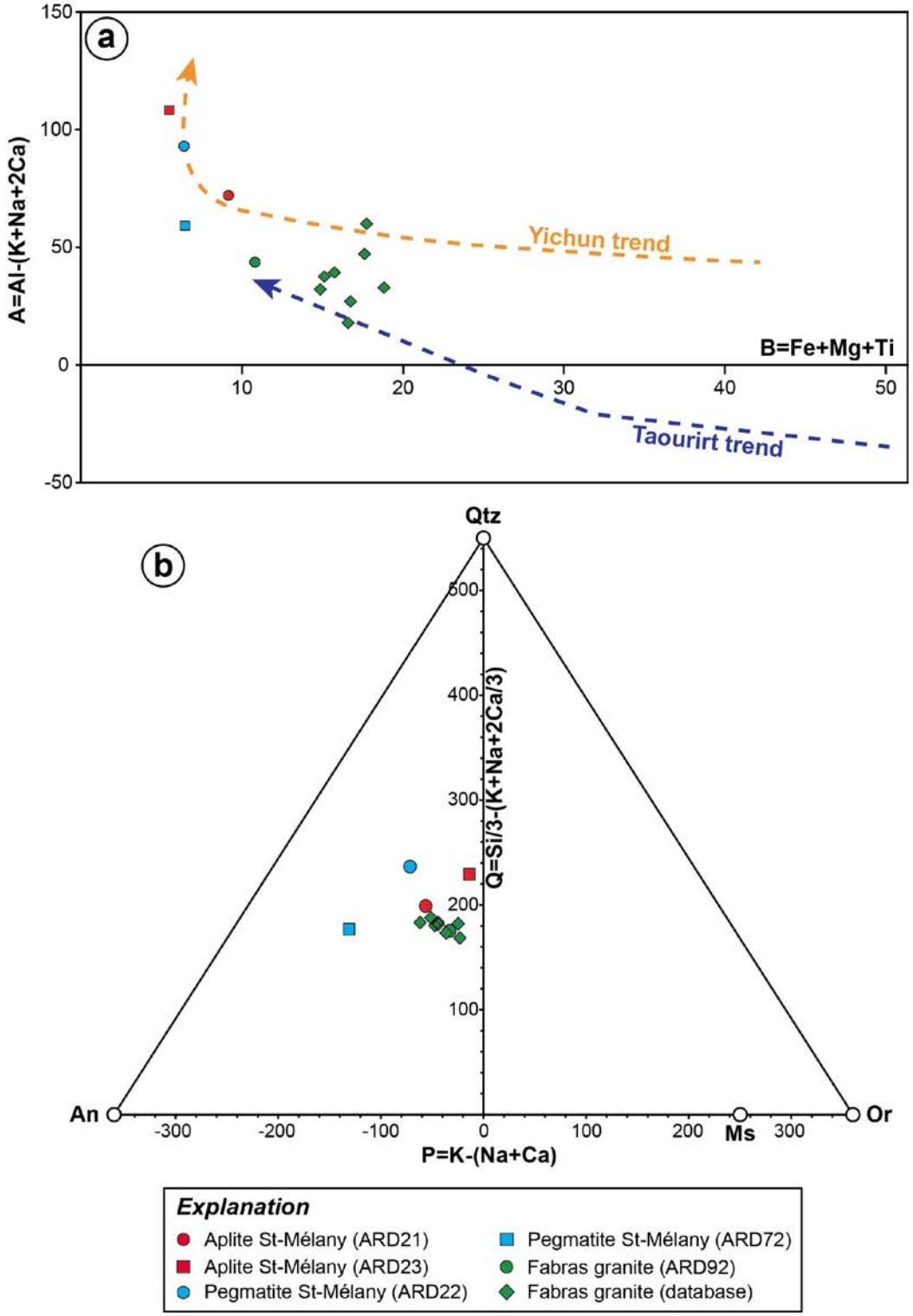

Fig. 99: Major element compositions of the Fabras granite and rare-metal aplites-pegmatites from St-Mélany projected in (a) the A-B diagram representing the peraluminous index A=Al-(Na+K+2Ca) as function of the differentiation index B=Fe+Mg+Ti (after Debon and Lefort, 1988) and in (b) the Q-P diagram representing the quartz content Q=Si/3-(K+Na+2Ca/3) as function of the relative proportions of feldspars P=K-(Na+Ca) (after Debon and Lefort, 1988). The data are plotted with unpublished data from the Fabras granite (Artemise database). Whole-rock data are given in Table 26.

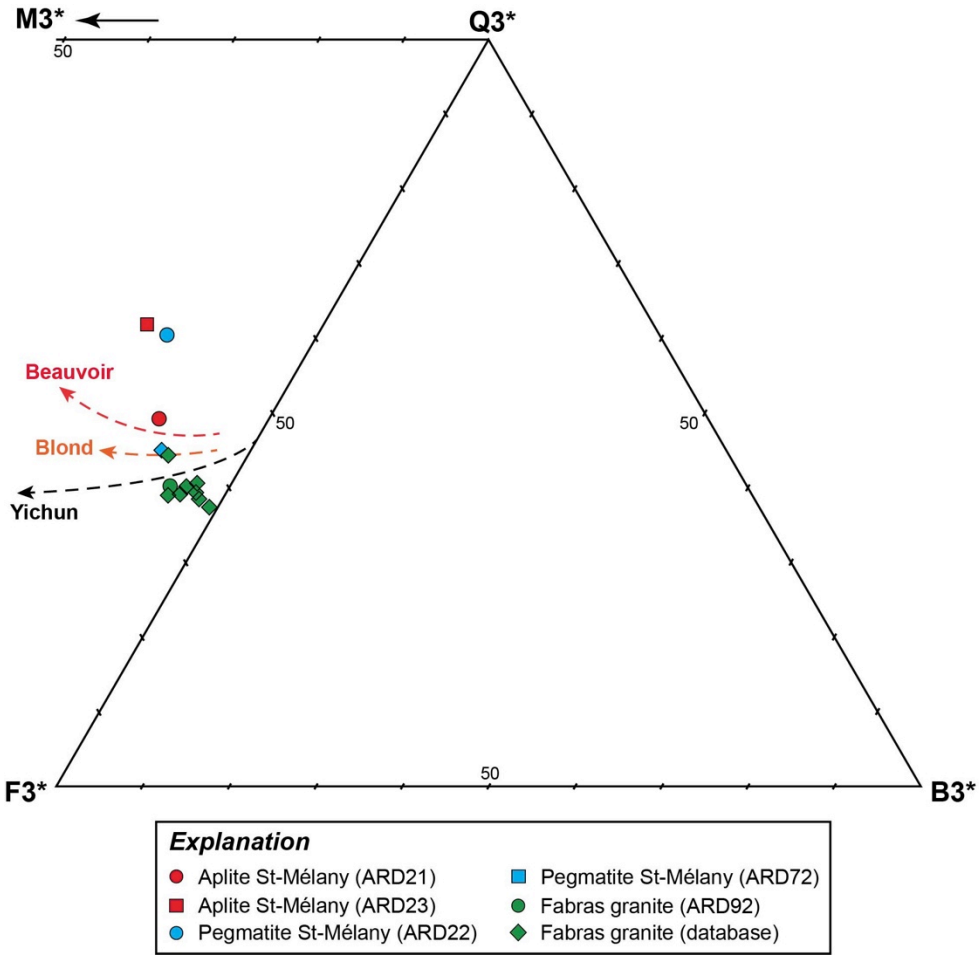

Fig. 100: Major element compositions of the Fabras granite and aplites-pegmatites from St-Mélany projected in the (QBF)3 diagram (after Debon and Lefort, 1988), where Q3=Si+7Al/2-5Ca-13(Na+K)/2, B3=-7Al/2+7Ca+7(Na+K)/2+8(Fe+Mg+Ti)/3 and F3=Al+3Ca+4(Na+K)-5(Fe+Mg+Ti)/3. The normalization of these parameters to the Q3+B3+F3 sum yield to the (Q3*B3*F3*) diagram, where Q3* represents the quartz pole, B3* the biotite pole and F3* the feldspar pole. A fourth summit M3*, symmetrical to B3* relatively to the Q3*-F3* segment and corresponding to the muscovite pole can be also projected. The data are plotted with unpublished data from the Fabras granite (Artemise database). Whole-rock data are given in Table 26.

5.4. Rare-metal aplites and pegmatites from St-Mélany

Two samples of aplites (ARD21 and ARD23; Fig. 97c) and pegmatites (ARD22 and ARD72; Fig. 97e) dykes that crosscut the St-Mélany mineralized veins have been collected. They are composed by a mineralogical assemblage of quartz, albite, K-feldspar and muscovite and contain disseminated accessory minerals of apatite, cassiterite and columbite-tantalite (Fig. 97d,f). The whole-rock geochemistry of the aplites and pegmatites show a high-P (0.4-1.1 wt.% P_2O_5) highly peraluminous composition (Al/CNK=1.23-1.55; Table 26). They show

a trace elements signature typical of the rare-metal granites characterized by high contents in Rb, Cs, U, Nb, Ta, W, Sn, P, Be and low contents in Mg, Ca, Sr, Ba, Y, Th, Zr, Hf, Sc, Ti, V, Cr, Fe, Mn compared to the UCC (Fig. 98a). Their REE patterns (Fig. 98b) show slight enrichment in LREE compared to HREE (La/Yb=3.4-11.1) with a negative Ce anomaly (Ce/Ce*=0.54-0.96) and a positive Eu anomaly (Eu/Eu*=1.00-3.91), typical of magmatic cumulates. They are particularly enriched in rare-metals with high concentrations in Sn (up to 242 ppm), W (up to 21 ppm), Ta (up to 145 ppm), Nb (up to 70 ppm), Rb (up to 696 ppm), Cs (up to 75 ppm) and Be (up to 317 ppm) (Table 26). In the A-B diagram (Fig. 99a), the data fall close to the Yichun fractionation trend (Marignac et al., 2016). In the Q-P diagram (Fig. 99b), the data follow a trend defined by quartz enrichment and albite fractionation. Considering they represent magmatic cumulates, this indicates that the aplites and pegmatites must have followed a greisenization trend to have their current compositions. This greisenization trend is easily visible in the (QBF)3 diagram (Fig. 100). It can be noted in the same diagram that the aplites and pegmatites from St-Mélany follow a distinct trend compared to the Fabras granite and the Rocles granite (muscovite-facies), which indicates thus that they were derived from an independent rare-metal granite.

Columbite-tantalite and cassiterite minerals have been studied in detail in one sample of rare-metal pegmatite (sample ARD72) in order to characterize the evolution of the magmatic system. The columbite-tantalite form sub-euhedral crystals, ranging from 10 to 450 µm in size, which are disseminated or found in clusters in the pegmatite. Observed in BSE imagery (Fig. 101), the largest crystals display a complex internal zoning composed of six constituents: (i) a small dark core, 5-10 µm in size, forming the nucleus of the crystals; (ii) a dark grey rim-I surrounding the core and passing in continuity to (iii) a dark grey rim-II; (iv) a discontinuous light grey rim, only a few µm-thick and slightly corrosive on the previous zones; (v) a dark grey rim-III crystallizing on the previous rim; and (vi) a late bright overgrowth, 1-50 µm in thickness, which corrode partially the crystalline rims. Small crystals (10-40 µm) constituted of the bright overgrowth are found disseminated in the pegmatite with larger crystals (up to 100 µm) of tantalite in overgrowth. The latter shows also a micrometer-scale internal zoning, which seems to be a growth zoning.

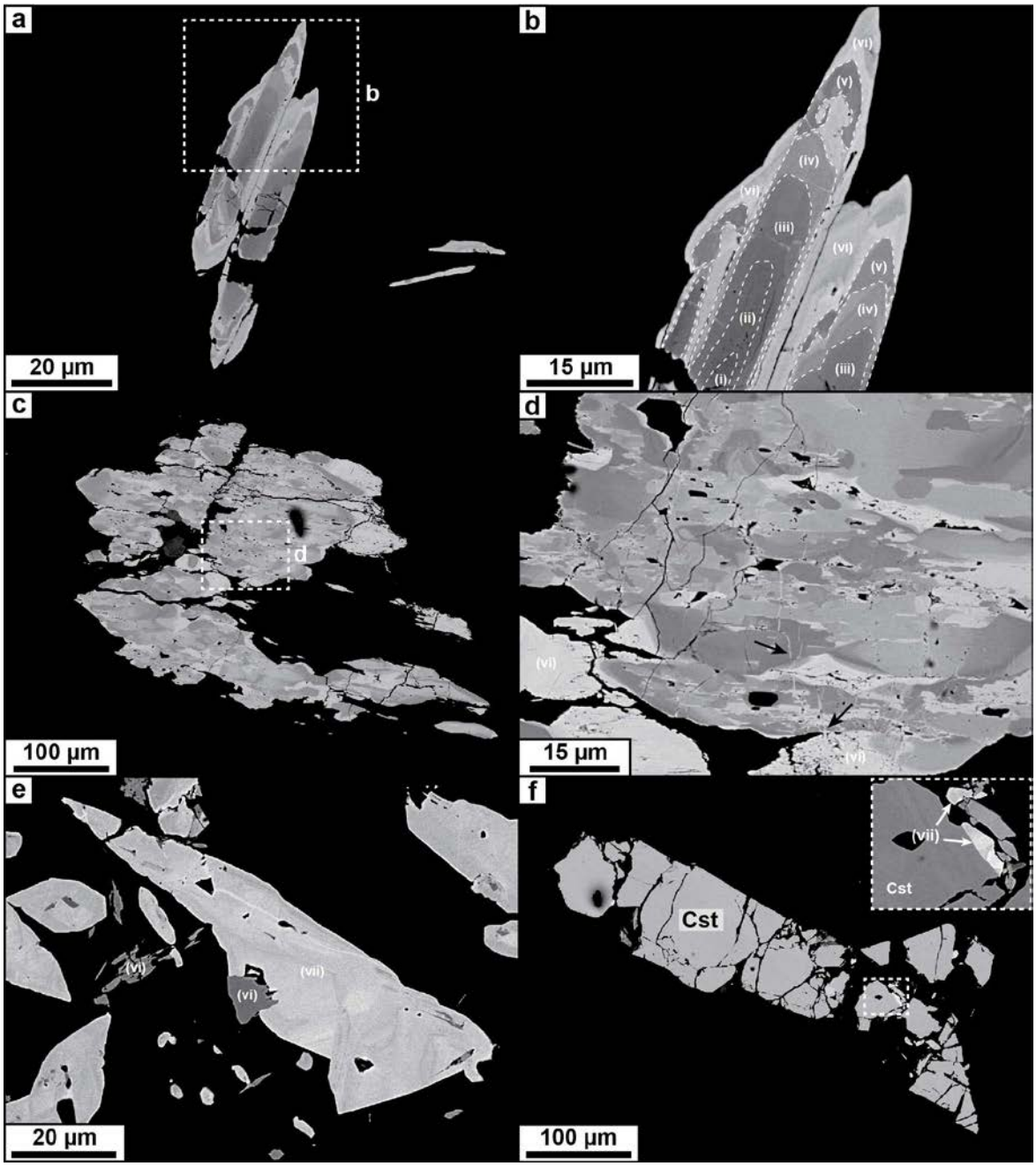

Fig. 101: BSE images of columbite-tantalite and cassiterite minerals from the rare-metal pegmatite from St-Mélany (sample ARD72). (a) Elongated crystal of columbite-tantalite disseminated in the pegmatite and showing a growth internal zoning. (b) Detailed view of the internal zoning composed by a succession of a dark core (i), dark rim-I (ii), dark rim-II (iii), light grey rim (iv), dark rim-III (v) and external bright overgrowth (vi). (c) Large crystal of columbite-tantalite composed by the aggregation of smaller crystals. (d) Detailed view showing the complex internal zoning of a large crystal of columbite-tantalite. Note the corrosion by the external bright overgrowth (vi) along micro-cracks (black arrows). (e) Late crystal of tantalite (vii) disseminated or in overgrowth on small crystals of the external bright overgrowth (vi). (f) Sub-euhedral crystal of cassiterite, homogeneous, and showing locally small overgrowths of tantalite (vii).

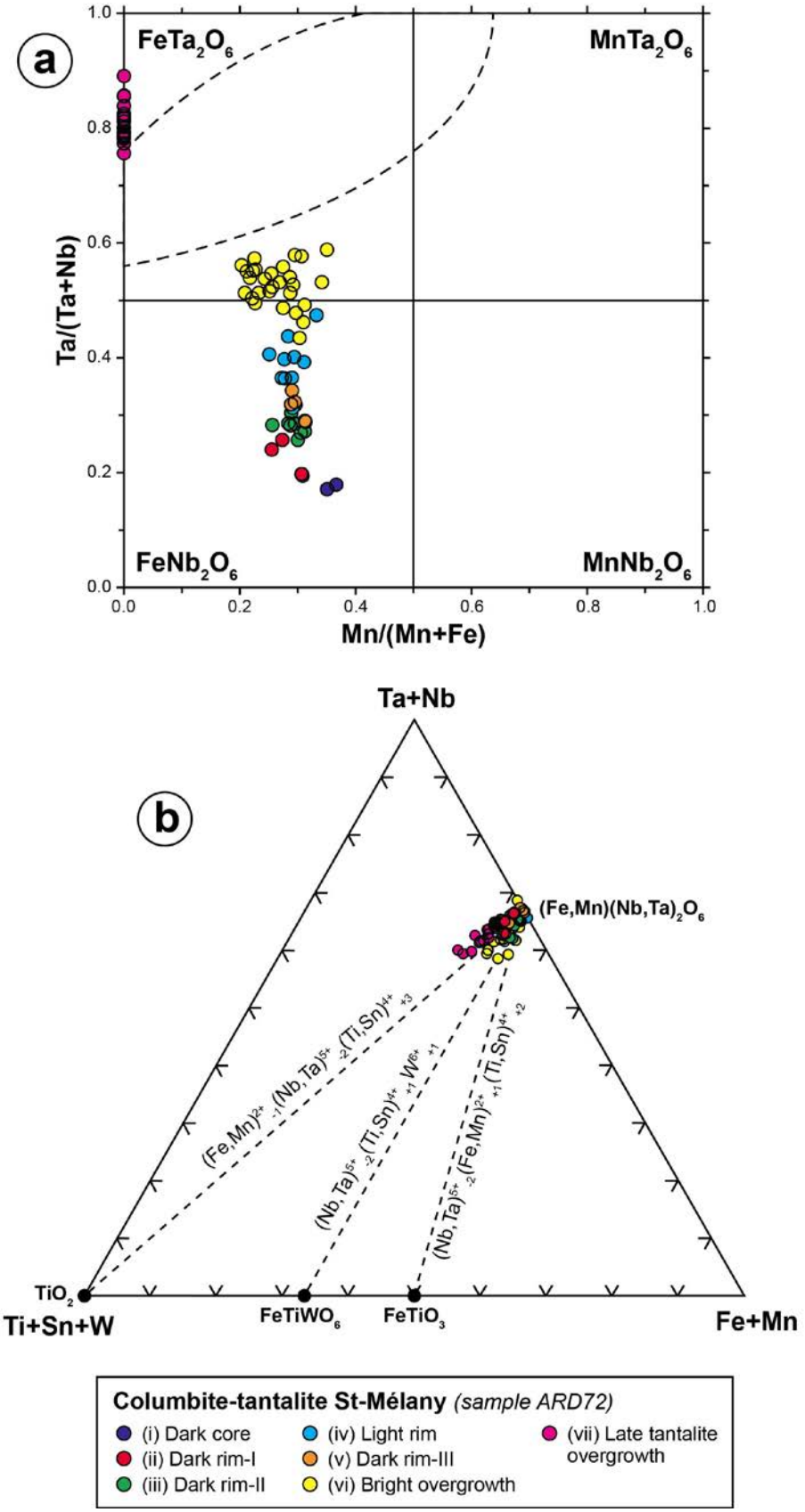

Fig. 102: Compositions of the columbite-tantalite minerals from the rare-metal pegmatite from St-Mélany (sample ARD72) in the columbite quadrilateral diagram (a) and in the ternary diagram (Nb+Ta)-(Sn+Ti+W)-(Fe+Mn) (b). The dash lines corresponds to the compositional gap of Černý et al. (1992).

Representative chemical compositions of the columbite-tantalites are given in Table 27. In the columbite quadrilateral (Fig. 102a), the composition of the columbite-tantalites show a geochemical evolution from a ferrocolumbite core toward a ferrotantalite external overgrowth, with Mn/(Mn+Fe) and Ta/(Ta+Nb) ratios ranging from 0.20 to 0.37 and from 0.17 to 0.59, respectively (Table 27). This geochemical evolution is typical of a magmatic fractionation trend. The late tantalite overgrowth is characterized by almost pure ferrotantalite compositions with Mn/(Mn+Fe)=0 and Ta/(Ta+Nb)=0.76-0.89 (Table 27). It may correspond to a magmatic-hydrothermal trend. In the ternary diagram (Nb+Ta)-(Sn+Ti+W)-(Fe+Mn) (24b), the data for core to overgrowth fall along the vector $FeNb_2O_6$ – $FeTiWO_6$ indicating the participation of the substitution mechanism $(Nb,Ta)^{5+}_{-2}(Ti,Sn)^{4+}_{+1}W^{6+}_{+1}$. The data for the late tantalite overgrowth fall along the vector $FeNb_2O_6$ – TiO_2 according to the substitution mechanism $(Fe,Mn)^{2+}_{-1}(Nb,Ta)^{5+}_{-2}(Ti,Sn)^{4+}_{+3}$. The cassiterite form large sub-euhedral crystals, up to 460 µm in size, which are fractured by apatite and appears to crystallize earlier than the columbite-tantalite found in overgrowth (Fig. 95f). The cassiterite has composition close to the ideal formula (SnO_2=97.8-100 wt.%) and shows a discrete internal zoning in BSE imagery, corresponding to zones with minor amounts of Ta_2O_5 (up to 1.5 wt.%).

In conclusion, the whole-rock geochemistry of the main regional magmatic rocks showed that the muscovite-facies of the Rocles granite (ca. 315 Ma) and the aplites and pegmatites from St-Mélany (ca. 305 Ma) represent potential sources of rare-metals in the studied area. Considering the structural relationships of the St-Mélany deposit, the Rocles granite represents the most attractive.

6. Micaschists from the Série Cévenole: effects of metamorphism and magmatism

Although variable in detail, the lithologies of the Série Cévenole are globally constant at the scale of the Drobie and lower Beaume valleys, and it has been shown that the M2 metamorphic grade was uniformly low in all the area (Toteu, 1981). This allows in principle to untangle the lithological effects from the possible effects of the prograde metamorphism or the contact metamorphism. In order to study the effects of the prograde M3 metamorphism, a transect from the epizone to the catazone was sampled in the micaschists along the Beaume valley. The Rocles granite sill being intercalated at the mesozone-catazone boundary, this transect may also allow to untangle the possible effects of the intrusion. To the 7 micaschists samples collected during the present study (referred as BMExx) were added 6 samples from an older sampling in the years 90's (referred as LAxxx) (Fig. 81). Another set of samples

(referred as ARDxx) was also collected on two transects in the Cévenol micaschists toward the Borne granite, in order to assess the contact metamorphism effects. One transect on the D220 road paralleling the Drobie valley was sampled in order to check the possible anomalies in the St-Mélany area (Fig. 81). Totally, this regional sampling is composed by 36 samples of the Cévenole micaschists. The whole-rock compositions data are presented in Table 28.

6.1. Whole-rock chemical composition of the Cévenol micaschists

The chemical compositions of the Cévenol micaschists have been represented in geochemical classification diagrams (Fig. 103) by distinguishing the metamorphic degree (epizone, mesozone, catazone). The majority of the data plot into the compositional field of greywackous shales. It can be noted that no clear distinction can be made based on major element geochemistry between the micaschists from the epizone, mesozone or catazone. The samples are essentially characterized by variations in SiO_2 (47.9-87.4 %) and Al_2O_3 (5.55-28.5 %) contents, as already described by Weisbrod (1970). Average major and trace element compositions for the Cévenol micaschists are given in Fig. 104. The mesozonal micaschists have globally the same trace element compositions than the epizonal micaschists but differ by higher contents in Cs, W, Mo, Sn and As (Fig. 104a). The sample of micaschist from the catazone shows however a very distinct composition, with lower contents in most of the trace elements, but its chemistry corresponds better to a quartzite (Fig. 104a). The three metamorphic units show similar REE patterns (Fig. 104b) with enrichment in LREE (La/Yb=8.4-12.3) and a negative Eu anomaly (Eu/Eu*=0.59-0.68). Moreover, a general trend of decrease in the REE contents from the epizone to the catazone can be observed (Fig. 104b). Regarding the Sn and W contents (Fig. 105), the micaschists show variable concentrations ranging from 2.2 to 14.5 ppm and 1.4 to 15.4 ppm, respectively (Table 28). The Sn contents are generally higher than the W contents with Sn/W ratios comprised between 0.5 and 5 (Fig. 105). The highest concentrations in Sn and W are found in the mesozone, which is also the host for the St-Mélany deposit. The micaschists enclosing the mineralized quartz veins from St-Mélany show geochemical anomalies in Sn (up to 14.5 ppm) and W (up to 15.4 ppm).

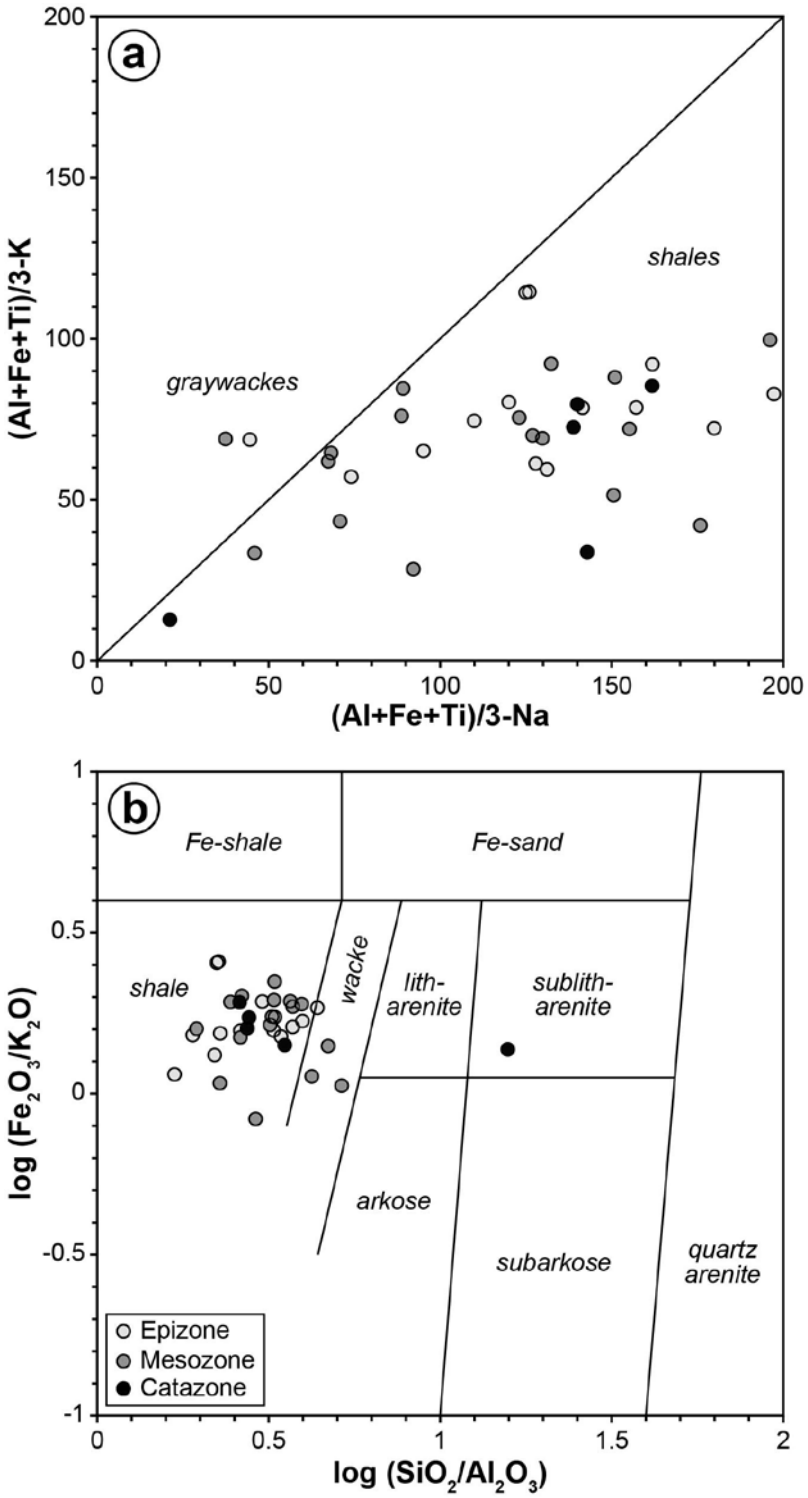

Fig. 103: Major element geochemistry of the Cévenol micaschists represented in the (a) (Al+Fe+Ti)/3-Na vs (Al+Fe+Ti)/3-K classification diagram (after Moine and de la Roche, 1968) and in the (b) log (SiO_2/Al_2O_3) vs log (Fe_2O_3/K_2O) classification diagram (after Herron, 1988). Data are given in Table 28.

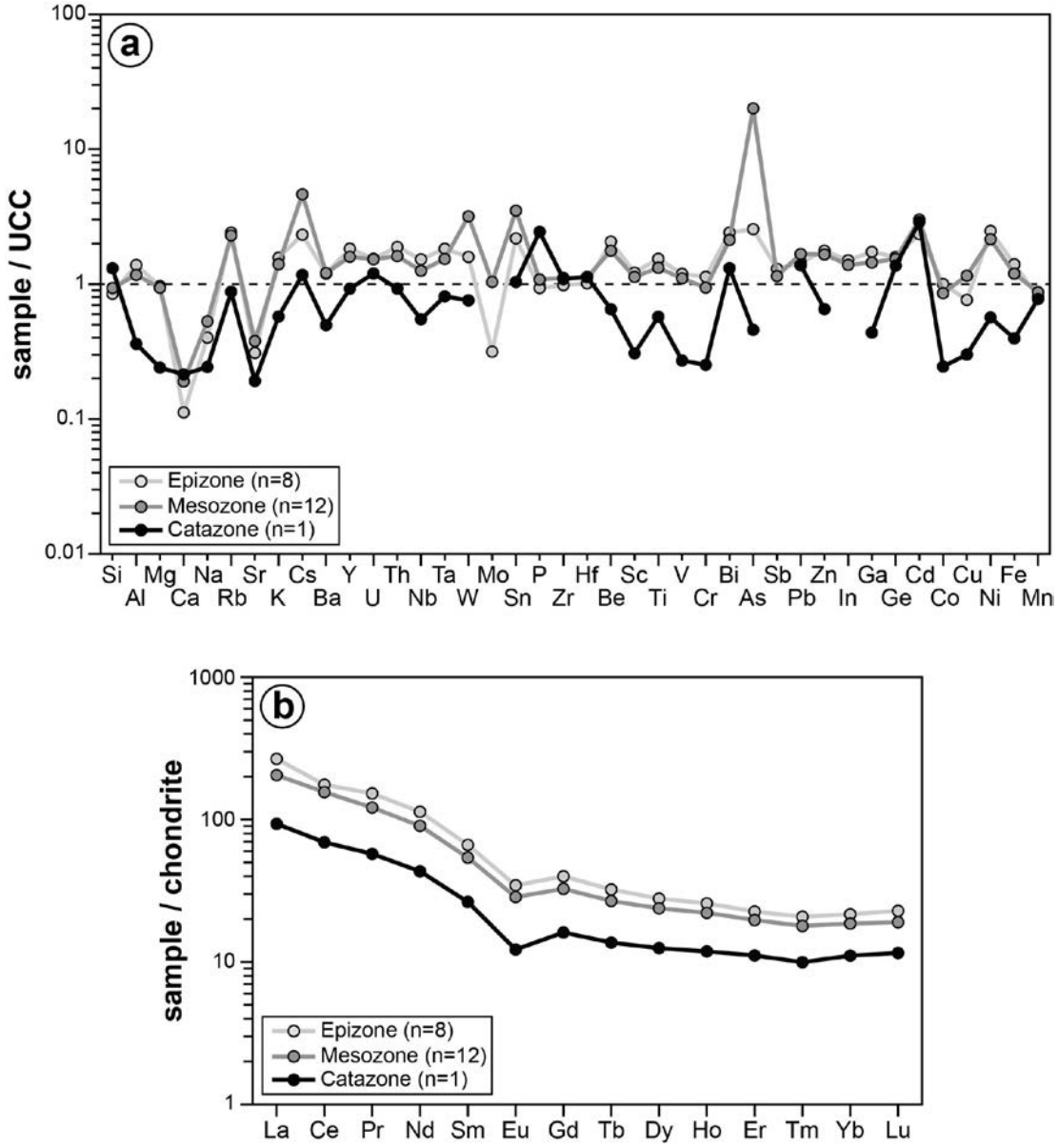

Fig. 104: Average geochemical compositions of the Cévenol micaschists. (a) Major and trace elements normalized by the upper continental crust (UCC, Rudnick and Gao, 2003). (b) REE contents normalized by the chondrite values (CI, Palme and O'Neill, 2014). Data are given in Table 28.

6.2. Mineralogical and geochemical study of the Ti-W oxides in the Cévenol micaschists

Paralleling the bulk chemistry, a detailed mineralogical and geochemical study was performed onto the Ti-oxides contained in the Cévenol micaschists for several reasons: (i) they represent the most abundant accessory minerals in the Cévenol schists; (ii) they are known to contain significant concentrations of W (e.g., Zack et al., 2004; Meinhold, 2010); (iii) they may react and reequilibrate during prograde metamorphism (e.g., Luvizotto et al.,

2009; Cave et al., 2015); and (iv) preliminary results suggested that their W content may be leached during the prograde metamorphism (Mangin et al., 1994).

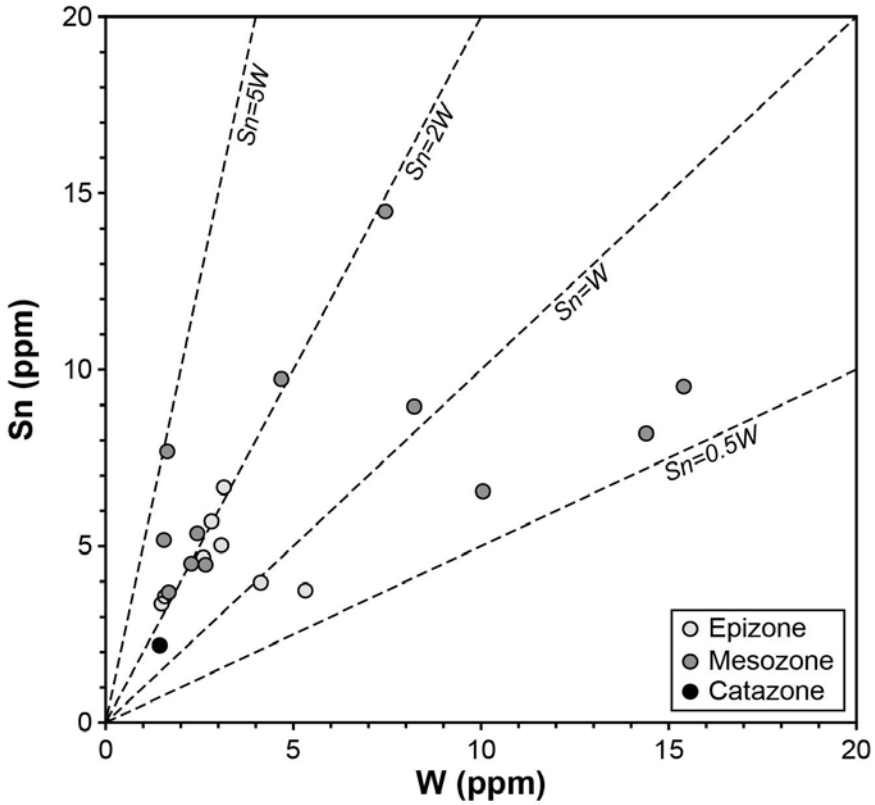

Fig. 105: W vs Sn contents in Cévenol micaschists.

6.2.1. Mineralogical and textural characterization of the Ti-oxides

Interpretation of the Ti-oxides compositional variations requires a good understanding of their precise paragenetic position in the studied samples. This in turn raises the question of the exact nature of the main regional schistosity ("S2"). It is true that during the D2 event, a schistosity appeared in the axial plane of F2 folds, marked by chlorite and muscovite. However, in the present-day epizone, chlorite and muscovite were reequilibrated under new P-T conditions, and in the mesozone (chlorite$^-$) and catazone (muscovite$^-$), newly formed biotite was pseudomorphic onto M2 chlorite or muscovite. Moreover, the prograde metamorphism M3 resulted in a renewal of dehydration and consequently of flattening perpendicularly to the schistosity. To summary, the S2 structure was everywhere reworked during the D3 event and should better be called a "S2-3" schistosity. In other words, given a mineral with an apparent syn-schistose nature, the problem may be to decide if it was truly syn-S2 or in fact syn-"S2-3".

- Ti-oxides in the Beaume transect: a LP-HT gradient

Epizone (sample BME4):

Micaschists from the epizone are characterized by a muscovite-chlorite metamorphic paragenesis typical of the greenschist facies (Fig. 106a). Garnet crystals are observed within the micaschists, but are systematically corroded and crosscut by the metamorphic chlorite, indicating an inherited origin. The Ti-oxides form opaque crystals in plane-polarized light, generally 100 to 500 µm in size, which are sub-euhedral and elongated in the schistosity plane (Fig. 106a). A few crystals are disposed obliquely with respect to the schistosity and are slightly twisted, suggesting that they were flattened. The Ti-oxides have been identified as ilmenite ($FeTiO_3$) minerals both by EDS analyses and Raman spectrometry. In BSE imagery (Fig. 107a), the ilmenite crystals show no internal zoning and contain occasionally micrometric inclusions of zircon and Ti-rich muscovite (up to 0.6 wt.% Ti). The latter may have form contemporaneously with the ilmenite and may correspond to co-crystallized phases. The ilmenite crystals are partially corroded by a TiO_2 phase, identified as anatase by Raman spectrometry, which replaces the ilmenite along crystalline borders always in association with chlorite (Fig. 107a,b).

Mesozone (samples BME5 to BME8):

In the lower mesozone (samples BME5 to BME6), the micaschists are characterized by a biotite-muscovite-cordierite metamorphic assemblage, corresponding to the lower amphibolite facies. In the upper mesozone (sample BME7 to BME8), the micaschists contain andalusite crystals growing on the cordierite, corresponding to an upper amphibolite facies. Transecting the chlorite$^-$ isograde is clearly associated with a major change in the Ti-oxide mineralogy, marked by the progressive transformation of ilmenite in anatase. The Ti-oxides crystals are less abundant than in the epizonal micaschists and have a dark grey to brown colour in plane-polarized light (Fig. 106b). They are sub-euhedral and show typically porous textures with quartz, K-feldspars and chlorite in infilling, which represent likely late retromorphosis phases. The size of the crystals decrease progressively with the metamorphism degree increase, from ca. 500 µm in average in the lower amphibolite facies (samples BME5 to BME6) down to ca. 100 µm in average in the upper amphibolite facies (samples BME7 to BME8) (Fig. 106c). In BSE imagery, the Ti-oxides crystals correspond to sub-euhedral anatase minerals, as confirmed by Raman spectrometry, which replaces partially some

preserved ilmenite crystals (Fig. 107c), up to the complete replacement by anatase (Fig. 107d). Anatase seems in turn corroded and replaced by retrograde chlorite (Fig. 107d). At the contact with the anatase, the chlorite contains highest Ti contents (up to 1 wt.%), suggesting that chlorite took its Ti content from the dissolution of anatase. A few crystals of ilmenite, 50 to 100 µm in size, were found locally preserved as relics minerals within the micaschists. In the upper mesozone (samples BME7 to BME8), the anatase shows locally a coexistence with rutile, which appears to progressively replace the anatase (Fig. 107e).

Mesozone-Catazone (samples BME9 to BME10):

At the end of the mesozone, (sample BME9, sillimanite-muscovite zone), only rutile was detected by Raman spectrometry forming highly corroded crystals disseminated into the micaschists (Fig. 107f). At the beginning of the catazone close to the footwall of the Rocles biotite-granite (sample BME10), the micaschists have a K-feldspar-garnet-sillimanite metamorphic paragenesis (Fig. 106d). The Ti-oxides consist in small crystals (100 µm in average) of ilmenite disseminated in the micaschists and associated with rutile in replacement as already seen in the mesozone (Fig. 106d). The ilmenite crystals correspond likely to relics crystals preserved during the prograde metamorphism. The rutile form sub-euhedral and show ragged crystalline borders, thus indicating partial dissolution (Fig. 107f). Retrograde chlorite is observed crosscutting and replacing lately the Ti-oxides.

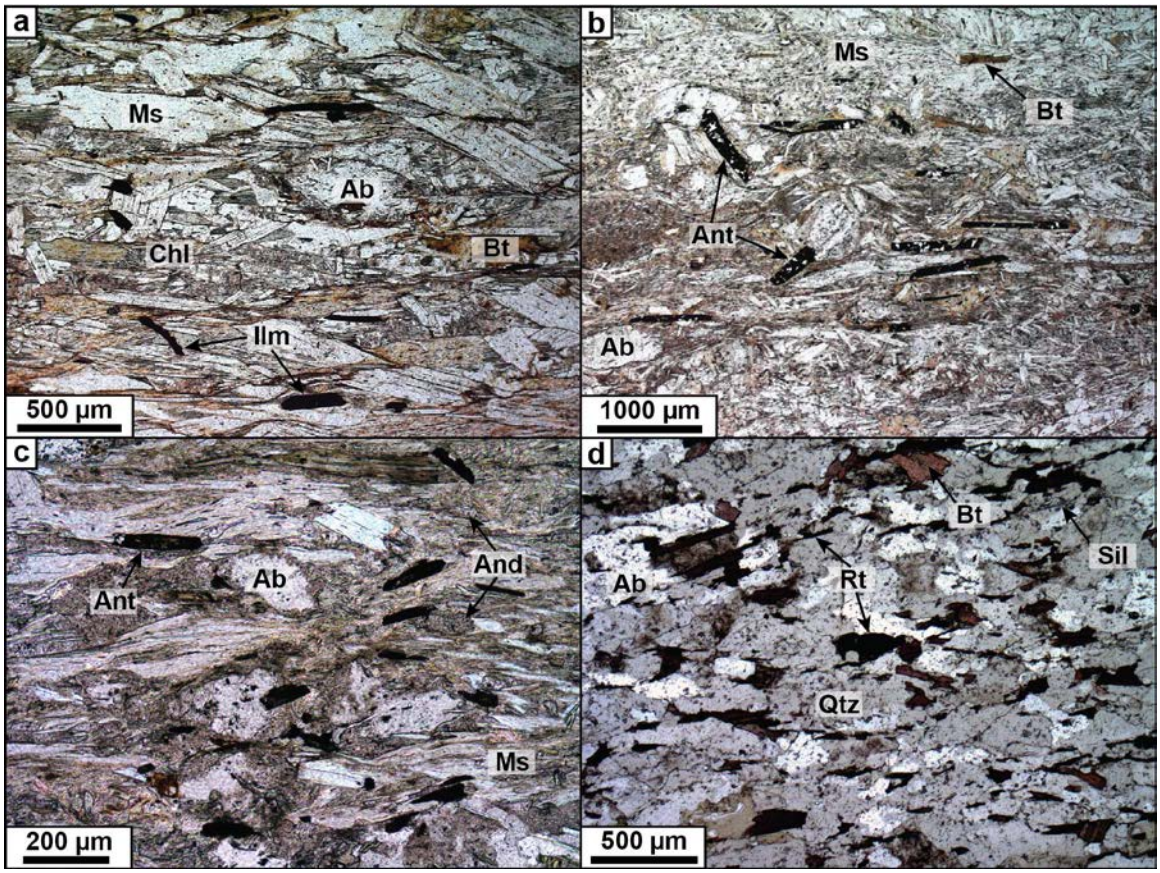

Fig. 106: Microphotographs in transmitted light of the Ti-W-oxides from the Cévenol micaschists in the Beaume valley. (a) Opaque crystals of ilmenite elongated or disposed obliquely within the schistosity of epizonal micaschist (sample BME4a). (b) Crystals of anatase partially corroded disseminated in the mesozonal micaschist (sample BME5a). (c) Small crystals of anatase in the mesozonal micaschists of upper amphibolite facies (sample BME7a). (d) Catazonal micaschists containing small and partially corroded rutile crystals (sample BME10b). Mineral abbreviations: Ab: albite; And: andalousite; Ant: anatase; Bt: biotite; Chl: chlorite; Ilm: ilmenite; Ms: muscovite; Qtz: quartz; Rt: rutile; Sil: sillimanite.

- Ti-oxides in the St-Mélany area: fingerprint of a W event

Two samples of the enclosing mesozonal micaschists from the St-Mélany deposit (samples ARD02 and ARD03) were also collected. The micaschists are characterized by a muscovite-biotite-cordierite metamorphic assemblage and contain numerous Ti-oxides, which are dark grey to brown colour in plane-polarized light and have been identified as anatase by Raman spectrometry. They commonly form sub-eudral crystals or polycrystalline aggregates, ranging from 100 to 500 µm in size, which are partially corroded by chlorite. In this respect, they show numerous similarities with those found in the micaschists from the lower mesozone in the Beaume valley.

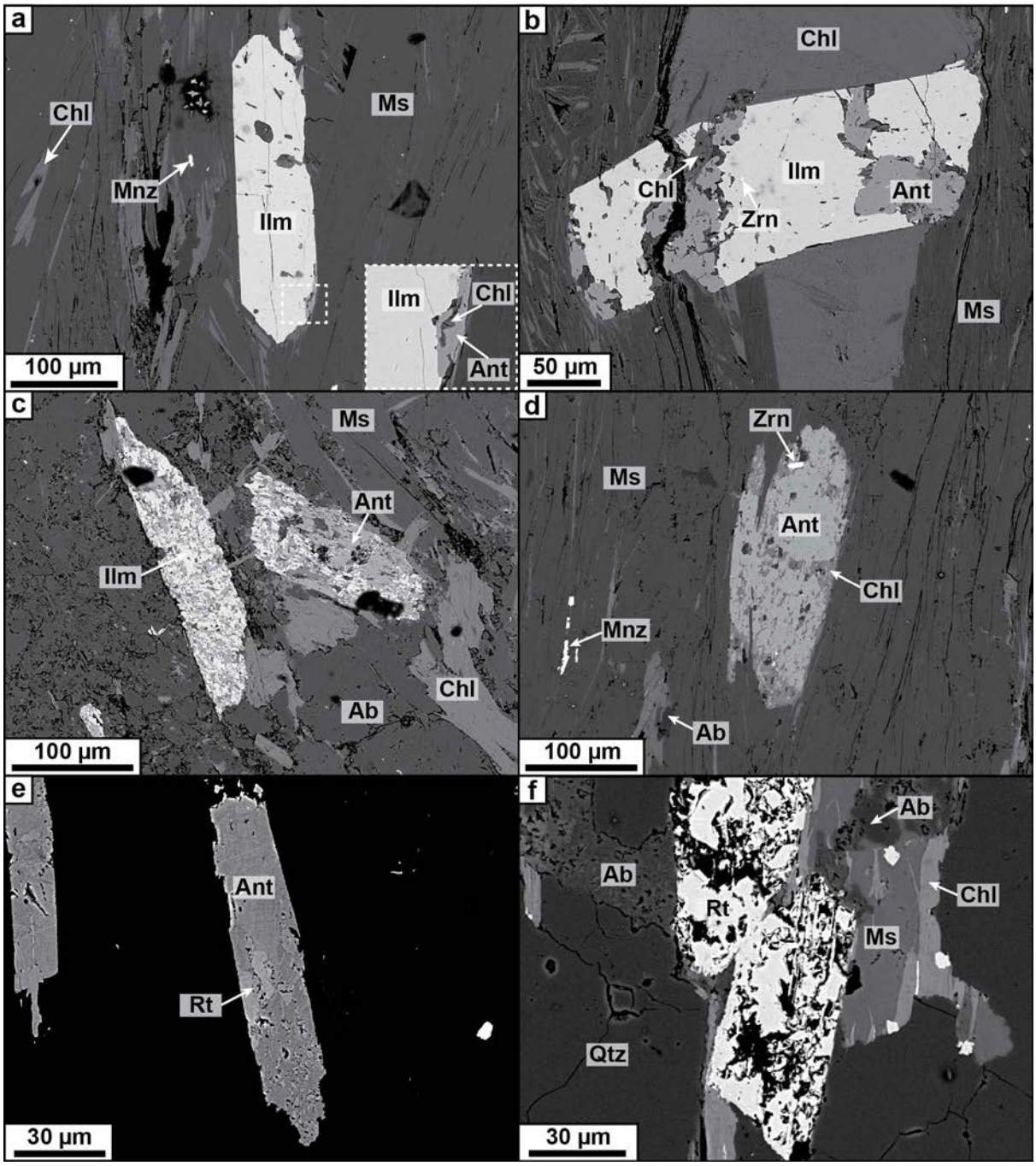

Fig. 107: BSE images of Ti-W-oxides from the Cévenol micaschists in the Beaume valley. (a) Sub-euhedral crystal of ilmenite in epizonal micaschist (sample BME4a). Note the corrosion by anatase along the crystalline border of ilmenite, in association with chlorite. (b) Sub-euhedral crystal of ilmenite partially replaced by anatase in epizonal micaschist (sample BME4a). (c) Ilmenite partially replaced by anatase and corroded by retrograde chlorite in mesozonal micaschist (sample BME6a). (d) Anatase crystal cut by retrograde chlorite in micaschist from the mesozone (sample BME6a). (e) Sub-euhedral crystal of anatase partially replaced by rutile in mesozonal micaschist (sample BME7a). (f) Corroded crystal of rutile in catazonal micaschist (sample BME10b). Mineral abbreviations: Ab: albite; Ant: anatase; Chl: chlorite; Ilm: ilmenite; Mnz: monazite; Ms: muscovite; Qtz: quartz; Rt: rutile; Zrn: zircon.

Observed in BSE imagery, the anatase crystals distinguish however by the presence of Nb-Sn-W-rich areas, as detected by EDS spectrometry (Fig. 108). Regular W-rich anatase bands (3.5-5.3 wt.% W), infra-micrometric to micrometric in width, are locally observed within the anatase (Fig. 108a,b) and may be interpreted as growth zoning. Anatase with high contents in Nb (2-3 wt.%), Sn (1.5-2 wt.%), W (1.4-2 wt.%) and Fe (0.8-1.2 wt.%) are also associated with the corroded anatase (Fig. 108c,d) and seems to be in overgrowth. These textural features indicate therefore that the anatase incorporated W, Sn and Nb during their crystallization. It should be noted that these rare-metal-rich anatase were only found in the micaschists enclosing the St-Mélany deposit among all the studied micaschists samples.

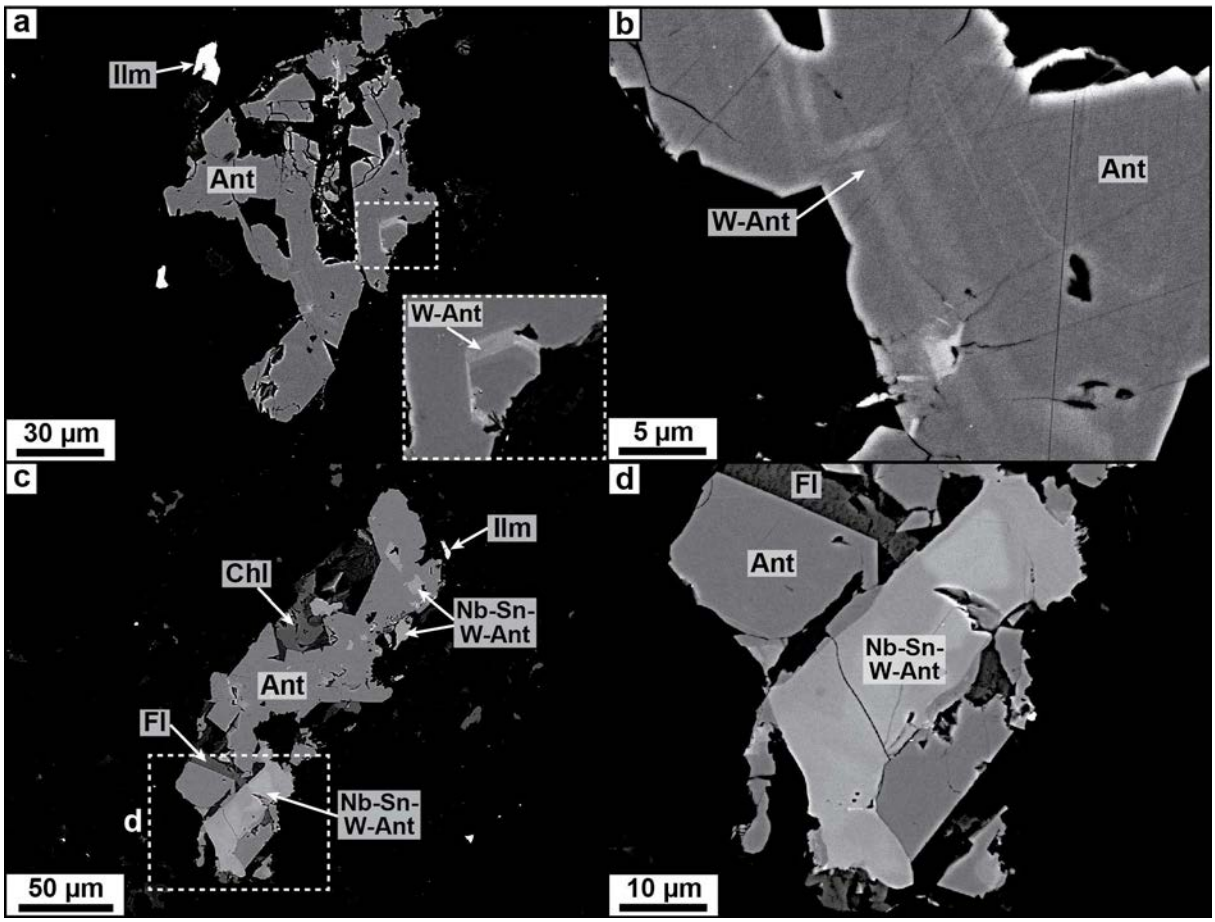

Fig. 108: BSE images of Ti-W-oxides from the Cévenol micaschists enclosing the St-Mélany deposit (sample ARD03a). (a) Anatase crystal showing W-rich internal zoning marked by growth zoning (inset). (b) Detail view of W-rich bands in anatase forming growth zoning. (c) Anatase crystal partially corroded by retrograde chlorite and showing Nb-Sn-W-rich area, associated with fluorite in overgrowth. (d). Detail view of the Nb-Sn-W-rich anatase associated with the anatase. Mineral abbreviations: Ant: anatase; Chl: chlorite; Fl: fluorite; Ilm: ilmenite.

6.2.2. Major and trace element compositions of the Ti-W oxides

Major and trace element compositions of the Ti-W-oxides from the Cévenol micaschists were determined by EMPA and LA-ICPMS. Data are given in Table 29.

- Beaume transect

Ilmenites from the epizone (sample BME4a), as well as the relics ilmenites found in the micaschists from the mesozone-catazone transition (sample BME10b), have compositions close to the pure formula (54-55 wt.% TiO_2; 43.1-44.9 wt.% FeO) with minor Mn (1.7-2 wt.% MnO) (Table 29). They contain relatively high contents (1200-37550 ppm) in Si, minor contents in Zn (up to 2000 ppm) and Nb (up to 1350 ppm), and trace contents (1-200 ppm) in Sc, V, Cr, Ni, Cu, Zr, Ta, Mo, Sn and W. Anatase and rutile have also compositions very close to the ideal formula (97-100 wt.% TiO_2) with minor contents of Fe (0.2-2.2 wt.% FeO), but they differ by their trace elements contents, particularly in W, Nb, Ta and Sn, which are generally higher than in ilmenite. Anatase from the mesozone contains minor contents in Nb (650-1750 ppm), Ta (30-180 ppm), W (3-130 ppm), Sn (1-100 ppm), V (50-370 ppm) and Sc (10-170 ppm). Rutile from the mesozone-catazone transition has also relatively high contents in W (up to 5350 ppm), Nb (up to 1350 ppm), Ta (up to 150 ppm) and Sn (up to 50 ppm). Selected trace elements contents of Ti-oxides from the Beaume micaschists as function of the metamorphism degree increase are shown in Fig. 109. A progressive increase is observed for W, Sn, Sc and V from the epizone (ilmenite) to the mesozone-catazone transition (rutile). In particular, the W content increases remarkably from 2 ppm in average in the epizone (sample BME4a) up to 2184 ppm in average at the mesozone-catazone transition (sample BME9b). At the beginning of the catazone close to the contact with the Rocles granite (sample BME10b), the W content decreases down to 40 ppm in average.

- St-Mélany area

Anatases from the micaschists hosting the St-Mélany deposit have the highest concentrations in rare-metals (Table 29). Indeed, they contain high contents in Sn (245-7480 ppm), W (300-5100 ppm), Nb (980-15000 ppm) and Ta (50-840 ppm). They have also very high concentrations in Zn (up to 35100 ppm) and Cu (up to 8630 ppm), which may be related to micro-inclusions of sulphides. The anatases that appear homogeneous on BSE imagery

(Fig. 108) contain in average 1220 ppm W, 390 ppm Sn and 1050 ppm Nb, whereas those showing W-rich zoning have in average 9000 ppm W, 210 ppm Sn and 620 ppm Nb, as determined by EMPA. The Nb-Sn-W-rich anatase marked by bright colour on BSE images contain in average 5520 ppm W, 12250 ppm Sn, 9660 ppm Nb and 340 ppm Ta.

6.2.3. Crystallization temperatures in Ti-oxides

Although the Zr-thermometer from Watson et al. (2006) was defined for rutile in equilibrium with quartz and zircon, it has been applied as first approximation to determine the crystallization temperatures of the different Ti-oxides (ilmenite, anatase and rutile) from the Beaume River valley. Results are shown in Fig. 110 and data are given in Table 29. Ilmenites from the epizone yield temperatures ranging from 318 to 534°C and show a mode around 350-400°C with an average temperature of 393°C (Fig. 110a). Anatases from the mesozone show slightly higher temperatures ranging from 334 to 537°C with average temperatures of 393°C (BME5a) and 444°C (BME7a) (Fig. 110b). Finally, rutiles from the mesozone-catazone transition yield the highest temperatures ranging from 379 to 617°C with average temperatures of 487°C (BME9b) and 458°C (BME10b) (Fig. 110c). Although progressively increasing with the metamorphic grade, these temperatures are clearly lower by more than 100°C than the peak M3 temperatures in the corresponding zones (see Barbey et al., 2015). This may be attributed to a bias due to the lack of equilibrium with zircon. A partial reequilibration during the retrograde path materialized by late chlorite may also be considered, but seems less likely. Indeed, in the latter case, one would rather expect uneven distribution of the temperature estimates.

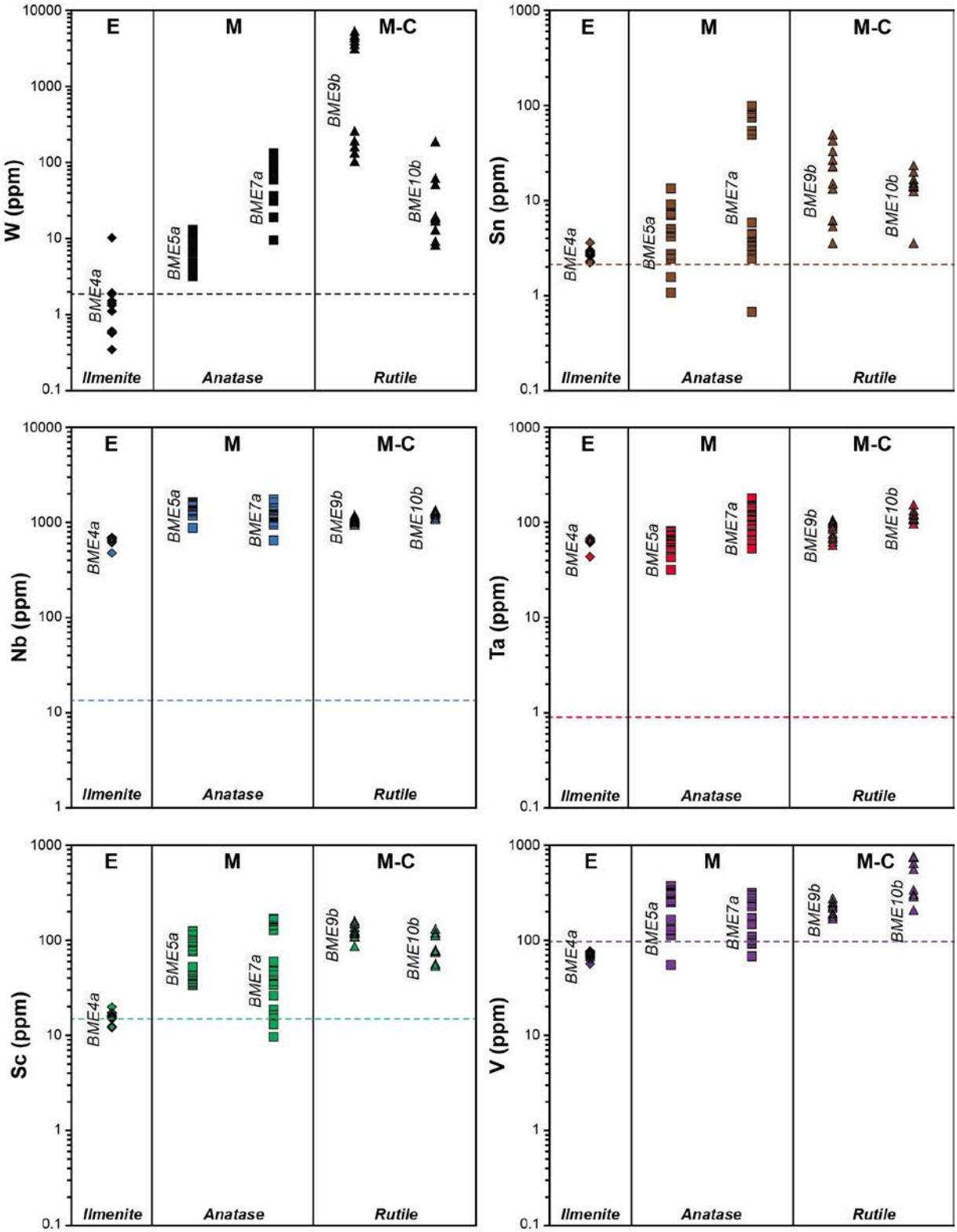

Fig. 109: Selected trace element compositions of Ti-oxides from the Beaume valley as function of the metamorphism degree increase. E: epizone (ilmenite; sample BME4a); M: mesozone (anatase; samples BME5a and BME7a); M-C: mesozone-catazone transition (rutile; BME9b and BME10b). Horizontal dash lines represent the clarke values for the upper continental crust (UCC from Rudnick and Gao, 2003). Data are given in Table 29.

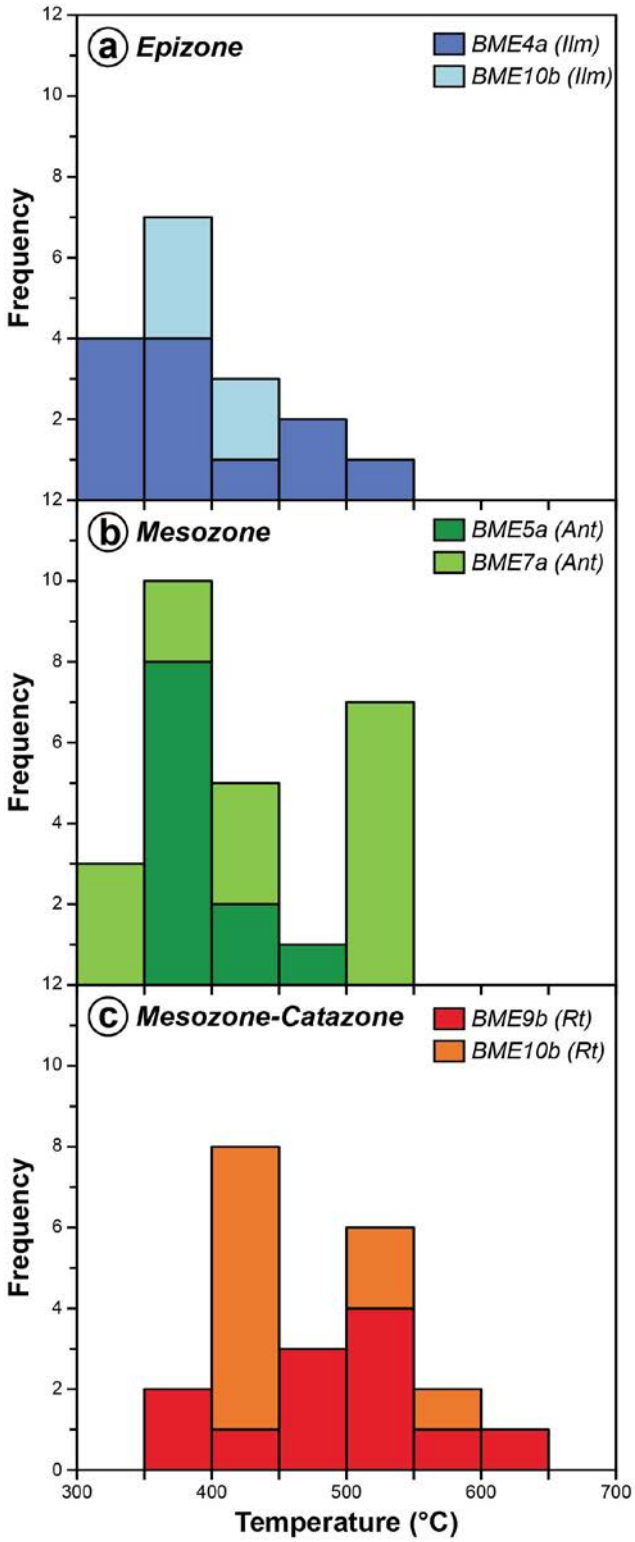

Fig. 110: Frequency histogram for Zr-in-Ti-oxides temperatures calculated using the thermometer defined by Watson et al. (2006). Data are given in Table 29.

7. Discussion

The previous results have shown the existence of potential magmatic sources of W in the North Cévennes area, as well as the possible evidence of W mobilization during the prograde metamorphism M3 as recorded by the Ti-oxides in the Cévenol micaschists. This raises therefore the question of the respective role of the metamorphic and magmatic events in the mobilization of W at the regional scale and the relationships with the St-Mélany Sn-W deposit.

7.1. Mobilization of W in relation with metamorphic and magmatic events

7.1.1. Ti-oxides as W-Sn traps during the prograde metamorphism

The whole-rock W and Sn contents in the micaschists from the Beaume valley profile (Fig. 111) may be possibly modelled as the superposition of two distinct phenomena: (i) a progressive decrease in W and Sn, from 3.2 ppm and 6.7 ppm respectively in the epizone to 1.4 ppm and 2.2 ppm respectively in the mesozone-catazone transition, would reflect a depletion in the micaschist during the prograde metamorphism; (ii) a more local enrichment in W and Sn correlated with the distance to the hanging-wall of the Rocles pluton may be tentatively interpreted as an input by the exsolved magmatic fluids, possibly from the muscovite-rich facies, which has relatively high concentrations in rare-metals (see 5.1). The detailed mineralogical and geochemical study of the Ti-oxides contained in the micaschists from the Beaume valley has showed a progressive crystallization of anatase in the mesozone passing to rutile in the catazone from the epizonal ilmenite during the M3 prograde metamorphism. These results appear similar to those found by Luvizotto et al. (2009) in the medium-grade micaschists from the Erzgebirge. However, according to our observations, the chlorite does not represent a co-crystallized phase with the anatase or rutile, but was rather formed during the retrograde dissolution of the Ti-oxides, as suggesting both by the corrosion textures and by the Ti enrichment in chlorite close to the reaction front. TiO_2 phases are known to contain high concentrations of high field strength elements (HFSE) such as W, Sn, Nb and Ta in substitutions to Ti and represent commonly the main mineral carriers of these elements in the host rocks (e.g., Zack et al., 2002, 2004; Meinhold et al., 2008; Meinhold, 2010).

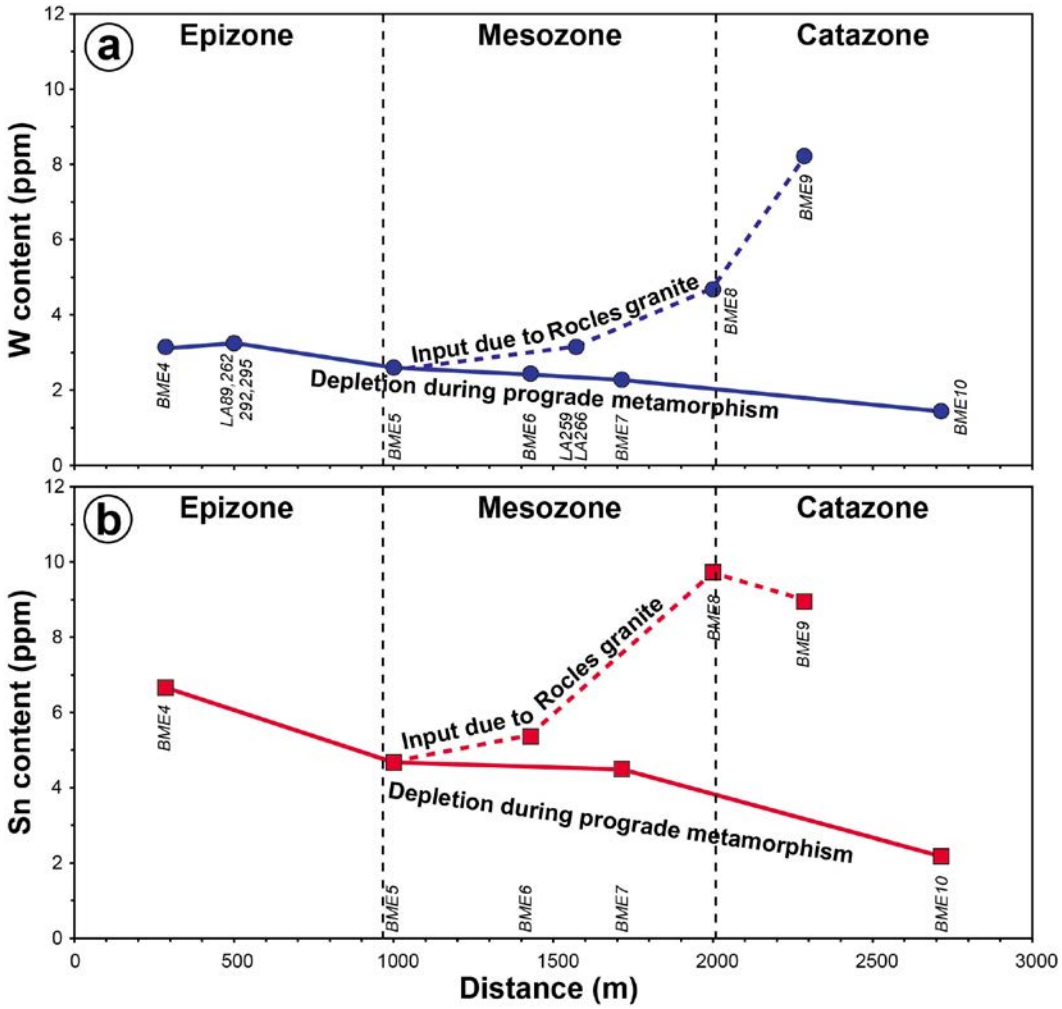

Fig. 111: Whole-rock contents in W (a) and Sn (b) in the micaschists along the Beaume valley transect and possible interpretation of the respective metamorphic and magmatic contributions. The location of the corresponding samples is shown on Fig. 81.

In the Beaume River profile, the progressive increase in the W and Sn contents in the Ti-oxides from the epizone (ca. 2 ppm W and 3 ppm Sn in ilmenite) to the catazone transition (ca. 1110 ppm W and 18 ppm Sn in rutile) may be thus put in relation with the overall volumic decrease in ilmenites as function of the metamorphism degree increase. Indeed, experimental studies have shown that rutile (and generally TiO_2) is highly soluble in chloride and fluoride-bearing metamorphic fluids in high-grade metamorphic conditions (P~0.5 GPa; T>700°C) (Rapp et al., 2010). This suggests that the dissolution of a large number of ilmenite crystals during the prograde metamorphism may release significant amounts of W and other elements, which in turn may be either mobilized by metamorphic fluids or be reincorporated in newly formed Ti-oxides (anatase, rutile) or coeval metamorphic biotite, as observed. Due to the overall decrease in the Ti-oxides amount (in volume), the prograde LP-HT metamorphism results in a loss of W and Sn in the micaschists, as shown in the interpreted

Beaume profile (Fig. 111), and possibly of other rare elements. This W may be then exported with the metamorphic fluids. The scheelite disseminations in calc-silicate rocks may represent the result of a metamorphic W mobilization, as demonstrated in the micaschists from the Montagne Noire by Gibert et al. (1992). There, the strata-bound scheelite-bearing calc-silicate gneisses resulted from the precipitation of W from CO_2-CH_4±N_2-rich metamorphic fluids at ca. 500°C and 2 kbar (Gibert et al., 1992). Finally, the W enrichment in the Ti-oxides found in the close proximity with the hanging-wall of the Rocles granite (Fig. 110) is more pronounced than expected given the contents from the epizone and the catazone. As for the whole-rock profile, this may be interpreted as a record of the interaction with the hosting-rocks of a magmatic-hydrothermal fluid derived from the Rocles granite, in which case the Ti-oxides would have acted as a trap for the W-Sn transported by this fluid.

7.1.2. The St-Mélany mesozone

As seen in Fig. 112, the surroundings of the St-Mélany deposit correspond to a W anomaly, with whole-rock contents between 6 and 15 ppm of W. It is also in the St-Mélany mesozonal micaschists that the Ti-oxides display the highest enrichment in W (up to 9000 ppm), Sn (up to 12250 ppm), Nb (up to 15000 ppm) and Ta (up to 840 ppm). As seen in Fig. 108, these oxides show a remarkable internal zoning in W showing alternating enrichment and depletion in rare-metals. This textural feature is strongly suggestive of successive influxes of a rare-metal-rich fluid superimposing their effects to the regional enrichment, as discussed above (see 7.1.1). In the same way as for the Beaume profile (Fig. 111), this in turn calls for the role for a rare-metal granite. In this respect, the Rocles muscovite-granite represents an attractive candidate because it is demonstrated to have been coeval with the M3 metamorphism and it contains elevated contents in Sn (up to 46 ppm) and W (up to 6.1 ppm). Due to its sill emplacement mode within the regional schistosity, this granite is indeed likely to be spatially close under the St-Mélany area. The two transects performed in the Cévenol micaschists toward the Borne granite (Fig. 112) may also be interpreted as reflecting the W depletion associated with the increase in LP-HT metamorphic grade. This trend is however obscured by two effects: (i) the development of the St-Mélany W anomaly; and (ii) an enrichment effect associated with the Borne contact metamorphism, which is however by far less spectacular than for the Rocles contact. However, the Borne granite being emplaced during the D4 event (ca. 305 Ma), i.e. approximately 10 Ma after the formation of the St-Mélany deposit, it clearly cannot be involved as source of the fluids and the metals.

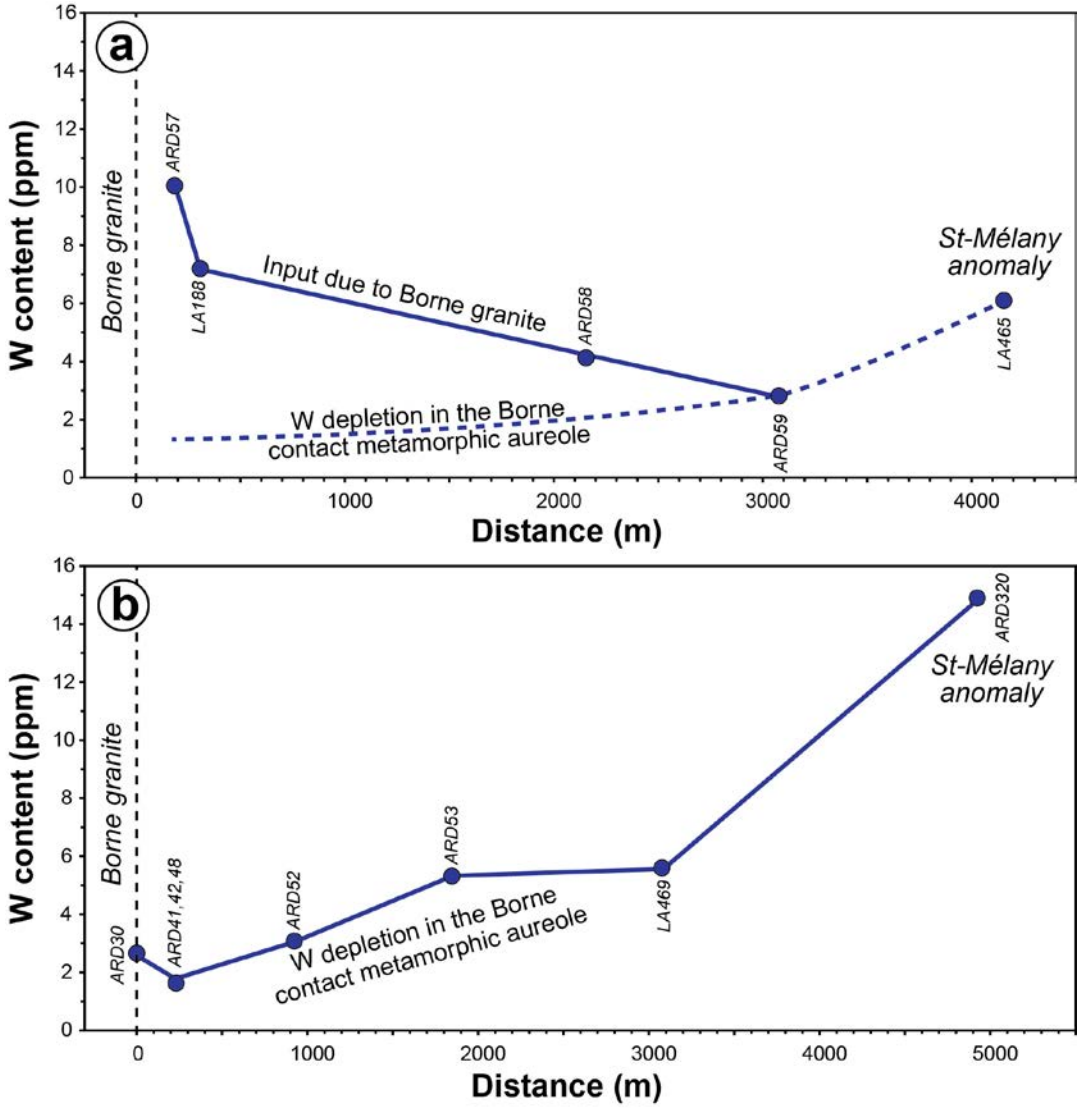

Fig. 112: Whole-rock contents in W in the micaschists along two transects, sub-parallel to the Drobie valley in direction of the Borne granite, and possible interpretation of the metamorphic and magmatic contributions. The location of the corresponding samples is shown on Fig. 81.

7.2. Relationships between the St-Mélany deposit and the late-Variscan metamorphism

7.2.1. Structural relationships with the regional deformation events

Field observations at St-Mélany indicate that the mineralized vein system was formed clearly after the deformation event D2 (ca. 340-330 Ma) responsible for the regional schistosity S2 and was emplaced under brittle conditions according to a hydraulic fracturing mode. The quartz veins suffered later a flattening plastic deformation (boudinage, folding) during compressive conditions at high temperature (T>500°C), as indicated by the quartz microstructures. They are then cut by the rare-metal aplites and pegmatites dykes dated at

306.5 ± 3.1 Ma (^{40}Ar-^{39}Ar on muscovite; Chauvet et al., 2012), thus indicating that the vein system was emplaced before the D4 event (ca. 305-300 Ma). It is then evident that the quartz vein system was formed under the M3 conditions, and suffered in part the effects of the D3 compressive event. In this regard, the age of 317.4 ± 4.7 Ma obtained on muscovite located at the selvage from the mineralized quartz veins may correspond to this episode, whereas the younger age of 298.4 ± 2.8 Ma obtained on the crystalline borders of the same muscovite may record recrystallization and resetting of the ^{40}Ar/^{39}Ar isotope system during later fluid circulation episode, as already shown by Tartèse et al. (2011) for instance. When the effects of the plastic deformation are removed, the reconstructed vein system may be interpreted as a shear zone system, with the main flat-lying veins corresponding to the "en echelon" tension joints, and the associated steep veins figuring the shear joints. Such structure would represent an inverse fault system, which is consistent with the overall compressive conditions of the D3 event. Structural analysis indicates that this compression was associated to a NNW-SSE direction (Fig. 85). A miniature equivalent of such a system, with field evidence for inverse movement, may be seen in the epizone of the Beaume River valley (Fig. 79d). At the opposite, the late aplites and pegmatites dykes were emplaced under extensional conditions in a normal fault, as indicated by the apparent normal movement (Fig. 83e). The internal deformation of the aplo-pegmatites and their whole-rock geochemistry typical of magmatic cumulates are consistent with a filter-press process.

7.2.2. Spatial relations with the regional fluid circulations

As described previously (see 2.2), several fluid circulations episodes are known in the Cévennes area, as recorded by the metamorphic quartz veins and the tourmalinites of regional extension. Quartz veins are frequently observed in the Cévenol micaschists and consist mostly in concordant syn-folial lenses of variable lateral extension, which were formed in shear zones during the nappe stacking (Arnaud et al., 2004). These early quartz veins are known in all the Cévennes schists nappe. However, in the surroundings of St-Mélany are concentrated a second type of quartz veins, which are discordant or sub-concordant on the regional schistosity and were clearly formed during the D3 compressive event (see 2.2). In the St-Mélany deposit, the vein system cuts these later metamorphic quartz lenses and represents one of the last significant hydrothermal episodes, associated with the deposition of the Sn-W mineralization at the end of the LP-HT metamorphic event. This evolving hydrothermal system may be tentatively interpreted as a progressive focusing of metamorphic fluid

circulations during the LP-HT event (ca. 320-315 Ma), in which case the St-Mélany quartz vein system may represent the final stage of a protracted process of concentration of fluid circulation in specific zones. In this model, the emplacement of large granitic bodies during the LP-HT metamorphism, such as the Rocles granite, may play a significant thermal role for the driving of regional-scale circulations of metamorphic fluids.

7.2.3. Timing of the Sn-W mineralization

Petrographic and structural study of the St-Mélany deposit showed that the Sn-W mineralization was contemporaneous with the late-kinematic D3 formation of the hosting quartz vein system. Indeed, cassiterite and wolframite are clearly earlier than the plastic deformation. They are fractured and partially corroded into the milky quartz and show evidences of undulose deformation visible in the cassiterite and in the scheelite formed after wolframite (Fig. 86). Moreover, their systematic positions at the quartz veins boundaries suggest that they crystallized early during the vein opening history. A relationship with the late metamorphic fluid circulations may thus be considered. Fluid inclusions studies realized by Noyé (1985) and Noyé and Weisbrod (1988) lead to the conclusion that the Sn-W mineralization results from the mixing of early aquo-carbonic (H_2O-CO_2±CH_4±N_2) hot fluids (350-400°C) with late aqueous (H_2O±CH_4) diluted fluids. The former may easily be interpreted as metamorphic fluids, whereas the latter may be derived from meteoric water. As already discussed in the preceding section (see 7.1), the prograde M3 metamorphism was likely responsible for the mobilization of a significant amount of W, and possibly of Sn, initially contained in the sedimentary protoliths. A direct contribution of this W to the St-Mélany mineralization is therefore a possibility. However, there are also evidences in the St-Mélany area for the circulation of a magmatic-hydrothermal fluid (likely derived from the evolved muscovite-Rocles granite), responsible for a W anomaly in the mesozonal schists. This of course strongly suggests the possibility of a contribution from this fluid to the St-Mélany W mineralization. Nevertheless, in the present state of knowledge, no magmatic-hydrothermal fluid is observed in the St-Mélany deposit. This apparent contradiction may be resolved by considering a two-stage process: (i) preconcentration stage leading to the formation of a regional W anomaly stocked in the Ti-oxides in relation with the emplacement of the evolved Rocles muscovite-granite; and (ii) remobilization stage consisting in the partial leaching of this W stock and reconcentration as wolframite in the major draining system recorded by the St-Mélany quartz vein system. This “telescopage” model may thus explain

why the primary magmatic-hydrothermal signature of the Rocles granite is blurred in this polyphase tectono-metamorphic context.

8. Conclusions

This work focused on the St-Mélany Sn-W deposit in the Cévennes area, which represents an interesting case study of hydrothermal quartz-cassiterite-wolframite veins hosted in mesozonal micaschists and located in the close vicinity of two heterochronous granites (Rocles and Borne) in a polyphase tectono-metamorphic regional context. Structural and petrographic study of the St-Mélany mineralized veins showed that this hydrothermal system formed during a polyphase vein opening, according to a typical hydraulic fracturing mode, and was lately affected by a plastic deformation in compressive conditions consistent with the D3 event at ca. 315 Ma. Geochemical analyses of the main regional magmatic rocks showed that the muscovite-facies of the Rocles granite (ca. 315 Ma) and the aplites and pegmatites from St-Mélany (ca. 305 Ma) represent two potential sources of rare-metals in the studied area. The latter crosscut the St-Mélany vein system and were emplaced under extensional conditions corresponding to the D4 event, i.e., temporally disconnected from the Sn-W mineralization. The Rocles granite was however emplaced during the M3 prograde metamorphism and could represent a potential source of Sn-W for the St-Mélany deposit. Whole-rock composition of the Cévenol micaschists revealed a W anomaly in the surroundings of St-Mélany. A transect realized along the Beaume valley in the micaschists showing a prograde metamorphism toward the contact with the Rocles granite revealed a progressive decrease in W and Sn from the epizone to the mesozone-catazone transition, which may reflect a depletion during the prograde metamorphism. The detailed mineralogical and geochemical study of the Ti-oxides contained in the micaschists from the Beaume valley has showed a progressive crystallization of anatase in the mesozone passing to rutile in the catazone from the epizonal ilmenite during the M3 prograde metamorphism. This mineralogical evolution is marked in particular by an increase in the W and Sn contents with the metamorphism degree increase. This suggests that the dissolution of a large number of ilmenite crystals during the prograde metamorphism may release significant amounts of W and other elements, which may be mobilized by regional metamorphic fluids. In the St-Mélany deposit, the mesozonal micaschists contain anatase crystals, which exhibit growth zoning marked by high enrichment in W (up to 9000 ppm), Sn (up to 12250 ppm), Nb (up to 15000 ppm) and Ta (up to 840 ppm). This indicates that the Ti-oxides crystallized during the

interaction with a rare-metal-rich fluid, which may represent a magmatic-hydrothermal fluid derived from the muscovite-Rocles granite, coeval with the M3 metamorphism. These results suggest that the St-Mélany Sn-W deposit was formed during a two-stage process, involving (i) a preconcentration stage by magmatic-hydrothermal fluids derived from the evolved Rocles muscovite-granite and resulting in a regional W anomaly stocked in the Ti-oxides; and (ii) a remobilization stage consisting in the partial leaching of this W stock by the regional metamorphic fluids during the M3 prograde metamorphism and yielding to their progressive concentration at St-Mélany forming the mineralized vein system. In conclusion, this work highlights the important role played by the metamorphic fluids in polyphase tectono-metamorphic setting for the formation of peri-batholitic Sn-W mineralization and opens new perspectives for the understanding of these complex hydrothermal systems at the crustal scale.

Table 24: Comparative table of the successive tectonic, metamorphic and magmatic events proposed for the French Massif Central (FMC) and for the Cévennes area (after Thierry et al., 2014).

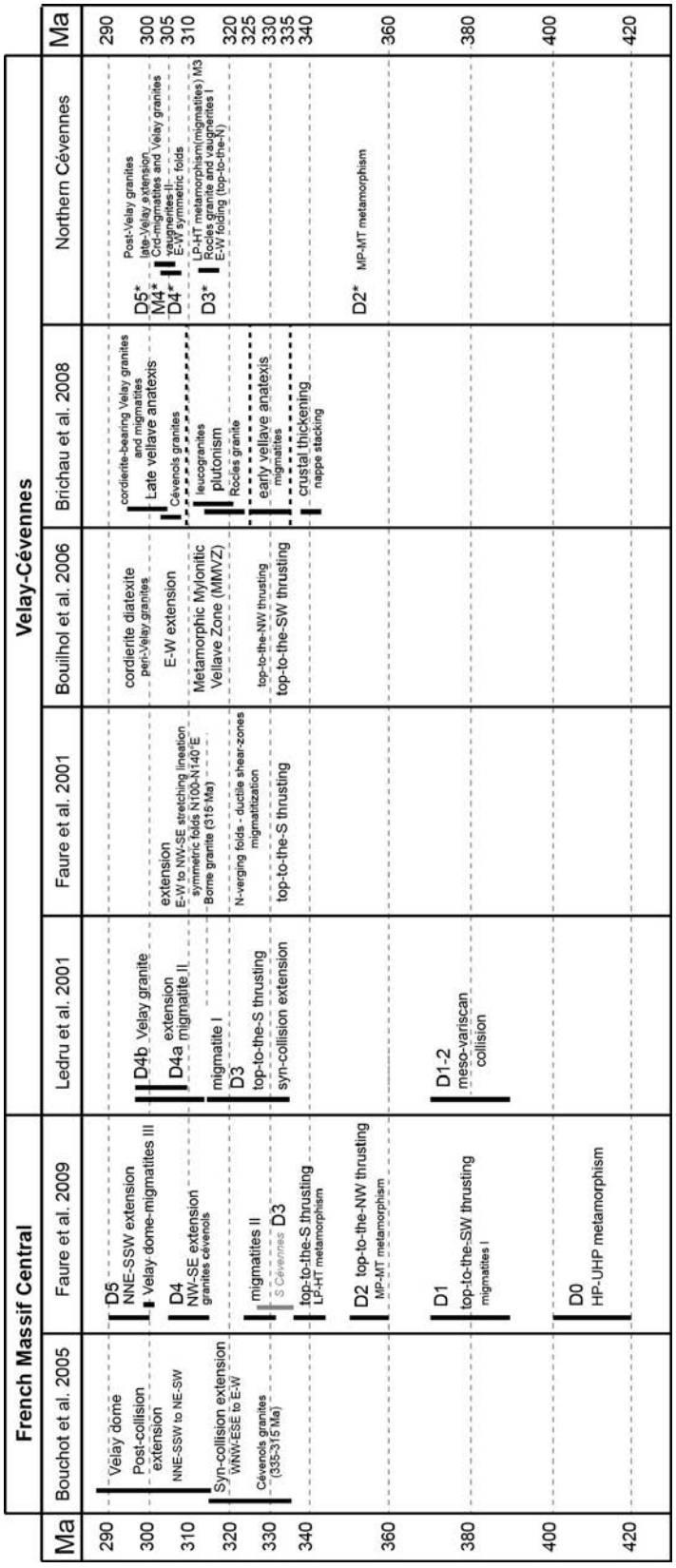

Table 25: $^{40}Ar/^{39}Ar$ analytical data for the selvage muscovite in the quartz mineralized veins from the St-Mélany deposit (sample ARD-13-12).

	Relative isotopic abundances (fAmps)*																Apparent age	
Sample	^{40}Ar	± (1σ)	^{39}Ar	± (1σ)	^{38}Ar	± (1σ)	^{37}Ar	± (1σ)	^{36}Ar	± (1σ)	Ca/K	± (1σ)	Cl/K	± (1σ)	$^{i}Ar^{*}/^{39}Ar_{i}$	± (1σ)	$^{40}Ar^{*}$ (%)	Age (Ma)	± (1σ)
ARD-13-12: selvage muscovite from quartz-cassiterite-wolframite vein																			
Spot 1	84.515	0.073	1.968	0.065	0.085	0.032	0.004	0.026	0.000	0.001	0.039	0.238	0.090	0.048	42.983	1.441	100.15	314.4	9.7
Spot 2	119.780	0.075	2.738	0.064	0.039	0.030	-0.060	0.026	0.002	0.001	-0.389	0.168	0.005	0.033	43.444	1.039	99.39	317.5	7.0
Spot 3	89.689	0.069	2.028	0.057	0.031	0.030	-0.007	0.029	0.003	0.001	-0.062	0.249	0.008	0.043	43.731	1.266	98.96	319.6	8.5
															Integrated age (spots 1-3):			**317.4**	**4.7**
Spot 4	91.489	0.075	2.272	0.058	0.099	0.029	0.007	0.028	0.001	0.001	0.052	0.220	0.091	0.038	40.108	1.056	99.68	295.0	7.2
Spot 5	87.758	0.079	2.150	0.061	0.055	0.031	0.040	0.026	0.002	0.001	0.335	0.214	0.039	0.043	40.525	1.181	99.34	297.8	8.0
Spot 6	122.918	0.077	2.850	0.062	-0.050	0.031	0.006	0.029	0.013	0.001	0.037	0.183	-0.089	0.032	41.717	0.936	96.79	305.9	6.3
Spot 7	124.853	0.071	3.121	0.060	0.036	0.030	0.006	0.027	0.000	0.001	0.036	0.154	-0.002	0.028	39.961	0.796	99.98	294.0	5.4
Spot 8	119.892	0.074	2.922	0.061	0.061	0.034	0.006	0.027	0.002	0.001	0.034	0.169	0.025	0.034	40.830	0.876	99.60	299.9	5.9
															Integrated age (spots 4-8):			**298.4**	**2.8**

* Corrected for blank, mass discrimination, and radioactive decay.
Sensitivity: 6.312E-17 ± 1.047E-18 (mol/fAmp).
Fluence J: 0.0044316 ± 2.25E-6

Table 26: Whole-rock chemical compositions of regional magmatic rocks from the North Cévennes area. bdl: below detection limit.

Sample	St-Mélany deposit						Borne	Rocles granite			Fabras
	Rare-metal aplite		*Rare-metal pegmatite*		*Lamprophyre*		granite	*Bt facies*	*Bt-Ms facies*	*Ms facies*	granite
	ARD21	ARD23	ARD22	ARD72	ARD25	ARD19	ARD33	ARD91	ARD67	ARD61	ARD92
Oxides (wt.%)											
SiO_2	74.32	74.85	75.53	72.04	56.59	54.35	69.30	72.79	73.86	75.31	73.00
Al_2O_3	15.07	15.60	14.60	15.87	14.26	13.80	14.55	13.81	13.80	14.68	14.58
Fe_2O_3	0.70	0.44	0.44	0.38	6.33	7.31	3.42	1.92	1.66	0.54	0.81
MnO	0.03	0.04	0.04	0.07	0.09	0.12	0.04	0.02	0.03	0.05	0.03
MgO	bdl	bdl	0.04	0.07	6.68	8.62	1.53	0.48	0.22	bdl	bdl
CaO	0.43	0.49	0.46	1.24	5.07	5.28	2.36	0.85	0.20	0.40	0.53
Na_2O	3.98	2.87	3.72	4.91	1.78	1.58	2.99	2.57	2.55	4.41	3.83
K_2O	3.76	4.13	2.67	2.33	4.43	4.49	3.73	5.81	6.22	4.15	4.70
TiO_2	0.03	bdl	bdl	bdl	1.14	1.16	0.49	0.29	0.23	0.04	0.05
P_2O_5	0.41	0.50	0.48	1.09	0.65	0.70	0.29	0.14	0.11	0.29	0.35
LOI	1.05	1.34	1.18	1.21	2.37	1.89	1.21	0.99	2.32	0.75	1.01
Total	99.78	100.26	99.16	99.21	99.39	99.27	99.90	99.65	101.2	100.6	98.90
Traces (ppm)											
As	123	35.8	12.1	3.00	12.0	30.6	2.34	bdl	bdl	1.82	bdl
Ba	43.3	44.4	41.2	121	1721	2721	727	533	330	50.1	85.5
Be	24.6	135	317	168	8.49	7.69	4.72	3.38	3.20	39.2	4.11
Bi	4.13	1.46	1.86	1.67	0.47	0.91	bdl	0.21	0.20	1.88	3.05
Cd	bdl	bdl	bdl	0.19	0.27	0.40	0.16	0.14	bdl	0.13	bdl
Co	bdl	0.51	bdl	bdl	25.1	29.7	7.01	2.68	1.83	bdl	bdl
Cr	7.27	6.81	4.78	4.27	355	451	48.9	10.8	9.62	4.80	4.92
Cs	59.8	34.2	43.2	75.3	62.5	82.4	14.6	5.86	5.72	16.8	43.8
Cu	bdl	bdl	bdl	bdl	17.2	24.4	bdl	bdl	9.34	5.00	bdl
Ga	31.4	30.9	26.8	30.2	20.8	19.1	20.4	17.9	17.2	21.7	24.8
Ge	3.75	4.92	5.26	4.94	1.59	1.81	1.74	1.14	0.92	2.53	1.69
Hf	1.28	1.81	0.65	2.10	9.43	9.38	6.55	5.02	3.39	1.10	1.01
In	bdl	bdl	bdl	bdl	0.08	0.08	bdl	bdl	bdl	bdl	bdl
Mo	bdl	bdl	bdl	bdl	1.28	bdl	bdl	bdl	bdl	bdl	bdl
Nb	31.6	50.8	46.4	70.1	18.7	17.8	15.2	8.18	8.22	20.0	18.1
Ni	bdl	bdl	5.69	bdl	47.4	148	13.6	bdl	bdl	bdl	bdl
Pb	9.53	18.5	8.87	25.6	29.0	49.2	32.8	54.3	54.3	29.1	6.47
Rb	662	607	696	572	352	300	211	217	263	427	554
Sc	1.75	bdl	bdl	bdl	17.9	21.0	10.0	4.12	3.79	1.13	2.31
Sb	0.24	bdl	bdl	bdl	bdl	bdl	bdl	bdl	0.29	bdl	bdl
Sn	176	116	183	242	16.1	15.1	7.40	4.20	11.1	45.8	48.6
Sr	34.9	39.2	37.4	82.9	564	540	421	205	84.0	25.6	33.5
Ta	23.6	33.3	49.4	145	1.62	1.56	1.98	0.82	0.93	18.4	6.92
Th	3.17	3.77	1.23	1.03	40.5	43.1	23.2	25.5	19.2	2.03	2.12
U	16.2	10.1	3.84	7.82	9.23	8.89	4.99	3.86	3.56	10.1	10.1
V	bdl	bdl	bdl	bdl	116	128	42.7	12.0	8.78	0.88	1.20
W	20.5	17.7	16.4	21.4	4.95	6.20	1.97	0.58	1.67	6.12	10.3
Y	3.98	3.16	1.88	2.84	24.5	30.3	21.9	11.5	9.49	3.82	5.79
Zn	54.6	36.8	49.0	34.9	94.3	109	37.3	50.9	34.6	52.3	41.0
Zr	19.2	19.6	5.98	20.3	360	367	248	161	100	17.3	20.2
La	1.77	2.03	1.71	1.32	54.4	55.7	57.5	40.4	19.1	2.36	2.23
Ce	3.34	2.16	1.65	1.47	124	126	116	83.1	56.0	4.83	4.74
Pr	0.41	0.38	0.32	0.26	16.5	17.1	12.8	10.2	5.26	0.58	0.57
Nd	1.44	1.47	1.25	1.03	71.3	72.9	45.6	37.4	19.3	2.04	1.96
Sm	0.37	0.36	0.29	0.33	13.8	14.1	7.90	7.35	4.25	0.51	0.55
Eu	0.12	0.31	0.14	0.44	2.45	2.63	1.44	0.98	0.56	0.09	0.09
Gd	0.38	0.41	0.29	0.36	8.18	9.30	5.65	4.89	3.01	0.44	0.52
Tb	0.08	0.07	0.05	0.07	1.01	1.20	0.77	0.60	0.40	0.08	0.12
Dy	0.54	0.41	0.30	0.43	5.22	6.25	4.25	2.76	2.05	0.56	0.91
Ho	0.11	0.08	0.06	0.08	0.92	1.12	0.80	0.42	0.34	0.11	0.18
Er	0.29	0.19	0.15	0.20	2.31	2.83	2.07	0.96	0.84	0.33	0.49
Tm	0.05	0.03	0.02	0.03	0.30	0.37	0.29	0.11	0.11	0.06	0.08
Yb	0.36	0.17	0.11	0.21	1.99	2.41	1.97	0.72	0.76	0.47	0.56
Lu	0.05	0.02	0.01	0.03	0.29	0.36	0.29	0.10	0.11	0.07	0.08

Table 27: Representative chemical compositions of columbite-tantalite from rare-metal pegmatite from St-Mélany (sample ARD72).

Rare-metal pegmatite from St-Mélany (sample ARD72)															
	(i) Dark core		*(ii) Dark rim-I*		*(iii) Dark rim-II*		*(iv) Light rim*		*(v) Dark rim-III*		*(vi) Bright overgrowth*			*(vii) Tantalite overgrowth*	
	a1	a22	a2	a3	a4	a20	a18	h6	a9	a29	a8	a13	a15	b8	b10	e4
Nb_2O_5	57.30	57.59	53.55	52.46	50.48	48.91	39.14	35.81	44.54	45.01	29.59	29.72	25.59	11.44	11.86	5.72
Ta_2O_5	19.66	20.90	21.93	21.48	30.96	31.98	43.64	46.31	35.35	35.08	49.92	47.90	48.30	68.57	71.65	77.62
FeO	12.18	11.43	12.75	12.66	13.35	13.24	12.44	12.35	12.45	12.27	12.85	11.64	12.32	13.71	13.74	13.04
MnO	6.49	6.53	5.58	5.52	5.79	5.27	5.11	4.82	5.14	4.91	3.61	5.21	4.47	0.00	0.00	0.00
WO_3	4.07	2.02	4.40	4.45	0.00	0.00	0.00	0.00	3.11	2.36	2.48	3.03	7.26	0.00	0.00	0.00
TiO_2	1.56	1.61	1.57	1.35	0.91	1.00	0.00	0.83	0.88	0.00	1.32	1.16	0.83	5.24	3.54	3.54
SnO_2	0.00	0.00	0.00	0.00	0.00	0.00	0.00	0.00	0.00	0.00	0.00	1.78	2.18	1.46	0.00	0.00
Total	101.3	100.1	99.78	97.92	101.5	100.4	100.3	100.1	101.5	99.63	99.77	100.4	100.9	100.4	100.8	99.92
Nb	1.57	1.59	1.50	1.50	1.43	1.41	1.20	1.11	1.30	1.34	0.94	0.94	0.82	0.39	0.41	0.21
Ta	0.32	0.35	0.37	0.37	0.53	0.55	0.80	0.86	0.62	0.63	0.96	0.91	0.93	1.40	1.48	1.68
Fe	0.62	0.58	0.66	0.67	0.70	0.71	0.70	0.71	0.67	0.68	0.76	0.68	0.73	0.86	0.87	0.87
Mn	0.33	0.34	0.29	0.30	0.31	0.28	0.29	0.28	0.28	0.27	0.22	0.31	0.27	0.00	0.00	0.00
W	0.06	0.03	0.07	0.07	0.00	0.00	0.00	0.00	0.05	0.04	0.05	0.05	0.13	0.00	0.00	0.00
Ti	0.07	0.07	0.07	0.06	0.04	0.05	0.00	0.04	0.04	0.00	0.07	0.06	0.04	0.30	0.20	0.21
Sn	0.00	0.00	0.00	0.00	0.00	0.00	0.00	0.00	0.00	0.00	0.00	0.05	0.06	0.04	0.00	0.00
Ta/(Ta+Nb)	0.17	0.18	0.20	0.20	0.27	0.28	0.40	0.44	0.32	0.32	0.50	0.49	0.53	0.78	0.78	0.89
Mn/(Mn+Fe)	0.35	0.37	0.31	0.31	0.31	0.29	0.29	0.28	0.29	0.29	0.22	0.31	0.27	0.00	0.00	0.00

Structural formulae were calculated on the basis of 6 atoms of oxygen.
bdl: below detection limit

Table 28: Whole-rock chemical compositions of the Cévenol micaschists. bdl: below detection limit.

	Epizone				Mesozone			
Sample	BME4	ARD52	ARD53	ARD58	ARD59	BME5	BME6	BME7
Oxides wt.%								
SiO_2	53.67	56.49	60.67	64.40	52.65	60.14	57.88	61.21
Al_2O_3	24.40	21.61	18.57	17.35	23.06	19.85	22.14	18.61
Fe_2O_3	7.16	7.14	6.40	6.17	8.65	7.83	7.63	7.64
MnO	0.10	0.05	0.08	0.05	0.07	0.07	0.17	0.07
MgO	2.23	1.63	2.31	1.82	2.75	2.40	1.66	2.47
CaO	0.52	0.25	0.14	0.03	0.03	0.37	0.24	0.34
Na_2O	1.62	0.56	1.75	0.45	0.37	1.44	0.78	2.11
K_2O	5.43	4.55	4.07	3.83	5.62	4.05	5.10	3.43
TiO_2	1.08	0.98	0.85	0.80	1.14	0.93	0.86	0.92
P_2O_5	0.11	0.16	0.20	0.13	0.07	0.14	0.11	0.15
LOI	3.99	5.92	3.94	4.19	4.87	3.58	4.15	3.54
Total	100.3	99.32	98.96	99.21	99.28	100.8	100.7	100.5
Traces (ppm)								
As	bdl	2.43	26.71	33.46	18.49	2.07	9.52	14.97
Ba	1045	771	996	612	801	670	660	597
Be	4.21	3.67	3.79	4.29	3.80	4.28	4.80	4.10
Bi	0.34	0.30	0.27	0.61	0.23	0.29	0.37	0.32
Cd	0.16	0.17	0.48	0.23	0.17	0.19	0.15	0.15
Co	18.63	17.66	10.29	9.54	16.73	20.87	18.09	18.56
Cr	119	96.66	96.64	87.52	109	99.41	101	97.25
Cs	4.71	20.19	14.38	20.93	11.33	7.47	13.62	8.19
Cu	21.26	26.01	32.18	27.63	7.73	24.74	20.25	24.04
Ga	34.75	31.26	26.86	25.53	33.22	28.18	31.65	26.65
Ge	2.52	2.21	1.36	2.34	2.60	2.34	3.11	2.51
Hf	5.03	4.95	5.54	4.58	6.62	5.18	3.37	5.28
In	0.10	0.08	bdl	bdl	0.09	0.09	0.10	0.07
Mo	bdl	bdl	bdl	0.54	bdl	0.57	bdl	bdl
Nb	20.45	18.19	15.49	14.43	22.55	17.25	15.92	16.73
Ni	46.32	36.69	25.68	28.00	50.74	44.96	46.03	42.36
Pb	16.87	26.18	31.76	25.31	14.41	22.41	28.61	13.05
Rb	249	213	182	217	233	192	264	166
Sc	23.33	18.57	16.08	16.40	19.91	19.28	20.05	18.77
Sb	0.31	0.23	1.28	1.12	0.51	0.20	bdl	0.27
Sn	6.66	5.02	3.74	3.96	5.70	4.67	5.36	4.50
Sr	117	74.21	106	31.91	46.29	69.29	86.00	88.93
Ta	1.82	1.65	1.40	1.31	1.85	1.59	1.48	1.50
Th	24.57	21.28	15.57	15.82	21.78	20.31	19.65	17.83
U	4.01	4.10	3.45	7.78	3.28	3.66	3.19	3.55
V	126	106	102	104	130	108	104	106
W	3.15	3.08	5.32	4.13	2.82	2.60	2.44	2.28
Y	37.18	38.18	36.74	36.27	39.38	34.87	29.29	33.24
Zn	96.43	116	110	89.92	126	119	165	111
Zr	164	172	198	165	237	168	110	177
La	67.88	66.68	47.01	44.44	61.15	53.97	58.63	50.49
Ce	99.20	127	93.78	87.73	122	102	114	96.17
Pr	15.37	15.00	10.72	10.32	14.53	12.08	13.27	11.52
Nd	57.11	54.91	40.37	39.18	54.19	45.12	48.32	43.02
Sm	10.51	10.37	7.83	7.92	10.52	8.64	9.05	8.32
Eu	2.01	2.02	1.45	1.61	2.20	1.78	1.76	1.77
Gd	7.69	8.07	6.70	6.84	8.59	7.13	6.45	6.90
Tb	1.19	1.22	1.02	1.05	1.25	1.06	0.96	1.04
Dy	7.23	7.12	6.19	6.29	7.27	6.45	5.64	6.25
Ho	1.46	1.43	1.30	1.33	1.46	1.32	1.14	1.25
Er	3.87	3.78	3.46	3.49	3.79	3.51	3.02	3.28
Tm	0.56	0.53	0.49	0.50	0.53	0.51	0.43	0.48
Yb	3.74	3.60	3.27	3.30	3.55	3.41	2.82	3.24
Lu	0.57	0.53	0.49	0.51	0.54	0.52	0.43	0.49

Table 28: Continued.

	Mesozone								Catazon
Sample	BME8	BME9	ARD02	ARD30	ARD41	ARD42	ARD48	ARD57	BME-10
Oxides wt.%									
SiO_2	69.29	71.48	59.97	54.60	67.09	62.37	64.30	56.73	87.36
Al_2O_3	14.71	13.85	18.31	22.32	15.89	19.29	16.30	21.48	5.55
Fe_2O_3	5.09	3.79	7.09	9.08	5.43	6.73	5.75	8.17	2.21
MnO	0.05	0.03	0.07	0.09	0.07	0.07	0.09	0.09	0.08
MgO	1.91	1.32	3.29	2.60	1.46	2.13	2.01	3.17	0.60
CaO	0.39	0.30	0.59	0.41	0.80	0.76	2.99	0.28	0.77
Na_2O	1.53	1.97	1.99	1.15	1.18	1.08	2.97	1.43	0.80
K_2O	3.62	3.58	3.63	4.71	4.80	3.88	3.03	4.06	1.61
TiO_2	0.67	0.75	0.91	1.01	0.90	0.91	0.64	0.94	0.37
P_2O_5	0.16	0.15	0.20	0.10	0.23	0.14	0.20	0.15	0.36
LOI	3.12	3.07	3.71	3.29	2.06	3.43	1.31	2.55	0.87
Total	100.6	100.3	99.74	99.35	99.91	100.8	99.58	99.05	100.6
Traces (ppm)									
As	378	26.88	33.00	48.08	4.33	11.67	51.49	60.81	2.20
Ba	585	552	780	666	871	707	701	700	312
Be	2.87	4.32	4.30	4.11	2.69	4.17	2.39	4.83	1.37
Bi	0.30	0.53	0.30	0.13	0.20	0.53	0.18	0.24	0.21
Cd	0.25	0.35	0.24	0.16	0.27	0.23	0.20	0.15	0.26
Co	5.24	3.25	17.03	20.95	12.48	18.24	9.24	21.97	4.24
Cr	69.65	71.09	98.85	112	71.76	92.36	30.99	113	23.21
Cs	24.55	20.55	25.12	32.98	16.13	16.32	13.65	45.51	5.74
Cu	19.98	28.49	30.78	63.91	25.79	16.93	13.91	15.26	8.42
Ga	19.97	18.17	27.52	31.77	23.41	26.42	21.79	31.64	7.65
Ge	1.90	1.74	1.92	2.38	1.79	2.36	1.50	2.30	1.92
Hf	5.44	9.98	5.45	4.36	12.33	4.76	5.93	4.50	5.99
In	bdl	bdl	0.08	bdl	bdl	bdl	bdl	bdl	bdl
Mo	0.52	1.56	0.67	bdl	bdl	bdl	0.97	1.09	bdl
Nb	12.49	14.24	15.88	18.11	17.03	14.97	9.98	17.40	6.60
Ni	23.22	14.54	49.04	46.45	24.80	42.60	9.91	47.68	9.80
Pb	26.10	50.77	11.48	38.12	29.36	24.02	19.06	34.59	23.45
Rb	178	198	214	275	202	174	134	211	73.73
Sc	11.16	11.36	18.00	21.23	13.92	19.18	18.74	20.27	4.31
Sb	0.58	1.04	0.81	0.21	0.21	0.25	bdl	0.49	bdl
Sn	9.73	8.95	14.48	4.47	5.17	3.69	7.68	6.55	2.18
Sr	99.57	145	76.85	117	140	159	212	99.70	61.32
Ta	1.15	1.39	1.47	1.71	1.58	1.40	0.83	1.69	0.73
Th	12.31	20.43	17.61	21.30	21.11	16.57	11.46	19.00	9.73
U	3.21	5.23	4.37	5.81	4.74	3.31	2.63	4.28	3.24
V	67.30	70.21	109	127	86.34	108	87.86	134	26.33
W	4.68	8.22	7.45	2.66	1.55	1.68	1.64	10.05	1.44
Y	32.46	30.98	33.31	36.61	41.35	36.65	29.33	34.57	19.43
Zn	90.22	51.54	122	97.10	78.31	154	85.62	112	43.77
Zr	184	378	176	149	478	165	223	155	211
La	42.13	53.44	45.76	61.41	55.49	52.85	36.38	54.04	22.54
Ce	82.74	97.20	88.61	120	115	100	74.74	107	42.95
Pr	9.71	12.12	10.92	13.97	12.80	12.37	8.74	12.30	5.40
Nd	37.10	44.52	41.79	51.62	48.36	45.65	33.52	45.43	20.52
Sm	7.41	8.50	8.48	9.93	9.48	8.70	6.72	8.79	4.06
Eu	1.57	1.63	1.41	1.83	1.88	2.17	1.50	1.75	0.72
Gd	6.13	6.57	7.10	7.95	7.77	7.36	5.83	7.14	3.34
Tb	0.94	0.99	1.07	1.17	1.16	1.13	0.86	1.08	0.52
Dy	5.63	5.81	6.49	6.93	7.07	6.77	5.27	6.47	3.20
Ho	1.15	1.17	1.30	1.41	1.49	1.38	1.10	1.31	0.67
Er	3.05	3.17	3.35	3.63	3.94	3.43	2.95	3.44	1.84
Tm	0.43	0.48	0.46	0.52	0.57	0.45	0.42	0.50	0.26
Yb	2.80	3.35	3.07	3.48	3.79	2.88	2.92	3.45	1.87
Lu	0.43	0.52	0.49	0.51	0.56	0.42	0.45	0.51	0.29

Table 29: Chemical compositions of Ti-oxides from the Cévenol micaschists in the Beaume Valley and in the St-Mélany deposit determined by EMPA and LA-ICPMS.

	Epizone				**Mesozone**							**Mesozone-Catazone transition**			
Sample	BME-4a (Ilmenite)				BME-5a (Anatase)				BME7a (Anatase)			BME9b (Rutile)			
EMPA	n=6				n=9				n=9			n=8			
wt.% ox	Mean	SD	Min	Max	Mean	SD	Min	Max	Mean	SD	Min	Max	Mean	SD	Min	Max
TiO_2	54.48	0.38	54.04	55.08	101.67	0.59	100.31	102.39	99.87	1.80	97.09	102.23	100.21	0.99	99.09	101.67
FeO	43.94	0.71	43.13	44.94	0.49	0.11	0.41	0.57	1.05	0.92	0.28	2.22	0.41	0.17	0.27	0.69
MnO	1.89	0.11	1.77	2.05	0.01	0.02	0.00	0.03	0.03	0.02	0.02	0.05	0.04	0.02	0.02	0.06
LA-ICPMS	n=12				n=13				n=15				n=12			
ppm	Mean	SD	Min	Max	Mean	SD	Min	Max	Mean	SD	Min	Max	Mean	SD	Min	Max
Si	7212	7178	1214	24055	6241	5082	937	18437	22484	19763	2250	70638	53924	45126	21510	182457
Sc	16	2.1	12	20	66	32	34	125	72	63	10	169	125	21	87	160
V	69	6.0	57	77	221	104	55	371	163	86	68	314	219	36	169	275
Cr	22	4.7	16	31	49	19	22	78	75	84	7.5	275	79	34	36	141
Ni	14	5.6	8.6	30	8.0	1.2	6.7	8.9	bdl	bdl	bdl	bdl	28	23	9.2	74
Cu	3.3	2.7	1.2	10.3	5.1	1.8	2.6	9.5	28	34	3.2	101	57	52	7.1	162
Zn	188	83	109	405	19	4.9	12	30	30	25	10	108	300	274	18	950
Zr	12	20	0.6	66	51	116	2.0	382	29	28	1.0	69	50	61	3	218
Nb	654	61	477	697	1407	214	876	1639	1210	258	647	1745	1069	70	942	1194
Ta	62	6.1	44	68	62	14	32	82	112	36	53	179	84	17	58	106
Mo	0.38	0.05	0.32	0.43	0.59	0.07	0.54	0.64	bdl	bdl	bdl	bdl	1.0	0.4	0.8	1.3
Sn	2.8	0.4	2.2	3.6	5.3	3.5	1.1	13.4	31	37	0.7	98	21	15	4	49
W	2.0	2.8	0.3	10.3	7.7	3.1	3.2	13.1	78	40	10	132	2184	2167	104	5349
T (°C)	393	70	318	534	431	98	360	662	444	82	334	537	487	70	379	617

Table 29: Continued.

	Mesozone-Catazone transition								St-Mélany			
Sample	BME10b (Ilmenite)				BME10b (Rutile)				ARD03a (Anatase)			
EMPA	n=4				n=7				n=26			
wt.% ox	Mean	SD	Min	Max	Mean	SD	Min	Max	Mean	SD	Min	Max
TiO_2	54.27	0.36	53.77	54.60	101.26	0.57	100.41	101.84	97.56	3.73	90.17	101.59
FeO	41.68	0.61	40.83	42.26	0.19	0.27	0.00	0.38	0.71	0.40	0.22	1.40
MnO	3.75	0.09	3.70	3.89	0.00	0.00	0.00	0.00	0.03	0.03	0.00	0.06
LA-ICPMS	n=5				n=10				n=15			
ppm	Mean	SD	Min	Max	Mean	SD	Min	Max	Mean	SD	Min	Max
Si	2734	2698	653	6473	13356	12764	1176	37551	34548	36856	5572	144940
Sc	46	8.3	35	58	90	28	54	132	86	17	56	107
V	174	23	140	206	488	223	208	759	815	906	124	2872
Cr	53	12	34	68	193	119	42	366	178	210	17	705
Ni	14	1.8	12	17	17	6.0	10	26	7.0	-	7.0	7.0
Cu	1.8	0.8	1.3	2.9	13	16	3.4	56	670	2393	2.6	8634
Zn	730	302	417	1182	548	864	8.8	2153	2747	9321	14	35103
Zr	4.6	0.7	3.9	5.4	34	53	6.1	172	32	36	1.8	108
Nb	651	28	601	668	1239	93	1082	1347	4591	4758	983	14983
Ta	74	4.9	65	77	119	18	97	154	278	261	51	839
Mo	0.8	0.2	0.6	1.0	3.1	-	3.1	3.1	bdl	bdl	bdl	bdl
Sn	6.8	0.4	6.3	7.5	15	5.1	3.6	23	1895	2535	245	7476
W	6.0	2.0	3.6	8.4	40	56	8.3	189	1714	1319	300	5102
T (°C)	394	6	388	401	458	66	407	599	458	71	356	566

PART III: Characterization of fluids and metals sources: hydrothermal vs magmatic deposits

Chapter 7: Fluid sources related to W-Sn mineralization in the Variscan French Massif Central: insights from the chemical and boron isotopic compositions of tourmaline

Abstract

Tourmaline is commonly associated with Sn-W deposits in the European Variscan belt, where it forms an accessory mineral phase, locally abundant, in granites and related pegmatites, greisen, hydrothermal quartz veins and breccia pipe systems. This work focuses on the tourmalinization associated with three hydrothermal W±Sn deposits (Puy-les-Vignes, Enguialès, St-Mélany), located in the French Massif Central (FMC), through an integrated approach combining mineralogical and textural observations, chemical compositions of major, minor and trace elements and boron isotopic analyses of tourmaline. In the three studied deposits, the tourmalinization represents the main hydrothermal alteration and occurs systematically through a multi-stage process, either during an early alteration stage, during the emplacement of the mineralized veins or during late fracturing episodes. The successive generations of tourmalines identified show numerous similarities between the three deposits, indicating that the tourmalinization occurs through a common boron metasomatism mechanism at the regional scale, involving several hydrothermal fluid circulations with time. Detailed analysis of representative tourmaline crystals indicate that the tourmalinization results from a discontinuous fluid mixing process in open system, which involves periodic inputs of hydrothermal fluids with different compositions over time. Reporting the compositions of tourmalines in the classical Al-Fe-Mg diagram from Henry and Guidotti (1985), it appears that four main fluid poles are sufficient to describe the chemical zonation in tourmalines by involving mixing trends between these different end-members. Interpretation of these fluid poles in terms of crustal reservoirs has been possible from the trace elements analysis of tourmalines and revealed the contribution of fluids equilibrated with granites, orthogneisses and metasedimentary rocks. Combining the trace element compositions and the boron isotope signatures of tourmalines, we propose that the boron source derived in majority from metasedimentary rocks in the three studied deposits. In this regard, we propose that the Para-Autochtonous Unit, located at the bottom of the three-nappe pile system of the FMC, represent an important metamorphic boron reservoir at the regional scale. Finally, the

tourmalines from the Puy-les-Vignes, Enguialès and St-Mélany deposits commonly show enrichment in Sn (36 ppm in average) and W (2.5 ppm in average), with Sn>W contents. In comparison, tourmalines from barren quartz-veins close to St-Mélany show no enrichment in Sn and W and have a distinct B isotope signature. Consequently, it may be proposed that the trace elements contents and the B isotopic composition of tourmaline may potentially serve as a proximal indicator of Sn-W mineralization and could help to distinguish between mineralized and barren zones.

Keywords:
Tourmaline; Sn-W mineralization; hydrothermal fluids; boron metasomatism; fluid mixing; boron isotopes; French Massif Central.

1. Introduction

Tourmaline is an ubiquitous mineral in magmatic-hydrothermal systems, generally associated with granites and related hydrothermal ore deposits (e.g., Slack and Trumbull, 2011). Its stability in a large number of geological environments, from sedimentary to hydrothermal, metamorphic and magmatic settings, makes of tourmaline an excellent petrogenetic indicator to determine the conditions of its host environment and the processes involved during its crystallization (e.g., Henry and Guidotti, 1985; Dutrow and Henry, 2011; London, 2011; van Hinsberg et al., 2011; van Hinsberg and Schumacher, 2011). The analysis of the chemical and isotopic composition of tourmaline give information about the physicochemical conditions of its crystallization in term of pressure, temperature, composition of the coexisting fluid(s) and of the host-rock, as well as the source(s) of the fluid(s) (e.g., Van den Bleeken et al., 2007; Marschall et al., 2008; van Hinsberg et al., 2011; Marschall and Jiang, 2011). Tourmaline is commonly associated with Sn-W deposits in the European Variscan belt, where it forms an accessory mineral phase, locally abundant, in granites and related pegmatites, greisen, hydrothermal quartz veins and breccia pipe systems (e.g., Kelly and Rye, 1979; Charoy, 1982; Derré, 1983; Jackson et al., 1989; Alikouss, 1993; London and Manning, 1995; Gloaguen, 2006). Tourmalinization (boron metasomatism) may affect metamorphic host-rocks and granites during fluid-rock interactions with boron-rich hydrothermal fluids (e.g., Charoy, 1982; Pollard et al., 1987; London and Manning, 1995). Although the spatial association between tourmalinization and the occurrence of ore deposits is well documented, the genetic relationship is however still debated concerning both the source of the fluids and the origin of tourmaline. In particular, since cases of intense tourmalinization without associated mineralization are known (e.g., Allman-Ward et al., 1982; Jiang et al., 2003; Demirel et al., 2009; Boushaba and Marignac, 2009; Dill et al., 2012).

Tourmaline is the main B-bearing mineral in Sn-W granite-related deposits and may form either at the magmatic stage (e.g., Dingwell et al., 1996; London, 1997; Wolf and London, 1997) or during the hydrothermal stage (e.g., Blamart et al., 1992; London and Manning, 1995; Williamson et al., 2000). Interpretation of the origin of tourmaline is mainly based on its internal texture and chemical composition (e.g., Manning, 1982; London and Manning, 1995). The crystallization of tourmaline requires high concentration of B (> 3 wt.% B), which has generally been interpreted as derived from a magmatic source (e.g., Taylor et al., 1992; London and Manning, 1995; Smith and Yardley, 1996; Williamson et al., 2010; Drivenes et al., 2015). Indeed, experimental studies have shown that high concentrations of B

in peraluminous granitic magmas (up to 1 wt.% B_2O_3) result in lowered solidus temperatures down to 650°C at 1 kbar, reduced melt viscosity and increase in the H_2O solubility (Pichavant and Manning, 1984; Pichavant, 1987; Dingwell et al., 1992). The crystallization of B-rich magma forms a separate aqueous fluid phase (vapour or liquid) at the magmatic-hydrothermal transition with the preferential partitioning of boron and other incompatible elements into the hydrothermal fluid (London et al., 1988; Hervig et al., 2002; Thomas et al., 2003; Schatz et al., 2004). Exsolution of the B-rich fluid phase produces greater mechanical energy and thus more extensive hydraulic fracturing of the host-rock, which may lead to the formation of breccia pipe and stockworks, associated with tourmalinization and silicification of the wall-rocks (Pollard et al., 1987; Halls, 1994). However, even if magmatic fluids may represent a possible source of boron, the latter does not have necessary a pure magmatic origin and may also be inherited from metamorphic country rocks.

Both empirical and experimental data indicate that boron may be mobilized from B-rich metapelites during prograde metamorphism (e.g., Moran et al., 1992; Henry and Dutrow, 1996; Sperlich et al., 1996; Nakano and Nakamura, 2001; Kawakami and Ikeda, 2003) or during hydrothermal fluid-rocks interactions (e.g., Weisbrod, 1987; von Goerne, 1999, 2001; London, 2011). In particular, the pioneer experimental work from Weisbrod (1987) demonstrated that the B solubility in hydrothermal aqueous fluids equilibrated with common pelitic assemblage at 1 kbar increases significantly with the temperature from 0.1 wt.% B_2O_3 at ca. 350°C in solution up to 2.5 wt.% B_2O_3 at ca. 700°C. This major result indicates that hot metamorphic fluids percolating through B-rich shales can mobilize significant contents of B in solution and such fluids may precipitate eventually important amounts of tourmalines. Thus, boron metasomatism does not necessarily imply the involvement of B-rich magmatic fluids. Marine sediments are known to represent a major reservoir of B in the crust, containing more than 80 ppm in average and up to 150 ppm of B, which may be fixed on clay minerals and micas (e.g., Ishikawa and Nakamura, 1993; Leeman and Sisson, 1996; Sanchez Bellon et al., 1997). In comparison, the B content in granites is generally lower ranging from 1 to 30 ppm in average (Leeman and Sisson, 1996) and can reach exceptionally high B concentrations >1000 ppm in the case of tourmaline-bearing granites (Pichavant and Manning, 1984). Furthermore, one isotopic study (O-H) of a Sn-mineralized quartz vein associated with tourmalinites has demonstrated a metamorphic origin of the fluid responsible for the tourmalinization (Blamart et al., 1992).

The aim of this chapter is to study the tourmalinization associated with W±Sn deposits from the French Massif Central (FMC), located in the internal zone of the Variscan belt, in

order to characterize the source of the hydrothermal fluids and the origin of boron. In this purpose, three W±Sn hydrothermal deposits located in different areas from the FMC have been selected: (i) the Puy-les-Vignes deposit in the Limousin area (NW FMC); (ii) the Enguialès deposit in the La Châtaigneraie area (SW FMC); and (iii) the St-Mélany deposit in the Cévennes area (SE FMC). In these deposits, the tourmalinization represents the main hydrothermal alteration and occurs systematically through a multi-stage process, either during an early alteration stage, during the emplacement of the mineralized veins or during late fracturing episodes. This study provides a complete characterization of the different generations of tourmaline associated within each deposit by combining petrographic and textural observations, major, minor and trace elements compositions and boron isotopic analyses.

2. Geological setting

The FMC belongs to the internal part of the West European Variscan belt, formed during the continental collision between Gondwana and Laurussia through the Upper Paleozoic (Faure et al., 2009 and references therein). The geological structure of the FMC has been classically described as a stack of metamorphic nappes that from the north to the south define three major units (Ledru et al., 1989; Faure et al., 2009): (i) the Upper Gneiss Unit (UGU), which is composed of migmatitic ortho- and paragneisses and contains the so-called "leptynite – amphibolite complex", formed by the bimodal association of mafic/ultramafic rocks with acidic rocks; (ii) the Lower Gneiss Unit (LGU) which consists of ortho- and paragneisses similar to those of the UGU; and (iii) the Para-Autochtonous Unit (PAU), dominated by metasedimentary units (micaschists, meta-greywackes and quartzites) that generally experienced Variscan low-grade metamorphism. Several W-Sn and rare-metal deposits are known in the FMC, mainly associated with large Carboniferous granites, and forming either peribatholitic or intragranitic stockworks, greisen, scheelite skarn or more rarely breccia pipes (Marignac and Cuney, 1999; Cuney et al., 2002; Bouchot et al., 2005). Tourmalinization represents generally a major hydrothermal alteration in the W-Sn peribatholitic deposits and is associated with the deposition of important amounts of tourmaline in the host-environment of the mineralized veins, commonly composed by metasedimentary rocks (micaschists and paragneisses). This study focuses on tourmaline-bearing samples coming from three W-Sn hydrothermal deposits in the FMC: Puy-les-Vignes, Enguialès and St-Mélany. These deposits are located in different tectono-metamorphic units,

but show several similarities in term of tourmalinization styles. They represent therefore interesting case studies allowing both to study the tourmalinization process in W-Sn granite-related deposits and to characterize the source of the boron fluids at a regional scale.

2.1. Puy-les-Vignes deposit

The Puy-les-Vignes deposit (Fig. 113) is located in the Limousin area in the northwestern part of the FMC and represents an atypical case of tourmaline-rich hydrothermal breccia pipe associated with a W mineralization in the Variscan belt. The deposit is hosted in the migmatitic biotite-sillimanite paragneisses of the LGU in close proximity with two peraluminous granites: (i) the Auriat granite, in the northeast, dated at 324 ± 1 Ma (U-Pb on zircon; Gebauer et al., 1981); and (ii) the Aureil granite, in the southwest, dated at 346 ± 14 Ma (Rb-Sr on whole rock; Duthou, 1978). Several mineralized W showings are known in the surroundings of Puy-les-Vignes, such as quartz-wolframite vein deposits (Le Moulard, Les Clauds, Etivaud, Chassagnat, Beynat), as well as a second similar breccia pipe at Les Caillaudoux, possibly also mineralized (Weppe, 1958). The pipe has an oval shape with dimensions 80 x 340 m at surface and is cut in two parts by a N30°E sinistral strike-slip fault ("faille limite") with a 120 m horizontal displacement (Weppe, 1951, 1958). The breccia is composed by angular to sub-angular polygenic and heterometric clasts of the country rocks (mainly gneisses and granites) cemented by a quartz matrix, which are systematically rimmed by an aureole of tourmalinite, of which the thickness varies from a few millimeters to ten centimeters, up to the complete tourmalinization of the fragments (Weppe, 1951, 1958). Quartz-wolframite-sulphides veins cut later the breccia pipe and are the host for the main W mineralization, even though the breccia itself contains a disseminated mineralization (see Chapter 4 for details). ^{40}Ar-^{39}Ar dating on muscovite closely associated with wolframite yielded to a plateau age of 323 ± 0.9 Ma (Cuney et al., 2002), suggesting a Namurian emplacement age of the tungsten mineralization.

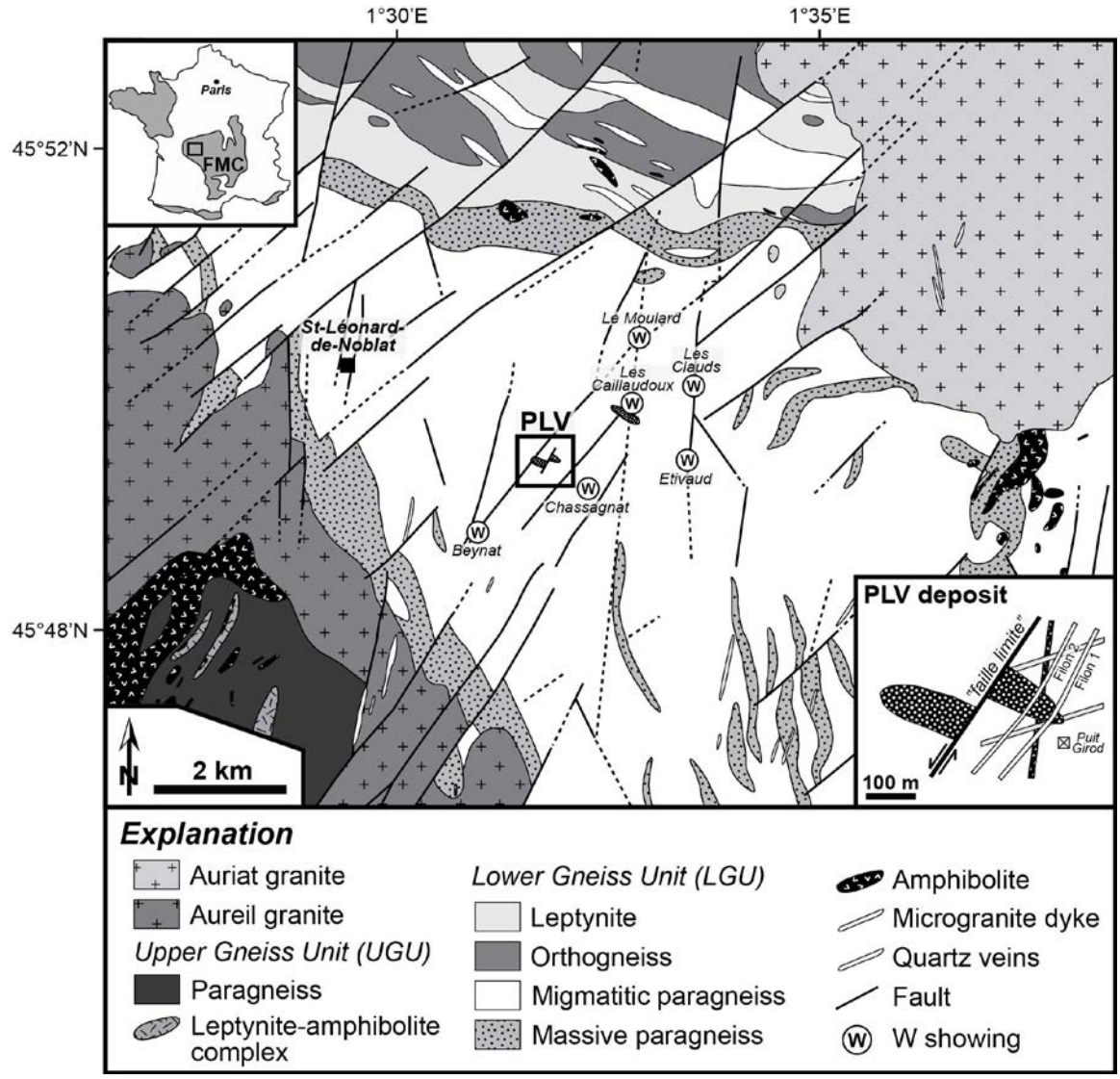

Fig. 113: Geological setting and location of the Puy-les-Vignes (PLV) deposit in the Limousin area, French Massif Central (FMC) (modified after Chenevoy et al., 1984).

2.2. Enguialès deposit

The Enguialès deposit (Fig. 114) is located in the La Châtaigneraie area in the southwest part of the FMC and consists in a dense network of quartz-ferberite veins, typically 10 to 50 cm thick, hosted in the micaschists of the LGU, which are overthrusted to the west by the micaschists of the PAU. This district hosts several tungsten occurrences, including quartz-wolframite vein deposits (Leucamp, Enguialès, Le Viala, Murols, Teissières-les-Bouliès, La Granière), intragranitic scheelite-bearing episyenite veins (Lafeuillade-en-Vézie) and disseminated scheelite deposits in calc-silicate rocks (Cazottes, Manhaval, Gimat) (Bogdanoff et al., 1987).

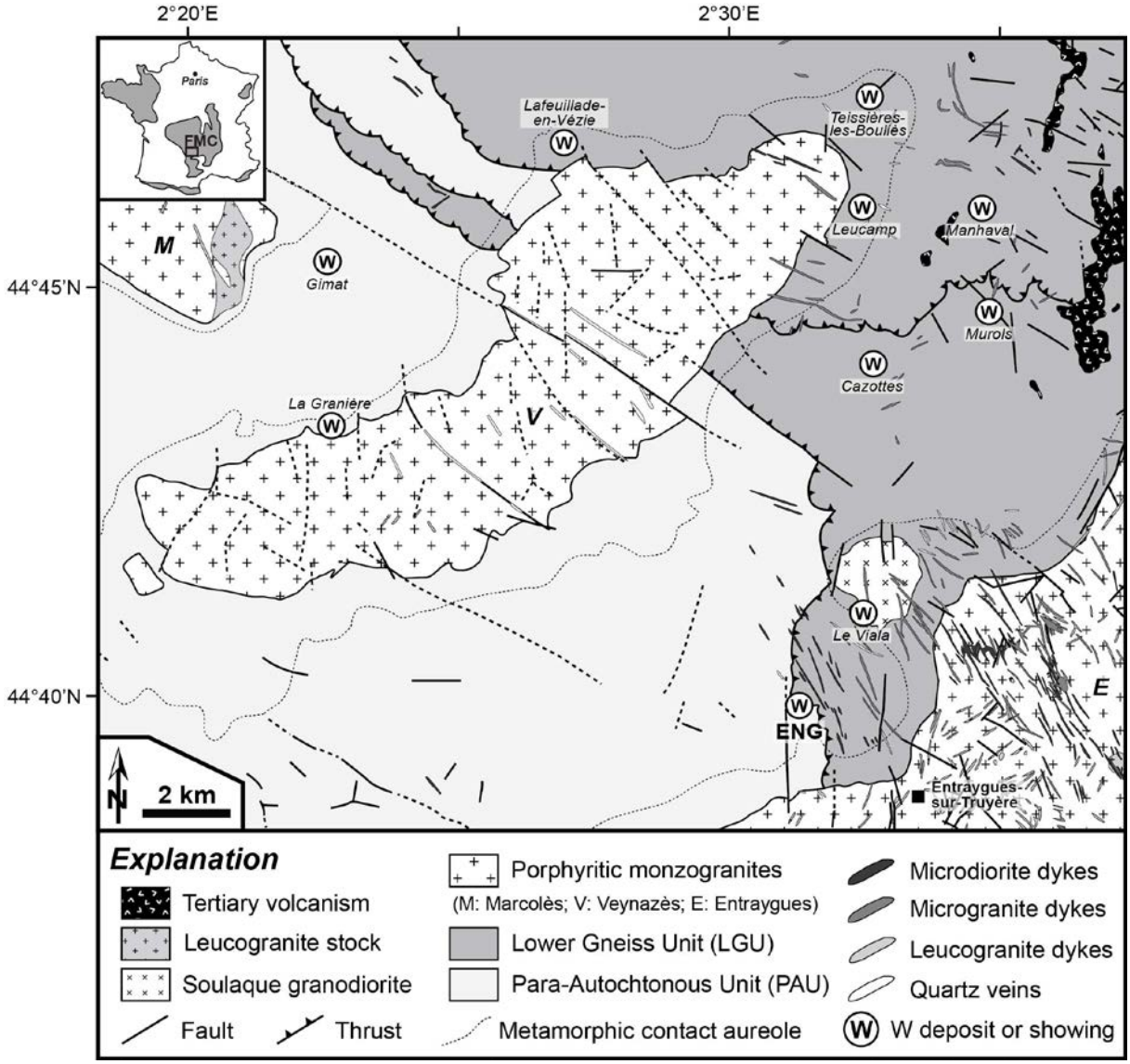

Fig. 114: Geological setting and location of the Enguialès (ENG) deposit in the La Châtaigneraie area, French Massif Central (FMC) (modified after Bogdanoff et al., 1989 and Goër de Herve et al., 2006).

The deposit cuts the regional schistosity in the contact metamorphic aureoles of two large Namurian biotite-cordierite porphyroid granites: (i) the Entraygues granite to the south corresponding to the western part of the Margeride granite has been dated at ca. 315-310 Ma (^{40}Ar-^{39}Ar on biotite; Monié et al., 2000); (ii) the Veinazès granite to the northwest dated between 323 ± 15 Ma (U-Pb on zircon; Monié et al., 2000), 314 ± 3 Ma and 313 ± 3 Ma (^{40}Ar-^{39}Ar on biotite; Monié et al., 2000). Geochronological data on the Margeride granitic complex yielded ages of 334 ± 7 Ma (U-Pb on zircon; Respaut, 1984), 323 ± 12 Ma (Rb-Sr on whole rock; Couturié et al., 1979), 314 ± 3 Ma (U-Pb on monazite; Pin, 1979), 309 ± 5 Ma (U-Pb on zircon; Duguet et al., 2006), 310 ± 3 Ma and 306 ± 3 Ma (^{40}Ar-^{39}Ar on biotite; Monié et al., 2000). These contrasting ages suggest that the Margeride granite may have

suffered several stages of sub-solidus high-temperature alterations during late fluid-rock interactions, as exemplified in the Armorian Massif (Tartèse et al., 2011). The Enguialès deposit is centred on a B-W-Bi geochemical anomaly of regional extension (Bogdanoff et al., 1987; Caia, 1989). Tourmalinization represents the main hydrothermal alteration and affects the micaschists at the selvages of the quartz-ferberite veins, forming massive tourmalinites up to several decimetres thickness at the contact with the quartz veins and passing progressively to tourmalinized micaschists (Derré, 1983; Caia, 1989). Muscovite from the selvage of a quartz-wolframite vein at Enguialès yielded ^{40}Ar-^{39}Ar ages of 305 ± 3 Ma and 306 ± 3 Ma, whereas a plateau age of 312 ± 3 Ma was obtained for a muscovite within the vein (Monié et al., 2000). The younger ages are coeval with the intrusions of small leucogranitic stocks in the Marcolès and Entraygues granites and dated at 306 ± 3 Ma (^{40}Ar-^{39}Ar on muscovite; Monié et al., 2000). Based on O-D isotopic data on the assumed equilibrium quartz-tourmaline, pressure-temperature conditions for the quartz-tourmalines veins at Enguialès have been estimated at 1.4 ± 0.4 kbar and 487 ± 34°C (Lerouge et al., 2000; Lerouge and Bouchot, 2009).

2.3. St-Mélany deposit

The St-Mélany Sn-W deposit (Fig. 115) is located in the Cévennes area in the southeast part of the FMC, at 10 km south from the Velay migmatitic dome. Other W showings are known in the surroundings of St-Mélany, such as quartz-wolframite veins (Serrecourte), scheelite skarn (Loubaresse) and disseminated scheelite in calc-silicate rocks. The deposit consists in a network of N110-140°E striking quartz-cassiterite±wolframite veins hosted in the mesozonal cordierite-biotite micaschists of the PAU, close to two granites: (i) the Rocles granite in the northeast was emplaced during the regional LP-MT compressive event dated at ca. 315 Ma during the Namurian (Barbey et al., 2015 and references therein). Chemical U-Th-Pb ages on monazite from the Rocles granite yield ages between 325 ± 4 Ma, 324 ± 4 Ma and 318 ± 3 Ma (Be Mezeme et al., 2006, 2007); (ii) the Borne granite in the southwest represents the eastern part of the Pont-de-Monvert granite and yields ages between 315 ± 5 Ma (Rb-Sr on whole rock; Mialhe, 1980), 307 ± 11 Ma (U-Pb on zircon; François, 2009) and 303 ± 3 Ma (U-Pb on monazite; Brichau et al., 2008). Recent dating of the Largentière granite, an eastern equivalent of the Borne granite in the same area, yields a Westphalian age of 304 ± 6 Ma (U-Pb on zircon; Couzinié et al., 2014). The mineralization in the St-Mélany deposit consists in a mineral paragenesis of cassiterite, wolframite, albite and apatite with minor beryl (Noyé,

1985). The Sn±W veins are cut by younger N20-N60°E striking dykes of aplo-pegmatites that yield a ^{40}Ar-^{39}Ar muscovite age of 306.5 ± 3.1 Ma (Chauvet et al., 2012). The micaschists are affected by a major hydrothermal alteration marked by a pervasive tourmalinization and muscovitization, which is of regional extension and appear without relationships with the Sn-W mineralization (Noyé and Weisbrod, 1988). Most of the muscovitization affecting the micaschists corresponds to hydrothermal retromorphosis, which is late compared to the main pervasive tourmalinization (Noyé, 1985; Noyé and Weisbrod, 1988).

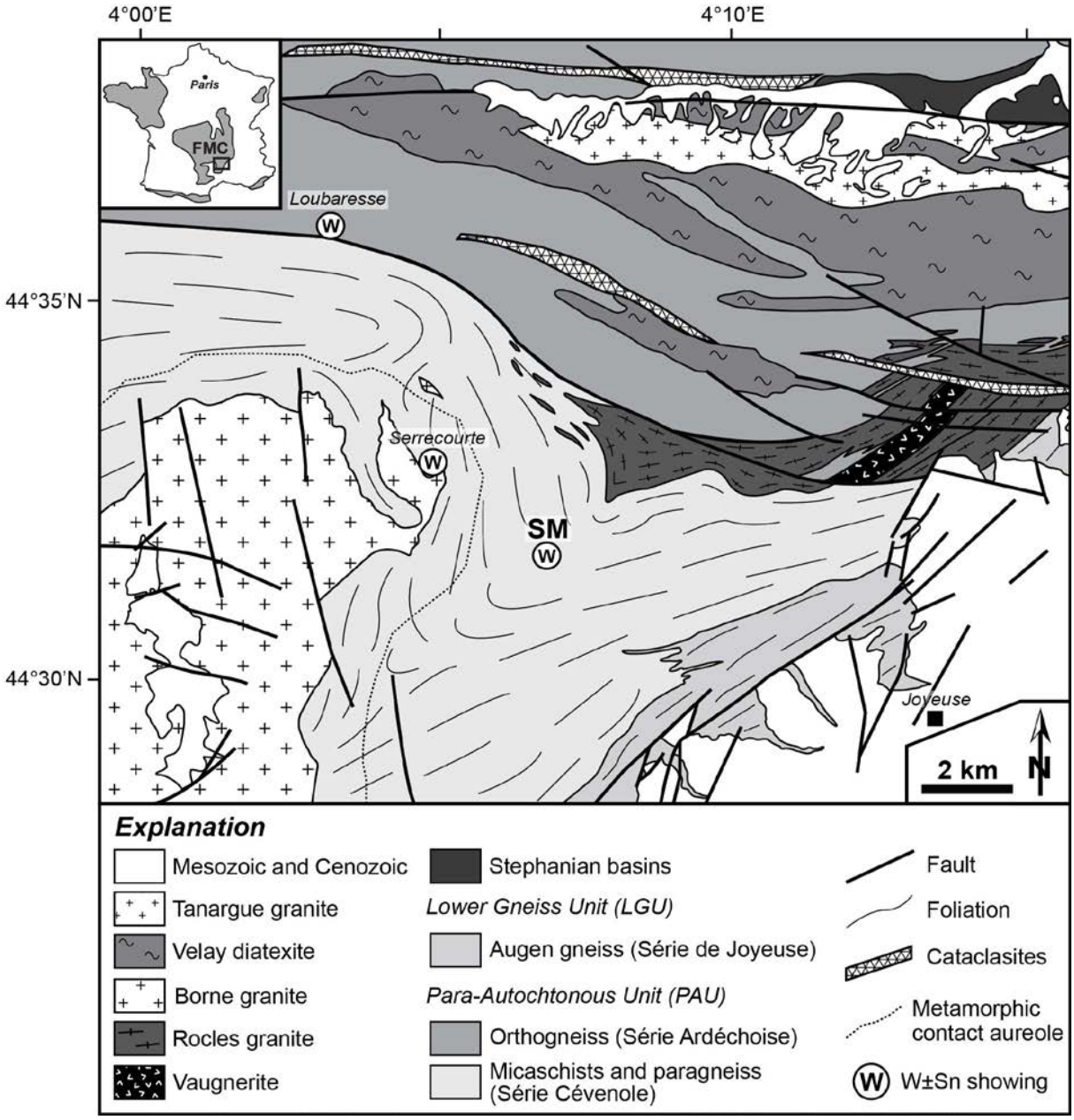

Fig. 115: Geological setting and location of the St-Mélany (SM) deposit in the Cévennes area, French Massif Central (FMC) (modified after Weisbrod et al., 1974).

3. Analytical methods

3.1. Scanning electron microscope

Mineralogical observations of tourmalines were performed at the GeoRessources laboratory (Vandœuvre-lès-Nancy, France) using a Jeol J7600F scanning electron microscope (SEM) equipped with a SDD-type EDS spectrometer coupled to an Oxford Wave WDS spectrometer. Backscattered electron (BSE) images were obtained on polished thin sections with an acceleration voltage of 15 kV, adjusting the electronic contrast to reveal internal zoning in tourmaline. SEM was used in order to study the internal textures of tourmaline and to select crystal sections for further chemical and isotopic analyses. Punctual EDS microanalyses were performed along profiles in selected crystals of tourmalines to determine precisely the major element variations along micrometre-scale oscillatory zoning. The major elements measured were calibrated using the same standards as for the electron microprobe analyses (see Table 30), with an analytical error < 1%.

3.2. Electron microprobe

Major and minor element composition of tourmalines was determined using an electron microprobe Cameca SX100 at the GeoRessources laboratory (Vandœuvre-lès-Nancy, France), operated with an acceleration voltage of 15 kV and a beam current of 12 nA. Calibration was realised using both natural and synthetic standards. The following elements were analysed using WDS spectrometers: Si, Al, Mg, Na, Fe, Mn, K, Ti, Ca and Cr. Counting times were 10 s on element peak and 5 s on background. Analytical error was < 1% for the element measured. Details of the WDS configuration are given in Table 30. Major and minor elements are expressed in weight per cent oxides (wt.%). Only analyses showing an analytical total between 85 and 90 wt.% were conserved. Structural formulae of tourmalines were calculated using the Excel spreadsheet from The Open University (UK) normalizing to 31 anions and assuming stoichiometric 3 apfu for B and 4 apfu for OH+F, based on the general formula $XY_3Z_6(T_6O_{18})(BO_3)_3V_3W$, where X=$Na^+$, Ca^{2+}, K^+ and vacancy (X□); Y=Fe^{2+}, Mg^{2+}, Mn^{2+}, Al^{3+}, Li^+, Fe^{3+} and Cr^{3+}; Z= Al^{3+}, Fe^{3+}, Mg^{2+}, Ti^{4+} and Cr^{3+}; T=Si^{4+}, Al^{3+} and B^{3+}; B=B^{3+}; V=OH^- and O^{2-}; and W=OH^-, F^- and O^{2-} (Hawthorne and Henry, 1999; Henry et al., 2011). The results presented here correspond to approximately 1,000 in situ electron probe microanalyses (EPMA).

3.3. Laser ablation ICPMS

Trace element compositions in tourmalines were measured by laser ablation inductively coupled plasma mass spectrometry (LA-ICPMS) at the GeoRessources laboratory (Université de Lorraine, Vandœuvre-lès-Nancy, France) using a Agilent 7500c quadrupole ICPMS coupled with a 193 nm GeoLas ArF Excimer laser (MicroLas, Göttingen, Germany). Laser ablation was performed with a constant 5 Hz pulse frequency and a constant fluence of 6 J/cm2 by focussing the beam at the sample surface using variable laser spot diameters between 24 and 90 μm. Helium was used as carrier gas to transport the laser-generated particles from the ablation cell to the ICPMS and argon was added as an auxiliary gas via a flow adapter before the ICP torch. Typical flow rates of 0.5 L/min for He and 0.9 L/min for Ar were used. The certified reference material NIST SRM 610 (concentrations from Jochum et al., 2011) was used as external standard for calibration of all analyses and was analysed twice at the beginning and at the end for each set of samples, following a bracketing standardization procedure. The reference material NIST SRM 612 was also used as control standard for the standardization. LA-ICPMS calibration was optimized for highest sensitivity on an intermediate m/Q range, while maintaining Th/U ~ 1 and ThO/Th < 0.5%, as determined on NIST SRM 610. The following 40 isotopes were measured with a dwell time of 10 ms for each: ^{7}Li, ^{9}Be, ^{29}Si, ^{45}Sc, ^{47}Ti, ^{51}V, ^{53}Cr, ^{59}Co, ^{60}Ni, ^{63}Cu, ^{66}Zn, ^{85}Rb, ^{88}Sr, ^{89}Y, ^{90}Zr, ^{93}Nb, ^{95}Mo, ^{118}Sn, ^{133}Cs, ^{137}Ba, ^{139}La, ^{140}Ce, ^{141}Pr, ^{146}Nd, ^{147}Sm, ^{153}Eu, ^{157}Gd, ^{159}Tb, ^{163}Dy, ^{165}Ho, ^{166}Er, ^{169}Tm, ^{172}Yb, ^{175}Lu, ^{181}Ta, ^{182}W, ^{208}Pb, ^{209}Bi, ^{232}Th and ^{238}U. Data reduction and absolute quantification of signals were performed using the software StalQuant, developed at ETH Zürich, Switzerland (see details in Fricker, 2012). For all analyses of tourmaline, the content of 29Si determined from EMPA analyses was used as internal standard. Limits of detection (LOD) were calculated using the 2σ criterion detailed in Longerich et al. (1996).

3.4. Secondary ion mass spectrometry

Boron isotopes in tourmaline were measured by secondary ion mass spectrometry (SIMS) using the Cameca IMS 1280-HR instrument at the CRPG-CNRS (Vandœuvre-lès-Nancy, France), following the analytical procedure described by Chaussidon and Albarède (1992). Analyses were performed on thin sections with a 20 nA beam of primary ions O^- accelerated at 13 kV. The secondary ions $^{10}B^+$ and $^{11}B^+$ were accelerated at 10 kV and were

measured in monocollection with a mass resolution M/ΔM=2000. Each calculated isotopic ratio $^{11}B/^{10}B$ corresponds to 30 cycles of measurement with counting times of 8 s per cycle at mass 10 and of 4 s at mass 11. The ablation spot size was fixed to 20 µm. Calibration was done on the NIST NBS951 reference material (Catanzaro et al., 1970). The $\delta^{11}B$ values expressed in ‰ were calculated by normalizing to the isotopic reference values of natural crystals of schorl and dravite (Dyar et al., 2001; Leeman and Tonarini, 2001).

4. Tourmalinization in the Puy-les-Vignes deposit

Tourmalinization in the Puy-les-Vignes deposit represents a major hydrothermal alteration. It affects mainly the clasts within the breccia, forming a black aureole of tourmalinite (Fig. 116a). Tourmaline forms during different stages of the paragenetic sequence of the deposit, leading to the formation of four generations of tourmaline. This relative chronology is based on the spatial localization, the petrography and the geochemistry of the tourmalines.

4.1. Petrography and internal textures of tourmalines

4.1.1. Greisen tourmalines (Tur 1)

They form sub-euhedral crystals, of green-brownish colour in plane-polarized light, ranging from 50 to 100 µm in size, which are disseminated in clusters within the internal part of the greisen (Fig. 116b) and are never found in the tourmalinized rims. The crystals are partially corroded by the quartz and muscovite of the greisen. Observed in BSE, they display an internal structure composed of four successive zones (Fig. 117a): (i) a light grey core forming the main part of the crystal, showing either homogenous texture or micrometre-scale oscillatory zoning; (ii) a light grey rim corresponding to the replacement of the initial core; (iii) an irregular bright overgrowth, of a few to 10 µm thickness, surrounding the core with textural evidences of corrosion; and (iv) a dark overgrowth of tens of µm wide, displaying locally synneusis texture. This first generation of tourmaline is interpreted to form during the early greisenization stage in the Puy-les-Vignes deposit.

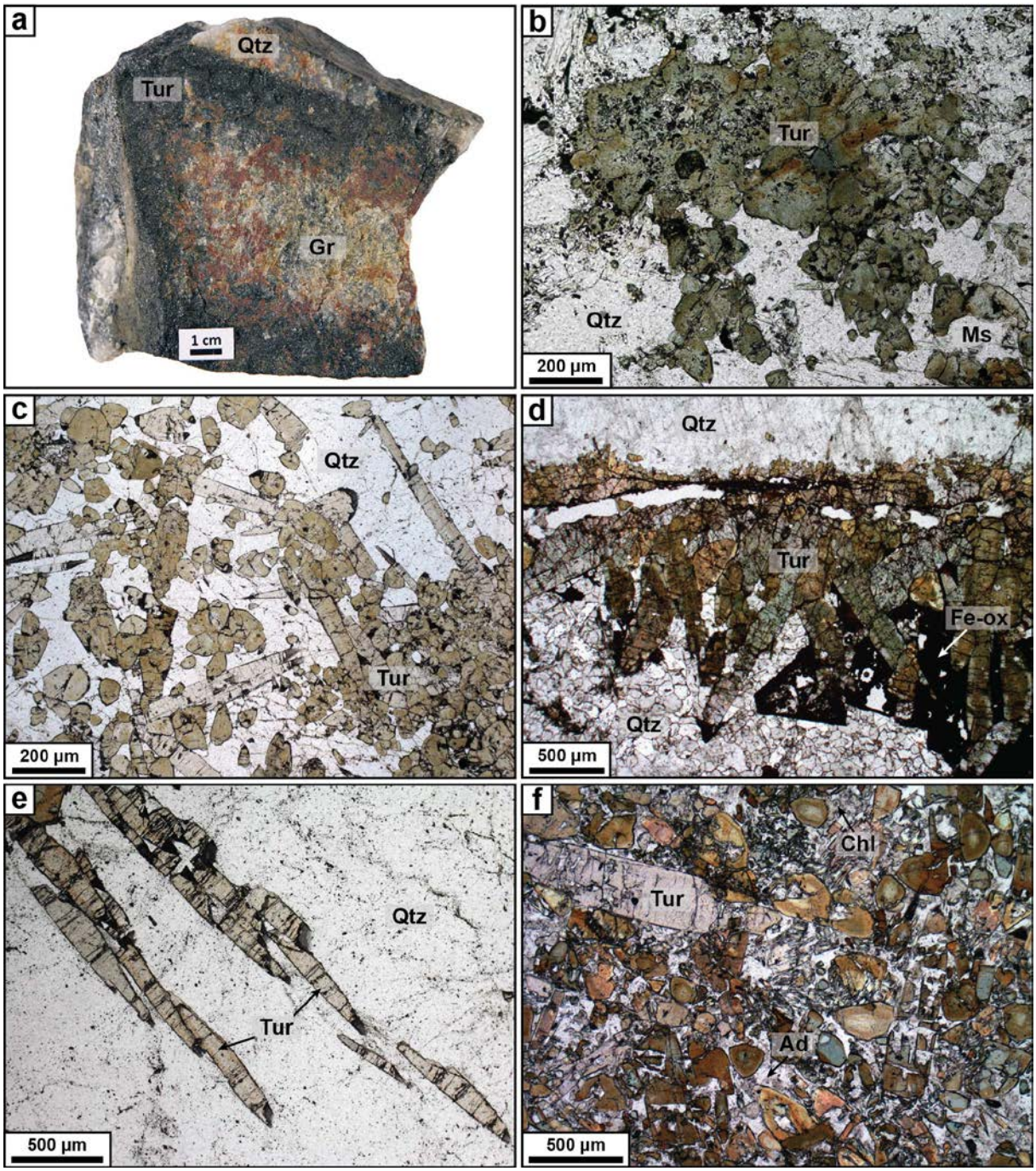

Fig. 116: Photographs of tourmalines from the Puy-les-Vignes deposit. (a) Representative sample of greisenized gneiss (Gr) rimmed by a centimetre-thick aureole of tourmalinite (Tur) cemented by quartz (Qtz) matrix (sample PLV-7571). (b) Tourmalines in cluster disseminated in the quartz-muscovite (Ms) assemblage in the greisen (sample PLV-02-08a). (c) Tourmalinite rim developed on a gneissic clast composed by the aggregation of tourmalines cemented by microcrystalline quartz (sample PLV-02-01a). (d) Tourmalinite rim on a granitic sample with minor late Fe-oxides (Fe-ox) showing sharp contact with the quartz of the breccia (sample PLV-02-04a). (e) Acicular tourmalines disseminated in the macrocrystalline quartz, forming the gangue of the breccia (sample PLV-02-05). (f) Late hydrothermal breccia composed of tourmaline clasts cemented by a matrix of adularia (Ad) and chlorite (Chl) (sample PLV-02-13b).

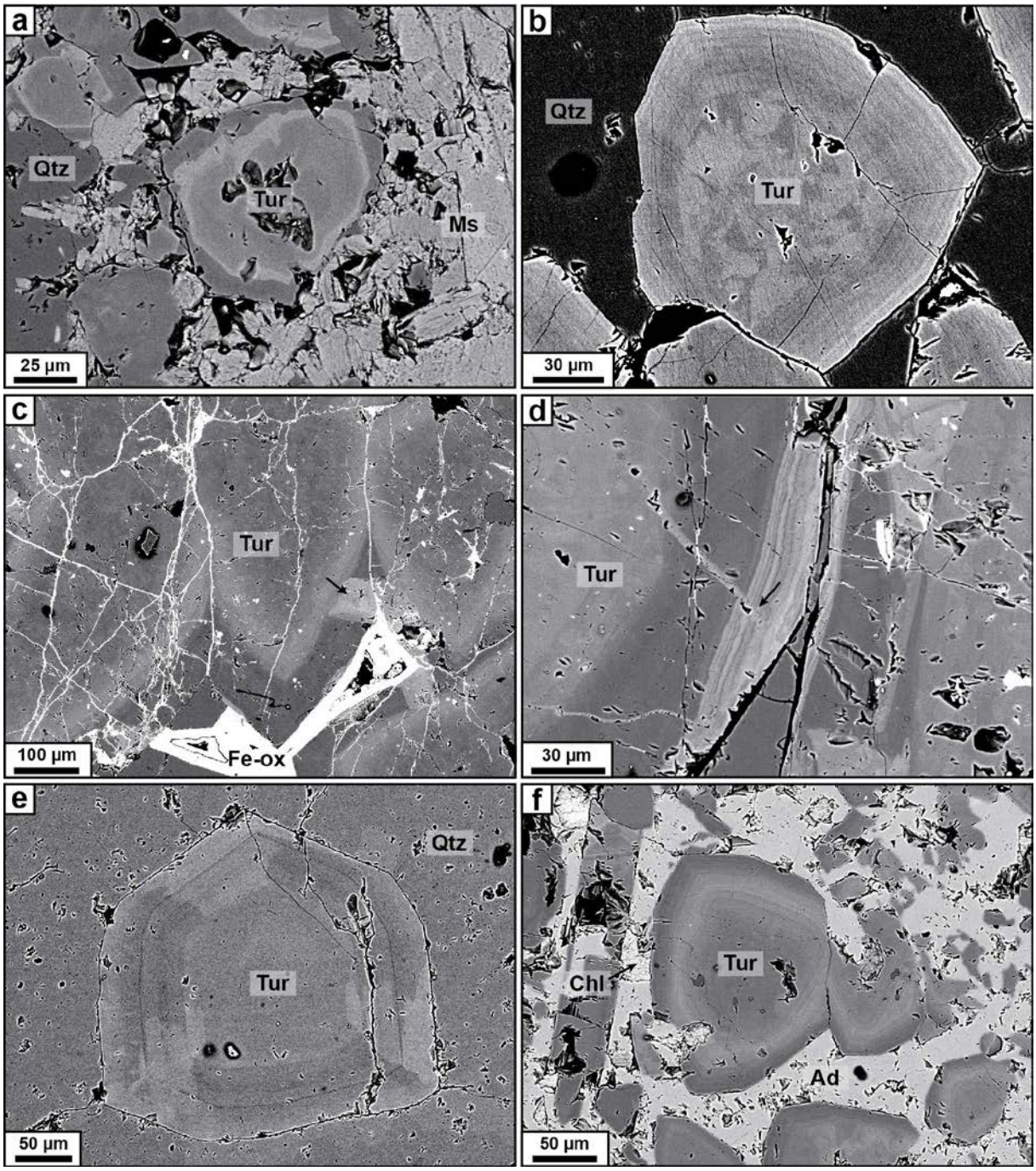

Fig. 117: BSE images of tourmalines from the Puy-les-Vignes deposit. (a) Tourmaline (Tur) from the greisen associated with neoformed quartz (Qtz) and muscovite (Ms) (sample PLV-02-08a). (b) Tourmaline with quartz in the tourmalinite rim developed on a greisenized gneissic sample, composed by a core surrounded by an overgrowth with intense oscillatory zoning (sample PLV-02-01a). (c) Tourmaline from the tourmalinite rim on a greisenized granitic sample, showing corrosion (arrow) and cut lately by Fe-oxides (Fe-ox) in infilling (sample PLV-02-04a). (d) Detail view of the late corrosion (arrow) cutting the crystalline borders of tourmaline on the granitic sample (sample PLV-02-04a). (e) Section of acicular tourmaline perpendicular to the c-axis showing sector zoning within macrocrystalline quartz (sample PLV-02-15). (f) Breccia tourmaline cemented in an adularia (Ad) and chlorite (Chl) matrix (sample PLV-02-13b).

4.1.2. Tourmalinites (Tur 2)

This second generation represents the most important stage of tourmalinization at Puy-les-Vignes. The tourmaline develops on the rims of the brecciated clasts (gneiss, granite) of the pipe, forming an aureole of tourmalinization, the thickness of which varies from a few millimetres to 10 centimetres, up to complete tourmalinization of the fragments (Fig. 116a). The contact with the quartz of the breccia is sharp, indicating that the tourmalinite forms before the quartz precipitation and the breccia-forming event (see Chapter 4 for details). The tourmalinite is formed by the aggregation of prismatic crystals of tourmaline, which are cemented by limpid macrocrystalline quartz. Regarding the lithology of the clast, the tourmaline display different features. Tourmaline developed on gneissic clasts have orange-brownish colour in plane-polarized light and range from 50 to 500 µm in size (Fig. 116c). Observed in BSE, the tourmaline crystals display an internal structure composed of three successive zones (Fig. 117b): (i) a small dark grey core showing a patchy texture; (ii) a discontinuous and irregular bright rim, of a few micrometres thickness, corresponding to the partial replacement of the core; and (iii) large overgrowth, forming the most important part of the crystal and showing a micrometre-scale oscillatory zoning. Tourmalines that formed on granitic clasts are larger in size, ranging from 100 µm up to a few millimetres, and have a green-brownish colour in plane-polarized light (Fig. 116d). In BSE imagery, the crystals show a different internal structure compared to the tourmalines on gneissic clast, composed of the following zones (Fig. 117c): (i) a dark grey core, which is commonly partially replaced by (ii) a dark rim; (iii) a bright overgrowth surrounds the core and shows a discrete oscillatory zoning at the micrometre-scale; (iv) a dark overgrowth with homogeneous texture; (v) a late corrosion, crosscutting and partially replacing the overgrowths (Fig. 117d).

4.1.3. Acicular tourmalines (Tur 3)

They are present within the quartz of the breccia and of the mineralized veins. They form large elongated euhedral crystals, with a green-blue colour or transparent in plane-polarized light and ranging from 500 µm to a few millimetres in size, and up to centimetre-size for the largest crystals (Fig. 116e). The tourmalines crystallized directly on the wall-rocks selvages. They are now found either as isolated or fan-like crystals disseminated within the quartz. The crystals are sometimes segmented within the quartz, suggesting that the tourmaline crystallization was followed by deformation of the quartz by a crack-seal

mechanism. In BSE imagery, the tourmalines show a dark homogeneous core forming the main part of the crystals, surrounding by a light rim of a few µm thickness. In sections perpendicular to the c-axis, tourmaline displays a visible sector zoning (Fig. 117e).

4.1.4. Breccia tourmalines (Tur 4)

This last generation of tourmalines is restricted to the late hydrothermal breccia stage at Puy-les-Vignes. The tourmalines form prismatic sub-euhedral crystals with an orange-brownish colour in plane-polarized light and ranging from 50 to 500 µm in size (Fig. 116f). The crystals are brecciated and cemented by a matrix of adularia and chlorite, with minor muscovite. In BSE imagery, their internal structure is composed of four successive zones (Fig. 117f): (i) a dark core showing a patchy texture, which is partially replaced by (ii) an irregular light grey rim; (iii) a bright overgrowth, passing progressively to (iv) a dark overgrowth displaying an oscillatory zoning at the micrometre-scale. The latter may represent an equivalent of the dark overgrowths of greisen tourmalines (Tur 1), based on chemical data (see 4.2.).

4.2. Chemical composition and crystal chemistry of tourmaline

4.2.1. Major elements

Representative chemical compositions of tourmaline from Puy-les-Vignes are given in Table 31. Tourmalines are members for a large majority of the alkali group, and for a minority of the X-vacant group (Fig. 118), according to the nomenclature of Henry et al. (2011). They represent mostly series of the dravite - schorl solid solution, with minor analyses falling in the foitite - Mg-foitite solid solution (Fig. 119). The compositional variability is mainly attributed to variable Fe/(Fe+Mg) and X□/(X□+Na) with an alkali-deficiency, as shown in Fig. 119, involving the main $Fe^{2+}_{-1}Mg^{2+}_{+1}$ and $(Fe^{2+}Na^{+})_{-1}(Al^{3+}\square)_{+1}$ coupled substitutions. In the Al-Fe-Mg diagram (Fig. 118), most of the tourmaline compositions fall in the metasediments field, with a few analyses falling in the field of the granites and pegmatites. Tourmalines from the greisen are mainly dravite, composing the core and dark overgrowth of the crystal, with low Fe/(Fe+Mg) values (0.28–0.54), except for the bright overgrowth, which has schorl composition with higher Fe/(Fe+Mg) values (0.56–0.64) (Fig. 119a). The core and the bright overgrowth have the highest Ti values (up to 0.18 apfu).

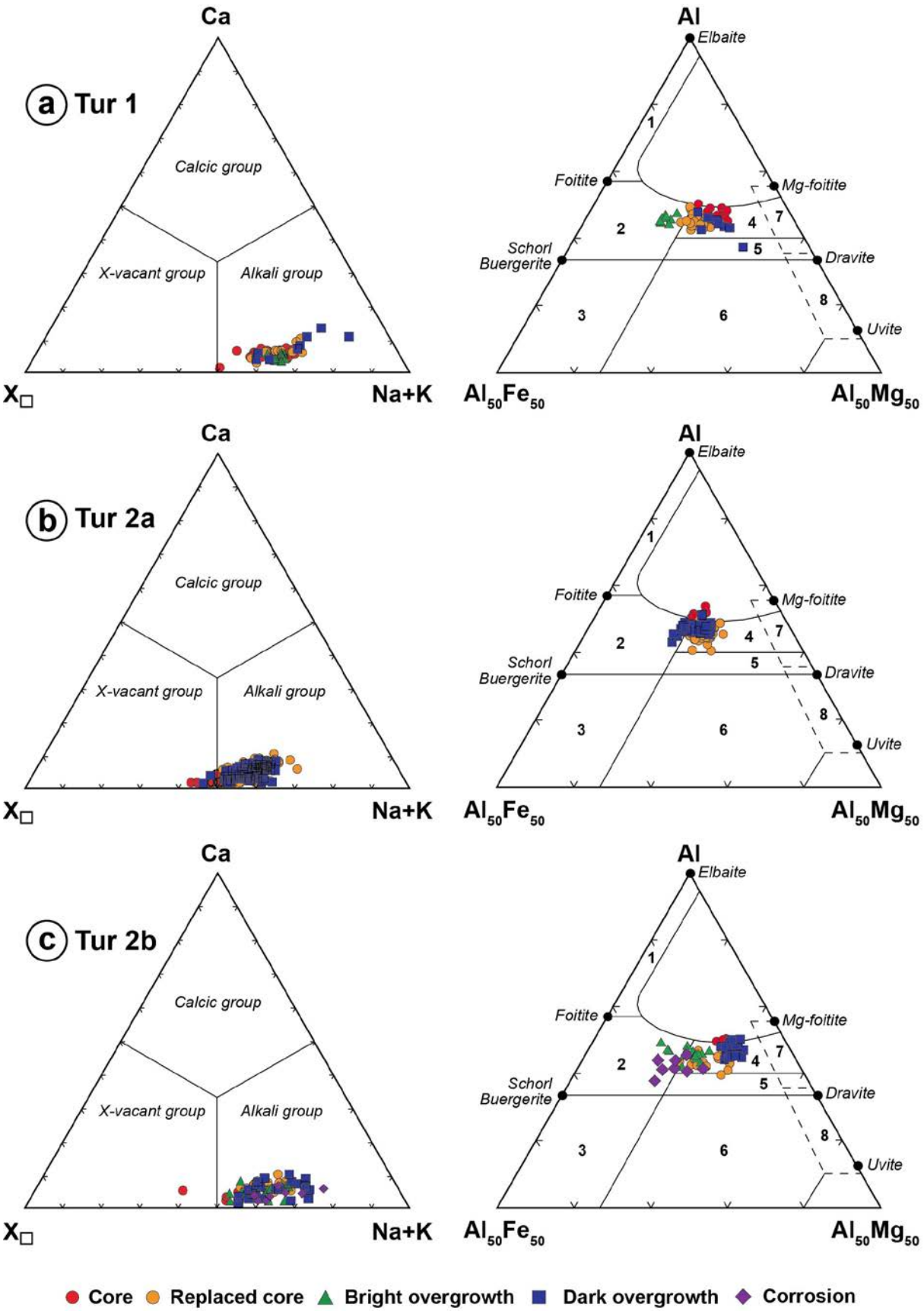
a Tur 1
b Tur 2a
c Tur 2b
Ca
Na+K
X□
Calcic group
X-vacant group
Alkali group
Al
Elbaite
Foitite
Mg-foitite
Schorl
Buergerite
Dravite
Uvite
Al50Fe50
Al50Mg50
1
2
3
4
5
6
7
8
Core
Replaced core
Bright overgrowth
Dark overgrowth
Corrosion

Fig. 118

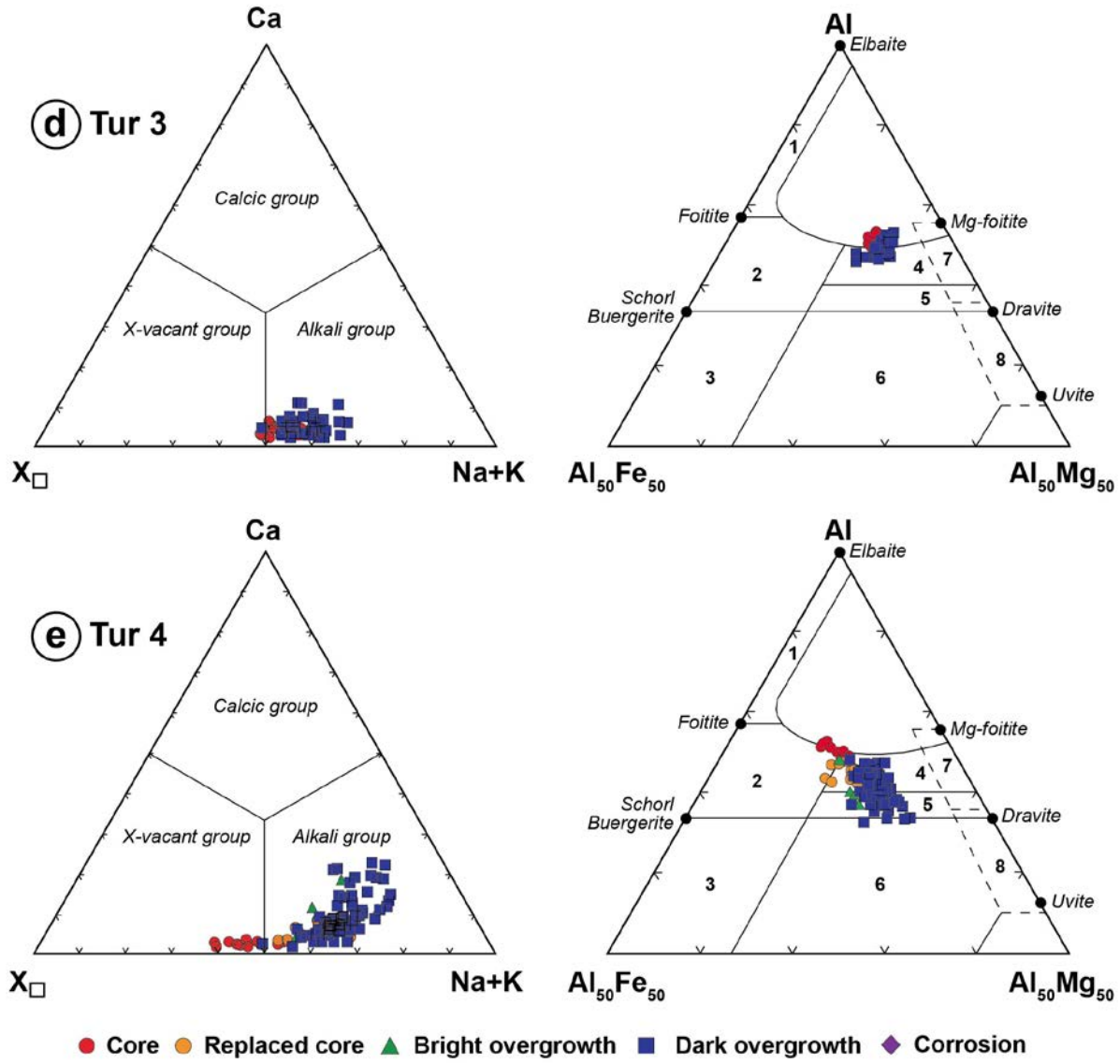

Fig. 118 (Continued): Ternary Ca-X□-Na+K diagram (after Hawthorne and Henry, 1999) and Al-Fe-Mg diagram (after Henry and Guidotti, 1985) for tourmalines from the Puy-les-Vignes deposit. (a) Tourmaline from greisen (Tur 1; samples PLV-02-08a and PV-5b). (b) Tourmaline in tourmalinites from gneissic clast (Tur 2a; sample PLV-02-01a). (c) Tourmaline in tourmalinites from granitic clast (Tur 2b; sample PLV-02-04a). (d) Acicular tourmaline in quartz (Tur 3; samples PLV-02-01c and PLV-02-15). (e) Tourmaline in late breccia (Tur 4; samples PLV-02-13a/b). The different fields in the Al-Fe-Mg diagram are from Henry and Guidotti (1985) and correspond to: (1) Li-rich granitoids, pegmatites and aplites; (2) Li-poor granitoids, pegmatites and aplites; (3) Fe^{3+}-rich quartz-tourmaline rocks (hydrothermally altered granites); (4) Al-rich metapelites and metapsammites; (5) Al-poor metapelites and metapsammites; (6) Fe^{3+}-rich quartz-tourmaline rocks, calc-silicate rocks and metapelites; (7) Low-Ca meta-ultramafics and Cr-V-rich metasediments; (8) Meta-carbonates and meta-pyroxenites.

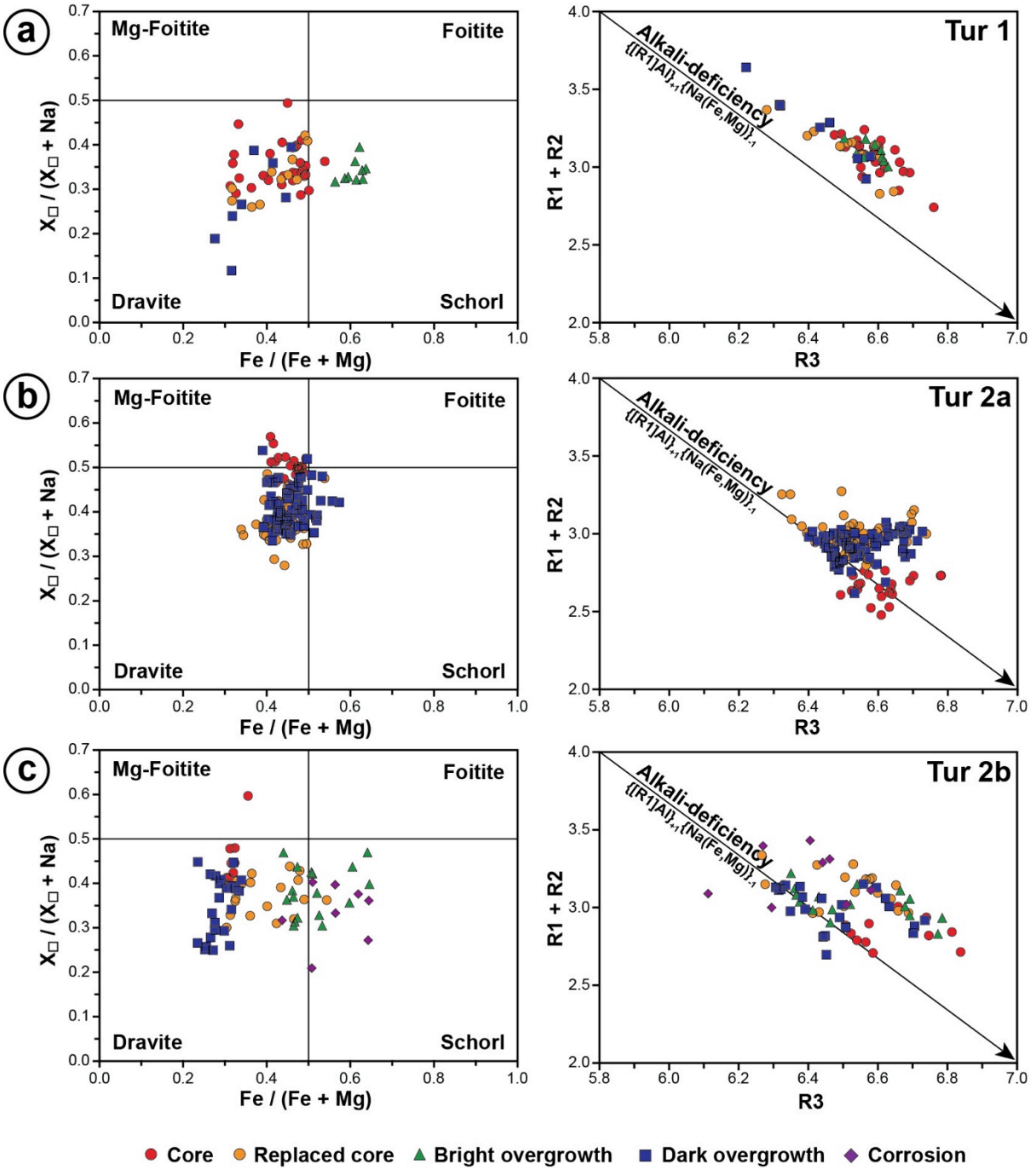

Fig. 119: Compositional diagrams for tourmalines from the Puy-les-Vignes deposit. Each generation of tourmaline is plotted in the X□/(X□+Na) vs Fe/(Fe+Mg) classification diagram (after Henry et al., 2011) and in the R1+R2 vs R3 diagram, where R1=Na+Ca, R2=Fe+Mg+Mn, and R3=Al+1.33Ti (after Manning, 1982). (a) Tourmaline from greisen (Tur 1; samples PLV-02-08a and PV-5b). (b) Tourmaline in tourmalinites from gneissic clast (Tur 2a; sample PLV-02-01a). (c) Tourmaline in tourmalinites from granitic clast (Tur 2b; sample PLV-02-04a). (d) Acicular tourmaline in quartz (Tur 3; samples PLV-02-01c and PLV-02-15). (e) Tourmaline in late breccia (Tur 4; samples PLV-02-13a/b).

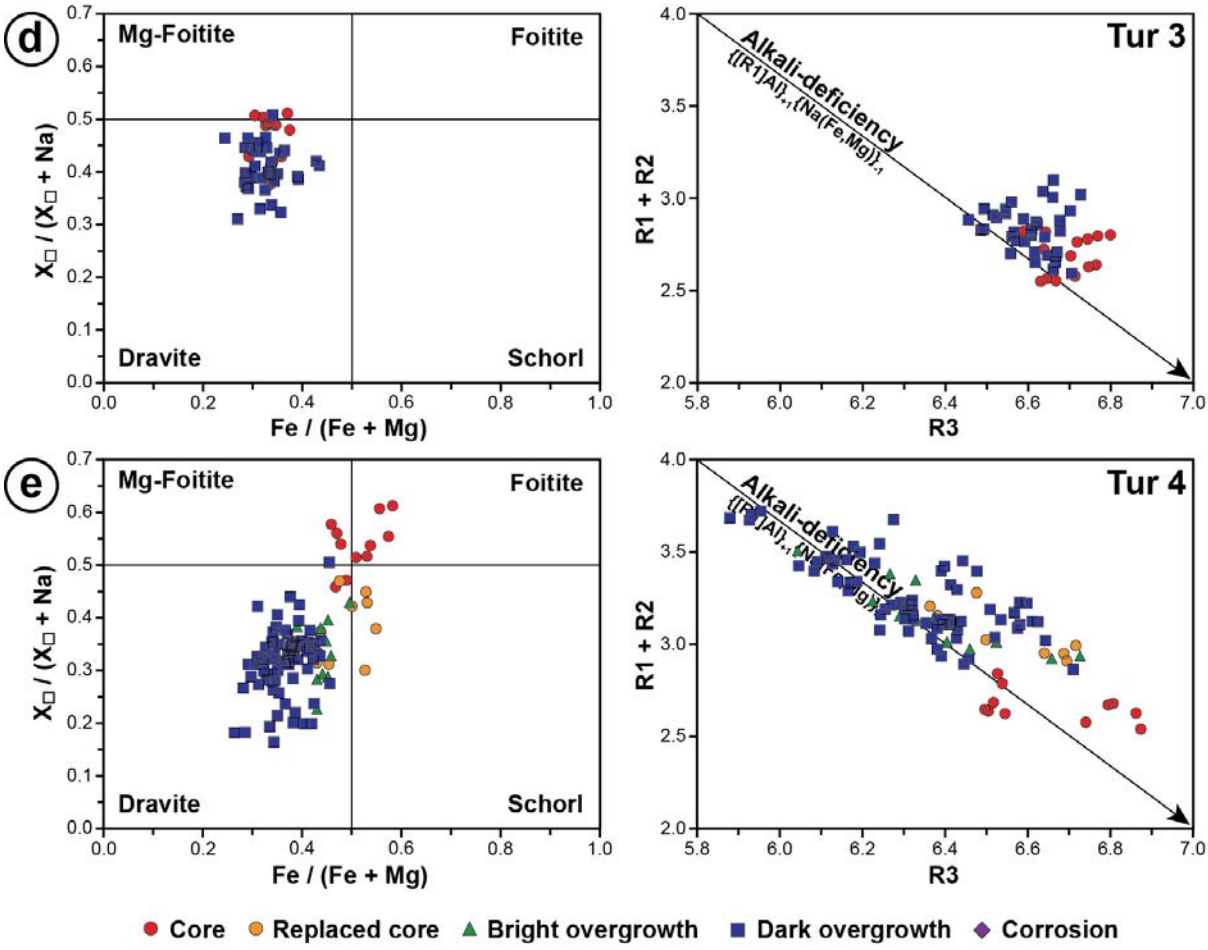

Fig. 119: Continued.

Tourmalines in the tourmalinites on the gneissic and granitic clasts distinguish by their composition. Tourmalines in tourmalinites from the gneissic clasts have limited compositional variations and are mainly dravite, characterized by minor variations in Fe/(Fe+Mg) (0.33–0.57) and X□/(X□+Na) (0.28–0.57) (Fig. 119b). The cores belong to the Mg-foitite sub-group and have the highest X□/(X□+Na) values (0.44–0.57), indicating that they are more alkali-deficient. The replaced cores have particularly high Ti values (up to 0.24 apfu). Tourmalines from tourmalinites on granitic clast distinguish by larger variability in Fe/(Fe+Mg) (0.23–0.64) and in X□/(X□+Na) values (0.21–0.60) (Fig. 119c). Whereas the core and dark overgrowth have dravitic composition, the bright overgrowth and the corrosion phase have schorlite composition, with higher Fe/(Fe+Mg) values (0.44–0.64), as well as the highest Ti contents (up to 0.34 apfu). The corrosion phase has in particular high content of Cr (up to 0.27 apfu). Acicular tourmalines also belong to the dravite sub-group and have limited variability in Fe/(Fe+Mg) (0.24–0.43) and X□/(X□+Na) (0.31–0.51) values (Fig. 119d). The cores distinguish from the overgrowth by higher X-site vacancies (0.38–0.51 apfu). Finally, the composition of tourmalines from the late breccia exhibits a wide range of Fe/(Fe+Mg) and

X□/(X□+Na) values (Fig. 119e). The cores have the highest X□/(X□+Na) values (0.46–0.61) and belong to the Mg-foitite – foitite solid solution, whereas the bright and dark overgrowths have dravite composition, with lower X□/(X□+Na) values (0.16–0.50) and the highest Ti values (up to 0.26 apfu) (Fig. 119e).

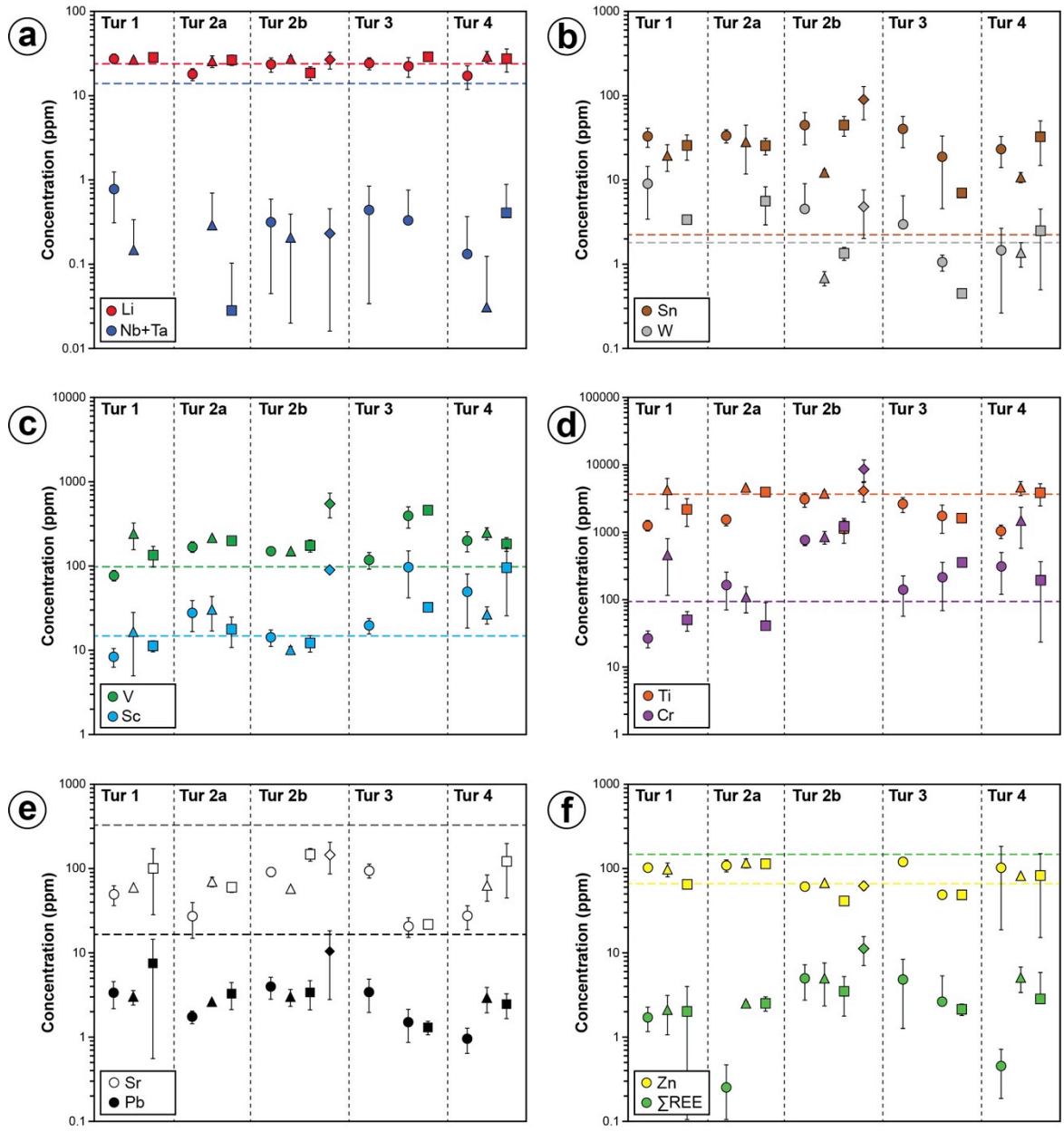

Fig. 120: Averages contents of selected trace elements in tourmalines from Puy-les-Vignes. Tur 1: greisen tourmalines (sample PLV-02-08a). Tur 2a: tourmalinites at the selvages of gneissic clast (sample PLV-02-01a). Tur 2b: tourmalinites at the selvages of granitic clast (sample PLV-02-04a). Tur 3: acicular tourmalines in quartz (samples PLV-02-01c and PLV-02-15). Tur 4: breccia tourmalines (samples PV-02-13a/b). The horizontal coloured dash lines represent the clarke values of the corresponding elements in the upper continental crust (UCC from Rudnick and Gao, 2003). Symbols correspond to: circle for core, triangle for rim, square for overgrowth and diamond for corrosion. Data are given in Table 32.

4.2.2. Trace elements

Trace elements compositions of tourmaline from Puy-les-Vignes are given in Table 32 and represented in Fig. 120. The different generations of tourmaline analysed are characterized by variable trace elements compositions, but have in common low concentrations in Rb, Sr, Cs, Mo, Nb, Ta, Y, REE, U, Th, Cu, Ni and Pb and high concentrations in Sn, W, V, Sc and Zn compared to the values of the upper continental crust (UCC from Rudnick and Gao, 2003). Greisen tourmalines have cores with relatively high concentrations in Li, Sn, W, Ba, Cs, Rb, Zn, with medium contents in Nb+Ta, compared with the others tourmalines. The dark overgrowths show lower concentrations in these elements compared to the cores, but have higher contents in Cr, Sr, Pb and Ti. Tourmalines associated with the tourmalinites from the rims of gneissic and granitic clasts have cores relatively enriched in Ti, V, Cr, Sn, Sc and depleted in Li, Cs. Minor variations are observed in the Pb, REE, Co and Zn contents between the tourmalines found on gneissic and granitic clasts, which likely reflects differences in the primary lithology. Acicular tourmalines have trace elements compositions close to those of tourmalinites from granitic clasts, with relatively high contents in W, Sn, Li, Nb+Ta, REE, Ti, V, Cr, Zn and Sr. Finally, the tourmalines associated with the late adularia-chlorite breccia have cores with low concentrations in Li, W, Cs, Co, Zn, Sr, Pb and REE and high concentrations in Cr, V and Sc. The bright and dark overgrowths surrounding the previous cores distinguish by relative enrichments in Sr, Sc, REE, Pb, Ti and Nb+Ta.

4.3. Boron isotopic composition

Boron isotopic compositions for representative tourmalines from Puy-les-Vignes are given in Table 33 and shown in Fig. 121. The $\delta^{11}B$ values vary from -7.48 to -0.45‰ and show generally isotopic differences between the cores, rims and overgrowths. Greisen tourmalines have cores with lower $\delta^{11}B$ values ranging from -5.68 to -3.43 ‰ compared to the rims and the external overgrowths, which have higher $\delta^{11}B$ values ranging from -2.89 to -1.06 ‰ and -2.77 to -1.61 ‰, respectively. The tourmalinites associated with the gneissic clasts have lighter $\delta^{11}B$ ratios with values from cores between -7.69 and -5.51 ‰, whereas the rims and external overgrowths show overlapping values falling between -6.76 and -4.95 ‰. The acicular tourmalines found within the quartz matrix of the breccia have similar $\delta^{11}B$ ratios ranging from -7.60 to -5.95 ‰ for the cores and -7.83 to -6.07 ‰ for the rims. The highest

$\delta^{11}B$ values are found in the cores of the breccia tourmalines, which are isotopically heavier (-1.71 to 0 ‰) than the rims and the overgrowths (-7.88 to -4.03 ‰) overlapping the $\delta^{11}B$ range from the tourmalinites and acicular tourmalines.

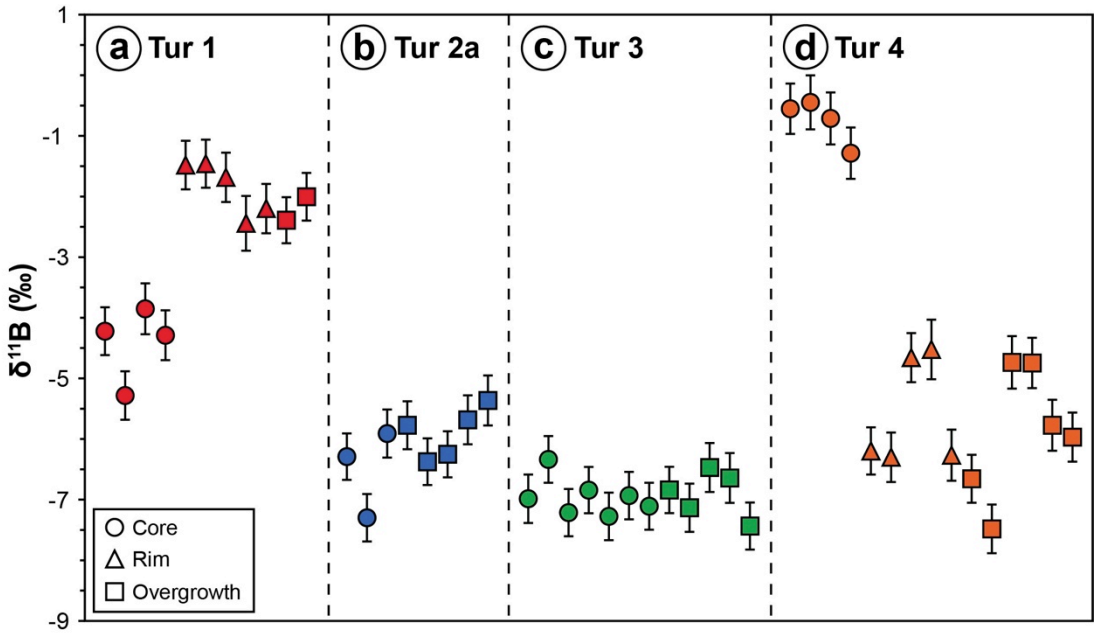

Fig. 121: Boron isotopic compositions of tourmalines from Puy-les-Vignes. (a) Tur 1: greisen tourmalines (sample PLV-02-08a). (b) Tur 2a: tourmalinites at the selvages of gneissic clast (sample PLV-02-01a). (c) Tur 3: acicular tourmalines in quartz (sample PLV-02-01c). (d) Tur 4: breccia tourmalines (sample PV-02-13b). Isotopic data are given in Table 33.

5. Tourmalinization in the Enguialès deposit

Tourmalinization in the Enguialès deposit affects mainly the enclosing micaschists in the close proximity of the W±Sn mineralized quartz veins. In the surroundings of the deposit (< 2 km) are observed along the Montsalvy road some quartz-tourmaline barren veins, up to 15 cm thick, which crosscut the biotite-cordierite micaschists in the contact metamorphic aureole of the Veinazès granite. These quartz-tourmaline veins show a diffuse tourmalinization of the enclosing micachists at the wall-rocks selvages and are deformed by a boudinage deformation. They show several similarities with the mineralized quartz-tourmaline veins in the Enguialès deposit. Two generations of tourmaline can be distinguished at Enguialès based on the petrographic observations and the chemical analyses.

5.1. Petrography and internal textures of tourmalines

5.1.1. Tourmalinites (Tur 1)

This first generation represents the main tourmalinization stage, forming a tourmalinite rim (tourmaline ± quartz) of a few millimetres up to several decimetres thickness developed in the micaschists at the hanging-walls of the quartz-wolframite veins (Fig. 122a). In the micaschists, the tourmaline crystals are disseminated in the schistosity underlined by muscovite and biotite, but are not wrapped by it (Fig. 122b, Fig. 123a), thus, suggesting that their crystallization is post-schistosity and likely occurs by replacement of the phyllosilicates by boron fluids (metasomatism). The tourmalinites are formed by the aggregation of prismatic tourmalinite crystals, partially corroded and cemented by microcrystalline quartz (Fig. 122c), showing textural evidence of undulose extinction and grain boundary migration. The contact between the tourmalinites and the quartz-wolframite veins is sharp, indicating a crack-seal opening mechanism. The quartz of the veins forms larger crystals, mm in size, which show similar evidence of plastic deformation than the quartz of the tourmalinite. This indicates that the tourmalinization and the vein opening formed before the plastic deformation episode. The tourmalinization appears related to the early pervasive alteration of the enclosing micaschists during early hydrothermal fluids circulations in pre-existing fractures. The tourmalines crystals are 50-500 μm in size and have typically an orange-brown colour in plane-polarized light. They contain commonly micro-inclusions of monazite, zircon or ilmenite, ranging from 10 to 100 μm in size, which likely represent crystals trapped during the growth of tourmaline. Observed in BSE, the tourmaline display an internal structure composed of four units (Fig. 123b): (i) a light grey core showing regularly a patchy texture; (ii) a dark rim surrounding the core; (iii) a bright overgrowth of a few μm thick; (iv) a large overgrowth forming the main part of the crystals and always displaying an intense oscillatory zoning at the micrometre-scale; and (v) a late corrosion phase, forming irregular veinlets crosscutting the core and oscillatory overgrowth and commonly associated with late Fe-oxides in infilling. Several sub-euhedral crystals of Ti-W-oxides (rutile?) are associated within the tourmalinites (Fig. 123c). These Ti-oxides display a complex internal zoning, including bright W-Fe-rich irregular zones containing up to 8 wt.% W and 2.7 wt.% Fe, and occasionally associated with wolframite and scheelite micro-inclusions. These Ti-W-oxides appear in infilling within the tourmaline and crosscut the microcrystalline quartz and could represent late invasive mineral phases in possible relation with the formation of the quartz-wolframite veins.

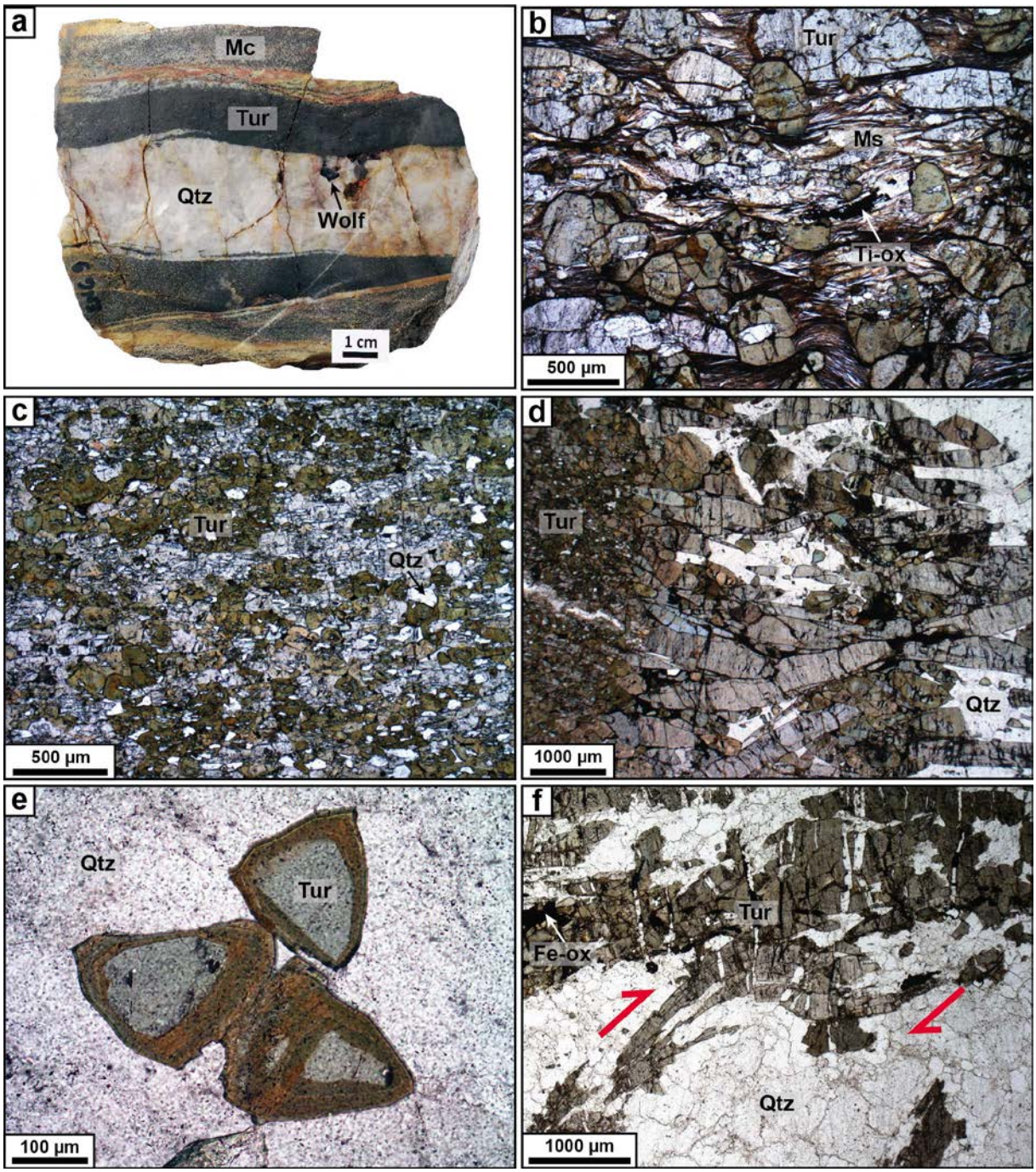

Fig. 122: Photographs of tourmalines from the Enguialès deposit. (a) Representative sample of quartz (Qtz)-wolframite (Wolf) vein, rimmed by a centimetre-thick aureole of tourmalinization (Tur), hosted in the micaschists (Mc) (sample ENG-9). (b) Tourmaline crystals disseminated within muscovite (Ms) and Ti-oxides (Ti-ox) in the schistosity of the micaschist (sample ENG-9a). (c) Tourmalinite developed at the selvage of the quartz-wolframite vein, composed by the aggregation of tourmalines crystals cemented by microcrystalline quartz (sample CHA-14-18). (d) Acicular tourmalines developed on the selvage of the tourmalinite and partially fragmented within the quartz of the vein (sample ENG-37). (e) Acicular tourmalines disseminated in macrocrystalline quartz of the veins, showing sections perpendicular to the c-axis with internal zoning (sample ENG-37). (f) Crystals of acicular tourmalines disseminated and segmented in the quartz vein, with minor Fe-oxides (Fe-ox) in late infilling, and deformed by a shearing deformation resulting in kink-fold (sample ENG-9b).

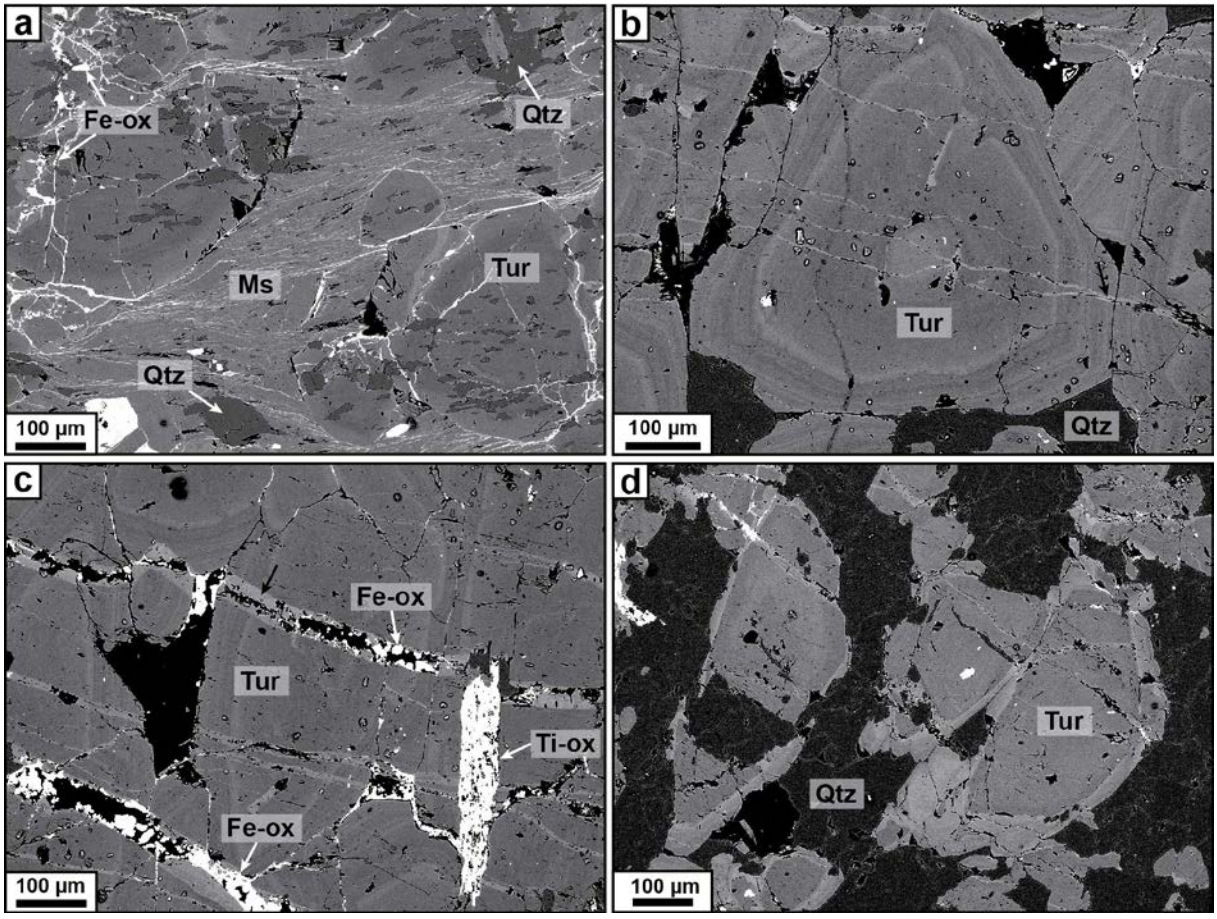

Fig. 123: BSE images of tourmalines from the Enguialès deposit. (a) Tourmaline crystals (Tur) in the schistosity underlined by muscovite (Ms) and partially corroded by quartz (Qtz) and late Fe-oxides (Fe-ox) (sample ENG-9a). (b) Tourmaline crystal in the tourmalinite showing a section perpendicular to the c-axis with an intense oscillatory zoning in the external overgrowth (sample ENG-9b). Note the late corrosion tourmaline in veinlets crosscutting the crystal. (c) Large veins of corrosion tourmaline associated with late Fe-oxides (Fe-ox) and Ti-oxides (Ti-ox) in infilling (sample ENG-9b). (d) Acicular tourmaline segmented in the quartz of the vein (sample ENG-9b). Note the light grey external overgrowth showing evidence of corrosion textures.

5.1.2. Acicular tourmalines (Tur 2)

This second generation corresponds to the formation of acicular crystals of tourmaline developing orthogonally to the selvages of the previous tourmalinites (Fig. 122d) or disseminated within the quartz of the veins (Fig. 122e). The crystals range from a few millimetres to centimetres in size and are blue-green in plane-polarized light. The tourmaline crystals on the wall-rocks selvages are cut or fragmented by the quartz of the vein, indicating that the tourmaline crystallization was followed by the deformation of the quartz by a crack-seal mechanism and recrystallization of the quartz. Acicular tourmalines observed within the quartz have a fan-like structure and are deformed by a shearing deformation (Fig. 122f),

parallel to the vein selvages, yielding to a kink-fold structure. The tourmalines show evidence of later extension marked by tension gashes at the µm-scale. The internal structure of the acicular tourmalines is formed by three successive zones in BSE imagery (Fig. 123d): (i) a light core with a patchy texture; (ii) a dark rim of a few µm thickness, surrounding the core; and (iii) a bright external corrosion forming invasive overgrowths, crosscutting the core and the rim, similarly as for the tourmalinite crystals.

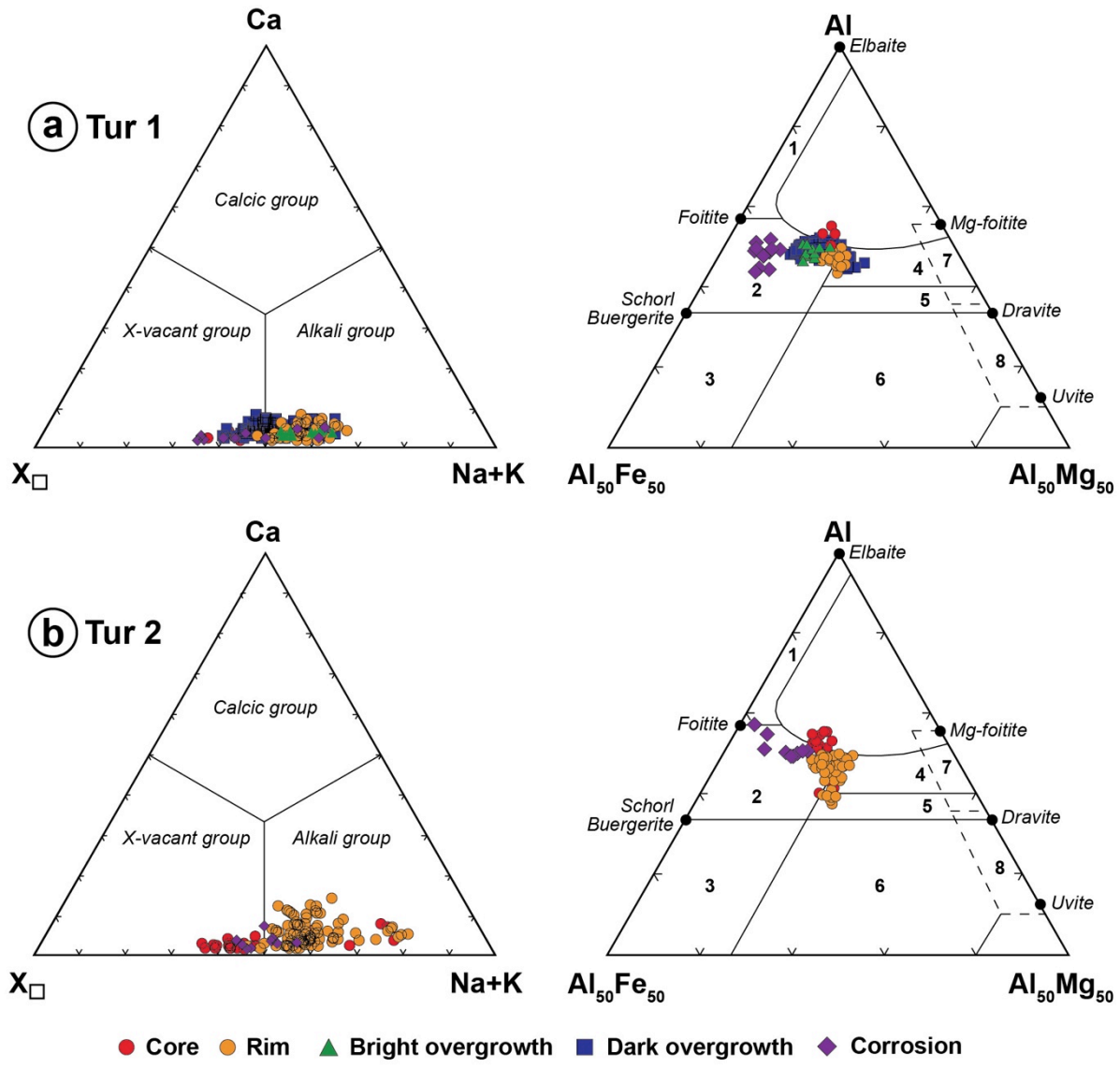

Fig. 124: Ternary Ca-X□-Na+K diagram (after Hawthorne and Henry, 1999) and Al-Fe-Mg diagram (after Henry and Guidotti, 1985) for tourmalines from the Enguialès deposit. (a) Tourmaline in tourmalinites from quartz veins selvages (Tur 1; samples ENG-9a/b). (b) Acicular tourmaline in quartz (Tur 2; samples ENG-9b, ENG-37; ENG-16b and CHA-14-18). The different fields in the Al-Fe-Mg diagram are from Henry and Guidotti (1985) and are the same than Fig. 118.

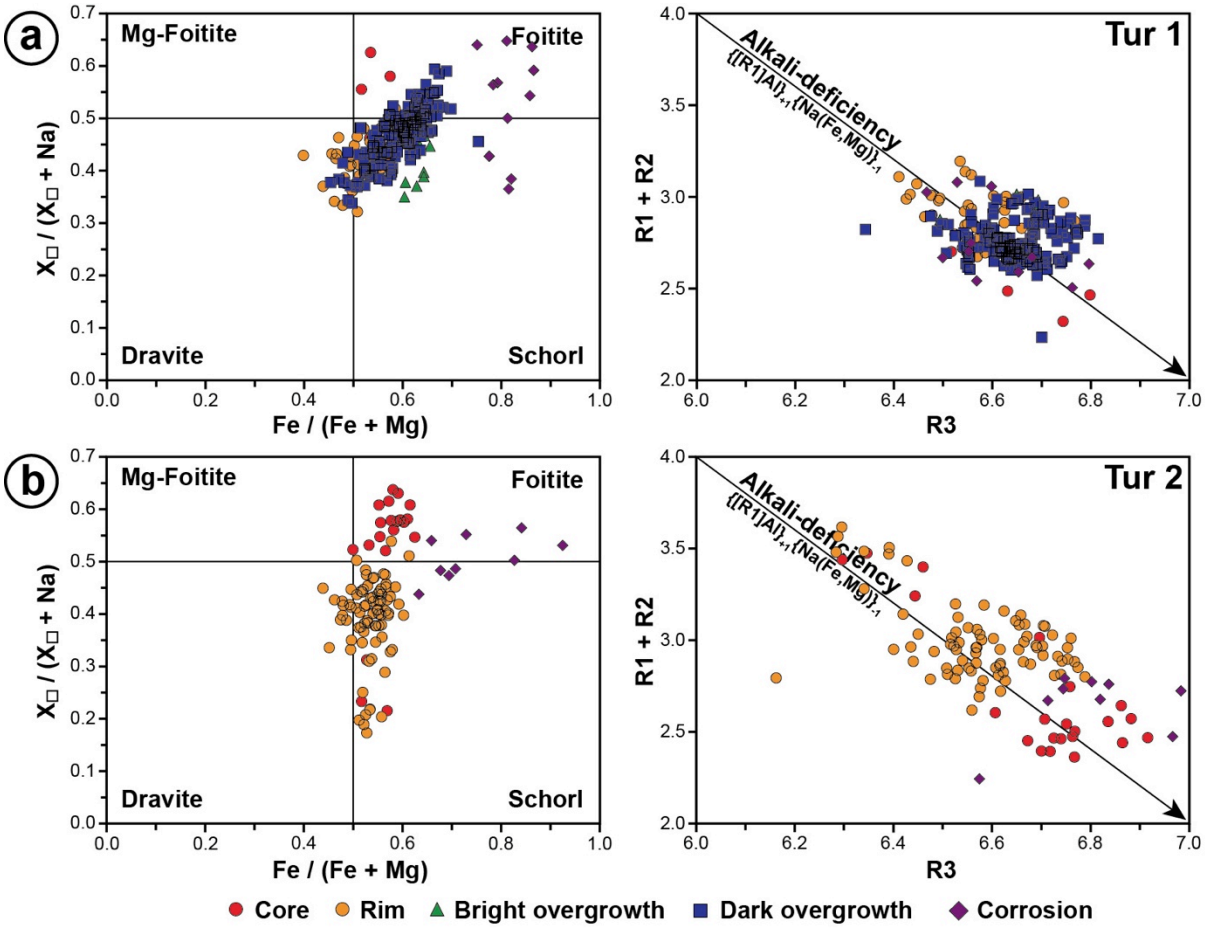

Fig. 125: Compositional diagrams for tourmalines from the Enguialès deposit. Each generation of tourmaline is plotted in the X□/(X□+Na) vs Fe/(Fe+Mg) classification diagram (after Henry et al., 2011) and in the R1+R2 vs R3 diagram, where R1=Na+Ca, R2=Fe+Mg+Mn, and R3=Al+1.33Ti (after Manning, 1982). (a) Tourmaline in tourmalinites from quartz veins selvages (Tur 1; samples ENG-9a/b). (b) Acicular tourmaline in quartz (Tur 2; samples ENG-9b, ENG-37; ENG-16b and CHA-14-18).

5.2. Chemical composition and crystal chemistry of tourmaline

5.2.1. Major elements

Representative chemical compositions of tourmaline from the Enguialès deposit are given in Table 34. Tourmalines are members of the alkali and X-vacant groups (Fig. 124), according to the nomenclature of Henry et al. (2011). They belong principally to the schorl and foitite groups (Fig. 125). The compositional variability is mainly attributed to variable Fe/(Fe+Mg) and X□/(X□+Na) with an alkali-deficiency, as shown in Fig. 125, involving the main $Fe^{2+}_{-1}Mg^{2+}_{+1}$ and $(Fe^{2+}Na^{+})_{-1}(Al^{3+}\square)_{+1}$ coupled substitutions. The tourmaline compositions fall in the fields of granitoids and peraluminous metasediments in the Al-Fe-Mg diagram (Fig. 124). The tourmalinites at the selvages of the quartz veins are characterized by

a foitite core surrounding by a schorl-dravite rim, whereas the overgrowths have schorl to foitite compositions (Fig. 125a). Acicular tourmalines in the quartz veins have similar compositions with a foitite core and a rim with variable X□/(X□+Na) values (0.17–0.54) (Fig. 125b). The late corrosion tourmaline has schorl to foitite composition, both in tourmalinites and acicular tourmalines, with high Ti content (up to 0.24 apfu).

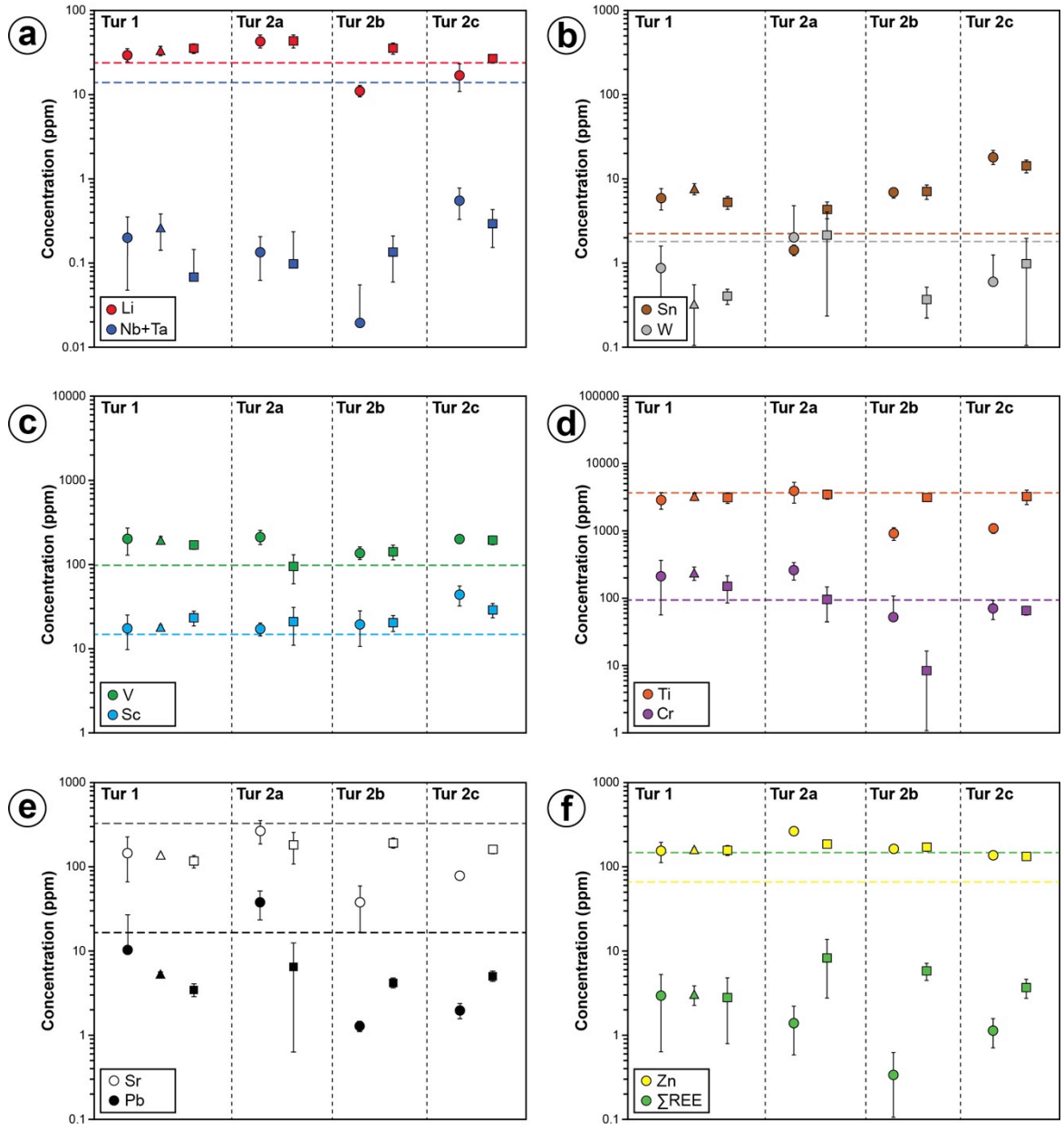

Fig. 126: Average contents of selected trace elements in tourmalines from Enguialès. Tur 1: tourmalinites at the selvages of the quartz-wolframite veins (samples ENG-9a/b). Tur 2a: acicular tourmalines in quartz (sample ENG-9b). Tur 2b: acicular tourmalines in quartz (samples ENG-37). Tur 2c: acicular tourmalines in quartz (sample CHA-14-18). The horizontal coloured dash lines represent the clarke values of the corresponding elements in the upper continental crust (UCC from Rudnick and Gao, 2003). Symbols correspond to: circle for core, triangle for rim and square for overgrowth. Data are given in Table 35.

5.2.2. Trace elements

Trace elements compositions of tourmaline from Enguialès are given in Table 35 and shown in Fig. 126. The tourmalines from Enguialès are commonly characterized by high concentrations in Li, Sn, V, Co, Zn, Cr and low concentrations in Sr, Cs, W, Nb+Ta, REE in comparison to the values of UCC. Tourmalinites have cores and overgrowths with similar trace elements compositions marked by relatively high contents in Li, Sn, V, Co, Cr, Zn and low contents in W. Acicular tourmalines show similar compositions with higher contents in Li (up to 53 ppm), Sn (up to 26 ppm) and W (up to 5.3 ppm).

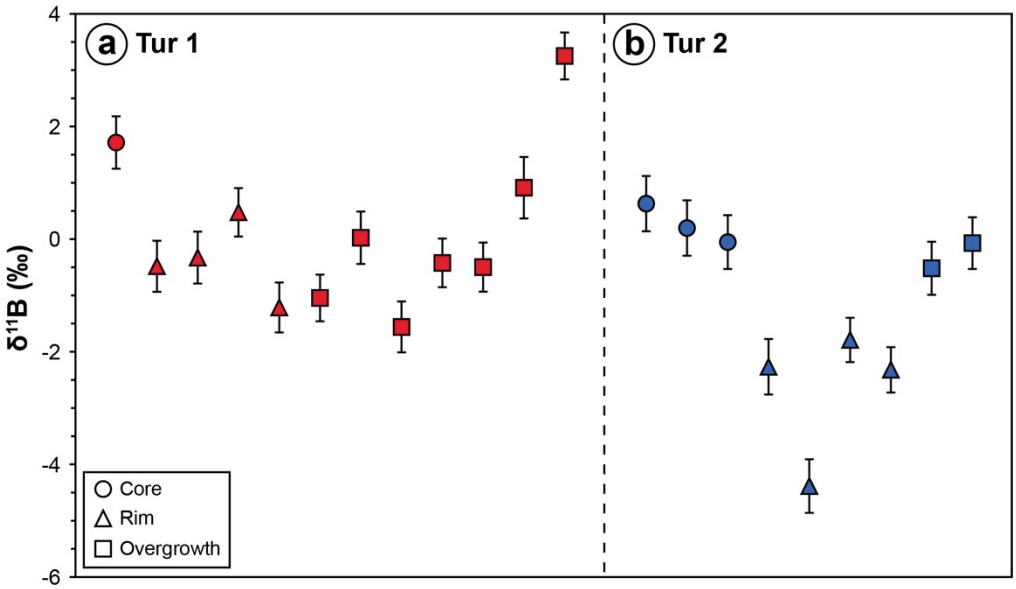

Fig. 127: Boron isotopic compositions of tourmalines from Enguialès. (a) Tur 1: tourmalinites at the selvages of the quartz-wolframite veins (samples ENG-9a/b). (b) Tur 2: acicular tourmalines in quartz (samples ENG-9b and CHA-14-18). Isotopic data are given in Table 36.

5.3. Boron isotopic composition

Boron isotope analyses for representative tourmalines from Enguialès are given in Table 36 and shown in Fig. 127. The $\delta^{11}B$ values range from -4.38 to 3.25 ‰. Tourmalines found in tourmalinites at the selvages of the quartz-wolframite veins show strong B isotopic variations within the crystals. The cores have relatively high $\delta^{11}B$ ratios comprised between 1.25 and 2.19 ‰, whereas the isotopic composition of the rims and the external overgrowths range from -1.65 to 0.91 ‰ and -2.01 to 3.67 ‰, respectively. Acicular tourmalines growing on the

tourmalinites have similar $\delta^{11}B$ ratios with overlapping values for the cores between -0.53 and 1.12 ‰ and for the external overgrowths between -0.99 and 0.39 ‰. The dark rims show however lighter $\delta^{11}B$ compositions with values ranging from -4.86 to -1.4 ‰.

6. Tourmalinization in the St-Mélany deposit

Tourmalinization in the St-Mélany deposit represents a major hydrothermal alteration affecting the enclosing micaschists, which results from the superposition of several B-metasomatism fluid episodes. At least, three successive generations of tourmalines can be distinguished in the St-Mélany deposit. Two of them are similar to two distinct tourmalinization types of regional extension known in the Cévennes area: (i) a first type ("Rocles-style") affecting the Cévenol micaschists in the proximity of the Rocles granite and marked by a diffuse tourmalinization of the micaschists; (ii) a second type ("Borne-Pont-de-Montvert-style") characterized by cm-thick tourmalinite veins with bleached selvages, that crosscut both the Borne granite in the north and the Pont-de-Montvert granite in the south, as well as their enclosing micaschists (see Chapter 6 for details).

6.1. Petrography and internal textures of tourmalines

6.1.1. Disseminated tourmalines (Tur 1a)

This first stage of tourmalinization affects the micaschists forming the host-rock. It corresponds to acicular crystals of tourmalines, millimetre in sizes, which are disseminated in the schistosity planes without preferential orientation (Fig. 128a). They have a light orange-brown colour in plane-polarized light and form typically fan-like structures that are commonly segmented in the schistosity planes (Fig. 128b). The crystals are superposed on the phyllosilicates underlining the schistosity and formed therefore after the development of the schistosity. The tourmalines are fractured by retrograde muscovite and chlorite and contain commonly micro-inclusions of fluoro-apatite, zircon or monazite, likely trapped during the tourmaline growth (Fig. 129a). Ti-Fe-W oxides are often associated with tourmaline and are likely related to the breakdown of biotite, from which they withdraw the Ti and Fe. Observed in BSE, the tourmaline crystals display three contrasting internal zones (Fig. 129a): (i) a light grey core homogeneous; (ii) a medium grey rim replacing core, showing patchy texture; and (iii) a dark overgrowth partially resorbing the core.

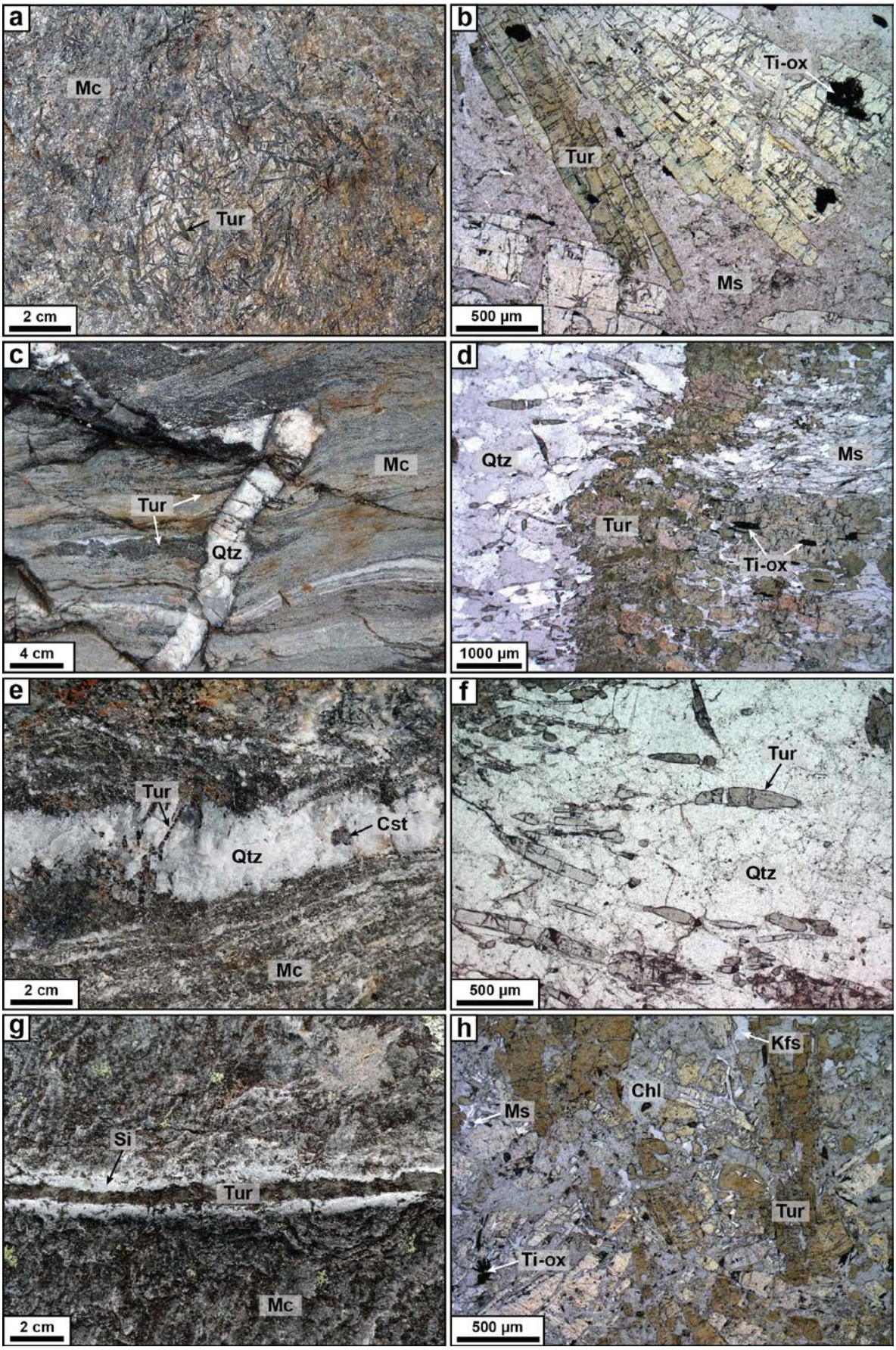
a
Mc
Tur
2 cm
b
Ti-ox
Tur
Ms
500 µm
c
Mc
Tur
Qtz
4 cm
d
Qtz
Ms
Tur
Ti-ox
1000 µm
e
Tur
Cst
Qtz
Mc
2 cm
f
Tur
Qtz
500 µm
g
Si
Tur
Mc
2 cm
h
Kfs
Chl
Ms
Tur
Ti-ox
500 µm

Fig. 128

Fig. 128: Photographs of tourmalines from the St-Mélany deposit. (a) Disseminated acicular crystals of tourmaline (Tur) in the micaschists (Mc). (b) Elongated tourmalines crystals developed on the muscovite (Ms) from the micaschist and associated with minor Ti-oxides (Ti-ox) (sample ARD-13-83b). (c) Tourmalinite at the selvage of quartz (Qtz) veins crosscutting the micaschists. Note the sharp contact between the quartz and the tourmalinite. (d) Tourmalinite developed at the selvage of the quartz veins, composed by the aggregation of tourmaline crystals diffusing in the schistosity planes, and associated with minor Ti-oxides (Ti-ox) (sample ARD-13-90). (e) Acicular tourmaline in quartz-cassiterite (Cst) veins, crosscutting the micaschist. Tourmaline crystals are typically segmented in the quartz. (f) Acicular tourmalines disseminated and segmented within the quartz vein (sample ARD-13-90). (g) Black tourmalinite vein rimmed by a white silicified border (Si) crosscutting the micaschist. (h) Breccia tourmalinite composed of tourmalines clasts cemented by an association of chlorite (Chl), K-feldspar (Kfs), muscovite, with disseminated Ti-oxides (sample ARD-13-10).

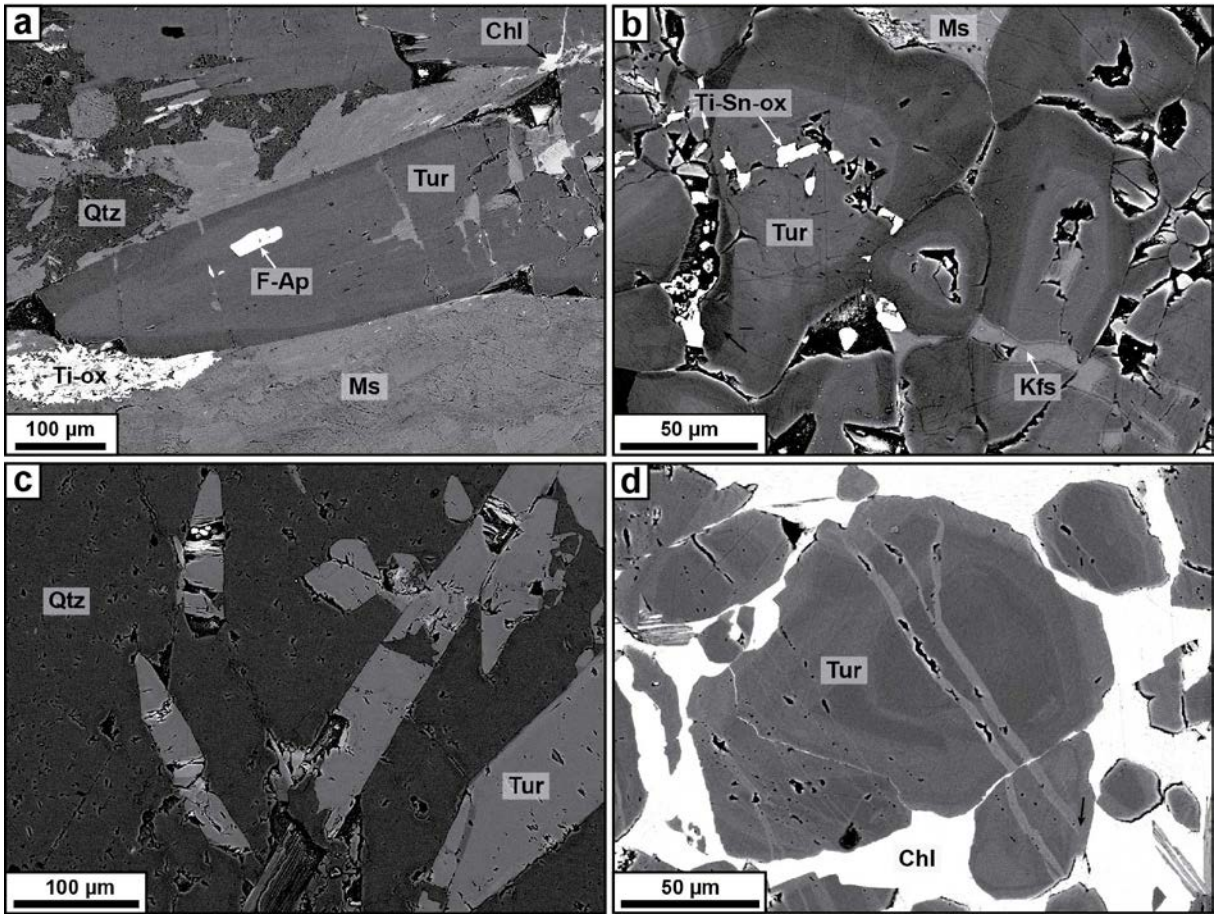

Fig. 129: BSE images of tourmalines from the St-Mélany deposit. (a) Elongated tourmaline (Tur) in muscovite (Ms), partially replaced by chlorite (Chl) in the micaschist in association with minor Ti-oxides (Ti-ox) and fluoro-apatite (F-Ap) (sample ARD-13-83b). (b) Tourmalines (Tur) in the tourmalinite selvage showing internal zoning and corrosion by K-feldspar (Kfs) with small Ti-Sn oxides (Ti-Sn-ox) in infilling (sample ARD-13-90). (c) Acicular tourmalines crystals (Tur) disseminated in the quartz (Qtz) veins (sample ARD-13-90). (d) Brecciated crystal of tourmaline (Tur) within chlorite (Chl), showing late corrosion schorl veins crosscutting the tourmaline (sample ARD-13-10).

6.1.2. Selvage tourmalinite (Tur 1b)

These tourmalines develop on the selvages of the quartz veins forming a cm-thick tourmalinization rim, which is diffuse in the schistosity planes of the micaschists (Fig. 128c). Since these tourmalines are diffuse within the micaschists and cannot be distinguished clearly, from a paragenetic point of view, from the disseminated tourmalines in the schistosity planes, we refer to them as Tur 1b. The tourmalinite is cut at the contact with the quartz vein and the tourmaline crystals are fragmented within the quartz. This indicates that the tourmalinization was limited to structural discontinuities in the micaschists, from which the boron fluids have circulated. Vein opening and quartz precipitation followed this pervasive alteration event during a later extension episode. In plane-polarized light, the tourmalines have a brown-orange colour and typically form prismatic elongated crystals of 100 to 500 μm in size (Fig. 128d). The crystals are commonly corroded by quartz and fractured by chlorite and K-feldspar in the micaschists. The tourmaline are often associated with several accessory minerals, such as fluoro-apatite and Ti-Sn-oxides (up to 3.4 wt.% Sn), which are in infilling within tourmaline (Fig. 129b). In BSE imagery, tourmalines have an internal structure composed of three units (Fig. 129b): (i) a light grey core with a patchy texture; (ii) a patchy zoning corresponding to a replaced core; (iii) a bright overgrowth of a few μm thickness surrounding by (iv) a dark grey external overgrowth.

6.1.3. Acicular tourmalines (Tur 2)

They form typically elongated and acicular crystals in the quartz-cassiterite veins, growing on the tourmalinite selvages and segmented within the quartz (Fig. 128e), indicating a crack-seal mechanism for the vein opening. They are also found as fragmented crystals disseminated within the quartz of the veins. They are millimetres in size and have a light green colour in plane-polarized light (Fig. 128f). Observed in BSE images, the crystals are composed by two internal zones (Fig. 129c): (i) a light grey core, homogeneous, forming the main part of the crystals and (ii) a bright overgrowth of a few μm thickness, surrounding the core. At the contact with the tourmalinites, a dark overgrowth showing oscillatory zoning is observed around the crystals. Locally, a corrosion phase cut the cores and rims.

6.1.4. Breccia tourmalines (Tur 3)

This last stage of tourmalinization is associated with late hydraulic fracturing of the micaschists forming black tourmalinite veins of a few centimetres thick crosscutting the regional schistosity (Fig. 128g). The veins show systematically bleached rims, from several millimetres up to a few centimetres in thickness, corresponding to the leaching and silicification of the micaschists at the hanging walls (Fig. 128g). At the outcrop scale, the tourmalinite veins corrodes and replaces partially the quartz veins, up to the complete tourmalinization of the quartz. Observed in plane-polarized light (Fig. 128h), the tourmalinite vein corresponds to a micro-breccia composed of clasts of tourmalines, ranging from 10 µm to a few mm in size, which are cemented by an association of chlorite with minor muscovite and K-feldspar (adularia?) and containing disseminated accessory minerals of monazite, apatite and Ti-W-Fe-oxides. The latter can contain up to 3.5 wt.% W and 2.2 wt.% Fe. In BSE imagery, the internal structure of the tourmaline crystals is composed of four zones (Fig. 129d): (i) a small dark core showing eventually sector zoning; (ii) a light grey rim with a regular oscillatory zoning at the micrometre-scale, which forms the main part of the crystals; (iii) a dark overgrowth of a few micrometre-thick around the previous rim; and (iv) a late corrosion overgrowth crosscutting the core and the external crystalline borders.

6.1.5. Tourmalines from the Beaume valley

These tourmalines are not located directly in the St-Mélany deposit, but are found in barren quartz veins, which crosscut the low-grade micaschists in the Beaume valley at around 7 km in the southeast of St-Mélany (see Chapter 6). Tourmaline is associated with K-feldspar, apatite and biotite within the quartz veins and form acicular crystals, which are millimetres in size and are disseminated within the quartz. Since these acicular tourmalines appear similar to the ones found in the quartz-cassiterite veins from St-Mélany (Tur 2), one sample of quartz-tourmaline vein from the Beaume valley was studied for comparison (sample ARD-13-05). In plane-polarized light, the crystals reveal a blue core, surrounding by a green rim. The same internal zoning is observed in BSE imagery showing very homogeneous crystals.

6.2. Chemical composition and crystal chemistry of tourmaline

6.2.1. Major elements

Representative chemical compositions of tourmaline from the St-Mélany deposit are given in Table 37. Tourmalines are mostly members of the alkali group, and in minority of the X-vacant group for some crystals (Fig. 130), and belong principally to the dravite-schorl solid solution (Fig. 131). The compositional variability is mainly attributed to variable X□/(X□+Na) values with an alkali-deficiency, as shown in Fig. 130, involving the main $(Fe^{2+}Na^{+})_{-1}(Al^{3+}\square)_{+1}$ coupled substitution. In the Al-Fe-Mg diagram from Henry and Guidotti (1985), most of the tourmalines fall into the field of the metasediments (Fig. 130). Disseminated tourmalines in the micaschists have a dravitic composition, composed by a core with higher Fe/(Fe+Mg) values (0.39–0.45) compared to the external overgrowth (0.34–0.37). The latter have the highest X□/(X□+Na) contents (0.35–0.44), indicating alkali-deficiency (Fig. 131a). Tourmalines at the selvages of the quartz veins show similar dravitic compositions for the cores, rims and dark overgrowths to the disseminated tourmalines with close values of Fe/(Fe+Mg) (0.35–0.47) and X□/(X□+Na) (0.15–0.42) contents (Fig. 131b). Only the bright overgrowths show a slight different composition evolving toward the foitite sub-group (Fig. 131b). Acicular tourmalines found in the quartz veins show however distinct major elements compositions compared to the previous tourmalines (Fig. 131c). The cores have compositions between the foitite and schorl sub-groups with relatively high Fe/(Fe+Mg) values (0.65–0.78), whereas the bright overgrowths have schorlite compositions with lower X□/(X□+Na) contents (0.20–0.35). The dark overgrowths and corrosions, locally observed, have however dravitic compositions. Breccia tourmalines associated with the late tourmalinite veins are composed of Mg-foitite core evolving to a rim and a dark overgrowth of dravitic composition (Fig. 131d). The external corrosion has also a dravite composition, but shows lower X□/(X□+Na) (0.11–0.45) contents. Finally, the tourmalines from the Beaume valley are characterized by compositions of dravite, which are similar to the tourmalines from St-Mélany with close values of Fe/(Fe+Mg) (0.42–0.47) and X□/(X□+Na) (0.24–0.44) (Fig. 131e).

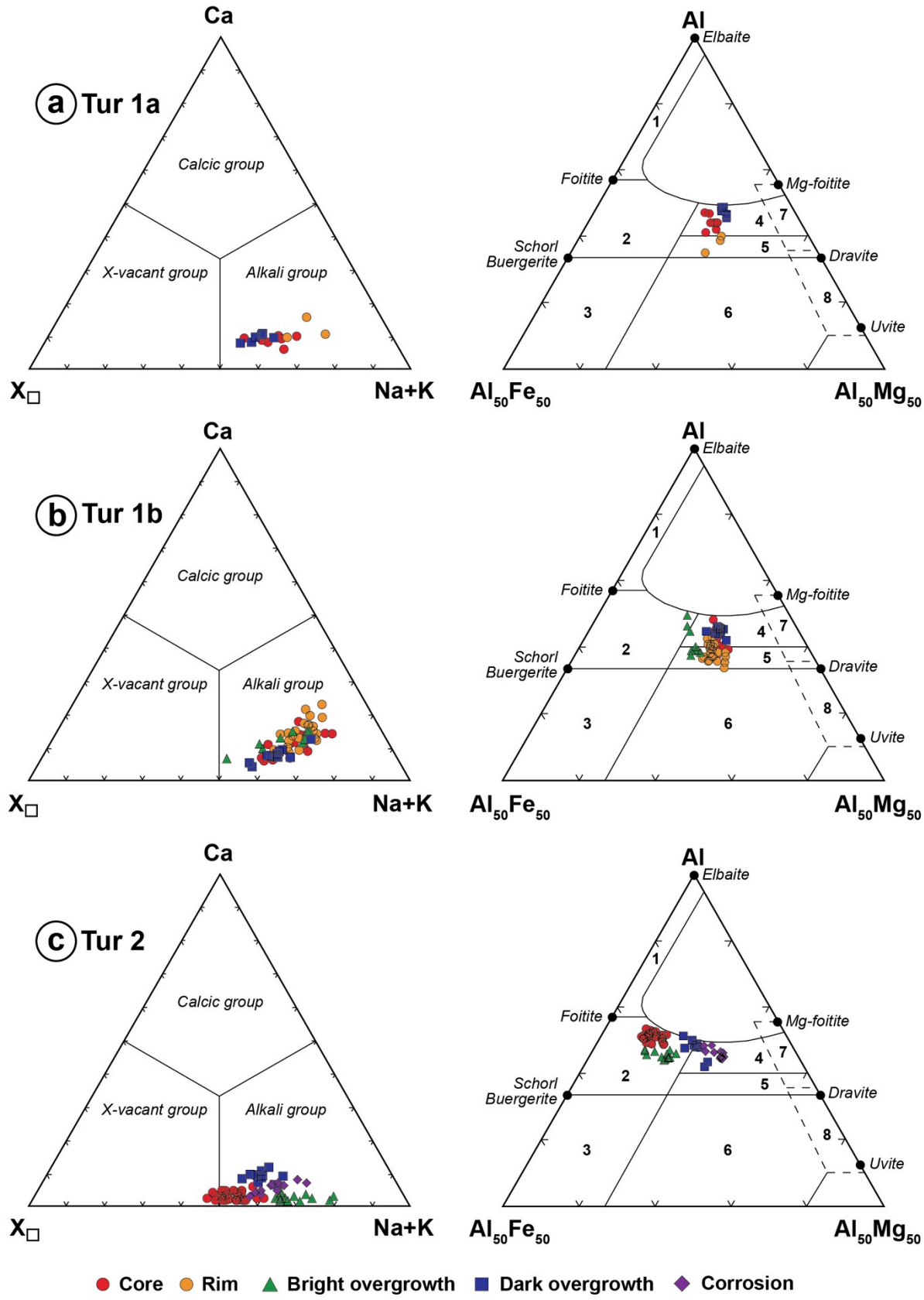
a Tur 1a
b Tur 1b
c Tur 2
Ca
Calcic group
X-vacant group
Alkali group
X□
Na+K
Al
Elbaite
Foitite
Mg-foitite
Schorl
Buergerite
Dravite
Uvite
1
2
3
4
5
6
7
8
Al50Fe50
Al50Mg50
Core
Rim
Bright overgrowth
Dark overgrowth
Corrosion

Fig. 130

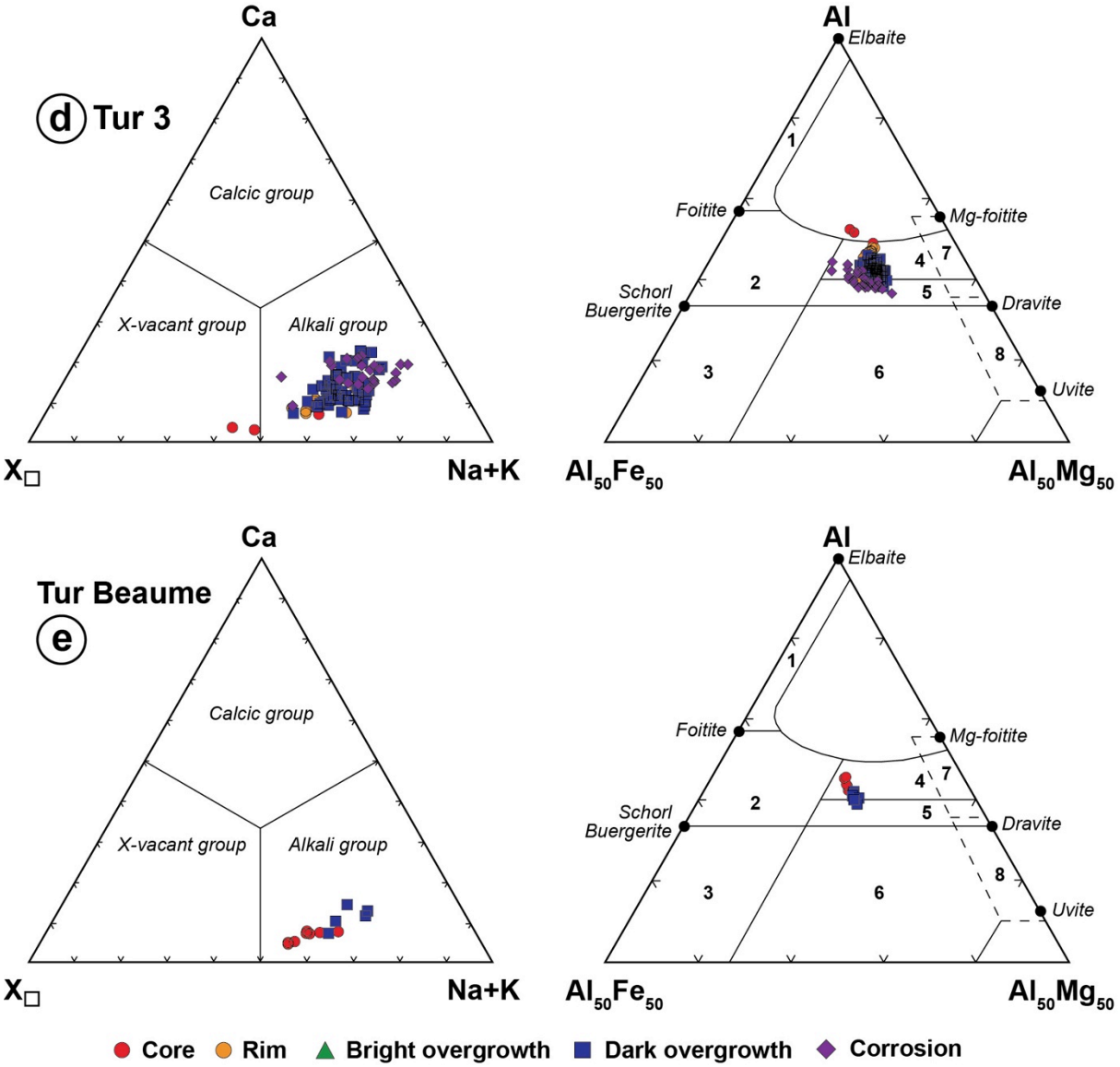

Fig. 130 (Continued): Ternary Ca-X□-Na+K diagram (after Hawthorne and Henry, 1999) and Al-Fe-Mg diagram (after Henry and Guidotti, 1985) for tourmalines from the St-Mélany deposit. (a) Disseminated tourmaline in the micaschists (Tur 1a; sample ARD-13-83b). (b) Tourmalinite at the selvage of the quartz veins (Tur 1b; sample ARD-13-90). (c) Acicular tourmalines in the quartz veins (Tur 2; sample ARD-13-90). (d) Tourmaline in the brecciated tourmalinite veins crosscutting the micaschists (Tur 3; sample ARD-13-10). (e) Tourmalines from the Beaume valley (sample ARD-13-05). The different fields in the Al-Fe-Mg diagram are from Henry and Guidotti (1985) and are the same than Fig. 118.

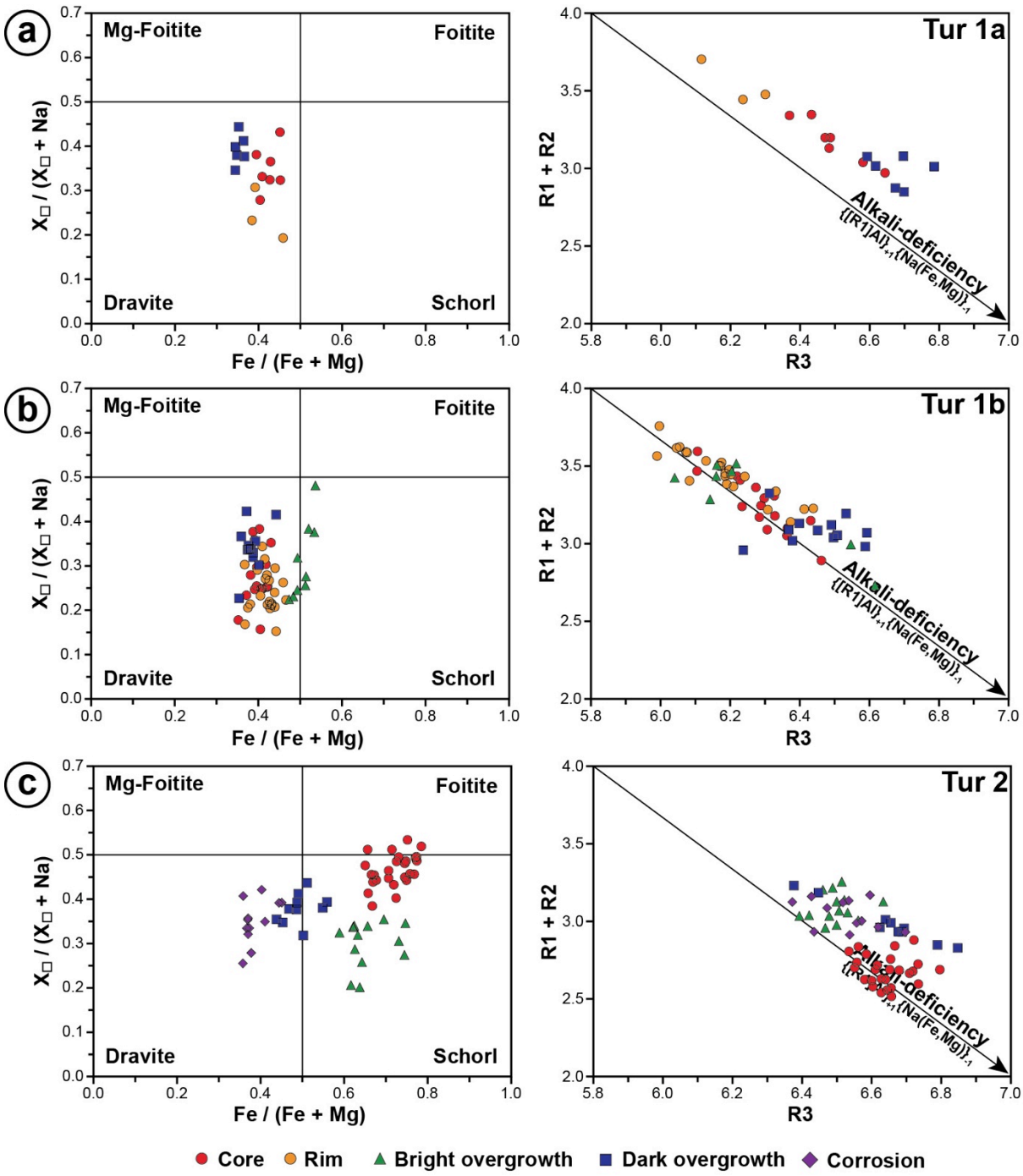

Fig. 131: Compositional diagrams for tourmalines from the St-Mélany deposit. Each generation of tourmaline is plotted in the X□/(X□+Na) vs Fe/(Fe+Mg) classification diagram (after Henry et al., 2011) and in the R1+R2 vs R3 diagram, where R1=Na+Ca, R2=Fe+Mg+Mn, and R3=Al+1.33Ti (after Manning, 1982). (a) Disseminated tourmaline in the micaschists (Tur 1a; sample ARD-13-83b). (b) Tourmalinite at the selvage of the quartz veins (Tur 1b; sample ARD-13-90). (c) Acicular tourmalines in the quartz veins (Tur 2; sample ARD-13-90). (d) Tourmaline in the brecciated tourmalinite veins crosscutting the micaschists (Tur 3; sample ARD-13-10). (e) Tourmalines from the Beaume valley (sample ARD-13-05).

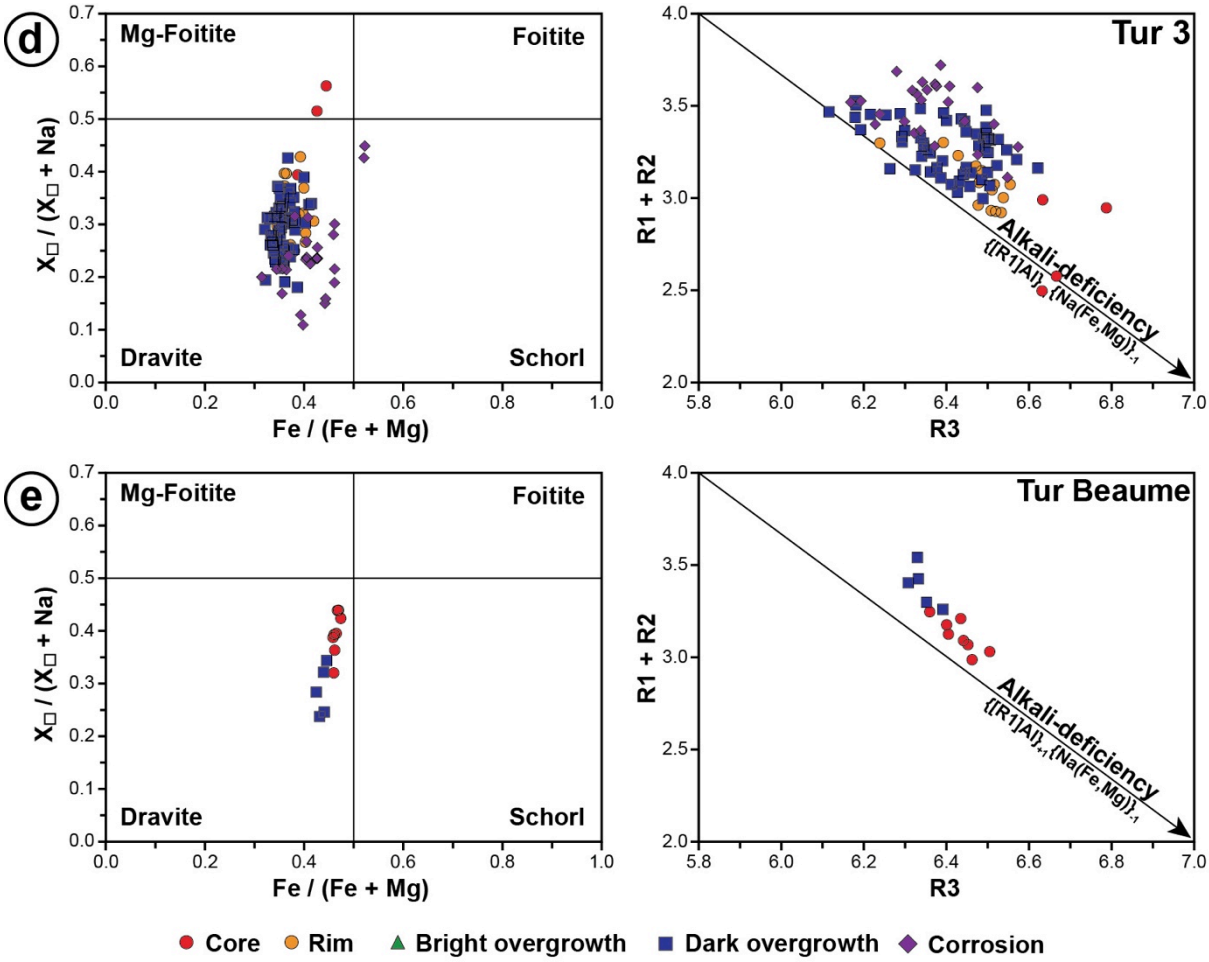

Fig. 131: Continued.

6.2.2. Trace elements

Trace elements compositions of tourmaline from St-Mélany are given in Table 38 and represented in Fig. 132. The tourmalines are commonly characterized by high contents in Li, Be, Sn, V, Sc and Zn and low contents in Ti, Cs, Nb+Ta, Sr, Ba and REE compared to the UCC. Disseminated tourmalines in the micaschists have close trace elements compositions compared to the cores from the tourmalines at the selvages of the quartz veins, containing in particular elevated contents in V (up to 391 ppm), Sc (up to 98 ppm), Cr (up to 346 ppm) and Pb (up to 81 ppm). The dark overgrowths from the tourmalinites have however lower contents in most of the trace elements (e.g., Be, Sn, V, Co, Cr, Sr, Sc) compared to the cores. Acicular tourmalines in overgrowth on the tourmalinites or disseminated in the mineralized quartz veins show distinct trace elements signatures in comparison with the others tourmalines. In particular, they contain very high concentrations in Li (up to 216 ppm), Sn (up to 352 ppm), W (up to 20 ppm), Zn (up to 1514 ppm) and very low contents in V (down to 12 ppm), Sc (down to 1.7 ppm) and no Cr. Breccia tourmalines in the late tourmalinite veins show

intermediate compositions compared with the previous tourmalines. Minor compositional variations in Li, Sc, Cr, Sr, Ti and REE differentiate the cores, rims and overgrowths. Finally, the tourmalines from the Beaume valley distinguish clearly from those from St-Mélany by higher contents in V, Co and Ni, and very low contents in Li, Sn and W.

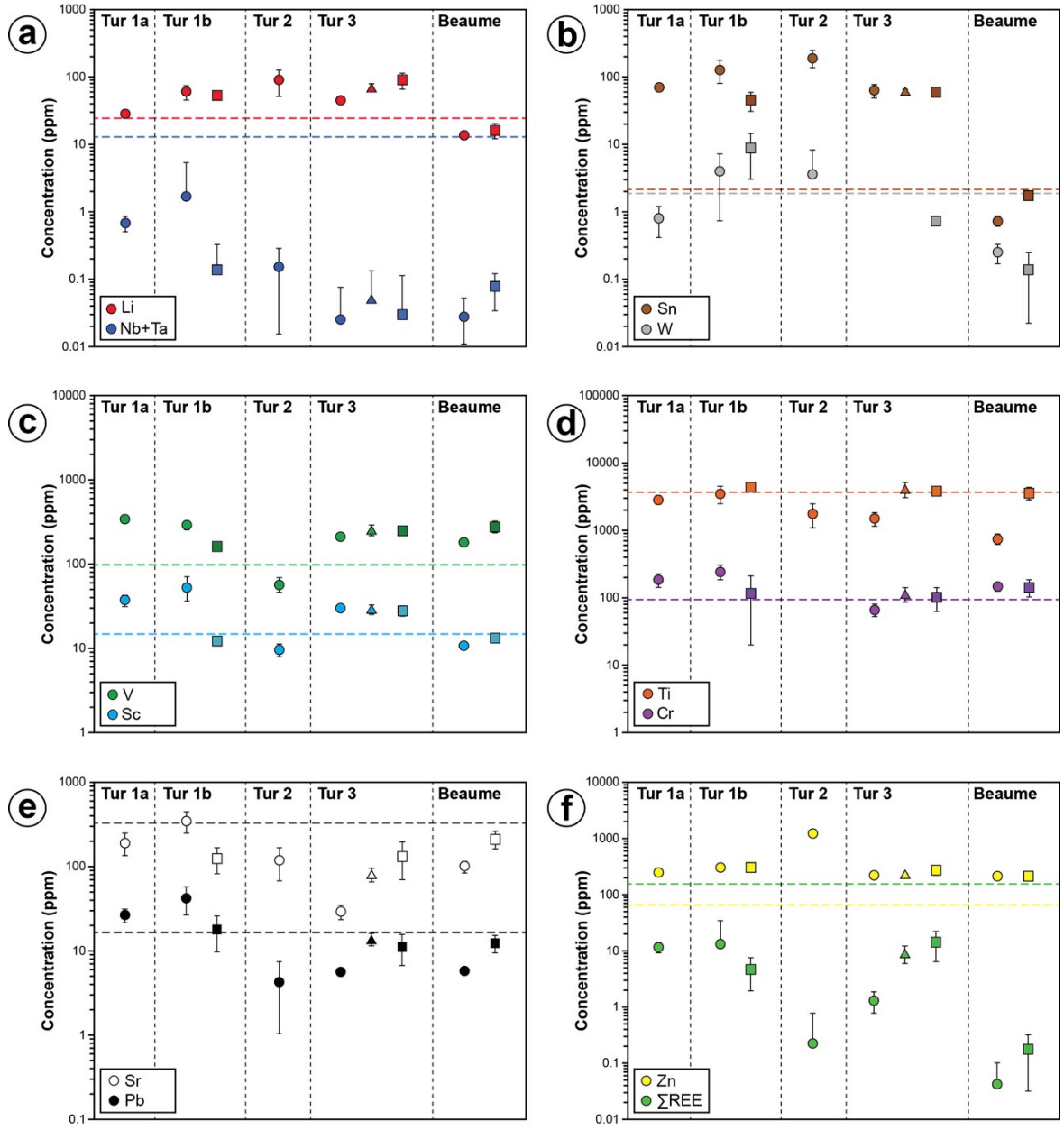

Fig. 132: Average contents of selected trace elements in tourmaline from St-Mélany. Tur 1a: disseminated tourmalines in the micaschists (sample ARD-13-83b). Tur 1b: tourmalinite at the selvages of the quartz-cassiterite veins (sample ARD-13-90). Tur 2: acicular tourmalines in the quartz-cassiterite veins (sample ARD-13-90). Tur 3: breccia tourmalines associated with the black tourmalinite veins (sample ARD-13-10). Beaume: acicular tourmalines from the Beaume valley (sample ARD-13-05). The horizontal coloured dash lines represent the clarke values of the corresponding elements in the upper continental crust (UCC from Rudnick and Gao, 2003). Symbols correspond to: circle for core, triangle for rim and square for overgrowth. Data are given in Table 38.

6.3. Boron isotopic composition

Boron isotopic compositions for representative tourmalines from St-Mélany are given in Table 39 and shown in Fig. 133. The tourmalines from St-Mélany have $\delta^{11}B$ values ranging from -6.03 to 1.51 ‰ and the different generations are clearly distinguished isotopically. Disseminated tourmalines in the micaschists are characterized by cores with $\delta^{11}B$ values between -1.27 and 0.39 ‰ and rims with $\delta^{11}B$ values between -2.04 and -1.2 ‰. Tourmalines found in the tourmalinized selvages of the quartz veins have a core with $\delta^{11}B$ ratios ranging from -3.78 to -2.82 ‰, whereas the rims and overgrowths are isotopically heavier with $\delta^{11}B$ ratios comprised between -2.85 and -1.16 ‰ and between -3.3 and -2.1 ‰, respectively. Acicular tourmalines in the quartz-cassiterite veins have the heaviest B isotopic compositions with lower $\delta^{11}B$ values for the cores (0.11-1.3 ‰) than the rims (0.91-1.94 ‰). At the opposite, the late breccia tourmalines associated with the black tourmalinite veins have the lightest B isotopic compositions. The cores distinguish by relatively higher $\delta^{11}B$ ratios (-5.63 to -3.77 ‰) than the rims (-6.46 to -4.76 ‰) and the external overgrowths (-5.80 to -4.79 ‰). Finally, the tourmalines from the Beaume valley found in quartz veins have intermediate $\delta^{11}B$ values ranging from -4.24 to -2.43 ‰. The cores and the rims have overlapping B isotopic compositions comprised between -4.41 and -2.01 ‰ and between -4.66 and -2.13 ‰, respectively.

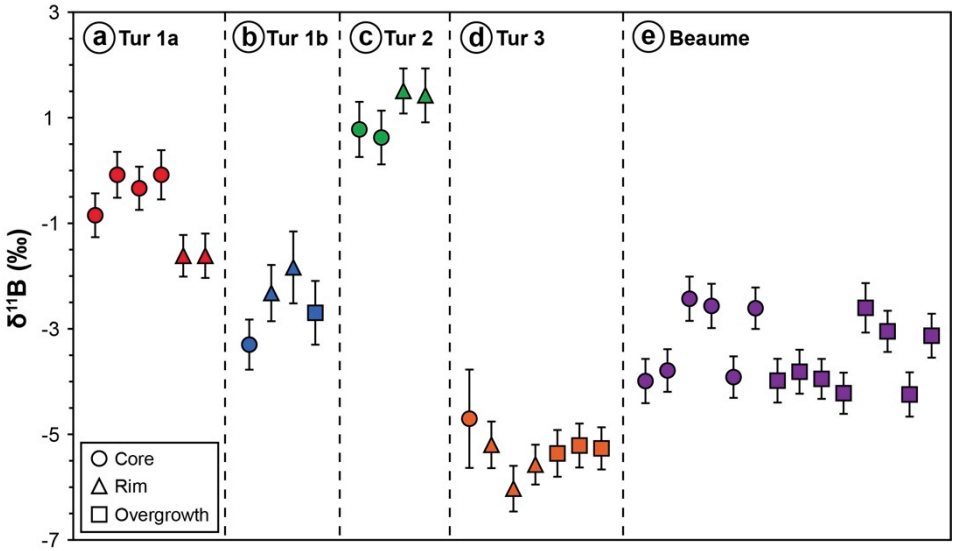

Fig. 133: Boron isotopic compositions of tourmaline from St-Mélany. (a) Tur 1a: disseminated tourmalines in the micaschists (sample ARD-13-83b). (b) Tur 1b: tourmalinites at the selvages of the quartz-cassiterite veins (sample ARD-13-90). (c) Tur 2: acicular tourmalines in the quartz-cassiterite veins (sample ARD-13-90). (d) Tur 3: breccia tourmalines associated with the black tourmalinite veins (sample ARD-13-10). (e) Beaume: Acicular tourmalines from the Beaume valley (sample ARD-13-05). Isotopic data are given in Table 39.

7. Discussion

7.1. Chemical variations in tourmalines and definition of fluid poles

7.1.1. Significance of the internal zoning in tourmalines: fractionation vs fluid mixing

Tourmalines from Puy-les-Vignes, Enguialès and St-Mélany show commonly complex internal zoning in BSE imagery, which reflects intra-crystalline compositional variations in major and minor elements. In particular, many tourmaline crystals have external overgrowths, which display fine-scale rhythmic zoning. Such features indicate that tourmaline crystallized in a fluid environment with fluctuating chemical composition and/or physical properties with time. Deciphering the chemical evolution at the growth band scale allows thus to reconstruct the nature of the hydrothermal fluid system, from which the tourmalines crystallized. Two main processes may explain the observed chemical variations, i.e., fractionation (close system) or fluid mixing (open system), or a combination of both. In open systems, the question arises about the nature of the incoming fluid(s), which may correspond either to one fluid of constant composition with time or itself evolving on the long term by fractionation, or the mixing between two or more fluids, incoming by alternation or mixing at the source or in the hydrothermal system. Detailed observations were conducted on representative tourmaline crystals from the Puy-les-Vignes and Enguialès deposits in order to identify the involved mechanism(s). X-ray element mapping of tourmaline crystals (Fig. 134) reveals intra-crystalline chemical discontinuities both in major (Fe, Mg) and minor (Ti, Ca) elements, corresponding to major compositional variations during the tourmaline crystallization. The corrosions are marked by compositional jumps, which are better explained by the influx of new fluid of distinct composition. However, the limited spatial resolution of the X-ray map does not allow determining in detail the evolution trends at the growth band scale, which are better highlighted by in situ punctual analyses. The EDS compositional profile within a representative tourmaline from Puy-les-Vignes (Fig. 135) shows a succession of rhythmic growth bands, each of them being characterized by an increase in the Fe/(Fe+Mg) value. At the first order, the Fe content increases progressively (0.93–1.18 apfu) in the external overgrowth, whereas the Mg content decreases (1.27–1.09 apfu). The Al content is more erratic with higher variations (6.27–6.46 apfu). Similarly, the Ca and Ti contents are highly variable along the overgrowth transect and do not appear correlated with other measured elements.

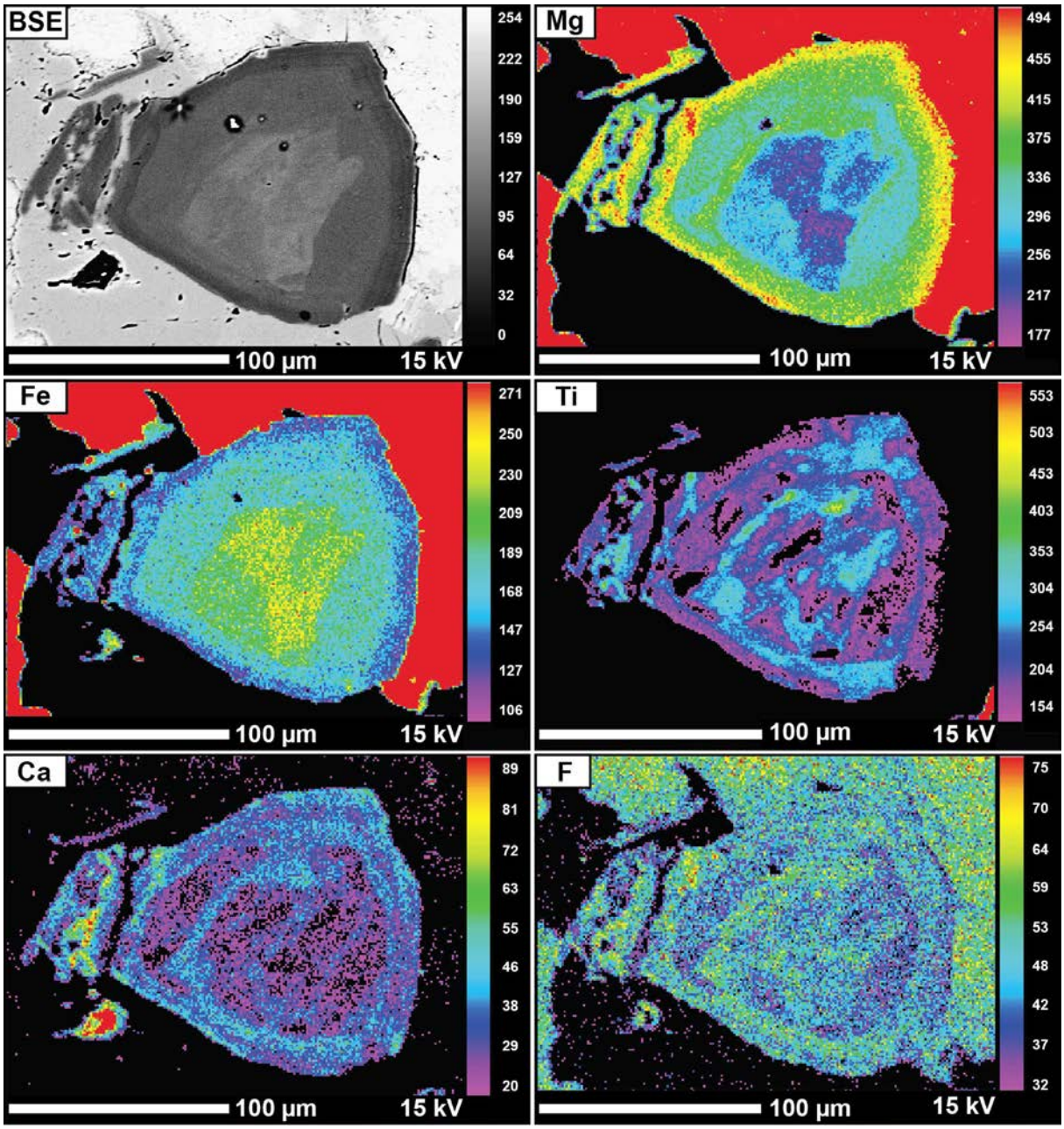

Fig. 134: Example of BSE and X-ray maps of Mg, Fe, Ti, Ca and F distribution in a zoned crystal of tourmaline from the Puy-les-Vignes deposit (Tur 4; sample PLV-02-13b).

At the second order, the transition from one growth band to another one is marked by compositional gaps corresponding to discontinuities visible on the BSE image (Fig. 135b), each growth band being composed by the alternation of a dark and a light band. The progressive increase in the Fe/(Fe+Mg) ratio with compositional gaps cannot therefore be interpreted as oscillatory zoning during in situ long-term fractionation or fractionation at the source of the hydrothermal fluid. Such characteristics are rather better explained by an apparent recharge in a less fractionated fluid with time. This is also confirmed by the absence of correlation between Al and Fe/(Fe+Mg), used here as a proxy for fractionation. Finally, the

significant variations in $\delta^{11}B$ at the crystal-scale (Fig. 136), up to 3 ‰, indicate the mixing between at least two fluids of distinct boron isotopic composition with time (e.g., Marschall et al., 2008). Consequently, all these features indicate that the crystallization of tourmaline results from a discontinuous fluid mixing process in open system, which involves periodic inputs of hydrothermal fluids with different compositions over time.

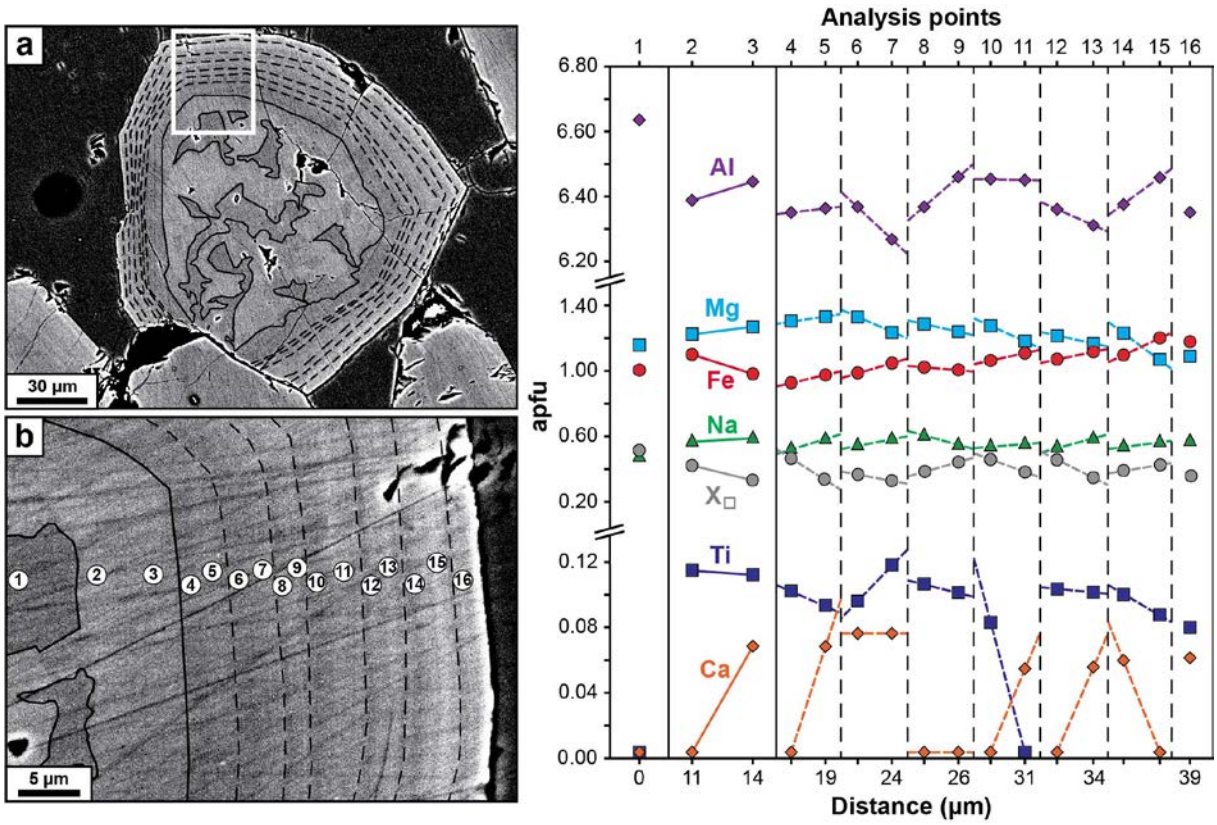

Fig. 135: EDS compositional profile in a tourmaline crystal from the tourmalinite on a gneissic clast from the Puy-les-Vignes deposit (Tur 2; sample PLV-02-01a). (a) BSE image of a tourmaline crystal section approximately perpendicular to the c-axis. Interpretation of the internal zoning is underlined with black dashed lines. (b) Detail view of the oscillatory zoning at the micrometre-scale in the external overgrowth and location of the EDS analyses points.

7.1.2. Interpretative model and definition of fluid poles

Considering that fluid mixing represents the major process explaining the chemical variations in tourmalines, this raises the question of the identification of the different end-members representative of the fluid poles. Since Al, Fe and Mg are the main elements showing major variations in tourmalines, the observed compositions may correspond to mixing trends between two or more possible fluid poles.

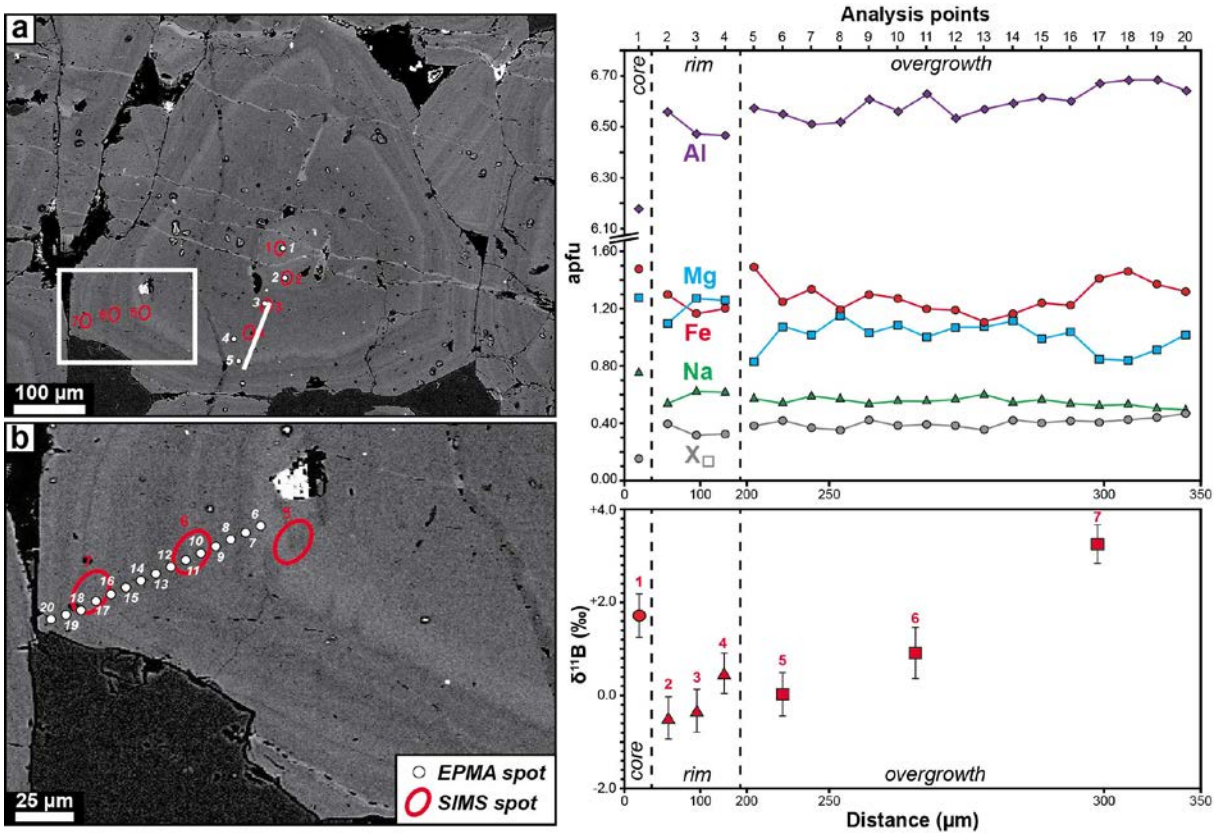

Fig. 136: Boron isotopes variations within a zoned tourmaline crystal from a tourmalinite of the Enguialès deposit (Tur 1; sample ENG-9b). The SIMS spots are represented by red ellipses with a major axis of 20 µm diameter.

In their study of the tourmalinites from the Ment granite, Boushaba and Marignac (2009) proposed a model to interpret the relative correlations in Al, Fe and Mg based on mixing trends between end-members, which may be identified in the Al-Fe-Mg diagram from Henry and Guidotti (1985). Following this methodology, it appears that the large majority of the tourmalines from the Puy-les-Vignes, Enguialès and St-Mélany deposits fall within the same quadrilateral in the Al-Fe-Mg diagram (Fig. 118, Fig. 124, Fig. 130). For each generation of tourmaline, the compositions from the different internal growth zones, i.e. core, rim and overgrowth, evolve into this quadrilateral and it appears that a few end-members are sufficient to describe the tourmaline zonation all along the history of the deposits by involving four main poles (Fig. 137): (i) an aluminous Fe-rich pole (A) which is projected in the upper part of the field of intra-granitic tourmalines and represent most the tourmaline compositions. In the detail, this pole can be actually sub-divided in two poles (A1) and (A2); (ii) an aluminous Mg-rich pole (B) projected in the upper part of the field of tourmalines from metasediments; (iii) a ferriferous pole (F) projected in the lower part of the field of intra-granitic tourmaline. In the same way, this pole can be sub-divided in two close poles (F1) and

(F2); and finally (iv) a magnesian pole (M) projected in the right bottom part of the field of the metasediments tourmalines, which can also be sub-divided in two poles (M1) and (M2). Mixing between these different poles may thus allow explaining the observed compositional variations in the tourmalines from the three deposits. In this regard, four main mixing trends between the different poles can be distinguished in the tourmalines studied: (i) mixing between the pole (M) with a mixing of poles (A) and (B), resulting in Al increasing correlated with Fe and anti-correlated with Mg decreasing; (ii) mixing of pole (F) with a mixing of poles (B) and (M), resulting in Al increasing correlated with Mg and anti-correlated with Fe decreasing; (iii) mixing of pole (B) with a mixing of poles (A) and (F) resulting in Al decreasing correlated with Mg and anti-correlated with Fe increasing; (iv) mixing of pole (A) with a mixing of poles (F) and (M) resulting in Al decreasing correlated with Fe and anti-correlated with Mg increasing.

7.1.3. Characterization of the mixing trends between the fluid poles

In the Al-Fe-Mg diagram (Fig. 137), the mixing trends between the four poles identified allow to characterize the chemical variations over time of the hydrothermal fluid systems crystallizing the tourmalines in the three studied deposits.

In the Puy-les-Vignes deposit (Fig. 118), the greisen tourmalines (Tur 1) have cores with compositions close to the pole (B), bright overgrowths falling on the pole (F1) and dark overgrowths correspond to the mixing trend between the poles (A1) and (M1). Tourmalines on the gneissic clasts (Tur 2a) have compositions close to the pole (A2), whereas those on the granitic clasts (Tur 2b) have cores and dark overgrowths falling close to the pole (B). The late corrosion tourmalines are clearly characterized by compositions toward the pole (F2). The acicular tourmalines (Tur 3) have core and overgrowths, which correspond to the composition of the pure (B) pole. Finally, breccia tourmalines (Tur 4) are the only one to have cores with composition of pole (A1) and with overgrowths showing a clear mixing trend toward the (M1) pole.

In the Enguialès deposit (Fig. 124), the tourmalinites (Tur 1) are characterized by cores with a composition of the pole (A1) and rims with compositions corresponding to a mixing trend between the pole (A1) and the pole (M2). The bright and dark overgrowths show small variations, which can be explained by a mixing between the poles (A1) and (F2). The acicular tourmalines (Tur 2) have similar compositions with cores falling on the (A1) pole and rims, which may correspond to a mixing between the pole (A1)-(A2) and the pole (M2).

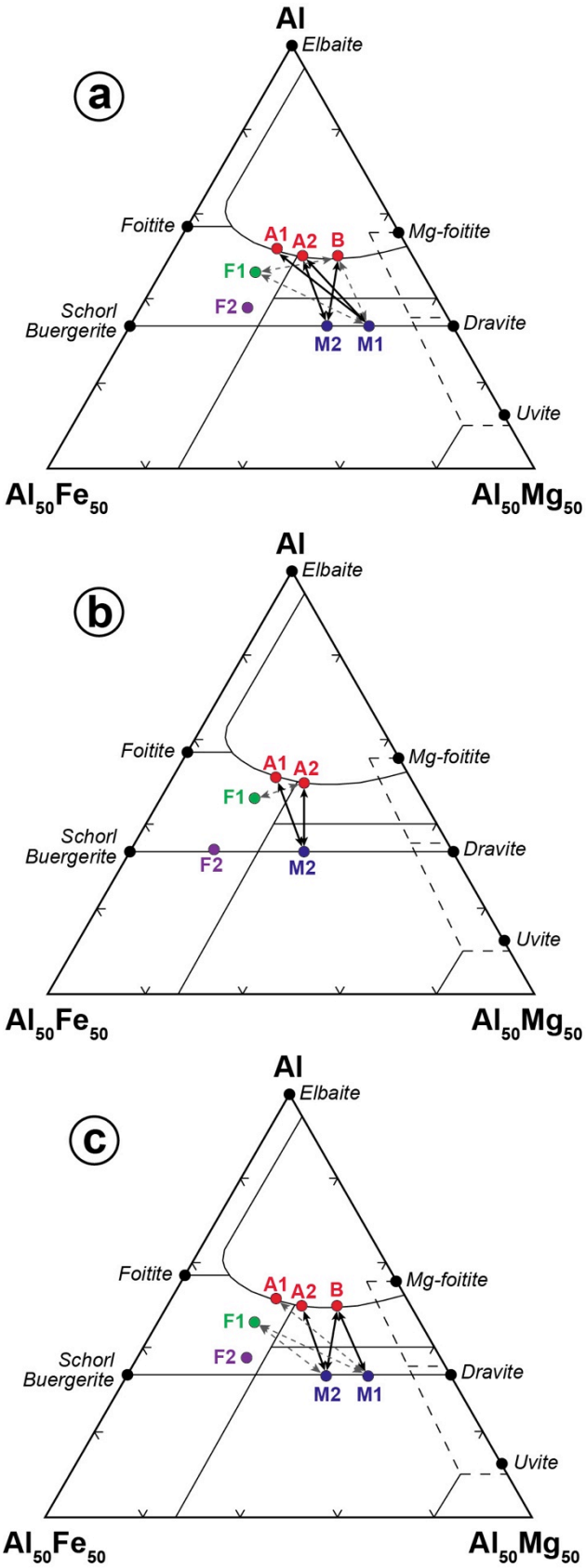

Fig. 137: Summary of the fluids poles and mixing trends observed in tourmaline from Puy-les-Vignes (a), Enguialès (b) and St-Mélany (c). Major trends are represented in dark solid lines and minor trends in grey dashed lines.

In the St-Mélany deposit (Fig. 130), the disseminated tourmalines (Tur 1a) and the selvages tourmalinites (Tur 2b) are both characterized by mixing trends between the pole (A2) and (M2). Acicular tourmalines (Tur 2) show however very distinct compositions marked by a core close to the (A1) pole, whereas the dark overgrowths show a mixing trend (A1)-(M2). Finally, the compositions of the late breccia tourmalines (Tur 3) and the tourmalines from the Beaume valley appear controlled by mixing trend between the poles (A2) and (M2).

In conclusion, the tourmalines from Puy-les-Vignes, Enguialès and St-Mélany are characterized by similar mixing trends involving four fluid poles (A, B, F, M). In particular, mixings between the aluminous poles (A) and (B) with the magnesian pole (M) appear frequent in most of the tourmalines.

7.2. Interpretation of the fluid poles in term of crustal reservoirs

Interpretation of the previously defined fluid poles in term of crustal reservoirs may be tentatively proposed from the trace elements compositions of tourmaline. Indeed, previous studies have already reported the utility of trace elements to distinguish between different fluid sources, particularly in complex magmatic-hydrothermal systems (e.g., Jiang and Palmer, 1998; Jiang et al., 2004, 2008; Marks et al., 2013; Drivenes et al., 2015).

In the Puy-les-Vignes deposit (Fig. 120; Table 32), the (M) pole falls in the field of tourmaline from metasediments and is characterized by medium trace elements compositions close to the clarke values of the UCC, without particular enrichment compared with the other tourmalines. This pole may correspond to fluid equilibrated with metasedimentary rocks, which constitute the enclosing rocks of the deposit (Fig. 113). The sub-division in poles (M1) and (M2) could then reflect lithology variations between micaschists and paragneisses, for instance. The (A) pole falls at the limit between the tourmalines from metasediments and granites in the Al-Fe-Mg diagram. It shows relative enrichment in Zn, V, Sc and Cr, and impoverishment in Ti, Sr, Pb, Li, REE compared to the UCC. This pole may correspond to the orthogneisses of the LGU (“Arc du Thaurion”), which are located at less than 10 km north from the deposit (Fig. 113). The pole (B) is characterized by relative enrichments in Li, Nb+Ta, W, Cs, Rb and Be, and depletion in Ti, Cr, Sc and V compared to the UCC. This geochemical signature is typical of an evolved granite. Since this pole shows a low Fe/Mg ratio, it may be interpreted as a Guéret-type granite, such as the Aureil granite, located at less than 5 km southwest of the Puy-les-Vignes deposit (Fig. 113). Finally, the pole (F), sub-divided in (F1) and (F2), has the lowest Al content and the highest Fe/Mg ratio. Its trace

element composition shows enrichments in V, Sc, Cr, Ti, Sn, Sr, REE, Y, Cu, Bi compared to the UCC, which correspond to intermediate compositions between felsic and mafic rocks. This pole may possibly be interpreted as the leptynite-amphibolite complex, which outcrops in the UGU, at less than 10 km southwest of Puy-les-Vignes.

In the Enguialès deposit (Fig. 126; Table 35), the pole (A) is characterized by enrichments in Li, Sn, W, V, Cr, Zn and impoverishments in Ti, REE, Nb+Ta compared to the UCC. This pole may represent an evolved granite, such as the Entraygues granite, located at less than 5 km south of the Enguialès deposit (Fig. 114). Tourmalines with compositions on a mixing trend between the poles (A) and (M) are characterized by trace elements compositions close to the UCC, excepted for Sn, V, Sc and Zn, which are enriched. This pole fall in the lower part of the tourmalines hosted in metasediments and may therefore represent metasedimentary rocks such as micaschists, which constitute the enclosing rocks of the Enguialès deposit.

At St-Mélany (Fig. 132; Table 38), the (A) pole is located in the intra-granitic field in the Al-Fe-Mg diagram and is characterized by enrichments in Li, Sn, W, Zn, medium contents in Nb+Ta, Sr, and impoverishments in V, Sc, Ti, Cr, Pb and REE compared to the UCC. This pole may correspond to a granitic pole with a high Fe/Mg ratio, which may be interpreted as the Rocles granite located at less than 2 km from the St-Mélany deposit (Fig. 115). At the opposite, the (M) pole characterized by a medium composition with minor enrichments in V, Ti, Cr, Pb compared to the UCC, may be interpreted as a metasedimentary pole, such as the enclosing Cévenol micaschists (Fig. 115).

The similarities of the mixing trends and fluid poles in the tourmalines from the three studied deposits suggest that they form regionally in a large hydrothermal system, where the fluid poles represent distinct crustal reservoirs. The temporal variability of the mixing suggests that the reservoirs are independent in space and implicated episodically in time to explain the zonation observed in tourmaline. Thus, it seems necessary that the separated fluid reservoirs be connected temporally via tectonic drains. In this purpose, two spatial scale of mixing must be considered: (i) a regional scale dominated by the mixing of external fluids from separated reservoirs, which are interconnected via crustal-scale drains, the opening of the latter being controlled by the regional tectonic stresses; (ii) a local scale allowing the internal mixing of the hydrothermal fluids within the deposit. In this last case, the access to the drains by the fluids is more likely controlled by the local tectonic structures and the permeability of the host-rocks. The succession of opening/closure of the tectonic joints allows then the fluid circulations, their mixing and the crystallization of zoned tourmaline. Whether

the composition of the fluids is significantly different, the latter will lead to a corrosion episode of the tourmaline.

7.3. Boron isotope signature in tourmalines: magmatic vs metamorphic source

It appears from the previous conclusions that metamorphic fluids play a major role in the tourmalinization process, which raises therefore the question of the source of boron. Previous B isotope studies on tourmaline from different Sn-W deposits in the Variscan belt concluded that boron had either a pure magmatic origin (e.g., Smith and Yardley, 1996; Pesquera et al., 2005; Ribeira da Costa et al., 2014; Drivenes et al., 2015) or a mixed magmatic-metamorphic origin (e.g., Jiang et al., 2008). However, the unambiguous distinction between B originating from granitic rocks or from metamorphic rocks is not always easy since there is a large overlap of their B isotopic composition. Indeed, the $\delta^{11}B$ values of tourmaline found in granites range from -15 to -5 ‰, whereas those from metamorphic rocks are comprise between -17 and +3 ‰ for tourmaline formed during prograde metamorphism and between -11 and +29 ‰ for those formed during retrograde metamorphism (Marschall and Jiang, 2011). Boron is known to be very mobile during fluid processes and especially through metamorphic dehydration reactions (van Hinsberg et al., 2011) and fluid-rock interactions (Weisbrod, 1987). Significant quantities of boron can be mobilized during the prograde metamorphism of sedimentary rocks by progressive decomposition of the phyllosilicates, which are the main primary hosts of boron containing up to 150 ppm (Leeman and Sisson, 1996; Sperlich et al., 1996; Nakano and Nakamura, 2001). Moreover, it has been experimentally demonstrated that B isotopes fractionate preferentially into the hydrothermal fluid phase rather than in minerals (Wunder et al., 2005; Meyer et al., 2008; Marschall et al., 2009). Consequently, the release of boron from metasedimentary rocks during the prograde to retrograde metamorphic path may represent a major source of B at a regional scale.

In the three deposits studied, the main tourmalinization episode is related to the early hydrothermal alteration leading to the formation of the tourmalinites at the selvages of the mineralized quartz-veins. This stage occurs systematically before the W mineralization episode and is likely controlled at the first order by the permeability of the country rocks and particularly by the existence of structural discontinuities playing the role of drains for fluid circulations. Detailed petrographic observations showed that tourmalinization appears as a diffuse process, which occurs by the progressive replacement of the phyllosilicates by B-rich

fluids (boron metasomatism), which is accompanied by the crystallization of tourmaline and chlorite with minor Ti-oxides. In the surroundings of Puy-les-Vignes and St-Mélany, no tourmaline-bearing granitic intrusions are known. In the Enguialès area, small tourmaline-bearing leucogranitic stocks are known, which crosscut the Marcolès and Entraygues porphyritic granites (Fig. 114). These intrusions were dated at 306 ± 3 Ma (^{40}Ar-^{39}Ar on muscovite; Monié et al., 2000) and appear temporally disconnected from the formation of the Enguialès W deposit according to the structural studies (see Chapter 1). Hence, a magmatic source of boron related to the intrusion of small leucogranitic bodies seems less probable in comparison with the large volume of boron-rich metasedimentary rocks, available in the surroundings of the deposits, which may be mobilized during the prograde metamorphism. Thus, it may be proposed that the boron was derived in majority from a metamorphic reservoir in the three studied deposits. In the La Châtaigneraie and the Cévennes area, the deposits are hosted in the micaschists from the PAU, which constitutes the main metasedimentary unit and is located at the bottom of the three-nappe pile system of the FMC (Ledru et al., 1989), and may therefore represent the source of boron. At Puy-les-Vignes (Fig. 113), the PAU is below the LGU enclosing the deposit, which would implicate the contribution of boron fluids derived from the underlying PAU at the regional scale.

7.4. W-Sn contents in tourmaline and implications for mineral exploration

The tourmalines from the Puy-les-Vignes, Enguialès and St-Mélany deposits commonly show enrichment in Sn (0.6-352 ppm) and W (0.1-20 ppm), with Sn contents (36 ppm in average) systematically higher than the W contents (2.5 ppm in average). The highest concentrations are found in tourmalines from St-Mélany, which contain up to 352 ppm Sn and 20 ppm W, which corresponds respectively to 168 and 11 times the clarke values of the UCC (Sn=2.1 ppm; W=1.9 ppm). Several studies already reported enrichments in Sn>W in tourmaline from cassiterite±wolframite-quartz-vein deposits (e.g., Williamson et al., 2000; Jiang et al., 2004; Mlynarczyk and Williams-Jones, 2006; Marks et al., 2013). This intriguing contrast may suggest that Sn is more easily incorporated into the tourmaline structure than W. Williamson et al. (2000) discussed the incorporation of tin and proposed that Sn^{4+}, with has an ionic radius of 0.69 Å in six coordination, is more easily incorporated within the tourmaline structure than Sn^{2+}, which has a very large ionic radius of 1.22 Å in eight coordination and 0.93 Å in six coordination. At the opposite, tungsten is usually present as W^{6+} in minerals with an ionic radius of 0.60 Å in octahedral coordination (Shannon, 1976), i.e., close to the

one of Sn^{4+}. However, the high charge-to-ionic-radius ratio of W^{6+} limits its substitution into the tourmaline, which may result likely in distortions of the crystalline network. Therefore, it seems likely that Sn is preferentially incorporated into the tourmaline structure than W, although it remains unknown which crystallochemical site(s) is occupied by these two elements. Sn^{4+} may possibly substitute to Ti^{4+} in tourmaline, which has an ionic radius of 0.6 Å, similar to the one of W^{6+} (Shannon, 1976). However, no statistical correlation was observed between Sn^{4+} and Ti^{4+}.

The high Sn and W contents in tourmaline from the three studied deposits raise the question about its use as a potential guide for mineral exploration. Indeed, the use of the chemical composition of tourmaline as a proximal indicator of mineralization has been already demonstrated, for instance in the case of orogenic gold deposits (e.g., Jiang et al., 2002), porphyry deposits (e.g., Baksheev et al., 2012) or massive sulphides deposits (e.g., Griffin et al., 1996). It can be noted that the highest Sn (±W) contents are found in acicular tourmalines disseminated in the quartz-wolframite-cassiterite veins and interpreted as syn-mineralization. In contrast, tourmalines associated with earlier and later stages have frequently lower W concentrations close or below the clarke value. Acicular tourmalines in the barren quartz veins from the Beaume valley, located at around 7 km from the St-Mélany showing, show no enrichment in Sn and W and are relatively depleted in these elements compared to the UCC. Moreover, they distinguish by a distinct B isotopic composition with a $\delta^{11}B$ difference of 4.5 ‰ in average compared to the acicular tourmalines from St-Mélany. These results suggest that in the case where regional tourmalinization are known, the trace elements contents and the B isotopic composition of tourmaline may potentially serve as a proximal indicator of Sn-W mineralization and could help to distinguish between mineralized and barren zones.

8. Conclusions

This work allowed to study the tourmalinization associated with three W±Sn deposits in the FMC through an integrated approach combining mineralogical and textural observations, chemical compositions of major, minor and trace elements and boron isotopic analyses of tourmaline. In the three studied deposits (Puy-les-Vignes, Enguialès, St-Mélany), the tourmalinization represents the main hydrothermal alteration and occurs systematically through a multi-stage process, either during an early alteration stage, during the emplacement of the mineralized veins or during late fracturing episodes. The successive generations of

tourmalines identified show numerous similarities between the three deposits, indicating that the tourmalinization occurs through a common boron metasomatism mechanism at the regional scale, involving several hydrothermal fluid circulations with time. Detailed analysis of representative tourmaline crystals indicate that the tourmalinization results from a discontinuous fluid mixing process in open system, which involves periodic inputs of hydrothermal fluids with different compositions over time. Reporting the compositions of tourmalines in the classical Al-Fe-Mg diagram from Henry and Guidotti (1985), it appears that the tourmaline from the three W±Sn deposits fall within the same quadrilateral and that four main fluid poles are sufficient to describe the chemical zonation in tourmalines all along the history of the deposits by involving mixing trends between these end-members. Interpretation of these fluid poles in terms of crustal reservoirs has been possible from the trace elements analysis of tourmalines and revealed the contribution of fluids equilibrated with granites, orthogneisses and metasedimentary rocks. The boron isotope signatures of tourmalines are not easy to interpret due to the large overlap of $\delta^{11}B$ values of the magmatic and metamorphic reservoirs. However, considering the possible reservoirs of boron in the three studied areas, it may be proposed that the boron source likely derived in majority from the metasedimentary rocks, which constitute the enclosing rocks of the three studied deposits. In this regard, the PAU seems to represent an important boron reservoir at the regional scale. Finally, the tourmalines from the Puy-les-Vignes, Enguialès and St-Mélany deposits commonly show enrichment in Sn (36 ppm in average) and W (2.5 ppm in average), with Sn>W contents. In comparison, tourmalines from barren quartz-veins close to St-Mélany show no enrichment in Sn and W and have a distinct B isotope signature. Consequently, it may be proposed that the trace elements contents and the B isotopic composition of tourmaline may potentially serve as a proximal indicator of Sn-W mineralization and could help to distinguish between mineralized and barren zones.

Table 30: WDS configuration used for EPMA of tourmaline.

Element	Standard	Crystal	Average detection limit (ppm)	Standard deviation (wt.%)
Si Kα	Albite	TAP	500	0.40
Al Kα	Al_2O_3	TAP	460	0.30
Na Kα	Albite	TAP	615	0.20
Mg Kα	Olivine	TAP	430	0.20
Fe Kα	Hematite	LIF	1710	0.50
Mn Kα	$MnTiO_3$	LIF	1600	0.15
K Kα	Orthose	LPET	340	0.05
Ti Kα	$MnTiO_3$	LPET	380	0.05
Ca Kα	Andradite	PET	610	0.10
Cr Kα	Cr_2O_3	PET	890	0.10

Table 31: Representative chemical compositions of tourmaline from Puy-les-Vignes.

	Tourmaline from greisen				Tourmalinites from gneissic clast				Tourmalinites from granitic clast				Acicular tourmalines				Breccia tourmalines			
	Sample PLV-02-08a				*Sample PLV-02-01a*				*Sample PLV-02-04a*				*Sample PLV-02-01c*				*Sample PLV-02-13b*			
	Core	Replaced core	Bright overgrowth	Dark overgrowth	Core	Replaced core	Dark overgrowth		Core	Bright overgrowth	Dark overgrowth	Corrosion	Core	Rim			Core	Replaced core	Bright overgrowth	Dark overgrowth
	1	4	6	10	10	13	16_1	16_2	68	70	86	8	1	2	3	4	43	52	44	47
SiO_2	36.68	35.95	35.88	36.75	36.87	36.32	36.44	36.61	36.41	35.41	35.85	35.93	36.97	36.86	36.15	36.79	36.93	35.45	35.62	36.54
TiO_2	0.23	0.48	0.40	0.33	0.21	1.04	0.71	0.74	0.20	0.65	0.79	1.09	0.32	0.27	0.70	0.35	0.20	0.93	1.03	0.67
Al_2O_3	34.55	33.86	33.86	32.46	35.83	33.69	34.26	33.94	35.93	34.23	34.13	30.01	35.61	35.82	34.27	34.89	33.31	31.45	30.79	31.50
Cr_2O_3	0.00	0.00	0.00	0.00	0.00	0.00	0.00	0.00	0.00	0.00	0.00	2.06	0.00	0.00	0.00	0.00	0.00	0.00	0.00	0.00
FeO	5.89	8.45	10.52	5.74	7.60	8.61	7.29	7.23	5.10	10.57	5.92	10.88	5.55	5.90	6.81	6.05	7.96	9.65	8.35	6.19
MgO	6.59	5.30	4.16	8.45	5.07	5.12	5.78	5.73	6.53	3.32	6.92	3.76	6.06	5.97	5.95	5.95	4.31	4.45	5.93	6.77
CaO	0.39	0.33	0.32	0.77	0.15	0.35	0.32	0.34	0.19	0.26	0.44	0.00	0.24	0.28	0.45	0.26	0.13	0.46	0.48	0.39
MnO	0.00	0.00	0.00	0.00	0.00	0.00	0.00	0.00	0.00	0.00	0.00	0.00	0.00	0.00	0.00	0.00	0.00	0.00	0.00	0.00
Na_2O	2.02	2.02	2.01	2.25	1.56	1.82	1.95	1.86	1.83	1.58	1.88	1.92	1.80	1.76	1.80	1.71	1.47	1.72	1.96	1.85
K_2O	0.00	0.00	0.00	0.00	0.00	0.00	0.00	0.00	0.00	0.00	0.00	0.00	0.00	0.00	0.00	0.00	0.05	0.05	0.05	0.06
F	0.00	0.00	0.00	0.00	0.00	0.00	0.00	0.00	0.00	0.00	0.00	0.00	0.00	0.00	0.00	0.00	0.00	0.00	0.00	0.00
H_2O*	3.73	3.59	3.67	3.45	3.75	3.70	3.72	3.71	3.74	3.63	3.76	3.58	3.76	3.76	3.70	3.73	3.64	3.56	3.57	3.62
B_2O_3*	10.81	10.65	10.63	10.78	10.88	10.73	10.78	10.76	10.85	10.52	10.91	10.37	10.90	10.91	10.73	10.80	10.56	10.31	10.35	10.50
Li_2O*	0.25	0.18	0.16	0.10	0.18	0.23	0.24	0.27	0.19	0.19	0.23	0.29	0.30	0.26	0.23	0.27	0.54	0.26	0.20	0.37
Total	101.1	101.0	101.6	101.7	102.1	101.6	101.5	101.2	101.0	100.4	100.8	99.88	101.5	101.8	100.8	100.8	99.10	98.29	98.34	98.46
Structural formula (apfu)																				
T-site																				
Si	5.90	5.87	5.87	5.92	5.89	5.89	5.88	5.92	5.83	5.85	5.89	6.02	5.89	5.87	5.86	5.92	6.08	5.98	5.98	6.05
Al	0.10	0.13	0.13	0.08	0.11	0.11	0.12	0.08	0.17	0.15	0.11	0.00	0.11	0.13	0.14	0.08	0.00	0.02	0.02	0.00
B	3.00	3.00	3.00	3.00	3.00	3.00	3.00	3.00	3.00	3.00	3.00	3.00	3.00	3.00	3.00	3.00	3.00	3.00	3.00	3.00
Z-site																				
Al	6.00	6.00	6.00	6.00	6.00	6.00	6.00	6.00	6.00	6.00	6.00	5.93	6.00	6.00	6.00	6.00	6.00	6.00	6.00	6.00
Mg	0.00	0.00	0.00	0.00	0.00	0.00	0.00	0.00	0.00	0.00	0.00	0.07	0.00	0.00	0.00	0.00	0.00	0.00	0.00	0.00
Cr	0.00	0.00	0.00	0.00	0.00	0.00	0.00	0.00	0.00	0.00	0.00	0.00	0.00	0.00	0.00	0.00	0.00	0.00	0.00	0.00
Fe^{3+}	0.00	0.00	0.00	0.00	0.00	0.00	0.00	0.00	0.00	0.00	0.00	0.00	0.00	0.00	0.00	0.00	0.00	0.00	0.00	0.00
Y-site																				
Al	0.44	0.38	0.39	0.09	0.64	0.32	0.39	0.38	0.61	0.52	0.57	0.00	0.59	0.59	0.40	0.54	0.46	0.23	0.07	0.14
Ti	0.03	0.06	0.05	0.04	0.03	0.13	0.09	0.09	0.02	0.08	0.02	0.14	0.04	0.03	0.09	0.04	0.02	0.12	0.13	0.08
Cr	0.00	0.00	0.00	0.00	0.00	0.00	0.00	0.00	0.00	0.00	0.00	0.27	0.00	0.00	0.00	0.00	0.00	0.00	0.00	0.00
Fe^{3+}	0.00	0.00	0.00	0.00	0.00	0.00	0.00	0.00	0.00	0.00	0.00	0.00	0.00	0.00	0.00	0.00	0.00	0.00	0.00	0.00
Mg	1.58	1.29	1.01	2.03	1.21	1.24	1.39	1.38	1.56	0.82	1.61	0.87	1.44	1.42	1.44	1.43	1.06	1.12	1.48	1.67
Mn	0.00	0.00	0.00	0.00	0.00	0.00	0.00	0.00	0.00	0.00	0.00	0.00	0.00	0.00	0.00	0.00	0.00	0.00	0.00	0.00
Fe^{2+}	0.79	1.15	1.44	0.77	1.02	1.17	0.98	0.98	0.68	1.46	0.66	1.53	0.74	0.79	0.92	0.81	1.10	1.36	1.17	0.86
Li*	0.16	0.12	0.11	0.06	0.11	0.15	0.15	0.17	0.12	0.13	0.14	0.20	0.20	0.17	0.15	0.17	0.36	0.18	0.14	0.25
X-site																				
Ca	0.07	0.06	0.06	0.13	0.03	0.06	0.06	0.06	0.03	0.05	0.04	0.00	0.04	0.05	0.08	0.04	0.02	0.08	0.09	0.07
Na	0.63	0.64	0.64	0.70	0.48	0.57	0.61	0.58	0.57	0.51	0.57	0.62	0.56	0.54	0.57	0.53	0.47	0.56	0.64	0.59
K	0.00	0.00	0.00	0.00	0.00	0.00	0.00	0.00	0.00	0.00	0.00	0.00	0.00	0.00	0.00	0.00	0.01	0.01	0.01	0.01
□	0.30	0.30	0.31	0.16	0.49	0.37	0.34	0.36	0.40	0.45	0.39	0.38	0.40	0.41	0.36	0.42	0.50	0.34	0.26	0.32
OH	4.00	4.00	4.00	4.00	4.00	4.00	4.00	4.00	4.00	4.00	4.00	4.00	4.00	4.00	4.00	4.00	4.00	4.00	4.00	4.00
F	0.00	0.09	0.00	0.30	0.00	0.00	0.00	0.00	0.00	0.00	0.00	0.00	0.00	0.00	0.00	0.00	0.00	0.00	0.00	0.00

Structural formula based on 31 anions (O, OH, F). B_2O_3, H_2O and Li_2O calculated by stoichiometry assuming B=3 apfu, OH+F=4 apfu and Li=15-total(T+Z+Y) and normalizing to 31 anions. * Calculated.

Table 32: Trace elements compositions of tourmalines (in ppm) from Puy-les-Vignes.

	Tourmaline from greisen *Sample PLV-02-08a*								**Tourmalinites from gneissic clast** *Sample PLV-02-01a*								**Acicular tourmalines** *Sample PLV-02-01c*			
	Core (n=6)				Rim (n=6)				Core (n=3)				Replaced core (n=2)				Core (n=12)			
	Dark overgrowth (n=2)												Dark overgrowth (n=15)							
	Mean	SD	Min	Max	Mean	SD	Min	Max	Mean	SD	Min	Max	Mean	SD	Min	Max	Mean	SD	Min	Max
Li	28	3.6	22	33	27	1.0	25	28	28	2.8	27	30	18	2.9	15	20	26	4.1	23	29	26	3.4	22	32	24	3.9	18	30
Be	16	-	16	16	4.8	-	4.8	4.8	14	-	14	14	12	2.1	11	14	47	-	47	47	23	-	23	23	10	4.9	3.7	16
Sc	8.4	2.1	5.2	11	17	12	6.7	37	11.3	1.7	10	12	28	11	19	40	30	13	21	40	18	7.0	11	39	20	4.1	14	27
Ti	1267	205	1015	1526	4263	2038	1720	7778	2187	966	1505	2870	1531	282	1352	1856	4617	162	4502	4731	3947	513	3379	4721	2616	657	1478	3705
V	78	11	64	96	240	84	108	323	134	37	108	161	170	24	146	195	216	3.2	214	218	200	20	172	235	118	26	73	166
Cr	27	7.5	17	37	460	344	45	968	50	16	39	62	164	93	98	229	109	46	77	142	41	49	9.2	114	141	84	21	289
Co	14	1.8	12	17	12	5.2	5.5	20	6.8	5.1	3.2	10	18	0.87	17	18	17	0.77	17	18	14	2.4	9.5	20	11	1.2	9.6	13.8
Ni	bdl	bdl	bdl	bdl	bdl	bdl	bdl	bdl	bdl	bdl	bdl	bdl	bdl	bdl	bdl	bdl	bdl	bdl	bdl	bdl	bdl	bdl	bdl	bdl	bdl	bdl	bdl	bdl
Cu	bdl	bdl	bdl	bdl	bdl	bdl	bdl	bdl	bdl	bdl	bdl	bdl	bdl	bdl	bdl	bdl	bdl	bdl	bdl	bdl	bdl	bdl	bdl	bdl	bdl	bdl	bdl	bdl
Zn	103	2.5	99	106	98	18	70	123	65	5.5	61	69	109	18	96	129	116	14	106	126	114	6.1	104	124	120	11	98	136
Rb	35	22	14	77	7.4	-	7.4	7.4	13	7.3	8.0	18	bdl	bdl	bdl	bdl	bdl	bdl	bdl	bdl	bdl	bdl	bdl	bdl	bdl	bdl	bdl	bdl
Sr	50	13	34	74	60	6.3	52	67	100	72	49	151	27	12	17	41	70	9.3	63	76	60	7.2	52	75	95	18	54	123
Y	bdl	bdl	bdl	bdl	bdl	bdl	bdl	bdl	0.60	-	0.60	0.6	bdl	bdl	bdl	bdl	bdl	bdl	bdl	bdl	0.14	-	0.14	0.14	0.66	0.86	0.13	2.5
Zr	1.7	-	1.7	1.7	0.57	-	0.6	0.6	2.3	2.3	0.72	4.0	0.75	-	0.75	0.75	bdl	bdl	bdl	bdl	0.57	-	0.57	0.57	2.2	2.5	0.56	8.3
Nb	0.78	0.47	0.32	1.6	0.27	0.1	0.2	0.4	bdl	bdl	bdl	bdl	bdl	bdl	bdl	bdl	0.58	-	0.58	bdl	0.23	-	0.23	0.23	0.36	0.20	0.15	0.73
Mo	bdl	bdl	bdl	bdl	bdl	bdl	bdl	bdl	bdl	bdl	bdl	bdl	bdl	bdl	bdl	bdl	bdl	bdl	bdl	bdl	3.5	1.6	2.6	5.8	1.3	-	1.3	1.3
Sn	33	8.4	23	44	19	6.8	12	31	26	8.5	20	32	33	6.0	27	38	28	17	17	40	26	5.7	17	38	40	16	21	81
Cs	2.5	1.5	0.9	4.9	bdl	bdl	bdl	bdl	1.0	-	1.0	1.0	bdl	bdl	bdl	bdl	bdl	bdl	bdl	bdl	bdl	bdl	bdl	bdl	bdl	bdl	bdl	bdl
Ba	77	62	20	193	4.3	-	4.3	4.3	24	5.0	20	27	bdl	bdl	bdl	bdl	bdl	bdl	bdl	bdl	2.3	0.16	2.1	2.4	0.53	-	0.53	0.53
La	0.68	0.26	0.34	1.04	0.71	0.28	0.37	1.2	1.4	-	1.4	1.4	bdl	bdl	bdl	bdl	0.75	0.20	0.61	0.89	0.82	0.12	0.58	1.1	2.0	3.4	0.32	13
Ce	1.0	0.30	0.63	1.4	1.2	0.49	0.56	1.8	1.3	1.0	0.62	2.0	0.38	0.02	0.36	0.39	1.6	0.20	1.4	1.7	1.4	0.24	1.2	2.1	1.6	0.48	0.42	2.3
Pr	bdl	bdl	bdl	bdl	0.18	-	0.18	0.18	bdl	bdl	bdl	bdl	bdl	bdl	bdl	bdl	0.11	-	0.11	0.11	0.18	0.04	0.12	0.23	0.14	0.04	0.09	0.19
Nd	bdl	bdl	bdl	bdl	0.50		0.50	0.50	bdl	bdl	bdl	bdl	bdl	bdl	bdl	bdl	bdl	bdl	bdl	bdl	0.72	-	0.72	0.72	0.48	0.19	0.34	0.77
Sm	bdl	bdl	bdl	bdl	bdl	bdl	bdl	bdl	bdl	bdl	bdl	bdl	bdl	bdl	bdl	bdl	bdl	bdl	bdl	bdl	bdl	bdl	bdl	bdl	0.56	-	0.56	0.56
Eu	0.43		0.43	0.43	0.32	0.07	0.27	0.37	bdl	bdl	bdl	bdl	bdl	bdl	bdl	bdl	0.30	-	0.30	0.30	0.38	0.11	0.24	0.55	0.41	0.10	0.20	0.54
Gd	bdl	bdl	bdl	bdl	bdl	bdl	bdl	bdl	bdl	bdl	bdl	bdl	bdl	bdl	bdl	bdl	bdl	bdl	bdl	bdl	bdl	bdl	bdl	bdl	bdl	bdl	bdl	bdl
Tb	bdl	bdl	bdl	bdl	bdl	bdl	bdl	bdl	bdl	bdl	bdl	bdl	bdl	bdl	bdl	bdl	bdl	bdl	bdl	bdl	0.15	-	0.15	0.15	bdl	bdl	bdl	bdl
Dy	bdl	bdl	bdl	bdl	bdl	bdl	bdl	bdl	bdl	bdl	bdl	bdl	bdl	bdl	bdl	bdl	bdl	bdl	bdl	bdl	bdl	bdl	bdl	bdl	bdl	bdl	bdl	bdl
Ho	bdl	bdl	bdl	bdl	bdl	bdl	bdl	bdl	bdl	bdl	bdl	bdl	bdl	bdl	bdl	bdl	bdl	bdl	bdl	bdl	bdl	bdl	bdl	bdl	0.07	-	0.07	0.07
Er	bdl	bdl	bdl	bdl	bdl	bdl	bdl	bdl	bdl	bdl	bdl	bdl	bdl	bdl	bdl	bdl	bdl	bdl	bdl	bdl	bdl	bdl	bdl	bdl	0.48	0.38	0.22	0.75
Tm	bdl	bdl	bdl	bdl	bdl	bdl	bdl	bdl	bdl	bdl	bdl	bdl	bdl	bdl	bdl	bdl	bdl	bdl	bdl	bdl	bdl	bdl	bdl	bdl	0.09	0.06	0.05	0.16
Yb	bdl	bdl	bdl	bdl	bdl	bdl	bdl	bdl	bdl	bdl	bdl	bdl	bdl	bdl	bdl	bdl	bdl	bdl	bdl	bdl	bdl	bdl	bdl	bdl	1.2	1.5	0.26	3.4
Lu	bdl	bdl	bdl	bdl	bdl	bdl	bdl	bdl	bdl	bdl	bdl	bdl	bdl	bdl	bdl	bdl	bdl	bdl	bdl	bdl	bdl	bdl	bdl	bdl	0.32	0.32	0.11	0.79
∑REE	1.7	0.55	1.0	2.4	2.1	1.0	1.2	3.9	2.0	2.0	0.62	3.4	0.25	0.22	0.10	0.39	2.5	0.11	2.4	2.6	2.5	0.48	1.9	3.7	4.8	3.6	0.74	15
Ta	bdl	bdl	bdl	bdl	0.16	0.04	0.13	0.19	bdl	bdl	bdl	bdl	bdl	bdl	bdl	bdl	bdl	bdl	bdl	bdl	0.19	-	0.19	0.19	0.26	0.15	0.12	0.60
W	8.9	5.5	4.0	19	bdl	bdl	bdl	bdl	3.4	0.32	3.2	3.6	bdl	bdl	bdl	bdl	bdl	bdl	bdl	bdl	5.6	2.7	1.6	9.2	3.0	3.5	0.31	8.9
Pb	3.4	1.2	2.4	5.7	3.0	0.58	2.0	3.8	7.5	7.0	2.6	12	1.7	0.30	1.5	1.9	2.6	0.04	2.6	2.7	3.3	1.2	1.8	7.2	3.4	1.5	2.0	7.7
Bi	bdl	bdl	bdl	bdl	0.95	-	0.9	0.9	bdl	bdl	bdl	bdl	bdl	bdl	bdl	bdl	bdl	bdl	bdl	bdl	12	-	12	12	0.39	0.34	0.15	0.64
Th	bdl	bdl	bdl	bdl	bdl	bdl	bdl	bdl	bdl	bdl	bdl	bdl	bdl	bdl	bdl	bdl	bdl	bdl	bdl	bdl	bdl	bdl	bdl	bdl	bdl	bdl	bdl	bdl
U	bdl	bdl	bdl	bdl	0.15	-	0.15	0.15	1.0	-	1.0	1.0	0.36	-	0.36	0.36	bdl	bdl	bdl	bdl	0.29	0.12	0.18	0.42	0.13	-	0.13	0.13

bdl: below detection limit

Table 32: Continued.

	Tourmalinites from granitic clast												Breccia tourmalines									
	Sample PLV-02-04a												*Sample PLV-02-13a/b*									
	Core (n=11)			Bright overgrowth (n=6)			Dark overgrowth (n=6)			Corrosion (n=4)			Core (n=7)			Bright overgrowth (n=9)			Dark overgrowth (n=9)		
	Mean	SD	Min	Mean	SD	Min	Mean	SD	Min	Mean	SD	Min	Mean	SD	Min	Mean	SD	Min	Mean	SD	Min	Max
Li	24	4.5	16	27	2.2	24	19	3.4	14	24	27	6.0	20	34	17	5.4	11	25	29	4.5	23	36	27	8.4	16	46
Be	7.0	2.6	3.8	12	bdl	bdl	8.3	4.9	4.0	14	10	8.6	5.1	23	7	5.3	3.1	16	9.1	2.2	6.0	11	9.3	7.3	4.0	20
Sc	14	3.2	10	20	10	1.1	8.5	12	12	2.7	9.7	17	90	6.9	81	98	49	31	26	118	27	6.1	18	36	96	70	17	228
Ti	3094	739	1925	4215	3767	317	3203	4066	1141	457	579	1907	4143	1334	2841	5998	1041	236	806	1384	4577	1064	2641	5760	3853	1396	1553	5802
V	150	14	125	175	150	4.0	145	154	175	29	141	227	552	180	404	804	200	53	89	238	245	40	161	287	183	34	135	222
Cr	759	116	562	988	845	178	716	1189	1228	276	1030	1775	8704	3075	6515	13058	310	190	26	531	1459	883	119	2385	194	171	13	419
Co	bdl	bdl	bdl	bdl	bdl	bdl	bdl	bdl	bdl	bdl	bdl	bdl	bdl	bdl	bdl	bdl	7.5	6.2	2.6	bdl	15	3.0	13	23	5.2	7.9	0.8	17
Ni	bdl	bdl	bdl	bdl	bdl	bdl	bdl	bdl	bdl	bdl	bdl	bdl	bdl	bdl	bdl	bdl	bdl	bdl	bdl	bdl	33	12	20	53	36	-	36	36
Cu	7.3	5.6	2.7	18	6.7	2.5	4.9	8.5	11	5.7	5.3	17	39	27	7.0	71	bdl	82	52	280	82	4.5	76	90	83	68	45	261
Zn	61	5.0	52	70	68	3.4	64	72	41	2.1	39	44	63	6.1	56	71	101	82	52	280	82	4.5	76	90	83	68	45	261
Rb	5.8	7.7	1.8	25	12	8.3	0.88	22	1.3	0.52	0.73	1.8	2.2	1.1	1.2	3.4	bdl	bdl	bdl	bdl	bdl	bdl	bdl	bdl	1.4	-	1.4	1.4
Sr	92	10	75	107	56	2.9	51	60	148	25	116	193	146	60	104	232	28	8.7	19	45	62	22	30	88	122	77	27	264
Y	3.4	2.5	0.12	8.3	2.6	1.5	0.82	5.1	1.5	2.5	0.18	5.9	10.5	4.7	5.1	16	bdl	bdl	bdl	bdl	bdl	bdl	bdl	bdl	bdl	bdl	bdl	bdl
Zr	101	58	1.2	165	84	36	40	130	29	51	3.3	121	99	38	67	144	0.6	0.5	0.18	0.9	bdl	bdl	bdl	bdl	bdl	bdl	bdl	bdl
Nb	0.35	0.25	0.09	0.89	0.25	0.18	0.08	0.52	bdl	bdl	bdl	bdl	0.31	0.20	0.15	0.53	0.31	0.29	0.11	0.6	0.28	-	0.28	0.28	0.6	0.17	0.42	0.8
Mo	bdl	bdl	bdl	bdl	bdl	bdl	bdl	bdl	0.5	-	0.5	0.5	bdl	bdl	bdl	bdl	bdl	bdl	bdl	bdl	bdl	bdl	bdl	bdl	bdl	bdl	bdl	bdl
Sn	45	19	14	71	12	1.0	11	13	45	12	37	67	90	38	63	147	23	9.4	13	39	11	1.5	8.0	13	33	18	7.7	69
Cs	1.3	1.1	0.4	3.3	3.4	2.1	1.3	6.4	0.36	-	0.36	0.36	0.75	-	0.75	0.75	bdl	bdl	bdl	bdl	bdl	1.1	1.1	1.1	bdl	bdl	bdl	bdl
Ba	12	29	0.70	92	2.8	1.5	0.88	5.5	1.8	-	1.8	1.8	4.0	2.4	2.1	7.0	bdl	bdl	bdl	bdl	bdl	bdl	bdl	bdl	bdl	bdl	bdl	bdl
La	0.65	0.14	0.51	1.0	1.0	0.58	0.71	2.2	0.73	0.11	0.53	0.85	0.90	0.34	0.57	1.4	0.22	0.02	0.20	0.23	1.3	0.49	0.6	2.1	0.9	0.8	0.24	2.9
Ce	1.3	0.35	0.95	2.1	1.7	1.0	1.1	3.7	1.3	0.23	1.1	1.7	2.1	0.47	1.4	2.6	0.39	0.25	0.15	0.8	3.0	1.7	1.3	6.9	1.4	1.4	0.24	5.0
Pr	0.12	0.05	0.08	0.23	0.22	0.17	0.11	0.55	0.15	0.04	0.09	0.20	0.24	0.09	0.13	0.32	0.07	0.01	0.07	0.08	0.19	0.04	0.14	0.24	0.23	0.14	0.11	0.44
Nd	0.57	0.11	0.41	0.70	0.74	0.32	0.48	1.2	0.73	-	0.73	0.73	1.3	0.55	0.92	1.7	0.23	-	0.23	0.23	0.9	0.08	0.8	0.9	1.4	-	1.4	1.4
Sm	0.34	-	0.34	0.34	bdl	bdl	bdl	bdl	bdl	bdl	bdl	bdl	0.9	-	0.86	0.86	bdl	bdl	bdl	bdl	bdl	bdl	bdl	bdl	bdl	bdl	bdl	bdl
Eu	0.43	0.06	0.28	0.49	0.28	0.06	0.21	0.35	0.49	0.15	0.28	0.72	0.58	0.10	0.45	0.69	bdl	bdl	bdl	bdl	bdl	0.02	0.33	0.38	0.47	0.18	0.29	0.8
Gd	0.77	-	0.77	0.77	bdl	bdl	bdl	bdl	0.50	-	0.50	0.50	1.2	0.53	0.62	1.7	bdl	bdl	bdl	bdl	1.6	-	1.6	1.6	bdl	bdl	bdl	bdl
Tb	0.14	-	0.14	0.14	0.09	-	0.09	0.09	0.10	-	0.10	0.10	0.3	0.05	0.21	0.31	bdl	bdl	bdl	bdl	bdl	bdl	bdl	bdl	bdl	bdl	bdl	bdl
Dy	0.74	0.39	0.45	1.6	bdl	bdl	bdl	bdl	0.76	-	0.76	0.76	1.6	0.55	0.95	2.1	bdl	bdl	bdl	bdl	bdl	bdl	bdl	bdl	bdl	bdl	bdl	bdl
Ho	0.19	0.08	0.12	0.33	0.15	0.08	0.10	0.24	0.21	-	0.21	0.21	0.50	0.15	0.38	0.67	bdl	bdl	bdl	bdl	0.15	0.04	0.11	0.18	bdl	bdl	bdl	bdl
Er	0.64	0.31	0.25	1.1	0.40	0.13	0.26	0.54	0.95	-	0.95	0.95	1.3	0.69	0.48	1.9	0.40	-	0.40	0.40	bdl	bdl	bdl	bdl	bdl	bdl	bdl	bdl
Tm	0.14	0.03	0.10	0.17	0.14	0.01	0.13	0.15	0.15	-	0.15	0.15	0.23	0.08	0.14	0.29	bdl	bdl	bdl	bdl	bdl	bdl	bdl	bdl	bdl	bdl	bdl	bdl
Yb	1.1	0.43	0.41	1.7	1.0	0.44	0.47	1.5	0.82	0.36	0.56	1.1	1.8	0.85	0.71	2.6	bdl	bdl	bdl	bdl	bdl	bdl	bdl	bdl	bdl	bdl	bdl	bdl
Lu	0.20	0.05	0.11	0.25	0.14	0.06	0.10	0.19	0.22	-	0.22	0.2	0.34	0.25	0.12	0.66	bdl	bdl	bdl	bdl	bdl	bdl	bdl	bdl	bdl	bdl	bdl	bdl
∑REE	5.0	2.2	2.1	9.1	5.0	2.6	2.3	9.8	3.5	1.7	2.0	6.7	11.4	4.3	5.6	15	0.45	0.27	0.00	0.8	5.1	1.7	2.7	7.8	2.8	3.0	0.48	11
Ta	0.09	0.02	0.07	0.11	bdl	bdl	bdl	bdl	bdl	bdl	bdl	bdl	bdl	bdl	bdl	bdl	bdl	bdl	bdl	bdl	bdl	bdl	bdl	bdl	0.41	0.12	0.32	0.50
W	4.5	4.5	0.50	15	0.68	0.13	0.61	0.84	1.3	0.24	1.2	1.5	4.8	2.8	1.7	8.4	1.5	1.2	0.6	2.8	1.4	0.44	1.0	2.1	2.5	2.0	1.1	3.9
Pb	4.0	1.2	2.8	7.3	3.0	0.67	2.3	3.9	3.4	1.3	2.0	5.2	10.5	7.8	2.1	19	1.0	0.32	0.7	1.6	2.9	1.0	1.5	4.5	2.5	0.8	1.1	4.1
Bi	1.0	0.75	0.37	2.5	1.0	0.64	0.50	1.9	0.89	0.67	0.19	1.6	7.7	4.8	0.91	12	bdl	bdl	bdl	bdl	bdl	bdl	bdl	bdl	bdl	bdl	bdl	bdl
Th	1.8	1.0	0.15	3.6	1.1	0.89	0.27	2.7	1.3	1.5	0.31	2.4	3.5	1.3	1.7	4.5	bdl	bdl	bdl	bdl	bdl	bdl	bdl	bdl	bdl	bdl	bdl	bdl
U	3.8	2.4	0.09	6.5	4.5	2.7	1.5	8.6	1.1	2.0	0.18	5.2	5.1	2.2	2.8	8.0	bdl	bdl	bdl	bdl	bdl	bdl	bdl	bdl	bdl	bdl	bdl	bdl

bdl: below detection limit

Table 33: Boron isotopic compositions of tourmalines from Puy-les-Vignes.

Sample	Zone	$\delta^{11}B$ (‰)	± 1σ
Greisen tourmaline (PLV-02-08a)			
PLV-02-08a_6	Core	-4.22	0.39
PLV-02-08a_2	Core	-5.28	0.40
PLV-02-08a_8	Core	-3.85	0.42
PLV-02-08a_9	Core	-4.29	0.41
PLV-02-08a_3	Rim	-1.48	0.40
PLV-02-08a_4	Rim	-1.46	0.40
PLV-02-08a_1	Rim	-1.68	0.41
PLV-02-08a_10	Rim	-2.44	0.45
PLV-02-08a_11	Rim	-2.20	0.41
PLV-02-08a_5	Overgrowth	-2.39	0.38
PLV-02-08a_7	Overgrowth	-2.00	0.39
Tourmalinite (PLV-02-01a)			
PLV-02-01a_1	Core	-6.29	0.38
PLV-02-01a_3	Core	-7.30	0.39
PLV-02-01a_7	Core	-5.91	0.40
PLV-02-01a_8	Rim	-5.77	0.40
PLV-02-01a_2	Overgrowth	-6.38	0.38
PLV-02-01a_4	Overgrowth	-6.25	0.38
PLV-02-01a_5	Overgrowth	-5.68	0.40
PLV-02-01a_6	Overgrowth	-5.36	0.41
Acicular tourmaline (PLV-02-01c)			
PLV-02-01c_1	Core	-6.98	0.40
PLV-02-01c_03	Core	-6.34	0.39
PLV-02-01c_05	Core	-7.21	0.39
PLV-02-01c_06	Core	-6.84	0.38
PLV-02-01c_07	Core	-7.28	0.39
PLV-02-01c_10	Core	-6.93	0.39
PLV-02-01c_12	Core	-7.11	0.39
PLV-02-01c_02	Rim	-6.84	0.38
PLV-02-01c_08	Rim	-7.13	0.40
PLV-02-01c_04	Rim	-6.47	0.40
PLV-02-01c_09	Rim	-6.64	0.41
PLV-02-01c_11	Rim	-7.44	0.39
Breccia tourmalines (PLV-02-13b)			
PLV-02-13b_1	Core	-0.55	0.41
PLV-02-13b_7	Core	-0.45	0.45
PLV-02-13b_13	Core	-0.71	0.43
PLV-02-13b_14	Core	-1.29	0.42
PLV-02-13b_2	Rim	-6.20	0.39
PLV-02-13b_3	Rim	-6.30	0.41
PLV-02-13b_5	Rim	-4.66	0.40
PLV-02-13b_11	Rim	-4.52	0.49
PLV-02-13b_12	Rim	-6.27	0.42
PLV-02-13b_4	Overgrowth	-6.66	0.40
PLV-02-13b_6	Overgrowth	-7.48	0.40
PLV-02-13b_8	Overgrowth	-4.74	0.43
PLV-02-13b_9	Overgrowth	-4.75	0.42
PLV-02-13b_10	Overgrowth	-5.77	0.42
PLV-02-13b_15	Overgrowth	-5.97	0.40

Table 34: Representative chemical compositions of tourmaline from Enguialès.

	Tourmalinites at selvages of quartz veins								**Acicular tourmalines**							
	Sample ENG-9a/b								*Sample ENG-9b*				*Sample ENG-37*			*Sample CHA-14-18*	
	Core		Rim	Bright overgrowth		Dark overgrowth		Corrosion	Core	Rim		Corrosion	Core	Rim	Corrosion	Core	Rim	
	1	2	2	3	4	7-2	7-3	7	8	15	14		1	2-2	9	1	3-1	3-2
SiO_2	36.53	36.76	36.03	35.70	35.68	36.14	36.27	35.79	36.32	35.95	35.69		36.50	35.92	36.37	36.58	36.58	36.54
TiO_2	0.00	0.46	0.33	0.78	0.75	0.62	0.65	0.41	0.67	0.94	0.30		0.11	0.48	0.00	0.14	0.29	0.27
Al_2O_3	33.30	35.11	34.07	33.64	33.99	34.58	34.13	34.56	32.01	32.43	35.82		36.17	34.00	32.98	35.75	35.59	35.67
Cr_2O_3	0.00	0.00	0.00	0.00	0.00	0.00	0.00	0.00	0.00	0.00	0.00		0.00	0.00	0.00	0.00	0.00	0.00
FeO	8.30	8.65	8.34	10.32	10.71	8.89	8.24	14.10	10.43	11.01	12.39		9.23	9.07	11.60	8.17	8.24	8.33
MgO	4.09	3.60	5.03	3.81	3.56	4.55	4.99	1.27	5.10	4.90	1.31		3.87	5.37	0.53	4.03	5.05	4.75
CaO	0.00	0.00	0.18	0.21	0.25	0.31	0.24	0.11	0.21	0.40	0.21		0.15	0.72	0.00	0.13	0.21	0.22
MnO	0.00	0.00	0.00	0.00	0.00	0.00	0.00	0.00	0.00	0.00	0.00		0.00	0.00	0.00	0.00	0.00	0.00
Na_2O	1.67	1.33	1.90	1.96	1.89	1.89	1.89	1.11	2.28	2.34	1.32		1.20	1.70	1.43	1.46	1.79	1.82
K_2O	0.00	0.00	0.00	0.00	0.00	0.00	0.00	0.00	0.17	0.00	0.00		0.00	0.00	0.00	0.00	0.00	0.00
F	0.00	0.00	0.00	0.00	0.00	0.00	0.00	0.00	0.00	0.00	0.00		0.00	0.00	0.00	0.00	0.00	0.00
H_2O*	3.61	3.69	3.44	3.50	3.50	3.58	3.52	3.63	3.66	3.67	3.66		3.72	3.62	3.55	3.71	3.71	3.70
B_2O_3*	10.47	10.70	10.62	10.57	10.60	10.73	10.70	10.52	10.60	10.65	10.61		10.79	10.70	10.28	10.75	10.87	10.86
Li_2O*	0.48	0.31	0.18	0.24	0.22	0.25	0.25	0.07	0.15	0.13	0.27		0.11	0.11	0.96	0.28	0.16	0.21
Total	98.44	100.60	100.12	100.72	101.15	101.54	100.88	101.57	101.59	102.42	101.58		101.86	101.69	97.69	100.99	102.49	102.37
Structural formula (apfu)																		
T-site																		
Si	6.07	5.97	5.90	5.87	5.85	5.85	5.89	5.91	5.96	5.87	5.85		5.88	5.83	6.15	5.91	5.85	5.85
Al	0.00	0.03	0.10	0.13	0.15	0.15	0.11	0.09	0.04	0.13	0.15		0.12	0.17	0.00	0.09	0.15	0.15
B	3.00	3.00	3.00	3.00	3.00	3.00	3.00	3.00	3.00	3.00	3.00		3.00	3.00	3.00	3.00	3.00	3.00
Z-site																		
Al	6.00	6.00	6.00	6.00	6.00	6.00	6.00	6.00	6.00	6.00	6.00		6.00	6.00	6.00	6.00	6.00	6.00
Mg	0.00	0.00	0.00	0.00	0.00	0.00	0.00	0.00	0.00	0.00	0.00		0.00	0.00	0.00	0.00	0.00	0.00
Cr	0.00	0.00	0.00	0.00	0.00	0.00	0.00	0.00	0.00	0.00	0.00		0.00	0.00	0.00	0.00	0.00	0.00
Fe^{3+}	0.00	0.00	0.00	0.00	0.00	0.00	0.00	0.00	0.00	0.00	0.00		0.00	0.00	0.00	0.00	0.00	0.00
Y-site																		
Al	0.52	0.70	0.47	0.39	0.42	0.46	0.43	0.64	0.14	0.11	0.77		0.74	0.34	0.57	0.73	0.56	0.58
Ti	0.00	0.06	0.04	0.10	0.09	0.08	0.08	0.05	0.08	0.12	0.04		0.01	0.06	0.00	0.02	0.03	0.03
Cr	0.00	0.00	0.00	0.00	0.00	0.00	0.00	0.00	0.00	0.00	0.00		0.00	0.00	0.00	0.00	0.00	0.00
Fe^{3+}	0.00	0.00	0.00	0.00	0.00	0.00	0.00	0.00	0.00	0.00	0.00		0.00	0.00	0.00	0.00	0.00	0.00
Mg	1.01	0.87	1.23	0.93	0.87	1.10	1.21	0.31	1.25	1.19	0.32		0.93	1.30	0.13	0.97	1.20	1.13
Mn	0.00	0.00	0.00	0.00	0.00	0.00	0.00	0.00	0.00	0.00	0.00		0.00	0.00	0.00	0.00	0.00	0.00
Fe^{2+}	1.15	1.18	1.14	1.42	1.47	1.20	1.12	1.95	1.43	1.50	1.70		1.24	1.23	1.64	1.10	1.10	1.12
Li*	0.32	0.20	0.12	0.16	0.15	0.16	0.16	0.05	0.10	0.08	0.18		0.07	0.07	0.65	0.18	0.10	0.14
X-site																		
Ca	0.00	0.00	0.03	0.04	0.04	0.05	0.04	0.02	0.04	0.07	0.04		0.03	0.13	0.00	0.02	0.04	0.04
Na	0.54	0.42	0.60	0.63	0.60	0.59	0.60	0.36	0.72	0.74	0.42		0.37	0.54	0.47	0.46	0.55	0.56
K	0.00	0.00	0.00	0.00	0.00	0.00	0.00	0.00	0.04	0.00	0.00		0.00	0.00	0.00	0.00	0.00	0.00
□	0.46	0.58	0.37	0.34	0.36	0.35	0.36	0.63	0.20	0.19	0.54		0.60	0.34	0.53	0.52	0.41	0.40
OH	4.00	4.00	3.76	3.84	3.83	3.87	3.82	4.00	4.00	4.00	4.00		4.00	3.92	4.00	4.00	3.95	3.95
F	0.00	0.00	0.24	0.16	0.17	0.13	0.18	0.00	0.00	0.00	0.00		0.00	0.08	0.00	0.00	0.05	0.05

Structural formula based on 31 anions (O, OH, F). B_2O_3, H_2O and Li_2O calculated by stoichiometry assuming B=3 apfu, OH+F=4 apfu and Li=15-total(T+Z+Y) and normalizing to 31 anions. * Calculated.

Table 35: Trace elements compositions of tourmaline (in ppm) from Enguialès.

	Tourmalinites at selvages of quartz veins												**Acicular tourmalines**							
	Sample ENG-9a/b												*Sample ENG-9b*							
	Core (n=16)				Replaced core (n=4)				Dark overgrowth (n=25)				Core (n=7)				Dark overgrowth (n=5)			
	Mean	SD	Min	Max	Mean	SD	Min	Max	Mean	SD	Min	Max	Mean	SD	Min	Max	Mean	SD	Min	Max
Li	30	5.3	21	42	33	4.3	29	38	36	4.6	27	45	44	7.7	31	53	44	7.7	33	52
Be	bdl	bdl	bdl	bdl	bdl	bdl	bdl	bdl	22	3.4	20	25	2.0	0.59	1.4	2.8	bdl	bdl	bdl	bdl
Sc	17	7.7	10	41	18	0.88	17	19	23	4.7	16	33	17	3.0	12	21	21	10	7.7	33
Ti	2885	796	1813	4735	3232	364	2826	3712	3113	555	2291	4550	3914	1335	2125	5626	3475	535	2662	3995
V	200	71	135	449	195	21	171	220	171	20	132	213	214	41	141	252	95	36	41	140
Cr	211	154	89	767	237	53	169	298	151	66	11	266	262	76	134	361	96	51	26	157
Co	23	7.3	14	38	25	0.89	23	25	18	2.6	14	27	32	2.4	28	36	26	10	16	42
Ni	115	5.7	109	121	16	2.2	14	18	9.2	2.5	4.2	12	38	8.3	32	55	28	14	11	39
Cu	5.2	5.1	1.7	8.8	bdl	bdl	bdl	bdl	bdl	bdl	bdl	bdl	6.2	-	6.2	6.2	bdl	bdl	bdl	bdl
Zn	154	42	113	258	161	5.6	156	168	157	19	108	194	266	20	240	292	186	15	166	205
Rb	1.6	1.6	0.38	3.4	bdl	bdl	bdl	bdl	bdl	bdl	bdl	bdl	bdl	bdl	bdl	bdl	bdl	bdl	bdl	bdl
Sr	146	80	72	318	138	7.0	131	145	117	20	57	153	270	84	128	364	182	74	103	268
Y	1.4	1.8	0.24	6.3	0.62	0.35	0.10	0.82	1.2	1.6	0.10	6.9	1.1	1.0	0.07	2.8	2.7	5.1	0.14	12
Zr	39	49	0.40	169	66	41	6.1	92	43	62	0.22	178	70	74	2.3	186	17	20	0.41	44
Nb	0.23	0.10	0.13	0.47	0.23	0.08	0.13	0.33	0.14	0.05	0.08	0.24	0.14	0.04	0.11	0.21	0.25	0.06	0.20	0.29
Mo	bdl	bdl	bdl	bdl	bdl	bdl	bdl	bdl	0.71	0.32	0.48	0.93	bdl	bdl	bdl	bdl	bdl	bdl	bdl	bdl
Sn	5.9	1.7	1.5	8.0	7.6	1.1	6.3	8.7	5.3	0.9	3.6	7.4	1.4	0.21	1.2	1.8	4.3	1.0	2.9	5.4
Cs	0.70	-	0.70	0.70	0.20	-	0.20	0.20	bdl	bdl	bdl	bdl	bdl	bdl	bdl	bdl	bdl	bdl	bdl	bdl
Ba	3.7	6.8	0.62	19	6.3	8.3	1.5	16	0.76	0.34	0.40	1.2	0.30	-	0.30	0.30	1.0	-	1.0	1.0
La	0.70	0.34	0.37	1.7	0.84	0.10	0.72	1.0	0.65	0.16	0.24	1.0	0.20	0.09	0.09	0.32	1.7	0.81	1.0	3.1
Ce	1.1	0.59	0.34	2.8	1.2	0.14	1.1	1.4	1.1	0.31	0.49	2.1	0.30	0.16	0.14	0.55	3.1	2.0	1.6	6.6
Pr	0.17	0.07	0.10	0.28	0.10	0.03	0.05	0.12	0.12	0.05	0.06	0.26	0.05	0.04	0.03	0.08	0.26	0.17	0.15	0.50
Nd	0.73	0.38	0.33	1.2	0.42	0.01	0.42	0.43	0.56	0.24	0.32	1.1	0.41	-	0.41	0.41	1.2	0.65	0.56	2.0
Sm	0.44	0.30	0.23	0.65	bdl	bdl	bdl	bdl	0.78	-	0.78	0.78	bdl	bdl	bdl	bdl	1.0	-	1.0	1.0
Eu	0.32	0.10	0.21	0.51	0.26	0.02	0.23	0.29	0.29	0.10	0.18	0.61	0.15	0.04	0.10	0.21	0.58	0.16	0.44	0.82
Gd	0.45	0.36	0.20	0.71	bdl	bdl	bdl	bdl	0.75	0.43	0.44	1.1	0.18	-	0.18	0.18	1.3	-	1.3	1.3
Tb	0.12	0.13	0.03	0.21	bdl	bdl	bdl	bdl	0.16	-	0.16	0.16	bdl	bdl	bdl	bdl	0.31	-	0.31	0.31
Dy	0.94	0.87	0.32	1.6	0.18	-	0.18	0.18	0.86	1.0	0.15	1.6	0.25	0.07	0.20	0.30	1.5	-	1.5	1.5
Ho	0.13	0.07	0.06	0.23	bdl	bdl	bdl	bdl	0.12	0.12	0.04	0.25	0.10	0.03	0.08	0.12	0.47	-	0.47	0.47
Er	0.54	0.32	0.32	0.90	0.18	0.04	0.15	0.21	0.41	0.23	0.20	0.85	0.36	0.06	0.32	0.43	1.1	-	1.1	1.1
Tm	0.11	0.07	0.03	0.15	0.05	-	0.05	0.05	0.08	0.05	0.04	0.16	0.10	0.06	0.05	0.17	bdl	bdl	bdl	bdl
Yb	0.76	0.33	0.43	1.2	0.41	0.10	0.34	0.48	0.75	0.29	0.28	1.2	0.69	0.19	0.50	0.88	2.4	-	2.4	2.4
Lu	0.12	0.06	0.07	0.16	0.09	0.02	0.06	0.11	0.14	0.06	0.09	0.25	0.13	0.07	0.07	0.20	0.52	-	0.52	0.52
∑REE	2.9	2.3	0.34	10	3.1	0.8	2.2	3.8	2.8	2.0	0.73	11	1.4	0.81	0.40	2.7	8.3	5.5	3.2	16
Ta	0.10	0.06	0.06	0.19	0.07	0.02	0.05	0.08	0.07	0.03	0.04	0.10	0.04	0.01	0.03	0.05	bdl	bdl	bdl	bdl
W	0.89	0.71	0.25	1.7	0.33	0.23	0.17	0.49	0.41	0.08	0.32	0.52	2.0	2.8	0.31	5.3	2.2	1.9	0.29	5.2
Pb	10	16	2.4	55	5.3	0.35	4.9	5.7	3.5	0.63	1.8	5.0	38	14	14	58	6.5	5.9	2.9	17
Bi	1.4	1.8	0.14	3.5	bdl	bdl	bdl	bdl	0.33	0.25	0.13	0.77	bdl	bdl	bdl	bdl	bdl	bdl	bdl	bdl
Th	0.29	0.16	0.08	0.47	0.10	0.01	0.09	0.11	0.34	0.25	0.11	1.0	0.23	0.12	0.11	0.42	5.0	5.1	1.4	8.7
U	0.87	0.55	0.22	1.7	1.1	0.61	0.29	1.7	0.94	0.87	0.13	2.6	1.7	1.6	0.13	4.3	2.2	2.8	0.45	5.5

bdl: below detection limit

Table 35: Continued.

	Acicular tourmalines															
	Sample ENG-37								*Sample CHA-14-18*							
	Core (n=11)				Overgrowth (n=11)				Core (n=13)				Overgrowth (n=9)			
	Mean	SD	Min	Max	Mean	SD	Min	Max	Mean	SD	Min	Max	Mean	SD	Min	Max
Li	11	1.7	9.1	14	36	5.5	25	46	17	6.2	7.6	24	27	2.8	23	32
Be	bdl	bdl	bdl	bdl	bdl	bdl	bdl	bdl	13	4.4	6.8	17	bdl	bdl	bdl	bdl
Sc	19	8.8	12	32	20	4.4	14	30	44	12	32	66	29	5.6	21	39
Ti	917	195	585	1149	3128	345	2658	3846	1095	181	753	1420	3234	777	1646	3917
V	138	24	118	178	142	28	108	193	202	20	170	240	195	23	160	216
Cr	52	56	6.2	188	8.4	8.1	1.7	20	71	22	46	116	66	10	54	86
Co	27	4.5	19	31	20	3.1	16	25	17	1.2	15	19	18	1.5	16	19
Ni	bdl	bdl	bdl	bdl	bdl	bdl	bdl	bdl	5.5	0.75	4.9	6.0	bdl	bdl	bdl	bdl
Cu	bdl	bdl	bdl	bdl	bdl	bdl	bdl	bdl	4.3	3.1	2.1	6.4	bdl	bdl	bdl	bdl
Zn	164	17	136	193	172	17	138	193	138	12	114	149	133	8.4	121	145
Rb	bdl	bdl	bdl	bdl	bdl	bdl	bdl	bdl	bdl	bdl	bdl	bdl	bdl	bdl	bdl	bdl
Sr	38	21	19	74	193	27	160	245	79	6.2	65	91	161	18	137	186
Y	bdl	bdl	bdl	bdl	0.10	0.06	0.03	0.18	0.12	0.07	0.03	0.23	0.07	0.02	0.06	0.09
Zr	0.20	0.06	0.11	0.27	0.26	0.16	0.05	0.38	0.67	0.61	0.17	2.1	0.17	0.09	0.11	0.34
Nb	0.09	-	0.09	0.09	0.15	0.02	0.12	0.19	0.48	0.16	0.21	0.75	0.30	0.08	0.21	0.49
Mo	bdl	bdl	bdl	bdl	bdl	bdl	bdl	bdl	2.8	2.7	0.50	5.8	bdl	bdl	bdl	bdl
Sn	6.9	1.0	5.3	8.3	7.1	1.4	3.8	9.0	18	3.5	12	26	14	2.5	10	17
Cs	bdl	bdl	bdl	bdl	bdl	bdl	bdl	bdl	bdl	bdl	bdl	bdl	bdl	bdl	bdl	bdl
Ba	bdl	bdl	bdl	bdl	0.52	0.10	0.45	0.59	0.27	0.07	0.17	0.37	0.36	-	0.36	0.36
La	0.10	0.05	0.05	0.19	1.7	0.34	1.3	2.4	0.30	0.11	0.13	0.42	1.1	0.24	0.84	1.7
Ce	0.16	0.09	0.07	0.36	2.7	0.57	1.9	3.9	0.47	0.19	0.19	0.78	1.7	0.34	1.3	2.4
Pr	0.06	0.02	0.04	0.08	0.25	0.06	0.16	0.38	0.05	0.02	0.02	0.07	0.15	0.04	0.12	0.25
Nd	bdl	bdl	bdl	bdl	0.79	0.15	0.62	1.1	0.22	0.09	0.12	0.39	0.49	0.18	0.27	0.81
Sm	bdl	bdl	bdl	bdl	0.13	-	0.13	0.13	bdl	bdl	bdl	bdl	bdl	bdl	bdl	bdl
Eu	0.19	0.10	0.06	0.27	0.54	0.08	0.42	0.67	0.20	0.02	0.15	0.23	0.31	0.13	0.14	0.56
Gd	bdl	bdl	bdl	bdl	bdl	bdl	bdl	bdl	0.12	-	0.12	0.12	bdl	bdl	bdl	bdl
Tb	0.01	-	0.01	0.01	bdl	bdl	bdl	bdl	bdl	bdl	bdl	bdl	bdl	bdl	bdl	bdl
Dy	bdl	bdl	bdl	bdl	bdl	bdl	bdl	bdl	bdl	bdl	bdl	bdl	bdl	bdl	bdl	bdl
Ho	bdl	bdl	bdl	bdl	bdl	bdl	bdl	bdl	0.01	-	0.01	0.01	bdl	bdl	bdl	bdl
Er	0.15	-	0.15	0.15	bdl	bdl	bdl	bdl	bdl	bdl	bdl	bdl	bdl	bdl	bdl	bdl
Tm	bdl	bdl	bdl	bdl	0.03	-	0.03	0.03	bdl	bdl	bdl	bdl	bdl	bdl	bdl	bdl
Yb	bdl	bdl	bdl	bdl	bdl	bdl	bdl	bdl	0.26	-	0.26	0.26	bdl	bdl	bdl	bdl
Lu	bdl	bdl	bdl	bdl	bdl	bdl	bdl	bdl	0.05	0.03	0.02	0.08	bdl	bdl	bdl	bdl
∑REE	0.34	0.28	0.13	0.89	5.8	1.3	3.5	8.5	1.1	0.43	0.36	1.9	3.7	0.93	2.5	5.5
Ta	0.04	-	0.04	0.04	0.04	0.01	0.03	0.05	0.12	0.04	0.09	0.22	0.07	0.02	0.04	0.09
W	bdl	bdl	bdl	bdl	0.37	0.15	0.27	0.47	0.60	0.65	0.11	2.0	0.99	0.98	0.33	2.4
Pb	1.3	0.18	0.94	1.6	4.2	0.56	3.1	4.9	2.0	0.41	1.5	3.1	5.0	0.70	3.6	5.8
Bi	0.06	0.04	0.03	0.09	0.82	1.1	0.10	2.9	0.05	-	0.05	0.05	0.32	0.33	0.08	0.56
Th	0.06	-	0.06	0.06	bdl	bdl	bdl	bdl	0.03	-	0.03	0.03	0.04	-	0.04	0.04
U	bdl	bdl	bdl	bdl	bdl	bdl	bdl	bdl	bdl	bdl	bdl	bdl	bdl	bdl	bdl	bdl

bdl: below detection limit

Table 36: Boron isotopic compositions of tourmaline from Enguialès.

Sample	Zone	$\delta^{11}B$ (‰)	± 1σ
Tourmalinite (ENG-9a/b)			
ENG-9b_1	Core	1.72	0.47
ENG-9b_2	Rim	-0.48	0.45
ENG-9b_3	Rim	-0.33	0.46
ENG-9b_4	Rim	0.48	0.43
ENG-9a_1	Rim	-1.21	0.44
ENG-9a_2	Overgrowth	-1.04	0.41
ENG-9b_5	Overgrowth	0.03	0.46
ENG-9a_3	Overgrowth	-1.56	0.45
ENG-9a_4	Overgrowth	-0.42	0.43
ENG-9a_5	Overgrowth	-0.50	0.44
ENG-9b_6	Overgrowth	0.91	0.55
ENG-9b_7	Overgrowth	3.25	0.42
Acicular tourmaline (ENG-9b)			
ENG-9b_8	Core	0.63	0.49
ENG-9b_11	Core	0.20	0.49
ENG-9b_9	Rim	-2.27	0.49
ENG-9b_10	Rim	-4.38	0.48
ENG-9b_12	Overgrowth	-0.52	0.47
ENG-9b_13	Overgrowth	-0.07	0.46
Acicular tourmaline (CHA-14-18)			
CHA-14-18_5	Core	-0.05	0.48
CHA-14-18_6	Rim	-1.79	0.39
CHA-14-18_7	Rim	-2.32	0.40

Table 37: Representative chemical compositions of tourmaline from St-Mélany.

	Disseminated tourmalines *Sample ARD-13-83b*				**Tourmalinite** *Sample ARD-13-90*				**Acicular tourmalines** *Sample ARD-13-90*				**Breccia tourmalines** *Sample ARD-13-10*				**Beaume tourmalines** *Sample ARD-13-05*			
	Core		Rim	Dark overgrowth	Core	Replaced core	Bright overgrowth	Dark overgrowth	Core	Bright overgrowth	Dark overgrowth	Corrosion	Core	Rim	Dark overgrowth	Corrosion	Core		Rim	
	1	2	8	4	10	13	3	1	20	2	7	4	1	2	3	10	1	5	13	14
SiO_2	36.34	36.78	36.99	37.31	37.32	36.15	36.45	36.93	35.73	35.87	36.17	36.57	36.71	36.01	36.34	35.25	37.40	36.44	36.27	36.00
TiO_2	0.42	0.55	0.50	0.85	0.59	1.06	1.22	0.63	0.23	0.57	0.39	0.81	1.17	0.86	0.92	0.74	0.17	0.31	0.66	0.74
Al_2O_3	33.24	33.68	32.36	35.38	32.17	30.70	32.86	32.62	34.71	32.76	34.53	33.68	34.19	32.23	32.76	32.54	33.98	32.83	32.58	32.10
Cr_2O_3	0.00	0.07	0.00	0.08	0.00	0.00	0.00	0.00	0.00	0.03	0.00	0.00	0.00	0.00	0.00	0.00	0.00	0.00	0.05	0.03
FeO	8.82	7.26	7.49	6.04	7.22	8.32	9.18	6.98	12.08	10.81	8.01	6.74	6.81	7.49	7.40	8.31	8.37	8.46	8.72	8.24
MgO	6.00	6.25	6.74	6.23	6.18	6.43	4.75	6.04	1.98	3.52	5.11	6.46	6.05	6.22	5.98	6.65	5.30	5.60	6.44	6.26
CaO	0.34	0.50	0.90	0.46	0.57	0.76	0.63	0.42	0.01	0.09	0.61	0.38	0.46	0.57	0.67	1.21	0.26	0.40	0.73	0.81
MnO	0.00	0.00	0.06	0.01	0.00	0.00	0.00	0.00	0.13	0.07	0.07	0.01	0.00	0.00	0.00	0.14	0.10	0.05	0.09	0.05
Na_2O	2.02	1.81	2.07	1.68	2.14	1.94	1.74	1.89	1.60	2.08	1.77	1.93	1.80	2.02	1.85	1.92	1.72	1.79	2.12	1.93
K_2O	0.00	0.00	0.00	0.00	0.00	0.00	0.00	0.00	0.00	0.00	0.00	0.00	0.00	0.00	0.00	0.00	0.00	0.00	0.00	0.00
F	0.00	0.00	0.00	0.00	0.00	0.00	0.00	0.00	0.00	0.00	0.00	0.00	0.00	0.00	0.00	0.00	0.00	0.00	0.00	0.00
H_2O*	3.69	3.72	3.72	3.81	3.70	3.62	3.69	3.68	3.63	3.61	3.70	3.72	3.75	3.64	3.68	3.66	3.73	3.65	3.70	3.65
B_2O_3*	10.70	10.79	10.77	11.04	10.73	10.49	10.69	10.66	10.52	10.47	10.73	10.77	10.87	10.56	10.66	10.60	10.82	10.59	10.73	10.59
Li_2O*	0.04	0.19	0.27	0.30	0.49	0.21	0.34	0.36	0.21	0.26	0.27	0.21	0.29	0.24	0.30	0.09	0.21	0.14	0.10	0.17
Total	101.61	101.60	101.86	103.19	101.12	99.67	101.54	100.22	100.83	100.14	101.36	101.28	102.10	99.85	100.55	101.11	102.06	100.27	102.18	100.58
Structural formula (apfu)																				
T-site																				
Si	5.90	5.93	5.97	5.87	6.04	5.99	5.93	6.02	5.90	5.96	5.86	5.90	5.87	5.93	5.93	5.78	6.01	5.98	5.88	5.91
Al	0.10	0.07	0.03	0.13	0.00	0.01	0.07	0.00	0.10	0.04	0.14	0.10	0.13	0.07	0.07	0.22	0.00	0.02	0.12	0.09
B	3.00	3.00	3.00	3.00	3.00	3.00	3.00	3.00	3.00	3.00	3.00	3.00	3.00	3.00	3.00	3.00	3.00	3.00	3.00	3.00
Z-site																				
Al	6.00	6.00	6.00	6.00	6.00	5.99	6.00	6.00	6.00	6.00	6.00	6.00	6.00	6.00	6.00	6.00	6.00	6.00	6.00	6.00
Mg	0.00	0.00	0.00	0.00	0.00	0.01	0.00	0.00	0.00	0.00	0.00	0.00	0.00	0.00	0.00	0.00	0.00	0.00	0.00	0.00
Cr	0.00	0.00	0.00	0.00	0.00	0.00	0.00	0.00	0.00	0.00	0.00	0.00	0.00	0.00	0.00	0.00	0.00	0.00	0.00	0.00
Fe^{3+}	0.00	0.00	0.00	0.00	0.00	0.00	0.00	0.00	0.00	0.00	0.00	0.00	0.00	0.00	0.00	0.00	0.00	0.00	0.00	0.00
Y-site																				
Al	0.27	0.32	0.12	0.44	0.14	0.00	0.23	0.27	0.66	0.37	0.45	0.30	0.32	0.18	0.23	0.06	0.43	0.33	0.10	0.12
Ti	0.05	0.07	0.06	0.10	0.07	0.13	0.15	0.08	0.03	0.07	0.05	0.10	0.14	0.11	0.11	0.09	0.02	0.04	0.08	0.09
Cr	0.00	0.01	0.00	0.01	0.00	0.00	0.00	0.00	0.00	0.00	0.00	0.00	0.00	0.00	0.00	0.00	0.00	0.00	0.01	0.00
Fe^{3+}	0.00	0.00	0.00	0.00	0.00	0.00	0.00	0.00	0.00	0.00	0.00	0.00	0.00	0.00	0.00	0.00	0.00	0.00	0.00	0.00
Mg	1.45	1.50	1.62	1.46	1.49	1.58	1.15	1.47	0.49	0.87	1.23	1.55	1.44	1.53	1.45	1.63	1.27	1.37	1.56	1.53
Mn	0.00	0.00	0.01	0.00	0.00	0.00	0.00	0.00	0.02	0.01	0.01	0.00	0.00	0.00	0.00	0.02	0.01	0.01	0.01	0.01
Fe^{2+}	1.20	0.98	1.01	0.80	0.98	1.15	1.25	0.95	1.67	1.50	1.09	0.91	0.91	1.03	1.01	1.14	1.12	1.16	1.18	1.13
Li*	0.03	0.13	0.17	0.19	0.32	0.14	0.22	0.24	0.14	0.17	0.17	0.13	0.19	0.16	0.20	0.06	0.14	0.10	0.06	0.11
X-site																				
Ca	0.06	0.09	0.16	0.08	0.10	0.13	0.11	0.07	0.00	0.02	0.11	0.07	0.08	0.10	0.12	0.21	0.04	0.07	0.13	0.14
Na	0.64	0.57	0.65	0.51	0.67	0.62	0.55	0.60	0.51	0.67	0.56	0.60	0.56	0.64	0.59	0.61	0.54	0.57	0.67	0.61
K	0.00	0.00	0.00	0.00	0.00	0.00	0.00	0.00	0.00	0.00	0.00	0.00	0.00	0.00	0.00	0.00	0.00	0.00	0.00	0.00
□	0.30	0.35	0.20	0.41	0.23	0.24	0.34	0.33	0.49	0.31	0.34	0.33	0.36	0.26	0.30	0.18	0.42	0.36	0.21	0.24
OH	4.00	4.00	4.00	4.00	4.00	4.00	4.00	4.00	4.00	4.00	4.00	4.00	4.00	4.00	4.00	4.00	4.00	4.00	4.00	4.00
F	0.00	0.00	0.00	0.00	0.00	0.00	0.00	0.00	0.00	0.00	0.00	0.00	0.00	0.00	0.00	0.00	0.00	0.00	0.00	0.00

Structural formula based on 31 anions (O, OH, F). B_2O_3, H_2O and Li_2O calculated by stoichiometry assuming B=3 apfu, OH+F=4 apfu and Li=15-total(T+Z+Y) and normalizing to 31 anions. * Calculated.

Table 38: Trace elements compositions of tourmaline (in ppm) from St-Mélany.

	Disseminated tourmalines				**Tourmalinites at the selvages of the mineralized quartz veins**								**Acicular tourmalines**			
	Sample ARD-13-83b				*Sample ARD-13-90*								*Sample ARD-13-90*			
	Core (n=18)				Core (n=24)				Dark overgrowth (n=2)				Core (n=27)			
	Mean	SD	Min	Max	Mean	SD	Min	Max	Mean	SD	Min	Max	Mean	SD	Min	Max
Li	28	3.2	22	36	60	15	39	95	54	0.34	54	54	89	39	51	216
Be	6.2	1.3	3.6	8.3	24	21	5.0	85	bdl	bdl	bdl	bdl	12	7.4	3.6	28
Sc	37	5.8	27	47	53	17	26	99	12	0.43	12	13	10	1.7	7.2	14
Ti	2822	385	2290	3467	3484	1006	1835	5678	4286	95	4219	4353	1770	683	977	3395
V	337	25	283	392	287	34	227	357	161	18	148	174	57	12	30	75
Cr	183	40	150	324	241	59	121	346	115	95	48	182	bdl	bdl	bdl	bdl
Co	12	1.6	10	16	11	3.8	7.2	22	3.2	0.75	2.7	3.7	32	3.8	26	43
Ni	55	5.8	46	63	22	8.0	13	46	bdl	bdl	bdl	bdl	44	40	4.9	183
Cu	bdl	bdl	bdl	bdl	bdl	bdl	bdl	bdl	bdl	bdl	bdl	bdl	bdl	bdl	bdl	bdl
Zn	254	19	213	283	303	26	253	348	304	11	297	312	1234	134	991	1514
Rb	5.9	6.2	1.2	17	0.85	-	0.85	0.85	bdl	bdl	bdl	bdl	4.1	6.2	0.34	11
Sr	190	55	118	320	344	97	174	510	125	43	95	155	118	51	53	232
Y	3.1	9.3	0.09	37	21	69	0.16	310	0.47	-	0.47	0.47	0.16	0.08	0.10	0.22
Zr	12	17	0.25	51	34	73	0.82	349	8.2	8.4	2	14	0.46	0.34	0.15	1.6
Nb	0.61	0.14	0.39	0.90	1.5	3.3	0.30	17	0.27	-	0.27	0.27	0.21	0.10	0.10	0.46
Mo	bdl	bdl	bdl	bdl	0.55	0.01	0.55	0.56	bdl	bdl	bdl	bdl	bdl	bdl	bdl	bdl
Sn	68	7.9	53	77	127	48	74	276	45	14	35	55	189	53	101	352
Cs	0.90	1.0	0.12	2.6	0.11	-	0.11	0.11	bdl	bdl	bdl	bdl	0.36	-	0.36	0.36
Ba	8.3	14	1.3	60	1.9	0.83	0.95	3.3	1.9	-	1.9	1.9	0.61	-	0.61	0.61
La	3.9	3.1	1.9	16	3.4	5.7	0.58	28	1.7	0.75	1.1	2.2	0.14	0.14	0.06	0.54
Ce	5.2	1.2	3.1	7.1	6.1	10	0.87	49	2.3	1.1	1.6	3.1	0.28	0.47	0.06	1.5
Pr	0.48	0.13	0.26	0.66	0.71	1.1	0.10	5.2	0.43	-	0.43	0.43	0.09	0.05	0.04	0.14
Nd	1.6	0.37	1.1	2.1	3.0	4.7	0.39	19	bdl	bdl	bdl	bdl	0.46	0.17	0.34	0.58
Sm	0.29	0.13	0.20	0.38	1.5	2.3	0.27	6.6	bdl	bdl	bdl	bdl	0.44	0.02	0.42	0.45
Eu	0.75	0.17	0.35	1.0	0.80	0.35	0.39	2.0	0.71		0.71	0.71	bdl	bdl	bdl	bdl
Gd	bdl	bdl	bdl	bdl	0.70	0.53	0.17	1.4	bdl	bdl	bdl	bdl	bdl	bdl	bdl	bdl
Tb	0.05	0.01	0.04	0.05	0.09	0.07	0.03	0.15	bdl	bdl	bdl	bdl	0.06	-	0.06	0.06
Dy	0.16	-	0.16	0.16	0.56	0.49	0.12	1.2	bdl	bdl	bdl	bdl	bdl	bdl	bdl	bdl
Ho	0.02	0.03	0.00	0.05	0.13	0.15	0.03	0.23	0.15	-	0.15	0.15	bdl	bdl	bdl	bdl
Er	0.10	0.11	0.00	0.21	0.35	0.34	0.09	0.89	bdl	bdl	bdl	bdl	bdl	bdl	bdl	bdl
Tm	bdl	bdl	bdl	bdl	bdl	bdl	bdl	bdl	bdl	bdl	bdl	bdl	bdl	bdl	bdl	bdl
Yb	0.26	0.14	0.15	0.46	0.39	-	0.39	0.39	bdl	bdl	bdl	bdl	bdl	bdl	bdl	bdl
Lu	0.06	0.03	0.02	0.09	0.09	0.07	0.03	0.19	bdl	bdl	bdl	bdl	bdl	bdl	bdl	bdl
∑REE	12	2.5	7.4	16	13	21	0.00	107	4.6	2.7	2.7	6.6	0.22	0.54	0.00	2.8
Ta	0.11	0.03	0.06	0.20	0.24	0.26	0.07	1.2	bdl	bdl	bdl	bdl	0.08	0.02	0.05	0.10
W	0.80	0.38	0.29	1.5	4.0	3.2	0.70	13	8.8	5.8	4.7	13	3.6	4.6	0.37	20
Pb	26	5.1	19	36	42	15	19	81	18	8.1	12	23	4.2	3.2	1.4	14
Bi	bdl	bdl	bdl	bdl	0.12	0.08	0.04	0.23	bdl	bdl	bdl	bdl	0.17	-	0.17	0.17
Th	1.4	3.5	0.06	11	0.47	0.37	0.03	1.2	bdl	bdl	bdl	bdl	bdl	bdl	bdl	bdl
U	0.33	0.49	0.09	1.5	0.46	0.30	0.08	1.0	1.1	-	1.1	1.1	bdl	bdl	bdl	bdl

bdl: below detection limit

Table 38: Continued.

	Breccia tourmalines *Sample ARD-13-10*										**Tourmalines from the Beaume valley** *Sample ARD-13-05*									
	Core (n=4)				Rim (n=6)				Dark overgrowth (n=21)				Core (n=10)				Rim (n=10)			
	Mean	SD	Min	Max	Mean	SD	Min	Max	Mean	SD	Min	Max	Mean	SD	Min	Max	Mean	SD	Min	Max
Li	45	2.7	43	49	70	8.4	57	82	89	24	63	136	13	1.4	11	16	16	4.2	12	24
Be	7.6	2.4	5.0	10	18	31	4.2	82	10	8.9	5.6	40	1.6	0.22	1.3	2.0	1.4	0.18	1.1	1.6
Sc	30	2.3	28	33	29	3.9	24	36	28	4.0	23	42	11	0.83	10	12	13	1.1	11	15
Ti	1503	352	1121	1972	4049	1005	3447	6078	3770	484	2650	5140	751	134	571	985	3549	724	1728	4432
V	207	6.2	201	216	253	38	194	305	244	23	194	286	181	14	153	209	276	46	182	357
Cr	66	14	54	79	113	27	68	136	103	40	41	165	144	19	112	189	143	41	79	219
Co	6.0	0.19	5.8	6.2	6.1	0.31	5.6	6.4	4.5	1.6	2.0	7.0	43	4.0	39	49	40	3.5	36	45
Ni	bdl	bdl	bdl	bdl	bdl	bdl	bdl	bdl	bdl	bdl	bdl	bdl	72	10	61	86	72	10	59	86
Cu	bdl	bdl	bdl	bdl	bdl	bdl	bdl	bdl	bdl	bdl	bdl	bdl	bdl	bdl	bdl	bdl	bdl	bdl	bdl	bdl
Zn	221	14	203	232	228	5.8	221	235	269	50	219	383	216	11	202	234	214	6.7	201	223
Rb	bdl	bdl	bdl	bdl	bdl	bdl	bdl	bdl	bdl	bdl	bdl	bdl	bdl	bdl	bdl	bdl	bdl	bdl	bdl	bdl
Sr	29	5.7	24	37	81	15	69	109	132	62	68	282	100	16	84	122	210	50	102	294
Y	0.14	-	0.14	0.14	0.17	0.11	0.10	0.30	0.57	0.23	0.24	0.77	bdl	bdl	bdl	bdl	0.02	0.01	0.02	0.03
Zr	bdl	bdl	bdl	bdl	0.26	0.17	0.15	0.45	0.50	0.27	0.00	0.74	bdl	bdl	bdl	bdl	0.04	0.01	0.03	0.05
Nb	bdl	bdl	bdl	bdl	0.15	0.06	0.11	0.19	0.21	0.10	0.13	0.32	0.03	0.01	0.02	0.05	0.08	0.03	0.05	0.12
Mo	bdl	bdl	bdl	bdl	bdl	bdl	bdl	bdl	bdl	bdl	bdl	bdl	0.24	-	0.24	0.24	bdl	bdl	bdl	bdl
Sn	63	15	46	78	60	4.5	54	66	58	6.1	48	72	0.73	0.13	0.56	0.98	1.7	0.21	1.4	2.1
Cs	bdl	bdl	bdl	bdl	0.29	-	0.29	0.29	3.0	-	3.0	3.0	bdl	bdl	bdl	bdl	bdl	bdl	bdl	bdl
Ba	0.81	-	0.81	0.81	1.5	0.85	0.78	2.8	2.3	0.64	1.4	3.2	0.19	0.03	0.16	0.23	0.26	0.13	0.10	0.50
La	0.45	0.22	0.26	0.72	2.5	0.97	2.1	4.5	4.1	2.0	1.9	10	0.05	0.02	0.04	0.06	0.06	0.04	0.03	0.17
Ce	0.80	0.39	0.50	1.4	4.3	1.38	3.5	7.1	7.0	3.5	3.3	18	0.03	0.03	0.01	0.08	0.09	0.07	0.02	0.24
Pr	0.13	-	0.13	0.13	0.39	0.14	0.29	0.67	0.68	0.36	0.26	1.8	0.08	0.11	0.01	0.16	0.01	0.01	0.01	0.02
Nd	bdl	bdl	bdl	bdl	1.2	0.47	0.83	2.0	2.4	1.3	1.3	6.4	bdl	bdl	bdl	bdl	bdl	bdl	bdl	bdl
Sm	bdl	bdl	bdl	bdl	0.30	-	0.30	0.30	0.89	0.26	0.57	1.2	bdl	bdl	bdl	bdl	bdl	bdl	bdl	bdl
Eu	0.13	-	0.13	0.13	0.31	0.11	0.20	0.52	0.67	0.36	0.37	1.5	bdl	bdl	bdl	bdl	0.04	0.03	0.02	0.11
Gd	bdl	bdl	bdl	bdl	bdl	bdl	bdl	bdl	0.46	0.04	0.43	0.48	bdl	bdl	bdl	bdl	bdl	bdl	bdl	bdl
Tb	bdl	bdl	bdl	bdl	bdl	bdl	bdl	bdl	0.12	-	0.12	0.12	bdl	bdl	bdl	bdl	bdl	bdl	bdl	bdl
Dy	bdl	bdl	bdl	bdl	0.17	-	0.17	0.17	bdl	bdl	bdl	bdl	bdl	bdl	bdl	bdl	bdl	bdl	bdl	bdl
Ho	bdl	bdl	bdl	bdl	bdl	bdl	bdl	bdl	bdl	bdl	bdl	bdl	bdl	bdl	bdl	bdl	0.01	-	0.01	0.01
Er	bdl	bdl	bdl	bdl	0.14	-	0.14	0.14	0.24	-	0.24	0.24	bdl	bdl	bdl	bdl	0.03	-	0.03	0.03
Tm	bdl	bdl	bdl	bdl	bdl	bdl	bdl	bdl	bdl	bdl	bdl	bdl	bdl	bdl	bdl	bdl	bdl	bdl	bdl	bdl
Yb	bdl	bdl	bdl	bdl	bdl	bdl	bdl	bdl	bdl	bdl	bdl	bdl	bdl	bdl	bdl	bdl	bdl	bdl	bdl	bdl
Lu	bdl	bdl	bdl	bdl	bdl	bdl	bdl	bdl	bdl	bdl	bdl	bdl	0.03	-	0.03	0.03	bdl	bdl	bdl	bdl
∑REE	1.3	0.54	0.90	2.1	8.9	3.0	7.1	15	14	8	5.1	38	0.04	0.06	0.00	0.16	0.18	0.14	0.03	0.54
Ta	0.10	-	0.10	0.10	bdl	bdl	bdl	bdl	bdl	bdl	bdl	bdl	0.03	-	0.03	0.03	0.02	0.01	0.01	0.03
W	bdl	bdl	bdl	bdl	bdl	bdl	bdl	bdl	0.36	0.51	0.00	0.72	0.25	0.08	0.19	0.30	0.14	0.11	0.07	0.31
Pb	5.6	0.40	5.2	6.1	14	2.3	12	18	11	4.5	4.4	17	5.8	0.39	5.2	6.4	12	3.0	6.7	16
Bi	bdl	bdl	bdl	bdl	bdl	bdl	bdl	bdl	bdl	bdl	bdl	bdl	0.52	-	0.52	0.52	bdl	bdl	bdl	bdl
Th	bdl	bdl	bdl	bdl	bdl	bdl	bdl	bdl	0.11	0.05	0.08	0.15	bdl	bdl	bdl	bdl	0.02	0.00	0.02	0.02
U	bdl	bdl	bdl	bdl	bdl	bdl	bdl	bdl	bdl	bdl	bdl	bdl	0.10	-	0.10	0.10	bdl	bdl	bdl	bdl

bdl: below detection limit

Table 39: Boron isotopic compositions of tourmaline from St-Mélany.

Sample	Zone	$\delta^{11}B$ (‰)	± 1σ
Disseminated tourmalines (ARD-13-83b)			
ARD-13-83b_1	Core	-0.85	0.42
ARD-13-83b_2	Core	-0.08	0.43
ARD-13-83b_3	Core	-0.34	0.41
ARD-13-83b_4	Core	-0.08	0.47
ARD-13-83b_5	Rim	-1.62	0.39
ARD-13-83b_6	Rim	-1.62	0.42
Tourmalinite (ARD-13-90)			
ARD-13-90_8	Core	-3.30	0.48
ARD-13-90_5	Rim	-2.32	0.53
ARD-13-90_6	Rim	-1.84	0.68
ARD-13-90_7	Overgrowth	-2.70	0.60
Acicular tourmalines (ARD-13-90)			
ARD-13-90_1	Core	0.78	0.52
ARD-13-90_3	Core	0.62	0.51
ARD-13-90_2	Rim	1.51	0.43
ARD-13-90_4	Rim	1.42	0.51
Breccia tourmalines (ARD-13-10)			
ARD-13-10_1	Core	-4.70	0.93
ARD-13-10_2	Rim	-5.20	0.44
ARD-13-10_3	Rim	-6.03	0.43
ARD-13-10_5	Rim	-5.58	0.38
ARD-13-10_4	Overgrowth	-5.36	0.44
ARD-13-10_6	Overgrowth	-5.21	0.42
ARD-13-10_7	Overgrowth	-5.27	0.40
Beaume tourmalines (ARD-13-05)			
ARD-13-05_04	Core	-3.99	0.42
ARD-13-05_05	Core	-3.79	0.40
ARD-13-05_06	Core	-2.43	0.42
ARD-13-05_09	Core	-2.57	0.42
ARD-13-05_10	Core	-3.92	0.39
ARD-13-05_14	Core	-2.61	0.39
ARD-13-05_01	Rim	-3.98	0.41
ARD-13-05_02	Rim	-3.81	0.42
ARD-13-05_03	Rim	-3.95	0.38
ARD-13-05_07	Rim	-4.22	0.39
ARD-13-05_08	Rim	-2.60	0.47
ARD-13-05_11	Rim	-3.05	0.39
ARD-13-05_12	Rim	-4.24	0.42
ARD-13-05_13	Rim	-3.13	0.42

Chapter 8: Geochemical signature of the rare-metal magmatic fluids exsolved from the Beauvoir granite (Massif Central, France) through LA-ICPMS analysis of primary fluid inclusions

Abstract

The Beauvoir granite, located in the Echassières granitic complex in the northeastern part of the French Massif Central, represents an exceptional case in the European Variscan belt of a rare-metal granite crosscutting a quartz-ferberite stockwork (La Bosse) with a vertical development of more than 100 m. The latter was strongly reworked by the rare-metal magmatic-hydrothermal fluids derived from the Beauvoir granite, resulting in a massive topazification. This study focuses on the LA-ICPMS analysis of primary fluid inclusions contained in quartz and topaz from the Beauvoir granite and from the La Bosse stockwork in order to characterize the geochemical composition of the magmatic fluids exsolved from the rare-metal Beauvoir granite. The L1-type fluid inclusions represent the earliest records of the primary fluids in the Beauvoir granite. Microthermometric data showed that these fluids are high temperature (500 to >600°C), saline (17-28 wt.% NaCl eq) and Li-rich (T_e < -70°C) with Na/Li ratios < 0.5. LA-ICPMS analyses show that the chemical composition of the fluid is dominated mainly by Li, Na, K, Cs, Sn, Rb as major cations with significant concentrations (10^2-10^3 ppm) in Nb, Ta and W as minor elements. Boiling of the L1 fluid yielded to the phase separation of a low- to moderate-salinity vapour (V2; 4.7-22 wt.% NaCl eq) and a high-salinity brine (L2; 32-48 wt.% NaCl eq) at ca. 450°C. LA-ICPMS analyses of these two types of fluid inclusions revealed that the L2-type fluid inclusions have among the highest concentrations in metals and show a preferential enrichment in most of the elements compared to the V2-type fluid inclusions. The evolution of the exsolved fluids in distance from the Beauvoir granite is characterized by a decrease in temperature and salinity, which can be interpreted in terms of cooling and thermal equilibration around the intrusion. Furthermore, the salinity decrease may indicate that the magmatic-hydrothermal fluids derived from the Beauvoir granite were more or less diluted by a very low salinity fluid, which may be possibly meteoric water, considering the relatively low depth emplacement (ca. 3 km) of the Beauvoir granite. These results demonstrate that the L1-type fluid inclusions conserved the pristine magmatic geochemical signature of the Beauvoir granite, and that this

signature remains also preserved in the fluid inclusions from the metasomatized La Bosse stockwork despite the distance from the granitic cupola roof (> 100 m) and the interaction with external fluids. Consequently, the geochemical signature of fluid inclusions may be proposed as a reliable pathfinder for the discovery of hidden rare-metal granitic cupolas at Echassières and more widely in the Limousin area.

Keywords:

Fluid inclusions; rare-metals; LA-ICPMS; hydrothermal fluids; Beauvoir granite; French Massif Central.

1. Introduction

Rare-metal deposits are mainly associated with peraluminous to peralkaline granites, granitic pegmatites and carbonatite complexes, which represent important economic resources for a large variety of elements such as Li, Be, Ta, Nb, REE and Zr (Pollard, 1995). Among these deposits, the rare-element pegmatites of the LCT (Lithium-Caesium-Tantalum) class and the peraluminous rare-metal granites (RMG) constitute two major groups of rare-metal mineralization (Linnen and Cuney, 2005; Černý and Ercit, 2005; Černý et al., 2005; Linnen et al., 2012). The European Variscan belt contains numerous occurrences of these two types of rare-metals deposits, which are mainly found in the Bohemian Massif, the Iberian Massif, the Cornwall, the Armorican Massif and the French Massif Central (FMC). These mineralization were formed between ca. 330 Ma and 300 Ma in various geodynamic settings (Marignac and Cuney, 1999; Cuney et al., 2002; Melleton et al., 2012, 2015). In France, the peraluminous Beauvoir granite represents an exceptional case of disseminated Sn-Li-Ta-Nb-Be mineralization with the potential to be an economic deposit, and has been extensively studied during the 1980s-1990s with the continuous core drilling of 900 m (GPF1) in the framework of the "Géologie Profonde de la France" program (Cuney and Autran, 1987). These studies led to a complete petrological, geochemical, geophysical, structural and geochronological description of the Beauvoir granite and of its host-environment and to the elaboration of integrated genetic model for this type of rare-metal deposit (Cuney et al., 1992; Raimbault et al., 1995).

The magmatic-hydrothermal evolution of RMG systems is relatively well constrained from a large number of works based both on natural examples (e.g., Cuney et al., 1992; Raimbault et al., 1995; Audétat et al., 2000a,b; Breiter et al., 2005; Johan and Johan, 2005) and on experimental approaches (e.g., Webster et al., 1989; Linnen, 1998; Linnen and Cuney, 2005; Veksler, 2004, 2005). The extreme rare-metal enrichment in these highly peraluminous granitic magmas has generally been interpreted as resulting from crystal fractionation (Černý et al., 2005). Deciphering the geochemical composition of the magmatic fluids exsolved from RMG is essential to better understand the behaviour of the elements during the late-stage of crystallization and the partitioning of the elements between the melt and the fluid phase at the magmatic-hydrothermal transition. Most of these data have been obtained from silicate melt inclusions studies, which represent direct witnesses of the crystallizing magma (e.g., Thomas et al., 2003, 2005; Webster et al., 2004; Badanina et al., 2004; Rickers et al., 2006). These works reported that late-stage residual melts are enriched in H_2O, fluxing elements (B, F, P)

and incompatible elements (e.g., Be, Sn, Rb, Cs, Nb, Ta, Li) and reflect the whole-rock bulk composition of the host-granite. At the magmatic-hydrothermal transition, residual melt may yield to the phase separation in a low-density vapour phase and in a high-density brine (Veksler, 2004, 2005). Analysis of the composition of coexisting melt and fluid inclusions trapped during phase separation in low phosphorus RMG showed that most of the trace elements partition into the aqueous fluid phase (Thomas et al., 2005; Rickers et al., 2006). However, few data remain available about the trace element composition of such magmatic-hydrothermal systems (e.g., Audétat et al., 2000a,b; Fabre et al., 2001).

The aims of this chapter are: (i) to determine the trace element composition of the magmatic fluid inclusions trapped in primary quartz and topaz crystals and to characterize the geochemical signature of the rare-metal-bearing fluids exsolved from the Beauvoir granite; (ii) to study the partitioning of the minor and trace elements between the co-existing volatile and brine phase resulting from the phase separation during the boiling of the early primary magmatic fluid; (iii) to determine the chemical evolution of the magmatic fluids exsolved from the Beauvoir granite during their interaction with the percolated enclosing micaschists in distance from the granitic cupola.

2. Geological setting

The Echassières granitic complex is located in the northeastern part of the FMC in the Sioule metamorphic series (Fig. 138). The complex includes a W-bearing quartz-vein system (La Bosse stockwork) and at least three successive granitic units that intruded into the micaschists of the Para-Autochtonous Unit (Cuney et al., 1992; Raimbault et al., 1995). From the older to the younger, these granitic units are (Fig. 139): (i) the La Bosse granite, concealed at depth, that is presumed to be related to the genesis of the tungsten deposit; (ii) the Colettes granite, which is a porphyritic biotite-muscovite-cordierite granite and overprints the La Bosse stockwork; and (iii) the Beauvoir topaz-lepidolite-albite granite, consisting in a peraluminous high phosphorus RMG with disseminated Sn-Li-Ta-Nb-Be mineralization, which crosscuts the Colettes granite. The Beauvoir granite is characterized by a vertical internal zoning (Fig. 139) marked by a magmatic foliation underlined by lepidolite, which separates three granitic units emplaced successively (Cuney et al., 1992; Raimbault et al., 1995): (i) B3 facies, which contains euhedral pink-colored K-feldspars and hosts commonly micaschists inclusions; (ii) B2 facies forming a lepidolite-rich granular granite with idiomorphic quartz crystals; (iii) B1 facies corresponding to an albite-lepidolite-rich granite

containing globular quartz crystals and anhedral perthitic K-feldspars. Generally, the abundance of accessory minerals (topaz, cassiterite, columbite-tantalite, Li-Be phosphates) tends to increase upward from the B3 to the B1 facies reflecting the increase in trace element contents (Cuney et al., 1992).

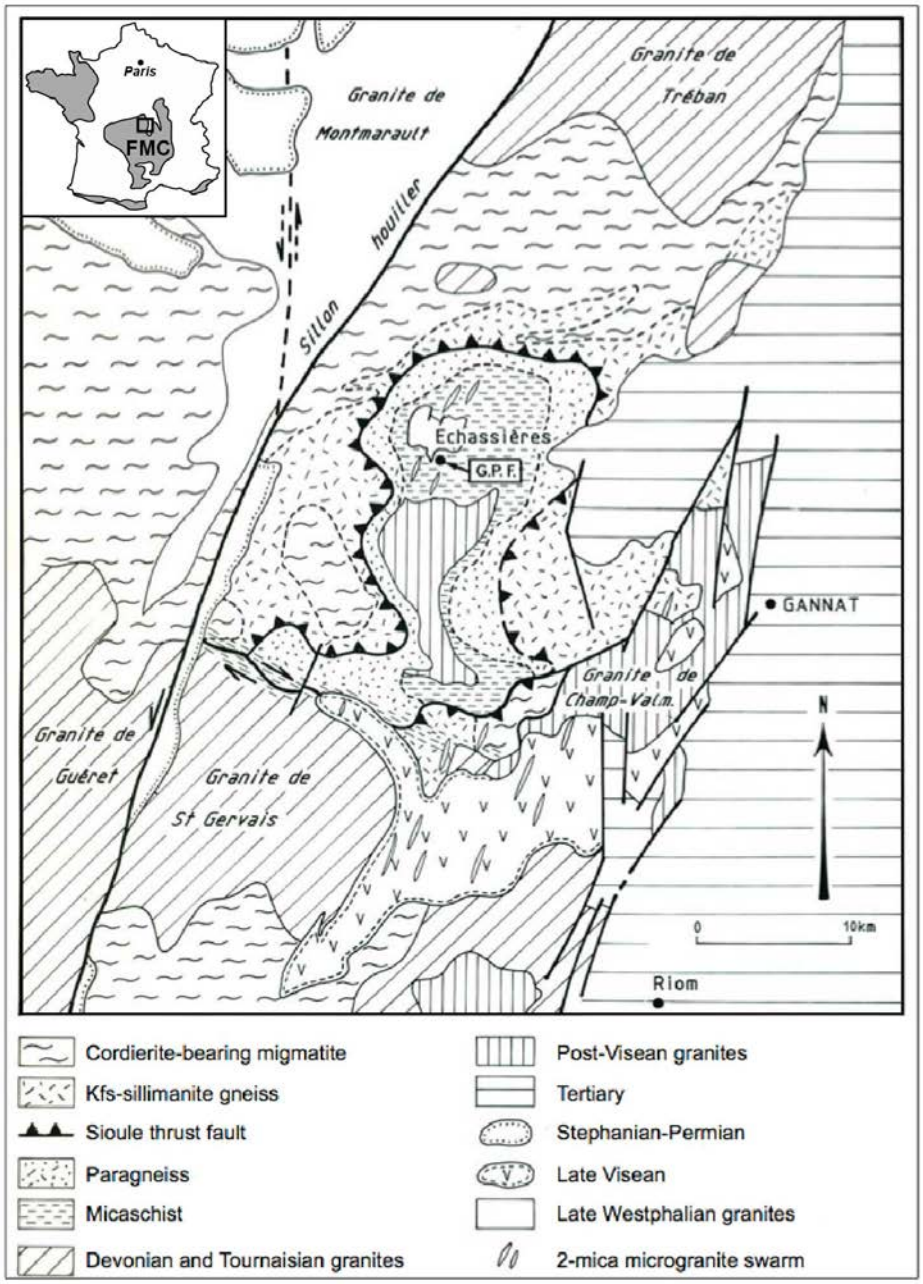

Fig. 138: Location and geological setting of the Echassières complex in the French Massif Central (FMC) (from Cuney and Autran, 1987).

The Beauvoir granite was emplaced at ca. 308 ± 2 Ma, based on an ^{40}Ar-^{39}Ar age on lepidolite from the B1 facies (Cheilletz et al., 1992). However, a recent U-Pb dating on a B1

columbite-tantalite yielded an age of 317 ± 6 Ma (Melleton et al., 2015). This age is significantly older than the ^{40}Ar-^{39}Ar age. Yet, there is no known high-temperature event in the Beauvoir system, which could have reopened the mica system late after the granite emplacement. The fluid-rock interaction leading to Li-muscovite partly replacing the lepidolite is due to the mixing of the magmatic fluid exsolved from the granite with an external fluid at high temperature (Cuney et al. 1992). Moreover, the late Mesozoic hydrothermal event dated at 151 ± 4 Ma (K-Ar on illite; Merceron et al., 1992) was too low in temperature (T≤ 250°C). The age of 308 ± 2 Ma must thus be considered as close to the magmatic emplacement age. Given the relatively large uncertainty associated to the columbo-tantalite age (± 6 Ma), an emplacement age close to the lower limit of the incertitude interval at ca. 310 Ma seems to be consistent both with the U-Pb and the Ar-Ar datings.

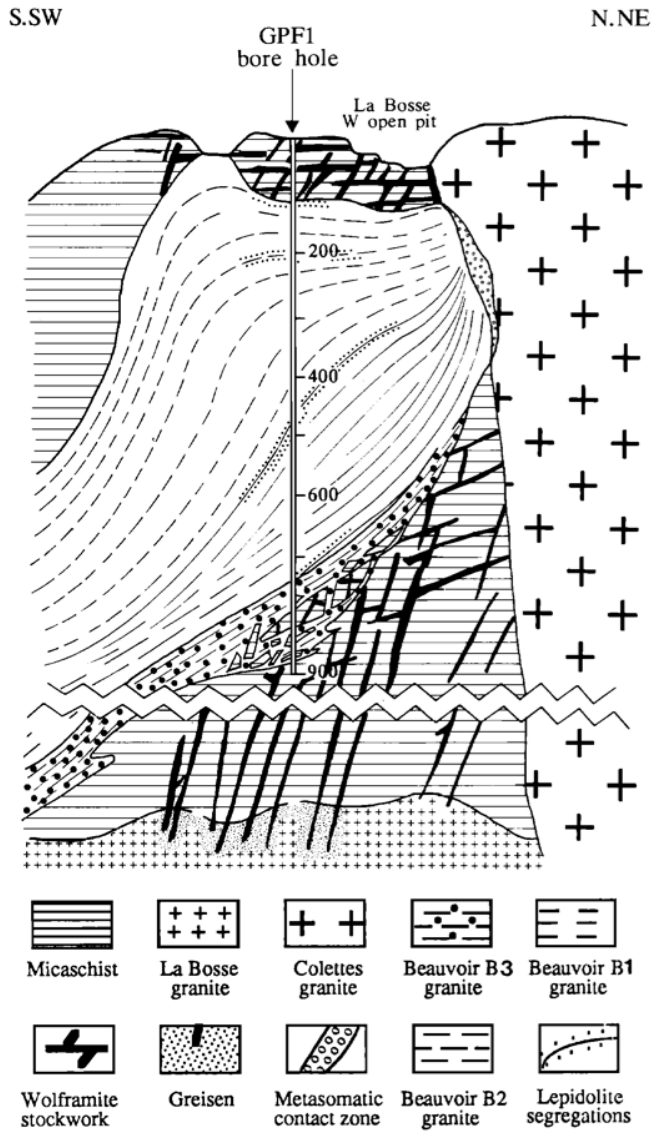

Fig. 139: Interpretative cross-section of the Beauvoir granite from the results of the GPF1 bore-hole (from Cuney et al., 1992).

The La Bosse W stockwork consists in a network of up to 0.6 m thick quartz-ferberite veins hosted in the micaschists (Fig. 139). There are two sets of veins, one parallel and one oblique to the regional foliation, resulting from hydraulic fracturing. Tungsten mineralization is polyphase at the vein scale, since three generations of quartz-ferberite veins have been recognized, emplaced by a crack-and-seal mechanism (Aubert, 1969; Aïssa et al., 1987a). The stockwork is crosscut by the Colettes granite and was overprinted by the contact metamorphic aureole. The Beauvoir granite is underlying the stockwork in surface, at about 100 m in the GPF1 bore-hole (Fig. 139), and closer to the surface in the present-day outliers from the Beauvoir kaolin quarry. Aplites and aplo-pegmatites issued from the granite crosscut the quartz-vein system. A strong reworking of the stockwork is marked by the crystallization of massive topaz ("topazites") at the expense of the quartz of the veins, in association with late Li-micas. Wolframite remains unaffected, to the exception of the formation within the ferberite of dissolution micro-cavities in which sequentially crystallized a Ta-enriched ferberite, a wolframoixiolite and a columbite-tantalite (Aïssa et al., 1987a).

Previous works on fluid inclusions in the Beauvoir granite system allowed to reconstruct the P-T-t conditions of fluid circulations and to make hypotheses on the nature of the different fluids generations (Aïssa et al., 1987b; Cuney et al., 1992): (i) Early magmatic fluids (L1) were only found in topaz from the B1 granite and correspond to high-temperature (490-590°C) brines (25-30 wt.% NaCl eq), which are rich in Li as indicated by low eutectic temperatures (T_e < -65°C) and direct LIBS measurements (Fabre et al., 2001). The exsolution of this fluid likely occurred at ca. 600°C and 0.8 kbars; (ii) Boiling of the L1 fluid occurred at high temperature (400-520°C) after a rapid decompression (~0.7 kbars) and yielded to the phase separation of a low- to moderate-salinity vapour (V2; 3-12 wt.% NaCl eq i.e., involving some remixing with the boiled brine) and a high-salinity brine (L2; 30-50 wt.% NaCl eq); (iii) A low-salinity (2-6 wt.% NaCl eq) aqueous fluid (L3) found in the Beauvoir granite was trapped at relatively low-temperature (330-420°C) and is interpreted to record a mixing between an external aqueous fluid with the magmatic brine L2 during the cooling of the granite, from both microthermometric data (Aïssa et al., 1987b) and stable isotopic data (Cuney et al., 1992); (iv) Later circulations involved several generations of aqueous fluids, including low-saline fluids (L4a; 0-10 wt.% NaCl eq; 120-350°C), moderate-saline brines (L4b; 20-26 wt.% NaCl eq; 200°C) and hyper-saline brines (L4c; 40-60 wt.% NaCl eq; 180-225°C). Fluid inclusions found in the topaz replacing the ferberite-quartz veins from the stockwork correspond to the same L1, L2 and V2 fluids than in the Beauvoir granite.

3. Materials and analytical methods

All analyses were performed at the GeoRessources laboratory (Université de Lorraine, Vandœuvre-lès-Nancy, France).

3.1. Studied material

The studied material come from two provenances: (i) samples of the Beauvoir granite taken from the drilling core of the B1 facies at the depth -25 m (sample B1-25; Fig. 140a) and -379 m (sample B1-379; Fig. 140b); (ii) samples of metasomatized topaz-quartz-ferberite veins from a surface outcrop (now inaccessible) of the La Bosse stockwork (samples ECH-X2 and ECH-11; Fig. 140c,d). Double-polished thick sections (150-200 μm thick) were prepared for microscopic observations of fluid inclusions using an Olympus BX51 optical microscope. The nomenclature used for fluid inclusions typology is the same than in Cuney et al. (1992). This study focuses principally on the early fluid inclusions (L1, L2 and V2) trapped in the primary quartz and topaz, and interpreted as the primary magmatic fluids exsolved from the Beauvoir granite (Aïssa et al., 1987b; Cuney et al., 1992). Petrographic characterization of fluid inclusions was based on the criteria established by Roedder (1984).

3.2. Microthermometry

Microthermometric measurements were realized on a Linkam THMS600 heating-cooling stage connected to an Olympus BX51 microscope. This system allows measurements in a temperature range between -190°C and 600°C and is connected to a cooling circuit for measuring temperatures above 300°C. Calibration was done before each analytical session using H_2O synthetic capillaries and H_2O-CO_2 natural fluid inclusions standards. The accuracy of measurements varies from ±0.2°C at low temperature to ±2°C at high temperature. The following phase transition temperatures were measured during the microthermometric experiments: the eutectic temperature (T_e) corresponding to the first visible melting, i.e. the apparition of the first visible liquid from the solid aqueous phase on heating; the ice melting temperature ($T_m$ice) corresponding to the final melting of solid aqueous phase; the final melting temperature of hydrohalite (T_mHh); the final melting temperature of halite (T_mHl); and the bulk homogenization temperature (T_H). Most of these phase transition temperatures were determined using a heating-cooling cycling method to obtain precise measurements and

to avoid metastability effects. Thick sections of the different samples were observed under the optical microscope in order to select fluid inclusions showing petrographic characteristics of the primary fluid inclusions identified by Aïssa et al. (1987b). Since magmatic fluid inclusions are rare and disseminated within the quartz and topaz crystals, the fluid inclusions previously selected by optical microscopy were firstly investigated at high temperature in order to select only those with T_H>300°C for further analyses. A progressive step-heating procedure was conducted to limit fracturing of the host-mineral and decrepitation of fluid inclusions. Fluid inclusions were progressively heated with a temperature rate of 30°C/min between room temperature and 200°C, then 20°C/min for 200°C<T<400°C, and finally 10°C/min for T>400°C. Measurement of phase transitions temperatures were done at low temperature of 0.5°C/min generally. Photographs of fluid inclusions after microthermometric measurements were then compared with the original pictures before the experiments in order to evaluate any leakage, such as the presence of micro-cracks or visual variations in shape and/or volume of the vapour phase. The selected fluid inclusions were then analysed during cryometric experiments.

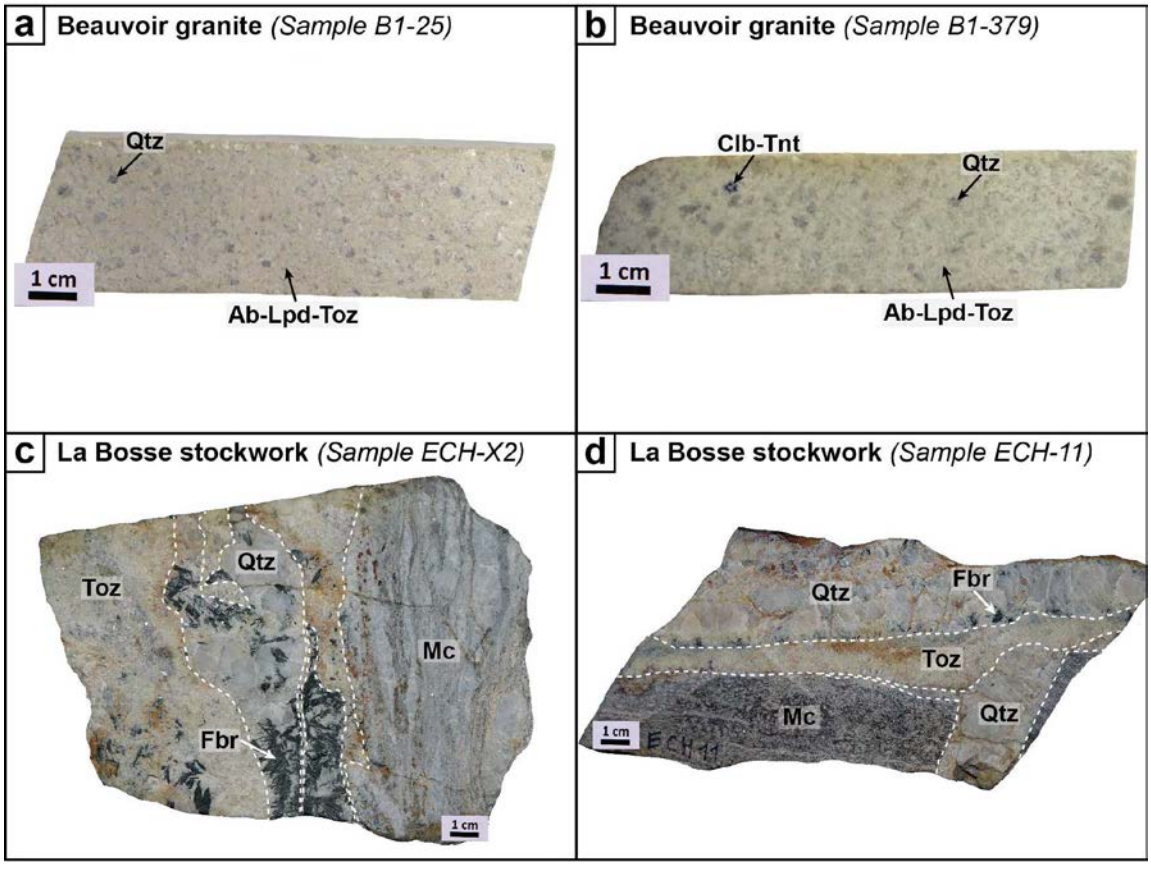

Fig. 140: Photographs of the studied samples from the Beauvoir granite (a: B1-25; b: B1-379) and the La Bosse stockwork (c: ECH-X2; d: ECH-11). Abbreviations: Ab: albite; Clb-Tnt: columbite-tantalite; Fbr: ferberite; Lpd: lepidolite; Mc: micaschist; Qtz: quartz; Toz: topaz.

3.3. Raman spectrometry

Fluid inclusions were analyzed by Raman spectrometry using a Horiba Jobin-Yvon LabRAM spectrometer equipped with a 1800 gr.mm^{-1} grating and an Edge filter. The confocal hole aperture is of 500 µm, the slit aperture is of 100 µm. The excitation beam is provided by a Stabilite 2017 Ar^+ laser (Spectra Physics, Newport Corporation) at 514.532 nm and a power of 400 mW, focused on the sample using x50 and x100 objectives equipped on an Olympus BX40 microscope. The laser beam diameter is around 1 µm. The signal-to-noise ratio was optimized ideally lower than 1 % by adjusting the acquisition time and accumulation number. All Raman analyses were done at room temperature. Salinity of the aqueous phase in fluid inclusions was estimated by following the method of Caumon et al. (2013) and is expressed in wt.% NaCl eq. The uncertainty of the measurement is ±0.3 wt.% NaCl. The quantitative analysis of the gas phases was determined using in-house calibration. Results are expressed in mol% relative to the volatile phase.

3.4. LA-ICPMS analysis

Chemical composition of the fluid inclusions was determined by laser ablation – inductively coupled plasma mass spectrometry (LA-ICPMS) using a Agilent 7500c quadrupole ICPMS coupled with a 193 nm GeoLas ArF Excimer laser (MicroLas, Göttingen, Germany). Laser ablation was performed with a constant 10 Hz pulse frequency by focusing the beam at the sample surface in the ablation cell with a Schwarzschild objective and using a stepwise opening procedure (Günther et al., 1998), starting the ablation with a laser spot diameter of 2 µm and stepwise increasing the spot diameter to the size of the fluid inclusion (from 10 to 80 µm). This procedure allows a controlled ablation by reducing the mechanical stress on the mineral surface, which limits the risk of splashing of the fluid (Günther et al., 1998). Helium was used as carrier gas to transport the laser-generated particles from the ablation cell to the ICPMS and argon was added as an auxiliary gas via a flow adapter before the ICP torch. Typical flow rates of 0.5 L/min for He and 0.87 L/min for Ar were used. The certified reference material NIST SRM 610 (concentrations from Jochum et al., 2011) was used as external standard for calibration of all analyses and was analyzed twice at the beginning and at the end for each set of samples, following a bracketing standardization procedure. The reference material NIST SRM 612 was also used as control standard for the standardization. LA-ICPMS calibration was optimized for highest sensitivity on an

intermediate m/Q range, while maintaining Th/U ~ 1 and ThO/Th < 0.5%, as determined on NIST SRM 610. The following isotopes were measured: ^{7}Li, ^{23}Na, ^{24}Mg, ^{29}Si, ^{39}K, ^{44}Ca, ^{55}Mn, ^{57}Fe with a dwell time of 10 ms, ^{85}Rb, ^{88}Sr with a dwell time of 35 ms and ^{93}Nb, ^{118}Sn, ^{133}Cs, ^{181}Ta, ^{182}W with a dwell time of 40 ms. Data reduction and absolute quantification of signals were performed using the software StalQuant, developed at ETH Zürich, Switzerland (see details in Fricker, 2012). For all analyses, ^{23}Na was used as internal standard for calculation of absolute concentrations. The molality of Na (in mol/kg) was calculated from the NaCl content (in wt.% eq) of the aqueous phase in fluid inclusions determined by Raman spectrometry or from the microthermometric data and following a charge-balancing method to an estimated chloride concentration (Allan et al., 2005). Limits of detection (LOD) were calculated using the 2σ criterion detailed in Longerich et al. (1996).

4. Results

4.1. Fluid inclusion petrography

Fluid inclusions were described at room temperature under the optical microscope according to their geometry, shape, number of visible phases, volume fraction of the vapour phase (Rv %) and their size. As shown in Table 40 summarizing the petrographic characteristics of the fluid inclusions observed in the Beauvoir granite and the La Bosse stockwork during the present work, it was indeed possible to retrieve the fluid inclusions types as described by Aïssa et al. (1987b).

4.1.1. Fluid inclusions in the Beauvoir granite

In the Beauvoir granite (facies B1; Fig. 141a,b), the quartz forms anhedral and millimetric globular magmatic crystals, which contain many fluid inclusions. Topaz forms generally limpid sub-euhedral crystals disseminated into the granite and contain less fluid inclusions than the quartz. The fluid inclusions in the quartz and topaz crystals form dense clouds of disseminated fluid inclusions. This represents a severe limitation to the identification of the different generations of fluid inclusions based on relative criteria of position or arrangement. L1-type fluid inclusions are generally found in clusters within the quartz and topaz and have irregular shapes with a size typically ranging from 10 to 23 μm, typically (Fig. 142a). They consist in multi-phase fluid inclusions at room temperature, with a

dominant aqueous phase containing a vapour bubble (Rv=40% in average) and small (< 5µm) refringent cubic solids, which appear to be halite (Fig. 142a). V2-type fluid inclusions consist in two-phase (liquid+vapour) irregularly shaped inclusions disseminated in clusters (Fig. 142b). They contain a dominant vapour phase (Rv>80%) and range approximately from 12 to 24 µm in size. Small cubic or rounded crystals of salts are observed occasionally. L2-type fluid inclusions (Fig. 142c) are characterized by irregular to regular shapes and have sizes comprised between 10 and 35 µm. They consist in multi-phase fluid inclusions, disseminated in clusters in the quartz and topaz, which are composed by a dominant aqueous phase and a small vapour phase (Rv=30% in average). Moreover, they contain multiple (n>2) cubic crystals of salts, corresponding generally to halite crystals (Fig. 142c). Late L3-type consists in regularly shaped two-phase (liquid+vapour) fluid inclusions of 15-20 µm in size and containing a small vapour bubble (Rv~40%). These fluid inclusions are less numerous within the granite. Finally, an intermediate type between the L2-type and the L3-type fluid inclusions was found and distinguish principally on the basis of the microthermometric data (see 4.2).

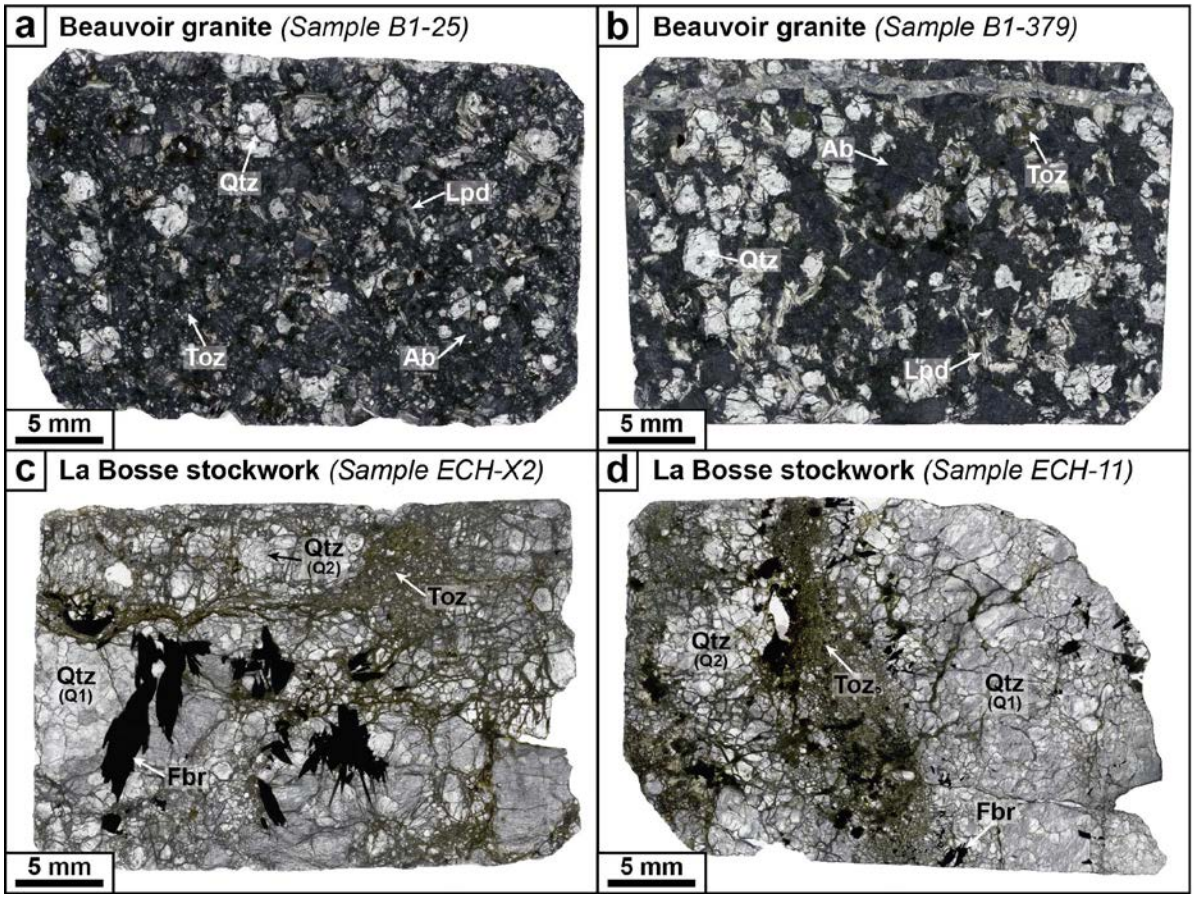

Fig. 141: Photographs of thick sections of the studied samples from the Beauvoir granite (a: B1-25; b: B1-379) and the La Bosse stockwork (c: ECH-X2; d: ECH-11). Abbreviations: Ab: albite; Fbr: ferberite; Lpd: lepidolite; Qtz: quartz; Toz: topaz.

4.1.2. Fluid inclusions in the La Bosse stockwork

In the topaz-bearing samples from the La Bosse stockwork (Fig. 141c,d), two types of quartz can be distinguished:

(i) Grey quartz (Q1) forming large crystals and containing numerous and small (< 10 µm) fluid inclusions, either disseminated or forming intragranular planes, corresponds to the primary quartz from the quartz-ferberite veins. The quartz is weakly deformed and the fluid inclusions appear as black decrepitated inclusions or deformed inclusions, due to the thermal effect of the Colettes granite emplacement (Aïssa et al., 1987b). They are not considered in the present study.

(ii) Limpid quartz (Q2) appearing as small interstitial or clustered crystals or as vein infillings within the altered quartz-ferberite veins.

The fluid inclusions encountered in either Q2 or in the topaz are of the same types as those found in the granite. Only few L1-type fluid inclusions were found in the quartz from the stockwork, being significantly less frequent than in the granite samples. They are multiphase (liquid+vapour+solids) with very irregular shapes and are small in size (10-24 µm). By contrast, V2- and L2-type fluid inclusions seem to be more frequent in the stockwork samples in comparison with the Beauvoir granite. V2-type fluid inclusions have regular to slightly irregular shapes with sizes ranging from 15 to 50 µm and are always found isolated or in clusters in the quartz and topaz crystals (Fig. 142d). The vapour phase represents ca. 60% of the total volume of the fluid inclusion. They contain occasionally small (< 5 µm) elongated refringent solids, which have a greenish colour in plane-polarized light and give no signal in Raman spectrometry typical of ionic solids. They are therefore interpreted as halite crystals. L2-type fluid inclusions were also found in the quartz and topaz. They have variable sizes (16-30 µm) with a small vapour bubble (Rv~30% in average) and contain several (n=1-3) small refringent solids of halite in the aqueous phase. Mixed L2-L3-type fluid inclusions are characterized by regular shapes and have a vapour phase representing 30 to 70% of the total volume (Fig. 142e). Their sizes range from 18 to 35 µm. They also contain cubic refringent solids of greenish colour, thought to be halite. Finally, the L3-type fluid inclusions are by far the most abundant fluid inclusions within the quartz and topaz crystals from the stockwork (Fig. 142f). They consist in two-phase (liquid+vapour) fluid inclusions, irregular to very regular in shape and ranging from 10 to 77 µm in size. The vapour phase occupies a variable volume comprised between 10 to 70% of the fluid inclusion.

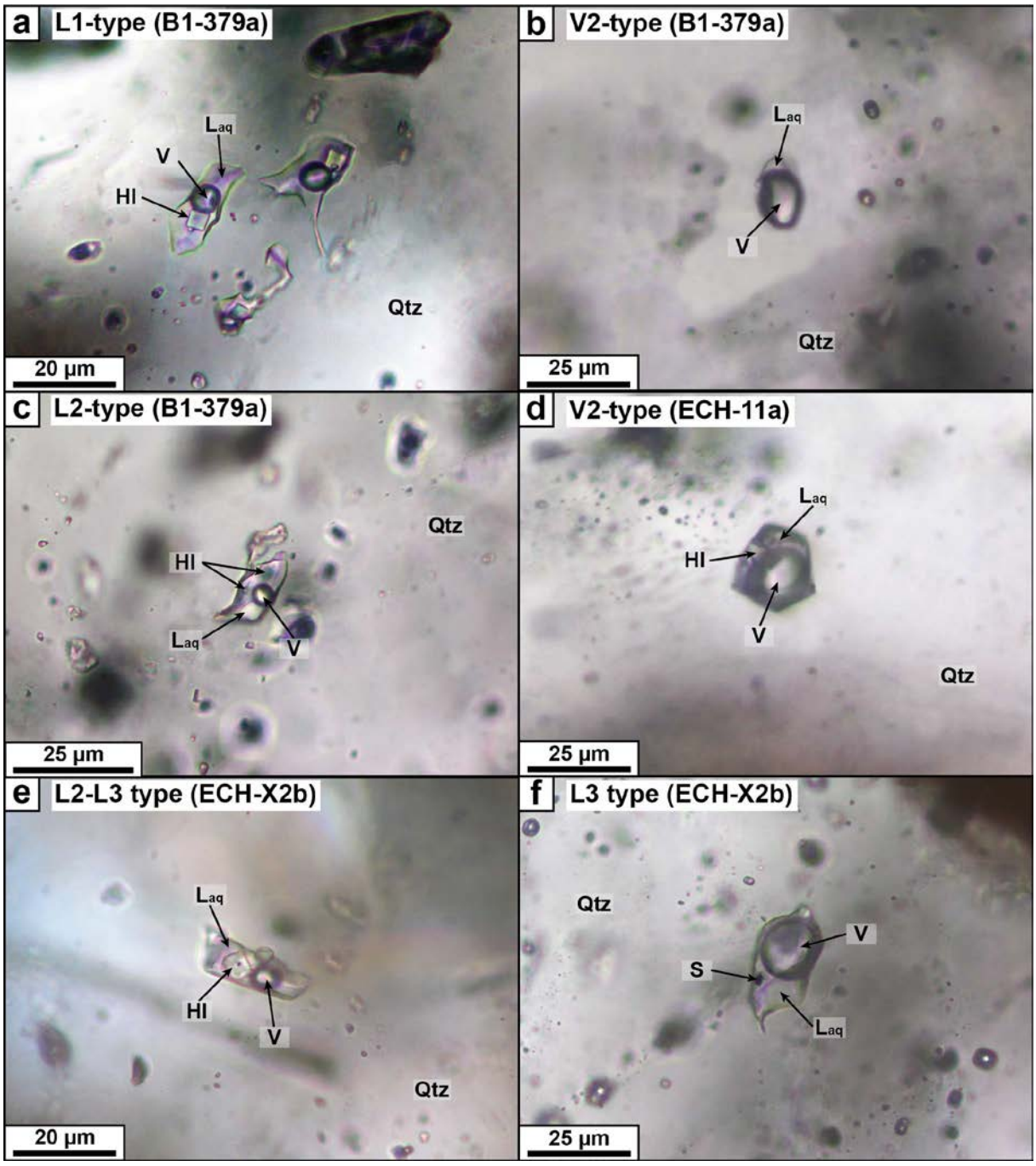

Fig. 142: Microphotographs showing the different types of fluid inclusions. Detailed description of each fluid inclusions type is given in the text. (a) L1-type fluid inclusion in globular quartz crystal from the Beauvoir granite (sample B1-379a). (b) V2-type fluid inclusion disseminated in the globular magmatic quartz from the Beauvoir granite (sample B1-379a). (c) L2-type fluid inclusions from a quartz crystal in the Beauvoir granite (sample B1-379a). (d) V2-type fluid inclusion isolated in the limpid quartz (Q2) from the La Bosse stockwork (sample ECH-11a). (e) Mixed L2-L3 fluid inclusion in limpid quartz (Q2) from the La Bosse stockwork (sample ECH-X2b). (f) L3-type fluid inclusion in limpid quartz (Q2) from the La Bosse stockwork (sample ECH-X2b). Abbreviations: Hl: halite; Laq: liquid aqueous phase; Qtz: quartz; S: unidentified solid; V: vapour phase.

4.2. Microthermometry and Raman results

Microthermometric and Raman data for the different fluid inclusions analysed are given in Table 40 and Fig. 143. The measurements of the T_H were strongly limited by the decrepitation of many fluid inclusions (ca. 75%) before bulk homogenization, despite the use of a slow temperature gradient (1-2 °C/min) during the heating phase. The decrepitation temperatures range from 250 to 500°C with a mode at ca. 400°C. Globally, the new results reproduce well the earlier findings of Aïssa et al. (1987b), including the systematic ΔT of ~100°C which is observed between the Th measurements in the Beauvoir granite, on one hand, and the La Bosse stockwork, on the other hand.

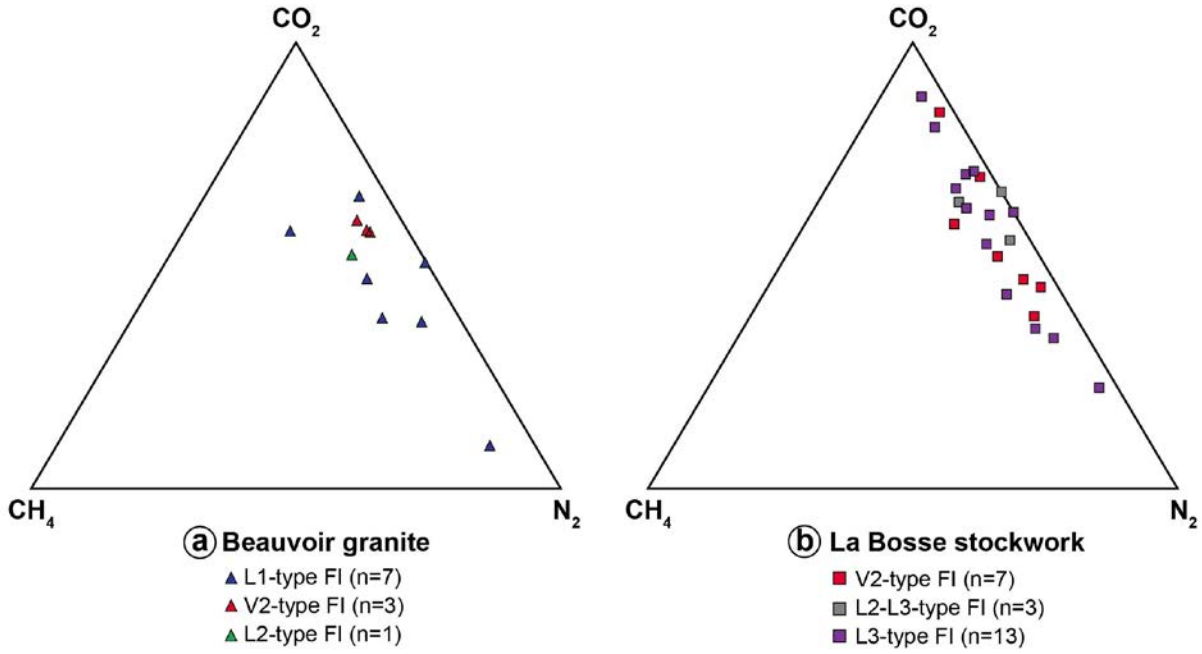

Fig. 143: Ternary diagrams CO_2-CH_4-N_2 showing the gas compositions of fluid inclusions from the Beauvoir granite (a) and the La Bosse stockwork (b) determined by Raman spectrometry. Representative Raman data of the different fluid inclusions analysed are given in Table 40.

4.2.1. L1-type fluid inclusions

They are characterized by very low eutectic temperatures (-80°C<T_e<-56°C) and low ice-melting temperatures (-39.9°C<$T_m$ice<-2.1°C). Hydrohalite melting was observed only in two fluid inclusions between -48.7 and -44°C. Most of the solids observed within the fluid inclusions correspond to halite crystals. Halite melting has been observed for fluid inclusions in the Beauvoir granite between 275 and 300°C, before the bulk homogenization, with an

average value of 287°C. One crystal of cassiterite (ca. 2 µm in size) has been identified by Raman spectrometry within a fluid inclusion of the Beauvoir granite (sample 379c, FI n°6a; Fig. 144). In the Beauvoir granite, the T_H (L) range from 491 to 600°C with an average value of 542°C. It should be noted that one fluid inclusion in a quartz crystal from the granite was not homogenized at 600°C, which is the upper limit of the Linkam stage used. In the La Bosse stockwork, the T_H (L) are lower and range from 377 to 468°C with an average value of 422°C. The composition of the vapour phase was only determined for fluid inclusions in the Beauvoir granite and is dominantly composed by CO_2 (9.7-65.6 mol%) and N_2 (20-82 mol%) with minor CH_4 (0.3-22 mol%) (Fig. 143; Table 40). No clathrate melting was observed in these fluid inclusions.

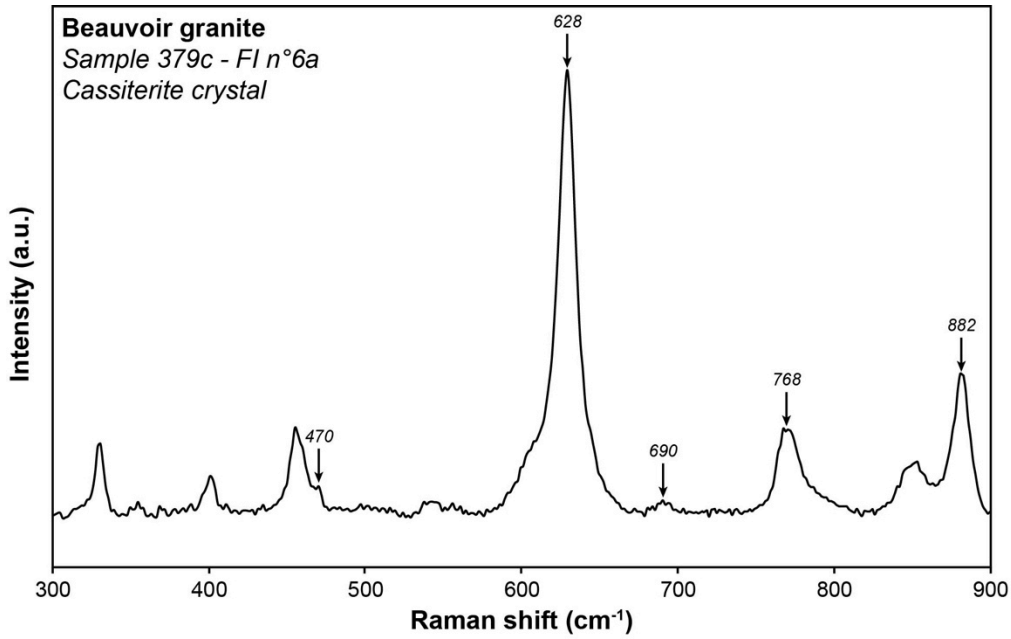

Fig. 144: Raman spectrum of a cassiterite crystal contained in a primary L1-type fluid inclusion within a magmatic quartz crystal of the Beauvoir granite (sample 379c, FI n°6a). The Raman shifts indicated on the spectrum corresponds to the Raman peaks of the cassiterite. The other peaks are those of the host quartz.

4.2.2. V2-type fluid inclusions

They show very low eutectic temperatures (-72°C<T_e<-65°C) and low ice-melting temperatures (-19.3°C<$T_m$ice<-1.4°C). One temperature of halite melting was measured in the granite at 300°C before the bulk homogenization. In the Beauvoir granite, the T_H (V) range from 375 to 595°C with an average temperature of 465°C. In the La Bosse stockwork, they

range from 342 to 490°C with an average temperature of 403°C. The majority of the bulk homogenization occurs in vapour phase, however a few were observed in supercritical phase (n=6). The volatile phase is dominantly composed by CO_2 (38.6-84.3 mol%), N_2 (12.9-53.6 mol%) and minor CH_4 (2.4-12.5 mol%) (Fig. 143; Table 40). Minor H_2S (1.7 mol% in average) was detected in V2-type fluid inclusions from the stockwork. V2 fluid inclusions represent low-density fluids, composed in majority by vapour H_2O with traces contents of volatils (CO_2, N_2, CH_4).

4.2.3. L2-type fluid inclusions

L2-type fluid inclusions have very low eutectic temperatures (-81°C<T_e<-52°C) and low ice-melting temperatures (-41.8°C<$T_m$ice<-1.6°C). Hydrohalite peritectic melting could not be observed in these fluid inclusions. Halite melting occur systematically before the bulk homogenization with T_mHl comprised between 215 and 407°C with average values of 359°C in the Beauvoir granite and 286°C in the La Bosse stockwork. In the Beauvoir granite, the T_H (L) range from 377 to 542°C with an average value of 455°C, whereas they range from 305 to 439°C with an average temperature of 375°C in the La Bosse stockwork. No clathrate melting was observed. The volatile phase is composed by CO_2 (52.4 mol%), N_2 (34.3 mol%) with minor CH_4 (13.2 mol%) (Fig. 143; Table 40) and represents only trace contents in the bulk composition of the L2-type fluid.

4.2.4. L2-L3-type fluid inclusions

They are characterized by very low eutectic temperatures (-73°C<T_e<-64°C) and low to relatively low ice-melting temperatures (-21.2°C<$T_m$ice<-1.2°C). Hydrohalite melting was not observed. Halite melting occurs before the bulk homogenization between 263 and 328°C in the stockwork with an average temperature of 286°C. Only one T_mHl was measured in the Beauvoir granite at 225°C. In the latter, the T_H (L) range from 407 to 414°C with an average temperature of 410°C. In the stockwork, the T_H (L) are comprised between 376 and 387°C with an average value of 382°C. The composition of the volatile phase was determined for L3-type fluid inclusions in the stockwork. The vapour phase is composed by CO_2 (55.7-66.5 mol%) and N_2 (26.6-40.5 mol%) dominantly, with minor CH_4 (0-9.2 mol%) (Fig. 143; Table 40).

4.2.5. L3-type fluid inclusions

They have very low eutectic temperatures (-72°C<T_e<-61°C) and low ice-melting temperatures (-4.3°C<$T_m$ice<-1.2°C). One T_mHl was measured at 292°C in a fluid inclusion from the stockwork. The T_H range from 338 to 398°C with an average temperature of 380°C in the stockwork. Within the Beauvoir granite, one T_H of 322°C was measured. The vapour phase is composed dominantly by CO_2 (22.6-87.9 mol%), N_2 (7.7-73.9 mol%) with minor CH_4 (0-10.5 mol%) (Fig. 143; Table 40).

4.3. Salinity calculation

Salinity of the fluid inclusions can be estimated in two ways: (i) from the microthermometric data by knowing the nature of the cations-dominant chemical system, which can be determined by the measurement of T_e and by using experimentally known model systems, such as H_2O-NaCl or H_2O-NaCl-$CaCl_2$ (Bodnar, 2003 and references therein); or (ii) from the Raman spectrometry analysis of the aqueous phase, which allows to estimate the chlorinity with a similar precision to the microthermometry (Caumon et al., 2013). Below is explained the calculation of the salinity of the fluid inclusions analysed (Table 40), which are reported hereafter in the salinity vs T_H diagram for the Beauvoir granite and the La Bosse stockwork (Fig. 145).

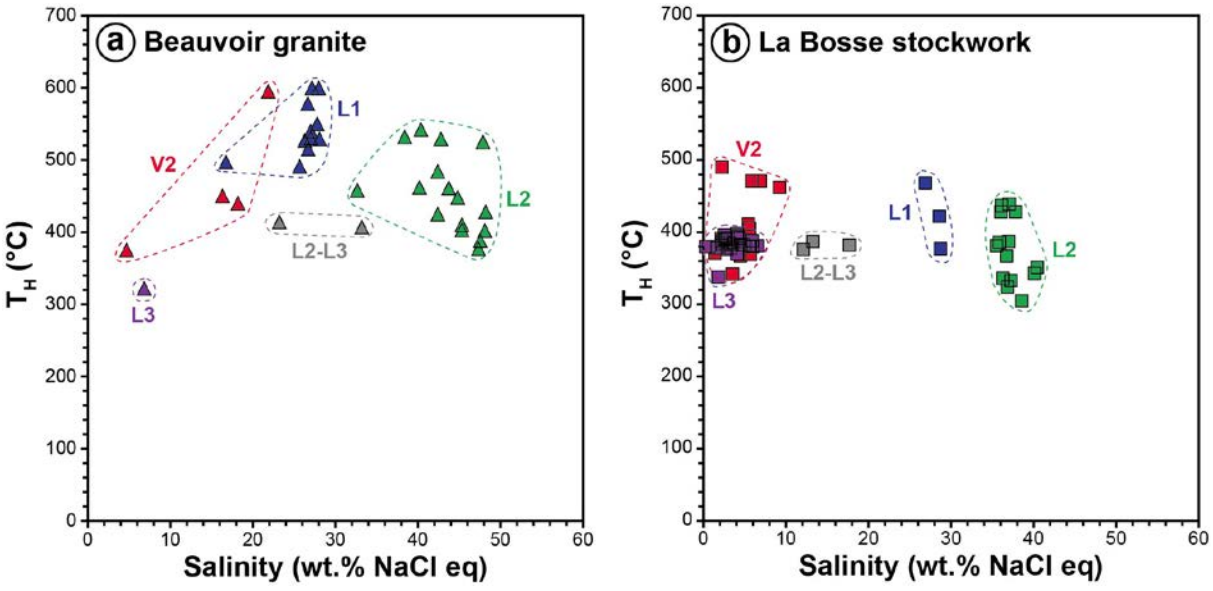

Fig. 145: Salinity vs T_H diagram for the different generations of fluid inclusions from the Beauvoir granite (a) and the La Bosse stockwork (b). Data are given in Table 40.

4.3.1. Estimation of the salinity for the L1-type fluid inclusions

From the microthermometric data:

All the L1-type fluid inclusions analysed in microthermometry have very low eutectic temperatures (-80°C<T_e<-60°C) with a mode value at -70°C, which are typical of the H_2O-NaCl-LiCl system (Monnin et al., 2002; Dubois et al., 2010). In this system, the salinity in wt.% NaCl eq of two-phase fluid inclusions can be estimated from the hydrohalite- and ice-melting temperatures, as well as the Na/Li ratio of the fluid (Dubois et al., 2010), whereas for halite-bearing fluid inclusions, ice melting and halite melting temperatures are sufficient to determine the system. However, hydrohalite-melting was very difficult to observe in the primary L1-type fluid inclusions, principally because of their small size (< 15 µm in average), and only two hydrohalite-melting temperatures could be measured, one in the Beauvoir granite (T_mHh=-44°C; B1-379c-6j), the other in the La Bosse stockwork (T_mHh=-48.7°C; ECH-X2b-44a) (Table 40). Based on the very similar $T_m$ice and considering that the two measured T_mHh are close, the hypothesis was made that all the inclusions shared the same T_mHh, and using the average value of T_mHh=-46°C for all the two-phase L1-type fluid inclusions, their salinity was estimated in the H_2O-NaCl-LiCl system (Dubois et al., 2010). A rough estimation by simply using the H_2O-NaCl model system (Bodnar 2003) was also performed. The salinity determined from the H_2O-NaCl-LiCl system ranges from 13.2 to 27.3 wt.% NaCl eq, while with the simple H_2O-NaCl, they should be estimated in the range from 16.7 to 38.2 wt.% NaCl eq.

From the Raman spectrometry:

As the T_mHl and $T_m$ice cannot always be measured easily in these fluid inclusions, the Raman spectrometry represents a good way to estimate the fluid salinity with a fast, systematic and reproducible acquisition. The estimated salinity ranges from 25.7 to 28.1 wt.% NaCl eq, with an accuracy better than ± 10% in average.

Synthesis:

The results are shown in Fig. 146 and given in Table 41. It appears that the salinity determined in the H_2O-NaCl-LiCl system is in good agreement with the one determined by Raman spectrometry, whereas the salinity determined in the H_2O-NaCl system appears always over-estimated compared with the two other salinities. Therefore, to overcome the lack in T_mHh measurements, the salinity determined by Raman spectrometry was selected when

available, and if not, the salinity determined using the H_2O-NaCl-LiCl system (in the way described in the preceding section) was chosen (see Table 40). By this method, it is finally found that the salinity of the L1-type fluid inclusions range from 16.7 to 28.1 wt.% NaCl eq in the Beauvoir granite, with an average value of 26 wt.% NaCl eq, while in the La Bosse stockwork, it ranges from 27 to 28.7 wt.% NaCl eq with an average value of 28 wt.% NaCl eq (Table 40). Judging from bulk salinity, they are therefore very similar.

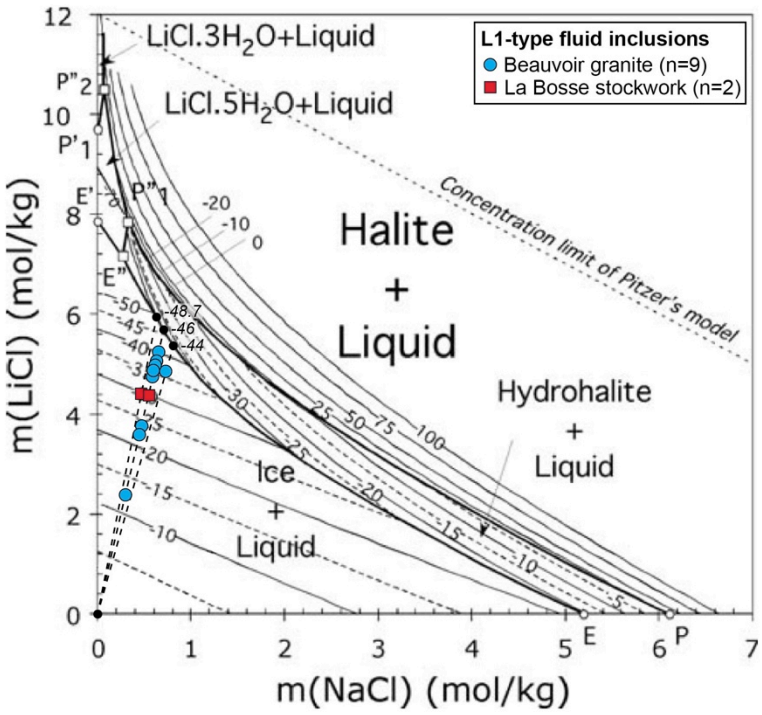

Fig. 146: Microthermometric data for the L1-type fluid inclusions represented in the m(NaCl) vs m(LiCl) diagram for the H_2O-NaCl-LiCl system (modified after Dubois et al., 2010).

4.3.2. Salinity estimated for the other fluid inclusions

The other types of fluid inclusions (V2, L2, L3, L2-L3) have also very low eutectic temperatures falling in the T_e range of the H_2O-NaCl-LiCl system (ca. -70°C). Since the hydrohalite melting could not been observed in these fluid inclusions, the salinity cannot be estimated by determining the molality in NaCl and LiCl, as for the L1-type fluid inclusions. In this case, the salinities were estimated by Raman spectrometry when possible or calculated in the H_2O-NaCl system (Bodnar, 2003) as the best possible approximation. The selected salinities are given in Table 40. Salinity of the V2-type fluid inclusions ranges from 4.7 to 21.9 wt.% NaCl eq in the Beauvoir granite with an average value of 15.3 wt.% NaCl eq, and

from 1.4 to 9.2 wt.% NaCl eq in the La Bosse stockwork with an average value of 4.5 wt.% NaCl eq. L2-type fluid inclusions are characterized by the highest salinities comprised between 32.6 and 48.2 wt.% NaCl eq with an average of 43.6 wt.% NaCl eq in the Beauvoir granite, and between 36.7 and 40.4 wt.% NaCl eq with an average value of 37.3 wt.% NaCl eq in the La Bosse stockwork. L2-L3-type fluid inclusions show salinities in the same interval values that those from the L1-type. They range from 23.2 to 33.2 wt.% NaCl eq in the Beauvoir granite with an average value of 28.2 wt.% NaCl eq, and from 12.1 to 17.7 wt.% NaCl eq in the La Bosse stockwork with an average value of 14.3 wt.% NaCl eq. Finally, the L3-type fluid inclusions have the lowest salinities in all the studied samples. The only L3-type fluid inclusion analysed in the Beauvoir granite has a salinity of 6.8 wt.% NaCl eq. In the La Bosse stockwork, the salinities range from 1.5 to 6.5 wt.% NaCl eq, with an average value of 3.7 wt.% NaCl eq.

4.4. Chemical composition of the fluid inclusions: LA-ICPMS measurements

The different generations of fluid inclusions were analysed by LA-ICPMS, with however a focus onto the L1, L2 and V2 families. The quality of the signals obtained depends highly of the size and of the depth of the fluid inclusions in the ablated mineral (quartz and topaz). A typical LA-ICPMS spectrum of L1-type fluid inclusion from the Beauvoir granite is shown in Fig. 147. The fluid inclusion signal is ca. 56 s in length and shows high signal/background ratios between 10^1 and 10^4 for most of the elements measured (Sn, Cs, Nb, Ta, W, Rb, Li). The Na signal is low due to the relatively high analytical background, which represents a technical limitation for the absolute quantification of the fluid inclusions signals. On the 47 fluid inclusions analysed by LA-ICPMS, only 28 yielded interpretable signals that were selected for the quantification. The salinity estimates previously calculated and reported in Table 40 were used to estimate the Na content for the quantification of the fluid inclusions signals and thus convert the ratios into bulk contents. Results are given in Table 42 and shown in Fig. 148. A discrepancy can be observed between the Na/Li ratios calculated from the microthermometric data and the LA-ICPMS data. Indeed, the Na/Li ratios estimated in the H_2O-NaCl-LiCl system fall in the range 0.4 - 0.5 (Table 41), whereas those calculated from the LA-ICPMS data are significantly higher comprised between 6 and 24 (Table 42). The latter are not consistent with (i) the very low eutectic temperatures (T_e < -70°C) indicating that Li is an abundant cation beside Na; and with (ii) preliminary LIBS data on primary fluid inclusions from the Beauvoir granite, which yielded Na/Li ratios comprised between 1.1 and

2.7 (Fabre et al., 2001). Therefore, it seems that the Li content is largely under-estimated by LA-ICPMS, thus resulting in high Na/Li ratios.

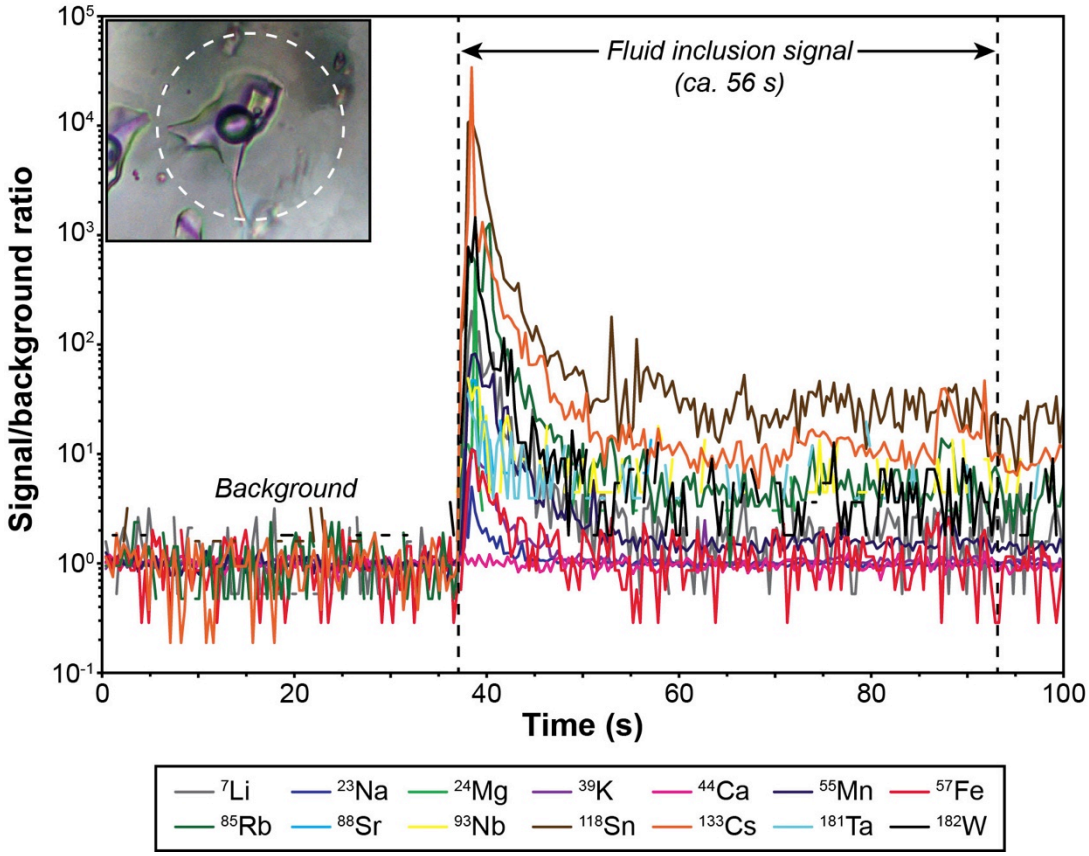

Fig. 147: Typical LA-ICPMS spectrum of a primary magmatic L1-type fluid inclusion hosted in a globular quartz crystal from the Beauvoir granite (sample B1-379a; inclusion n°A6b). The ablated fluid inclusion (picture in inset) was 17 µm in size using a laser spot diameter of 32 µm (dashed white circle). LA-ICPMS results are given in Table 42.

4.4.1. Fluid inclusions in the Beauvoir granite

L1-type fluid inclusions (n=5): they are characterized by very high contents in Na (103 500 – 110 600 ppm), Sn (1170 – 38 450 ppm), Cs (22 200 – 75 650 ppm), K (3230 – 41 720 ppm), high contents in Mn (8930 – 29 300 ppm), Fe (12 550 – 16 800 ppm), Rb (4110 – 13 850 ppm), Li (4450 – 17 960 ppm), W (920 – 2970 ppm) and minor contents in Nb (36 – 1450 ppm), Ta (18 – 180 ppm) and Sr (16 – 130 ppm). Their Na/Li and Na/K ratios range from 6.2 to 24 and 2.5 to 32, respectively.

V2-type fluid inclusions (n=2): they have lower concentrations in most of the measured elements compared to the L1-type fluid inclusions and also among all the analysed fluid

inclusions in the Beauvoir granite. They are characterized by relatively high contents in Na (71 600 – 86 200 ppm), Li (25 440 – 28 480 ppm), K (33 850 – 46 200 ppm), Cs (19 100 – 21 600 ppm), Mn (2640 – 22 400 ppm), Rb (7360 – 11 100 ppm) and moderate contents in Sn (1100 – 4270 ppm) and W (250 – 550 ppm), yielding to ratios Na/Li~3 and Na/K~2.

L2-type fluid inclusions (n=6): they have among the highest concentrations of the fluid inclusions analysed. They have very high contents in Na (158 200 – 189 700 ppm), K (35 350 – 1 280 400 ppm), Cs (23 700 – 42 150 ppm), Sn (14 300 – 75 050 ppm), Mn (44 550 – 865 000 ppm), high contents in Li (7370 – 335 930 ppm), Fe (26 600 – 220 000 ppm), Rb (14 950 – 44 100 ppm) and moderate to minor contents in W (1230 – 4250 ppm), Sr (32 – 84 ppm), Nb (11 – 1590 ppm), Ta (2 – 2280 ppm). The Na/Li and Na/K ratios range from 0.3 to 23 and 0.1 to 2.6, respectively.

L2-L3-type fluid inclusion (n=1): one fluid inclusion was analysed in a quartz crystal from the Beauvoir granite. It shows comparable concentrations with the L1-type fluid inclusions with very high content in Na (130 650 ppm), Sn (23 150 ppm), Cs (18 000 ppm), high contents in K (46 400 ppm), Mn (33 050 ppm), Fe (15 300 ppm), Rb (10 200 ppm), moderate contents in W (890 ppm), Li (5700 ppm) and trace contents in Sr (20 ppm) and Nb (6.3 ppm). This L2-L3-type fluid inclusion has Na/Li~23 and Na/K~3.

4.4.2. Fluid inclusions in the La Bosse stockwork

L1-type fluid inclusions (n=3): they show similar compositions with the L1-type from the Beauvoir granite. They have very high contents in Na (106 250 – 112 950 ppm), Fe (58 600 – 141 800 ppm), Mn (25 300 – 115 200 ppm), K (19 350 – 58 500 ppm), high contents in Cs (9750 – 14 800 ppm), moderate contents in Rb (1130 – 1940 ppm), Li (5740 – 9050 ppm), Sn (580 – 5870 ppm), W (185 – 230 ppm) and Sr (64 – 200 ppm). Their Na/Li and Na/K ratios range from 12 to 20 and 1.9 to 5.5, respectively.

V2-type fluid inclusions (n=3): they show the lowest concentrations compared with the L1- and L2-types in the La Bosse stockwork. Their composition is dominated by high contents in Na (5500 – 27 150 ppm), K (19 350 – 58 500 ppm), Fe (16 600 – 49 200 ppm) and moderate contents in Cs (370 – 5950 ppm), Sn (60 – 26 200 ppm), Rb (560 – 5230 ppm), Mn (450 – 25 200 ppm), Mg (1925 – 21 250 ppm), Sr (54 – 630 ppm), W (310 – 2220 ppm) and Li (2740 –

5930 ppm). Their Na/Li and Na/K ratios are comprised between 1 – 6.5 and 0.05 – 2.6, respectively.

L2-type fluid inclusions (n=4): they have the highest concentrations among the analysed fluid inclusions from the La Bosse stockwork. They have very high contents in Na (141 300 – 144 400 ppm), K (51 500 – 166 500 ppm), Fe (54 700 –232 400 ppm), Cs (10 900 – 83 600 ppm), high contents in Sn (2215 – 21 600 ppm), Mn (33 350 – 98 950 ppm) and moderate contents in Rb (2410 – 7400 ppm), W (240 – 1310 ppm), Li (4260 – 10 370 ppm) and Sr (91 – 560 ppm). In some of these fluid inclusions, Nb (63 – 110 ppm) and Ta (17 ppm) were detected. The Na/Li and Na/K ratios of the L2-type fluid inclusions range from 14 to 33 and 0.9 to 2.7, respectively.

L3-type fluid inclusions (n=4): these fluid inclusions were analysed in the quartz and topaz from the metasomatized stockwork. They are characterized by high contents in Na (13 800 – 22 050 pm), K (3000 – 17 700 ppm), Fe (24 150 – 170 500 ppm), Mn (21 850 – 59 550 ppm), Cs (1150 – 20 800 ppm), Sn (200 – 14 900 ppm), moderate contents in Rb (610 – 3340 ppm), Sr (15 – 4520 ppm), Li (925 – 3090 ppm), W (920 – 1400 ppm) and trace contents in Nb (57 – 160 ppm) and Ta (1.8 ppm). The Na/Li and Na/K ratios are comprised between 2.9 – 19 and 1.2 – 5.9, respectively.

5. Discussion

5.1. Magmatic signature of the early primary fluids from the Beauvoir granite

L1-type fluid inclusions represent the earliest records of the primary fluids in the Beauvoir granite. Microthermometric data showed that the fluids are high temperature (500 to >600°C), saline (17-28 wt.% NaCl eq) and Li-rich (T_e < -70°C). These temperatures are in accordance with the solidus temperature of the Beauvoir granite determined experimentally (Pichavant et al., 1987). LA-ICPMS analyses of the fluid inclusions reveal that the chemical composition of the fluid is dominated mainly by Li, Na, K, Cs, Sn, Rb as major cations with significant concentrations (10^2-10^3 ppm) in Nb, Ta and W as minor elements.

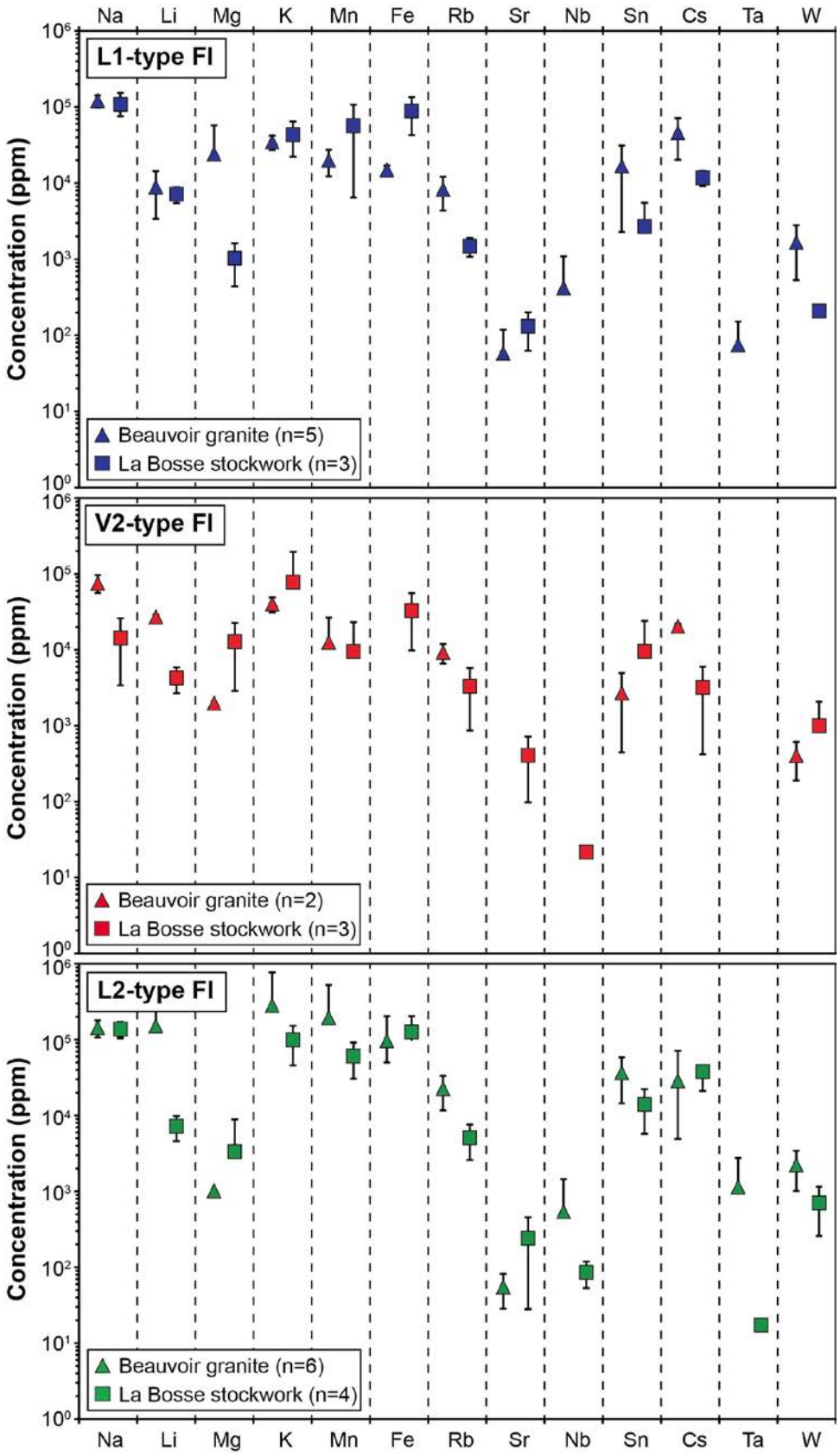

Fig. 148: Minor and trace elements contents in L1-, V2- and L2-types fluid inclusions (FI) from the Beauvoir granite and the La Bosse stockwork determined by LA-ICPMS. The values represented correspond to the average and standard deviations of the concentrations determined. Data are given in Table 42.

The very high concentration of Sn in the L1 fluid (up to 4 wt.% Sn) and highly variable appears suspect. Although, one micro-crystal of cassiterite was detected by Raman spectrometry, this does not necessarily indicate that the magmatic fluid was over-saturated relatively to SnO_2, but could possibly reflect the heterogeneous trapping of nano- to micro-inclusions of cassiterite. Nb content is higher in average than the Ta content in the fluids (Nb/Ta=5.6) and reaches several tens to one thousand of ppm. Nb is known to have been precipitate during the topazification of the wolframite stockwork (Aissa et al., 1987b), but not Ta. This may indicate the higher mobility of Nb compared to Ta in the magmatic-hydrothermal fluid derived from the Beauvoir granite. The fluid has very low contents in Ca and Sr and has a Na/K ratio close to 2. The composition of the L1-fluids contained in the primary quartz from the Beauvoir granite can be compared with the whole-rock composition of the B1 facies (Fig. 149). It appears that the primary L1 fluid is more enriched than the B1 facies granite in average for most of the elements (W, Nb, Mg, Fe, Mn, Cs, Sn, Rb, Na). Ta and K have close concentrations in the B1 granite and in the L1 fluid, suggesting maybe no particular partitioning.

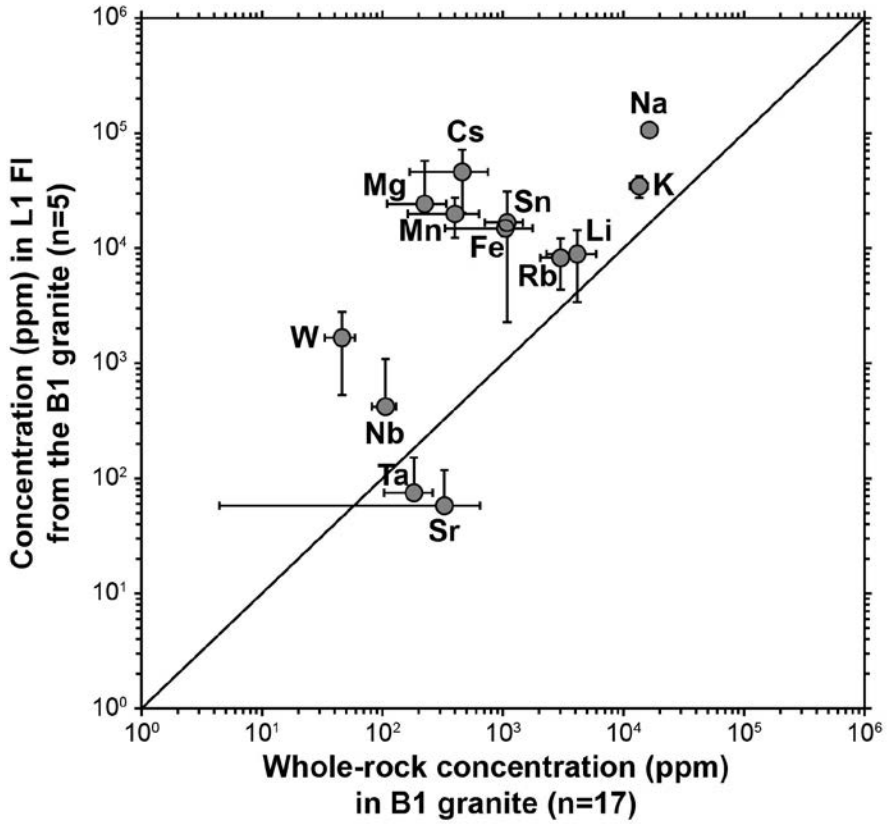

Fig. 149: Average concentrations of L1-type fluid inclusions (FI) contained in primary quartz from the Beauvoir granite vs average whole-rock concentrations of the B1 granite compiled from Cuney et al. (1992) and Raimbault et al. (1995).

The behaviour of Sr cannot be really discussed due to the large incertitude, however one can expect that it may follow the behaviour of Rb and be concentrated preferentially into the fluid phase. Ca was systematically below the limits of detection (LOD~3000 ppm) in the L1-type fluid inclusions, which indicates that its concentration was low in the primary fluid. This is also consistent with the low Ca content (0.7 wt.% CaO in average) in the Beauvoir granite (Cuney et al., 1992; Raimbault et al., 1995). F and Cl have not been measured by LA-ICPMS since they have high first ionization potentials, yielding to elevated LOD due to low sensitivity. However, there are several evidences that the primary magmatic fluid from the Beauvoir granite were F- and Cl-rich: (i) the high salinity determined in the L1-type fluid inclusions strongly indicates that Cl represents a major anion in the fluid; (ii) the very high content of Sn in the fluid inclusions suggests very high amounts of Cl, which is known to complex efficiency Sn in solution (Heinrich, 1990); (iii) the relatively high contents of Nb and Ta suggest high concentration of F in the magmatic fluids, which has been shown to increase significantly the solubility of these elements in hydrothermal solutions (e.g., Linnen and Cuney, 2005; Zaraisky et al., 2010; Timofeev et al., 2015); (iv) the high content in F and Al of the magmatic fluids is also demonstrated by the metasomatic topazites, which overprinted the early quartz-ferberite stockwork, those the magmatic origin has been inferred by the presence of primary L1-type fluid inclusions in the topaz (Aïssa et al., 1987b; Cuney et al., 1992). As comparison, elevated contents in F (ca. 4 wt.%) and Cl (ca. 0.3 wt.%) were found in primary melt inclusions from the Zinnwald rare-metal granites (Webster et al., 2004). Finally, the L1 fluid was likely under-saturated in SiO_2 and has slightly interacted with the enclosing rocks during its exsolution, which explains the dissolution of the quartz veins from the La Bosse stockwork. Consequently, the enrichment in incompatible lithophile elements within the L1 fluid reflects the high whole-rock concentrations in the B1 granite and indicates that the L1-type fluid inclusions preserved the pristine magmatic signature of the Beauvoir granite.

5.2. Element partitioning between co-existing vapour and brine phases during early boiling

Access to the major to trace elements composition of the co-existing V2- and L2-type fluid inclusions formed during the early boiling of the primary L1 fluid at ca. 400-520°C (Cuney et al., 1992) allows to study the element partitioning between the low-density vapour and the high-density brine phases. The average concentrations determined for the V2- and L2-

type fluid inclusions in the Beauvoir granite and the La Bosse stockwork are shown in Fig. 150. Although, the number of fluid inclusions analysed remains limited (n=2-6), it appears that the majority of the elements measured is preferentially concentrated into the aqueous phase in the Beauvoir granite (Fig. 150a). Whereas Cs, Rb, Na and Mg are close to the equilibrium line, W, Sn Li and Mn show however a clear preferential enrichment into the L2-type fluid inclusions. In the La Bosse stockwork (Fig. 150b), the trend is slightly different because W is more concentrated into the vapour phase, whereas Cs and Na are more concentrated into the aqueous phase. This difference may possibly reflect the interaction of the L2 and V2 fluids with external fluids in distance from the granite. This element partitioning is similar to the results of Audétat et al. (2000b), who showed that most of the elements exsolved from the crystallizing Mole granite, including W, Sn, Na, K, Li, Cs, partitioned preferentially into the brine phase.

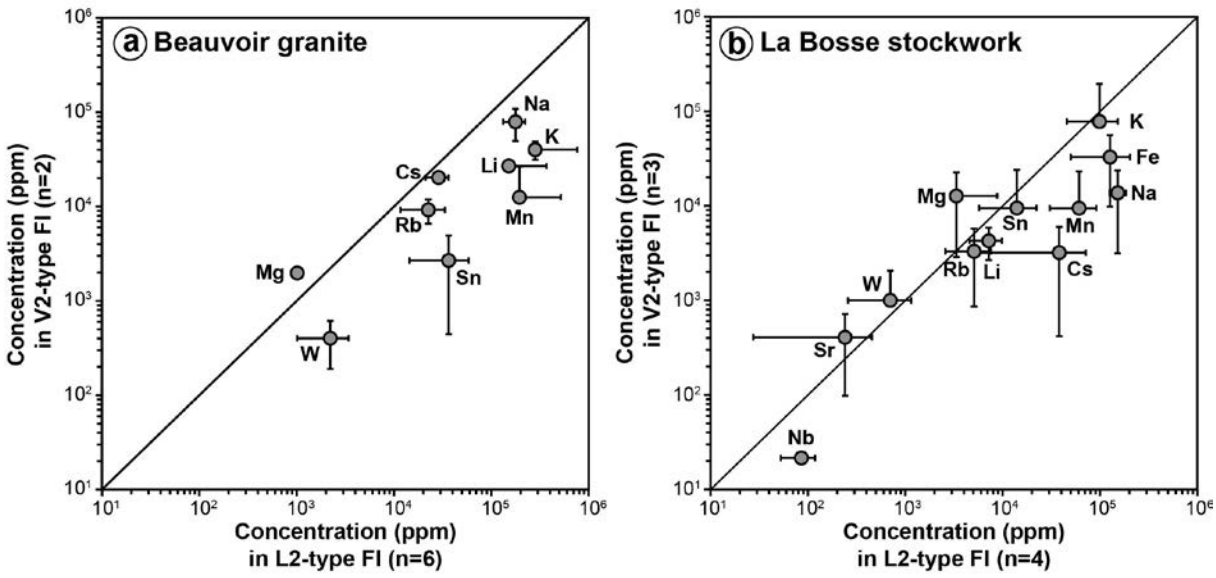

Fig. 150: Element partitioning between the V2- and L2-type fluid inclusions (FI) from the Beauvoir granite (a) and the La Bosse stockwork (b).

5.3. Chemical evolution of the magmatic fluids exsolved from the Beauvoir granite

The Beauvoir granite constitutes a remarkable case in the West European Variscan belt of a rare-metal granite crosscutting a quartz-ferberite stockwork with a vertical development of more than 100 m. The quartz-topaz vein from this study comes from the old La Bosse quarry (now filled with the wastes from the nearby kaolin quarry), at about 100 m above the granite and several 100 m laterally from the cupola (Fig. 139). This means that when the

magmatic-hydrothermal fluids issued from the B1 granite reached the stockwork, they had travelled through the enclosing micaschists and had therefore likely interacted with them. A comparison between the fluids found within the granite and those from the stockwork should therefore allow to quantify this interaction. Although the fluids encountered in the stockwork are mimetic at the first order with those of the Beauvoir granite, as seen in the previous section, microthermometric data also show that the T_H and the salinity are systematically lower in fluid inclusions from the La Bosse stockwork (Fig. 145). The T_H decrease is of 60 to 120°C in average from the granite to the stockwork, which is readily interpretable in terms of a cooling and thermal equilibration in the temperature gradient around the intrusion (Aissa et al., 1987b). The salinity decrease is of 3 to 10 wt.% NaCl eq in average, which, owing to the fact that the characteristic cationic ratios remain unchanged, likely means that the fluids issued from the Beauvoir granite were more or less diluted by a very low salinity fluid. This is turn is quite feasible, since the emplacement level of the pluton, estimated at ca. 3 km from the inclusions studies (Aïssa et al., 1987b) readily allows access to meteoric water coming from the surface. By contrast, there is no direct evidence for interaction with metamorphic fluids. There are indeed evidences of fluids of metamorphic derivation in the fluid inclusions from the metasomatized stockwork, but they are the same, and in the same few quantity, than in fluid inclusions from the granite, meaning that they are inherited. The very limited volatile content in the Beauvoir fluid inclusions was tentatively interpreted by Aïssa et al. (1987b) as due to the enclaving of micaschists in the Beauvoir melt, and in particular to the possible release of volatile-rich fluid inclusions in metamorphic quartz and quartz veins from the incorporated stockwork. When considered in detail, however, the chemistry of the L1, L2 and V2 fluids exhibit small, but significant, differences between the Beauvoir granite and the La Bosse stockwork, that may be interpreted as recording fluid-rock interaction of the magmatic fluids on their way outside the pluton (Fig. 148). Some of them may be due to direct interactions with the mineralized stockwork. For instance, the W enrichment in some V2 fluid inclusions may come from interaction with the wolframite, whereas the lack of Nb and Ta in L2 fluid inclusions may be the result of their trapping in the wolframoixiolite and columbo-tantalite crystallizing in microvugs within topazite-enclosed wolframites. Other elements, however, may be directly due to interaction with the micaschists, such as Sr, Fe, Mg, Mn and K. Nevertheless, it remains that the geochemical signature of the rare-metal granite is preserved in the fluid inclusions from the metasomatized La Bosse stockwork despite the distance from the granitic cupola roof and the interaction with external fluids. Consequently, it may be tentatively proposed that the geochemical signature of fluid inclusions may serve as

a highly reliable pathfinder for the discovery of hidden rare-metal granitic cupolas in the surroundings of the Echassières granitic complex and more widely in the Limousin area and elsewhere in the world.

6. Conclusions

This work allowed to characterize the geochemical signature of the magmatic fluids issued from the rare-metal Beauvoir granite intrusive in the Echassières granitic complex. The different generations of fluid inclusions (L1, L2, V2 and L3), initially identified by Aïssa et al. (1987b) were retrieved during this study. The L1-type fluid inclusions represent the earliest records of the primary fluids in the Beauvoir granite. Microthermometric data showed that these fluids are high temperature (500 to >600°C), saline (17-28 wt.% NaCl eq) and Li-rich (T_e < -70°C) with Na/Li ratios < 0.5. LA-ICPMS analyses show that the chemical composition of the fluid is dominated mainly by Li, Na, K, Cs, Sn, Rb as major cations with significant concentrations (10^2-10^3 ppm) in Nb, Ta and W as minor elements. Moreover, the massive topazification overprinting the La Bosse stockwork in surface indicates that the L1 fluid contained very high contents in F. Hence, the L1-type fluid inclusions preserved the pristine magmatic signature of the Beauvoir granite. Boiling of the L1 fluid yielded to the phase separation of a low- to moderate-salinity vapour (V2; 4.7-22 wt.% NaCl eq) and a high-salinity brine (L2; 32-48 wt.% NaCl eq) at ca. 450°C. LA-ICPMS analyses of these two types of fluid inclusions revealed that the L2-type fluid inclusions have among the highest concentrations in metals and show a preferential enrichment in most of the elements metals compared to the V2-type fluid inclusions. The evolution of the exsolved fluids in distance from the Beauvoir granite is characterized by a decrease in temperature and salinity, which can be interpreted in terms of cooling and thermal equilibration around the intrusion. Furthermore, the salinity decrease may indicate that the magmatic-hydrothermal fluids issued from the Beauvoir granite were more or less diluted by a very low salinity fluid, which may be possibly meteoric water considering the relatively low depth emplacement (ca. 3 km) of the Beauvoir granite. These results show that the geochemical signature of the rare-metal granite is preserved in the fluid inclusions from the metasomatized La Bosse stockwork despite the distance from the granitic cupola roof (> 100 m) and the interaction with external fluids. Consequently, it may be tentatively proposed that the geochemical signature of fluid inclusions may serve as a highly reliable pathfinder for the discovery of hidden rare-metal granitic cupolas at Echassières and more widely in the Limousin area.

Table 40: Petrography, microthermometry and compositional Raman data for the different fluid inclusions from the Beauvoir granite and the La Bosse stockwork.

	Petrography			Microthermometry				Salinity	Gas composition (mol %)				
FI type	n	Rv (%)	Size (µm)	T_e (°C)	$T_m$ice (°C)	T_mHh (°C)	T_mHl (°C)	T_{fl} (°C)	wt.% NaCl eq	n	CO_2	N_2	CH_4	H_2S
Beauvoir granite														
L1-type	11	20; 60; 40	10-23	-78; -56; -73	-39.9; -2.1	-44	275; 300; *287*	491; >600; *542*	16.7; 28.1; *26*	7	9.7; 65.6; *43.8*	20; 81.8; *46*	0.3; 22.2; *10.2*	-
V2-type	4	80; 90; 90	12-24	-72	-19.3	-	300	375; 595; *465*	4.7; 21.9; *15.3*	3	57.5; 60.1; *58.5*	31.5; 35.2; *33.7*	7.2; 8.4; *7.8*	-
L2-type	13	20; 40; 30	10-35	-77; -52	-39.9; -1.6	-	215; 407; *359*	377; 542; *455*	32.6; 48.2; *43.6*	1	52.4	34.3	13.2	-
L2-L3-type	2	30	30	-64	-21.2	-	225	407; 414; *410*	23.2; 33.2; *28.2*	-	-	-	-	-
L3-type	1	40	16	-61	-4.26	-	-	322	6.8	-	-	-	-	-
La Bosse stockwork														
L1-type	3	40; 40; 40	10-24	-80	-30; -8	-48.7	-	377; 468; *422*	27; 28.7; *28*	-	-	-	-	-
V2-type	16	60; 80; 60	15-47	-65	-6; -1.4; -3.5	-	-	342; 490; *403*	1.4; 9.2; *4.5*	7	38.6; 84.3; *55.7*	12.9; 53.6; *36.6*	2.4; 12.5; *5.9*	0; 6.3; *1.7*
L2-type	14	30; 40; 30	16-30	-81; -60	-41.8; -2.5	-	263; 328; *286*	305; 439; *375*	36.7; 40.4; *37.3*	-	-	-	-	-
L2-L3-type	3	60; 70; 60	18-35	-73	-1.7; -1.2	-	-	376; 387; *382*	12.1; 17.7; *14.3*	3	55.7; 66.5; *62.1*	26.6; 40.5; *33.5*	0; 9.2; *4.3*	-
L3-type	27	10; 70; 40	10-77	-72; -61; -72	-2.9; -0.15; -2.1	-	292	338; 398; 380	1.5; 6.5; *3.7*	13	22.6; 87.9; *58*	7.7; 73.9; *36*	0; 10.5; *5.9*	-

Values indicated correspond respectively to the minimum, maximum and mode values. Mean values are indicated in italics.
-: not determined

Table 41: Comparison of the salinity calculated for the L1-type fluid inclusions in the H_2O-NaCl system (Bodnar, 2003), H_2O-NaCl-LiCl system (Dubois et al., 2010) and determined by Raman spectrometry (Caumon et al., 2013).

			Microthermometry				Salinity in H_2O-NaCl system (Bodnar and Vityk, 1994)		Salinity in H_2O-NaCl-LiCl system (Dubois et al., 2010)					Salinity Raman
Sample	FI n°	Mineral	T_e (°C)	$T_m$ice (°C)	T_mHh (°C)	T_mHl (°C)	wt.% NaCl eq (1)	wt.% NaCl eq (2)	m(LiCl)	m(NaCl)	wt% LiCl	wt.% NaCl	Na/Li	wt.% NaCl eq	wt.% NaCl eq
B1-379a	A-6a	Qtz	-73.0	-37.8	~ -46*	-	34.21	-	5.00	0.62	16.98	2.90	0.41	26.3	27.0
B1-379a	A-6b	Qtz	-73.0	-34.8	~ -46*	-	31.89	-	4.80	0.60	16.43	2.83	0.41	25.5	26.3
B1-379a	A-6c	Qtz	-69.0	-35.8	~ -46*	-	32.63	-	4.90	0.61	16.71	2.87	0.41	25.9	26.7
B1-379c	C-1	Qtz	-	-22.1	~ -46*	300	-	38.16	3.60	0.48	12.93	2.38	0.44	20.2	28.1
B1-25a	A-4	Toz	-78.0	-37.1	~ -46*	275	-	36.33	5.00	0.62	16.98	2.90	0.41	26.3	25.7
B1-25a	B-1	Qtz	-64.0	-23.0	~ -46*	290	-	37.41	3.70	0.48	13.24	2.37	0.43	20.6	27.2
B1-379c	5b	Toz	-55.7	-39.9	~ -46*	-	36.04	-	5.20	0.70	17.48	3.24	0.45	27.3	-
B1-379c	6j	Toz	-69.8	-36.1	-44.0	-	32.86	-	4.80	0.70	16.35	3.29	0.48	25.8	-
B1-25a	10	Qtz	-62.8	-12.8	~ -46*	-	16.73	-	2.20	0.30	8.40	1.58	0.45	13.2	-
ECH-X2b	44a	Qtz	-80.5	-29.9	-48.7	-	28.57	-	4.40	0.50	15.34	2.40	0.38	23.6	-
ECH-X2b	44b	Qtz	-	-30.0	~ -46*	-	28.66	-	4.40	0.51	15.33	2.45	0.38	23.6	-

Salinity in the H_2O-NaCl system were calculated using the ice-melting temperature (1) and the halite dissolution temperature (2).

*: estimated value calculated from the average of T_mHh values of B1-379c-6j (-44°C) and ECH-X2b-44a (-48.7°C).

-: not determined

Table 42: Chemical compositions of fluid inclusions from the Beauvoir granite and the La Bosse stockwork determined by LA-ICPMS.

Fl type	Sample	Fl n°	Host-mineral	Size µm	Salinity wt.% NaCl eq	Concentrations (ppm)																	Mass ratios	
						Na	Li	Mg	K	Ca	Mn	Fe	Rb	Sr	Nb	Sn	Cs	Ta	W				Na/Li	Na/K
Beauvoir granite																								
L1-type	B1-379a	9a	Qtz	20	27.0	106250	9140	bdl	23150	bdl	8930	bdl	5000	bdl	180	6250	34550	130	bdl				12	4.6
L1-type	B1-379a	A6a	Qtz	23	27.0	106250	4450	bdl	36560	bdl	21300	12550	9030	16	bdl	18750	22200	18	1110				24	2.9
L1-type	B1-379a	A6b	Qtz	17	26.3	103500	8240	775	41720	bdl	29300	15300	13850	31	41	38450	71700	24	2970				13	2.5
L1-type	B1-379a	A6c	Qtz	19	26.7	105100	4670	bdl	3230	bdl	22800	16800	9330	130	36	18950	75650	22	920				23	32.5
L1-type	B1-379c	C1	Qtz	14	28.1	110600	17960	47700	40000	bdl	17000	bdl	4110	bdl	1450	1170	25900	180	bdl				6.2	2.8
V2-type	B1-379a	10a	Qtz	14	18.2	71600	25440	bdl	33850	bdl	22400	bdl	7360	bdl	bdl	4270	19100	bdl	250				2.8	2.1
V2-type	B1-379c	15v	Qtz	24	21.9	86200	28480	1980	46200	bdl	2640	bdl	11100	bdl	bdl	1100	21600	bdl	550				3.0	1.9
L2-type	B1-379a	7a	Qtz	30	48.1	189300	10900	bdl	82550	bdl	56900	26600	19250	32	17	42500	33600	bdl	1380				17	2.3
L2-type	B1-379c	6l	Toz	15	42.4	166850	7370	bdl	65350	bdl	56900	bdl	14950	bdl	bdl	30150	24100	bdl	2080				23	2.6
L2-type	B1-379c	6m	Toz	25	40.4	159000	11730	1010	72800	bdl	58450	bdl	15600	84	bdl	38850	24550	bdl	2130				14	2.2
L2-type	B1-379c	8a	Qtz	30	44.8	176300	27210	bdl	107150	bdl	85600	41800	20600	49	11	14300	23700	2.2	1230				6.5	1.6
L2-type	B1-379c	8c	Qtz	30	48.2	189700	335930	bdl	1280400	bdl	865000	220000	44100	bdl	bdl	17600	24150	bdl	bdl				0.6	0.1
L2-type	B1-379c	9a	Qtz	20	40.2	158200	513150	bdl	82600	bdl	44550	bdl	20600	bdl	1590	75050	42150	2280	4250				0.3	1.9
L2-L3-type	B1-379a	7b	Qtz	30	33.2	130650	5700	bdl	46400	bdl	33050	15300	10200	20	6.3	23150	18000	2.5	890				23	2.8
La Bosse stockwork																								
L1-type	ECH-X2b	6	Qtz	24	27.0	106250	9050	615	19350	bdl	115200	141800	1130	64	bdl	580	9750	bdl	230				12	5.5
L1-type	ECH-X2b	44a	Qtz	16	28.6	112550	6740	bdl	52600	bdl	25300	58600	1410	200	bdl	1710	10800	bdl	bdl				17	2.1
L1-type	ECH-X2b	44b	Qtz	10	28.7	112950	5740	1450	58500	bdl	30400	66150	1940	130	bdl	5870	14800	bdl	185				20	1.9
V2-type	ECH-X2b	D4	Qtz	42	6.9	27150	4160	1925	10500	bdl	450	16600	4130	630	22	2200	3300	bdl	2220				6.5	2.6
V2-type	ECH-11b	1a	Qtz	20	1.4	5500	5930	21250	10150	bdl	25200	bdl	560	540	bdl	26200	5950	bdl	480				0.9	0.5
V2-type	ECH-11b	22a	Qtz	30	2.6	10250	2740	15060	213600	bdl	2730	49200	5230	54	bdl	60	370	bdl	310				3.7	0.05
L2-type	ECH-X2b	B2	Toz	16	36.7	144400	6110	9700	61950	bdl	39500	90900	3500	560	110	16200	10900	17	1310				24	2.3
L2-type	ECH-X2c	21a	Qtz	25	36.3	142850	8060	230	115100	bdl	71800	129000	7400	150	bdl	21600	41700	bdl	670				18	1.2
L2-type	ECH-X2c	22	Qtz	30	35.9	141300	4260	110	51500	bdl	33350	54700	2410	91	bdl	2215	16150	bdl	240				33	2.7
L2-type	ECH-11a	17a	Qtz	25	36.1	142050	10370	bdl	166500	bdl	98950	232400	7040	165	63	16000	83600	bdl	585				14	0.9
L3-type	ECH-X2c	9b	Toz	25	3.5	13800	3090.0	4150	6600	bdl	28650	67300	1000	1900	160	8900	20800	bdl	1100				4.5	2.1
L3-type	ECH-X2b	A4	Qtz	77	4.5	17700	925	7810	3000	bdl	21850	24150	610	15.0	57	2870	1150	1.8	920				19	5.9
L3-type	ECH-X2b	C3b	Qtz	32	5.6	22050	7610	26260	17700	bdl	59550	170500	3340	4520	87	14900	10150	bdl	1400				2.9	1.2
L3-type	ECH-11a	8a	Qtz	16	4.1	16150	1850	bdl	5700	bdl	bdl	bdl	690	bdl	bdl	200	3300	bdl	bdl				8.7	2.8

bdl: below detection limit; Qtz: quartz; Toz: topaze.

GENERAL DISCUSSION AND CONCLUSIONS

1. Relationships between the W events and the late Variscan thermal evolution

1.1. Crustal melting during the late Carboniferous

As pointed out by Romer and Kroner (2015, 2016), the first-order control for W endowment at the scale of the Variscan belt was the deposition and tectonic accumulation of Ediacaran to Cambrian sediments at the Gondwana margin, whereas at the province or district scale, the main control was the disposal of a focussed heat flow driven by magmatic processes (heat advection). In fact, the Variscan orogeny was the first tectono-magmatic cycle experienced by the Gondwana-derived sediments, explaining the efficiency of tungsten (and other rare metals) concentration in relation with the maturation of the immature Variscan crust of Europe (Marignac and Cuney, 1999).

In the French Massif Central (FMC), the Late Carboniferous was characterized by the competition of compression and extension at the regional scale (e.g., Bouchot et al., 2005). This was due to the complex interaction, in time and space, of two opposite processes. On the one hand, on its western and eastern (in present coordinates) boundaries, the newly-born European plate issued from Devonian and Early Carboniferous subductions/collisions was submitted to compressive forces due to the on-going collisions of the Alleghanian (to the west) and Uralian (to the east) orogenic belts, that were not to end up until the Early Permian. This was pointed out as early as 1975 by Arthaud and Matte, who underlined the importance of the Late Carboniferous wrench fault system (e.g., South Armorican Shear Zone and its eastern prolongation) as a response to this extended field stress environment. On the other hand, starting from the end of the Devonian, a succession of lithospheric delamination events allowed both strong mantle-crust interactions and the massive production of felsic melts, and development of extensional conditions in the middle and upper crust. As a result, anomalous heat flows are recorded in the Variscan crust as either LP-HT metamorphic belts, such as in the Pyrenees (Laumonier et al., 2010 and references therein) or the southern FMC (Cévennes: Montel et al., 1992; Montagne Noire: Faure et al., 2014), or more local granite intrusions. The large Late Carboniferous Velay granite dome (ca. 305-300 Ma), with its pervasive cordierite-bearing migmatite aureole (Barbey et al., 2015), is a striking example of linking crustal-scale HT metamorphism with batholith-scale granite intrusion. The earlier giant Margeride batholith (ca. 340-330 Ma) is another example (e.g., Talbot et al., 2005).

The complementary information given by deep crust xenoliths found in the Tertiary Bournac volcano (E FMC) documents the importance of thermal events affecting the lower

crust since the end of the Devonian, at least in the southern FMC, with in particular the dating of two UHT granulite-yielding events in the lower crust at the end of the Carboniferous at 320-300 Ma and 300-280 Ma (Rossi et al., 2006) (Fig. 151). It is not before the Early Permian (ca. 285 Ma) that the beginning of a return to stationary geotherms is recorded in the Bournac xenoliths, at a time when the end of the Uralian and Alleghanian orogenesis allowed the generalisation of extensional conditions at the plate scale, at the origin of the ubiquist Permian basin and range provinces and associated magmatism (e.g., Praeg, 2004; McCann et al., 2006).

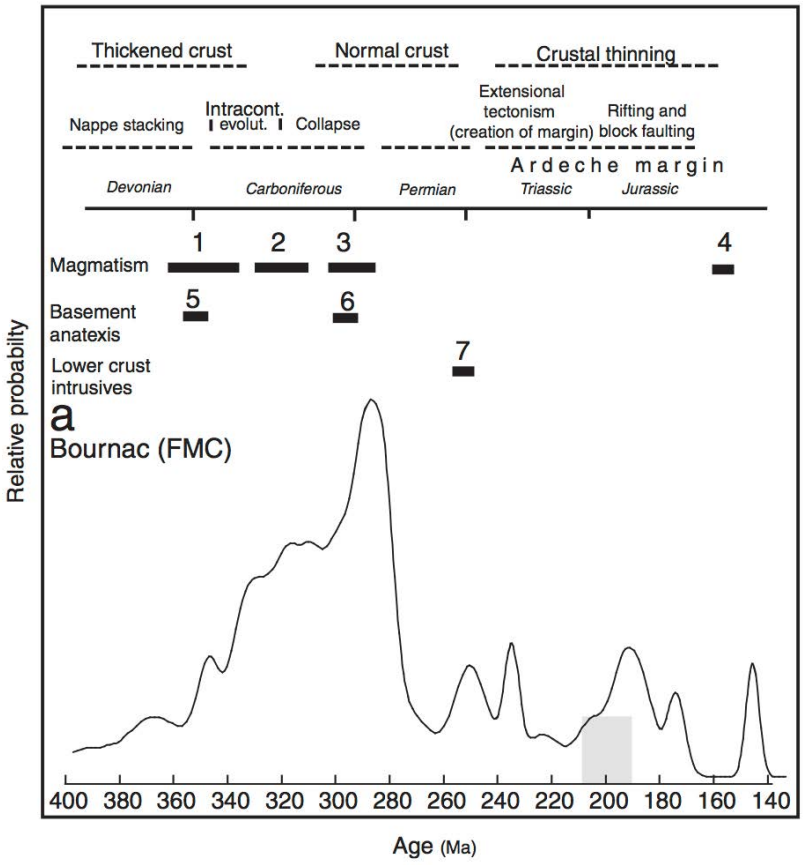

Fig. 151: Relative probability plot of U-Pb zircon ages from the Bournac volcano (eastern French Massif Central) and relationships with the main magmatism and geodynamic events (from Rossi et al., 2006).

1.2. From the W point of view

A result of the present work is a refining of the time-heat relationships for the W deposits at the scale of the FMC.

1.2.1. W events in the northern FMC (Limousin)

At the N Limousin scale, the first thermal event is Late Devonian-Early Tournaisian and is marked by the Guéret-type granite emplaced at ca. 360-350 Ma (e.g., Duthou et al., 1984; Bertrand et al., 2001), to which belongs the Aureil granite at the SW of Puy-les-Vignes. The lamprophyre dyke crosscut by the Puy-les-Vignes pipe (Chapter 4) is possibly of the same age. A second major event corresponds to the emplacement of the Millevaches and Brame-St-Sylvestre leucogranitic complexes during the Late Namurian (or Serpukhovian) at ca. 330-325 Ma (e.g., Holliger et al., 1986; Rolin et al., 2014), to which also pertains the Auriat granite at the NE of Puy-les-Vignes. The leucogranite dyke overprinted by the breccia pipe is also likely of the same age. Immediately following began the exhumation of the leucogranite complexes during the Early Namurian (or Bashkirian) at ca. 325-320 Ma (Scaillet et al., 1996; Le Carlier de Veslud et al., 2013; Rolin et al., 2014). This episode is also coeval with the first recorded hydrothermal event at Puy-les-Vignes, i.e. the greisenization (Fig. 67; Chapter 4), which is clearly retrograde for the regional Late Devonian migmatites. The wolframite deposition age is well dated at ca. 317 Ma (U-Pb on wolframite; Chapter 1), following the first brecciation stage, with the development of the tourmaline crackle-breccia, and the coeval W-rutiles (see Chapter 4). This occurred on a continued retrograde path, as demonstrated by the biotite to chlorite transformation (from Bt-Ms to Ms-Chl assemblages, i.e., from mesozone to epizone) in the breccia clasts. This Late Namurian episode corresponds also in the N Limousin to the emplacement of the La Porcherie leucogranite dated at 317 ± 3 Ma (U-Pb on zircon; Lafon and Respaut, 1988). It is also the age of migmatites exhumed from the bottom of the Millevaches leucogranite by the activity of the Pradines fault and dated at 316 ± 2 Ma (U-Pb on monazite from leucosomes; Gébelin et al., 2009). Apart from these exhumed rocks, this HT event is not documented at the present erosion level in N Limousin, suggesting that it was restricted to a deeper part of the nappe pile.

The Puy-les-Vignes rare-metal leucogranite, dated at ca. 314 Ma in this work (Chapter 4), is easily correlated with the belt of rare-metal granites (RMG) and rare-metal pegmatites (RMP) running W-E from the Blond to the Beauvoir plutons. As seen in Fig. 152, the age of this belt is however difficult to constrain, because of several discrepancies. The Beauvoir granite yields a 308 ± 2 Ma age by Ar-Ar dating on lepidolite (Cheilletz et al., 1992), but a 317 ± 6 Ma age by U-Pb dating on a magmatic columbite-tantalite (Melleton et al., 2015), and these ages are not mutually compatible. There is however no known post-magmatic high-temperature event at Beauvoir, which could have reset the Ar-Ar age, and looking at the

consistency of Ar-Ar (Li-mica) and U-Pb (columbite-tantalite) ages at Chédeville (Fig. 152), it may be proposed that at Beauvoir it is the Ar-Ar age which is the most reliable. In the same way, the Blond granite yields ages at 311 ± 0.5 Ma by Ar-Ar dating on Li-muscovite (Alexandrov et al., 2002) and at 319 ± 7 Ma by U-Pb dating on zircon (Alexandrov et al., 2000). These ages seem again mutually not compatible. In the latter case, however, as observed by Cuney and Marignac (2015), all the zircons from the Blond granite are strongly zoned, with a core and a rim. In fact, the obtained ages spread from ca. 340 Ma to ca. 309 Ma, and the published age of 319 ± 7 Ma is an average. A better interpretation is that the ages are a mixture between an inherited core at ≥ 340 Ma (likely the age of the hosting Guéret-type Cieux-Vaulry granite) and a magmatic rim at ca. 311 Ma, the likely age of the Blond granite (Cuney and Marignac, 2015). Other ages for RMG were obtained: (i) by Ar-Ar on Li-mica only, such as for the Richemont rhyolite, which yielded an Ar-Ar age on lepidolite at 313 ± 1.4 Ma (Cuney et al., 2002); (ii) by both Ar-Ar on Li-mica and U-Pb on columbite-tantalite, as exemplified by the Chédeville pegmatite (Ar-Ar ages at 309 ± 0.9 Ma and 310 ± 1.5 Ma; Cheilletz et al., 1992; Cuney et al., 2002; U-Pb age at 309 ± 5 Ma; Melleton et al., 2015) and the Montebras granite (Ar-Ar age on lepidolite at 309.9 ± 0.7 Ma; Cuney et al., 2002; U-Pb age at 314 ± 4 Ma; Melleton et al., 2015). Finally, it seems that as a best estimate, the RMG generation spread a range of ages during the Westphalian (or Moscovian) in the 314-308 Ma interval (Fig. 152). The 314 ± 4 Ma age of the Puy-les-Vignes RMG (Chapter 4) is evidently consistent with this interval. The "N Limousin RMG event" would thus appear to slightly post-date the migmatite event recorded by Gébelin et al. (2009), but would more or less be coeval with the activity of some significant wrench shear zones such as the Pradines and the Marches faults, the latter being suspected by Melleton et al. (2015) to have controlled RMG emplacement.

The late age recorded at Puy-les-Vignes (ca. 300 Ma; Ar-Ar on adularia) may be correlated with another large thermal event, expressed to the north in the St-Sylvestre leucogranitic complex by the generation of episyenites, well dated at 305 ± 1 Ma (Ar-Ar on muscovite; Scaillet et al., 1996) and 301 ± 2 Ma (Rb-Sr on whole-rock and minerals; Turpin et al., 1990), and interpreted as due to the circulation of HT vapours, generated at depth at temperature ≥ 400°C (Cathelineau, 1986). The development of the large corresponding hydrothermal system (also recorded by the penetrative chloritisation of the Brame-St-Sylvestre complex) involves a deep heat source. In the same way, the coeval gold-depositing hydrothermal systems developed in the southern Limousin imply a source of ≥ 400°C moderately saline fluids (Souhassou, 2001; Boiron et al., 2003). In the latter case, the source

of heat and deep fluids is suspected to have been a deep-seated Velay-type granite and its migmatite aureole (Marignac et al., 2000). The Blond-centered hydrothermal system, which generated the ca. 298 Ma Vaulry deposit (U-Pb on wolframite; Chapter 1), is another manifestation of this large-scale thermal event affecting the Limousin crust at the end of the Carboniferous, during the Stephanian (or Gzhelian).

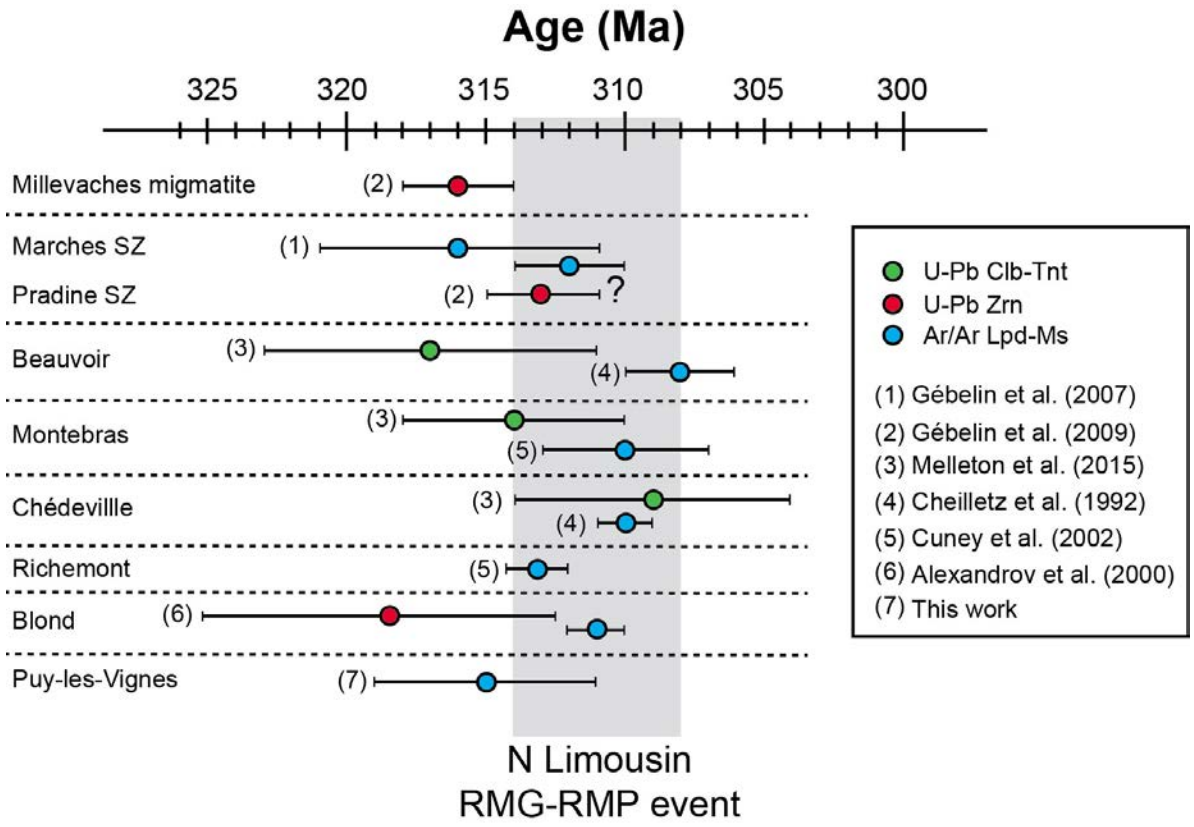

Fig. 152: Synthesis of the geochronological data for the rare-metal granites and pegmatites (RMG-RMP) from the Limousin area (NW French Massif Central).

1.2.2. W events in the southern FMC (Cévennes and Châtaigneraie)

In the N Cévennes, no magmatic event is dated prior to the LP-HT metamorphic event (M3) at ca. 315 Ma (i.e., more or less coeval with the deep thermal event leading to migmatites in the N Limousin). However, numerous bodies of a porphyritic Bt-granite are known to the east of the catazonal domain, which are demonstrably earlier than the M3 migmatites (Thierry et al., 2014) and look very similar to the Margeride granite. The latter, which is dated at 334 ± 7 Ma (U-Pb on zircon; Respaut, 1984), is clearly southwardly overthrusted (biotite-sillimanite-bearing shear zones) on the country rocks from the Para-Autochthonous Unit (PAU), and therefore is interpreted as late-kinematic for the South

Cévennes thrusting event (Ledru et al., 2001). The peraluminous Rocles granite is coeval with the LP-HT metamorphic event and the associated deformations, and the small W deposit of St-Mélany is proved on a structural analysis basis to have been formed under late-kinematic conditions (Chapter 6). This is confirmed by direct U-Pb dating on wolframite (315 ± 15 Ma; Chapter 1) and by Ar-Ar dating of the vein muscovite selvages (Chapter 6). The later yielded two ages: a core age at ca. 317 ± 5 Ma and a rim age at 298 ± 3 Ma. The former is interpreted as recording the crystallization of muscovite. As schematically described in Fig. 153, this is possible because the N Cévennes pile suffered the beginning of a quick exhumation just after the M3 peak (Montel et al., 1992; Barbey et al., 2015), and would have been favoured if the muscovite crystallized on this exhumation path, not too far from the mesozone isograde. The rim age of ca. 300 Ma results from the reheating experienced by the N Cévennes pile at the time of the Velay event (M4 geotherm) quickly followed by a cooling on the M4 geotherm.

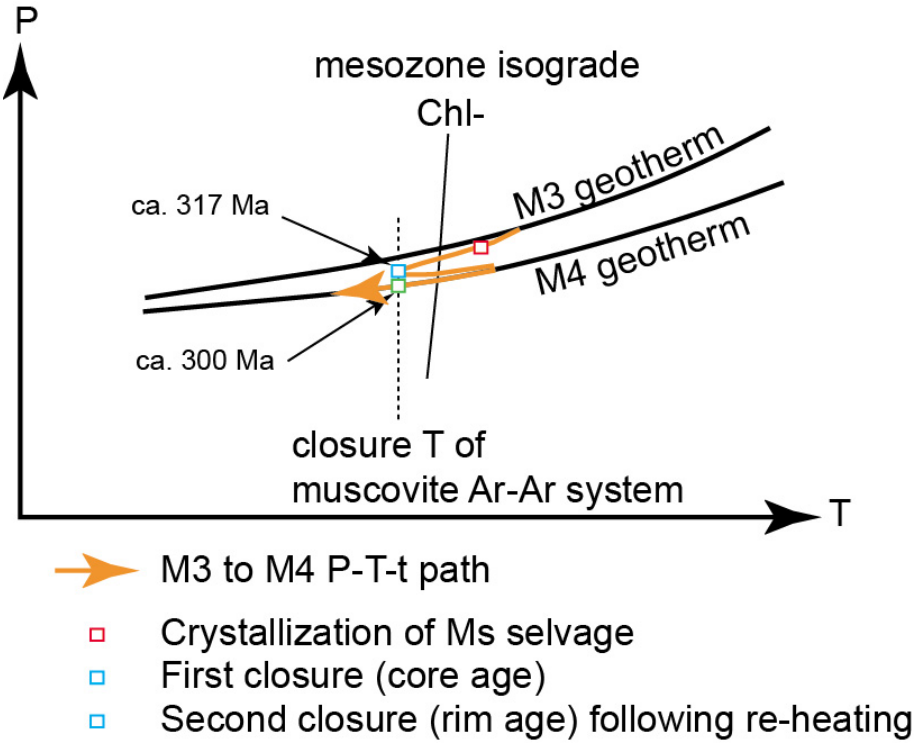

Fig. 153: Conceptual P-T-t path of the muscovite at the selvage of the quartz mineralized veins from the St-Mélany deposit. The geotherms are from Montel et al. (1992).

Clustering between ca. 305 and ca. 300 Ma (Stephanian), a series of granite intrusions affected the N Cévennes, with the Borne A-type pluton in the south, and the large Velay pluton and the late Tanargue and Fabras granites to the north. At the St-Mélany locality, these events are recorded as lamprophyre and aplite-pegmatite dykes, the latter with a clear RMG-

RMP (PHP-type of Linnen and Cuney, 2005) affinity (Chapter 6). The latest magmatic events in the N Cévennes Variscan history occurred in the Early Permian-Stephanian, in relation with the development of the Prades-Jaujac coal basin dated at 296 ± 7 Ma (U-Pb on zircons from intercalated tuffs; Bruguier et al., 2003).

In the La Châtaigneraie, the emplacement of Margeride-like plutons in epizonal rocks of the PAU is the first recorded magmatic activity (W-Margeride to the S and Veinazes to the N of the Enguialès deposit). There is a large contact metamorphic aureole around these plutons, with an external "spotted zone" and an internal "hornfels" zone. The Enguiales deposit is located on what is described (Derré, 1983; Caia, 1989) as an apophysis of this aureole, with a Bt zone at the outcrop and a "spotted" zone at depth, but the mining works were nowhere as deep as to meet the inferred intrusion beneath the deposit. The old works are no more accessible, but "spotted" schists may be found in the mining dumps. They effectively show elliptic spots (~1 cm) of altered cordierite. These spots are however very similar with those which, in the N Cévennes, record the beginning of the mesozone. Also, the 1:50 000 geological map (Goër de Herve et al., 2006) shows that the "hornfels" zone is offsetting the "spotted" zone. It may therefore be suspected that the thermal history of the area is more complicated than currently assumed, and would demand further investigations.

Whatever the significance of this LP-HT metamorphic overprint onto the epizonal rocks, it is observed that the thermal aureole surrounding Enguiales is spatially associated with fluid circulations, in a way very reminiscent of the N Cévennes at St-Mélany. Whereas at the regional scale quartz veining appears very scarce in the epizonal schists, when getting close to the Enguiales deposit (and the same seems true for the nearby Leucamp deposit as well) a series of quartz veins, several tens meter in long and up to 50 cm thick, are observed to develop. These veins are mostly sub-concordant to the regional schistosity, exhibiting conspicuous boudinage, but may also been oblique, and in that case suffered flattening, resulting into folding. The Enguiales deposit itself is made of two sets of pene-contemporaneous veins, one set subconcordant to the regional schistosity, the other strongly discordant, without conspicuous deformation at the outcrop scale (although quartz may exhibit plastic deformation to some extent at the thin section scale). The veins are surrounded by tourmalinite selvages, which are very similar to the "Rocles-type" tourmalinites of the N Cévennes, and may be affected by more or less syn-hydrothermal shearing at the microscope scale (Chapter 7) and, as in the N Cévennes, pre-dated the quartz veins opening, although later acicular tourmalines are associated to the veining and are affected by crack-sealing. All

these observations point to a similar relationship between regional fluid circulation and deformation and the development of the wolframite-bearing vein systems at Enguiales and at St-Mélany. One is therefore expecting also a similar age (or older at Enguiales, if the thermal advection is really associated with the Margeride event). In this respect, the existing data are rather disturbing. Two Ar-Ar ages are known (Monié et al., 2000), one from a muscovite from the vein selvage, yielding a ca. 305 Ma age, the other from a muscovite taken from a microvug in the quartz, with a 312 Ma age. While the former may evidently be rejuvenated by later fluid circulation at the quartz-surrounding rocks contact, the latter may be closer to the mineralization age, although the paragenetic position of this in-vug muscovite is not known, being altogether likely later than the wolframite. The U-Pb age obtained on the wolframite at ca. 275 Ma (Chapter 1) is evidently too young, and calls for some kind of rejuvenation of the wolframite during a later alteration event such as the ferberitization. The paragenetic evolution at Enguiales is unfortunately poorly documented, due to a lack of samples from the active workings, only a very few wolframite-bearing samples having been found at the surface in the mine wastes. It is only known that a strong scheelitization event occurred somewhere in the history (Derré, 1983; Caia, 1989).

At the regional scale, two other magmatic events are observed. One consists in a series of small intrusions and NE-trending leucogranite dykes, which are dated at ca. 306 Ma (Ar-Ar on muscovite; Monié et al., 2000) and are believed by some workers to be responsible for the Enguiales deposit (Gama, 2000; Lerouge et al., 2000). The second is represented by a swarm of NW-trending dykes of microgranite and microgranodiorite, to which the Soulaque granodiorite stock is likely related (Demange et al., 1988a). A K/Ar Permian age of 274 ± 8 Ma was obtained by Bellon and Gibert (1981) for a microdiorite dyke in the north of the Entraygues granite. It is possible that the postulated rejuvenation of the Enguiales wolframite be related to the corresponding thermal event.

1.2.3. Conclusion

From a purely thermal point of view, the histories of the northern and southern segments of the Variscan FMC are strikingly parallel, although the tectonic context, on the one hand, and the relative importance of each event, on the other hand, may be quite different. From the ca. 330-325 Ma event to the very beginning of the Permian, it is remarkable that each thermal pulse at the crustal scale was associated to a W-depositing event in one or the other part of the belt. Although developed at the scale of the belt, and associated with large peraluminous

batholiths, the Late Namurian (or Serpukhovian) event at ca. 330-325 Ma is of limited importance from the W point of view, to the noticeable exception of the La Bosse stockwerk in the Echassières complex. It is apparently the Westphalian (or Moscovian) event at ca. 315 Ma associated with the LP-HT tectono-metamorphic episode, which has the greatest importance, with the Puy-les-Vignes and Enguialès major deposits, and the small St-Mélany occurrence. At the end of the cycle, the large middle crustal anomalies associated to the intrusion of Velay-type plutons at ca. 300 MA are again of limited significance for the tungsten, with only the small Vaulry occurrence, although they are clearly responsible for the gold endowment of the FMC. This late delamination event seems however responsible for the formation of RMG and RMP, in relation with incipient granulitization starting at ca. 315-310 Ma, according to the findings in the Bournac xenoliths (Rossi et al., 2006).

2. The source problems

2.1. St-Mélany: towards an integrated model

2.1.1. Tourmaline: the boron source

It is a striking fact that neither the Rocles nor the Borne granites are normally tourmaline-bearing, whereas tourmalinization is clearly spatially related to the granite environment. It is however known experimentally that a fluid equilibrated with a B-containing aluminium saturated mineral assemblage may dissolve significant quantities of boron, as temperature is increasing, up to 2.5% B_2O_3 at 700°C (Weisbrod, 1987). Metapelites are a good example of such an assemblage, and, when issued from marine sediments, contain effectively boron, more than 80 ppm as an average, and up to 150 ppm (Leeman and Sisson, 1996). The metapelitic rocks of the Cévenole series, considered as metaturbidites, are aluminium saturated as shown by the appearance of cordierite and/or andalusite in the mesozone, with some graphite-bearing pyrophyllite schists in the epizone (Weisbrod, 1970). Metamorphic fluids issued from the prograde LP-HT M3 metamorphism are thus expected to be enriched in boron, and when following a retrograde path, are therefore an evident source of boron for metasomatic tourmalinization. The same process of boron remobilization from metasediments by heated fluids was demonstrated, for instance, in the contact metamorphism aureole of the Skiddaw granite by Bebout et al. (1999).

Two types of tourmalinization are observed in the St-Mélany area (Chapter 7). Both

types are joint-controlled, and thus were formed in a context of enhanced permeability, allowing channelling of the fluids when beginning to leave the metamorphic environment. A first type, the “Rocles-type”, is well expressed in the vicinity of the Rocles pluton roof, and results from the transformation of micas (yielding Al, Fe, and Mg) into tourmaline along the schistosity, starting from a joint. The late-kinematic origin of this tourmalinization event seems clear, meaning that it resulted from retrograde fluid circulation at the end of the M3 event. This is corroborated by the fact that they are earlier than the St-Mélany W-bearing quartz vein system, itself demonstrated late-kinematic, and resulting from metamorphic fluid circulation (Chapter 7). A second “Borne-type” is mainly found at the Borne-schists boundary, as tourmaline veins with bleached selvages, clearly resulting of a joint-controlled B-rich fluid circulation, with extraction of Al, Fe and Mg from destroyed micas in the selvage. Such veins may overprint the Borne granite, and they seem mainly controlled by the late leucogranite dykes. They are thus the likely expression of the contact metamorphism fluids leaving the main Borne contact aureole. Their late character is confirmed by the observation of them overprinting the earlier Rocles-type tourmalinites in the Drobie river valley.

Rocles-type tourmaline: what is learned from trace element contents

Whereas a main metapelite source for B and the water involved in Rocles-type tourmalinization is thus demonstrated, the consideration of trace elements leads to a slightly more complicated view. As seen in the Chapter 7, two sources are in fact fingerprinted in these tourmalines. A first, metasedimentary, source is not surprising and is indeed expected. There is however a second source, with apparently a clear granitic signature marked in particular by the input of rare metals. These two end-member sources are as a rule simultaneously participating to the tourmaline growth, involved in mixing processes, with varying with time ratios between the end-members, suggesting independent inflow of the corresponding fluids. The participation of a granite-derived fluid is thus demonstrated.

Nature of the granite-derived fluid: what was learned from the Ti-oxides

An important conclusion of the study of the W (and Sn) behaviour in the prograde metamorphism along a S-N profile along the Baume River valley (Chapter 6) was that, whereas W was leached from the metapelites with increasing metamorphic grade, a distinct W (and Sn) re-enrichment was observed in relation with the Rocles granite roof, the rare metals being trapped within the then recrystallizing Ti-oxides (anatase in the mesozone, and rutile at higher grade). Moreover, observations in the St-Mélany area lead to the conclusion of a

pulsatile rare metal input, suggestive of the involvement of a magmatic-hydrothermal fluid, likely derived from the most evolved Rocles facies, the roofing Ms-granite. It becomes now clear that this fluid was also involved in the growth of the Rocles-type tourmalines. The next question is evidently: was also this fluid involved in the St-Mélany mineralization?

The source of W: what is really learned from the wolframite fingerprinting?

As seen in Chapter 2, the trace element signature of the St-Mélany wolframite is very reminiscent of that in an evolved granite such as the Rocles Ms-granite. The involvement of the magmatic-hydrothermal fluid associated with the latter would thus seem unescapable, on the model of the Mole granite mineralization (Audétat et al., 2000a,b). There are however severe objections to this idea. First, no fluid with an evident magmatic signature has been recognised in the St-Mélany quartz vein system by the fluid inclusions study from Noyé (1985). Second, all the structural and mineralogical evidence imply a very late-kinematic development of the St-Mélany vein system, in an already retrograde metamorphic environment, in an area of concentrated fluid flowing, post-dating the main tourmalinization event in which is documented the involvement of the magmatic fluid. Third, there is a problem in the wolframite signature itself. As seen in Fig. 30 (Chapter 2), the wolframite is distinctly enriched in Nb-Ta relative to the granite. Moreover, the Nb to Ta ratio is nearly inverted, the strong negative Nb anomaly typical of the evolved granites being transformed into a strong positive anomaly in the wolframite. Even if the global Nb-Ta enrichment was due to a favourable partition coefficient, it is very unlikely that preferential Nb enrichment in wolframite be due to a specific crystal chemistry effect. Despite the presence of late aplite/pegmatite dykes of a RMG lineage, the consideration of a granitic source more evolved than the Rocles Ms-granite is unlikely. In fact, even if Nb and Ta are by far more enriched in a granite like the B1 Beauvoir facies (> 150 ppm), the Nb negative anomaly remains. It is the same when the magmatic fluid is considered (Chapter 8). Despite a significant increase of the Nb/Ta ratio in the fluid, the negative anomaly is not removed. This observation is consistent with both the prediction of Ballouard et al. (2016) and the empirical observations of Marignac et al. (2000), converging toward the notion of rather Ta-enriched fluids evolving from rare-metal melts. To solve the contradiction, it may be proposed to pay more attention to the Rocles Ms-granite-related rare-metal anomaly in the mesozone micaschists. As already stated, the anomaly is hosted in the Ti-oxides, and, it appears that the St-Mélany Ti-oxides present exactly the same positive anomaly in Nb and Ta as the St-Mélany wolframite. It is therefore proposed that it was precisely the leaching of a volume of rocks affected by the rare metal

anomaly that was at the origin of the metals to be concentrated in the W-Sn deposit. This would have occurred during the short-lived retrograde path following the M3 thermal peak, and could be related to the chloritization that is seen to affect the anatase in many samples from the M3 mesozone.

2.1.2. Synthesis

To summarize, the W (and Sn) concentration observed in the St-Mélany quartz vein system may be seen as the result from the combination of several more or less independent processes occurring in the same time interval and under the medium grade conditions of a LP-HT metamorphism (Fig. 154): (i) trapping of the metals released from a crystallizing evolved granitic magma (to become the Rocles Ms-granite), through their transport by the magmatic-hydrothermal fluid and their incorporation in the Ti-oxides that independently evolved in the prograde LP-HT metamorphism. This first stage lead to the formation of a significant volume of micaschists with some rare-metal endowment; (ii) progressive focussing of metamorphic fluids evolved from the same prograde metamorphism and subjected to cooling on their way upward (prone to boron metasomatism and tourmaline formation), forced to flow in a more and more restricted draining system of transient joints; and (iii) fortuitous channelling of these fluids through a portion of the enriched rare-metal volumes of rock. By contrast, the obvious absence of any active draining system at the time of the Borne intrusion may explain why, despite of the presence of a (small) rare metal anomaly in the contact aureole, no W (or Sn) concentration is known in the periphery of the intrusion.

2.2. Is the model exportable? The Enguialès case

Some of the favourable factors that were identified at St-Mélany seem to be present in the Enguialès context: (i) the same time-space progressive focussing of metamorphic fluids, culminating with the Enguialès quartz vein system, and apparently the same late-kinematic development of tourmalinization and the quartz veins (see above); (ii) the attested predominance of metamorphic fluids of the C-O-H-N-NaCl system in the fluid inclusions from the quartz veins (Ramboz, 1980); (iii) the attested existence of rare metal-enriched Ti-oxides in the vicinity of the deposit (Gama, 2000; Lerouge et al., 2007);

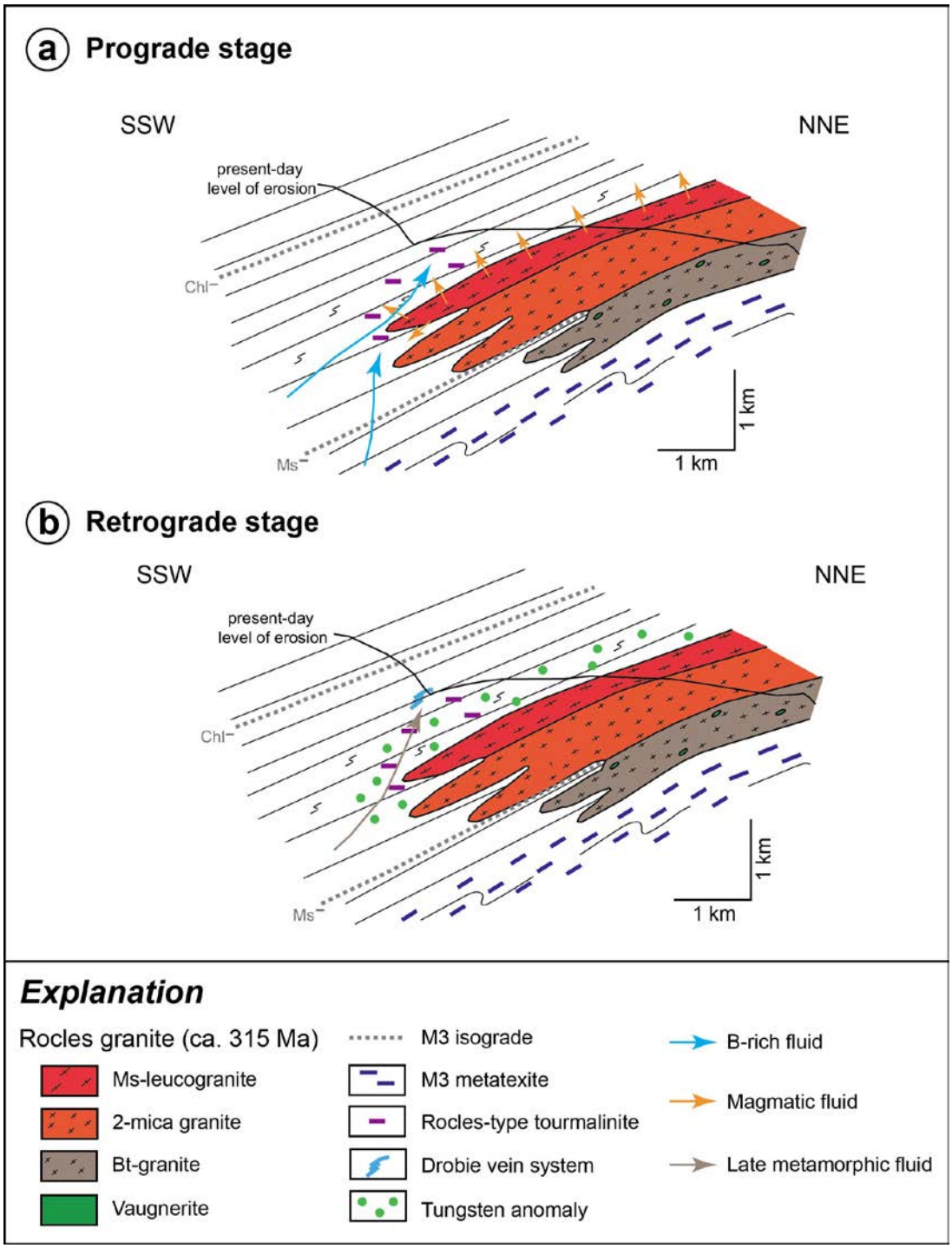

Fig. 154: Conceptual model for the genesis of the St-Mélany deposit at ca. 315 Ma. (a) Prograde stage: the syn-kinematic Rocles granite releases magmatic fluids into the surrounding rocks, whereas metamorphic devolatilization yields B-rich fluids, able to react with metamorphic biotite under decreasing temperature gradient, to produce the Rocles-type tourmalinites. Reacting with the surrounding rocks, the metamorphic fluids create a tungsten anomaly. (b) Retrograde stage: at the end of the M3 event, the late metamorphic fluids going out from the metamorphic pile leach the tungsten anomaly, and when focused by such a structure as the Drobie late-kinematic vein system, be at the origin of the St-Mélany W deposit.

(iv) the same fingerprinting of both a metasedimentary and a granitic end-member fluid sources in the selvage tourmalines; and (v) the same multi-element diagram for wolframite, with a pronounced Nb-Ta positive anomaly. Based on the anomalous rare-metal content of the Ti-oxides, Gama (2000) considered that the formation of the Enguialès deposit was related to the late leucogranite system intrusive in the Margeride pluton at ca. 306 Ma (Monié et al., 2000), and proposed that a hidden leucogranite stock was emplaced beneath the deposit. Reinforcing this model, consideration of the $\delta^{18}O$ isotopic composition of coexisting tourmaline and quartz in the vein system lead some authors (Lerouge et al., 2000; Lerouge and Bouchot, 2009) to the conclusion that a purely magmatic-hydrothermal fluid was responsible for the genesis of the deposit. This conclusion was however based on the assumption of the isotopic equilibrium between quartz and the tourmaline, which, given the complex tectonic evolution at the microscopic scale, marked by a succession of crack-seal processes affecting the already crystallized tourmaline and accompanied by new quartz deposition, may at least be questioned, if not simply discarded. Indeed, previous studies in other quartz vein systems with complex history (e.g., Au Limousin: Souhassou, 2001; W Vaulry: Vallance et al., 2001) showed that to get reliable $\delta^{18}O$ isotopic data, only small wafers of quartz containing a well-identified population of fluid inclusions are amenable to significant isotopic analyses. Moreover, as discussed in the preceding section, that a magmatic fluid may be involved in the tourmaline episode does not necessarily mean that it was responsible for the later crystallization of wolframite. To summary, the weight of the evidence at hand seems to be more in favour of a St-Mélany-type model for the Enguialès deposit than a classical orthomagmatic model, although it is evident that a definitive conclusion must await further investigations (in particular, a survey of the fluid inclusions in wolframite).

2.3. Increasing the complexity: the Puy-les-Vignes system

A first problem to be addressed in the Puy-les-Vignes system is the source of boron involved for the pervasive tourmaline crackle-breccia. As for the systems from the southern FMC, there is no particular evidence for the presence of a B-rich granitic melt in the N Limousin. Yet, the local environment consists in high-grade paragneisses, which were likely boron-depleted under prograde metamorphic conditions prior to the formation of the Puy-les-Vignes hydrothermal system. Moreover, there is no evidence of a new metamorphic cycle affecting these gneisses. However, as discussed in a preceding section, there is evidence at the

N Limousin scale, of the existence at depth of such a metamorphic cycle, yielding migmatites at the expense of the PAU metasediments, at ca. 317 Ma. It may thus be thought that the boron needed for the production of the Puy-les-Vignes crackle-breccia was issued from an active prograde metamorphism at a deeper level in the metamorphic pile, likely at the expense of the Dronne micaschists from the PAU. The Puy-les-Vignes breccia pipe would therefore be the result of a strong focussing of the B-bearing devolatilization fluids through the "carapace" of the gneiss from the LGU. Such a fluid focussing, driven either by a crystallizing granite or migmatites at depth, would have been favoured by the crossing of tectonic lineaments at Puy-les-Vignes, as suggested by the crossing of lamprophyre and leucogranite dykes. In this perspective, the succession at Puy-les-Vignes of the tourmaline crackle-breccia and the superimposed "explosive" quartz breccia, the latter being characterized by strong hydraulic fracturing and pressure-assisted opening allowing rotation of metric clasts prior to quartz sealing, is highly suggestive of a parallel with the progressive fluid focussing described in the southern W-systems. A possible conceptual model for the genesis of the Puy-les-Vignes deposit is shown in Fig. 155.

There is however an evident difference in the sizes of the Puy-les-Vignes and the southern systems. This may be put in relation with another difference, i.e., the multiplicity of fluid sources involved in the Puy-les-Vignes tourmaline. As seen in Chapter 6, at least four distinct end-members may be identified at Puy-les-Vignes, of which two are common to all the studied systems, i.e., an evolved granite-related fluid, and a metasediment source, while two others, that are specific to Puy-les-Vignes, may be identified to the orthogneisses from the LGU (e.g., the Thaurion gneisses), and to the so-called LA (leptyno-amphibolite) assemblage from the UGU. As discussed in the Chapter 6, the different end-members are involved in complex mixing relationships, with however the metasediment end-member being most often present. This is consistent with a boron source in a metasedimentary unit, which would evidently be identified to the Dronne micaschists, whereas the other sources correspond to the draining of more local units. In this perspective, however, the granite source sets a specific problem, since a distant source like the La Porcherie granite is evidently poorly feasible. It must then be speculated that an evolved granite was emplaced at depth under Puy-les-Vignes, in a position similar to the Rocles granite in the N Cévennes, or, to take a reference in the northern FMC, to the St-Mathieu granite in the western Limousin.

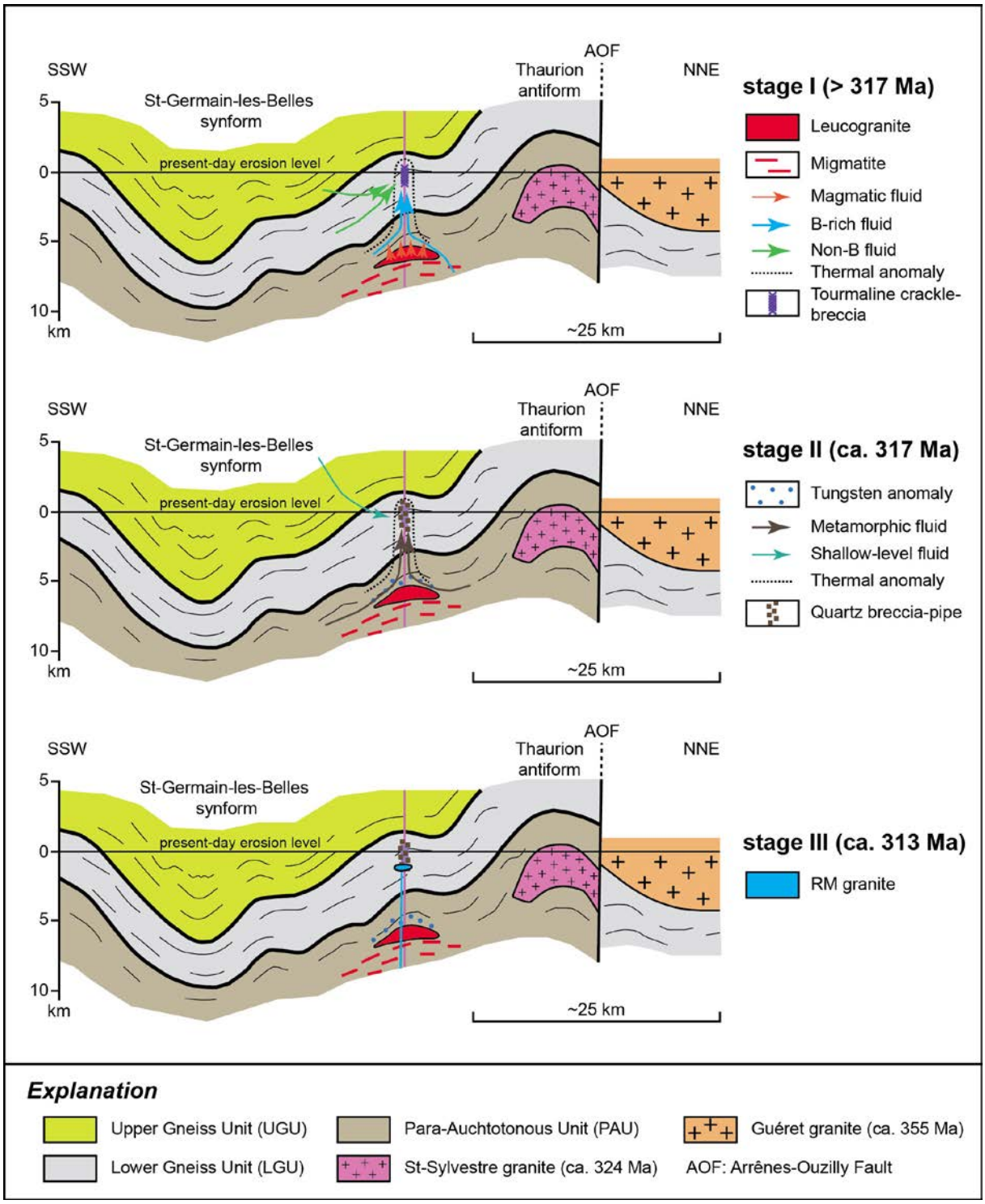

Fig. 155: Conceptual model for the genesis of the Puy-les-Vignes W-bearing breccia pipe. The cross-section is inspired from Lardeaux et al. (2014). Stage I: B-rich fluids are issued from the devolatilization of the Para-Autochtonous metapelites under a LP-HT metamorphic gradient. Following a tectonic-controlled chimney (intersection of earlier magmatic dykes), they are focused into the superincombent gneisses of the LGU where they form a tourmaline crackle-breccia pipe. Linked to the corresponding heat advection and development of a thermal anomaly, fluids from the UGU and LGU may be mobilized and mixed with the B-rich fluids yielding the complex zoning patterns observed in the tourmalines of the crackle-breccia. Coeval intrusion at depth of a leucogranite yields magmatic fluids and development of a tungsten anomaly in the surrounding metapelites of

the PAU. Stage II: the late metamorphic fluids are in turn focused towards the LGU and create the quartz breccia-pipe superimposed to the tourmaline crackle-breccia. On their way, they leach the preceding tungsten anomaly and thus may form the Puy-les-Vignes deposit. More surficial fluids may be mobilized due to the protracted thermal anomaly, and contribute to the W deposition according to the fluid inclusions study findings of Alikouss (1993). Stage III: later on, renewal of deep-seated magmatic activity produces the intrusion of a rare-metal granite into the breccia pipe.

Similarly to the south FMC, the trace element fingerprint of the Puy-les-Vignes wolframite (Chapter 2) calls for a strict relationship with an evolved granite, but, as for the southern wolframites, it exhibits a strong positive Nb-Ta anomaly. The same kind of explanation may thus be envisaged, calling for a relay of the magmatic signature by trapping of rare metals in the hanging wall of the hypothetical deep intrusion, and subsequent remobilization. Although quite speculative, this model presents a double advantage: (i) it explains the time gap between the first expression of a magmatic fluid, recorded in the tourmaline crackle-breccia, and the main quartz brecciation associated with wolframite deposition; and (ii) it explains why fluid inclusion studies fail to reveal the participation of a magmatic fluid in the quartz-wolframite breccia and vein systems at Puy-les-Vignes (Alikouss, 1993). It may also be emphasized that, beyond the obvious differences, the Puy-les-Vignes hydrothermal system shares important similarities with the south FMC W deposits. Thus, it would appear that the main W endowment of the FMC would have occurred at about the same time, under the same type of metamorphic regime and following the same style of metallogenic system, ultimately controlled by the first main lithospheric delamination event following the latest contractional processes in the FMC part of the belt (Marignac and Cuney, 1999).

3. Other W deposits: alternative to the preceding model

3.1. Vaulry deposit

The small intra-granitic Vaulry deposit is hosted in a rare-metal granite (Blond massif), but was formed long after the cooling of the latter (Vallance et al., 2001). A notable difference in comparison with other W deposits is the absence of tourmaline. However, as in the other deposits, the fluid inclusions studies (Vallance et al., 2001) failed to reveal the participation of a magmatic fluid, wolframite and cassiterite deposition being related to the mixing between a

hot moderately saline fluid (with only traces of a volatile component) and a cooler low-salinity fluid. Preliminary data obtained on fluid inclusions hosted in wolframite show similarities with those in the quartz and cassiterite. They show in particular that wolframite deposition occurred earlier than cassiterite, in response to a near isothermal dilution process (Fig. 156).

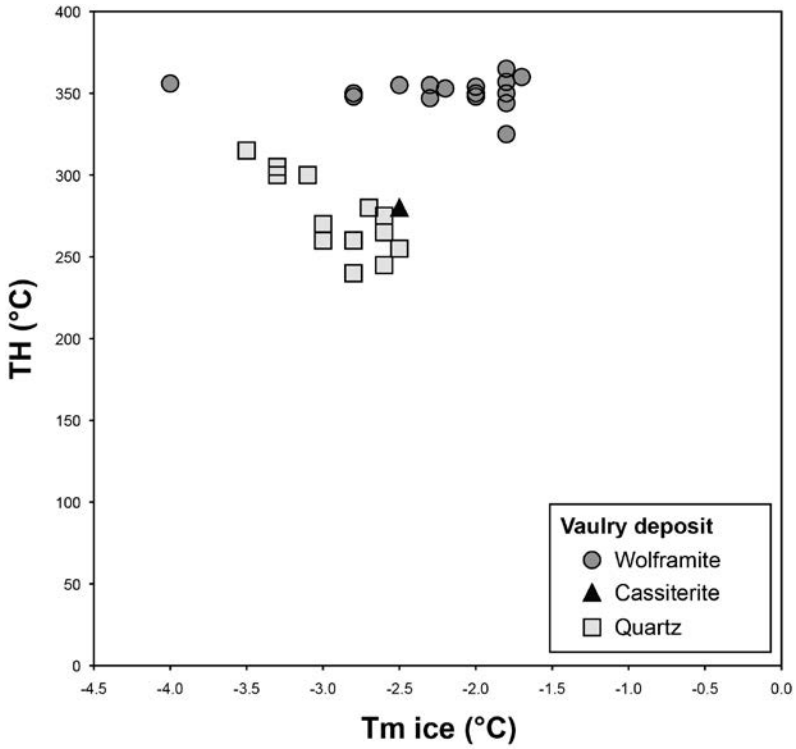

Fig. 156: Preliminary data on primary fluid inclusions contained in wolframite from the Vaury deposit and comparison with the existing data on cassiterite and quartz (Vallance et al., 2001). Microthermometric analyses of fluid inclusions in wolframite were performed at the University of Geneva (Switzerland) using an Olympus XM10 infrared camera.

$\delta^{18}O$ isotopic measurements allowed Vallance et al. (2001) to interpret the low-salinity fluid as a poorly exchanged meteoric water, while the heavier and more saline component is closer to a metamorphic fluid. This is very similar to the fluid end-members found in the S Limousin gold deposits (Boiron et al., 2003), and as for those, a connection with the emplacement at great depth of a Velay-type batholith and the associated migmatite aureole may be envisaged. Yet, the Vaulry wolframite shows the same pattern with a strong Nb-Ta anomaly as other wolframites from the FMC, implying a granite connection without direct intervention of a magmatic fluid. As for the other deposits, an intermediate rare-metal preconcentration is therefore required. However, in the Vaulry deposit case, this

preconcentration may be the Blond granite itself. Indeed, the columbite-tantalite that are part of the magmatic assemblage may play the same role as the Ti-oxides in the other systems, and their interaction with late fluids percolating through the granite may be the source of the Nb-Ta anomaly recorded in the wolframite. This hypothesis should however be tested by a study of the behaviour of rare metal-bearing minerals, which is at the moment lacking.

3.2. St Goussaud deposit

The St-Goussaud showing, dated at ca. 327 Ma (U-Pb on wolframite; Chapter 1) is hosted in the more evolved part of the Brame-St-Sylvestre peraluminous pluton (Cuney and Friedrich, 1987), in a quartz vein system which suffered plastic deformation in a flat-lying shear zone affecting the granite (Alikouss, 1993). Fluid inclusions studies revealed the same type of fluids as at Vaulry (Alikouss, 1993), and the St-Goussaud wolframite exhibits the same Nb-Ta anomaly as elsewhere in the FMC. As for the Vaulry deposit, a rare-metal preconcentration within the St-Goussaud granite may be proposed.

4. Conclusions and perspectives

4.1. Toward the definition of a conceptual model

4.1.1. Metallogenic system approach

According to this work, a first approach to a class of metallogenic system (part of the "mineral system" of McCuaig et al., 2010) can be applied to the peri-batholithic W-Sn quartz vein systems from the FMC. These models include: (i) a fundamental role for more or less evolved granites as the ultimate sources of W and/or Sn; (ii) a close relationship with the regional events of fluid production in relation with anomalous heat flow; (iii) a determining role for a progressive focussing of these fluids toward the metal trap. In this perspective, these models present some similarities with the classical petroleum system of oil geologists. On the one hand, the primary migration is represented by the transfer from an evolved granite, corresponding to the source rock, to the surrounding rocks by magmatic fluids. In the constitution of this peri-granitic metal stock, the Ti-oxides play apparently a major role. On the other hand, the secondary migration represents the flushing of these peri-granitic metal stocks by the prograde metamorphism through progressive draining toward specific traps. The

focussing mechanism may be of tectonic (e.g., St-Mélany, Enguialès) or hydromechanical (e.g., Puy-les-Vignes) nature. The last stage of the metallogenic system, i.e. the trapping, was not the target of the present work. It is however possible based on previous works to suggest some hypotheses. W deposition may be due for instance to the dilution of metamorphic fluids by the influx of low-salinity and cooler fluids, which is documented in many studies (e.g., Giuliani, 1984, 1987; Noyé, 1985; Alikouss, 1993; Vindel et al., 1995; Noronha et al., 1999). Moreover, it was shown by Gibert et al. (1992) that W solubility is strongly decreased in presence of N_2. In this regard, it can be noticed that N_2-rich fluids are equally documented in many W deposits in the European Variscan belt (e.g., Ramboz et al., 1985; Vindel et al., 1995). Concerning the solubility of cassiterite, it is known that the redox conditions and the pH have some influence (Heinrich, 1990). It is evident that further works are needed both from experimental works and fluids inclusions studies. In summary, the existence of a deposit will depend on the conjunction of these two series of events, which are independent, although connected in time and space, whereas the metal endowment will depend on the intensity/efficiency of both processes.

4.1.2. Advantages and limits of the model

Advantages

This model presents the advantages to explain the apparent lack of magmatic fluids as a major component of the hydrothermal system at the trap level, and do not require significant preconcentration in W and/or Sn. The involved granite does not need to be more evolved than a typical peraluminous granite of the AKL-family (Stussi, 1989), which are widespread in the FMC. There is altogether no need for an enriched metasedimentary environment at the local scale. The geochemical background of the late Neoproterozoic - Early Palaeozoic sediments appear sufficient even when the enrichment is not greater than twice the clarke value (W=1.9 ppm; Sn=2.1 ppm in the UCC), as shown in the Cévennes area (Chapter 6). Moreover, as far as the W mobilized during prograde metamorphism is either lost or trapped as scheelite-bearing calc-silicate gneisses, any enrichment at the level of the deposit formation would not be efficient. The model also helps to understand why so many are the granites and so few are the related deposits, although W can be easily extracted from a granitic melt with the exsolved magmatic fluid as tungstate species (Wood and Samson, 2000). The contrary would have been expected. It would appear that W is systematically trapped outside the non-mineralized pluton (e.g., Borne granite in Cévennes), but not systematically leached thereafter. Further works are

needed to check the hypothesis about non-mineralized pluton.

Limits

It must be emphasized that the proposed model applies to intermediate depths of granite emplacement (i.e., 1-2 kbar), being admitted that shallower intrusions may yield magmatic-hydrothermal deposits, such as for instance for the Mole granite in Australia (Audétat et al., 2000a,b). Also, if a trap existed before and was impacted by the intrusion of an evolved granite, the formation of a magmatic-hydrothermal deposit would be conceivable, although no well documented example is known at the moment. In order to better validate this model, further works are required. In particular, it will be desirable: (i) to assess the possible role of Ti-rich biotite of the high-grade zone in the trapping of metals; (ii) to realize other geochemical profiles along regional metamorphic isograde and contact aureoles; and (iii) to systematically document fluid inclusions in wolframite.

4.2. Implications of the model and generalization to other Variscan deposits

Considered at the regional scale, the proposed models are characterized by a vertical extension more than lateral and as proposed at Puy-les-Vignes may be of crustal-scale. It is likely that the richer will be the system in metals, the larger will be its size, which may eventually reach a crustal-scale size. There are several indications that these systems are part of largest magmatic-hydrothermal systems, as indicated by the successive magmatic and hydrothermal events in a same location, thus suggesting a crustal-scale tectonic control. It is in particular remarkable that rare-metal granite systems frequently followed in time and sometimes overprinted in space the W-Sn system, as recorded at Puy-les-Vignes, Echassières and St-Mélany. Such coincidence opens new exploration perspectives for the discoveries of hidden W deposits in brown fields, where large magmatic-hydrothermal systems are already known. It is likely that the model may be extended to many peri-batholitic W-Sn systems found worldwide, in which the identified fluids correspond either to high-temperature C-O-H-N metamorphic fluids or to low-salinity colder fluids, without clear indication of the implication of a magmatic fluid (see Marignac and Cathelineau, 2010 for a critical review). Stable isotope (O, H) data from the main quartz of mineralized veins show generally a large range of compositional around the “magmatic box”, interpreted as recording the mixing between meteoric water and a magmatic fluid. However, as discussed in Marignac and Cathelineau (2010), there are several evidences that the fluid interpreted as magmatic has

more likely a metamorphic origin. The implication of metamorphic fluids has been already proposed in W deposits from Cornwall (e.g., Wilkinson, 1990), Iberia (e.g., Noronha et al., 1999) and the FMC (e.g., Vallance et al., 2001). Geochemical anomalies in W and Sn around tungsten deposits are known both at Hemerdon (Beer and Ball, 1986) and at Panasqueira (Polya, 1989) (Fig. 157). In both cases, the W and Sn contents are 10-500 times the clarke value in the enclosing micaschists hosting the mineralized veins and decrease progressively with distance from the deposit. At Panasqueira, the W-Sn contents fall in the background value of the Beira schists only at more than 15 km from the deposit (Polya, 1989). Moreover, it can be noted that the observed decreasing trends show a depletion in W in comparison with the expected theoretical trends. The apparent difference may suggest a later remobilization of W in the country rocks. In this perspective, the existence around Puy-les-Vignes of an anomalous W halo more than 2 km in radius, as indicated by the stream sediments geochemistry (Bertrand et al., 2015), may be therefore relevant.

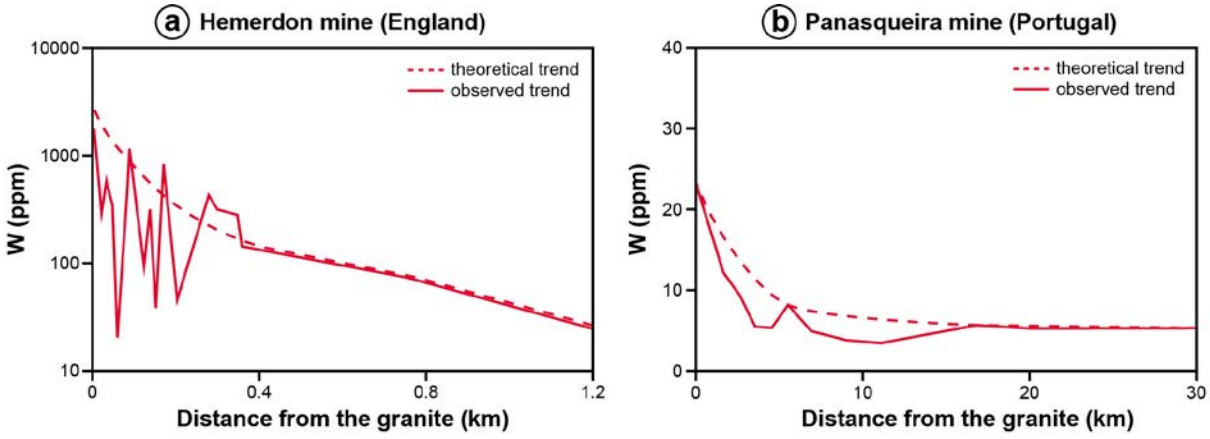

Fig. 157: Geochemical haloes in W around the Hemerdon deposit (Beer and Ball, 1986) and the Panasqueira deposit (Polya, 1989). Note the difference between the observed and the theoretical trends suggesting the remobilization of W in the country rocks.

4.3. Time-space framework of the W metallogenic system in the Variscan orogenic evolution

At the province scale, the coincidence of wolframite ages with the timing of the major thermal events is remarkable. In particular, the apparently widespread LP-HT events at ca. 317-315 Ma seem to be coeval with a W pulse at the scale of the FMC. This time interval is coincident with the turning point in the history of the European Variscan belt, between the north-Variscan Late Devonian-Early Carboniferous and the south-Variscan Late

Carboniferous collisional orogens (Schulmann et al., 2014). This major change is attributed to a reconfiguration of the European plate boundaries. The ca. 317-315 Ma time interval is also coincident with the first UHT granulitic event in the lower crust, seen in the Bournac enclave (Rossi et al., 2006). In this regard, it is also striking that a major RMG event seems to closely follow the main W pulse. It is indeed thought that there is a strong link between granulitization and the production of rare-metal melts (Cuney and Barbey, 2014). This succession of thermal and magmatic events may thus tentatively be put in relation with a major delamination event at the scale of the FMC.

Nevertheless, it remains difficult to place the W-Sn metallogenic systems in the frame of the Variscan geodynamic evolution and to understand in detail the magmatic-hydrothermal genetic processes, for three main reasons: (i) the current lack of consensus about the Late Carboniferous history of the FMC, as exemplified in the Limousin area (Faure et al., 2009 and references therein); (ii) the fact that most of the workings on W deposits in the FMC are now old (mainly from the 1980's) and are of limited access in the field, which necessities new studies in the light of the current conceptual model and analytical methods; and (iii) the relative paucity of relevant ages for the magmatic and metamorphic events, due either to old ages partly uncertain (e.g., old whole-rock Rb-Sr ages) or to the contradiction between U-Th-Pb chemical ages and U-Pb LA-ICPMS ages on monazite, which can yield differences up to 20 Ma (Poujol et al., 2016). Consequently, further works seems required, in particular on dating of granites, in order to propose a comprehensive metallogenic system of W-Sn hydrothermal mineralization in the European Variscan belt.

REFERENCES

A

Aïssa, M., Marignac, C., Weisbrod A., (1987a). Le stockwerk à ferbérite d'Echassières : évolution spatiale et temporelle ; cristallochimie des ferbérites. In Géologie profonde de la France, Echassières : le forage scientifique. Une clé pour la compréhension des mécanismes magmatiques et hydrothermaux associés aux granites à métaux rares (eds. M. Cuney and A. Autran). *Géologie de la France*, 2-3, 311-333.

Aïssa, M., Weisbrod, A., Marignac, C. (1987b). Caractéristiques chimiques et thermodynamiques des circulations hydrothermales du site d'Echassières. In Géologie profonde de la France, Echassières : le forage scientifique. Une clé pour la compréhension des mécanismes magmatiques et hydrothermaux associés aux granites à métaux rares (eds. M. Cuney and A. Autran). *Géologie de la France*, 2-3, 335-350.

Ait Malek, H. (1997). Pétrologie, géochimie et géochronologie d'associations acides-basiques: exemples du Sud-Est du Velay (Massif Central Français) et de l'Anti-Atlas occidental (Maroc). Ph.D. thesis, Institut National Polytechnique de Lorraine, Nancy, 268p.

Albrecht, M., Derrey, I.T., Horn, I., Schuth, S., Weyer, S. (2014). Quantification of trace element contents in frozen fluid inclusions by UV-fs-LA-ICP-MS analysis. *Journal of Analytical Atomic Spectrometry*, 29, 1034-1041.

Alekseev, V.I., Gembitskaya, I.M., Marin, Y.B. (2011). Wolframoixiolite and niobian ferberite from zinnwaldite granitic rocks of the Chukchi Peninsula. *Geology of Ore Deposits*, 53, 639-648.

Alexandre, P., Le Carlier de Veslud, C., Cuney, M., Ruffet, G., Virlogeux, D., Cheilletz, A. (2002). Datation $^{40}Ar/^{39}Ar$ des leucogranites sous couverture du complexe plutonique de Charroux-Civray (Vienne). *Comptes Rendus Geoscience*, 334, 1141-1148.

Alexandrov, P., Cheilletz, A., Deloule, E., Cuney, M. (2000). 319±7 Ma crystallization age for the Blond granite (northwest Limousin, French Massif Central) obtained by U/Pb ion-probe dating of zircons. *Comptes Rendus de l'Académie des Sciences*, Paris*, 330,* 617-622.

Alexandrov, P., Ruffet, G., Cheilletz, A. (2002). Muscovite recrystallization and saddle-shaped $^{40}Ar/^{39}Ar$ age spectra: example from the Blond granite (Massif Central, France). *Geochimica et Cosmochimica Acta*, 60, 1793-1807.

Alikouss, S. (1993). Contribution à l'étude des fluides crustaux : approche analytique et expérimentale. Ph.D. thesis, Institut National Polytechnique de Lorraine, France, 255p.

Allan, M.M., Yardley, B.W., Forbes, L.J., Shmulovich, K.I., Banks, D.A., Shepherd, T.J. (2005). Validation of LA-ICP-MS fluid inclusion analysis with synthetic fluid inclusions. *American Mineralogist*, 90, 1767-1775.

Allman-Ward, P., Halls, C., Rankin, A., Bristow, C. (1982). An intrusive hydrothermal breccia body at Wheal Remfry in the western part of the St Austell granite pluton, Cornwall, England. In Metallization Associated with Acid Magmatism (eds A.M. Evans), John Wiley & Sons Ltd, London, 1-28.

Anderson, A.J., Wirth, R., Thomas, R. (2008). The alteration of metamict zircon and its role in the remobilization of high-field-strengths elements in the Georgeville granite, Nova Scotia. *The Canadian Mineralogist*, 46, 1-18.

Anderson, E.D., Atkinson Jr, W.W., Marsh, T., Iriondo, A. (2009). Geology and geochemistry of the Mammoth breccia pipe, Copper Creek mining district, southeastern Arizona: evidence for a magmatic–hydrothermal origin. *Mineralium Deposita*, 44, 151-170.

Anglin, C.D., Jonasson, I.R., Franklin, J.M., (1996). Sm-Nd dating of scheelite and tourmaline: implications for the genesis of Archean gold deposits, Val d'Or, Canada. *Economic Geology*, 91, 1372-1382.

Arnaud, F., Boullier, A.M., Burg, J.P. (2004). Shear structures and microstructures in micaschists: the Variscan Cévennes duplex (French Massif Central). *Journal of Structural Geology*, 26, 855-868.

Arniaud, D., Dupuy, C., Dostal, J. (1984). Geochemistry of Auriat granite (Massif Central, France). *Chemical Geology*, 45, 263-277.

Arthaud, F., Matte, P. (1975). Les décrochements tardi-hercyniens du Sud-Ouest de l'Europe. Géométrie et essai de reconstitution des conditions de la déformation. *Tectonophysics*, 25, 139-171.

Aubert, G. (1969). Les coupoles granitiques de Montebras et d'Echassières (Massif Central Français) et la genèse de leurs minéralisations en étain, lithium, tungstène et béryllium. *Mémoires du BRGM*, 46, 350p.

Audétat, A., Günther, D., Heinrich, C.A. (1998). Formation of a magmatic-hydrothermal ore deposit: insights with LA-ICP-MS analysis of fluid inclusions. *Science*, 279, 2091-2094.

Audétat, A., Günther, D., Heinrich, C.A. (2000a). Magmatic-hydrothermal evolution in a fractionating granite: A microchemical study of the Sn-W-F-mineralized Mole Granite (Australia). *Geochimica et Cosmochimica Acta*, 64, 3373-3393.

Audétat, A., Günther, D., Heinrich, C.A. (2000b). Causes for large-scale metal zonation

around mineralized plutons: fluid inclusion LA-ICP-MS evidence from the Mole Granite, Australia. *Economic Geology*, 95, 1563-1581.

Audion, A.S., Labbé, J.F. (2012). Panorama mondial 2011 du marché du tungstène. Rapport Public BRGM, RP-61341-FR, 108p.

Aurisicchio, C., De Vito, C., Ferrini, V., Orlandi, P. (2001). Nb-Ta oxide minerals from miarolitic pegmatites of the Baveno pink granite, NW Italy. *Mineralogical Magazine*, 65, 509-522.

Aurisicchio, C., De Vito, C., Ferrini, V., Orlandi, P. (2002). Nb and Ta oxide minerals in the Fonte Del Prete granitic pegmatite dike, Island of Elba, Italy. *The Canadian Mineralogist*, 40, 799-814.

B

Badanina, E.V., Veksler, I.V., Thomas, R., Syritso, L.F., Trumbull, R.B. (2004). Magmatic evolution of Li–F, rare-metal granites: a case study of melt inclusions in the Khangilay complex, Eastern Transbaikalia (Russia). *Chemical Geology*, 210, 113-133.

Baker, E.M., Andrew, A.S. (1991). Geologic, fluid inclusion, and stable isotope studies of the gold-bearing breccia pipe at Kidston, Queensland, Australia. *Economic Geology*, 86, 810-830.

Baksheev, I.A., Prokof'ev, V.Y., Zaraisky, G.P., Chitalin, A.F., Yapaskurt, V.O., Nikolaev, Y.N., Tikhomirov, P.L., Nagornaya, E.V., Rogacheva, L.I., Gorelikova, N.V., Kononov, O.V. (2012). Tourmaline as a prospecting guide for the porphyry-style deposits. *European Journal of Mineralogy*, 24, 957-979.

Ballouard, C., Poujol, M., Boulvais, P., Branquet, Y., Tartèse, R., Vigneresse, J.L. (2016). Nb-Ta fractionation in peraluminous granites: A marker of the magmatic-hydrothermal transition. *Geology*, 44, 231-234.

Ballouard, C., Poujol, M., Boulvais, P., Mercadier, J., Tartese, R., Venneman, T., Deloule, E., Jolivet, M., Kéré, I., Cathelineau, M., Cuney, M. (2017). Magmatic and hydrothermal behavior of uranium in syntectonic leucogranites: The uranium mineralization associated with the Hercynian Guérande granite (Armorican Massif, France). *Ore Geology Reviews*, 80, 309-331.

Barbey, P., Macaudière, J., Marignac, C., Jabbori, J. (2005). Les concentrations à sillimanite du Sud Velay et l'évolution P–T–t fini-hercynienne dans le Massif Central (France). *Comptes Rendus Geoscience*, 337, 872-879.

Barbey, P., Villaros, A., Marignac, C., Montel, J.M. (2015). Multiphase melting, magma

emplacement and P-T-time path in late-collisional context: the Velay example (Massif Central, France). *Bulletin de la Société Géologique de France*, 186, 93-116.

Bau, M. (1996). Controls on the fractionation of isovalent trace elements in magmatic and aqueous systems: evidence from Y/Ho, Zr/Hf, and lanthanide tetrad effect. *Contributions to Mineralogy and Petrology*, 123, 323-333.

Be Mezeme, E., Cocherie, A., Faure, M., Legendre, O., Rossi, P. (2006). Electron microprobe monazite geochronology of magmatic events: examples from Variscan migmatites and granitoids, Massif Central, France. *Lithos*, 87, 276-288.

Be Mezeme, E., Faure, M., Chen, Y., Cocherie, A., Talbot, J.Y. (2007). Structural, AMS and geochronological study of a laccolith emplaced during Late Variscan orogenic extension: the Rocles pluton (SE French Massif Central). *International Journal of Earth Sciences*, 96, 215-228.

Bebout, G.E., Cooper, D.C., Bradley, A.D., Sadofsky, S.J. (1999). Nitrogen-isotope record of fluid-rock interactions in the Skiddaw Aureole and granite, English Lake District. *American Mineralogist*, 84, 1495-1505.

Beer, K.E., Ball, T.K. (1986). Tin and tungsten in pelitic rocks from S.W. England and their behaviour in contact zones of granites and in mineralized areas. *Proceedings of the Ussher Society*, 6, 330-337.

Belissont, R., Boiron, M.C., Luais, B., Cathelineau, M. (2014). LA-ICPMS analyses of minor and trace elements and bulk Ge isotopes in zoned Ge-rich sphalerites from the Noailhac–Saint-Salvy deposit (France): Insights into incorporation mechanisms and ore deposition processes. *Geochimica et Cosmochimica Acta*, 126, 518-540.

Belkasmi, M., Cuney, M. (1998). Les columbo-tantalites zonées du granite de Montebras (Massif Central Français). Implications pétrogénétiques. *Comptes Rendus de l'Académie des Sciences*, Paris, 326, 459-465.

Belkasmi, M., Cuney, M., Pollard, P.J., Bastoul, A. (2000). Chemistry of the Ta-Nb-Sn-W oxide minerals from the Yichun rare metal granite (SE China): genetic implications and comparison with Moroccan and French Hercynian examples. *Mineralogical Magazine*, 64, 507-523.

Bell, K., Anglin, C.D., Franklin, J.M. (1989). Sm-Nd and Rb-Sr isotope systematics of scheelites: Possible implications for the age and genesis of vein-hosted gold deposits. *Geology*, 17, 500-504.

Bellanger, D. (1980). Vaugnérites et roches associées des Cévennes médianes : quelques aspects pétrologiques et géochimiques. Ph.D. thesis, Université de Lyon, France, 185p.

Bellon, H., Gibert, J.P. (1981). Analyses radiométriques (K-Ar) des associations plutoniques et hypovolcaniques hercyniennes de la region Nord-Margeride (Massif Central, France). *Bulletin de la Société Géologique de France*, 7, 429-437.

Belousova, E.A., Griffin, W.L., O'Reilly, S.Y., Fisher, N.I. (2002). Apatite as an indicator mineral for mineral exploration: trace-element compositions and their relationship to host rock type. *Journal of Geochemical Exploration*, 76, 45-69.

Berger, J., Féménias, O., Ohnenstetter, D., Bruguier, O., Plissart, G., Mercier, J.C.C., Demaiffe, D. (2010). New occurrence of UHP eclogites in Limousin (French Massif Central): age, tectonic setting and fluid–rock interactions. *Lithos*, 118, 365-382.

Bermanec, V., Tomašić, N., Kniewald, G., Back, M.E., Zagler, G. (2008). Niobioaeschynite-(Y), a new member of the aeschynite group from the Bear Lake Diggings, Haliburton County, Ontario, Canada. *The Canadian Mineralogist*, 46, 395-402.

Berry, W.B., Wilde, P., Quinby-Hunt, M.S., Orth, C.J. (1986). Trace element signatures in Dictyonema Shales and their geochemical and stratigraphic significance. *Norsk Geologisk Tidsskrift*, 66, 45-51.

Berthier, F., Duthou, J.L., Roques, M. (1979). Datation géochronologique Rb/Sr sur roches totales du granite de Guéret (Massif Central). Age fini-Dévonien de mise en place de l'un de ses faciès types. *Bulletin BRGM*, 1, 31–42.

Bertrand, J.M., Leterrier, J., Cuney, M., Brouand, M., Stussi, J.M., Delaperriere, E., Virlojeux, D. (2001). Géochronologie U-Pb sur zircons de granitoïdes du Confolentais, du massif de Charroux-Civray (Poitou) et de Vendée. *Géologie de la France*, 1-2, 167-180.

Bertrand, G., Charles, N., Melleton, J., Tourlière, B., Cassard, D., Dupuy, J.J., Gloaguen, E., Loiselet, C., Angel, J.M., Berthier, H. (2015). Réévaluation du potentiel français en ressources minérales : retraitement des données géochimiques de l'Inventaire et établissement de fiches de cibles minières. Synthèse des travaux réalisés de 2013 à 2015. Rapport final. BRGM/RP-65165-FR, 434p.

Best, M.G., Christiansen, E.H., Deino, A.L., Grommé, C.S., Tingey, D.G. (1995). Correlation and emplacement of a large, zoned, discontinuously exposed ash flow sheet; the $^{40}Ar/^{39}Ar$ chronology, paleomagnetism, and petrology of the Pahranagat Formation, Nevada. *Journal of Geophysical Research*, 100, 24593-24609.

Béziat, P., Prouhet, J.P., Tollon, F. (1980). Le district de Montredon-Labessonnié (Tarn): W, Sn, F. Publications du 26e Congrès Géologique International (Paris): Gisements français, 7, 42p.

Blamart, D., Boutaleb, M., Sheppard, S., Marignac, C., Weisbrod, A. (1992). A comparative

thermobarometric (chemical and isotopic) study of a tourmalinized pelite and its Sn-Be vein, Walmès, Morocco. *European Journal of Mineralogy*, 4, 355-368.

Bleiner, B., Hametner, K., Günther, D. (2000). Optimization of a laser ablation-inductively coupled plasma "time of flight" mass spectrometry system for short transient signal acquisition. *Fresenius Journal of Analytical Chemistry*, 368, 37-44.

Blevin, P.L., Chappell, B.W. (1995). Chemistry, origin, and evolution of mineralized granites in the Lachlan Fold Belt, Australia: the metallogeny of I- and S-type granites. *Economic Geology*, 90, 1604-1619.

Bodnar, R.J. (2003). Introduction to aqueous-electrolyte fluid inclusions. In Fluid Inclusions: Analysis and Interpretation (eds. I. Samson, A. Anderson and D. Marshall). *Mineralogical Association of Canada, Short Course*, 32, 81-99.

Bogdanoff, S., Cirodde, J.L., Donnot, M. (1989). The nappes of La Châtaigneraie, southwest Massif Central, France. *Tectonophysics*, 157, 69-79.

Bogdanoff, S., Cirodde, J.L., Ploquin, A., Ramboz, C., Le Chapelain, J.R., Mignon, R. (1987). Exploration for tungsten in the Châtaigneraie district. *Chronique de la Recherche Minière*, 487, 11-30.

Boiron, M.C., Cathelineau, M., Banks, D.A., Fourcade, S., Vallance, J. (2003). Mixing of metamorphic and surficial fluids during the uplift of the Hercynian upper crust: consequences for gold deposition. *Chemical Geology*, 194, 119–141.

Bonazzi, P., Menchetti, S. (1999). Crystal chemistry of aeschynite-(Y) from the Western Alps: residual electron density on difference-Fourier map. *European Journal of Mineralogy*, 11, 1043-1049.

Bonazzi, P., Zoppi, M., Dei, L. (2002). Metamict aeschynite-(Y) from the Evje-Iveland district (Norway): heat-induced recrystallization and dehydrogenation. *European Journal of Mineralogy*, 14, 141-150.

Bonne, A., Moreau, J. (1973). Etude structurale du gisement de wolframite d'Enguialès (Massif Central Français). *Mineralium Deposita*, 8, 57-63.

Borovinskaya, O., Hattendorf, B., Tanner, M., Gschwind, S., Günther, D. (2013). A prototype of a new inductively coupled plasma time-of-flight mass spectrometer providing temporally resolved, multi-element detection of short signals generated by single particles and droplets. *Journal of Analytical Atomic Spectrometry*, 28, 226-233.

Bouchot, V., Milesi, J.P., Ledru, P. (2000). Crustal scale hydrothermal palaeofield and related Au, Sb, W orogenic deposits at 310-305 Ma (French Massif Central, Variscan Belt). *SGA News*, 10, 6–12.

Bouchot, V., Ledru, P., Lerouge, C., Lescuyer, J.L., Milesi, J.P. (2005). Late Variscan mineralizing systems related to orogenic processes: The French Massif Central. *Ore Geology Reviews*, 27, 169-197.

Bouilhol, P., Leyreloup, A.F., Delor, C., Vauchez, A., Monié, P. (2006). Relationships between lower and upper crust tectonic during doming: the mylonitic southern edge of the Velay metamorphic core complex (Cévennes-French Massif Central). *Geodinamica Acta*, 19, 137-153.

Boushaba, A., Marignac, C. (2009). La nature des fluides hydrothermaux des tourmalinites du massif granitique Permien du Ment, Maroc Central. In L'hydrothermalisme en domaine continental : fonctionnement, ressource et patrimoine (S. Gallino and C. Gauchon, eds.). *Collection EDYTEM*, 9, 33-48.

Bowles, J.F.W. (1990). Age dating of individual grains of uraninite in rocks from electron microprobe analysis. *Chemical Geology*, 83, 47-53.

Breiter, K., Sokolova, M., Sokol, A. (1991). Geochemical specialization of the tin bearing granitoid massifs of NW Bohemia. *Mineralium Deposita*, 26, 298-306.

Breiter, K., Fryda, J., Seltmann, R., Thomas, R. (1997). Mineralogical evidence for two magmatic stages in the evolution of an extremely fractionated P-rich rare-metal granite: the Podlesi Stock, Krusne Hory, Czech Republic. *Journal of Petrology*, 38, 1723-1739.

Breiter, K., Förster, H.J., Seltmann, R. (1999). Variscan silicic magmatism and related tin-tungsten mineralization in the Erzgebirge-Slavkovský les metallogenic province. *Mineralium Deposita*, 34, 505-521.

Breiter, K., Müller, A., Leichmann, J., Gabašová, A. (2005). Textural and chemical evolution of a fractionated granitic system: the Podlesí stock, Czech Republic. *Lithos*, 80, 323-345.

Breiter, K., Škoda, R., Uher, P. (2007). Nb-Ta-Ti-W-Sn-oxide minerals as indicators of a peraluminous P-and F-rich granitic system evolution: Podlesí, Czech Republic. *Mineralogy and Petrology*, 91, 225-248.

Breiter, K., Škoda, R. (2012). Vertical zonality of fractionated granite plutons reflected in zircon chemistry: the Cínovec A-type versus the Beauvoir. *Geologica Carpathica*, 63, 383-398.

Brevart, O., Dupré, B., Allègre, C.J. (1982). Metallogenic provinces and the remobilization process studied by lead isotopes: lead-zinc ore deposits from the Southern Massif Central, France. *Economic Geology*, 77, 564-575.

Brichau, S., Respaut, J.P., Monié, P. (2008). New age constraints on emplacement of the

Cévenol granitoids, South French Massif Central. *International Journal of Earth Sciences*, 97, 725-738.

Bril, H. (1982). Fluid inclusions study of Sn-W-Au, Sb- and Pb-Zn mineralizations from the Brioude-Massiac district (French Massif Central). *Tschermaks Mineralogische und Petrographische Mitteilungen*, 30, 1-16.

Bril, H., Beaufort, D. (1989). Hydrothermal alteration and fluid circulation related to W, Au, and Sb vein mineralizations, Haut Allier, Massif Central, France. *Economic Geology*, 84, 2237-2251.

Bril, H., Bonhomme, M.G., Marcoux, E., Baubron, J.C. (1991). Ages K/Ar des minéralisations de Brioude-Massiac (W-Au-As-Sb; Pb-Zn), Pontgibaud (Pb-Ag; Sn) et Labesette (As-Pb-Sb-Au): Place de ces districts dans l'évolution géotectonique du Massif central français. *Mineralium Deposita*, 26, 189-198.

Bril, H., Marignac, C., Cathelineau, M., Tollon, F., Cuney, M., Boiron, M.C. (1994). Metallogenesis of the French Massif Central: time-space relationships between ore deposition and tectono-magmatic events. In Pre-Mesozoic Geology in France and Related Areas (eds. J. Chantraine, J. Rolet, D.S. Santallier, A. Piquet and J.D. Keppie). Springer, Berlin Heidelberg, 379-402.

Bruguier, O., Becq-Giraudon, J.F., Champenois, M, Deloule, E., Ludden, J., Mangin, D. (2003). Application of in situ zircon geochronology and accessory phase chemistry to constraining basin development during post-collisional extension: a case-study from the French Massif Central. *Chemical Geology*, 201, 319-336.

Buhl, J.C., Willgallis, A. (1985). On the hydrothermal synthesis of wolframite. *Chemical Geology*, 48, 93-102.

Burruss, R.C. (2003). Petroleum fluid inclusions, an introduction. In Fluid Inclusions: Analysis and Interpretation (eds. I. Samson, A. Anderson and D. Marshall). *Mineralogical Association of Canada, Short Course, 32,* 159-174.

C

Caia, G. (1989). Les gîtes de tungstène du secteur d'Enguialès - Le Viala dans leur contexte géologique (Châtaigneraie, Massif Central Français). Ph.D. thesis, Université d'Orléans, France, 155p.

Campbell, A., Petersen, U. (1988). Chemical zoning in wolframite from San Cristobal, Peru. *Mineralium Deposita*, 23, 132-137.

Cardellach, E., Canals, A., Pujals, I. (1996). La composicion isotopica del azufre y del plomo

en las mineralizaciones de Zn-Pb del valle de Aran (Pirineo Central) y su significado metalogenetico. *Estudios Geológicos*, 52, 189-195.

Carignan, J., Hild, P., Mevelle, G., Morel, J., Yeghicheyan, D. (2001). Routine analyses of trace elements in geological samples using flow injection and low pressure on- line liquid chromatography coupled to ICP- MS: a study of geochemical reference materials BR, DR- N, UB- N, AN- G and GH. *Geostandards Newsletter*, 25, 187-198.

Catanzaro, E.J., Champion, C.E., Garner, E.L., Marinenko, G., Sappenfield, K.M., Shields, W.R. (1970). Standard reference materials: boric acid isotopic and assay standard reference materials. *US National Bureau of Standards, Special Publication*, N°260-17, 70p.

Cathelineau, M. (1986). The hydrothermal alkali metasomatism effects on granitic rocks: quartz dissolution and related subsolidus changes. *Journal of Petrology*, 27, 945-965.

Cathelineau, M., Boiron, M.C., Holliger, P., Poty, B. (1990). Metallogenesis of the French part of the Variscan orogen. Part II: Time-space relationships between U, Au and Sn-W ore deposition and geodynamic events – mineralogical and U-Pb data. *Tectonophysics*, 177, 59-79.

Cathelineau, M., Boiron, M.C., Fourcade, S., Ruffet, G., Clauer, N., Belcourt, O., Coulibaly, Y., Banks, D.A., Guillocheau, F. (2012). A major Late Jurassic fluid event at the basin/basement unconformity in western France: $^{40}Ar/^{39}Ar$ and K-Ar dating, fluid chemistry, and related geodynamic context. *Chemical Geology*, 322, 99-120.

Caumon, M.C., Dubessy, J., Robert, P., Tarantola, A. (2013). Fused-silica capillary capsules (FSCCs) as reference synthetic aqueous fluid inclusions to determine chlorinity by Raman spectroscopy. *European Journal of Mineralogy*, 25, 755-763.

Cave, B.J., Stepanov, A.S., Craw, D., Large, R.R., Halpin, J.A., Thompson, J. (2015). Release of trace elements through the sub-greenschist facies breakdown of detrital rutile to metamorphic titanite in the Otago Schist, New Zealand. *The Canadian Mineralogist*, 53, 379-400.

Cepedal, A., Fuertes-Fuente, M., Martin-Izard, A., González-Nistal, S., Barrero, M. (2008). Gold-bearing As-rich pyrite and arsenopyrite from the El Valle gold deposit, Asturias, northwestern Spain. *The Canadian Mineralogist*, 46, 233-247.

Černý, P., Ercit, T.S. (1989). Mineralogy of Niobium and Tantalum: Crystal Chemical Relationships, Paragenetic Aspects and Their Economic Implications. In Lanthanides, Tantalum and Niobium (P. Möller, P. Černý and F. Saupé, eds.). Springer-Verlag, Berlin

and Heidelberg, 27-79.

Černý, P., Ercit, T.S. (2005). The classification of granitic pegmatites revisited. *The Canadian Mineralogist*, 43, 2005-2026.

Černý, P., Goad, B.E., Hawthorne, F.C., Chapman, R. (1986). Fractionation trends of the Nb- and Ta-bearing oxide minerals in the Greer Lake pegmatitic granite and its pegmatite aureole, southeastern Manitoba. *American Mineralogist*, 71, 501-517.

Černý, P., Ercit, T.S., Wise, M.A. (1992). The tantalite-tapiolite gap: Natural assemblages versus experimental data. *The Canadian Mineralogist*, 30, 587–596.

Černý, P., Ercit, T.S., Wise, M.A., Chapman, R., Buck, H.M. (1998). Compositional, structural and phase relationships in titanian ixiolite and titanian columbite-tantalite. *The Canadian Mineralogist*, 36, 547-561.

Černý, P., Chapman, R., Masau, M. (2000). Two-stage exsolution of a titanian (Sc, Fe^{3+})(Nb, Ta)O_4 phase in niobian rutile from Southern Norway. *The Canadian Mineralogist*, 38, 907-913.

Černý, P., Blevin, P.L., Cuney, M., London, D. (2005). Granite-related ore deposits. *Economic Geology*, 100th Anniversary Volume, 337-370.

Černý, P., Novák, M., Chapman, R., Ferreira, K.J. (2007). Subsolidus behavior of niobian rutile from the Písek region, Czech Republic: a model for exsolution in W-and Fe^{2+}>> Fe^{3+}-rich phases. *Journal of Geosciences*, 52, 143-159.

Chakhmouradian, A.R., Reguir, E.P., Kressall, R.D., Crozier, J. Pisiak, L.K., Sidhu, R., Yang, P. (2015). Carbonatite-hosted niobium deposit at Aley, northern British Columbia (Canada): Mineralogy, geochemistry and petrogenesis. *Ore Geology Reviews*, 64, 642-666.

Chalier, M., Sabourdy, G. (1987). Les lamprophyres du granite hyperalumineux du Saint-Sylvestre (Limousin, Massif Central français): caractères pétrologiques et origine. *Comptes Rendus de l'Académie des Sciences*, Paris, 305, 99-104.

Chalier, M., Virlogeux, D., Duthou, J.L. (1994). Les lamprophyres du district aurifère de Saint Yriex (Limousin, Massif Central français). Age Rb/Sr Autunien et relations chronologiques avec le dépôt de l'or. *Comptes Rendus de l'Académie des Sciences*, Paris, 319, 1511-1518.

Charonnat, X., Chauvet, A., Faure, M. (1999). Contexte structural des minéralisations aurifères tardi-hercyniennes des Cévennes (Massif central français). *Comptes Rendus de l'Académie des Sciences, Paris*, 328, 463-469.

Charoy, B. (1982). Tourmalinization in Cornwall, England. In Mineralization associated with

acid magmatism (Evans, A.M. Ed.), 63-70.

Charoy, B. (1979). Définition et importance des phénomènes deutériques et des fluides associés dans les granites. Conséquence métallogéniques. Ph.D. thesis, Institut National Polytechnique de Lorraine, France, 364p.

Chauris, L., Marcoux, E. (1994). Metallogeny of the Armorican Massif. In Pre-Mesozoic Geology in France and Related Areas (eds. J. Chantraine, J. Rolet, D.S. Santallier, A. Piquet and J.D. Keppie). Springer, Berlin Heidelberg, 243-264.

Chaussidon, M., Albarède, F. (1992). Secular boron isotope variations in the continental crust: an ion microprobe study. *Earth and Planetary Science Letters*, 108, 229–241.

Chauvet, A., Volland-Tuduri, N., Lerouge, C., Bouchot, V., Monié, P., Charonnat, X., Faure, M. (2012). Geochronological and geochemical characterization of magmatic-hydrothermal events within the Southern Variscan external domain (Cévennes area, France). *International Journal of Earth Sciences*, 101, 69-86.

Che, X.D., Linnen, R.L., Wang, R.C., Aseri, A., Thibault, Y. (2013). Tungsten solubility in evolved granitic melts: An evaluation of magmatic wolframite. *Geochimica et Cosmochimica Acta*, 106, 84-98.

Cheilletz, A., Archibald, D., Cuney, M., Charoy, B. (1992). Ages $^{40}Ar/^{39}Ar$ du leucogranite à topaze-lépidolite de Beauvoir et des pegmatites sodolithiques de Chédeville (Nord Massif Central, France). Significations pétrologique et géodynamique. *Comptes Rendus de l'Académie des Sciences*, Paris, 315, 329-336.

Chen, Y., Clark, A.H., Farrar, E., Wasteneys, H.A.H.P., Hodgson, M.J., Bromley, A.V. (1993). Diachronous and independent histories of plutonism and mineralization in the Cornubian Batholith, southwest England. *Journal of the Geological Society*, London, 150, 1183-1191.

Chen, Y.J., Pirajno, F., Li, N., Guo, D.S., Lai, Y. (2009). Isotope systematics and fluid inclusion studies of the Qiyugou breccia pipe-hosted gold deposit, Qinling Orogen, Henan province, China: implications for ore genesis. *Ore Geology Reviews*, 35, 245-261.

Chen, H., Kyser, T.K., Clark, A.H. (2011). Contrasting fluids and reservoirs in the contiguous Marcona and Mina Justa iron oxide-Cu(-Ag-Au) deposits, south-central Peru. *Mineralium Deposita*, 46, 677-706.

Chenevoy, M., Constans, J.E., Recoing, M. (1984). Carte géologique à 1/50 000 Saint-Léonard-de-Noblat et notice explicative. Editions BRGM, 44p.

Chesley, J., Halliday, A., Scrivener, R. (1991). Samarium–neodymium direct dating of fluorite

mineralization. *Science*, 252, 949–951.

Chesley, J., Halliday, A., Kyser, T., Spry, P. (1994). Direct dating of Mississippi Valley-type mineralization; use of Sm–Nd in fluorite. *Economic Geology*, 89, 1192–1199.

Chèvremont, P., Floc'h, J.P., Ménillet, F., Stussi, J.M., Delbos, R., Sauret, B., Blès, J.L., Courbe, C., Vuaillat, D., Gravelat, C. (1996). Notice explicative de la carte géologique à 1/50 000, feuille Rochechouart (687), France. BRGM Editions, Orélans.

Christensen, J.N., Halliday, A.N., Leigh, K.E., Randell, R.N., Kesler, S.E. (1995). Direct dating of sulphides by Rb-Sr: A critical test using the Polaris Mississippi Valley-type Zn-Pb deposit. *Geochimica et Cosmochimica Acta*, 59, 5191-5197.

Ciceri, E., Recchia, S., Dossi, C., Yang, L., Sturgeon, R.E. (2008). Validation of an isotope dilution, ICP-MS method based on internal mass bias correction for the determination of trace concentrations of Hg in sediment cores. *Talanta*, 74, 642-647.

Cloos, M. (1993). Lithospheric buoyancy and collisional orogenesis: Subduction of oceanic plateaus, continental margins, island arcs, spreading ridges, and seamounts. *Geological Society of America Bulletin*, 105, 715-737.

Cnudde, V., Boone, M.N. (2013). High-resolution X-ray computed tomography in geosciences: A review of the current technology and applications. *Earth-Science Reviews*, 123, 1-17.

Cordeiro, P.F.O., Brod, J.A., Palmieri, M., Oliveira, C.G., Barbosa, E.S.R., Santos, R.V., Gaspar, J.C., Assis, L.C. (2011). The Catalão I niobium deposit, central Brazil: Resources, geology and pyrochlore chemistry. *Ore Geology Reviews*, 41, 112-121.

Costa, M.M., Neiva, A.M.R., Azevedo, M.R., Corfu, F. (2014). Distinct sources for syntectonic Variscan granitoids: Insights from the Aguiar da Beira region, Central Portugal. *Lithos*, 196-197, 83-98.

Costa, S. (1990). De la collision continentale à l'extension tardi-orogénique : 100 millions d'années d'histoire varisque dans le Massif Central Français. Une étude chronologique par la méthode ^{40}Ar-^{39}Ar. Ph.D. thesis, Université de Montpellier, France, 441p.

Couturié, J.P., Vachette-Caen, M., Vialette, Y. (1979). Age Namurien d'un laccolite granitique différencié par gravité : le granite de la Margeride (Massif Central Français). *Comptes Rendus de l'Académie des Sciences*, Paris, 291, 449-452.

Couzinié, S., Moyen, J.F., Villaros, A., Paquette, J.L., Scarrow, J.H., Marignac, C. (2014). Temporal relationships between Mg-K mafic magmatism and catastrophic melting of the Variscan crust in the southern part of Velay complex (Massif Central, France). *Journal of Geosciences*, 59, 69-86.

Cuney, M., Autran, A. (1987). Objectifs généraux du projet GPF Echassières n°1 et résultats essentiels acquis par le forage de 900 m sur le granite albitique à topaze-lépidolite de Beauvoir. In Géologie profonde de la France, Echassières : le forage scientifique. Une clé pour la compréhension des mécanismes magmatiques et hydrothermaux associés aux granites à métaux rares (eds. M. Cuney and A. Autran). *Géologie de la France*, 2-3, 7-24.

Cuney, M., Barbey, P. (2014). Uranium, rare metals, and granulite-facies metamorphism. *Geoscience Frontiers*, 5, 729-745.

Cuney, M., Friedrich, M. (1987). Physicochemical and crystal-chemical controls on accessory mineral paragenesis in granitoïds. Implications for uranium metallogenesis. *Bulletin de Minéralogie*, 110, 235-247.

Cuney, M., Kyser, K. (2008). Hydrothermal uranium deposits related to igneous rocks. In Recent and not-so-recent developments in uranium deposits and implications for exploration (eds. M. Cuney and K. Kyser). *Mineralogical Association of Canada, Short Course Series*, 39, Quebec, 119-162.

Cuney, M., Marignac, C. (2015). Rare metal, W and U deposits and related granites from the NE French Massif Central. Field Guide for the 13th Biennial SGA Meeting, 24–27 August 2015, Nancy, France, 155p.

Cuney, M., Le Fort, P., Wang, Z.X. (1984). Uranium and thorium geochemistry and mineralogy in the Manaslu leucogranite (Nepal, Himalaya). In Geology of Granites and their Metallogenetic Relations (eds. X. Kewqin and T. Guangchi), Proceedings of the Int. Symposia, Nanjing, China, Oct. 26-30, 1982, 853-73.

Cuney, M., Friedrich, M., Blumenfeld, P., Bourguignon, A., Boiron, M.C., Vigneresse, J.L., Poty, B. (1990). Metallogenesis in the French part of the Variscan orogen. Part I: U preconcentrations in pre-Variscan and Variscan formations - a comparison with Sn, W and Au. *Tectonophysics*, 177, 39-57.

Cuney, M., Marignac, C., Weisbrod, A. (1992). The Beauvoir topaz-lepidolite albite granite (Massif Central, France): the disseminated magmatic Sn-Li-Ta-Nb-Be mineralization. *Economic Geology*, 87, 1766-1794.

Cuney, M., Brouand, M., Stussi, J.M. (2001). Le magmatisme hercynien en Vendée. Corrélations avec le socle du Poitou et l'Ouest du Massif Central français. *Géologie de la France*, 1-2, 117-142.

Cuney, M., Alexandrov, P., Le Carlier de Veslud, C., Cheilletz, A., Raimbault, L., Ruffet, G., Scaillet, S. (2002). The timing of W-Sn rare-metals mineral deposit formation in the

Western Variscan chain in their orogenic setting: the case of the Limousin area (Massif Central, France). In The Timing and Location of Major Ore Deposits in an Evolving Orogen (eds. D.J. Blundell, F. Neubauer and A. Von Quadt). *Geological Society of London, Special Publication*, 204, 213-228.

D

Davis, D.W., Schandl, E.S., Wasteneys, H.A. (1994). U-Pb dating of minerals in alteration halos of Superior Province massive sulfide deposits: syngenesis versus metamorphism. *Contributions to Mineralogy and Petrology*, 115, 427-437.

Dazé, A., Lee, J.K., Villeneuve, M. (2003). An intercalibration study of the Fish Canyon sanidine and biotite $^{40}Ar/^{39}Ar$ standards and some comments on the age of the Fish Canyon Tuff. *Chemical Geology*, 199, 111-127.

De Vito, C., Pezzotta, F., Ferrini, V., Aurisicchio, C. (2006). Nb-Ti-Ta oxides in the gem-mineralized and "hybrid" Anjanabonoina granitic pegmatite, Central Madagascar: a record of magmatic and postmagmatic events. *The Canadian Mineralogist*, 44, 87-103.

Debon, F., Lefort, P. (1988). A cationic classification of common plutonic rocks and their magmatic associations: principles, method, applications. *Bulletin de Minéralogie*, 111, 493-510.

Decrée, S., Deloule, E., De Putter, T., Dewaele, S., Mees, F., Baele, J.M., Marignac, C. (2014). Dating of U-rich heterogenite: new insights into U deposit genesis and U cycling in the Katanga Copperbelt. *Precambrian Research*, 241, 17-28.

Decrée, S., Deloule, E., Ruffet, G., Dewaele, S., Mees, F., Marignac, C., Yans, J., De Putter, T. (2010). Geodynamic and climate controls in the formation of Mio-Pliocene world-class oxidized cobalt and manganese ores in the Katanga province, DR Congo. *Mineralium Deposita*, 45, 621-629.

Decrée, S., Marignac, C., De Putter, T., Yans, J., Clauer, N., Dermech, M., Aloui, K., Baele, J.M. (2013). The Oued Belif Hematite-Rich Breccia: A Miocene Iron Oxide Cu-Au-(U-REE) Deposit in the Nefza Mining District, Tunisia. *Economic Geology*, 108, 1425-1457.

Demange, M., Nicolas, V.A., Soler, P., Giouse, H. (1988a). Le gisement tungstifère de Leucamp (Cantal, France). Contrôles géologiques et minéralisations. *Bulletin de la Société Géologique de France*, 8, 559-570.

Demange, M., Nicolas, V.A., Soler, P., Giouse, H. (1988b). Le batholite composite du Veynazès (Cantal, France) : pétrographie, géologie et géochimie. Relations avec le

gisement tungstifère de Leucamp. *Bulletin de la Société Géologique de France*, 8, 839-850.

Demange, M., Pascal, M. L., Raimbault, L., Armand, J., Forette, M. C., Serment, R., Touil, A. (2006). The Salsigne Au-As-Bi-Ag-Cu Deposit, France. *Economic Geology*, 101, 199-234.

Demirel, S., Göncüoğlu, M.C., Topuz, G., Isik, V. (2009). Geology and chemical variations in tourmaline from the quartz–tourmaline breccias within the Kerkenez granite–monzonite massif, Central Anatolian Crystalline Complex, Turkey. *The Canadian Mineralogist*, 47, 787-799.

Derré, C. (1983). La province à Sn-W ouest-européenne. Histoire de divers types de gisements du Massif Central, des Pyrénées et du Portugal. Distributions des gisements. Ph.D. thesis, Université Paris VI, 2 vol., I, 345p., II, 421p.

Deveaud, S., Gumiaux, C., Gloaguen, E., Branquet, Y. (2013). Spatial statistical analysis applied to rare-element LCT-type pegmatite fields: an original approach to constrain faults-pegmatites-granites relationships. *Journal of Geosciences*, 58, 163-182.

Deveaud, S., Millot, R., Villaros, A. (2015). The genesis of LCT-type granitic pegmatites, as illustrated by lithium isotopes in micas. *Chemical Geology*, 411, 97-111.

Dewaele, S., De Clercq, F., Hulsbosch, N., Piessens, K., Boyce, A., Burgess, R., Muchez, P. (2016). Genesis of the vein-type tungsten mineralization at Nyakabingo (Rwanda) in the Karagwe–Ankole belt, Central Africa. *Mineralium Deposita*, 51, 283-307.

Didier, A., Bosse, V., Boulvais, P., Bouloton, J., Paquette, J.L., Montel, J.M., Devidal, J.L. (2013). Disturbance versus preservation of U–Th–Pb ages in monazite during fluid–rock interaction: textural, chemical and isotopic in situ study in microgranites (Velay Dome, France). *Contributions to Mineralogy and Petrology*, 165, 1051-1072.

Dill, H.G., Garrido, M.M., Melcher, F., Gomez, M.C., Luna, L.I. (2012). Depth-related variation of tourmaline in the breccia pipe of the San Jorge porphyry copper deposit, Mendoza, Argentina. *Ore Geology Reviews*, 48, 271-277.

Dingwell, D.B., Knoche, R., Webb, S.L., Pichavant, M. (1992). The effect of B_2O_3 on the viscosity of haplogranitic liquids. *American Mineralogist*, 77, 457-461.

Dingwell, D.B., Pichavant, M., Holtz, F. (1996). Experimental studies of boron in granitic melts. In Boron, mineralogy, petrology and geochemistry in the Earth's crust (Grew, E., Anovitz, L., eds.). *Reviews in Mineralogy*, 33, 331–385.

Dove, P.M., Rimstidt, J.D. (1985). The solubility and stability of scorodite, $FeAsO_4.2H_2O$. *American mineralogist*, 70, 838-844.

Downes, H., Shaw, A., Williamson, B.J., Thirlwall, M.F. (1997). Sr, Nd and Pb isotopic evidence for the lower crustal origin of Hercynian granodiorites and monzogranites, Massif Central, France. *Chemical Geology*, 136, 99-122.

Drivenes, K., Larsen, R.B., Müller, A., Sørensen, B.E., Wiedenbeck, M., Raanes, M.P. (2015). Late-magmatic immiscibility during batholith formation: assessment of B isotopes and trace elements in tourmaline from the Land's End granite, SW England. *Contributions to Mineralogy and Petrology*, 169, 1-27.

Dubessy, J., Ramboz, C., Nguyen-Trung, C., Cathelineau, M., Charoy, B., Cuney, M., Leroy, J., Poty, B., Weisbrod, A. (1987). Physical and chemical controls (fO_2, T, pH) of the opposite behaviour of U and Sn-W as exemplified by hydrothermal deposits in France and Great-Britain, and solubility data. *Bulletin de Minéralogie*, 110, 261-281.

Dubois, M., Monnin, C., Castelain, T., Coquinot, Y., Gouy, S., Gauthier, A., Goffé, B. (2010). Investigation of the H_2O-NaCl-LiCl System: A Synthetic Fluid Inclusion Study and Thermodynamic Modeling from -50° to +100°C and up to 12 mol/kg. *Economic Geology*, 105, 329-338.

Duguet, M., Bogdanoff, S., Turland, M., Nehlig, P., Lebret, P., Ricordel, C., Simon-Coinçon, R., Thiry, M. (2006). Notice explicative de la feuille Entraygues-sur-Truyère à 1/50 000, BRGM Edition, 173p.

Dupuis, C., Beaudoin, G. (2011). Discriminant diagrams for iron oxide trace element fingerprinting of mineral deposit types. *Mineralium Deposita*, 46, 319-335.

Duthou, J.L. (1978). Les granitoïdes du Haut Limousin (Massif central français), chronologie Rb/Sr de leur mise en place; le thermo-métamorphisme carbonifère. *Bulletin de la Société Géologique de France*, 20, 229-235.

Duthou, J.L., Cantagrel, J.M., Didier, J., Vialette, Y. (1984). Palaeozoic granitoids from the French Massif Central: age and origin studied by ^{87}Rb-^{87}Sr system. *Physics of the Earth and Planetary Interiors*, 35, 131-144.

Dutrow, B.L., Henry, D.J. (2011). Tourmaline: a geological DVD. *Elements*, 7, 301-306.

Dyar, M.D., Wiedenbeck, M., Robertson, D., Cross, L.R., Delaney, J.S., Ferguson, K., Francis, C.A., Grew, E.S., Guidotti, C.V., Hervig, R.L., Hughes, J.M., Husler, J., Leeman, W., McGuire, A.V., Rhede, D., Rothe, H., Paul, R.L., Richards, I. and Yates, M. (2001). Reference minerals for the microanalysis of light elements. *Geostantards Newsletter*, 25, 441-463.

E

Ebougué, Z. (1995). Magmas ultimes peralumineux à métaux rares : mise en évidence de processus de différenciation extrême dans des dykes (Région de Blond, Massif Central Français). Ph.D. thesis, Université de Nancy, France, 417p.

Eggins, S.M., Kinsley, L.P.J., Shelley, J.M.G. (1998). Deposition and element fractionation processes during atmospheric pressure laser sampling for analysis by ICP-MS. *Applied Surface Science*, 127-129, 278-286.

Eglinger, A., Ferraina, C., Tarantola, A., André-Mayer, A-S., Vanderhaeghe, O., Boiron, M-C., Dubessy, J., Richard, A., Brouand, M. (2014a). Hypersaline fluids generated by high-grade metamorphism of evaporites: fluid inclusion study of uranium occurrences in the Western Zambian Copperbelt. *Contributions to Mineralogy and Petrology*, 167, 1-28.

Eglinger, A., Tarantola, A., Durand, C., Ferraina, C., Vanderhaeghe, O., André-Mayer, A-S., Paquette, J-L. and Deloule, E. (2014b). Uranium mobilization by fluids associated with Ca–Na metasomatism: A P–T–t record of fluid–rock interactions during Pan-African metamorphism (Western Zambian Copperbelt). *Chemical Geology*, 386, 218-237.

Ercit, T.S. (2005). Identification and alteration trends of granitic-pegmatite-hosted (Y,REE,U,Th)-(Nb,Ta,Ti) oxide minerals: a statistical approach. *The Canadian Mineralogist*, 43, 1291-1303.

Estrade, G., Salvi, S., Beziat, D., Rakotovao, S., Rakotondrazafy, R. (2014). REE and HFSE mineralization in peralkaline granites of the Ambohimirahavavy alkaline complex, Ampasindava peninsula, Madagascar. *Journal of African Earth Sciences*, 94, 141-155.

European Commission (2014). Report on Critical Raw Materials for the EU. Technical Report, European Commission (Enterprise and Industry), Brussels, Belgium, 41p.

Ewing, R.C. (1975a). Alteration of metamict, rare-earth, AB_2O_6-type Nb-Ta-Ti oxides. *Geochimica et Cosmochimica Acta*, 39, 521-530.

Ewing, R.C. (1975b). The crystal chemistry of complex Niobium and Tantalum oxides. IV. The metamict state: Discussion. *American Mineralogist*, 60, 728-733.

F

Fabre, C. (2000). Reconstitution chimique des paléofluides par spectrométrie d'émission optique couplée à l'ablation laser. Applications aux fluides alpins et aux fluides de bassins. Ph.D. thesis, Université de Nancy, 296p.

Fabre, C., Boiron, M.C., Dubessy, J., Moissette, A. (1999). Determination of ions in individual fluid inclusions by laser ablation optical emission spectroscopy: development and applications to natural fluid inclusions. *Journal of Analytical Atomic Spectrometry*,

14, 913-922.

Fabre, C., Boiron, M.C., Dubessy, J., Cathelineau, M., Banks, D. (2002). Palaeofluid chemistry of a single fluid event: a bulk and in-situ multi-technique analysis (LIBS, Raman Spectroscopy) of an Alpine fluid (Mont-Blanc). *Chemical Geology*, 182, 249-264.

Fabre, C., Boiron, M.C., Marignac, C., Aïssa, M. (2001). Li-F-rich magmatic fluids exsolved from rare metal granites: the example of the Beauvoir granite (French Massif Central); a microthermometric and LIBS study. XVI ECROFI abstract, Porto 2001, 7, 145-147.

Faure, M. (1995). Late orogenic carboniferous extensions in the Variscan French Massif Central. *Tectonics*, 14, 132-153.

Faure, M., Charonnat, X., Chauvet, A. (1999). Schéma structural et évolution tectonique du domaine para-autochtone cévenol de la chaîne hercynienne (Massif central français). *Comptes Rendus de l'Académie des Sciences*, Paris, 328, 401-407.

Faure, M., Charonnat, X., Chauvet, A., Chen, Y., Talbot, J.Y., Martelet, G., Courrioux, G., Monié, P., Milesi, J.P. (2001). Tectonic evolution of the Cévennes para-autochthonous domain of the Hercynian French Massif Central and its bearing on ore deposits formation. *Bulletin de la Société Géologique de France*, 172, 687-696.

Faure, M., Lardeaux, J-M., Ledru, P. (2009). A review of the pre-Permian geology of the Variscan French Massif Central. *Comptes Rendus Geoscience*, 341, 202–213.

Faure, M., Cocherie, A., Gaché, J., Esnault, C., Guerrot, C., Rossi, P., Wei, L., Qiuli, L. (2014). Middle Carboniferous intracontinental subduction in the Outer zone of the Variscan belt (Montagne Noire axial zone, French Massif Central): Multimethod geochronological approach of polyphase metamorphism. *Geological Society, London, Special Publications*, 405, 289-311.

Fayek, M., Kyser, T.K., Riciputi, L.R. (2002). U and Pb isotope analysis of uranium minerals by ion microprobe and the geochronology of the McArthur River and Sue Zone uranium deposits, Saskatchewan, Canada. *The Canadian Mineralogist*, 40, 1553-1569.

Feng, C., Zeng, Z., Zhang, D., Qu, W., Du, A., Li, D., She, H. (2011). SHRIMP zircon U–Pb and molybdenite Re–Os isotopic dating of the tungsten deposits in the Tianmenshan–Hongtaoling W–Sn orefield, southern Jiangxi Province, China, and geological implications. *Ore Geology Reviews*, 43, 8-25.

Ferenc, S., Uher, P. (2007). Magnesian wolframite from hydrothermal quartz veins in the Rochovce granite exocontact, Ochtiná, Western Carpathians, Slovakia. *Neues Jahrbuch für Mineralogie Abhandlungen*, 183, 165-172.

Fletcher, C.J.N. (1977). The geology, mineralization, and alteration of Ilkwang Mine, Republic of Korea; a Cu-W-bearing tourmaline breccia pipe. *Economic Geology*, 72, 753-768.

Förster, H.J. (2010). Late-Variscan granites of the Aue – Schwarzenberg Zone (western Erzgebirge, Germany): Composition of accessory minerals and mineralogical mass balance of the lanthanides and actinides. *Zeitschrift für Geologische Wissenschaften*, 38, 125-144.

Förster, H.J., Rhede, D., Hecht, L. (2008). Chemical composition of radioactive accessory minerals: implications for the evolution, alteration, age, and uranium fertility of the Fichtelgebirge granites (NE Bavaria, Germany). *Neues Jahrbuch für Mineralogie Abhandlungen,* 185, 161-182.

Förster, H.J., Romer, R.L. (2010). Carboniferous magmatism. In Pre-Mesozoic Geology of Saxo-Thuringia – From the Cadomian Active Margin to the Variscan Orogen (eds. U. Linnemann and R. L. Romer). Schweizerbart, Stuttgart, 287-308.

François, T. (2009). Contraintes géochimiques et géochronologiques sur l'origine et la mise en place des granites du Mont Lozère. M.Sc. thesis, Université de Montpellier, France, 39p.

Frei, R., Nägler, T.F., Schönberg, R., Kramers, J.D. (1998). Re-Os, Sm-Nd, U-Pb, and stepwise lead leaching isotope systematics in shear-zone hosted gold mineralization: Genetic tracing and age constraints of crustal hydrothermal activity. *Geochimica et Cosmochimica Acta*, 62, 1925-1936.

Fricker, M.B. (2012). Design of ablation cells for LA-ICP-MS: from modeling to high spatial resolution analysis applications. Ph.D. thesis, ETH Zürich, 173 p.

Frost, J.K. (1996). Geochemistry of black shales of the New Albany Group (Devonian-Mississippian) in the Illinois Basin: relationships between lithofacies and the carbon, sulfur, and iron contents. Illinois State Geological Survey, Circular no. 557, 32p.

G

Gäbler, H.E., Rehder, S., Bahr, A., Melcher, F., Goldmann, S. (2013). Cassiterite fingerprinting by LA-ICPMS. *Journal of Analytical Atomic Spectrometry*, 28, 1247-1255.

Gama, S. (2000). Evénements métallogéniques à W-Bi (Au) à 305 Ma en Châtaigneraie du Cantal : apport d'une analyse multi-spectrométrique (micro PIXE-PIGE et Raman) des minéraux et des fluides occlus à l'identification des sources de fluides hydrothermaux.

Ph.D. thesis, Université d'Orléans, France, 249 p.

García-Sansegundo, J., Martin-Izard, A., Gavaldà, J. (2014). Structural control and geological significance of the Zn-Pb ores formed in the Benasque Pass area (Central Pyrenees) during the post-late Ordovician extensional event of the Gondwana margin. *Ore Geology Reviews*, 56, 516-527.

Gawęda, A., Muller, A., Stein, H., Kądziolko-Gawel, M., Mikulski, S. (2013). Age and origin of the tourmaline-rich hydraulic breccias in the Tatra Granite, Western Carpathians. *Journal of Geosciences*, 58, 133-148.

Gebauer, H., Bernard-Griffiths, J., Gnünenfelder, M. (1981). U/Pb zircon and monazite dating of mafic-ultramafic complex and its country rocks. Example: Sauviat-sur-Vige, French Massif Central. *Contributions to Mineralogy and Petrology*, 76, 292-300.

Gébelin, A., Roger, F., Brunel, M. (2009). Syntectonic crustal melting and high-grade metamorphism in a transpressional regime, Variscan Massif Central, France. *Tectonophysics*, 477, 229-243.

Genna, D., Gaboury, D. (2015). Deciphering the hydrothermal evolution of a VMS System by LA-ICPMS using trace elements in pyrite: an example from the Bracemac-McLeod Deposits, Abitibi, Canada, and implications for exploration. *Economic Geology*, 110, 2087-2108.

George, L.L., Cook, N.J., Ciobanu, C.L. (2016). Partitioning of trace elements in co-crystallized sphalerite–galena–chalcopyrite hydrothermal ores. *Ore Geology Reviews*, 77, 97-116.

Ghaderi, M., Palin, J.M., Campbell, I.H., Sylvester, P.J. (1999). Rare earth element systematics in scheelite from hydrothermal gold deposits in the Kalgoorlie-Norseman region, Western Australia. *Economic Geology*, 94, 423-437.

Gibert, F., Moine, B., Schott, J., Dandurand, J.L. (1992). Modeling of the transport and deposition of tungsten in the scheelite-bearing calc-silicate gneisses of the Montagne Noire, France. *Contributions to Mineralogy and Petrology*, 112, 371-384.

Giesen, C., Wang, H.A.O., Schapiro, D., Zivanovic, N., Jacobs, A., Hattendorf, B., Schüffler, P.J., Grolimund, D., Buhmann, J.M., Brandt, S., Varga, Z., Wild, P.J., Günther, D., Bodenmiller, B. (2014). Highly multiplexed imaging of tumor tissues with subcellular resolution by mass cytometry. *Nature Methods*, 11, 417-422.

Giuliani, G. (1984). Les concentrations filoniennes à tungstène-étain du massif granitique des Zaër (Maroc Central): Minéralisations et phases fluides associées. *Mineralium Deposita*, 19, 193-201.

Giuliani, G. (1987). La cassitérite zonée du gisement de Sokhret Allal (Granite des Zaër; Maroc Central): composition chimique et phases fluides associées. *Mineralium Deposita*, 22, 253-261.

Gloaguen, E. (2006). Apports d'une étude intégrée sur les relations entre granites et minéralisations filoniennes (Au et Sn-W) en contexte tardi-orogénique (Chaîne Hercynienne, Galice centrale, Espagne). Ph.D. thesis, Université d'Orléans, France, 574p.

Gloaguen, E., Branquet, Y., Boulvais, P., Moëlo, Y., Chauvel, J.J., Chiappero, P.J., Marcoux, E. (2007). Palaeozoic oolitic ironstone of the French Armorican Massif: a chemical and structural trap for orogenic base metal-As-Sb-Au mineralisation during Hercynian strike-slip deformation. *Mineralium Deposita*, 42, 399-422.

Goër de Herve, A., Bogdanoff, S., Couturié, J.P. (2006). Carte géologique de Entraygues-sur-Truyère au 1/50 000, BRGM Edition, Orléans.

Goldmann, S., Melcher, F., Gäbler, H-E., Dewaele, S., De Clercq, F., Muchez, P. (2013). Mineralogy and trace element chemistry of ferberite/reinite from tungsten deposits in Central Rwanda. *Minerals*, 3, 121-144.

Goldstein, R.H. (2001). Fluid inclusions in sedimentary and diagenetic systems. *Lithos*, 55, 159-193.

Gomes, M.E.P., Neiva, A.M.R. (2002). Petrogenesis of tin-bearing granites from Ervedosa, Northern Portugal: the importance of magmatic processes. *Chemie der Erde-Geochemistry*, 62, 47-72.

Graham, J., Thornber, M.R. (1974). The crystal chemistry of complex Niobium and Tantalum oxides. I. Structural classification of MO_2 phases. *American Mineralogist*, 59, 1026-1039.

Griffin, W.L., Slack, J.F., Ramsden, A.R., Win, T.T., Ryan, C.G. (1996). Trace elements in tourmalines from massive sulfide deposits and tourmalinites: Geochemical controls and exploration applications. *Economic Geology*, 91, 657-675.

Gromet, L.P., Haskin, L.A., Korotev, R.L., Dymek, R.F. (1984). The "North American shale composite": its compilation, major and trace element characteristics. *Geochimica et Cosmochimica Acta*, 48, 2469-2482.

Gschwind, S., Flamigni, L., Koch, J., Borovinskaya, O., Groh, S., Niemax, K., Günther, D. (2011). Capabilities of inductively coupled plasma spectrometry for the detection of nanoparticles carried by monodisperse microdroplets. *Journal of Analytical Atomic Spectrometry*, 26, 1166-1174.

Gschwind, S., Hagendorfer, H., Frick, D.A., Günther, D. (2013). Mass quantification of nanoparticles by single droplet calibration using inductively coupled plasma mass spectrometry. *Analytical Chemistry*, 85, 5875–5883.

Guérangé-Lozes, J., Burg, J.P. (1990). Les nappes varisques du sud-ouest du Massif Central (carte géologiques et structurales à 1/250 000 Montpellier et Aurillac). *Géologie de la France,* 3-4, 71-106.

Guion, J.L. (1984). Contribution à l'étude géologique et gîtologique du district à tungstène, étain et fluor de Montredon-Labessonnié (Tarn). Ph.D. thesis, Université de Toulouse, France, 246p.

Gulson, B.L., Jones, M.T. (1992). Cassiterite: potential for direct dating of mineral deposits and a precise age for the Bushveld complex granites. *Geology*, 20, 355–358.

Günther, D., Koch, J. (2008). Formation of aerosols generated by laser ablation and their impact on elemental fractionation in LA-ICPMS. In Laser Ablation ICPMS in the Earth Sciences: Current Practices and Outstanding Issues (ed. P. Sylvester). *Mineralogical Association of Canada, Short Course,* 40, 19-34.

Günther, D., Frischknecht, R., Heinrich, C.A., Kahlert, H.J. (1997). Capabilities of an Argon Fluoride 193 nm excimer laser for laser ablation inductively coupled plasma mass spectometry microanalysis of geological materials. *Journal of Analytical Atomic Spectrometry*, 12, 939-944.

Günther, D., Audétat, A., Frischknecht, R., Heinrich, C.A. (1998). Quantitative analysis of major, minor and trace elements in fluid inclusions using laser ablation-inductively coupled plasma mass spectrometry. *Journal of Analytical Atomic Spectrometry*, 13, 263-270.

Guoliang, G., Zhixiong, C. (1992). Compositional characteristics of wolframite in tin deposits, Dupangling, Guangxi. *Chinese Journal of Geochemistry*, 11, 156-167.

Guoliang, G., Zhixiong, C. (1994). Compositional characteristics and existing forms of major, trace and rare – earth elements in cassiterite, Dupangling tin ore field, Guangxi. *Chinese Journal of Geochemistry*, 13, 85-95.

H

Halls, C. (1994). Energy and mechanism in the magmatic-hydrothermal evolution of the Cornubian batholith: a review. In Metallogeny of collisional orogens (Seltmann, R., Kämpf, H. and Möller, P., eds.). Czech Geological Survey, Prague, 274-294.

Hawthorne, F.C., Henry, D.J. (1999). Classification of the minerals of the tourmaline group.

European Journal of Mineralogy, 11, 201-215.

Heinrich, C.A. (1990). The chemistry of hydrothermal tin-(tungsten) ore deposition. *Economic Geology*, 85, 457-481.

Heinrich, C.A., Pettke, T., Halter, W.E., Aigner-Torres, M., Audétat, A., Günther, D., Hattendorf, B., Bleiner, D., Guillong, M., Horn, I. (2003). Quantitative multi-element analysis of minerals, fluid and melt inclusions by laser-ablation inductively-coupled-plasma mass-spectrometry. *Geochimica et Cosmochimica Acta,* 67, 3473-3497.

Hem, S.R., Makovicky, E. (2004). The system Fe–Co–Ni–As–S. II. Phase relations in the (Fe, Co, Ni)$As_{1.5}S_{0.5}$ section at 650 and 500°C. *The Canadian Mineralogist*, 42, 63-86.

Henry, D.J., Guidotti, C.V. (1985). Tourmaline as a petrogenetic indicator mineral: an example from the staurolite-grade metapelites of NW Maine. *American Mineralogist*, 70, 1-15.

Henry, D.J., Dutrow, B.L. (1996). Metamorphic tourmaline and its petrologic applications. In Boron: Mineralogy, Petrology and Geochemistry (Grew, E.S., Anovitz, L.M., eds.). *Reviews in Mineralogy*, 33, 503–557.

Henry, D.J., Dutrow, B.L. (2012). Tourmaline at diagenetic to low-grade metamorphic conditions: Its petrologic applicability. *Lithos*, 154, 16-32.

Henry, D.J., Novák, M., Hawthorne, F.C., Ertl, A., Dutrow, B.L., Uher, P., Pezzotta, F. (2011). Nomenclature of the tourmaline-supergroup minerals. *American Mineralogist*, 96, 895-913.

Herron, M.M. (1988). Geochemical classification of terrigenous sands and shales from core or log data. *Journal of Sedimentary Petrology*, 58, 820-829.

Hervig, R.L., Moore, G.M., Williams, L.B., Peacock, S.M., Holloway, J.R., Roggensack, K. (2002). Isotopic and elemental partitioning of boron between hydrous fluid and silicate melt. *American Mineralogist*, 87, 769-774.

Hetzel, A., Böttcher, M.E., Wortmann, U.G., Brumsack, H.J. (2009). Paleo-redox conditions during OAE 2 reflected in Demerara Rise sediment geochemistry (ODP Leg 207). *Palaeogeography, Palaeoclimatology, Palaeoecology*, 273, 302-328.

Holliger, P., Cuney, M., Friedrich, M., Turpin, L. (1986). Age Carbonifère de l'unité de Brâme du complexe granitique peralumineux de Saint Sylvestre (N.O. Massif Central) défini par les données isotopiques U-Pb sur zircon et monazite. *Comptes Rendus de l'Académie des Sciences*, Paris, 303, 1309-1314.

Hsieh, H-F., Chang, W-S., Hsieh, Y-K., Wang, C-F. (2011). Using dried-droplet laser ablation inductively coupled plasma mass spectrometry to quantify multiple elements in whole

blood. *Analytica Chimica Acta*, 699, 6-10.

Hsu, L.C. (1976). The stability relations of the wolframite series. *American Mineralogist*, 61, 944-955.

Hsu, L.C. (1981). Phase relations of some tungstate minerals under hydrothermal conditions. *American Mineralogist*, 66, 298-308.

Irber, W. (1999). The lanthanide tetrad effect and its correlation with K/Rb, Eu/Eu*, Sr/Eu, Y/Ho, and Zr/Hf of evolving peraluminous granite suites. *Geochimica et Cosmochimica Acta*, 63, 489-508.

I

Ishihara, S. (1981). The granitoid series and mineralization. *Economic Geology*, 75th Anniversary Volume, 458-484.

Ishikawa, T., Nakamura, E. (1993). Boron isotope systematics of marine sediments. *Earth and Planetary Science Letters*, 117, 567-580.

J

Jackson, N.J., Willis-Richards, J., Manning, D.A., Sams, M.S. (1989). Evolution of the Cornubian ore field, southwest England: Part II. Mineral deposits and ore-forming processes. *Economic Geology*, 84, 1101-1133.

Jackson, S. (2008). Calibration strategies for elemental analysis by LA-ICPMS. In Laser Ablation ICPMS in the Earth Sciences: Current Practices and Outstanding Issues (ed. P. Sylvester). *Mineralogical Association of Canada, Short Course*, 40, 169-188.

Jackson, S.E., Pearson, N.J., Griffin, W.L., Belousova, E.A. (2004). The application of laser ablation-inductively coupled plasma-mass spectrometry to in situ U–Pb zircon geochronology. *Chemical Geology*, 211, 47–69.

Jacobsen, J.B.E., McCarthy, T.S., Laing, G.J. (1976). The copper-bearing breccia pipes of the Messina district South Africa. *Mineralium Deposita*, 11, 33-45.

Jamieson, R.A., Unsworth, M.J., Harris, N.B., Rosenberg, C.L., Schulmann, K. (2011). Crustal melting and the flow of mountains. *Elements*, 7, 253-260.

Jiang, S.Y., Radvanec, M., Nakamura, E., Palmer, M., Kobayashi, K., Zhao, H-X., Zhao, K-D. (2008). Chemical and boron isotopic variations of tourmaline in the Hnilec granite-related hydrothermal system, Slovakia: Constraints on magmatic and metamorphic fluid evolution. *Lithos*, 106, 1-11.

Jiang, S.Y., Palmer, M. R. (1998). Boron isotope systematics of tourmaline from granites and pegmatites; a synthesis. *European Journal of Mineralogy*, 10, 1253-1265.

Jiang, S.Y., Palmer, M.R., Yeats, C.J. (2002). Chemical and boron isotopic compositions of tourmaline from the Archean Big Bell and Mount Gibson gold deposits, Murchison Province, Yilgarn craton, Western Australia. *Chemical Geology*, 188, 229-247.

Jiang, S.Y., Yang, J.H., Novák, M., Selway, J. (2003). Chemical and boron isotopic compositions of tourmaline from the Lavicky leucogranite, Czech Republic. *Geochemical Journal*, 37, 545-556.

Jiang, S.Y., Yu, J.M., Lu, J.J. (2004). Trace and rare-earth element geochemistry in tourmaline and cassiterite from the Yunlong tin deposit, Yunnan, China: implication for migmatitic–hydrothermal fluid evolution and ore genesis. *Chemical Geology*, 209, 193-213.

Jochum, K. P., Stoll, B. (2008). Reference materials for elemental and isotopic analyses by LA-(MC)-ICPMS: Successes and outstanding needs. In Laser Ablation ICPMS in the Earth Sciences: Current Practices and Outstanding Issues (ed. P. Sylvester). *Mineralogical Association of Canada, Short Course*, 40, 147-168.

Jochum, K.P., Weis, U., Stoll, B., Kuzmin, D., Yang, Q., Raczek, I., Jacob, D.E., Stracke, A., Birbaum, K., Frick, D.A., Günther, D., Enzweiler, J. (2011). Determination of reference values for NIST SRM 610-617 glasses following ISO guidelines. *Geostandards and Geoanalytical Research*, 35, 397–429.

Johan, M.D.V., Johan, Z. (1994). Accessory minerals of the Cínovec (Zinnwald) granite cupola, Czech Republic Part 1: Nb-, Ta-and Ti-bearing oxides. *Mineralogy and Petrology*, 51, 323-343.

Johan, Z., Johan, V. (2005). Accessory minerals of the Cínovec (Zinnwald) granite cupola, Czech Republic: indicators of petrogenetic evolution. *Mineralogy and Petrology*, 83, 113-150.

K

Kawakami, T., Ikeda, T. (2003). Boron in metapelites controlled by the breakdown of tourmaline and retrograde formation of borosilicates in the Yanai area, Ryoke metamorphic belt, SW Japan. *Contributions to Mineralogy and Petrology*, 145, 131-150.

Kelly, W.C., Rye, R.O. (1979). Geologic, fluid inclusion, and stable isotope studies of the tin-tungsten deposits of Panasqueira, Portugal. *Economic Geology*, 74, 1721-1822.

Kempe, U., Wolf, D. (2006). Anomalously high Sc contents in ore minerals from Sn–W deposits: possible economic significance and genetic implications. *Ore Geology Reviews*, 28, 103-122.

Klementová, M., Rieder, M. (2004). Exsolution in niobian rutile from the pegmatite deposit at Greenbushes, Australia. *The Canadian Mineralogist*, 42, 1859-1870.

Klemme, S., Prowatke, S., Münker, C., Magee, C. W., Lahaye, Y., Zack, T., Kasemann, S.A., Cabato, E.J.A., Kaeser, B. (2008). Synthesis and preliminary characterisation of new silicate, phosphate and titanite reference glasses. *Geostandards and Geoanalytical Research*, 32, 39-54.

Kontak, D.J. (1990). The East Kemptville topaz-muscovite leucogranite, Nova Scotia, geological setting and whole rock geochemistry. *The Canadian Mineralogist*, 28, 787-825.

Krachler, M., Zheng, J., Fisher, D., Shotyk, W. (2005). Analytical procedures for improved trace element detection limits in polar ice from Arctic Canada using ICP-MS. *Analytica Chimica Acta,* 530, 291-298.

Kroner, U., Romer, R.L. (2010). The Saxo-Thuringian Zone – tip of the Armorican spur and part of the Gondwana plate. In Pre-Mesozoic Geology of Saxo-Thuringia – From the Cadomian Active Margin to the Variscan Orogen (eds. U. Linnemann and R. L. Romer). Schweizerbart, Stuttgart, 371-394.

Kroner, U., Romer, R.L. (2013). Two plates - many subduction zones: the Variscan orogeny reconsidered. *Gondwana Research*, 24, 298-329.

Kuiper, K.F., Deino, A., Hilgen, F.J., Krijgsman, W., Renne, R., Wijbrans, J.R. (2008). Synchronizing Rock Clocks of Earth History. *Science*, 320, 500-504.

Kumtabtim, U., Siripinyanond, A., Auray-Blais, C., Ntwari, A., Becker, J.S. (2011). Analysis of trace metals in single droplet of urine by laser ablation inductively coupled plasma mass spectrometry. *International Journal of Mass Spectrometry,* 307, 174-181.

Kutscher, D.J., Fricker, M.B., Hattendorf, B., Bettmer, J., Günther, D. (2011). Systematic studies on the determination of Hg-labelled proteins using laser ablation-ICPMS and isotope dilution analysis. *Analytical and Bioanalytical Chemistry,* 401, 2691-2698.

Kyle, J.R., Ketcham, R.A. (2015). Application of high resolution X-ray computed tomography to mineral deposit origin, evaluation, and processing. *Ore Geology Reviews*, 65, 821-839.

L

Lach, P., Mercadier, J., Dubessy, J., Boiron, M.C., Cuney, M. (2013). In Situ Quantitative Measurement of Rare Earth Elements in Uranium Oxides by Laser Ablation‐Inductively Coupled Plasma‐ Mass Spectrometry. *Geostandards and Geoanalytical*

Research, 37, 277-296.

Lafon, J. M., Respaut, J.P. (1988). Géochronologie U-Pb et leucogranites varisques : cas des massifs de Grand-Rieu et de la Porcherie (Limousin), Massif Central Français. *Bulletin de Minéralogie*, 111, 225–237.

Lancelot, J.R., de Saint André, B., de la Boisse, H. (1984). Systématique U-Pb et évolution du gisement d'uranium de Lodève (France). *Mineralium Deposita*, 19, 44-53.

Lancelot, J.R., Sarazin, G., Allègre, C.J. (1971). Composition isotopique du plomb et du soufre des galènes liées aux formations sédimentaires. Interprétations géologiques et géophysiques. *Contributions to Mineraloly and Petrology*, 32, 315-333.

Langmuir, D. (1976). Uranium solution-mineral equilibria at low temperatures with applications to sedimentary ore deposits. *Geochimica et Cosmochimica Acta*, 42, 547-569.

Lardeaux, J.M., Ledru, P., Daniel, I., Duchene, S. (2001). The Variscan French Massif Central - a new addition to the ultra-high pressure metamorphic 'club': exhumation processes and geodynamic consequences. *Tectonophysics*, 332, 143-167.

Lardeaux, J.M., Schulmann, K., Faure, M., Janoušek, V., Lexa, O., Skrzypek, E., Edel, J.B., Štípská, P. (2014). The Moldanubian Zone in the French Massif Central, Vosges/Schwarzwald and Bohemian Massif revisited: differences and similarities. *Geological Society, London, Special Publications*, 405, 7-44.

Laumonier, B., Marignac, C., Cheilletz, A., Macaudière, J. (1991). Relations entre tectoniques superposées, migmatitisations et mise en place des granites sur l'exemple de la bordure sud du dôme du Velay (région de Laviolle, Ardèche, France). *Comptes Rendus de l'Académie des Sciences*, Paris, 313, 937-944.

Laumonier, B., Marignac, C., Kister, P. (2010). Polymetamorphism and crustal evolution of the eastern Pyrenees during the Late Carboniferous Variscan orogenesis. *Bulletin de la Société Géologique de France*, 181, 411-428.

Le Carlier de Veslud, C., Alexandre, P., Ruffet, G., Cuney, M., Cheilletz, A. (2013). A two-stage exhumation in Western French Massif Central: New geochronological evidences of syn-collisional extension. *Lithos*, 175-176, 1-15.

Le Guen, M., Orgeval, J.J., Lancelot, J. (1991). Lead isotope behaviour in a polyphased Pb-Zn ore deposit: Les Malines (Cévennes, France). *Mineralium Deposita*, 26, 180-188.

Le Guen, M., Lescuyer, J.L., Marcoux, E. (1992). Lead-isotope evidence for a Hercynian origin of the Salsigne gold deposit (Southern Massif Central, France). *Mineralium Deposita*, 27, 129-136.

Lecumberri-Sanchez, P., Romer, R.L., Lüders, V., Bodnar, R.J. (2014). Genetic relationship between silver-lead-zinc mineralization in the Wutong deposit, Guangxi Province and Mesozoic granitic magmatism in the Nanling belt, southeast China. *Mineralium Deposita*, 49, 353-369.

Ledru, P., Lardeaux, J.M., Santallier, D., Autran, A., Quenardel, J.M., Floc'h, J.P., Lerouge, G., Maillet, N., Marchand, J., Ploquin, A. (1989). Où sont les nappes dans le Massif Central Français ? *Bulletin de la Société Géologique de France*, 3, 605-618.

Ledru, P., Courrioux, G., Dallain, C., Lardeaux, J.M., Montel, J.M., Vanderhaeghe, O., Vitel, G. (2001). The Velay dome (French Massif Central): melt generation and granite emplacement during orogenic evolution. *Tectonophysics*, 342, 207-237.

Leeman, W.P., Sisson, V.B. (1996). Geochemistry of boron and its implications for crustal and mantle processes. In Boron: mineralogy, petrology and geochemistry in the earth's crust (Grew, E.S. and Anovitz, L.M. eds). *Reviews in Mineralogy*, 33, 645–707.

Leeman, W.P., Tonarini, S. (2001). Boron isotopic analysis of proposed borosilicate mineral reference samples. *Geostantards Newsletter*, 25, 399-403.

Legros, H., Marignac, C., Mercadier, J., Cuney, M., Richard, A., Wang, R. C., Charles, N., Lespinasse, M.Y. (2016). Detailed paragenesis and Li-mica compositions as recorders of the magmatic-hydrothermal evolution of the Maoping W-Sn deposit (Jiangxi, China). *Lithos*, 264, 108-124.

Lehmann, B. (1990). Metallogeny of tin. Springer, Berlin-Heidelberg-New York, 212p.

Leisen, M., Boiron, M.C., Richard, A., Dubessy, J. (2012). Determination of Cl and Br concentrations in individual fluid inclusions by combining microthermometry and LA-ICPMS analysis: Implications for the origin of salinity in crustal fluids. *Chemical Geology,* 330-331, 197-206.

Lerouge, C., Bouchot, V. (2009). Conditions of formation and origin of fluids of quartz-tourmaline veins in the La Châtaigneraie tungstiferous district (Massif Central, France): fluid inclusions and stable isotopes. *Bulletin de la Société Géologique de France*, 180, 263-270.

Lerouge, C., Bouchot, V., Guerrot, C. (2000). Fluids and the W (±As,Au) ore deposits of the Enguialès-Leucamp District, La Châtaigneraie, French Massif Central. *Journal of Geochemical Exploration*, 69-70, 343-347.

Lerouge, C., Deschamps, Y., Piantone, P., Gilles, C., Breton, J. (2007). Metal-carrier accessory minerals associated with W±Sn mineralization, La Châtaigneraie tungsten ore district, Massif Central, France. *The Canadian Mineralogist*, 45, 875-889.

Leroy, J. (1978). The Margnac and Fanay uranium deposits of the La Crouzille District (western Massif Central, France); geologic and fluid inclusion studies. *Economic Geology*, 73, 1611-1634.

Leroy, J., Sonet, J. (1976). Contribution à l'étude géochronologique des filons de lamprophyres recoupant le granite à deux micas de Saint-Sylvestre (Limousin-Massif Central français). *Comptes Rendus de l'Académie des Sciences,* Paris, 283, 1477-1480.

Linnemann, U., Hofmann, M., Romer, R.L., Gerdes, A. (2010). Transitional stages between the Cadomian and Variscan orogenies: Basin development and tectono-magmatic evolution of the southern margin of the Rheic Ocean at the Saxo-Thuringian Zone (North Gondwana shelf). In Pre-Mesozoic Geology of Saxo-Thuringia – From the Cadomian Active Margin to the Variscan Orogen (eds. U. Linnemann and R.L. Romer). Schweizerbart, Stuttgart, 59-98.

Linnen, R.L. (1998). The solubility of Nb-Ta-Zr-Hf-W in granitic melts with Li and Li+ F; constraints for mineralization in rare metal granites and pegmatites. *Economic Geology*, 93, 1013-1025.

Linnen, R.L., Van Lichtervelde, M., Černý, P. (2012). Granitic pegmatites as sources of strategic metals. *Elements*, 8, 275-280.

Linnen, R.L., Cuney, M. (2005). Granite-related rare-element deposits and experimental constraints on Ta-Nb-W-Sn-Zr-Hf mineralization. In Rare-Element Geochemistry and Mineral Deposits (eds. R.L. Linnen and I.M. Samson). *Geological Association of Canada, Short Course Notes*, 17, 45-68.

Lister, B. (1978). The preparation of twenty ore standards, IGS 20-39. Preliminary work and assessment of analytical data. *Geostandards Newsletter*, 2, 157-186.

Llorens, T., Moro, M.C. (2012). Oxide minerals in the granitic cupola of the Jálama Batholith, Salamanca, Spain. Part I: accessory Sn, Nb, Ta and Ti minerals in leucogranites, aplites and pegmatites. *Journal of Geosciences*, 57, 25-43.

Llorens, T., Moro, M.C. (2012). Oxide minerals in the granitic cupola of the Jálama Batholith, Salamanca, Spain. Part II: Sn, W and Ti minerals in intra-granitic quartz veins. *Journal of Geosciences*, 57, 155-171.

London, D. (2011). Experimental synthesis and stability of tourmaline: a historical overview. *The Canadian Mineralogist*, 49, 117-136.

London, D., Manning, D.A.C. (1995). Chemical variation and significance of tourmaline from southwest England. *Economic Geology*, 90, 495-519.

London, D. (1997). Estimating abundances of volatiles and other mobile components in

evolved silicic melts through mineral-melt equilibria. *Journal of Petrology*, 38, 1691–1706.

London, D., Hervig, R.L., Morgan, G.B. (1988). Melt-vapor solubilities and elemental partitioning in peraluminous granite-pegmatite systems: experimental results with Macusani glass at 200 MPa. *Contributions to Mineralogy and Petrology*, 99, 360-373.

Longerich, H.P., Jackson, S.E., Günther, D. (1996). Laser ablation inductively coupled plasma mass spectrometric transient signal data acquisition and analyte concentration calculation. *Journal of Analytical Atomic Spectrometry*, 11, 899-904.

Loukola-Ruskeeniemi, K., Heino, T. (1996). Geochemistry and genesis of the black shale-hosted Ni-Cu-Zn deposit at Talvivaara, Finland. *Economic Geology*, 91, 80-110.

Lüders, V., Romer, R.L., Cabral, A.R., Schmidt, C., Banks, D.A., Schneider, J. (2005). Genesis of itabirite-hosted Au-Pd-Pt-bearing hematite-(quartz) veins, Quadrilátero Ferrífero, Minas Gerais, Brazil: Constraints from fluid inclusion infrared microthermometry, bulk crush-leach analysis and U-Pb systematics. *Mineralium Deposita*, 40, 289-306.

Ludwig, K.R. (1993). ISOPLOT: a plotting and regression program for radiogenic-isotope data. U.S. Geological Survey, Open File Report, 91–445, 1–42.

Ludwig, K.R., Grauch, R.I., Nutt, C.J., Nash, J.T., Frishman, D., Simmons, K.R. (1987). Age of uranium mineralization at the Jabiluka and Ranger uranium deposits, Northern Territory, Australia: new U–Pb isotope evidence. *Economic Geology*, 82, 857–874.

Ludwig, K.R., Simmons K.R. (1991). U-Pb dating of uranium ores in collapse-breccia pipes, Grand Canyon region. In Source, transport and deposition of metals (eds. M. Pagel and J.L. Leroy) A.A. Balkema, Rotterdam, 405-408.

Lumpkin, G.R., Ewing, R.C. (1992). Geochemical alteration of pyrochlore group minerals: Microlite subgroup. *American Mineralogist*, 77, 179-188.

Lumpkin, G.R., Ewing, R.C. (1995). Geochemical alteration of pyrochlore group minerals: Pyrochlore subgroup. *American Mineralogist*, 80, 732-743.

Lumpkin, G.R., Ewing, R.C. (1996). Geochemical alteration of pyrochlore group minerals: Betafite subgroup. *American Mineralogist*, 81, 1237-1248.

Luvizotto, G.L., Zack, T., Meyer, H.P., Ludwig, T., Triebold, S., Kronz, A., Münker, C., Stockli, D.F., Prowatke, S., Klemme, S., Jacob, D.E., von Eynatten, H. (2009). Rutile crystals as potential trace element and isotope mineral standards for microanalysis. *Chemical Geology*, 261, 346-369.

Luvizotto, G.L., Zack, T., Triebold, S., von Eynatten, H. (2009). Rutile occurrence and trace

element behavior in medium-grade metasedimentary rocks: example from the Erzgebirge, Germany. *Mineralogy and Petrology*, 97, 233-249.

M

Macaudière, J., Marignac, C., Weisbrod, A. (1987). Grandes nappes synschisteuses collisionnelles dans la catazone hercynienne des Cévennes médianes (Massif Central français). *Comptes Rendus de l'Académie des Sciences,* Paris, 304, 1195-1199.

Mangin, D., Marignac, C., Chaussidon, M. (1994). Mobilité du tungstène dans le métamorphisme régional : l'exemple des Cévennes (Massif Central Français). 15^{e} Réunion des Sciences de la Terre, 26-28 April 1994, Nancy, France.

Manning, D.A.C. (1982). Chemical and morphological variation in tourmalines from the Hub Kapong batholith of peninsular Thailand. *Mineralogical Magazine*, 45, 139-147.

Manning, D.A.C. (1991). Chemical variation in tourmaline from south-west England. *Read at the Annual Conference of the Ussher Society*, 327-332.

Marcoux, E. (1987). Isotopes du plomb et paragenèses métalliques, traceurs de l'histoire des gîtes minéraux. Illustration des concepts de source, d'héritage et de regionalism dans les gîtes français . Applications en recherché minière. Ph.D. thesis, Université de Clermont-Ferrand, Doc BRGM, 117, France, 413p.

Marcoux, E., Bril, H. (1986). Héritage et sources des métaux d'après la géochimie isotopique du plomb. *Mineralium Deposita*, 21, 35-43.

Marcoux, E., Moëlo, Y., Picot, P., Baubron, J.C. (1988). Evolution minéralogique et isotopique (Pb) du filon sulfuré complexe des Borderies (Massif Central Français) – Implications métallogéniques. *Mineralium Deposita*, 23, 58-70.

Marcoux, E., Lescuyer, J.L., Milesi, J.P. (1990). Géochimie isotopique du plomb du gisement de Chessy et des minéralisations volcanosédimentaires de la série de la Brévenne (Massif Central). Implications métallogéniques et conséquences pour l'exploration. *Chronique de la Recherche Minière*, 501, 3-11.

Marcoux, E., Moëlo, Y. (1991). Lead isotope geochemistry and paragenetic study of inheritance phenomena in metallogenesis: examples from base metal sulfide deposits in France. *Economic Geology*, 86, 106-120.

Marcoux, E., Joubert, M., Lescuyer, J.L. (1991). Origine des minéralisations stratiformes de la bordure du Canigou (Pyrénées-orientales, France) : apport de la géochimie isotopique du plomb. *Comptes Rendus de l'Académie des Sciences*, Paris, 312, 281-287.

Marcoux, E., Cassard, D., Chabod, J.C. (1993). Source hercynienne du gisement filonien Zn

(Ge) de Saint-Salvy (Tarn, France). *Comptes Rendus de l'Académie des Sciences*, Paris, 316, 1091-1098.

Marignac, C., Cuney, M. (1999). Ore deposits of the French Massif Central: insight into the metallogenesis of the Variscan collision belt. *Mineralium Deposita*, 34, 472-504.

Marignac, C., Cathelineau, M. (2010). The nature of ore-forming fluids in peri-batholitic Sn-W deposits and a classification. In Proceedings of the 10th Biennial SGA Meeting: Smart Science for Exploration and Mining, Townsville (Williams et al. eds), Vol. 1, 245-247.

Marignac, C., Leroy, J., Macaudière, J., Pichavant, M., Weisbrod, A. (1980). Evolution tectonométamorphique d'un segment de l'orogène hercynien : les Cévennes médianes, Massif Central français. *Comptes Rendus de l'Académie des Sciences*, Paris, 291, 605-608.

Marignac, C., Cathelineau, M., Boiron, M.C., Fourcade, S., Vallance, J., Souhassou, M. (2000). The Q-Au lodes of W Europe: towards the definition of a Variscan-type of shear-zone hosted gold deposits. In A Geode-GeoFrance 3D Workshop on Orogenic Gold Deposits in Europe with emphasis on the Variscides (eds. V. Bouchot and R. Moritz). Doc BRGM, 297, 82-85.

Marignac, C., Belkasmi, M., Chalal, Y., Kesraoui, M. (2001). W–Nb–Ta oxides as markers of the magmatic to hydrothermal transition condition in rare-metal granites. In Mineral Deposits at the Beginning of the 21st Century (Piestrzyñski, A. et al., Eds.). Proceedings of the Joint Sixth Biennial SGA-SEG Meeting, Kraków, Poland, 26-29 August 2001, 441– 448.

Marignac, C., Aïssa, D.E., Bouabsa, L., Kesraoui, M., Nedjari, S. (2016). The Hoggar Gold and Rare Metals Metallogenic Province of the Pan-African Tuareg Shield (Central Sahara, South Algeria): An Early Cambrian Echo of the Late Ediacaran Murzukian Event? In Mineral Deposits of North Africa (M. Bouabdellah and J.F. Slack eds.). Springer International Publishing, 371-404.

Marks, M.A., Marschall, H.R., Schühle, P., Guth, A., Wenzel, T., Jacob, D.E., Barth, M., Markl, G. (2013). Trace element systematics of tourmaline in pegmatitic and hydrothermal systems from the Variscan Schwarzwald (Germany): the importance of major element composition, sector zoning, and fluid or melt composition. *Chemical Geology*, 344, 73-90.

Marschall, H.R., Altherr, R., Kalt, A., Ludwig, T. (2008). Detrital, metamorphic and metasomatic tourmaline in high-pressure metasediments from Syros (Greece): intra-

grain boron isotope patterns determined by secondary-ion mass spectrometry. *Contributions to Mineralogy and Petrology*, 155, 703-717.

Marschall, H.R., Meyer, C., Wunder, B., Ludwig, T., Heinrich, W. (2009). Experimental boron isotope fractionation between tourmaline and fluid: confirmation from in situ analyses by secondary ion mass spectrometry and from Rayleigh fractionation modelling. *Contributions to Mineralogy and Petrology*, 158, 675-681.

Marschall, H.R., Jiang, S.Y. (2011). Tourmaline isotopes: no element left behind. *Elements*, 7, 313-319.

Matte, P. (2001). The Variscan collage and orogeny (480-290 Ma) and the tectonic definition of the Armorica microplate: a review. *Terra Nova*, 13, 122-128.

McCann, T. (2008). The Geology of Central Europe: Precambrian and Palaeozoic. *Geological Society of London*, 784p.

McCann, T., Pascal, C., Timmerman, M.J., Krzywiec, P., López-Gómez, J., Wetzel, A., Krawczyk, C.M., Rieke, H., Lamarche, J. (2006). Post-Variscan (end Carboniferous-Early Permian) basin evolution in Western and Central Europe. *Geological Society of London, Memoirs*, 32, 355-388.

McCuaig, T.C., Beresford, S., Hronsky, J. (2010). Translating the mineral systems approach into an effective exploration targeting system. *Ore Geology Reviews*, 38, 128-138.

Meinhold, G. (2010). Rutile and its applications in earth sciences. *Earth-Science Reviews*, 102, 1-28.

Meinhold, G., Anders, B., Kostopoulos, D., Reischmann, T. (2008). Rutile chemistry and thermometry as provenance indicator: an example from Chios Island, Greece. *Sedimentary Geology*, 203, 98-111.

Melcher, F., Graupner, T., Gäbler, H.E., Sitnikova, M., Henjes-Kunst, F., Oberthür, T., Gerdes, A., Dewaele, S. (2015). Tantalum–(niobium–tin) mineralisation in African pegmatites and rare metal granites: constraints from Ta–Nb oxide mineralogy, geochemistry and U–Pb geochronology. *Ore Geology Reviews*, 64, 667-719.

Melgarejo, J.C., Costanzo, A., Bambi, A.C.J.M., Gonçalves, A.O., Neto, A.B. (2012). Subsolidus processes as a key factor on the distribution of Nb species in plutonic carbonatites: The Tchivira case, Angola. *Lithos*, 152, 187-201.

Melleton, J., Gloaguen, E., Frei, D., Novák, M., Breiter, K. (2012). How are the emplacement of rare-element pegmatites, regional metamorphism and magmatism interrelated in the Moldanubian domain of the Variscan Bohemian Massif, Czech Republic? *The Canadian Mineralogist*, 50, 1751-1773.

Melleton, J., Gloaguen, E., Frei, D. (2015). Rare-elements (Li-Be-Ta-Sn-Nb) magmatism in the European Variscan Belt, a review. In Proceedings of the 13th Biennial SGA Meeting, 24–27 August 2015, Nancy, France (eds. A. S. André-Mayer, M. Cathelineau, P. Muchez, E. Pirard and S. Sindern), Vol. 2, 807-810.

Mercadier, J., Cuney, M., Lach, P., Boiron, M. C., Bonhoure, J., Richard, A., Leisen, M., Kister, P. (2011). Origin of uranium deposits revealed by their rare earth element signature. *Terra Nova*, 23, 264-269.

Merceron, T., Bonhomme, M.G., Fouillac, A.M., Vivier, G., Meunier, A. (1987). Pétrologie des altérations hydrothermales du sondage GPF Echassières n°1. In Géologie profonde de la France, Echassières : le forage scientifique. Une clé pour la compréhension des mécanismes magmatiques et hydrothermaux associés aux granites à métaux rares (eds. M. Cuney and A. Autran). *Géologie de la France*, 2-3, 259-269.

Merceron, T., Vieillard, P., Fouillac, A.M., Meunier, A. (1992). Hydrothermal alterations in the Echassières granitic cupola. *Contributions to Mineralogy and Petrology*, 112, 279-292.

Meyer, C., Wunder, B., Meixner, A., Romer, R.L., Heinrich, W. (2008). Boron-isotope fractionation between tourmaline and fluid: an experimental re-investigation. *Contributions to Mineralogy and Petrology*, 156, 259-267.

Miahle, J. (1980). Le massif granitique de la Borne : étude pétrographique, géochimique, géochronologique et structurale. Ph.D. thesis, Université de Clermont-Ferrand, France, 170p.

Michard-Vitrac, A., Albarède, F., Allègre C.J. (1981). Lead isotopic composition of Hercynian granitic K-feldspars constrains continental genesis. *Nature*, 291, 460-464.

Mir, A.R., Bhat, Z.A., Alvi, S.H., Balaram, V. (2015). Geochemistry of black shales from Singhbhum mobile belt, Eastern India: implications for paleo-weathering and provenance. *Himalayan Geology*, 36, 126-133.

Mlynarczyk, M.S., Williams-Jones, A.E. (2006). Zoned tourmaline associated with cassiterite: implications for fluid evolution and tin mineralization in the San Rafael Sn–Cu deposit, southeastern Peru. *The Canadian Mineralogist*, 44, 347-365.

Moine, B., de la Roche, H. (1968). Nouvelle approche du problème de l'origine des amphibolites à partir de leur composition chimique. *Comptes Rendus de l'Académie des Sciences*, Paris, 267, 2084-2087.

Möller, P., Dulski, P., Szacki, W., Malow, G., Riedel, E. (1988). Substitution of tin in cassiterite by tantalum, niobium, tungsten, iron and manganese. *Geochimica et*

Cosmochimica Acta, 52, 1497-1503.

Monecke, T., Kempe, U., Monecke, J., Sala, M., Wolf, D. (2002). Tetrad effect in rare earth element distribution patterns: a method of quantification with application to rock and mineral samples from granite-related rare metal deposits. *Geochimica et Cosmochimica Acta*, 66, 1185-1196.

Monié, P., Respaut, J.P., Brichaud, S., Bouchot, V., Faure, M., Roig, J.Y. (2000). $^{40}Ar/^{39}Ar$ and U-Pb geochronology applied to Au-W-Sb metallogenesis in the Cévennes and Châtaigneraie districts (Southern Massif Central, France). In A Geode-GeoFrance 3D Workshop on Orogenic Gold Deposits in Europe with emphasis on the Variscides (eds. V. Bouchot and R. Moritz). Doc BRGM, 297, 77-79.

Monnin, C., Dubois, M., Papaiconomou, N., Simonin, J.P. (2002). Thermodynamics of the $LiCl+H_2O$ system. *Journal of Chemical and Engineering Data*, 47, 1331-1336.

Montel, J.M., Marignac, C., Barbey, P., Pichavant, M. (1992). Thermobarometry and granite genesis: the Hercynian low- P, high- T Velay anatectic dome (French Massif Central). *Journal of Metamorphic Geology*, 10, 1-15.

Moran, A.E., Sisson, V.B., Leeman, W.P. (1992). Boron depletion during progressive metamorphism: implications for subduction processes. *Earth and Planetary Science Letters*, 111, 331-349.

Morelli, R.M., Creaser, R.A., Selby, D., Kontak, D.J., Horne, R.J. (2005). Rhenium-osmium geochronology of arsenopyrite in Meguma group gold deposits, Meguma Terrane, Nova Scotia, Canada: evidence for multiple gold-mineralizing events. *Economic Geology*, 100, 1229-1242.

Morgan, J.W., Wandless, G.A. (1980). Rare earth element distribution in some hydrothermal minerals: evidence for crystallographic control. *Geochimica et Cosmochimica Acta*, 44, 973-980.

Mougeot, R., Respaut, J.P., Ledru, P., Marignac, C. (1997). U-Pb chronology on accessory minerals of the Velay anatectic dome (French Massif Central). *European Journal of Mineralogy*, 9, 141-156.

Mourey, Y. (1985). Le leucogranite à topaze de Chavence. Un nouvel exemple de massif à Sn, W, Li dans le Nord du Massif Central Français. *Comptes Rendus de l'Académie des Sciences*, Paris, 300, 951-954.

Mouthier, B. (2005). La mine de tungstène de Puy-les-Vignes (Haute-Vienne). Connaissance et Sauvegarde de Saint-Léonard, 2^{e} édition, 256 p.

Müller, A., Halls, C. (2005). Rutile - the tin-tungsten host in the intrusive tourmaline breccia

at Wheal Remfry, SW England. In Mineral Deposit Research: Meeting the Global Challenge (Mao, J. and Bierlein, F.P., eds.). Proceedings of the Eighth Biennial SGA Meeting, Beijing, China, 441-444.

Munoz, M., Baron, S., Boucher, A., Béziat, D., Salvi, S. (2015). Mesozoic vein-type Pb-Zn mineralization in the Pyrenees: lead isotopic and fluid inclusion evidence from the Les Argentières and Lacore deposits. *Comptes Rendus Geoscience*, 348, 322-332.

Munz, I.A. (2001). Petroleum inclusions in sedimentary basins: systematics, analytical methods and applications. *Lithos*, 55, 195-212.

Myers, D.P., Hieftje, G.M. (1993). Preliminary design considerations and characteristics of an inductively coupled-plasma-time-of-flight mass spectrometer. *Microchemical Journal*, 48, 259-277.

N

Nadoll, P., Angerer, T., Mauk, J. L., French, D., Walshe, J. (2014). The chemistry of hydrothermal magnetite: a review. *Ore Geology Reviews*, 61, 1-32.

Nakai, S., Halliday, A.N., Kesler, S.E., Jones, H.D., Kyle, J.R., Lane, T.E. (1993). Rb-Sr dating of sphalerites from Mississippi Valley-type (MVT) ore deposits. *Geochimica et Cosmochimica Acta*, 57, 417-427.

Nakano, T., Nakamura, E. (2001). Boron isotope geochemistry of metasedimentary rocks and tourmalines in a subduction zone metamorphic suite. *Physics of the Earth and Planetary Interiors*, 127, 233-252.

Nakashima, K., Watanabe, M., Soeda, A. (1986). Regional and local variations in the composition of the wolframite series from SW Japan and possible factors controlling compositional variations. *Mineralium Deposita*, 21, 200-206.

Nasdala, L., Wenzel, M., Vavra, G., Irmer, G., Wenzel, T., Kober, B. (2001). Metamictisation of natural zircon: accumulation versus thermal annealing of radioactivity-induced damage. *Contributions to Mineralogy and Petrology*, 141, 125-144.

Nasraoui, M., Bilal, E. (2000). Pyrochlores from the Lueshe carbonatite complex (Democratic Republic of Congo): a geochemical record of different alteration stages. *Journal of Asian Earth Sciences*, 18, 237-251.

Neiva, A.M.R. (1996). Geochemistry of cassiterite and its inclusions and exsolution products from tin and tungsten deposits in Portugal. *The Canadian Mineralogist*, 34, 745-768.

Neiva, A.M.R. (2008). Geochemistry of cassiterite and wolframite from tin and tungsten quartz veins in Portugal. *Ore Geology Reviews*, 33, 221-238.

Neiva, A.M.R., Williams, I.S., Lima, S.M., Teixeira, R.J.S. (2012). U–Pb and $^{39}Ar/^{40}Ar$ data constraining the ages of the source, emplacement and recrystallization/cooling events from late- to post-D3 Variscan granites of the Gouveia area, central Portugal. *Lithos*, 153, 72–83.

Nicolas, V.A. (1985). Le gisement wolframifère de Leucamp dans son environnement géologique (Châtaigneraie du Cantal, France). Ph.D. thesis, Ecole Nationale Supérieure des Mines de Paris, France, 384p.

Noblet, C., Lefort, J.P. (1990). Sedimentological evidence for a limited separation between Armorica and Gondwana during the Early Ordovician. *Geology*, 18, 303–306.

Noronha, F. (1983). Estudo metallogénico da área tungstífera da Borralha. Ph.D. thesis, University of Porto, Portugal, 477p.

Noronha, F., Vindel, E., López García, J.Á., Dória, A., García García, E., Boiron, M.C., Cathelineau, M. (1999). Fluids related to tungsten ore deposits in Northern Portugal and Spanish Central System: a comparative study. *Revista de la Sociedad Geológica de España*, 12, 397-403.

Noronha, F., Cathelineau, M., Boiron, M.C., Banks, D.A., Dória, A., Ribeiro, M.A., Nogueira, P., Guedes, A. (2000). A three stage fluid flow model for Variscan gold metallogenesis in northern Portugal. *Journal of Geochemical Exploration*, 71, 209-224.

Noyé, F. (1985). Etude métallogénique des indices à étain-tungstène de Saint Mélany (Ardèche, France). Ph.D. thesis, Institut National Polytechnique de Lorraine, France, 285p.

Noyé, F., Weisbrod, A. (1988). Les indices stanno-wolframifères de Saint Mélany (Cévennes Médianes, Ardèche, Massif Central Français). In Gisements métallifères dans leur contexte géologique (Johan, Z. and Ohnenstetter, D. eds), Doc. BRGM, 158, 175-194.

O

Oh, M.S., Marcoux, E., Calvez, J.Y., Touray, J.C. (1989). Anomalous unradiogenic lead from strata-bound Zn-Pb-Cu mineralization in the Saint Georges-Sur-Loire synclinorium (Armorican Massif, France). *Economic Geology*, 84, 1436-1443.

Ohnenstetter, D., Piantone, P. (1992). Pyrochlore-group minerals in the Beauvoir peraluminous leucogranite, Massif Central, France. *The Canadian Mineralogist*, 30, 771-784.

Okrusch, M., Hock, R., Schüssler, U., Brummer, A., Baier, M., Theisinger, H. (2003). Intergrown niobian rutile phases with Sc- and W-rich ferrocolumbite: An electron-

microprobe and Rietveld study. *American Mineralogist*, 88, 986-995.

P

Pačevski, A., Götzinger, M., Dimitrijević, R., Cvetković, L. (2007). Oscillatory zoning in wolframite from Osanica, near Bor, Serbia. *Neues Jahrbuch für Mineralogie Abhandlungen*, 184, 151-160.

Palme, H., O'Neill, H.S.C. (2014). Cosmochemical estimates of mantle composition. Treatise on geochemistry, 2nd Edition, 1-39.

Passchier, C.W., Trouw, R.A.J. (2005). Microtectonics, Springer, 366 pp.

Pavlova, G.G., Palessky, S.V., Borisenko, A.S., Vladimirov, A.G., Seifert, T., Phan, L.A. (2015). Indium in cassiterite and ores of tin deposits. *Ore Geology Reviews*, 66, 99-113.

Perini, G., Cebria, J.M., Lopez-Ruiz, J., Doblas, M. (2004). Carboniferous-Permian mafic magmatism in the Variscan belt of Spain and France: implications for mantle sources. In Permo-Carboniferous Magmatism and Rifting in Europe (eds. M. Wilson, E.R. Neumann, G.R. Davies, M.J. Timmerman, M. Heeremans, B.T. Larsen). *Geological Society of London, Special Publication*, 223, 415-438.

Pesquera, A., Torres-Ruiz, J., Gil-Crespo, P.P., Jiang, S.Y. (2005). Petrographic, chemical and B-isotopic insights into the origin of tourmaline-rich rocks and boron recycling in the Martinamor Antiform (Central Iberain Zone, Salamanca, Spain). *Journal of Petrology*, 46, 1013-1044.

Pettke, T., Diamond, L.W. (1995). Rb-Sr isotopic analysis of fluid inclusions in quartz: evaluation of bulk extraction procedures and geochronometer systematics using synthetic fluid inclusions. *Geochimica et Cosmochimica Acta*, 59, 4009-4027.

Pettke, T., Heinrich, C.A., Ciocan, A.C., Günther, D. (2000). Quadrupole mass spectrometry and optical emission spectroscopy: detection capabilities and representative sampling of short transient signals from laser-ablation. *Journal of Analytical Atomic Spectrometry*, 15, 1149-1155.

Pettke, T., Halter, W.E., Webster, J.D., Aigner-Torres, M., Heinrich, C.A. (2006). Accurate quantification of melt inclusion chemistry by LA-ICPMS: a comparison with EMP and SIMS and advantages□and possible limitations of these methods. *Lithos*, 78, 333-361.

Pettke, T., Oberli, F., Heinrich, C.A. (2010). The magma and metal source of giant porphyry-type ore deposits, based on lead isotope microanalysis of individual fluid inclusions. *Earth and Planetary Science Letters*, 296, 267-277.

Pettke, T., Oberli, F., Audétat, A., Wiechert, U., Harris, C.R., Heinrich, C.A. (2011).

Quantification of transient signals in multiple collector inductively coupled plasma mass spectrometry: accurate lead isotope ratio determination by laser ablation of individual fluid inclusions. *Journal of Analytical Atomic Spectrometry*, 26, 475-492.

Pettke, T., Oberli, F., Audétat, A., Guillong, M., Simon, A.C., Hanley, J.J., Klemm, L.M. (2012). Recent developments in element concentration and isotope ratio analysis of individual fluid inclusions by laser ablation single and multiple collector ICP-MS. *Ore Geology Reviews*, 244, 10-38.

Pfaff, K., Romer, R.L., Markl, G. (2009). U-Pb ages of ferberite, chalcedony, agate, 'U-mica' and pitchblende: constraints on the mineralization history of the Schwarzwald ore district. *European Journal of Mineralogy*, 21, 817-836.

Pichavant, M. (1987). Effects of B and H_2O on liquidus phase relations in the haplogranite system at 1 kbar. *American Mineralogist*, 72, 1056-1070.

Pichavant, M., Manning, D. (1984). Petrogenesis of tourmaline granites and topaze granites: the contribution of experimental data. *Physics of the Earth and Planetary Interiors*, 35, 31-50.

Pichavant, M., Boher, M., Stenger, J.F., Aïssa, M., Charoy, B. (1987). Relations de phase des granites de Beauvoir à 1 et 3 kbar, en condition de saturation en H_2O. In Géologie profonde de la France, Echassières : le forage scientifique. Une clé pour la compréhension des mécanismes magmatiques et hydrothermaux associés aux granites à métaux rares (eds. M. Cuney and A. Autran). *Géologie de la France*, 2-3, 77–85.

Pieczka, A. (2010). Primary Nb-Ta minerals in the Szklary pegmatite, Poland: New insights into controls of crystal chemistry and crystallization sequences. *American Mineralogist*, 95, 1478-1492.

Pin, C. (1979). Géochronologie U-Pb et microtectonique des séries métamorphiques antéstéphaniennes de l'Aubrac et de la région de Marvejols (Massif Central). Ph.D. thesis, Université de Montpellier, France, 205p.

Plimer, I.R. (1974). Pipe-like molybdenite-wolframite-bismuth deposits of wolfram camp, North Queensland, Australia. *Mineralium Deposita*, 9, 95-104.

Plimer, I.R., Lu, J., Kleeman, J.D. (1991). Trace and rare earth elements in cassiterite - sources of components for the tin deposits of the Mole Granite, Australia. *Mineralium Deposita*, 26, 267-274.

Pollard, P.J. (1995). A special issue devoted to the geology of rare metal deposits. Geology of rare metal deposits: an introduction and overview. *Economic Geology*, 90, 489-494.

Pollard, P.J., Pichavant, M., Charoy, B. (1987). Contrasting evolution of fluorine- and boron-

rich tin systems. *Mineralium Deposita*, 22, 315-321.

Polya, D.A. (1988). Compositional variation in wolframites from the Barroca Grande mine, Portugal: evidence for fault-controlled ore formation. *Mineralogical Magazine*, 52, 497-503.

Polya, D.A. (1989). Chemistry of the main-stage ore-forming fluids of the Panasqueira W-Cu (Ag)-Sn deposit, Portugal; implications for models of ore genesis. *Economic Geology*, 84, 1134-1152.

Poujol, M., Pitra, P., Van den Driessche, J., Tartèse, R., Ruffet, G., Paquette, J. L., Poilvet, J. C. (2016). Two-stage partial melting during the Variscan extensional tectonics (Montagne Noire, France). *International Journal of Earth Sciences*, 1-24.

Praeg, D. (2004). Diachronous Variscan late-orogenic collapse as a response to multiple detachments: a view from the internides in France to the foreland in the Irish Sea. In Permo-Carboniferous Magmatism and Rifting in Europe (eds. M. Wilson, E.R. Neumann, G.R. Davies, M.J. Timmerman, M. Heeremans and B.T. Larsen). *Geological Society of London, Special Publication*, 223, 89-138.

R

Raimbault, L. (1984). Géologie, pétrographie et géochimie des granites et minéralisations associées de la région de Meymac (Haute Corrèze, France). Ph.D. thesis, Ecole Nationale Supérieure des Mines de Paris, France, 482p.

Raimbault, L. (1985). Utilisation des spectres de terres rares des minéraux hydrothermaux (apatite, fluorine, scheelite, wolframite) pour la caractérisation des fluides minéralisateurs et l'identification des magmas sources et des processus évolutifs. *Bulletin de Minéralogie*, 108, 737-744.

Raimbault, L. (1998). Composition of complex lepidolite-type granitic pegmatites and of constituent columbite-tantalite, Chédeville, Massif Central, France. *The Canadian Mineralogist*, 36, 563-583.

Raimbault, L., Burnol, L. (1998). The Richemont rhyolite dyke, Massif Central, France: a subvolcanic equivalent of rare-metal granites. *The Canadian Mineralogist*, 36, 265-282.

Raimbault, L., Baumer, A., Dubru, M., Benkerrou, C., Croze, V., Zahm, A. (1993). REE fractionation between scheelite and apatite in hydrothermal conditions. *American Mineralogist*, 78, 1275-1285.

Raimbault, L., Cuney, M., Azencott, C., Duthou, J.L., Joron, J.L. (1995). Geochemical evidence for a multistage magmatic genesis of Ta-Sn-Li mineralization in the granite at

Beauvoir, French Massif Central. *Economic Geology*, 90, 548-576.

Ramboz, C. (1980). Géochimie et étude des phases fluides de gisements et indices d'étain-tungstène du sud du Massif Central (France). Ph.D. thesis, Institut National Polytechnique de Lorraine, France, 278p.

Ramboz, C., Schnapper, D., Dubessy, J. (1985). The P-V-T-X-fO_2 evolution of H_2O-CO_2-CH_4-bearing fluid in a wolframite vein: Reconstruction from fluid inclusion studies. *Geochimica et Cosmochimica Acta*, 49, 205-219.

Rapp, J.F., Klemme, S., Butler, I.B., Harley, S.L. (2010). Extremely high solubility of rutile in chloride and fluoride-bearing metamorphic fluids: an experimental investigation. *Geology*, 38, 323-326.

Rauchenstein-Martinek, K., Wagner, T., Wälle, M., Heinrich, C.A. (2014). Gold concentrations in metamorphic fluids: a LA-ICPMS study of fluid inclusions from the Alpine orogenic belt. *Chemical Geology,* 385, 70-83.

Ren, S.K., Walshe, J.L., Paterson, R.G., Both, R.A., Andrew, A. (1995). Magmatic and hydrothermal history of the porphyry-style deposits of the Ardlethan tin field, New South Wales, Australia. *Economic Geology*, 90, 1620-1645.

René, M., Škoda, R. (2011). Nb-Ta-Ti oxides fractionation in rare-metal granites: Krásno-Horní Slavkov ore district, Czech Republic. *Mineralogy and Petrology*, 103, 37-48.

Renne, P.R., Norman, E.B. (2001). Determination of the half-life of ^{37}Ar by mass spectrometry. *Physical Review C*, 63 (047302).

Renne, P.R., Swisher, C.C., Deino, A.L., Karner, D.B., Owens, T.L., DePaolo, D.J. (1998). Intercalibration of standards, absolute ages and uncertainties in $^{40}Ar/^{39}Ar$ dating. *Chemical Geology*, 145, 117-152.

Renne, P.R., Cassata, W.S., Morgan, L.E. (2009). The isotopic composition of atmospheric argon and $^{40}Ar/^{39}Ar$ geochronology: time for a change? *Quaternary Geochronology*, 4, 288-298.

Resano, M., McIntosh, K.S., Vanhaecke, F. (2012). Laser ablation-inductively coupled plasma-mass spectrometry using a double-focusing sector field mass spectrometer of Mattauch-Herzog geometry and an array detector for the determination of platinum group metals and gold in NiS buttons obtained by fire assay of platiniferous ores. *Journal of Analytical Atomic Spectrometry*, 27, 165-173.

Respaut, J.P. (1984). Géochronologie et géochimie isotopique U-Pb de la minéralisation uranifère de la mine des Pierres Plantées (Lozère) et de son encaissant: le massif granitique de la Margeride. Ph.D. thesis, Université de Montpellier, France, 122p.

Respaut, J.P., Cathelineau, M., Lancelot, J.R. (1991). Multistage evolution of the Pierres-Plantées uranium ore deposit (Margeride, France): evidence from mineralogy and U-Pb systematics. *European Journal of Mineralogy*, 3, 85-103.

Ribeiro da Costa, I., Mourão, C., Récio, C., Guimarães, F., Antunes, I.M., Farinha Ramos, J., Barriga, F.J.A.S., Palmer, M.R., Milton, J.A. (2014). Tourmaline occurrences within the Penamacor-Monsanto granitic pluton and host-rocks (Central Portugal): genetic implications of crystal-chemical and isotopic features. *Contributions to Mineralogy and Petrology*, 167, 1-23.

Rice, C.M., Darke, K.E., Still, J.W., Lachowski, E.E. (1998). Tungsten-bearing rutile from the Kori Kollo gold mine, Bolivia. *Mineralogical Magazine*, 62, 421-429.

Richard, A., Rozsypal, C., Mercadier, J., Banks, D.A., Cuney, M., Boiron, M.C., Cathelineau, M. (2012). Giant uranium deposits formed from exceptionally uranium-rich acidic brines. *Nature Geoscience*, 5, 142-146.

Rickers, K., Thomas, R., Heinrich, W. (2006). The behavior of trace elements during the chemical evolution of the H_2O-, B-, and F-rich granite–pegmatite–hydrothermal system at Ehrenfriedersdorf, Germany: a SXRF study of melt and fluid inclusions. *Mineralium Deposita*, 41, 229-245.

Roddick, J.C. (1983). High precision intercalibration of ^{40}Ar-^{39}Ar standards. *Geochimica et Cosmochimica Acta*, 47, 887-898.

Roedder, E. (1984). Fluid inclusions. In Ribbe, P.H. (Ed.), *Reviews in Mineralogy. Mineralogical Society of America,* vol. 12, 646 pp.

Roig, J.Y., Faure, M., Maluski, H. (2002). Superimposed tectonic and hydrothermal events during the late- orogenic extension in the Western French Massif Central: a structural and $^{40}Ar/^{39}Ar$ study. *Terra Nova*, 14, 25-32.

Rolin, P., Marquer, D., Cartannaz, C., Rossi, P. (2014). Carboniferous magmatism related to progressive pull-apart opening in the western French Massif Central. *Bulletin de la Société Géologique de France*, 185, 171-189.

Romer, R.L. (2003). Alpha-recoil in U-Pb geochronology: effective sample size matters. *Contributions to Mineralogy and Petrology*, 145, 481-491.

Romer, R.L., Wright, J.E. (1992). U-Pb dating of columbites: a geochronological tool to date magmatism and ore deposits. *Geochimica et Cosmochimica Acta*, 56, 2137-2142.

Romer, R.L., Lehmann, B. (1995). U-Pb columbite age of Neoproterozoic Ta-Nb mineralization in Burundi. *Economic Geology*, 90, 2303-2309.

Romer, R.L., Rötzler, J. (2003). Effect of metamorphic reaction history on the U-Pb dating of

titanite. In Geochronology: Linking the isotopic record with petrology and textures (eds. D. Vance, A. Müller and I. Villa). *Geological Society of London, Special Publication*, 220, 147-158.

Romer, R.L., Lüders, V. (2006). Direct dating of hydrothermal W mineralization: U-Pb age for hübnerite ($MnWO_4$), Sweet Home Mine, Colorado. *Geochimica et Cosmochimica Acta*, 70, 4725-4733.

Romer, R.L., Rötzler, J. (2011). The role of element distribution for the isotopic dating of metamorphic minerals. *European Journal of Mineralogy*, 23, 17-33.

Romer, R.L., Kroner, U. (2015). Sediment and weathering control on the distribution of Paleozoic magmatic tin-tungsten mineralization. *Mineralium Deposita*, 50, 327-338.

Romer, R.L., Kroner, U. (2016). Phanerozoic tin and tungsten mineralization – tectonic controls on the distribution of enriched protoliths and heat sources for crustal melting. *Gondwana Research*, 31, 60-95.

Romer, R.L., Heinrich, W., Schröder-Smeibidl, B., Meixner, A., Fischer, C.O., Schulz, C. (2005). Elemental dispersion and stable isotope fractionation during reactive fluid-flow and fluid immiscibility in the Bufa del Diente aureole, NE-Mexico: Evidence from radiographies and Li, B, Sr, Nd, and Pb isotope systematics. *Contributions to Mineralogy and Petrology*, 149, 400-429.

Romer, R.L., Thomas, R., Stein, H.J., Rhede, D. (2007). Dating multiply overprinted Sn-mineralized granites-examples from the Erzgebirge, Germany. *Mineralium Deposita*, 42, 337-359.

Rossi, P., Cocherie, A., Fanning, C.M., Deloule, E. (2006). Variscan to eo-Alpine events recorded in European lower-crust zircons sampled from the French Massif Central and Corsica, France. *Lithos*, 87, 235-260.

Rudnick, R.L., Gao, S. (2003). Composition of the Continental Crust. In Treatise on Geochemistry Vol. 3 (Eds. Rudnick, R.L.). Elsevier, Amsterdam, pp 1–64.

Ruffet, G., Innocent, C., Michard, A., Féraud, G., Beauvais, A., Nahon, D., Hamelin, B. (1996). A geochronological $^{40}Ar/^{39}Ar$ and $^{87}Rb/^{86}Sr$ study of K–Mn oxides from the weathering sequence of Azul, Brazil. *Geochimica et Cosmochimica Acta*, 60, 2219–2232.

S

Sakharkar, M.V., Sharma, J., Ray, R.K., Biswas, A.K. (1997). Characterization of synthesized wolframite minerals and their leach residues. *Hydrometallurgy*, 44, 65-69.

Salvi, S., Williams-Jones, A.E. (2005). Alkaline Granite-Syenite Deposits. In Rare-element geochemistry and mineral deposits (Linnen, R.L. And Samson, I.M. Eds). *Geological Association of Canada, Short Course Notes,* 17, 315-341.

Salvi, S., Williams-Jones, A.E. (2006). Alteration, HFSE mineralisation and hydrocarbon formation in peralkaline igneous systems: Insights from the Strange Lake Pluton, Canada. *Lithos*, 91, 19-34.

Samama, J-C. (1971). Paléoplacers à tungstène-étain dans les séries métamorphiques du Vivarais oriental. *Comptes Rendus de l'Académie des Sciences*, Paris, 272, 516-518.

Sanchez Bellon, A., Mosser, C., Cardona, J.P., Roquin, C., Pardo, E.S. (1997). Contribution of multivariate geochemical analysis and mineralogical study in the characterization of sediments: the Miocene-Pliocene boundary in the Sorbas Basin (SE Spain). *Clay Minerals*, 32, 517-530.

Scaillet, S., Cheilletz, A., Cuney, M., Farrar, E., Archibald D.A. (1996). Cooling pattern and mineralization history of the Saint Sylvestre and western Marche leucogranite pluton, French Massif Central: I. $^{40}Ar/^{39}Ar$ isotopic constraints. *Geochimica et Cosmochimica Acta*, 60, 4653-4671.

Scambelluri, M., Philippot, P. (2001). Deep fluids in subduction zones. *Lithos*, 55, 213-227.

Schatz, O.J., Dolejš, D., Stix, J., Williams-Jones, A.E., Layne, G.D. (2004). Partitioning of boron among melt, brine and vapour in the system haplogranite-H_2O-NaCl at 800°C and 100 MPa. *Chemical Geology*, 210, 135-147.

Schilling, G.D., Andrade, F.J., Barnes, J.H., Sperline, R.P., Denton, M.B., Barinaga, C.J., Koppenaal, D.W. and Hieftje, G.M. (2007). Continuous simultaneous detection in mass spectrometry. *Analytical Chemistry*, 79, 7662-7668.

Schlegel, T.U., Wälle, M., Steele-MacInnis, M. and Heinrich, C.A. (2012). Accurate and precise quantification of major and trace element compositions of calcic-sodic fluid inclusions by combined microthermometry and LA-ICPMS analysis. *Chemical Geology*, 334, 144-153.

Schmid, R., Romer, R.L., Franz, L., Oberhänsli, R., Martinotti, G. (2003). Basement-cover sequences within the UHP unit of the Dabie Shan. *Journal of Metamorphic Geology*, 21, 531–538.

Schulmann, K., Catalán, J.R.M., Lardeaux, J.M., Janoušek, V., Oggiano, G. (2014). The Variscan Orogeny: extent, timescale and the formation of the European Crust. *Geological Society of London, Special Publications*, 405, 1-6.

Seedorff, E., Einaudi, M. (2004). Henderson Porphyry molydenum system, Colorado: II.

Decoupling of introduction and deposition of metals during geochemical evolution of hydrothermal fluids. *Economic Geology*, 99, 39–72.

Severac, J.L. (1982). Etude géologique, minéralogique et géochimique des minéralisations en tungstène de Fumade (Tarn). Ph.D. thesis, Université Paul Sabatier, Toulouse, France, 144p.

Shannon, R.D. (1976). Revised effective ionic radii and systematic studies of interatomic distances in halides and chalcogenides. *Acta Crystallographica*, 32, 751–767.

Sharygin, V.V., Sobolev, N.V., Channer D.M.DeR. (2009). Oscillatory-zoned crystals of pyrochlore-group minerals from the Guaniamo kimberlites, Venezuela. *Lithos*, 1125, 976-985.

Shaw, A., Downes, H., Thirlwall, M.F. (1993). The quartz-diorites of Limousin: elemental and isotopic evidence for Devono-Carboniferous subduction in the Hercynian belt of the French Massif Central. *Chemical Geology*, 107, 1-18.

Shepherd, T.J., Chenery, S.R. (1995). Laser ablation ICP-MS elemental analysis of individual fluid inclusions: an evaluation study. *Geochimica et Cosmochimica Acta*, 59, 3997-4007.

Shepherd, T.J., Darbyshire, D.P.F. (1981). Fluid inclusion Rb-Sr isochrons for dating mineral deposits. *Nature*, 290, 578-579.

Sillitoe, R. (1985). Ore-related breccias in volcanoplutonic arcs. *Economic Geology*, 80, 1467-1514.

Sillitoe, R.H., Sawkins, F.J. (1971). Geologic, mineralogic and fluid inclusion studies relating to the origin of copper-bearing tourmaline breccia pipes, Chile. *Economic Geology*, 66, 1028-1041.

Simmons, S.F., Simpson, M.P., Reynolds, T.J. (2007). The significance of clathrates in fluid inclusions and the evidence for overpressuring in the Broadlands-Ohaaki geothermal system, New Zealand. *Economic Geology*, 102, 127-135.

Sinclair, A.J., Macquar, J.C., Rouvier, H. (1993). Re-evaluation of lead isotopic data, southern Massif Central, France. *Mineralium Deposita*, 28, 122-128.

Sinclair, W.D. (2007). Porphyry deposits. In Mineral Deposits of Canada: A Synthesis of Major Deposit-Types, District Metallogeny, the Evolution of Geological Provinces, and Exploration Methods (ed. W. D. Goodfellow). *Geological Association of Canada, Mineral Deposits Division, Special Publication*, No. 5, 223-243.

Skewes, M.A., Holmgren, C., Stern, C.R. (2003). The Donoso copper-rich, tourmaline-bearing breccia pipe in central Chile: petrologic, fluid inclusion and stable isotope

evidence for an origin from magmatic fluids. *Mineralium Deposita*, 38, 2-21.

Škoda, R., Novák, M. (2007). Y,REE,Nb,Ta,Ti-oxide (AB_2O_6) minerals from REL-REE euxenite-subtype pegmatites of the Třebíč Pluton, Czech Republic; substitutions and fractionation trends. *Lithos*, 95, 43-57.

Slack, J.F., Trumbull, R. (2011). Tourmaline as a recorder of ore-forming processes. *Elements*, 7, 321-326.

Smith, M.P., Yardley, B.W.D. (1996). The boron isotopic composition of tourmaline as a guide to fluid processes in the southwestern England orefield: an ion microprobe study. *Geochimica et Cosmochimica Acta*, 60, 1415-1427.

Smith, M.P., Savary, V., Yardley, B.W.D., Valley, J.W., Royer, J.J., Dubois, M. (1998). The evolution of the deep flow regime at Soultz-sous-Forêts, Rhine Graben, eastern France: evidence from a composite quartz vein. *Journal of Geophysical Research*, 103, 27, 223-237.

Smith, S.R., Foster, G.L., Romer, R.L., Tindle, A.G., Kelley, S.P., Noble, S.R., Horstwood, M., Breaks, F.W. (2004). U–Pb columbite–tantalite chronology of rare-element pegmatites using TIMS and Laser Ablation–Multi Collector–ICP–MS. *Contributions to Mineralogy and Petrology*, 147, 549–564.

So, C.S., Shelton, K.L., Chi, S.J., Yun, S.T. (1991). Geochemical studies of the Gyeongchang W-Mo Mine, Republic of Korea; progressive meteoric water inundation of a magmatic hydrothermal system. *Economic Geology*, 86, 750-767.

Solomovich, L.I., Trifonov, B.A., Sabelnikov, S.E. (2012). Geology and mineralization of the Uchkoshkon tin deposit associated with a breccia pipe, Eastern Kyrgyzstan. *Ore Geology Reviews*, 44, 59-69.

Somarin, A.K., Ashley, P. (2004). Hydrothermal alteration and mineralisation of the Glen Eden Mo-W-Sn deposit: a leucogranite-related hydrothermal system, Southern New England Orogen, NSW, Australia. *Mineralium Deposita*, 39, 282-300.

Soufi, M. (1988). Etude des magmatismes leucogranitique et ongonitique de Blond (Haut Limousin, Massif Central Français). Relations avec une mise en place syntectonique du massif granitique. Ph.D. thesis, Université de Nancy, France, 304p.

Souhassou, M. (2001). Les circulations fluides dans le batî Sud-Limousin à la fin du Carbonifère : Relations entre les systèmes hydrothermaux de la faille d'Argentat et Saint-Yrieix : conséquences pour le dépôt de l'or. Ph.D. thesis, Institut National Polytechnique de Lorraine, 243p.

Spell, T.L., McDougall, I. (2003). Characterization and calibration of $^{40}Ar/^{39}Ar$ dating

standards. *Chemical Geology*, 198, 189-211.

Sperlich, R., Giere, R., Frey, M. (1996). Evolution of compositional polarity and zoning in tourmaline during prograde metamorphism of sedimentary rocks in the Swiss Central Alps. *American Mineralogist*, 81, 1222–1236.

Spier, C.A., Vasconcelos, P.M., Oliveira, S.M.B. (2006). $^{40}Ar/^{39}Ar$ geochronological contraints on the evolution of lateritic iron deposits in the Quadrilatero Ferrifero, Minas Gerais, Brazil. *Chemical Geology*, 234, 79–104.

Steiger, R.H., Jäger, E. (1977) Subcommission on geochronology: convention on the use of decay constants in geo- and cosmochronology. *Earth and Planetary Science Letters*, 36, 359-362.

Stein, H.J., Sundblad, K., Markey, R.J., Motuza, G. (1998). Re–Os ages for Archean molybdenite and pyrite, Kuittila-Kivisuo, Finland, and Proterozoic molybdenite, Kabeliai, Lithuania: testing the chronometer in a metamorphic and metasomatic setting. *Mineralium Deposita*, 33, 329–345.

Stein, H.J., Morgan, J.W., Scherstén, A. (2000). Re-Os dating of low-level highly radiogenic (LLHR) sulfides: the Harnäs gold deposit, southwest Sweden, records continental-scale tectonic events. *Economic Geology*, 95, 1657-1671.

Štemprok, M., Pivec, E., Landgrová, A. (2005). The petrogenesis of a wolframite-bearing greisen in the Vykmanov granite stock, Western Krušné hory pluton (Czech Republic). *Bulletin of Geosciences*, 80, 163-184.

Stipp, M., Stuènitz, H., Heilbronner, R., Schmid, S. M. (2002). The eastern Tonale fault zone: a 'natural laboratory' for crystal plastic deformation of quartz over a temperature range from 250 to 700°C. *Journal of Structural Geology*, 24, 1861-1884.

Stoffell, B., Appold, M.S., Wilkinson, J.J., McClean, N.A., Jeffries, T.E. (2008). Geochemistry and Evolution of Mississippi Valley-Type Mineralizing Brines from the Tri-State and Northern Arkansas Districts Determined by LA-ICP-MS Microanalysis of Fluid Inclusions. *Economic Geology*, 103, 1411–1435.

Sturgeon, R.E., Lam, J.W.H., Saint, A. (2000). Analytical characteristics of a commercial ICP orthogonal acceleration time-of-flight mass spectrometer (ICP-TOFMS). *Journal of Analytical Atomic Spectrometry*, 15, 607-616.

Stussi, J.M. (1989). Granitoid chemistry and associated mineralization in the French Variscan. *Economic Geology*, 84, 1363-1381.

Swart, P.K., Moore, F. (1982). The occurrence of uranium in association with cassiterite, wolframite, and sulphide mineralization in South-West England. *Mineralogical*

Magazine, 46, 211-215.

Sylvester, P.J., Ghaderi, M. (1997). Trace element analysis of scheelite by excimer laser ablation-inductively coupled plasma-mass spectrometry (ELA-ICPMS) using a synthetic silicate glass standard. *Chemical Geology*, 141, 49-65.

Sylvester, P.J. (2008). Matrix effects in laser ablation-ICPMS. In Laser Ablation ICPMS in the Earth Sciences: Current Practices and Outstanding Issues (Sylvester, P. Ed.). *Mineralogical Association of Canada, Short Course Series*, Vol. 40, 67-78.

T

Talbot, J.Y., Martelet, G., Courrioux, G., Chen, Y., Faure, M. (2004). Emplacement in an extensional setting of the Mont Lozère–Borne granitic complex (SE France) inferred from comprehensive AMS, structural and gravity studies. *Journal of Structural Geology*, 26, 11-28.

Tanner, M., Günther, D. (2008). A new ICP-TOFMS. Measurement and readout of mass spectra with 30 μs time resolution, applied to in-torch LA-ICP-MS. *Analytical and Bioanalytical Chemistry*, 391, 1211-1220.

Tanner, M., Günther, D. (2009). Short transient signals, a challenge for inductively coupled plasma mass spectrometry, a review. *Analytica Chimica Acta*, 633, 19–28.

Tartèse, R., Ruffet, G., Poujol, M., Boulvais, P., Ireland, T.R. (2011). Simultaneous resetting of the muscovite K-Ar and monazite U-Pb geochronometers: a story of fluids. *Terra Nova*, 23, 390-398.

Taylor, R.P., Ikingura, J.R., Fallick, A.E., Huang, Y., Watkinson, D.H. (1992). Stable isotope compositions of tourmalines from granites and related hydrothermal rocks of the Karagwe-Ankolean belt, northwest Tanzania. *Chemical Geology*, 94, 215-227.

Tessier, B. (1989). Mise en place, pétrographie, géochimie et minéralogie des granites associés aux skarns minéralisés en tungstène de Fumade (Tarn, France). Ph.D. thesis, Université Pierre et Marie Curie, Paris VI, France, 375p.

Thierry, J., Marignac, C., Ledru, P., Reboulet, S., Dagain, J., Naud, G., Roger, J., Laumonier, B., Vernhet, Y. (2014). Evolution géologique de l'Ardèche cristalline, Notice explicative de la feuille Privas à 1/50 000, BRGM Edition, 99-131.

Thomas, R., Förster, H-J., Heinrich, W. (2003). The behaviour of boron in a peraluminous granite-pegmatite system and associated hydrothermal solutions: a melt and fluid-inclusion study. *Contributions to Mineralogy and Petrology*, 144, 457-472.

Thomas, R., Förster, H. J., Rickers, K., Webster, J. D. (2005). Formation of extremely F-rich

hydrous melt fractions and hydrothermal fluids during differentiation of highly evolved tin-granite magmas: a melt/fluid-inclusion study. *Contributions to Mineralogy and Petrology*, 148, 582-601.

Timofeev, A., Migdisov, A.A., Williams-Jones, A.E. (2015). An experimental study of the solubility and speciation of niobium in fluoride-bearing aqueous solutions at elevated temperature. *Geochimica et Cosmochimica Acta*, 158, 103-111.

Tindle, A.G., Webb, P.C. (1989). Niobian wolframite from Glen Gairn in the Eastern Highlands of Scotland: A microprobe investigation. *Geochimica et Cosmochimica Acta*, 53, 1921-1935.

Tomašić, N., Gajović, A., Bermanec, V., Rajić, M. (2004). Recrystallization of metamict Nb-Ta-Ti-REE complex oxides: a coupled X-ray-diffraction and Raman spectroscopy. Study of aeschynite-(Y) and polycrase-(Y). *The Canadian Mineralogist*, 42, 1847-1857.

Tornos, F., Casquet, C., Relvas, J.M.R.S., Barriga, F.J.A.S., Sáez, R. (2002). The relationship between ore deposits and oblique tectonics: the SW Iberian Variscan Belt. In The Timing and Location of Major Ore Deposits in an Evolving Orogen (eds. D. J. Blundell, F. Neubauer and A. von Quadt, A). *Geological Society of London, Special Publications*, 204, 179-198.

Toteu, F. (1981). Utilisation des analyses chimico-minéralogiques et microstructurales dans la reconstitution des événements tectono-métamorphiques des formations polycycliques. Exemple du Vivarais cristallin, Ardèche, France. Ph.D. thesis, Institut National Polytechnique de Lorraine, Nancy, 177p.

Toteu, F., Macaudière, J. (1984). Complex synkinematic and postkinematic garnet porphyroblast growth in polymetamorphic rocks. *Journal of Structural Geology*, 6, 669-677.

Touret, J.L.R. (2001). Fluids in metamorphic rocks. *Lithos*, 55, 1-25.

Trumbull, R.B., Slack, J.F., Krienitz, M.S., Belkin, H.E., Wiedenbeck, M. (2011). Fluid sources and metallogenesis in the Blackbird Co–Cu–Au–Bi–Y–REE district, Idaho, USA: insights from major-element and boron isotopic compositions of tourmaline. *The Canadian Mineralogist*, 49, 225-244.

Turpin, L., Leroy, J.L., Sheppard, S.M. (1990). Isotopic systematics (O, H, C, Sr, Nd) of superimposed barren and U-bearing hydrothermal systems in a Hercynian granite, Massif Central, France. *Chemical Geology*, 88, 85-98.

U

Ulrich, T., Günther, D., Heinrich, C.A. (1999). Gold concentrations of magmatic brines and the metal budget of porphyry copper deposits. *Nature*, 399, 676-679.

V

Vallance, J., Cathelineau, M., Marignac, C., Boiron, M.C., Fourcade, S., Martineau, F., Fabre, C. (2001). Microfracturing and fluid mixing in granites: W-(Sn) ore deposition at Vaulry (NW French Massif Central). *Tectonophysics*, 336, 43-61.

Van den Bleeken, G., Corteel, C., Van den haute, P. (2007). Epigenetic to low-grade tourmaline in the Gdoumont metaconglomerates (Belgium): A sensitive probe of its chemical environment of formation. *Lithos*, 95, 165-176.

van Hinsberg, V.J., Schumacher, J.C. (2011). Tourmaline as a petrogenetic indicator mineral in the Haut-Allier metamorphic suite, Massif Central, France. *The Canadian Mineralogist*, 49, 177-194.

van Hinsberg, V.J., Henry, D.J., Marschall, H.R. (2011). Tourmaline: an ideal indicator of its host environment. *The Canadian Mineralogist*, 49, 1-16.

Van Lichtervelde, M., Salvi, S., Beziat, D., Linnen, R.L. (2007). Textural features and chemical evolution in tantalum oxides: magmatic versus hydrothermal origins for Ta mineralization in the Tanco Lower pegmatite, Manitoba, Canada. *Economic Geology*, 102, 257-276.

Vasconcelos, P.M., Becker, T.A., Renne, P.R., Brimhall, G.H. (1992). Age and duration of weathering by ^{40}K–^{40}Ar and $^{40}Ar/^{39}Ar$ analysis of potassium-manganese oxides. *Science*, 258, 451–455.

Veksler, I.V. (2004). Liquid immiscibility and its role at the magmatic–hydrothermal transition: a summary of experimental studies. *Chemical Geology*, 210, 7-31.

Veksler, I.V. (2005). Element enrichment and fractionation by magmatic aqueous fluids: Experimental constraints on melt-fluid immiscibility and element partitioning. In Rare-Element Geochemistry and Mineral Deposits (eds. R.L. Linnen and I.M. Samson). *Geological Association of Canada, Short Course Notes*, 17, 69-85.

Velasco, F., Pesquera, A., Herrero, J.M. (1996). Lead isotope study of Zn-Pb ore deposits associated with the Basque-Cantabrian basin and Paleozoic basement, Northern Spain. *Mineralium Deposita*, 31, 84-92.

Vermeesch, P. (2012). On the visualisation of detrital age distributions. *Chemical Geology*, 312, 190-194.

Vindel, E., Lopez, J.A., Boiron, M.C., Cathelineau, M., Prieto, A.C. (1995). P-V-T-X-fO_2

evolution from wolframite to sulphide depositional stages in intragranitic W-veins. An example from the Spanish Central System. *European Journal of Mineralogy*, 7, 675-688.

Von Goerne, G., Franz, G., Robert, J.L. (1999). Upper thermal stability of tourmaline + quartz in the system $MgO–Al_2O_3–SiO_2–B_2O_3–H_2O$ and $Na_2O–MgO–Al_2O_3–SiO_2–B_2O_3–H_2O–HCl$ in hydrothermal solutions and siliceous melts. *The Canadian Mineralogist*, 37, 1025-1039.

Von Goerne, G., Franz, G., Heinrich, W. (2001). Synthesis of tourmaline solid solutions in the system $Na_2O–MgO–Al_2O_3–SiO_2–B_2O_3–H_2O–HCl$ and the distribution of Na between tourmaline and fluid at 300 to 700°C and 200 MPa. *Contributions to Mineralogy and Petrology*, 141, 160-173.

von Raumer, J.F., Stampfi, G.M., Bussy, F. (2003). Gondwana-derived microcontinents – the constituents of the Variscan and Alpine collisional orogens. *Tectonophysics*, 365, 7-22.

von Seckendorff, V., Timmerman, M.J., Kramer, W., Wrobel, P. (2004). New $^{40}Ar/^{39}Ar$ ages and geochemistry of late Carboniferous to early Permian lamprophyres and related volcanic rocks in the Saxothuringian Zone of the Variscan Orogen (Germany). In Permo-Carboniferous Rifting and Magmatism in Europe (eds. M. Wilson, E.R. Neumann, G.R. Davies, M.J. Timmerman, M. Heeremans, B.T. Larsen). *Geological Society of London, Special Publications*, 223, 335-359.

W

Wälle, M., Heinrich, C.A. (2014). Fluid inclusion measurements by laser ablation sector-field ICP-MS. *Journal of Analytical Atomic Spectrometry*, 29, 1052-1057.

Wang, H.A.O., Grolimund, D., Giesen, C., Borca, C.N., Shaw-Stewart, J.R.H., Bodenmiller, B., Günther, D. (2013). Fast chemical imaging at high spatial resolution by laser ablation inductively coupled plasma mass spectrometry. *Analytical Chemistry*, 85, 10,107–10,116.

Wang, R.C., Fontan, F., Monchoux, P. (1992). Minéraux disséminés comme indicateurs du caractère pegmatitique du granite de Beauvoir, Massif d'Echassières, Allier, France. *The Canadian Mineralogist*, 30, 763-770.

Wang, R.C., Fontan, F., Xu, S.J., Chen, X.M., Monchoux, P. (1997). The association of columbite, tantalite and tapiolite in the Suzhou granite, China. *The Canadian Mineralogist*, 35, 699-706.

Watson, E.B., Wark, D.A., Thomas, J.B. (2006). Crystallization thermometers for zircon and

rutile. *Contributions to Mineralogy and Petrology*, 151, 413-433.

Weber, C., Barbey, P. (1986). The role of water, mixing processes and metamorphic fabric in the genesis of the Baume migmatites (Ardèche, France). *Contributions to Mineralogy and Petrology*, 92, 481-491.

Webster, J.D., Holloway, J.R., Hervig, R.L. (1989). Partitioning of lithophile trace elements between H_2O and H_2O+CO_2 fluids and topaz rhyolite melt. *Economic Geology*, 84, 116-134.

Webster, J., Thomas, R., Förster, H.J., Seltmann, R., Tappen, C. (2004). Geochemical evolution of halogen-enriched granite magmas and mineralizing fluids of the Zinnwald tin-tungsten mining district, Erzgebirge, Germany. *Mineralium Deposita*, 39, 452-472.

Weisbrod A., Samama J.C., Elmi S., Berger E., Feys R. (1974). Carte géologique à 1/50 000 de Largentière (864). BRGM Editions, Orléans.

Weisbrod, A. (1970). Pétrologie du socle métamorphique des Cévennes Médianes (Massif Central Français). Reconstitution sédimentologique et approche thermodynamique du métamorphisme. Ph.D. thesis, Université de Nancy, 4 vol., 530p.

Weisbrod, A. (1987). Boron content of hydrothermal solutions and tourmaline solubility. *Terra Cognita*, 7, 408-409.

Weisbrod, A. (1988). Caractères généraux des phases fluides dans les indices et gisements de tungstène et d'étain. In Gisements métallifères dans leur contexte géologique (Johan, Z. and Ohnenstetter, D. eds.), Doc. BRGM, 158, 9-14.

Weisbrod, A., Pichavant, M., Marignac, C., Macaudière, J., Leroy, J. (1980). Relations structurales et chronologiques entre le magmatisme basique, les granitisations et l'évolution tectonométamorphique tardi-hercynienne dans les Cévennes médianes, Massif central français. *Comptes Rendus de l'Académie des Sciences*, Paris, 291, 665-668.

Weppe, M. (1951). Contribution à l'étude des gîtes de tungstène français : Puy-les-Vignes (Haute Vienne), La Châtaigneraie (Cantal). Revue de Géologie appliquée et de Prospection minière, Société d'Impressions Typographiques, Nancy, 210p.

Weppe, M. (1958). Contribution à la géologie minière et à la minéralogie minière. Les gisements de wolfram de Leucamp, Puy-les-Vignes, Montbelleux. Société d'Impressions Typographiques, Nancy, 196p.

Wilkinson, J.J., Stoffell, B., Wilkinson, C.C., Jeffries, T.E., Appold, M.S. (2009). Anomalously metal-rich fluids form hydrothermal ore deposits. *Science*, 323, 764-767.

Williamson, B.J., Spratt, J., Adams, J.T., Tindle, A.G., Stanley, C.J. (2000). Geochemical

constraints from zoned hydrothermal tourmalines on fluid evolution and Sn mineralization: an example from fault breccias at Roche, SW England. *Journal of Petrology*, 41, 1439-1453.

Williamson, B.J., Müller, A., Shail, R.K. (2010). Source and partitioning of B and Sn in the Cornubian batholith of southwest England. *Ore Geology Reviews*, 38, 1-8.

Wilson, M., Neumann, E.R., Davies, G.R., Timmerman, M.J., Heeremans, M., Larsen, B.T. (2004). Permo-Carboniferous magmatism and rifting in Europe: introduction. In Permo-Carboniferous Magmatism and Rifting in Europe (eds. M. Wilson, E. R. Neumann, G. R. Davies, M. J. Timmerman, M. Heeremans and B. T. Larsen). *Geological Society of London, Special Publications*, 223, 1-10.

Wolf, M.B., London, D. (1997). Boron in granitic magmas: stability of tourmaline in equilibrium with biotite and cordierite. *Contributions to Mineralogy and Petrology*, 130, 12–30.

Wong, L., Davis, D.W., Krogh, T.E., Robert, F. (1991). U-Pb zircon and rutile chronology of Archean greenstone formation and gold mineralization in the Val d'Or region, Quebec. *Earth and Planetary Science Letters*, 104, 325-336.

Wood, S.A., Samson, I.M. (2000). The hydrothermal geochemistry of tungsten in granitoid environments: I. Relative solubilities of ferberite and scheelite as a function of T, P, pH, and mNaCl. *Economic Geology*, 95, 143-182.

Wunder, B., Meixner, A., Romer, R.L., Wirth, R., Heinrich, W. (2005). The geochemical cycle of boron: constraints from boron isotope partitioning experiments between mica and fluid. *Lithos*, 84, 206-216.

Y

Yang, K., Bodnar, R.J. (2004). Orthomagmatic origin for the Ilkwang Cu–W breccia-pipe deposit, southeastern Kyongsang Basin, South Korea. *Journal of Asian Earth Sciences*, 24, 259-270.

Yardley, B.W., Bodnar, R.J. (2014). Fluids in the continental crust. *Geochemical Perspectives*, 3, 1-123.

Yuan, S.D., Peng, J.T., Hu, R.Z., Li, H.M., Shen, N.P., Zhang, D.L. (2008). A precise U–Pb age on cassiterite from the Xianghualing tin–polymetallic deposit (Hunan, South China). *Mineralium Deposita*, 43, 375–382.

Z

Zachariáš, J., Frýda, J., Paterová, B., Mihaljevič, M. (2004). Arsenopyrite and As-bearing

pyrite from the Roudný deposit, Bohemian Massif. *Mineralogical Magazine*, 68, 31-46.

Zack, T., Kronz, A., Foley, S.F., Rivers, T. (2002). Trace element abundances in rutiles from eclogites and associated garnet mica schists. *Chemical Geology*, 184, 97-122.

Zack, T., Von Eynatten, H., Kronz, A. (2004). Rutile geochemistry and its potential use in quantitative provenance studies. *Sedimentary Geology*, 171, 37-58.

Zaraisky, G.P., Korzhinskaya, V., Kotova, N. (2010). Experimental studies of Ta_2O_5 and columbite–tantalite solubility in fluoride solutions from 300 to 550°C and 50 to 100 MPa. *Mineralogy and Petrology*, 99, 287-300.

Zartman, R.E., Doe, B.R. (1981). Plumbotectonics – The model. *Tectonophysics*, 75, 135-162.

Zhu, J.C., Li, R.K., Li, F.C., Xiong, X.L., Zhou, F.Y., Huang, X.L. (2001). Topaz–albite granites and rare-metal mineralization in the Limu district, Guangxi Province, southeast China. *Mineralium Deposita*, 36, 393-405.

LIST OF FIGURES

List of figures

LIST OF TABLES

List of tables